NEUTRON STRUCTURE FUNCTIONS MEASURED WITH SPECTATOR TAGGING

by

Svyatoslav Tkachenko
B.S. June 1997, Odessa State Polytechnic University
M.S. May 2004, University of Virginia

A Dissertation Submitted to the Faculty of
Old Dominion University in Partial Fulfillment of the
Requirement for the Degree of

DOCTOR OF PHILOSOPHY

PHYSICS

OLD DOMINION UNIVERSITY
December 2009

Approved by:

Sebastian Kuhn (Director)

John Adam

Gail Dodge

Rocco Schiavilla

Leposava Vuskovic

ABSTRACT

NEUTRON STRUCTURE FUNCTIONS MEASURED WITH SPECTATOR TAGGING

Svyatoslav Tkachenko
Old Dominion University, 2009
Director: Dr. Sebastian Kuhn

We know much less about the neutron than the proton due to the absence of free neutron targets. Neutron information has to be extracted from data on nuclear targets like deuterium. This requires corrections for off-shell and binding effects which are not known from first principles and therefore are model-dependent. As a consequence, the same data can be interpreted in different ways, leading to different conclusions about important questions such as the value of the d/u quark ratio at large momentum fraction x. The Barely Off-shell NUcleon Structure (BONUS) experiment at Jefferson Lab addressed this problem by tagging spectator protons in coincidence with inelastic electron scattering from deuterium. A novel compact radial time projection chamber was built to detect low-momentum, backward moving protons, ensuring that the scattering took place on a loosely bound neutron. The scattered electron was detected with Jefferson Lab's CLAS spectrometer. Data were taken at beam energies of 2, 4 and 5 GeV. Results on the extracted structure function F_2^n of the neutron, both in the resonance and deep inelastic regions are presented. Dependence of the results on the spectator kinematics, angle and momentum, is investigated. In addition, tests of the spectator model for different angles and momenta are performed.

©Copyright, 2010, by Svyatoslav Tkachenko, All Rights Reserved

ACKNOWLEDGMENTS

I would like to thank those who contributed to this work. I would like to start with my parents, Svetlana and Mihail Tkachenko. They started all this in Odessa, Ukraine (then, it was Odessa, USSR) many years ago. They turned me into what I am now, and this work would be impossible without them for many reasons. I would like to thank my wife, Olga Cherepanova, who has been my help and inspiration for the last several years. Special thanks to my son, Artiom Tkachenko, who worked hard on not letting me get bored in the last months of my graduate work. And to conclude this honorable list, I would like to thank my advisor, Sebastian Kuhn, a great person and scientist: I learnt a lot from him; he was the kind of "boss" that everybody would dream of, and I just hope that my future superiors are going to be like him.

Since I do not want to double the size of this thesis, I will stop listing names, but I want to reiterate that I am thanking everybody who helped me in this research, who helped bringing me up, who taught me something about physics, life, and life in physics, and those who simply brightened one (or more) of my days with their smiles. Greatest thanks to all of you, best wishes to those of you who are living, and RIP to those who are no longer with us.

TABLE OF CONTENTS

Page

List of Tables . . . vii
List of Figures . . . xx

Chapter

I Introduction . . . 1

II Physics review . . . 3
II.1 Nucleon structure . . . 3
II.2 Scattering experiments . . . 5
II.3 Elastic form factors . . . 8
II.4 Resonant structure . . . 15
II.5 Deep inelastic scattering . . . 20
II.5.1 Deep inelastic scattering cross-section and structure functions 20
II.5.2 Scaling and partons . . . 25
II.6 Quark-hadron duality . . . 27
II.7 Deuterium . . . 32
II.7.1 Static properties of the deuteron . . . 32
II.7.2 The deuteron wavefunction . . . 36
II.7.3 Deuteron in scattering experiments . . . 39
II.8 Tagged structure functions . . . 43
II.8.1 Spectator tagging . . . 45
II.8.2 Corrections to impulse approximation . . . 48
II.8.3 Alternative way of extracting F_2 structure function . . . 60

III Experimental setup . . . 62
III.1 Accelerator facility . . . 62
III.2 Hall B and CLAS . . . 63
III.2.1 Drift chambers . . . 66
III.2.2 Cherenkov counters . . . 69
III.2.3 Time of flight detector . . . 70
III.2.4 Electromagnetic calorimeter . . . 71
III.2.5 Target . . . 73
III.2.6 DVCS magnet . . . 74
III.3 Radial Time Projection Chamber . . . 75
III.3.1 Time projection chambers . . . 75
III.4 BONuS RTPC . . . 80

IV Data analysis . . . 88
IV.1 Running conditions . . . 88
IV.2 Preliminary analysis . . . 89
IV.2.1 Drift chambers . . . 89

IV.2.2 Time of flight system . . . 97
IV.2.3 Forward electromagnetic calorimeter . . . 101
IV.2.4 RTPC calibration . . . 104
IV.2.5 Momentum corrections . . . 107
IV.2.6 RTPC momentum corrections . . . 125
IV.3 Cuts and corrections to the data . . . 126
IV.3.1 Experimental data . . . 126
IV.3.2 Accidental background subtraction . . . 129
IV.3.3 Simulated data . . . 130
IV.4 High level physics analysis . . . 133
IV.4.1 Experimental data . . . 133
IV.4.2 Simulated data . . . 134
IV.5 Presentation of data . . . 141
IV.6 Extraction of F_{2n} . . . 142

V Results . . . 146
V.1 Systematic errors . . . 146
V.2 Results and discussion . . . 149
V.2.1 W^* dependence . . . 150
V.2.2 θ_{pq} dependence . . . 153
V.3 Summary . . . 154

APPENDICES

A Partons: quarks and gluons . . . 264
B Some kinematic variables . . . 267
C Residues . . . 270

BIBLIOGRAPHY . . . 271

VITA . . . 276

LIST OF TABLES

		Page
1	Neutron constants, from reference [6]	6
2	Proton constants, from reference [6]	6
3	Ground state properties of the deuteron [28], [31].	33
4	DVCS magnet dimensions.	75
5	Supply settings and electrode voltages in the RTPC during operation of the experiment. The suffixes on the GEM label refer to the inner (i) and outer (o) surfaces of the GEMs. All voltages are of negative polarity and are referenced to ground. The table is taken from H. Fenker [68].	87
6	Triggers collected in the BONuS experiment.	89
7	Beam energy values deduced from Hall A measurements, GeV	117
8	Uncertainties for missing energy and momentum spreads for 4 beam energies, GeV.	118
9	Summary of quark properties (light quarks), from reference [6]	264
10	Summary of quark properties (heavy quarks), from reference [6]	264

LIST OF FIGURES

		Page
1	The ratio of per nucleon cross-sections on iron and deuterium as a function of Bjorken x.	4
2	The electron scattering diagram, the sum of the lowest order electron-photon vertex and all amputated loop corrections.	8
3	World data on the proton form factors.	12
4	Values of G_M^n taken from ratio measurements on deuterium and polarized ^{3}He measurements.	13
5	World data on G_E^n.	14
6	Scattering process corresponding to the transverse helicity conserving amplitude $A_{1/2}$.	17
7	Scattering process corresponding to the transverse helicity non-conserving amplitude $A_{3/2}$.	17
8	Scattering process corresponding to the longitudinal helicity non-conserving amplitude $C_{1/2}$.	18
9	Proton resonance transition amplitudes.	19
10	Neutron resonance transition amplitudes.	20
11	Inclusive electroproduction cross-section data from Jefferson Lab at Q^2=1.5 GeV/c^2 as a function of invariant mass squared.	21
12	An attempt to find the neutron resonance distribution as a simple difference between those of the deuterium and proton.	22
13	The $eN \rightarrow eN^{(*)}$ process describing elastic scattering as well as resonance excitation.	23
14	The $eN \rightarrow eX$ process describing deep inelastic scattering.	23
15	The invariant mass (W) distribution.	24
16	The elastic scattering off quasi-free quark.	26
17	The ratio of neutron to proton structure functions as a function of Bjorken x, extracted from SLAC proton and deuteron data [17], assuming different prescriptions for nuclear corrections.	28
18	Extracted F_2 data in the nucleon resonance region for hydrogen and deuterium targets as functions of the Nachtman scaling variable ξ.	30
19	Virtual photon scattering from parton, leading twists.	31
20	Scheme of a nucleon-nucleon potential as a function of distance r between nucleons.	37
21	The deuteron u and w reduced radial wavefunctions calculated with the Argonne $v18$ potential.	39
22	The deuteron S wave function in configuration space and in momentum space, calculated from the Argonne v_{18} potential.	40
23	The deuteron elastic structure function $A(Q^2)$ for $Q^2 > 1$ GeV/c^2.	41
24	The deuteron elastic structure function $B(Q^2)$.	42
25	The deuteron structure function F_2^D per nucleon at $Q^2 = 1.925$ GeV/c^2.	44

26 Two main diagrams contributing to the spectator reaction in the region of $\alpha > 1$. 46
27 The ratio of nuclear spectral functions calculated in the light cone and instant form formalisms as a function of light cone momentum fraction α_s. 49
28 Ratio of the plane wave impulse approximation (PWIA) corrected for the target fragmentation (TF) to the pure PWIA calculation. 51
29 Ratio $R_n \equiv F_2^{n(eff)}(W^2, Q^2, p^2)/F_2^n(W^2, Q^2)$ of the bound to free neutron structure functions in the covariant spectator model. 53
30 Ratio $R_n \equiv F_2^{n(eff)}(W^2, Q^2, p^2)/F_2^n(W^2, Q^2)$ of the bound to free neutron structure functions in the relativistic quark spectral function approach. 54
31 Ratio of the bound to free neutron structure functions calculated in the instant form approach. 55
32 The α_s dependence of the ratio of the light cone spectral function with FSI effects included calculated in DWIA framework, to that without FSI effects. 57
33 The debris-nucleon effective cross-section as a function of the longitudinal distance. 58
34 The momentum and angular dependence of the ratio of the spectral function calculated accounting for FSI to the spectral function calculated in the impulse approximation. 59
35 The schematics of the accelerator. 63
36 CLAS in Hall B. 64
37 CLAS, 2-dimensional view. 65
38 CLAS, 3-dimensional view. 66
39 Representation of a portion of the layout of a Region 3 chamber. . . . 67
40 Vertical cut of the drift chambers transverse to the beam line. 68
41 Hexagonal cell drift lines with and without magnetic field. 68
42 Exploded view of one of the six CLAS EC modules [60]. 72
43 Target tube with fixtures attached. 74
44 The classical TPC with gaseous sensitive volume. 76
45 BONuS data readout scheme. 77
46 An enlarged view of a GEM electrode. 78
47 Electric field lines and equipotential lines in GEM holes. 79
48 Simulation of Moeller tracks in the DVCS solenoid (S. Kuhn). 81
49 Schematics of the BONuS RTPC. See text for details. 83
50 Exploded view of the BONuS RTPC. 84
51 An RTPC event. 86
52 Residuals for six sectors before the alignment. 92
53 Residuals for six sectors after the alignment. 93
54 DC resolutions after the DC calibration. 98
55 The geometric mean in ADC counts for the fifth paddle of the first sector. 101

56 The RF offset *vs* the vertex z coordinate. 102
57 The ratio of logarithms of energy attenuation as reported by the left and right PMTs ($\ln AL/\ln AR$ *vs* the hit position x (in cm) along the scintillator. 103
58 Comparison of coordinates as reported by the CLAS and RTPC. . . . 106
59 The dE/dx distribution of particles registered by the RTPC before the RTPC gain calibration. 108
60 The dE/dx distribution of particles registered by the RTPC after the RTPC gain calibration. 109
61 Invariant mass, W, distribution for the p(e,e′)p reaction before momentum corrections. 110
62 Raw and corrected invariant mass distributions for pre-selected 5 pass events. 120
63 Raw and corrected invariant mass distributions for inclusive 5 pass events. 120
64 Missing energy distributions before and after the CLAS momentum corrections. 121
65 z component of missing momentum distributions before and after the CLAS momentum corrections. 122
66 The difference between expected and measured momenta before the CLAS momentum corrections as a function of ϕ. 123
67 The difference between expected and measured momenta after the CLAS momentum corrections as a function of ϕ. 124
68 Momentum distributions and the difference between measured and true spectator momenta. 127
69 The electron distribution shown as a function of the azimuthal angle relative to the sector mid-plane and the polar angle. 129
70 The distribution of $\Delta z = z_{electron} - z_{spectator}$ for 2 GeV events before the Δz cut was applied. 131
71 Inclusive W distributions for experimental and simulated data. 132
72 The W and W^* distributions of the quasi-elastic simulation for the 4 GeV data. 137
73 The W and W^*distributions of the quasi-elastic simulation for 5 GeV beam energy. 138
74 The W and W^* distributions of the inelastic simulation for the 4 GeV data. 139
75 The W and W^*distributions of the inelastic simulation for 5 GeV beam energy. 140
76 Raw data, raw data with subtracted accidental background, and elastic simulation cross-normalized with experimental data. 144
77 Model (lines) and measured effective (markers) F_{2n} are shown as functions of x^* for two Q^2 bins for 5.254 GeV energy. 155

78 Ratio of experimental data with subtracted accidental background and elastic tail to the full simulation in the PWIA spectator picture is shown as a function of W^*. Data are for Q^2 from 0.22 to 0.45 $(\mathrm{GeV}/c)^2$, $\cos\theta_{pq}$ from -0.75 to -0.25. The beam energy is 2.140 GeV. 157
79 Ratio of experimental data with subtracted accidental background and elastic tail to the full simulation in the PWIA spectator picture is shown as a function of W^*. Data are for Q^2 from 0.22 to 0.45 $(\mathrm{GeV}/c)^2$, $\cos\theta_{pq}$ from -0.25 to 0.25. The beam energy is 2.140 GeV. 158
80 Ratio of experimental data with subtracted accidental background and elastic tail to the full simulation in the PWIA spectator picture is shown as a function of W^*. Data are for Q^2 from 0.22 to 0.45 $(\mathrm{GeV}/c)^2$, $\cos\theta_{pq}$ from 0.25 to 0.75. The beam energy is 2.140 GeV. 159
81 Ratio of experimental data with subtracted accidental background and elastic tail to the full simulation in the PWIA spectator picture is shown as a function of W^*. Data are for Q^2 from 0.45 to 0.77 $(\mathrm{GeV}/c)^2$, $\cos\theta_{pq}$ from -0.75 to -0.25. The beam energy is 2.140 GeV. 160
82 Ratio of experimental data with subtracted accidental background and elastic tail to the full simulation in the PWIA spectator picture is shown as a function of W^*. Data are for Q^2 from 0.45 to 0.77 $(\mathrm{GeV}/c)^2$, $\cos\theta_{pq}$ from -0.25 to 0.25. The beam energy is 2.140 GeV. 161
83 Ratio of experimental data with subtracted accidental background and elastic tail to the full simulation in the PWIA spectator picture is shown as a function of W^*. Data are for Q^2 from 0.45 to 0.77 $(\mathrm{GeV}/c)^2$, $\cos\theta_{pq}$ from 0.25 to 0.75. The beam energy is 2.140 GeV. 162
84 Ratio of experimental data with subtracted accidental background and elastic tail to the full simulation in the PWIA spectator picture is shown as a function of W^*. Data are for Q^2 from 0.77 to 1.10 $(\mathrm{GeV}/c)^2$, $\cos\theta_{pq}$ from -0.75 to -0.25. The beam energy is 2.140 GeV. 163
85 Ratio of experimental data with subtracted accidental background and elastic tail to the full simulation in the PWIA spectator picture is shown as a function of W^*. Data are for Q^2 from 0.77 to 1.10 $(\mathrm{GeV}/c)^2$, $\cos\theta_{pq}$ from -0.25 to 0.25. The beam energy is 2.140 GeV. 164
86 Ratio of experimental data with subtracted accidental background and elastic tail to the full simulation in the PWIA spectator picture is shown as a function of W^*. Data are for Q^2 from 0.77 to 1.10 $(\mathrm{GeV}/c)^2$, $\cos\theta_{pq}$ from 0.25 to 0.75. The beam energy is 2.140 GeV. 165
87 Effective and model F_{2n} structure functions are shown as functions of W^*. Data are for Q^2 from 0.22 to 0.45 $(\mathrm{GeV}/c)^2$, $\cos\theta_{pq}$ from -0.75 to -0.25. The beam energy is 2.140 GeV. 166
88 Effective and model F_{2n} structure functions are shown as functions of W^*. Data are for Q^2 from 0.22 to 0.45 $(\mathrm{GeV}/c)^2$, $\cos\theta_{pq}$ from -0.25 to 0.25. The beam energy is 2.140 GeV. 167

89 Effective and model F_{2n} structure functions are shown as functions of W^*. Data are for Q^2 from 0.22 to 0.45 $(\mathrm{GeV}/c)^2$, $\cos\theta_{pq}$ from -0.25 to 0.25. The beam energy is 2.140 GeV. 168
90 Effective and model F_{2n} structure functions are shown as functions of W^*. Data are for Q^2 from 0.45 to 0.77 $(\mathrm{GeV}/c)^2$, $\cos\theta_{pq}$ from -0.75 to -0.25. The beam energy is 2.140 GeV. 169
91 Effective and model F_{2n} structure functions are shown as functions of W^*. Data are for Q^2 from 0.45 to 0.77 $(\mathrm{GeV}/c)^2$, $\cos\theta_{pq}$ from -0.25 to 0.25. The beam energy is 2.140 GeV. 170
92 Effective and model F_{2n} structure functions are shown as functions of W^*. Data are for Q^2 from 0.45 to 0.77 $(\mathrm{GeV}/c)^2$, $\cos\theta_{pq}$ from 0.25 to 0.75. The beam energy is 2.140 GeV. 171
93 Effective and model F_{2n} structure functions are shown as functions of W^*. Data are for Q^2 from 0.77 to 1.10 $(\mathrm{GeV}/c)^2$, $\cos\theta_{pq}$ from -0.75 to -0.25. The beam energy is 2.140 GeV. 172
94 Effective and model F_{2n} structure functions are shown as functions of W^*. Data are for Q^2 from 0.77 to 1.10 $(\mathrm{GeV}/c)^2$, $\cos\theta_{pq}$ from -0.25 to 0.25. The beam energy is 2.140 GeV. 173
95 Effective and model F_{2n} structure functions are shown as functions of W^*. Data are for Q^2 from 0.77 to 1.10 $(\mathrm{GeV}/c)^2$, $\cos\theta_{pq}$ from 0.25 to 0.75. The beam energy is 2.140 GeV. 174
96 Effective and model F_{2n} structure functions are shown as functions of x^*. Data are for Q^2 from 0.22 to 0.45 $(\mathrm{GeV}/c)^2$, $\cos\theta_{pq}$ from -0.75 to -0.25. The beam energy is 2.140 GeV. 175
97 Effective and model F_{2n} structure functions are shown as functions of x^*. Data are for Q^2 from 0.22 to 0.45 $(\mathrm{GeV}/c)^2$, $\cos\theta_{pq}$ from -0.25 to 0.25. The beam energy is 2.140 GeV. 176
98 Effective and model F_{2n} structure functions are shown as functions of x^*. Data are for Q^2 from 0.22 to 0.45 $(\mathrm{GeV}/c)^2$, $\cos\theta_{pq}$ from 0.25 to 0.75. The beam energy is 2.140 GeV. 177
99 Effective and model F_{2n} structure functions are shown as functions of x^*. Data are for Q^2 from 0.45 to 0.77 $(\mathrm{GeV}/c)^2$, $\cos\theta_{pq}$ from -0.75 to -0.25. The beam energy is 2.140 GeV. 178
100 Effective and model F_{2n} structure functions are shown as functions of x^*. Data are for Q^2 from 0.45 to 0.77 $(\mathrm{GeV}/c)^2$, $\cos\theta_{pq}$ from -0.25 to 0.25. The beam energy is 2.140 GeV. 179
101 Effective and model F_{2n} structure functions are shown as functions of x^*. Data are for Q^2 from 0.45 to 0.77 $(\mathrm{GeV}/c)^2$, $\cos\theta_{pq}$ from 0.25 to 0.75. The beam energy is 2.140 GeV. 180
102 Effective and model F_{2n} structure functions are shown as functions of x^*. Data are for Q^2 from 0.77 to 1.10 $(\mathrm{GeV}/c)^2$, $\cos\theta_{pq}$ from -0.75 to -0.25. The beam energy is 2.140 GeV. 181

103 Effective and model F_{2n} structure functions are shown as functions of x^*. Data are for Q^2 from 0.77 to 1.10 (GeV/c)^2, $\cos\theta_{pq}$ from -0.25 to 0.25. The beam energy is 2.140 GeV. 182
104 Effective and model F_{2n} structure functions are shown as functions of x^*. Data are for Q^2 from 0.77 to 1.10 (GeV/c)^2, $\cos\theta_{pq}$ from 0.25 to 0.75. The beam energy is 2.140 GeV. 183
105 Ratio of experimental data with subtracted accidental background and elastic tail to the full simulation in the PWIA spectator picture is shown as a function of $\cos\theta_{pq}$. Data are for Q^2 from 0.22 to 0.45 (GeV/c)^2, W^* from 1.00 to 1.35 GeV. The beam energy is 2.140 GeV. 184
106 Ratio of experimental data with subtracted accidental background and elastic tail to the full simulation in the PWIA spectator picture is shown as a function of $\cos\theta_{pq}$. Data are for Q^2 from 0.22 to 0.45 (GeV/c)^2, W^* from 1.35 to 1.60 GeV. The beam energy is 2.140 GeV. Error bars are statistical only. Systematic errors are shown as a blue band. 185
107 Ratio of experimental data with subtracted accidental background and elastic tail to the full simulation in the PWIA spectator picture is shown as a function of $\cos\theta_{pq}$. Data are for Q^2 from 0.22 to 0.45 (GeV/c)^2, W^* from 1.60 to 1.85 GeV. The beam energy is 2.140 GeV. 186
108 Ratio of experimental data with subtracted accidental background and elastic tail to the full simulation in the PWIA spectator picture is shown as a function of $\cos\theta_{pq}$. Data are for Q^2 from 0.22 to 0.45 (GeV/c)^2, W^* from 1.85 to 2.20 GeV. The beam energy is 2.140 GeV. 187
109 Ratio of experimental data with subtracted accidental background and elastic tail to the full simulation in the PWIA spectator picture is shown as a function of $\cos\theta_{pq}$. Data are for Q^2 from 0.45 to 0.77 (GeV/c)^2, W^* from 1.00 to 1.35 GeV. The beam energy is 2.140 GeV. 188
110 Ratio of experimental data with subtracted accidental background and elastic tail to the full simulation in the PWIA spectator picture is shown as a function of $\cos\theta_{pq}$. Data are for Q^2 from 0.45 to 0.77 (GeV/c)^2, W^* from 1.35 to 1.60 GeV. The beam energy is 2.140 GeV. 189
111 Ratio of experimental data with subtracted accidental background and elastic tail to the full simulation in the PWIA spectator picture is shown as a function of $\cos\theta_{pq}$. Data are for Q^2 from 0.45 to 0.77 (GeV/c)^2, W^* from 1.60 to 1.85 GeV. The beam energy is 2.140 GeV. 190
112 Ratio of experimental data with subtracted accidental background and elastic tail to the full simulation in the PWIA spectator picture is shown as a function of $\cos\theta_{pq}$. Data are for Q^2 from 0.77 to 1.10 (GeV/c)^2, W^* from 1.00 to 1.35 GeV. The beam energy is 2.140 GeV. 191
113 Ratio of experimental data with subtracted accidental background and elastic tail to the full simulation in the PWIA spectator picture is shown as a function of $\cos\theta_{pq}$. Data are for Q^2 from 0.77 to 1.10 (GeV/c)^2, W^* from 1.35 to 1.60 GeV. The beam energy is 2.140 GeV. 192

114 Ratio of experimental data with subtracted accidental background and elastic tail to the full simulation in the PWIA spectator picture is shown as a function of $\cos\theta_{pq}$. Data are for Q^2 from 0.77 to 1.10 $(\mathrm{GeV}/c)^2$, W^* from 1.60 to 1.85 GeV. The beam energy is 2.140 GeV. 193
115 Ratio of experimental data with subtracted accidental background and elastic tail to the full simulation in the PWIA spectator picture is shown as a function of W^*. Data are for Q^2 from 0.77 to 1.10 $(\mathrm{GeV}/c)^2$, $\cos\theta_{pq}$ from -0.75 to -0.25. The beam energy is 4.217 GeV. 194
116 Ratio of experimental data with subtracted accidental background and elastic tail to the full simulation in the PWIA spectator picture is shown as a function of W^*. Data are for Q^2 from 0.77 to 1.10 $(\mathrm{GeV}/c)^2$, $\cos\theta_{pq}$ from -0.25 to 0.25. The beam energy is 4.217 GeV. 195
117 Ratio of experimental data with subtracted accidental background and elastic tail to the full simulation in the PWIA spectator picture is shown as a function of W^*. Data are for Q^2 from 0.77 to 1.10 $(\mathrm{GeV}/c)^2$, $\cos\theta_{pq}$ from 0.25 to 0.75. The beam energy is 4.217 GeV. 196
118 Ratio of experimental data with subtracted accidental background and elastic tail to the full simulation in the PWIA spectator picture is shown as a function of W^*. Data are for Q^2 from 1.10 to 2.23 $(\mathrm{GeV}/c)^2$, $\cos\theta_{pq}$ from -0.75 to -0.25. The beam energy is 4.217 GeV. 197
119 Ratio of experimental data with subtracted accidental background and elastic tail to the full simulation in the PWIA spectator picture is shown as a function of W^*. Data are for Q^2 from 1.10 to 2.23 $(\mathrm{GeV}/c)^2$, $\cos\theta_{pq}$ from -0.25 to 0.25. The beam energy is 4.217 GeV. Error bars are statistical only. Systematic errors are shown as a blue band. . . . 198
120 Ratio of experimental data with subtracted accidental background and elastic tail to the full simulation in the PWIA spectator picture is shown as a function of W^*. Data are for Q^2 from 1.10 to 2.23 $(\mathrm{GeV}/c)^2$, $\cos\theta_{pq}$ from 0.25 to 0.75. The beam energy is 4.217 GeV. 199
121 Ratio of experimental data with subtracted accidental background and elastic tail to the full simulation in the PWIA spectator picture is shown as a function of W^*. Data are for Q^2 from 2.23 to 4.52 $(\mathrm{GeV}/c)^2$, $\cos\theta_{pq}$ from -0.75 to -0.25. The beam energy is 4.217 GeV. 200
122 Ratio of experimental data with subtracted accidental background and elastic tail to the full simulation in the PWIA spectator picture is shown as a function of W^*. Data are for Q^2 from 2.23 to 4.52 $(\mathrm{GeV}/c)^2$, $\cos\theta_{pq}$ from -0.25 to 0.25. The beam energy is 4.217 GeV. 201
123 Ratio of experimental data with subtracted accidental background and elastic tail to the full simulation in the PWIA spectator picture is shown as a function of W^*. Data are for Q^2 from 2.23 to 4.52 $(\mathrm{GeV}/c)^2$, $\cos\theta_{pq}$ from 0.25 to 0.75. The beam energy is 4.217 GeV. 202
124 Effective and model F_{2n} structure functions are shown as functions of W^*. Data are for Q^2 from 0.77 to 1.10 $(\mathrm{GeV}/c)^2$, $\cos\theta_{pq}$ from -0.75 to -0.25. The beam energy is 4.217 GeV. 203

125 Effective and model F_{2n} structure functions are shown as functions of W^*. Data are for Q^2 from 0.77 to 1.10 $(\mathrm{GeV}/c)^2$, $\cos\theta_{pq}$ from -0.25 to 0.25. The beam energy is 4.217 GeV. 204
126 Effective and model F_{2n} structure functions are shown as functions of W^*. Data are for Q^2 from 0.77 to 1.10 $(\mathrm{GeV}/c)^2$, $\cos\theta_{pq}$ from 0.25 to 0.75. The beam energy is 4.217 GeV. 205
127 Effective and model F_{2n} structure functions are shown as functions of W^*. Data are for Q^2 from 1.10 to 2.23 $(\mathrm{GeV}/c)^2$, $\cos\theta_{pq}$ from -0.75 to -0.25. The beam energy is 4.217 GeV. 206
128 Effective and model F_{2n} structure functions are shown as functions of W^*. Data are for Q^2 from 1.10 to 2.23 $(\mathrm{GeV}/c)^2$, $\cos\theta_{pq}$ from -0.25 to 0.25. The beam energy is 4.217 GeV. 207
129 Effective and model F_{2n} structure functions are shown as functions of W^*. Data are for Q^2 from 1.10 to 2.23 $(\mathrm{GeV}/c)^2$, $\cos\theta_{pq}$ from 0.25 to 0.75. The beam energy is 4.217 GeV. 208
130 Effective and model F_{2n} structure functions are shown as functions of W^*. Data are for Q^2 from 2.23 to 4.52 $(\mathrm{GeV}/c)^2$, $\cos\theta_{pq}$ from -0.75 to -0.25. The beam energy is 4.217 GeV. 209
131 Effective and model F_{2n} structure functions are shown as functions of W^*. Data are for Q^2 from 2.23 to 4.52 $(\mathrm{GeV}/c)^2$, $\cos\theta_{pq}$ from -0.25 to 0.25. The beam energy is 4.217 GeV. 210
132 Effective and model F_{2n} structure functions are shown as functions of W^*. Data are for Q^2 from 2.23 to 4.52 $(\mathrm{GeV}/c)^2$, $\cos\theta_{pq}$ from 0.25 to 0.75. The beam energy is 4.217 GeV. 211
133 Effective and model F_{2n} structure functions are shown as functions of x^*. Data are for Q^2 from 0.77 to 1.10 $(\mathrm{GeV}/c)^2$, $\cos\theta_{pq}$ from -0.75 to -0.25. The beam energy is 4.217 GeV. 212
134 Effective and model F_{2n} structure functions are shown as functions of x^*. Data are for Q^2 from 0.77 to 1.10 $(\mathrm{GeV}/c)^2$, $\cos\theta_{pq}$ from -0.25 to 0.25. The beam energy is 4.217 GeV. 213
135 Effective and model F_{2n} structure functions are shown as functions of x^*. Data are for Q^2 from 0.77 to 1.10 $(\mathrm{GeV}/c)^2$, $\cos\theta_{pq}$ from 0.25 to 0.75. The beam energy is 4.217 GeV. 214
136 Effective and model F_{2n} structure functions are shown as functions of x^*. Data are for Q^2 from 1.10 to 2.23 $(\mathrm{GeV}/c)^2$, $\cos\theta_{pq}$ from -0.75 to -0.25. The beam energy is 4.217 GeV. 215
137 Effective and model F_{2n} structure functions are shown as functions of x^*. Data are for Q^2 from 1.10 to 2.23 $(\mathrm{GeV}/c)^2$, $\cos\theta_{pq}$ from -0.25 to 0.25. The beam energy is 4.217 GeV. 216
138 Effective and model F_{2n} structure functions are shown as functions of x^*. Data are for Q^2 from 1.10 to 2.23 $(\mathrm{GeV}/c)^2$, $\cos\theta_{pq}$ from 0.25 to 0.75. The beam energy is 4.217 GeV. 217

139 Effective and model F_{2n} structure functions are shown as functions of x^*. Data are for Q^2 from 2.23 to 4.52 $(\mathrm{GeV}/c)^2$, $\cos\theta_{pq}$ from -0.75 to -0.25. The beam energy is 4.217 GeV. 218
140 Effective and model F_{2n} structure functions are shown as functions of x^*. Data are for Q^2 from 2.23 to 4.52 $(\mathrm{GeV}/c)^2$, $\cos\theta_{pq}$ from -0.25 to 0.25. The beam energy is 4.217 GeV. 219
141 Effective and model F_{2n} structure functions are shown as functions of x^*. Data are for Q^2 from 2.23 to 4.52 $(\mathrm{GeV}/c)^2$, $\cos\theta_{pq}$ from 0.25 to 0.75. The beam energy is 4.217 GeV. 220
142 Ratio of experimental data with subtracted accidental background and elastic tail to the full simulation in the PWIA spectator picture is shown as a function of $\cos\theta_{pq}$. Data are for Q^2 from 0.77 to 1.10 $(\mathrm{GeV}/c)^2$, W^* from 1.00 to 1.35 GeV. The beam energy is 4.217 GeV. 221
143 Ratio of experimental data with subtracted accidental background and elastic tail to the full simulation in the PWIA spectator picture is shown as a function of $\cos\theta_{pq}$. Data are for Q^2 from 0.77 to 1.10 $(\mathrm{GeV}/c)^2$, W^* from 1.35 to 1.60 GeV. The beam energy is 4.217 GeV. 222
144 Ratio of experimental data with subtracted accidental background and elastic tail to the full simulation in the PWIA spectator picture is shown as a function of $\cos\theta_{pq}$. Data are for Q^2 from 0.77 to 1.10 $(\mathrm{GeV}/c)^2$, W^* from 1.60 to 1.85 GeV. The beam energy is 4.217 GeV. 223
145 Ratio of experimental data with subtracted accidental background and elastic tail to the full simulation in the PWIA spectator picture is shown as a function of $\cos\theta_{pq}$. Data are for Q^2 from 0.77 to 1.10 $(\mathrm{GeV}/c)^2$, W^* from 1.85 to 2.20 GeV. The beam energy is 4.217 GeV. Error bars are statistical only. Systematic errors are shown as a blue band. 224
146 Ratio of experimental data with subtracted accidental background and elastic tail to the full simulation in the PWIA spectator picture is shown as a function of $\cos\theta_{pq}$. Data are for Q^2 from 0.77 to 1.10 $(\mathrm{GeV}/c)^2$, W^* from 2.20 to 2.68 GeV. The beam energy is 4.217 GeV. 225
147 Ratio of experimental data with subtracted accidental background and elastic tail to the full simulation in the PWIA spectator picture is shown as a function of $\cos\theta_{pq}$. Data are for Q^2 from 1.10 to 2.23 $(\mathrm{GeV}/c)^2$, W^* from 1.00 to 1.35 GeV. The beam energy is 4.217 GeV. 226
148 Ratio of experimental data with subtracted accidental background and elastic tail to the full simulation in the PWIA spectator picture is shown as a function of $\cos\theta_{pq}$. Data are for Q^2 from 1.10 to 2.23 $(\mathrm{GeV}/c)^2$, W^* from 1.35 to 1.60 GeV. The beam energy is 4.217 GeV. 227
149 Ratio of experimental data with subtracted accidental background and elastic tail to the full simulation in the PWIA spectator picture is shown as a function of $\cos\theta_{pq}$. Data are for Q^2 from 1.10 to 2.23 $(\mathrm{GeV}/c)^2$, W^* from 1.60 to 1.85 GeV. The beam energy is 4.217 GeV. 228

150 Ratio of experimental data with subtracted accidental background and elastic tail to the full simulation in the PWIA spectator picture is shown as a function of $\cos\theta_{pq}$. Data are for Q^2 from 1.10 to 2.23 $(\mathrm{GeV}/c)^2$, W^* from 1.85 to 2.20 GeV. The beam energy is 4.217 GeV. 229
151 Ratio of experimental data with subtracted accidental background and elastic tail to the full simulation in the PWIA spectator picture is shown as a function of $\cos\theta_{pq}$. Data are for Q^2 from 1.10 to 2.23 $(\mathrm{GeV}/c)^2$, W^* from 2.20 to 2.68 GeV. The beam energy is 4.217 GeV. 230
152 Ratio of experimental data with subtracted accidental background and elastic tail to the full simulation in the PWIA spectator picture is shown as a function of $\cos\theta_{pq}$. Data are for Q^2 from 2.23 to 4.52 $(\mathrm{GeV}/c)^2$, W^* from 1.00 to 1.35 GeV. The beam energy is 4.217 GeV. 231
153 Ratio of experimental data with subtracted accidental background and elastic tail to the full simulation in the PWIA spectator picture is shown as a function of $\cos\theta_{pq}$. Data are for Q^2 from 2.23 to 4.52 $(\mathrm{GeV}/c)^2$, W^* from 1.35 to 1.60 GeV. The beam energy is 4.217 GeV. 232
154 Ratio of experimental data with subtracted accidental background and elastic tail to the full simulation in the PWIA spectator picture is shown as a function of $\cos\theta_{pq}$. Data are for Q^2 from 2.23 to 4.52 $(\mathrm{GeV}/c)^2$, W^* from 1.60 to 1.85 GeV. The beam energy is 4.217 GeV. Error bars are statistical only. Systematic errors are shown as a blue band. 233
155 Ratio of experimental data with subtracted accidental background and elastic tail to the full simulation in the PWIA spectator picture is shown as a function of $\cos\theta_{pq}$. Data are for Q^2 from 2.23 to 4.52 $(\mathrm{GeV}/c)^2$, W^* from 1.85 to 2.20 GeV. The beam energy is 4.217 GeV. 234
156 Ratio of experimental data with subtracted accidental background and elastic tail to the full simulation in the PWIA spectator picture is shown as a function of $\cos\theta_{pq}$. Data are for Q^2 from 2.23 to 4.52 $(\mathrm{GeV}/c)^2$, W^* from 2.20 to 2.68 GeV. The beam energy is 4.217 GeV. 235
157 Ratio of experimental data with subtracted accidental background and elastic tail to the full simulation in the PWIA spectator picture is shown as a function of W^*. Data are for Q^2 from 1.10 to 2.23 $(\mathrm{GeV}/c)^2$, $\cos\theta_{pq}$ from -0.75 to -0.25. The beam energy is 5.254 GeV. 236
158 Ratio of experimental data with subtracted accidental background and elastic tail to the full simulation in the PWIA spectator picture is shown as a function of W^*. Data are for Q^2 from 1.10 to 2.23 $(\mathrm{GeV}/c)^2$, $\cos\theta_{pq}$ from -0.25 to 0.25. The beam energy is 5.254 GeV. 237
159 Ratio of experimental data with subtracted accidental background and elastic tail to the full simulation in the PWIA spectator picture is shown as a function of W^*. Data are for Q^2 from 1.10 to 2.23 $(\mathrm{GeV}/c)^2$, $\cos\theta_{pq}$ from 0.25 to 0.75. The beam energy is 5.254 GeV. 238

160 Ratio of experimental data with subtracted accidental background and elastic tail to the full simulation in the PWIA spectator picture is shown as a function of W^*. Data are for Q^2 from 2.23 to 4.52 $(\mathrm{GeV}/c)^2$, $\cos\theta_{pq}$ from -0.75 to -0.25. The beam energy is 5.254 GeV. 239
161 Ratio of experimental data with subtracted accidental background and elastic tail to the full simulation in the PWIA spectator picture is shown as a function of W^*. Data are for Q^2 from 2.23 to 4.52 $(\mathrm{GeV}/c)^2$, $\cos\theta_{pq}$ from -0.25 to 0.25. The beam energy is 5.254 GeV. Systematic errors are shown as a blue band. 240
162 Ratio of experimental data with subtracted accidental background and elastic tail to the full simulation in the PWIA spectator picture is shown as a function of W^*. Data are for Q^2 from 2.23 to 4.52 $(\mathrm{GeV}/c)^2$, $\cos\theta_{pq}$ from 0.25 to 0.75. The beam energy is 5.254 GeV. Error bars are statistical only. Systematic errors are shown as a blue band. . . . 241
163 Effective and model F_{2n} structure functions are shown as functions of W^*. Data are for Q^2 from 1.10 to 2.23 $(\mathrm{GeV}/c)^2$, $\cos\theta_{pq}$ from -0.75 to -0.25. The beam energy is 5.254 GeV. 242
164 Effective and model F_{2n} structure functions are shown as functions of W^*. Data are for Q^2 from 1.10 to 2.23 $(\mathrm{GeV}/c)^2$, $\cos\theta_{pq}$ from -0.25 to 0.25. The beam energy is 5.254 GeV. 243
165 Effective and model F_{2n} structure functions are shown as functions of W^*. Data are for Q^2 from 1.10 to 2.23 $(\mathrm{GeV}/c)^2$, $\cos\theta_{pq}$ from 0.25 to 0.75. The beam energy is 5.254 GeV. 244
166 Effective and model F_{2n} structure functions are shown as functions of W^*. Data are for Q^2 from 2.23 to 4.52 $(\mathrm{GeV}/c)^2$, $\cos\theta_{pq}$ from -0.75 to -0.25. The beam energy is 5.254 GeV. 245
167 Effective and model F_{2n} structure functions are shown as functions of W^*. Data are for Q^2 from 2.23 to 4.52 $(\mathrm{GeV}/c)^2$, $\cos\theta_{pq}$ from -0.25 to 0.25. The beam energy is 5.254 GeV. 246
168 Effective and model F_{2n} structure functions are shown as functions of W^*. Data are for Q^2 from 2.23 to 4.52 $(\mathrm{GeV}/c)^2$, $\cos\theta_{pq}$ from 0.25 to 0.75. The beam energy is 5.254 GeV. 247
169 Effective and model F_{2n} structure functions are shown as functions of x^*. Data are for Q^2 from 1.10 to 2.23 $(\mathrm{GeV}/c)^2$, $\cos\theta_{pq}$ from -0.75 to -0.25. The beam energy is 5.254 GeV. 248
170 Effective and model F_{2n} structure functions are shown as functions of x^*. Data are for Q^2 from 1.10 to 2.23 $(\mathrm{GeV}/c)^2$, $\cos\theta_{pq}$ from -0.25 to 0.25. The beam energy is 5.254 GeV. 249
171 Effective and model F_{2n} structure functions are shown as functions of x^*. Data are for Q^2 from 1.10 to 2.23 $(\mathrm{GeV}/c)^2$, $\cos\theta_{pq}$ from 0.25 to 0.75. The beam energy is 5.254 GeV. 250
172 Effective and model F_{2n} structure functions are shown as functions of x^*. Data are for Q^2 from 2.23 to 4.52 $(\mathrm{GeV}/c)^2$, $\cos\theta_{pq}$ from -0.75 to -0.25. The beam energy is 5.254 GeV. 251

173 Effective and model F_{2n} structure functions are shown as functions of x^*. Data are for Q^2 from 2.23 to 4.52 (GeV/c)^2, $\cos\theta_{pq}$ from -0.25 to 0.25. The beam energy is 5.254 GeV. 252
174 Effective and model F_{2n} structure functions are shown as functions of x^*. Data are for Q^2 from 2.23 to 4.52 (GeV/c)^2, $\cos\theta_{pq}$ from 0.25 to 0.75. The beam energy is 5.254 GeV. 253
175 Ratio of experimental data with subtracted accidental background and elastic tail to the full simulation in the PWIA spectator picture is shown as a function of $\cos\theta_{pq}$. Data are for Q^2 from 1.10 to 2.23 (GeV/c)^2, W^* from 1.00 to 1.35 GeV. The beam energy is 5.254 GeV. 254
176 Ratio of experimental data with subtracted accidental background and elastic tail to the full simulation in the PWIA spectator picture is shown as a function of $\cos\theta_{pq}$. Data are for Q^2 from 1.10 to 2.23 (GeV/c)^2, W^* from 1.35 to 1.60 GeV. The beam energy is 5.254 GeV. 255
177 Ratio of experimental data with subtracted accidental background and elastic tail to the full simulation in the PWIA spectator picture is shown as a function of $\cos\theta_{pq}$. Data are for Q^2 from 1.10 to 2.23 (GeV/c)^2, W^* from 1.60 to 1.85 GeV. The beam energy is 5.254 GeV. 256
178 Ratio of experimental data with subtracted accidental background and elastic tail to the full simulation in the PWIA spectator picture is shown as a function of $\cos\theta_{pq}$. Data are for Q^2 from 1.10 to 2.23 (GeV/c)^2, W^* from 1.85 to 2.20 GeV. The beam energy is 5.254 GeV. 257
179 Ratio of experimental data with subtracted accidental background and elastic tail to the full simulation in the PWIA spectator picture is shown as a function of $\cos\theta_{pq}$. Data are for Q^2 from 1.10 to 2.23 (GeV/c)^2, W^* from 2.20 to 2.68 GeV. The beam energy is 5.254 GeV. 258
180 Ratio of experimental data with subtracted accidental background and elastic tail to the full simulation in the PWIA spectator picture is shown as a function of $\cos\theta_{pq}$. Data are for Q^2 from 2.23 to 4.52 (GeV/c)^2, W^* from 1.00 to 1.35 GeV. The beam energy is 5.254 GeV. 259
181 Ratio of experimental data with subtracted accidental background and elastic tail to the full simulation in the PWIA spectator picture is shown as a function of $\cos\theta_{pq}$. Data are for Q^2 from 2.23 to 4.52 (GeV/c)^2, W^* from 1.35 to 1.60 GeV. The beam energy is 5.254 GeV. 260
182 Ratio of experimental data with subtracted accidental background and elastic tail to the full simulation in the PWIA spectator picture is shown as a function of $\cos\theta_{pq}$. Data are for Q^2 from 2.23 to 4.52 (GeV/c)^2, W^* from 1.60 to 1.85 GeV. The beam energy is 5.254 GeV. 261
183 Ratio of experimental data with subtracted accidental background and elastic tail to the full simulation in the PWIA spectator picture is shown as a function of $\cos\theta_{pq}$. Data are for Q^2 from 2.23 to 4.52 (GeV/c)^2, W^* from 1.85 to 2.20 GeV. The beam energy is 5.254 GeV. 262

184 Ratio of experimental data with subtracted accidental background and elastic tail to the full simulation in the PWIA spectator picture is shown as a function of $\cos\theta_{pq}$. Data are for Q^2 from 2.23 to 4.52 $(\mathrm{GeV}/c)^2$, W^* from 2.20 to 2.68 GeV. The beam energy is 5.254 GeV. 263
185 Scattering of an electron with initial 4-momentum k off a proton with initial momentum p. 268

CHAPTER I

INTRODUCTION

Great progress has been made in our understanding of nuclear and nucleon structure in the last century. Hundreds of experiments have been conducted, hundreds of theoretical models have been constructed. From the detection of the nucleus itself by Rutherford to the detection of its constituents, the proton and the neutron, also known as nucleons, to the discovery of the constituents of the nucleons themselves, we know immensely more about matter now than we did a hundred years ago. Still, many unanswered questions remain. From the basic untouched questions of a possible substructure of quarks and a possible derivation of nuclear forces from first principles to much-worked-on questions of elastic form factors, there is much work left to do in nuclear and nucleon physics.

This work is dedicated to analyzing the BoNuS experiment. This experiment took place in Hall B of Jefferson Lab in autumn of 2005. A new experimental technique was utilized allowing us to access data in the low-momentum target fragmentation region, where protons are spectators of the reactions that take place on neutrons in deuterium, thus facilitating access to neutron data. A novel Radial Time Projection Chamber capable of registering protons with momenta down to 70 MeV/c was used in conjunction with the CLAS detector in which scattered electrons were registered. A thin deuterium gas target was used, and data on slow protons, spectators of the electron-neutron reaction, were collected.

This technique allowed us to emulate a neutron target, which is not provided by Nature, by means of a deuterium target. This way we collected neutron data with a minimum amount of model dependence that usually plagues scientists' attempts to study the neutron's inner structure. Thus, we can explore: the link between the resonance structure and the quark structure at high energies, thereby studying quark-hadron duality and its region of applicability, the proton-to-neutron structure function ratio and consequently the up-to-down quark distribution ratio, and the non-perturbative quark-gluon dynamics in a bound hadron system.

The particular goal of this work is to find the neutron unpolarized structure

This dissertation uses *Physical Review D* as the journal model.

function F_{2n} and to study how the effective structure function extracted from measurements on a bound neutron varies with the kinematics of the spectator proton. Ultimately, we are interested in the ratio of the neutron to proton structure functions F_{2n}/F_{2p}.This ratio can be converted to the ratio of up and down quark distributions in the nucleons thus allowing us to access the nucleon structure. While F_{2p} is relatively well known, F_{2n} has only been accessed using nuclear targets, which for inclusive experiments requires models for the nuclear physics and a subtraction of F_{2p} background. This ratio is sensitive to different symmetry breaking mechanisms, and the precise knowledge of it will let us eliminate some theoretical models that have very different predictions for the high-x behavior of the ratio.

CHAPTER II

PHYSICS REVIEW

As mentioned previously, we know a lot about nucleons, but we would like to know even more. We know less about neutrons than about protons since there are no free neutron targets provided by Nature. In addition, nucleons are known to change their properties when put into nuclei (see figure 1), so that performing an experiment on a nuclear target containing neutrons does not give us a definitive answer on free neutron properties. As a result, the wealth of our knowledge of nucleon structure data concentrates mainly on protons. Neutron data, which have been acquired mainly by doing experiments on deuterium and applying nuclear corrections to the data, have big and largely model dependent uncertainties.

The BONuS experiment tried to remedy this by measuring electron scattering off almost free neutrons. The used method accesses neutron data with a minimum of uncertainty associated with nuclear corrections. Measuring neutron structure with the accuracy comparable with that of proton measurements will allow to determine valence quark content at high x, check Bloom-Gilman duality, determine neutron resonance structure, and find neutron elastic form factors.

II.1 NUCLEON STRUCTURE

There are two kinds of nucleons, particles that comprise the atomic nucleus: the proton and the neutron. According to contemporary views, they form an isospin doublet, and can be transformed into each other by means of the "isospin rotation". They both consist of two kinds of valence quarks[a]: up and down, the neutron having two down and one up quark, and the proton having two up and one down quark. This composition is responsible for the similarities as well as differences in the neutron and proton properties.

The proton is a subatomic particle with an electric charge of +1 (measured in units of the electron charge) that represents a hydrogen nucleus. The neutron is a

[a]According to the current scientific views quarks are one of two kinds of fundamental spin 1/2 particles, along with leptons. Quarks interact through all four fundamental forces. They are fermions and come in six "flavors": up, down, strange, charm, bottom and top. Their charge, expressed in units of the electron charge, is fractional. Up and down are the two lightest flavors of quarks, their masses are below 10 MeV (the exact values are not known at the moment), and their charges are: $q_u = (2/3)e$, q_d = -(1/3)e, where e is the electron charge. See appendix A for more.

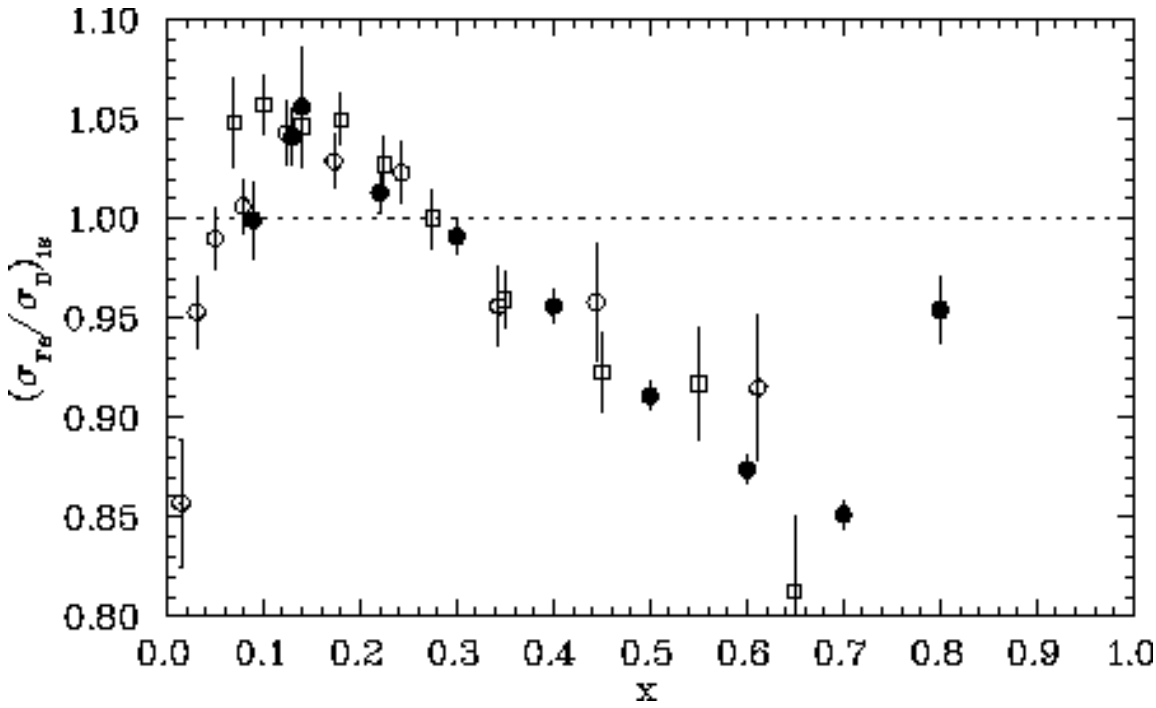

FIG. 1: The ratio of per nucleon cross-sections on iron and deuterium as a function of Bjorken x from EMC (hollow circles) [1], SLAC (solid circles) [2], and BCDMS (squares) [3]. The data have been averaged over Q^2 and corrected for neutron excess.

neutral particle that is only found in nuclei more complicated than hydrogen, and only accompanied by protons. Unlike the proton, the neutron is not a stable particle in its free state, decaying through β-decay with a half life of 885.7 $\pm$ 0.8 seconds:

$$n \rightarrow p + e^{-} + \overline{\nu}_e. \tag{1}$$

This is another factor complicating investigation of neutrons.

As a result, the neutron was discovered later than the proton (which was detected and recognized by Rutherford in 1918). The neutron's discovery is attributed to Chadwik (1932), who showed [4] that the neutral radiation emitted by some elements subjected to bombardment with α-particles was not a type of the γ-radiation, as had been thought before, but rather a new type of particle with no electric charge and mass close to that of the proton.

In spite of such striking differences, the proton and neutron are indeed siblings, and they also bear some similarities: they are both composite particles, which is witnessed, for example, by their magnetic moments; they both interact through all four fundamental forces: electromagnetic, weak nuclear, strong nuclear and gravitational. They are both spin 1/2 particles, also known as fermions.

Still, the aforementioned differences are large indeed, to which the fact that we know more about the proton than about the neutron can be attributed. The differences are not limited to charge and stability. Of the other ones, I would like to mention a puzzling negative charge radius on the neutron. It can be explained by either a π^{-} cloud surrounding the neutron core, or by the spin-spin forces pushing d quarks to the periphery of the neutron (see, e.g. [5]) (the proton has an intuitive positive charge radius). See tables 1 and 2 for the compilation of the most important constants associated with the neutron and proton structure.

II.2 SCATTERING EXPERIMENTS

Scattering is the main tool for studying subatomic particles. It consists of colliding two or more particles and examining how they scatter as a result of the collision. A lot of useful information can be extracted using this method. There are different

TABLE 1: Neutron constants, from reference [6]

Mass, MeV	939.565360±0.000081
Mean life, s	885.7±0.8
Magnetic moment, Bohr magnetons	-1.91304273±0.00000045
Electric dipole moment, 10^{-25} $e$cm	<0.63
Mean-square charge radius[a], fm^2	-0.1161±0.0022
Electric polarizability, 10^{-4} fm^3	11.6±1.5
Magnetic polarizability, 10^{-4} fm^3	3.7±2.0
Charge, $10^{-21}e$	-0.4±0.1

[a]Found using the neutron-electron scattering length b_{ne} as $\langle r_n^2 \rangle = 3(m_e a_0/m_n) b_{ne}$, where m_e and m_n are the masses of the electron and the neutron correspondingly, and a_0 is the Bohr radius.

TABLE 2: Proton constants, from reference [6]

Mass, MeV	938.27200±0.00004
Mean life, s	$> 1.6\times10^{25}$
Magnetic moment, Bohr magnetons	2.792847337±0.000000029
Electric dipole moment, 10^{-23} $e$cm	-4 ± 6
Charge radius, fm	0.870±0.008
Electric polarizability, 10^{-4} fm^3	12.0±0.7
Magnetic polarizability, 10^{-4} fm^3	1.6±0.6
$\lvert q_p + q_e \rvert / e$[a]	$< 1.0\times10^{-21}$

[a]The limit is from neutrality-of-matter experiments; it assumes $q_n = q_p + q_e$.

kinds of scattering depending on whether the colliding particles are moving towards each other in the lab frame (this is what we see in colliders) or whether a beam of particles is incident upon a quasi-stationary (fixed target experiments). Also, when one studies nucleons (which is what we are aiming at in the BONuS experiment), different particles can be "thrown" at nuclei: electron, photon, neutrinos, etc. All these experiments are needed, as they complement each other, but here I will concentrate on electron-nucleon fixed target scattering since this is what was used in the BONuS experiment.

In our case we are dealing with a fixed target experiment. Deuterium (the "source" of neutrons for BONuS) was located in a target, off which an electron beam was scattered and the angular distribution of the scattered electrons was measured. In the case of elastic scattering (leaving the target intact), this angular distribution, also known as the cross-section, can be calculated as

$$\frac{d\sigma}{d\Omega} = \left(\frac{d\sigma}{d\Omega}\right)_{point} |F(q^2)|^2, \tag{2}$$

where q is the 4-momentum transfer (the difference between incoming and scattered electron momenta), $F(q^2)$ contains the information about the composite nature of the target (more on this in coming sections), and $\left(\frac{d\sigma}{d\Omega}\right)_{point}$ is the cross-section we would have if an electron scattered off a point particle:

$$\left(\frac{d\sigma}{d\Omega}\right)_{point} = \left(\frac{\alpha Z E}{2p^2 \sin^2 \theta_e/2}\right)^2 (1 - \beta^2 \sin^2 \frac{\theta}{2}), \tag{3}$$

where α is the electromagnetic coupling constant, Z is the charge of the target, E is the energy of the incident electron, p is the magnitude of its momentum, θ_e is the scattering angle of the electron, and β is the speed of electron in units of the speed of light. Usually, cross-sections are calculated in the lab frame. In this case, we need to take the recoil of the target into account and this is what I will call Mott cross-section:

$$\left(\frac{d\sigma}{d\Omega}\right)_{Mott} = \left(\frac{\alpha Z E}{2p^2 \sin^2 \theta_e/2}\right)^2 \frac{E'}{E}(1 - \beta^2 \sin^2 \frac{\theta_e}{2}), \tag{4}$$

where E' is the energy of the scattered electron.

The cross-section expresses the probability of an interaction. It can be later used to find expectation values of any observables of the reaction. Thus, the cross-section is all we need to extract almost any information on the reaction under consideration.

II.3 ELASTIC FORM FACTORS

Elastic form factors[b] are observables that contain information on the composite nature of nucleons. In the simplest form (coinciding with the historical development of the form factors [7]), they can be introduced as

$$\frac{d\sigma}{d\Omega} = \left(\frac{d\sigma}{d\Omega}\right)_{Mott} [F(q)]^2, \tag{5}$$

where $F(q)$ is a form factor (see equation (4) for details on $\left(\frac{d\sigma}{d\Omega}\right)_{Mott}$).

This simple form does not shed much light on the nature of the form factors. For this, we would need to abolish the kindergarten level simplicity and introduce a form containing some physics details.

Consider an example of electron scattering beyond the lowest (tree) level in QED (figure 2).

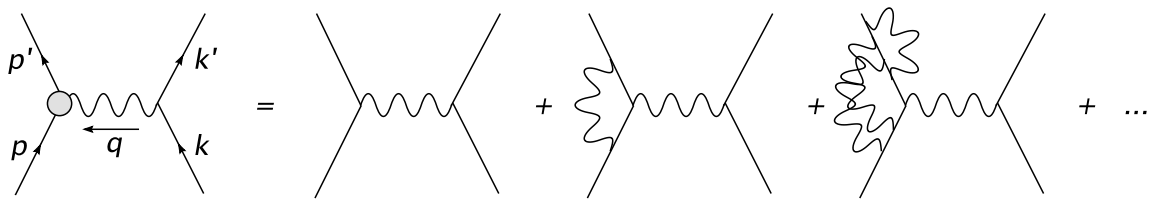

FIG. 2: The electron scattering diagram, the sum of the lowest order electron-photon vertex and all amputated loop corrections, from [10].

Let us see how different calculating this diagram would be from calculating the tree-level one. Call the vertex denoted by the grey blob, $-ie\Gamma^\mu(p', p)$. Then, the amplitude for the shown scattering process is [10]

$$iM = ie^2 \left(\bar{u}(p')\Gamma^\mu(p', p)u(p)\right) \frac{1}{q^2} \left(\bar{u}(k')\gamma_\mu(k', k)u(k)\right), \tag{6}$$

where M is the scattering amplitude, $\bar{u}, u$ are Dirac spinors, γ_μ is the Dirac matrix, and the initial, final and momentum exchange vectors p, p', and q are shown on figure 2.

In general, Γ^μ is some expression that involves p, p', γ_μ, constants, and pure numbers. At the tree level, it is equal to γ^μ. Due to Lorentz invariance and Γ^μ

[b] These observables are used for the description of elastic scattering. All the reactions described in this section are elastic unless noted otherwise.

transforming as a vector, the possible form for it must be a linear combination of vectors (γ^μ, p, p' or their linear combinations in our case). Using the combinations $p' + p$ and $p' - p$ for convenience, we have

$$\Gamma^\mu = \gamma^\mu \cdot A + (p'^\mu + p^\mu) \cdot B + (p'^\mu - p^\mu) \cdot C. \tag{7}$$

Coefficients A,B, and C must be scalars. Thus, they can involve ordinary numbers, constants, and momentum exchange q^2. If we apply Ward identity

$$q_\mu \Gamma^\mu = 0, \tag{8}$$

we can see that the third term of (7) does not vanish automatically when dotted into q_μ, and thus its coefficient must be zero. Conventionally rearranging the rest of (7) with the help of Gordon's identity

$$\bar{u}(p')\gamma^\mu u(p) = \bar{u}(p') \left(\frac{p'^\mu + p^\mu}{2m} + \frac{i\sigma^{\mu\nu} q_\nu}{2m} \right) u(p), \tag{9}$$

where $\sigma^{\mu\nu} = \frac{i}{2}[\gamma^\mu, \gamma^\nu]$, and substituting A and B with conventional F_1 and F_2, we arrive at the final expression

$$\Gamma^\mu(p', p) = \gamma^\mu F_1(q^2) + \frac{i\sigma^{\mu\nu} q_\nu}{2m} F_2(q^2), \tag{10}$$

where the dependence of the coefficients on the only non-trivial scalar, q^2, is shown explicitly.[c]

These coefficients, F_1 and F_2 are the form factors. To lowest order, $F_1 = 1$, and $F_2 = 0$. The derivation given for the electron case used general symmetry principles, and the structure (10) can be applied to any fermions. But in the case of composite particles (proton, neutron), we should not expect Dirac equation values of 1 and 0 to be a good approximation to the form factors.

Let us go into more details. F_1 is the helicity non-flip Dirac form factor, and F_2 is the helicity flip Pauli form factor. In plane-wave Born approximation, the cross-section for elastic electron-nucleon scattering is

$$\frac{d\sigma}{d\Omega} = \left(\frac{d\sigma}{d\Omega} \right)_{Mott} \left((F_1^2 + \kappa^2 \tau F_2^2) + 2\tau (F_1 + \kappa F_2)^2 \tan^2 \frac{\theta_e}{2} \right), \tag{11}$$

where $\tau = Q^2/(4M_N^2)$, M_N is the nucleon mass, and κ denotes the nucleon anomalous magnetic moment.

[c] $Q^2 = -q^2$ is often used instead of q^2, mainly as a matter of convenience. I will use Q^2 from now on (see Appendix B for more on kinematic variables).

There are certain benefits in using not these form factors themselves, but their linear combinations. The ones used most often are the Sachs form factors [28]:

$$G_E(Q^2) = F_1(Q^2) - \tau\kappa F_2(Q^2); \tag{12}$$

$$G_M(Q^2) = F_1(Q^2) + \kappa F_2(Q^2), \tag{13}$$

where G_E and G_M are the Sachs electric and magnetic form factors respectively. These new form factors have the following properties:

$$G_E^p(0) = 1; \quad G_E^n(0) = 0; \tag{14}$$

$$G_M^{p,n}(0) = \mu^{p,n}, \tag{15}$$

where superscripts p and n denote proton and neutron, respectively, and μ denotes nucleon magnetic moments. In the Breit frame[d], the electric and magnetic nucleon form factors can be written as Fourier transforms of the transverse nucleon charge and magnetization distributions, respectively.

Using Sachs form factors allows us to determine them separately using, for example, the Rosenbluth formula for scattering off a proton:

$$\frac{d\sigma}{d\Omega} = \left(\frac{d\sigma}{d\Omega}\right)_{Mott} \frac{1}{\epsilon}\left(\tau(G_M^p)^2 + \epsilon(G_E^p)^2\right)\frac{1}{1+\tau}, \tag{16}$$

where $\epsilon = 1/[1 + 2(1+\tau)\tan^2(\theta_e/2)]$ is the linear polarization of the virtual photon. Thus, measuring the cross-section at fixed Q^2 as a function of ϵ provides us with the information on each of the form factors. Polarization transfer measurements are another technique used to access form factor information that became very popular in the last decade or so. They allow us to access the ratio of the form factors by measuring the transverse and longitudinal polarizations of the scattered nucleon. For example, in the case of the proton:

$$\frac{G_E^p}{G_M^p} = -\frac{P_t}{P_l}\frac{E_e + E_e'}{2M}\tan\frac{\theta_e}{2}, \tag{17}$$

where P_t and P_l are transverse and longitudinal polarizations of the scattered proton, E_e and E_e' are the initial and final energies of the electron, and M is the proton mass.

[d] A particular Lorentz frame defined by $\vec{p}\,' = -\vec{p}$, that is the nucleon momentum after the collision has the same magnitude and opposite direction as the nucleon momentum before the interaction [32]. There is no energy transfer to the target in this frame.

In the limit of large momentum transfer, the two proton form factors and the magnetic form factor of a neutron are nearly identical to each other except for a scaling factor[e] [28]:

$$G_E^p(Q^2) = \frac{1}{\mu_p} G_M^p(Q^2) = \frac{1}{|\mu_n|} |G_M^n|(Q^2) \equiv G(Q^2), \tag{18}$$

where μ_p and μ_n are the magnetic dipole moments of the proton and neutron, respectively. The function $G(Q^2)$ may be described by a dipole form:

$$G(Q^2) = \left(\frac{1}{1 + (Q/Q_0)^2} \right)^2, \tag{19}$$

with parameter Q_0 found (by fitting (19) to experimental data) to be 0.84 GeV/c [28].

The electric form factor of the neutron $G_E^n(Q^2)$ is only known at relatively small momentum transfers and is found to be much smaller than the corresponding magnetic form factor [28]. There are two reasons why measuring $G_E^n(Q^2)$ is difficult at high Q^2:

- The value of τ in (16) increases with Q^2, and as a result, the scattering cross-section is dominated by the magnetic form factor at high Q^2.
- There are no fixed neutron targets with good enough luminosity, and the neutron data have to be deduced from nuclear experiments (more on this item throughout the thesis).

A substantial amount of data on the proton form factors exist (see, for example, figure 3). Unfortunately, their neutron counterparts are known less accurately, and over a smaller kinematic range (see figures 4 and 5). Even the better known proton form factors have their own unsolved mysteries, like the discrepancy between the results obtained through the Rosenbluth technique and polarization technique[f] (see, for example reference [11] and figure 3).

[e] Several years ago, this relationship was a decent approximation of the global data, but in the last decade experimental data started showing very significant deviations of (18) from being a true equality (see, for example, reference [8], or any other review paper).

[f] This discrepancy is currently attributed to the two-photon exchange contribution, but a satisfactory experimental proof is still lacking.

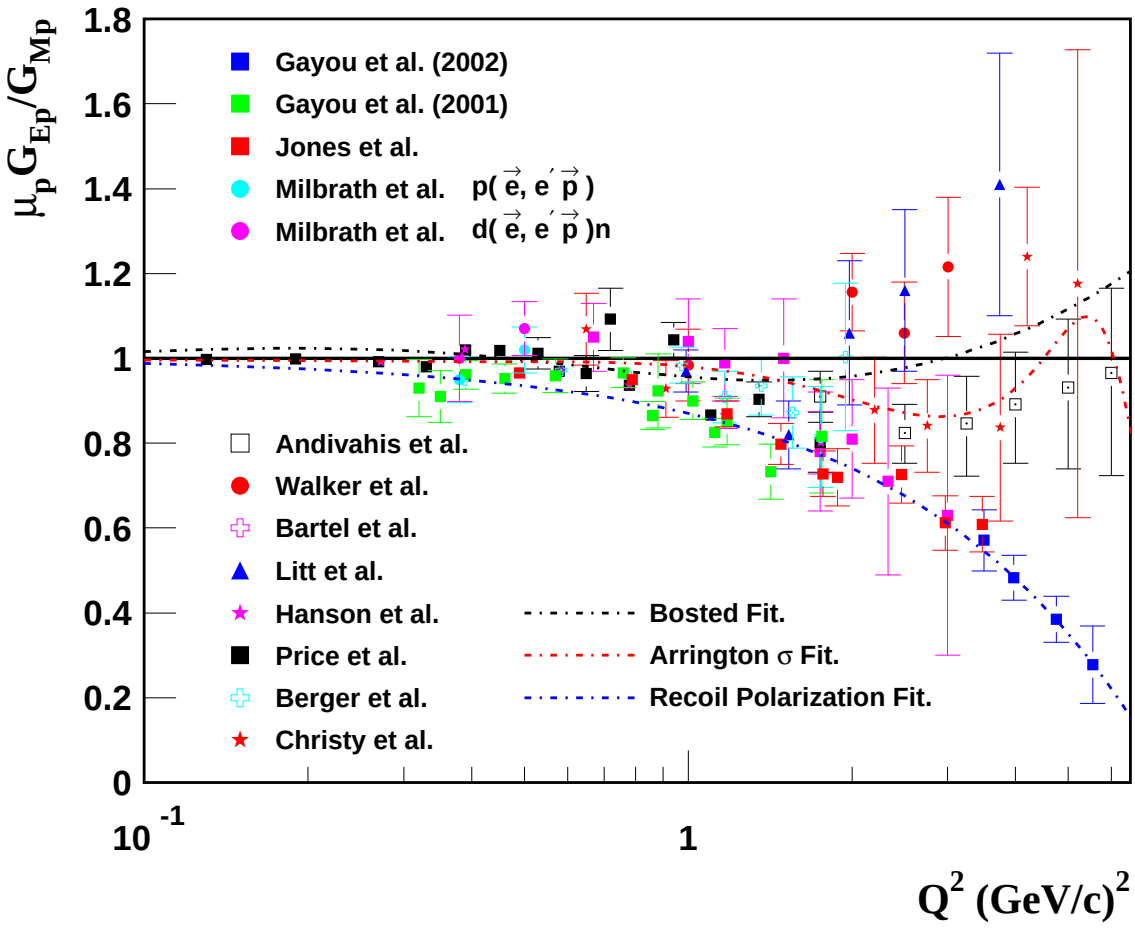

FIG. 3: Proton form factor ratio $\mu_p G_{Ep}/G_{Mp}$ by Rosenbluth separations and recoil polarization. In addition, the fits of Arrington, Bosted, and recoil polarization are also shown. From [9].

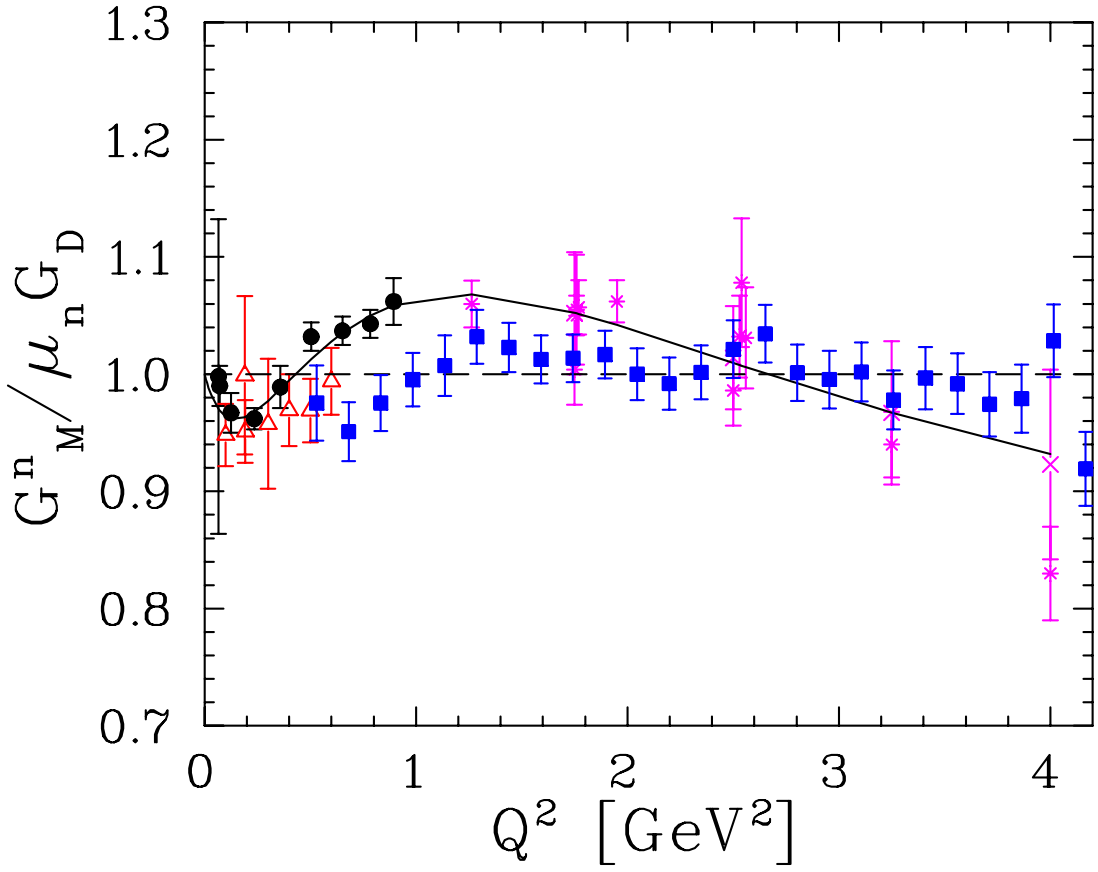

FIG. 4: Values of G_M^n taken from ratio measurements on deuterium and polarized ^{3}He measurements. The circles are extractions from the ratio of $e-n$ to $e-p$ quasielastic scattering; the open triangles are from measurements on polarized ^{3}He; the solid squares are the CLAS preliminary results; the crosses and asterisks are points obtained from quasielastic e-n scattering on light nuclei. The solid line is a fit to the experimental data. From [8].

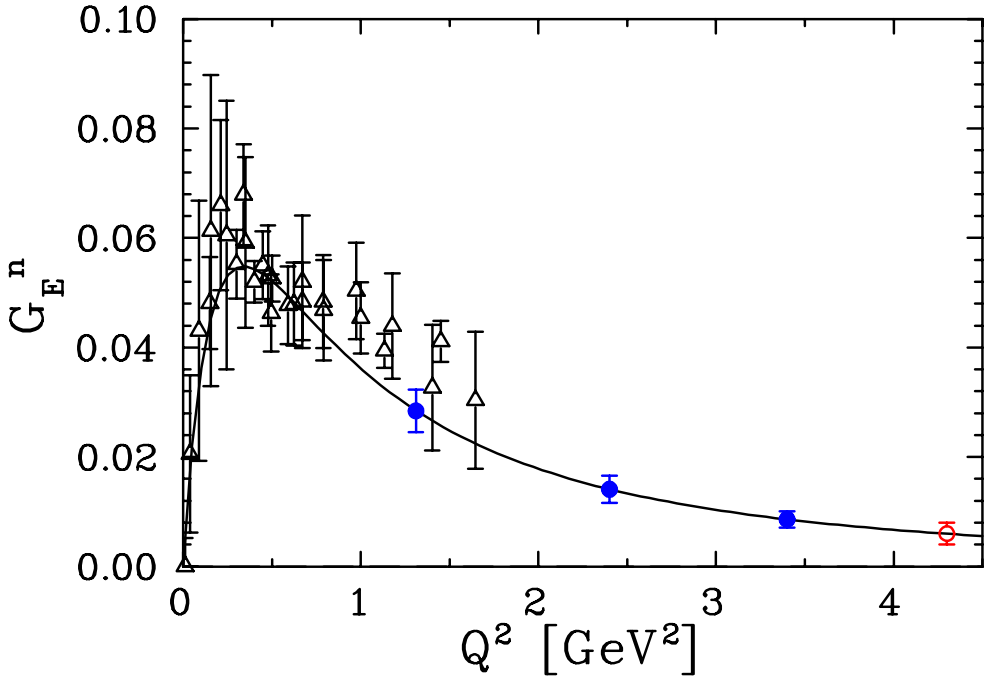

FIG. 5: World data on G_E^n including a recently completed Jefferson Lab Hall A measurement (solid circles), and an approved Hall C measurement (hollow circle). From [8].

II.4 RESONANT STRUCTURE

So far, we dealt with electron-nucleon scattering in which final state nucleons are in their ground state (*i.e.* elastic scattering, $e + N \rightarrow e + N$). The extension of this reaction is the one in which the electron shares a larger fraction of its initial energy with the nucleon, thus exciting it, and the final state nucleon is in an excited state (also known as a resonant state or resonance): $e + N \rightarrow e + R$, where R denotes a resonance.

In nuclear physics, a resonance is a peak located around a certain energy found in differential cross sections of scattering experiments. These peaks are associated with subatomic particles (such as Nucleons, Delta baryons, Upsilon mesons, tauons) and their excitations (see, for example, the upper panel of figure 11). These particles are not stable and their lifetime is connected to their resonant peak width as

$$\Gamma = \frac{1}{T}, \tag{20}$$

where Γ is resonance width, and T is the resonance lifetime. About 120 baryons and baryon resonances are known [6], [12]. Baryons are usually identified by their names and masses[g]. I will discuss only baryons comprised of the lightest, u and d, quarks. The particle name is N or Δ for baryons having isospin 1/2 or 3/2, respectively. Resonances are characterized by adding $L_{2I,2J}$ behind the particle name where L defines the lowest orbital momentum required when they disintegrate into a ground state nucleon and a pseudoscalar meson, I and J are isospin and total angular momentum, respectively.

Resonance peaks can be easily seen in the cross-section between W (see appendix B) of 1 and 2 GeV (that is, between the elastic peak and "continuum"), see the upper panel of figure 11. The most prominent low mass resonances are: $\Delta(1232)P_{33}$, $N(1440)P_{11}$, $N(1520)D_{13}$, $N(1535)S_{11}$, and $N(1688)F_{15}$ (numbers in brackets are masses of the resonances in MeV).[h]

Resonant behavior is usually extracted from cross-sections either on hydrogen (for protons) or nuclear (for neutrons) targets. As will be mentioned later, resonances are very valuable for connecting the region where constituent quark models are describing

[g] Where mass is usually the invariant mass of the unobserved final state of the inclusive reaction, W. See appendix B for more.

[h] In inclusive electron scattering, we can see only three regions of overlapping resonances (figure 11, upper panel). To distinguish individual resonances, we need to use a different technique, *e.g.* $\mathrm{N}(\pi, \pi')$ or $\mathrm{N}(\gamma, \pi)$.

the data well with the region where perturbative quantum chromodynamics (QCD) is a good description. A lot of effort has been and is being put into studying them.

Analogously to elastic scattering, reactions involving resonances can be described with the help of form factors (*transition* form factors now), that contain all the information about the electromagnetic structure of the baryon. These form factors are the charge and current transition matrix elements.

Transitions between a nucleon state |N> and a resonant state |R> can be expressed in terms of dimensionless helicity[i] matrix elements[j]:

$$G_H = \frac{1}{M_N} < R, \lambda' | \varepsilon^\mu J_\mu | N, \lambda >, \tag{21}$$

where λ denotes helicity, and the polarization vectors $\varepsilon^{\pm,0}$ correspond to right and left circularly polarized photons, and longitudinally polarized photons, respectively.

Equivalently, electromagnetic transition matrix elements are expressed in terms of helicity amplitudes:

$$A_{1/2} = \sqrt{\frac{2\pi\alpha}{K_R}} G_+, \quad A_{3/2} = \sqrt{\frac{2\pi\alpha}{K_R}} G_-, \quad C_{1/2} = \sqrt{\frac{2\pi\alpha}{K_R}} \frac{|\vec{q}|}{Q} G_0, \tag{22}$$

where K_R is the equivalent real photon energy at the resonance position.

The transverse amplitude $A_{1/2}$ is helicity-conserving (see figure 6), whereas transverse amplitude $A_{3/2}$ (see figure 7) and longitudinal $C_{1/2}$ (see figure 8) are helicity-flip amplitudes. Using the transition form factors, one can write the inelastic scattering cross-section for a resonance as

$$\frac{d\sigma}{dE' d\Omega_e} = \sigma_{Mott} f_{rec} \left(\frac{|G_E|^2 + \tau^* |G_T|^2}{1 + \tau^*} + 2\tau^* |G_T|^2 \tan^2 \theta_e/2 \right) R(W). \tag{23}$$

In analogy with the Sachs form factors for elastic scattering, the resonance longitudinal and transverse form factors are written as

$$G_0 = G_E, \quad \frac{1}{2}(|G_+|^2 + |G_-|^2) = \tau^* |G_T|^2. \tag{24}$$

A resonance line shape of the following form is introduced

$$R(W) = \frac{2\pi^{-1} W_R M_N \Gamma_R}{(W^2 - W_R^2)^2 + W_R^2 \Gamma_R^2}, \tag{25}$$

[i] Projection of the particle spin onto the direction of particle momentum.

[j] The discussion below follows the treatment of [15].

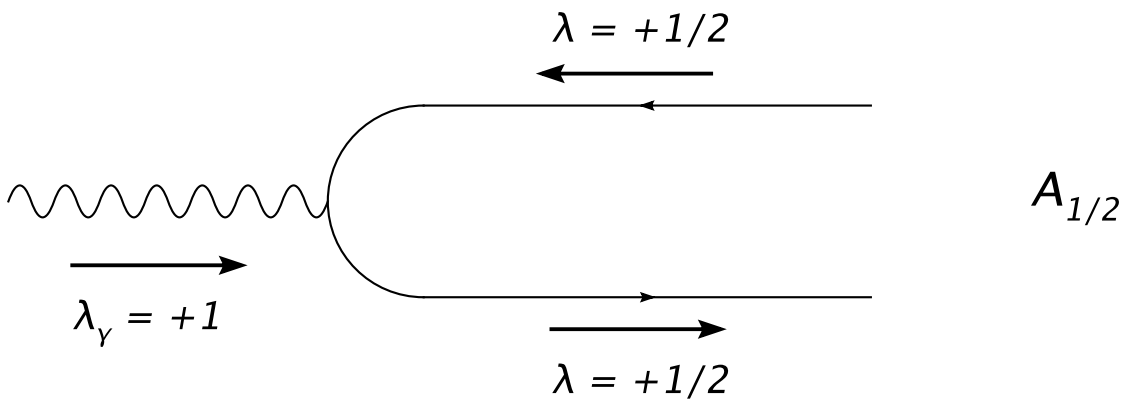

FIG. 6: Scattering process corresponding to the transverse helicity conserving amplitude $A_{1/2}$.

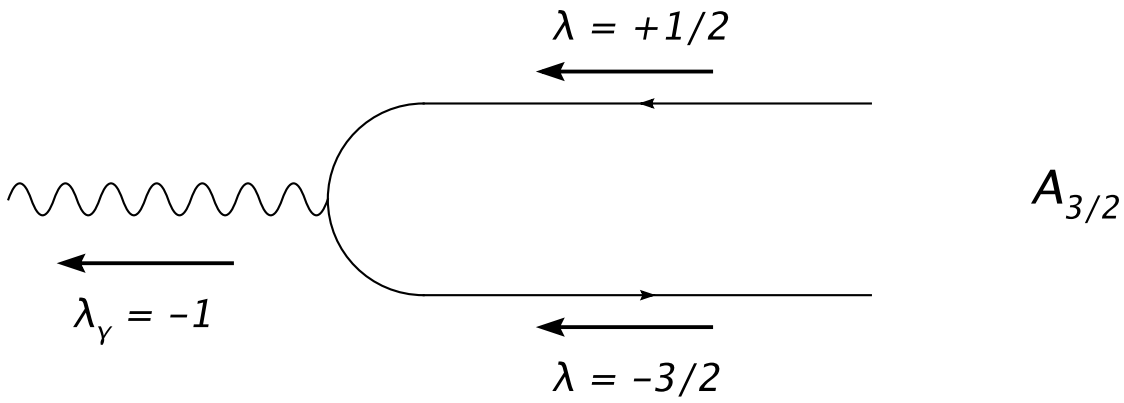

FIG. 7: Scattering process corresponding to the transverse helicity non-conserving amplitude $A_{3/2}$.

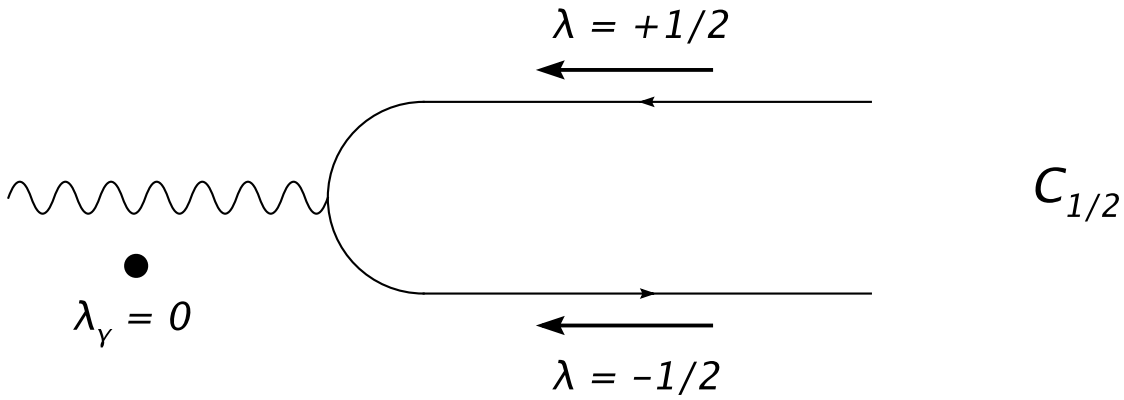

FIG. 8: Scattering process corresponding to the longitudinal helicity non-conserving amplitude $C_{1/2}$.

where W_R and Γ_R are resonance mass and width. The analogous kinematic quantity ($Q^2/4M_N^2$ for the elastic case) is

$$\tau^* = \frac{(Q^2 + W_R^2 - M_N^2)^2}{4M_N^2 Q^2}. \tag{26}$$

The recoil factor (which is E'/E for the elastic case) is

$$f_{rec} = \frac{E'}{E}\frac{1}{1 - (W_R^2 - M_N^2)/2M_N E}. \tag{27}$$

In the limit of a very narrow resonance, in which $W_R = M_N$ and $W_R\Gamma \to 0$, $R(W)$ becomes a δ-function and the cross-section reduces to that for elastic scattering.

Thus, knowledge of the resonance form factors lets us describe resonance transitions in the same way as knowledge of elastic form factors lets us describe elastic reactions.

The resonant region is a bridge between the low Q^2 region in which data can be explained rather successfully by the constituent quark models, and the high Q^2 region in which perturbative quantum chromodynamics (QCD), pQCD, is presumed to be valid. The unresolved problem is two-fold: on one hand, the processes governing resonance transitions themselves are not fully understood, on the other hand, the threshold at which pQCD description becomes **the** description is not known yet. The spread of opinions about the latter reaches orders of magnitude [13]. Additionally, the understanding of the phenomenon of quark-hadron duality (see section II.6) requires

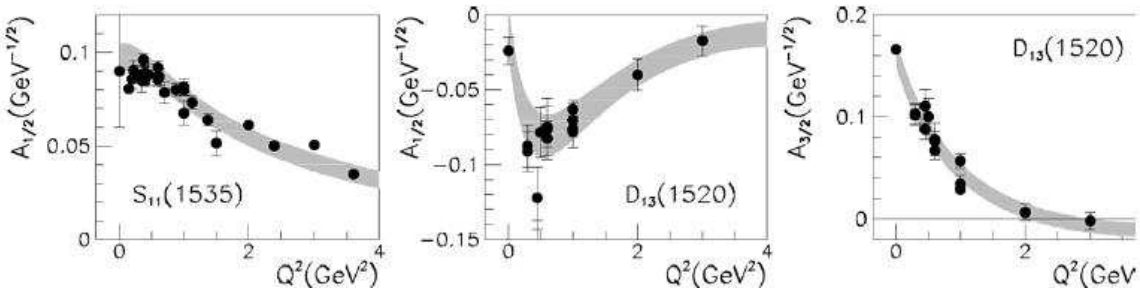

FIG. 9: Proton resonance transition amplitudes (from reference [14]). World data on the contributing helicity conserving ($A_{1/2}$) and helicity non-conserving ($A_{3/2}$) amplitudes are shown for two low lying resonances. The gray band shows the quark model prediction.

thorough knowledge of the resonance region behavior. More experimental resonance data are needed, in particular, on the neutron, as discussed later.

The experimental situation has the usual trend: although a lot of data have been accumulated on proton transitions, not much is known about their neutron counterparts [16]. See, for example, figures 9 and 10, which contain the world data on three particular resonance transition amplitudes. The discrepancy in the number of data points is striking indeed. The difficulties of extracting neutron data by applying nuclear corrections to the deuterium data can be seen in figure 11. The figure shows the inclusive resonance electroproduction cross-section data. They were obtained at Jefferson Lab (JLab) at $Q^2 = 1.5$ GeV/c^2 for hydrogen and deuterium targets at matched kinematics. It can be seen that, at $W^2 > 2$ GeV/c^2 the deuterium data are so smeared that none of the higher resonances can be really seen. And a simple subtraction clearly yields nonsense as can be seen from figure 12. What one gets for the neutron "resonant picture" is a resonance distribution turned upside down.

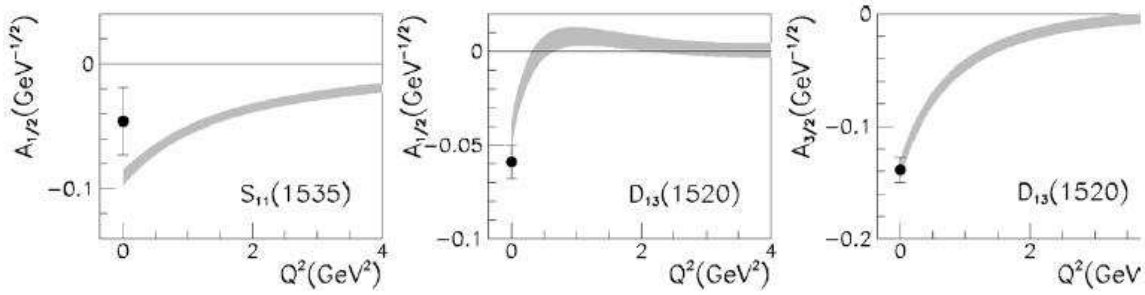

FIG. 10: Same as figure 9, but for neutron resonance transition amplitudes (from reference [14]). The point at $Q^2 = 0$ is the Particle Data Group estimate.

II.5 DEEP INELASTIC SCATTERING

II.5.1 Deep inelastic scattering cross-section and structure functions

In the previous sections we went from looking at a nucleon as a whole using elastic scattering to probing deeper by exciting resonant states of the nucleon. If we want to look even deeper and look at the inner structure of the nucleon, we need to turn to even larger energy probes. This sounds simple enough, but there is a problem introduced by this "simple" approach: the nucleon will break up and the initial state completely lose its initial identity thus requiring a new formalism to be constructed. Pictorially, we are going from the nice and clean picture of figure 13 to the mess of figure 14. Or, looking at the invariant mass distribution (figure 15), we are going from the elastic peak at $W \approx 0.94$ GeV to the resonant region between 1.2 and 2 GeV to the structureless continuum beyond that.

Now, how do we quantitatively describe deep inelastic scattering (DIS)? The derivation of the vertex form in section II.3 did not care about the final states. Thus, equation (10) should describe the vertex for the inelastic case as well, and the cross-section equation shape should be similar to what we had before. Indeed, for both inelastic and elastic cases, the cross-section can be written in the form

$$\frac{d\sigma}{dE'd\Omega} = \frac{4\alpha^2 E'^2}{Q^4}\Big(\quad \Big). \tag{28}$$

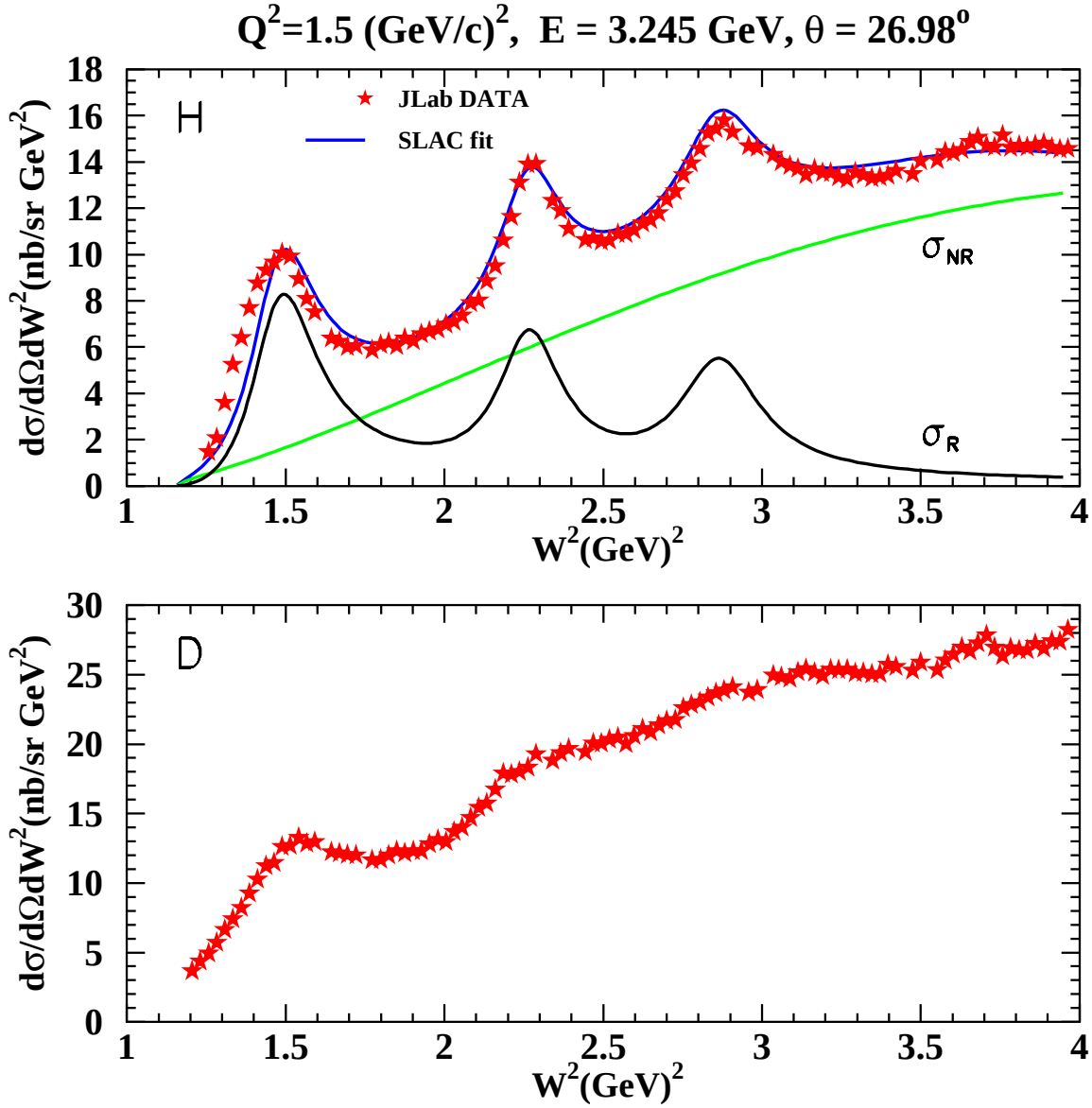

FIG. 11: Inclusive electroproduction cross-section data from Jefferson Lab at Q^2=1.5 GeV/c^2 (from [16]) as a function of invariant mass squared. The upper panel shows hydrogen data with global resonant fit and non-resonant background fit. The lower panel shows deuterium data at the same kinematics.

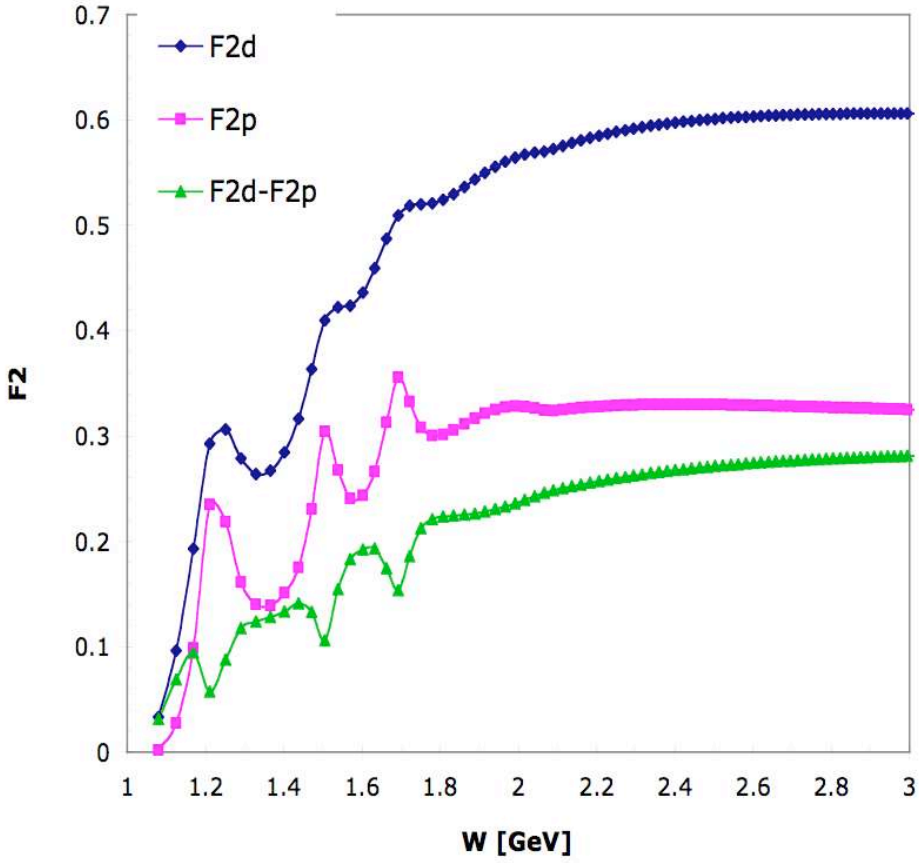

FIG. 12: An attempt to find the neutron resonance distribution as a simple difference between those of the deuterium and proton.

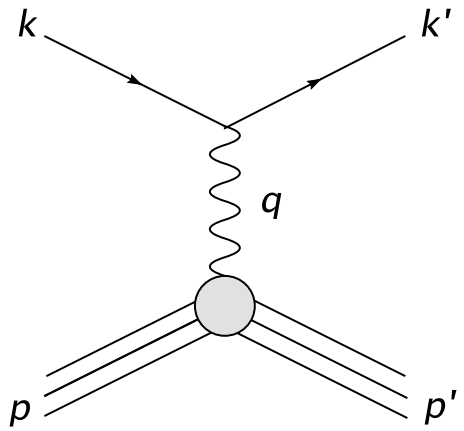

FIG. 13: The $eN \rightarrow eN^{(*)}$ process describing elastic scattering as well as resonance excitation. In the former case, the outgoing particle (momentum p') is the same as incoming (momentum p). In the latter, the outgoing particle is in a resonant state.

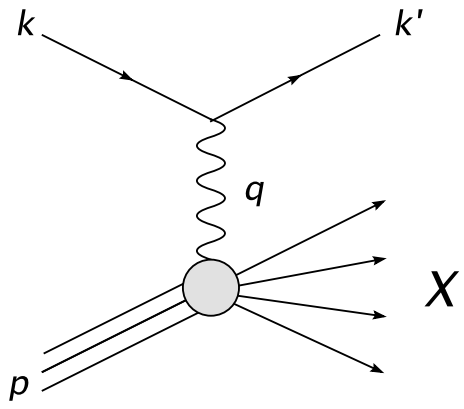

FIG. 14: The $eN \rightarrow eX$ process describing deep inelastic scattering where new particles are created in the final state.

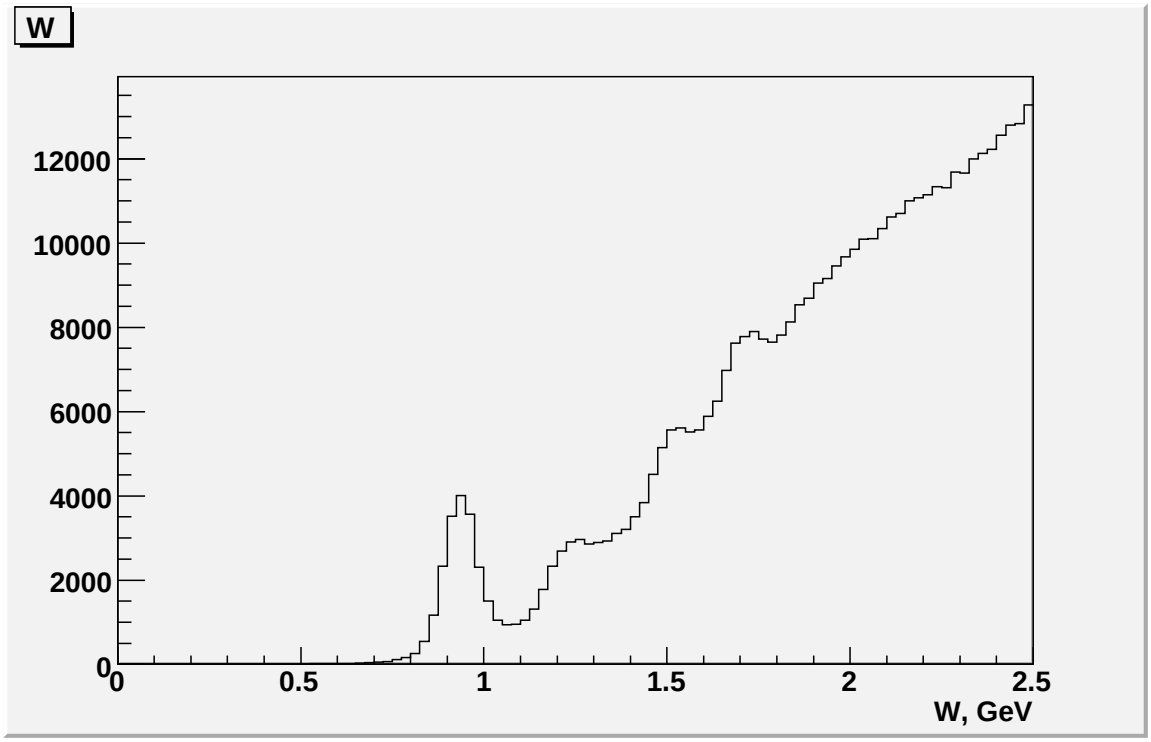

FIG. 15: The invariant mass (W) distribution in the region stretching from the elastic peak (the peak at around 1 GeV) to the inelastic continuum. Three resonance bumps can be seen between 1 and 2 GeV (Δ resonance at W of 1.232 GeV, S_{11}/D_{13} peak at around 1.5 GeV, and F_{15} peak at around 1.7 GeV). This picture was made using BONuS hydrogen data.

For elastic scattering ($eN \to eN$),

$$\left(\quad \right) = \left(\frac{G_E^2 + \tau G_M^2}{1+\tau} \cos^2 \frac{\theta_e}{2} + 2\tau G_M^2 \sin^2 \frac{\theta_e}{2} \right) \delta(\nu - \frac{Q^2}{2M}), \tag{29}$$

where the energy conserving delta function is shown explicitly. For DIS we have [32]

$$\left(\quad \right) = W_2(\nu, Q^2) \cos^2 \frac{\theta_e}{2} + 2W_1(\nu, Q^2) \sin^2 \frac{\theta_e}{2}, \tag{30}$$

where W_1 and W_2 are the structure functions, analogous to the elastic form factors in the elastic case, and transition form factors in the resonant case.

II.5.2 Scaling and partons

To continue our discussion, let us remember Rutherford's experiment that discovered nuclei: some of the α-particles incident on atoms would suddenly scatter at a big angle, thus indicating that they ran into some hard scattering center somewhere inside. If the energy of electrons probing the nucleon's structure is raised so that they are capable of resolving really small distances, the energy and angular distributions of the scattered electrons will start looking as if an elastic scattering off a structureless spin-half Dirac particle (to be called quark) took place.

Thus, we got another turn of the spiral: elastic scattering at a new level. At this scale proton structure functions should turn into elastic ones [32]:

$$2W_1^{point} = \frac{Q^2}{2m^2} \delta(\nu - \frac{Q^2}{2m}), \tag{31a}$$

$$W_2^{point} = \delta(\nu - \frac{Q^2}{2m}), \tag{31b}$$

where m is the mass of the scattering center on which the elastic scattering occurred (quark). And, at large Q^2, we can represent inelastic electron-proton scattering as elastic electron-quark scattering. Instead of figure 14, we get figure 16.

At this scale, inelastic structure functions exhibit a remarkable quality which will become apparent if we rewrite (31) in the following form[k]:

$$2mW_1^{point}(\nu, Q^2) = \frac{Q^2}{2m\nu} \delta \left(1 - \frac{Q^2}{2m\nu} \right), \tag{32a}$$

$$\nu W_2^{point}(\nu, Q^2) = \delta \left(1 - \frac{Q^2}{2m\nu} \right). \tag{32b}$$

[k]Equations (31) and (32) are somewhat naive, since quarks are not at rest inside nucleons. To account for that, one needs to replace the quark mass m with xM, where x is the fraction of the nucleon momentum carried by the quark in the Infinite Momentum Frame, and M is the mass of the nucleon.

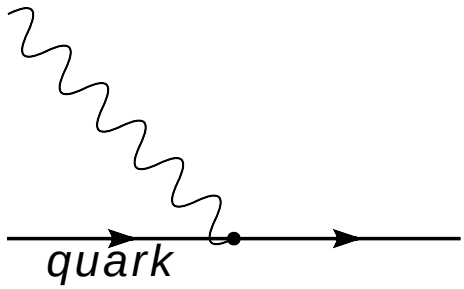

FIG. 16: The elastic scattering off quasi-free quark.

As one can see, both of them depend only on the ratio $\frac{Q^2}{2\nu}$, which is proportional to Bjorken $x = \frac{Q^2}{2M\nu}$ in the lab frame, but not on Q^2 or ν independently. This incredible property is called scaling.

Thus, at Q^2 large enough to resolve nucleon constituents,

$$MW_1(\nu, Q^2) \to F_1(x), \tag{33a}$$

$$\nu W_2(\nu, Q^2) \to F_2(x), \tag{33b}$$

where x is Bjorken x (see appendix B for more). Using the $F_1(x)$ and $F_2(x)$ structure functions, the DIS cross-section can be written as

$$\frac{d\sigma}{d\Omega} = \frac{4\alpha^2 E'^2}{Q^4}\left(\frac{F_2(x)}{\nu}\cos^2\frac{\theta_e}{2} + 2\frac{F_1(x)}{M}\sin^2\frac{\theta_e}{2}\right) \tag{34}$$

In this picture, DIS off a nucleon can be viewed as an incoherent sum of scattering off all the constituents (see, for example, [27]). Then, it should be no surprise that we can connect the inelastic cross-section to the distribution of partons inside the nucleon. And, since the information on the composite nature of the nucleon is by construction hidden into the structure functions, those should be the ones containing the "connection".

Indeed, if we denote f_i to be the probability that a struck parton of kind i and charge e_i carries momentum fraction x, simple manipulations will let us identify:

$$F_1(x) = \frac{1}{2}\sum_i e_i^2 f_i(x), \tag{35a}$$

$$F_2(x) = \sum_i e_i^2 x f_i(x). \tag{35b}$$

Thus, DIS structure functions not only contain information allowing us to extract cross-section, and consequently physical quantities associated with the scattering, but also invaluable details of the internal composition of nucleons[l], shedding light on some of the innermost workings of Nature.

The problem is, our current knowledge of DIS structure functions is unsatisfactory, especially in the case of the neutron. Just to give a quick example, we can look at figure 17. Due to the model dependence of the data analysis, three completely different theories can be supported using the same experimental data set. The situation is alarming, to say the least, and requires finding some model-independent approach to extracting neutron structure functions.

Knowledge of the valence quark distributions at large x is important for several reasons: assumptions on the large-x behavior were built into the global analysis of parton distribution functions [19]; determining d/u experimentally would shed light on the mechanisms behind the spin-flavor symmetry breaking [16]; quark distributions at large x are important for estimating backgrounds in searches for new physics beyond standard models in new high-energy colliders (*e.g.*, LHC).

II.6 QUARK-HADRON DUALITY

Although more than three decades passed since QCD was established to be the theory governing strong force interactions, its inner workings are still not completely clear. The degrees of freedom appearing in the QCD Lagrangian (quarks and gluons) are not observed in nature as real degrees of freedom, being lumped into hadrons which we can observe instead. Due to asymptotic freedom[m] the partons[n] can still be effectively studied at high momentum scale Q.

But at low Q QCD is a strongly interacting theory, thus making the perturbative treatment of parton interactions impossible. Since our knowledge of quantum systems is largely based on applications of perturbation theory, this makes usage of partons as degrees of freedom highly inconvenient, and the hadron description is used in this region (see for example section II.4).

[l] See appendix A for more.

[m] The phenomenon of the strong coupling constant being small at high momenta (or, equivalently, small distances), which allows perturbative treatment of the strong force in the region of high momenta.

[n] Quarks and gluons.

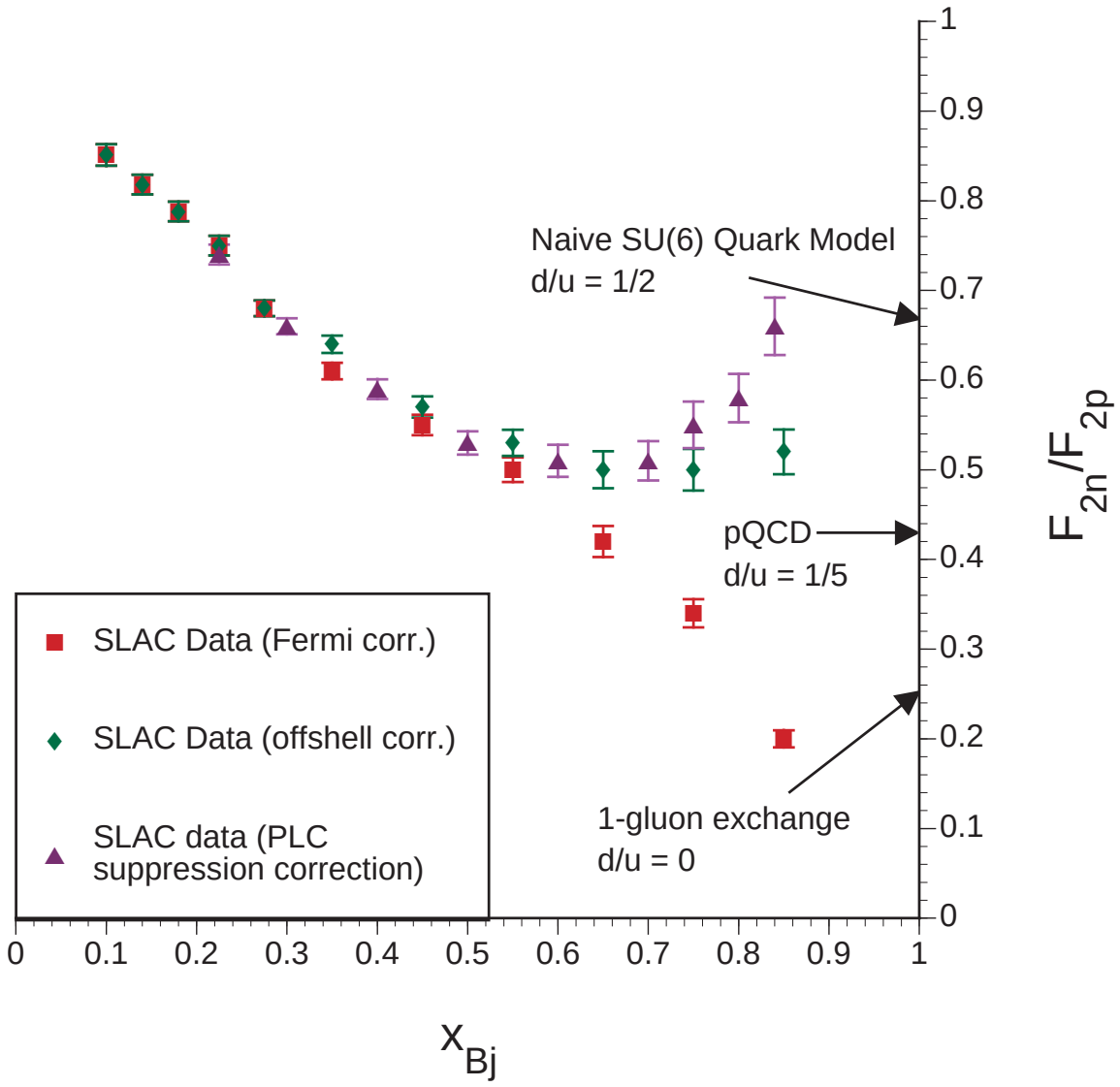

FIG. 17: The ratio of neutron to proton structure functions as a function of Bjorken x, extracted from SLAC proton and deuteron data, assuming different prescriptions for nuclear corrections. Several theoretical predictions for the $x \to 1$ limits are shown [16]: "SU(6) quark model", in which quark wave functions are represented by SU(6) symmetry group which is a simple convolution of SU(3) flavor and SU(2) spin groups; "pQCD model" (also known as helicity conservation model) in which scattering off the quark having the same helicity as the nucleon dominates; "1-gluon exchange model" (also known as scalar diquark dominance model) in which scattering off u quarks dominate. For more details see [18], [19], [20]

There is, however, a surprising connection between high- and low-Q regions. Almost forty years ago observations showed that the behavior of low-energy cross-sections averaged over some energy intervals closely resembles that at asymptotically high Q. In particular, it was observed [21] that the resonance structure function (or transition form factor) at low W averages to the global scale curve which describes high W data (see figure 18 for a contemporary illustration). This connection between hadronic and partonic regimes got the name of quark-hadron duality.

Currently, duality is formulated in terms of the operator product expansion (OPE) of moments of structure functions. According to OPE[o], at $Q^2 \gg \Lambda^2_{\rm QCD}$, where $\Lambda_{\rm QCD}$ is the cutoff of the region which cannot be explored perturbatively, the moments of structure functions can be expanded in powers of $1/Q^2$. For example, the nth moment of the F_2 structure function,

$$\int_0^1 F_2(x)x^n\,dx = M_2^{(n)} = \sum_{\tau=2,4,...}^{\infty} \frac{A_\tau^{(n)}(\alpha_s(Q^2))}{Q^{\tau-2}}, \quad n = 2,4,6,..., \tag{36}$$

where $A_\tau^{(n)}$ are the matrix elements with twist[p] $\leq \tau$. In this treatment soft and hard contributions to scattering are separated in each of the terms of the sum, thus allowing separate treatment of them. Here the soft contribution is hidden in $A_\tau^{(n)}$ coefficients. For the leading twist $\tau = 2$,

$$A_2^{(n)} P^{\mu_1}\cdots P^{\mu_n} = \langle P|\bar{\psi}\gamma\{^{\mu_1}\gamma_5 iD^{\mu_2}\cdots iD^{\mu_n}\}\psi|P\rangle, \tag{37}$$

where P is the nucleon momentum, D^μ is the covariant derivative, and the braces denote symmetrization of indices and subtraction of traces.

Leading twist terms correspond to virtual photons scattering incoherently from one parton (see figure 19a), whereas higher twists involve multiple partonic fields (see figure 19b, 19c). The lowest moment of the F_2 structure function is called the Bloom-Gilman integral. Using the Bloom-Gilman integral, we can write duality in mathematical terms as

$$\frac{2M_N}{Q^2}\int_0^{\nu_m} d\nu\ \nu W_2(\nu,Q^2) = \int_{x_m}^1 dx\ F_2(x), \tag{38}$$

where $\nu W_2(\nu, Q^2)$ is the actually observed structure function in the resonance region, the upper limit on the ν integration, $\nu_m = (W_m^2 - M^2 + Q^2)/2M$, where $W_m \approx 2$ GeV,

[o]See [22] for more on OPE.

[p]The mass dimension minus the spin of an operator

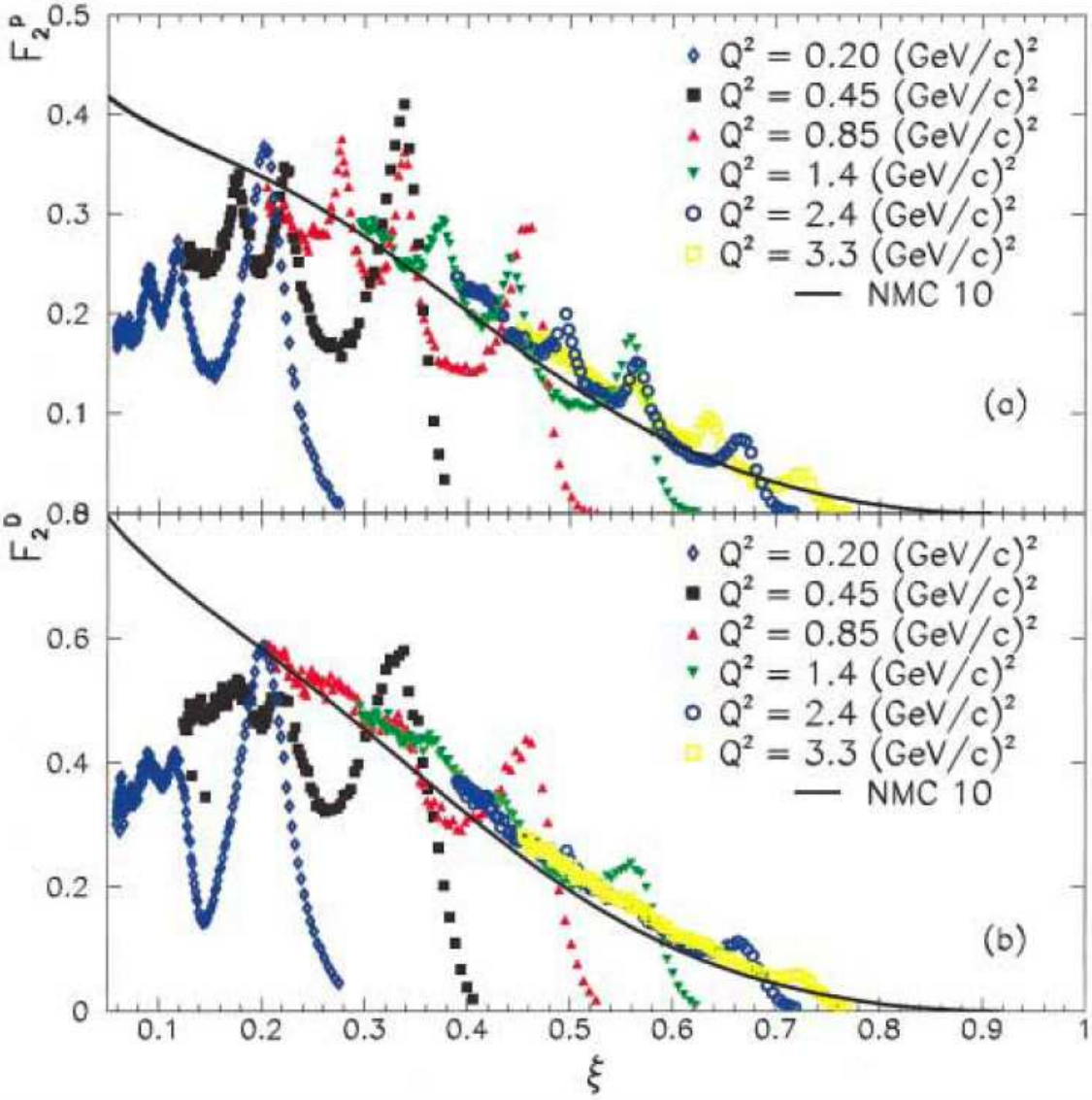

FIG. 18: Extracted F_2 data in the nucleon resonance region for hydrogen (a) and deuterium (b) targets as functions of the Nachtman scaling variable ξ (see appendix B). The solid curves indicate the result of the fit to deep inelastic data for a fixed Q^2 of 10 $(\mathrm{GeV}/c)^2$ (from reference [23]).

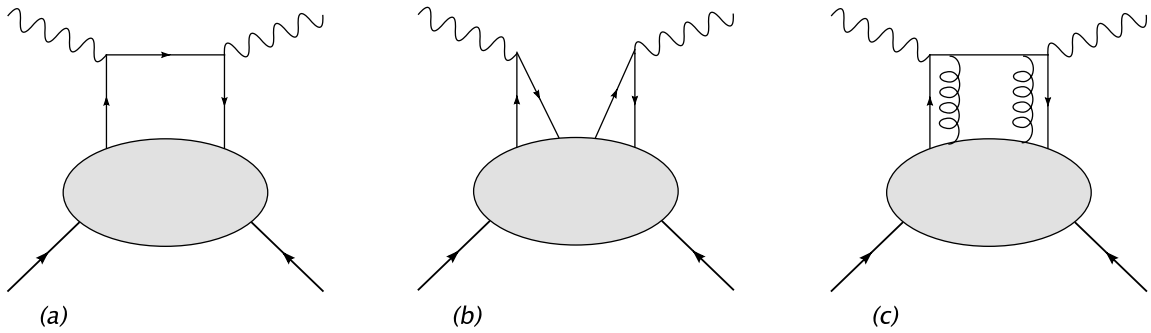

FIG. 19: (a) Leading twist diagram. (b) Higher twist four quark contribution. (c) Higher twist two gluon contribution.

is chosen so that the integral of the scaling function covers the resonance region data, $x_m = Q^2/2M\nu_m$, and $F_2(x)$ is the structure function in the asymptotic DIS limit. If there are no contributions from higher twist terms, duality is exact. Thus, for duality to work, the higher order terms need to be suppressed. In the QCD domain, where Q^2 is high, this is not a problem, since higher twist terms will have a very large Q^2 in the denominator, but for moderate to low Q^2, higher twist terms should somehow cancel, thus suppressing the interaction between the scattered quark and the hadronic system.

Duality does not have a simple intuitive explanation since the nature of the processes at low and high Q^2 is really different. At high Q^2, QCD assumes that the virtual photon interacts only with one parton, with each additional interaction being suppressed by $1/Q^2$ which make their contributions negligible. On the other hand, at low Q^2 an incoming photon coherently interacts with the whole hadron. The difference between these two kinds of interactions is analogous to the difference between $(a + b)^2$ and $(a^2 + b^2)$ expressions. Such expressions can be equal only if all the interference terms cancel out, and there is no reason why this should be the case. Nevertheless, the duality appears to work very well, down to Q^2 values of the order of 1 GeV/c^2 [22].

Besides duality being an interesting phenomenon in itself, its understanding would allow precision studies of the high Bjorken x region, which is hard to study experimentally for technical reasons, at least at the moment. Duality could also provide

an efficient average low energy description of hadronic physics used in the interpretation of neutrino oscillations and high energy experiments, as well as more detailed understanding of hadronization.

More data are needed to understand duality. The aforementioned cancellation of the interference terms could be a fortuitous accident in the proton, due purely to the charge assignments[q]. Thus, neutron data are especially interesting, since the neutron's charge assignments are different.

II.7 DEUTERIUM

Deuterium is a stable isotope of hydrogen with a natural abundance of approximately 1 atom in 6500 of hydrogen. Its nucleus, the deuteron, is the simplest composite nuclear system, and as such, is the simplest laboratory for nuclear physics provided by Nature. It is one of only four stable nuclides with an odd number of protons and odd number of neutrons, and it is the only stable two-nucleon system in Nature.

The deuteron is widely used for extracting nuclear properties due to its relative simplicity compared to other nuclei. It is also a valuable tool for extracting neutron information since the deuteron is the simplest nucleus containing neutrons, while having a very small binding energy thus facilitating the study of its components. This is how it was used in the BoNuS experiment, as an emulation of a neutron target.

II.7.1 Static properties of the deuteron

The deuteron is a unique nucleus. Its binding energy, 2.2 MeV, is much less than the average value between a pair of nucleons in any other stable nucleus. The precise determination of the deuteron binding energy from the neutron radiative capture by hydrogen combined with measuring the deuteron mass makes an accurate knowledge of the neutron mass possible. Due to the small binding energy, the deuteron has no excited states, and all of the measurements are guaranteed to be made in the ground state. A compilation of some ground state properties of the deuteron is given in table 3.

[q]Indeed, the sum of squares of quark charges in the proton is $\frac{2}{3}^2 + \frac{2}{3}^2 + (-\frac{1}{3})^2 = 1$, which is exactly the square of the sum: $(\frac{2}{3} + \frac{2}{3} - \frac{1}{3})^2 = 1$, whereas for the neutron the sum of squares is $(-\frac{1}{3})^2 + (-\frac{1}{3})^2 + (\frac{2}{3})^2 = \frac{2}{3}$, but the square of the sum is $(\frac{2}{3} - \frac{1}{3} - \frac{1}{3})^2 = 0$

TABLE 3: Ground state properties of the deuteron [28], [31].

Ground state property	Value
Mass, M_d	1875.612762(75) MeV
Binding energy, E^B	2.22457312(22) MeV
Spin and parity, J^π	1^+
Isospin, I	0
Magnetic dipole moment, μ_d	$0.857438230(24)\mu_N$
Electric quadrupole moment, Q_d	0.28590(30) $e$fm^2
Matter radius, r_d	1.975(3) fm
Charge radius, r_{ch}	2.130(10) fm

Angular momentum structure

Since the deuteron's parity is positive, its orbital angular momentum is bound to be even. To see that, we can separate the deuteron wave function into 3 parts: the intrinsic wave function of the proton, the intrinsic wave function of the neutron, and the orbital wave function for their relative motion. Since the proton and neutron are just two states of the nucleon, they have the same intrinsic parity, and thus the product of their parities is even. Then the parity of the deuteron is determined by the parity of the wave function of the relative orbital motion. Its parity is determined by the orbital angular momentum. The argument goes as follows. For states with a definite orbital angular momentum $\mathbf{L}$, the angular dependence in the wave function is given by spherical harmonics. Under a parity inversion spherical harmonics transform as

$$Y_{LM}(\theta,\phi) \underset{P}{\rightarrow} Y_{LM}(\pi-\theta,\pi+\phi) = (-1)^L Y_{LM}(\theta,\phi), \tag{39}$$

where $Y_{LM}(\theta,\phi)$ are spherical harmonics, and θ and ϕ are the polar and azimuthal angles, respectively. As is seen from (39), the parity of $Y_{LM}(\theta,\phi)$ is $(-1)^L$, and angular momentum has to be even to provide positive parity. This in turn necessitates the deuteron to have spin equal to 1. Since the spin of the ground state of the deuteron is $J=1$, where $\mathbf{J}=\mathbf{L}+\mathbf{S}$, the possible values of $\mathbf{S}$, the sum of the intrinsic spins of the two nucleons, are 0 and 1. One cannot couple $\mathbf{S}=0$ with even values of L to form a $J=1$ state. Thus, $S=1$.

The deuteron has two possible orbital angular momentum states: S-state and D-state, with the S-state being dominant (approximately 96%). The deuteron isospin

is $T = 0$.[r]

Magnetic dipole moment

The deuteron magnetic moment was measured by Rabi *et al.* in 1934 by measuring the deflection of a deuteron ("deuton") beam by a magnetic field [29]. Since then many measurements utilizing different methods have been performed and the value of "0.75 ± 0.2 nuclear units" has been greatly improved upon (see table 3). There are two sources of the magnetic dipole moment of a nucleus:

- Each nucleon has an intrinsic magnetic moment;
- Orbital motion of a proton carrying net charge results in electric current producing magnetic field.

To explicitly account for these two sources, we can write the magnetic moment operator as[s]

$$\boldsymbol{\mu_d} = g_p \mathbf{s_p} + g_n \mathbf{s_n} + \frac{1}{2}\mathbf{L}, \tag{40}$$

where $\mathbf{L}$ is the orbital angular momentum of nucleons relative motion, $\mathbf{s_n}$, $\mathbf{s_p}$ are neutron and proton spins, respectively, and gyromagnetic ratios for proton and neutron are [t]

$$g_p = 5.585695\mu_N, \tag{41a}$$

$$g_n = -3.826085\mu_N. \tag{41b}$$

The measured value of the magnetic dipole moment (see table 3) confirms the presence of both $^3S_1$ and $^3D_1$ states in the deuteron. Indeed, for the S-state alone, the magnetic moment would be:

$$\mu_d = \mu_p + \mu_n = 0.879805\mu_N, \tag{42}$$

whereas for the D-state it can be calculated from

$$\mu_d = \frac{1}{4(J+1)}((g_p + g_n)(J(J+1) - L(L+1) + S(S+1)) + (J(J+1) + L(L+1) - S(S+1))) \tag{43}$$

[r] There is no two-nucleon bound state that couples to $T = 1$ isospin, which is illustrated by the non-existence of two-proton and two-neutron configurations.

[s] In the equation (40), it is assumed that proton and neutron masses are close enough, so that we can assign each of them half of the total relative angular momentum.

[t] Here we assumed that the structure of the bound nucleon is the same as that of the free one, hence we can use g_p and g_n of free nucleons and bound ones interchangeably.

(J being the total angular momentum of the state) to be $0.310\mu_N$ for a pure D-state, even further away from the measured value. The admixture of S- and D-states would be the most probable cause of these deviations although some contribution from virtual mesons exchanged between nucleons play a role [28].

Electric quadrupole moment

The electric quadrupole operator measures the lowest order departure of a charge distribution from the spherical shape:

$$Q_0 = e(3\langle z\rangle^2 - \langle r\rangle^2), \tag{44}$$

where e is the charge of the distribution, z is the z-coordinate, and r is the radial distance. Hence the discovery of the electric quadrupole moment of the deuteron in 1939 [30] meant that the nuclear force is not central, thus being more complicated than had been thought; this later became evidence for the role of pions in nuclear physics [31]. It also provides more evidence for the deuteron wavefunction having an admixture of the D-state, since the spherically symmetric S-state has a zero electric quadrupole moment.

Deuteron size

There are two "sizes" we can use for the deuteron: the spread of its charge distribution, the charge radius r_{ch}, and the spread of matter, the matter radius r_m (see table 3). The former is defined by scattering experiments, $r_{ch}^2 = -6dG_c/dQ^2\ |_{Q^2=0}$, where G_c is an elastic form factor defined later, whereas the latter is defined through the deuteron wavefunction (discussed later as well) and is related to the charge radius via

$$r_{ch}^2 = r_m^2 + \Delta r_m^2 + r_p^2 + r_n^2 + \frac{3}{4}\left(\frac{\hbar}{m_p}\right)^2, \tag{45}$$

where r_p=0.862(12) fm is the proton charge rms radius, r_n^2 = -0.113(5) fm^2 is the neutron charge rms radius, Δr_m^2 is a contribution from non-nucleonic degrees of freedom and is close to zero, and $m_p = 938.272309(28)$ MeV is the proton mass. The last term in the right-hand side is the Darwin-Foldy term providing a relativistic correction for the Zitterbewegung.

II.7.2 The deuteron wavefunction

As was already mentioned, the deuteron wavefunction in the non-relativistic limit should represent an admixture of S-state and D-state wavefunctions. We can write it in general form as

$$\psi_D = \frac{u(r)}{r}\Upsilon^M_{101} + \frac{\omega(r)}{r}\Upsilon^M_{121}, \tag{46}$$

where r is the radial coordinate, $u(r)$ and $\omega(r)$ are reduced radial wavefunctions for S and D states respectively, and

$$\Upsilon^M_{JLS} = \sum_{m_L,m_S} \langle J, M|L, m_L; S, m_S\rangle Y_{LM}(\theta,\phi)|S, m_S\rangle \tag{47}$$

are spin spherical harmonics (Y_{LM} are spherical harmonics).

The Hamiltonian of the system is

$$H = T_1 + T_2 + V, \tag{48}$$

where T_i is the kinetic energy of particle i and V is the two-body potential. The wavefunction has to satisfy the quantum equation of state, the Schroedinger equation (49)

$$i\frac{\partial\Psi_D}{\partial t} + H\Psi_D = 0 \tag{49}$$

(Ψ_D is the deuteron wavefunction, t is the time), in the non-relativistic case [32], and the Weinberg equation in the relativistic case (The relativistic case is too involved to be briefly shown here, see reference [48] for more).

Solving these equations is complicated by the fact that the nuclear potential is not known exactly. From experimental data we know that it has three distinct regions: the hard core, scalar boson exchange region, and pion exchange region (see figure 20). It has also been shown [49] that the most general form of the non-relativistic potential is

$$\begin{aligned} V(r^2,p^2,L^2;\boldsymbol{\sigma_1},\boldsymbol{\sigma_2},\boldsymbol{\tau_1},\boldsymbol{\tau_2}) = {} & V_0(r^2,p^2,L^2) + V_\sigma(r^2,p^2,L^2)\boldsymbol{\sigma_1}\cdot\boldsymbol{\sigma_2} + V_\tau(r^2,p^2,L^2)\boldsymbol{\tau_1}\cdot\boldsymbol{\tau_2} \\ & + V_{\sigma\tau}(r^2,p^2,L^2)(\boldsymbol{\sigma_1}\cdot\boldsymbol{\sigma_2})(\boldsymbol{\tau_1}\cdot\boldsymbol{\tau_2}) + V_{LS}(r^2,p^2,L^2)\mathbf{L}\cdot\mathbf{S} \\ & + V_{LS\tau}(r^2,p^2,L^2)(\mathbf{L}\cdot\mathbf{S})(\boldsymbol{\tau_1}\cdot\boldsymbol{\tau_2}) + V_T(r^2,p^2,L^2)S_{12} \\ & + V_{T\tau}(r^2,p^2,L^2)S_{12}\boldsymbol{\tau_1}\cdot\boldsymbol{\tau_2} + V_Q(r^2,p^2,L^2)Q_{12} \\ & + V_{Q\tau}(r^2,p^2,L^2)Q_{12}\boldsymbol{\tau_1}\cdot\boldsymbol{\tau_2} + V_{PP}(r^2,p^2,L^2)(\boldsymbol{\sigma_1}\cdot\boldsymbol{p})(\boldsymbol{\sigma_2}\cdot\boldsymbol{p}) \\ & + V_{PP\tau}(r^2,p^2,L^2)(\boldsymbol{\sigma_1}\cdot\boldsymbol{p})(\boldsymbol{\sigma_2}\cdot\boldsymbol{p})(\boldsymbol{\tau_1}\cdot\boldsymbol{\tau_2}), \end{aligned} \tag{50}$$

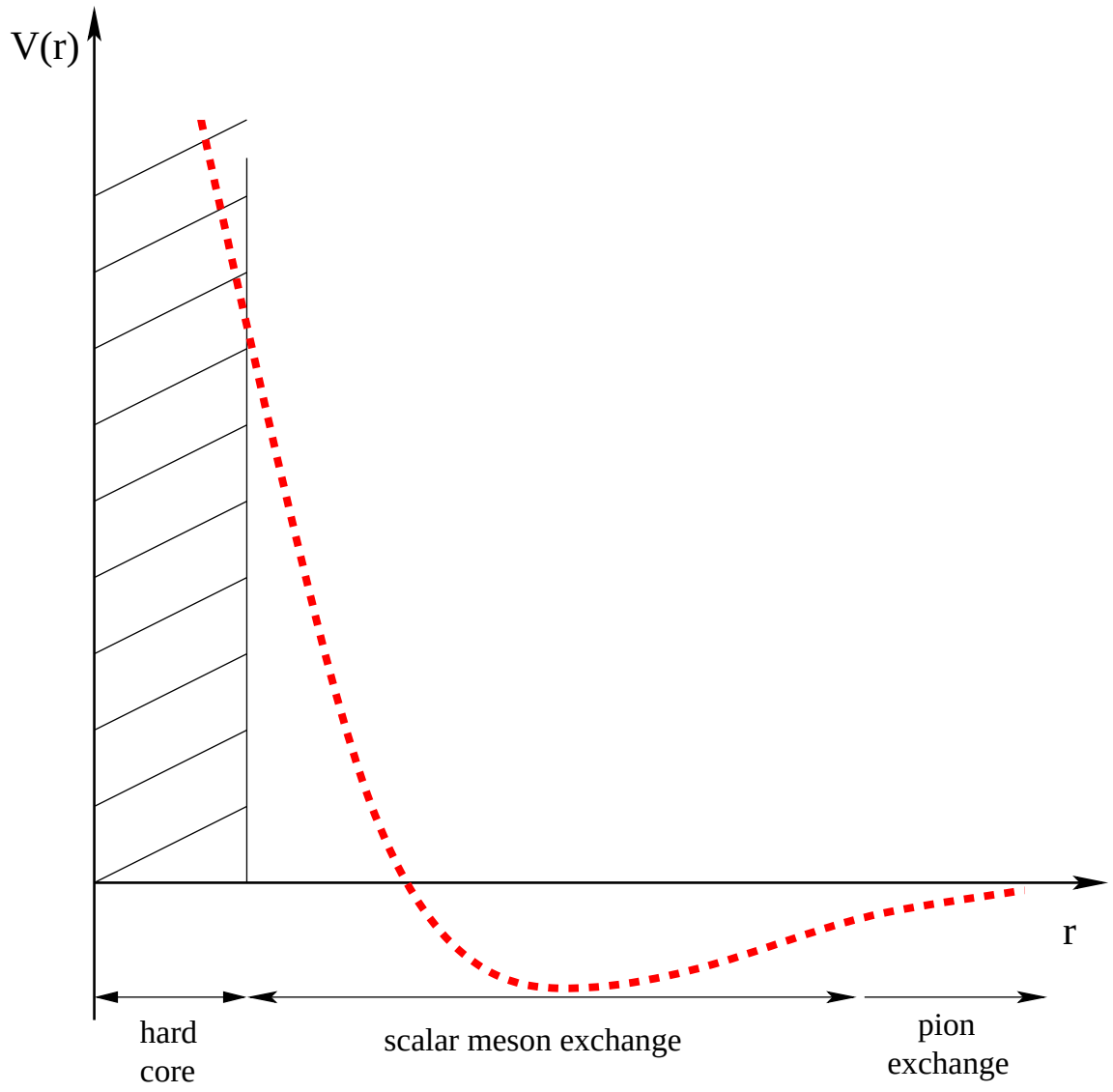

FIG. 20: Schematic diagram showing different parts of a nucleon-nucleon potential as a function of distance r between nucleons [28]. The hard core radius is around 0.4 fm and it takes more than 1 GeV energy to bring nucleons closer than (twice) this distance. The main part of the attraction lies at intermediate ranges, at radius $\sim$1 fm, and is believed to be dominated by the exchange of scalar mesons. The long range part, starting at around 2 fm, is due to the single-pion exchange.

where r is the relative radial coordinate, $\mathbf{r} = \mathbf{r_1} - \mathbf{r_2}$, the vector difference of individual nucleon coordinates, $\mathbf{p} = \frac{1}{2}(\mathbf{p_1} - \mathbf{p_2})$, $\boldsymbol{\sigma}_1$ and $\boldsymbol{\sigma}_2$ are spin operators of the nucleons, $\boldsymbol{\tau}_1$ and $\boldsymbol{\tau}_2$ are isospin operators of the nucleons, $\mathbf{L}$ is the relative orbital angular momentum operator, $\mathbf{S}$ is the total spin operator, the tensor operator is

$$S_{12} = \frac{3}{r^2}(\boldsymbol{\sigma_1} \cdot \boldsymbol{r})(\boldsymbol{\sigma_2} \cdot \boldsymbol{r}) - \boldsymbol{\sigma_1} \cdot \boldsymbol{\sigma_2}, \tag{51}$$

the two-body spin-orbit operator is

$$\mathbf{L} \cdot \mathbf{S} = \frac{1}{2}\mathbf{L} \cdot (\boldsymbol{\sigma_1} + \boldsymbol{\sigma_2}), \tag{52}$$

where $\ell_{1,2}$ are orbital angular momenta of each of the nucleons, and the quadratic spin operator is

$$Q_{12} = \frac{1}{2}((\boldsymbol{\sigma_1} \cdot \boldsymbol{L})(\boldsymbol{\sigma_2} \cdot \boldsymbol{L}) + (\boldsymbol{\sigma_1} \cdot \boldsymbol{L})(\boldsymbol{\sigma_2} \cdot \boldsymbol{L})). \tag{53}$$

The radial dependence and strength of each of the 12 terms are given by the 12 functions $V_0(r)$,$V_\sigma(r)$, etc. These functions are determined by fits to experimental data with hopes to get them from first principles once our understanding of QCD is developed enough.

The complicated form of (50) illustrates difficulties in deriving it from scratch. On top of that, the derivation of the nuclear potential from first principles must stem from quark-quark interactions. The problem here is that carrying out QCD calculations at the low energy at which nuclear physics operates is out of reach at the moment.

As a result, the best potentials we have at the moment (Paris [83], Bonn [84], Argonne [85], etc) utilize our knowledge of hadrons as much as possible and treat phenomenologically the aspects, mainly short-range interactions, of which we have incomplete knowledge [28]. These potentials have been quite successful in describing available data, and although the first principle derivation of the nuclear potential is still absent, we have very good substitutes to work with. Thus, provided the potential, we can solve for the wavefunction. The form of the wavefunction is very similar for all modern potentials. An example of the reduced radial wavefunctions for the $v18$ potential are given in figure 21. The u and w functions in momentum space are given by

$$u(p) = \int_0^\infty u(r) j_0(pr) r dr, \tag{54a}$$

$$w(p) = -\int_0^\infty w(r) j_2(pr) r dr, \tag{54b}$$

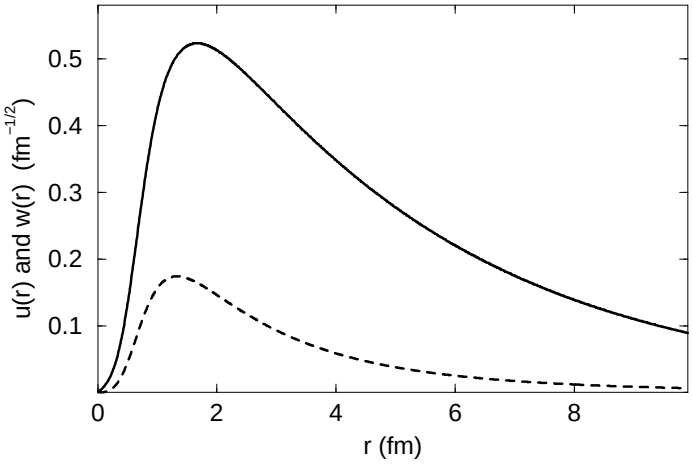

FIG. 21: The u (S-state) (solid line) and w (D-state) (dotted line) reduced radial wavefunctions calculated with the Argonne $v18$ potential (from reference [31]).

where $j_0(pr)$ and $j_2(pr)$ are Bessel functions of the 0^{th} and 2^{nd} order, correspondingly. The deuteron S wave function in configuration space and in momentum space is illustrated in figure 22.

II.7.3 Deuteron in scattering experiments

Following the treatment of lepton-nucleon scattering from the previous sections, I will concentrate on unpolarized elastic and inelastic scattering off the deuteron, although it is not possible to completely avoid mentioning polarization in this case.

Elastic scattering

In the Born approximation of a one-photon exchange mechanism, the unpolarized elastic scattering differential cross-section can be written as [33]

$$\frac{d\sigma}{d\Omega} = \sigma_{Mott}\frac{E'}{E}(A(Q^2) + B(Q^2)\tan^2(\theta/2)), \tag{55}$$

where σ_{Mott} is the Mott cross-section (see (4)), E' and E are the final and initial energies of the electron, θ is the scattering angle, and $A(Q^2)$ and $B(Q^2)$ are the elastic structure functions.

This is reminiscent of the electron-nucleon scattering case except that the deuteron is a spin-1 particle and consequently the structure functions depend on

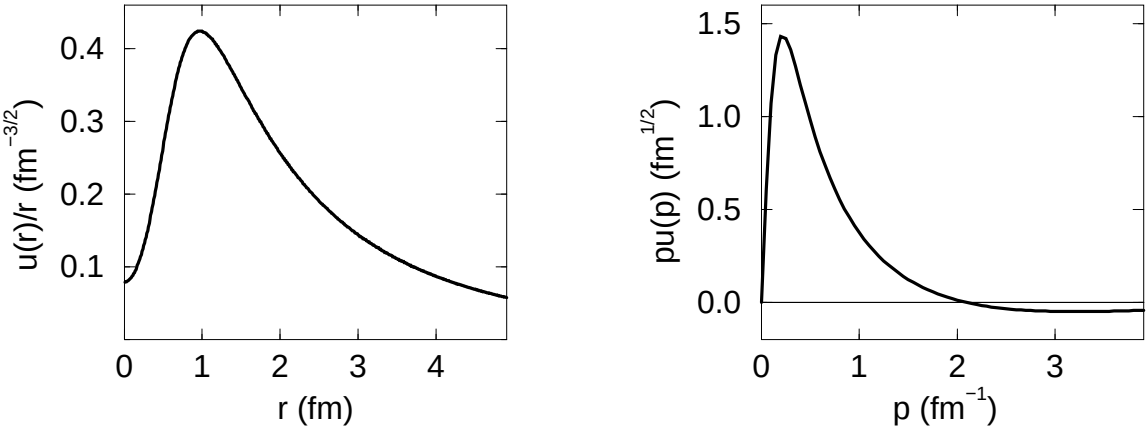

FIG. 22: The deuteron S wave function in configuration space and in momentum space, calculated from the Argonne v_{18} potential (from reference [31]).

three elastic form factors:

$$A(Q^2) = G_C^2(Q^2) + \frac{8}{9}\eta^2 G_Q^2(Q^2) + \frac{2}{3}\eta G_M^2(Q^2), \tag{56a}$$

$$B(Q^2) = \frac{4}{3}\eta(1+\eta)G_M^2(Q^2), \tag{56b}$$

where $\eta = Q^2/(4M_D)$, with M_D being the deuteron mass, and G_C, G_Q, G_M are the form factors. The bad news here is that we have two structure functions which we can measure in experiments and three form factors on which they depend (*i.e.* two equations with three unknowns). Thus, we have to turn to polarized scattering to get more equations and solve for G_C, G_Q and G_M. The illustrations of the A and B structure functions are shown in figures 23 and 24 from reference [46].

Inelastic scattering

The unpolarized inelastic electron-deuteron scattering cross-section can be written as [34]

$$\frac{d^2\sigma}{d\Omega dE'} = \sigma_{Mott}(W_{2D}(\nu, Q^2) - 2W_{1D}(\nu, Q^2)\tan^2(\theta/2)), \tag{57}$$

where W_{1D}, W_{2D} are deuteron inelastic structure functions, and ν is the energy transfer in the reaction. In the same way it was done for nucleon scattering, we can

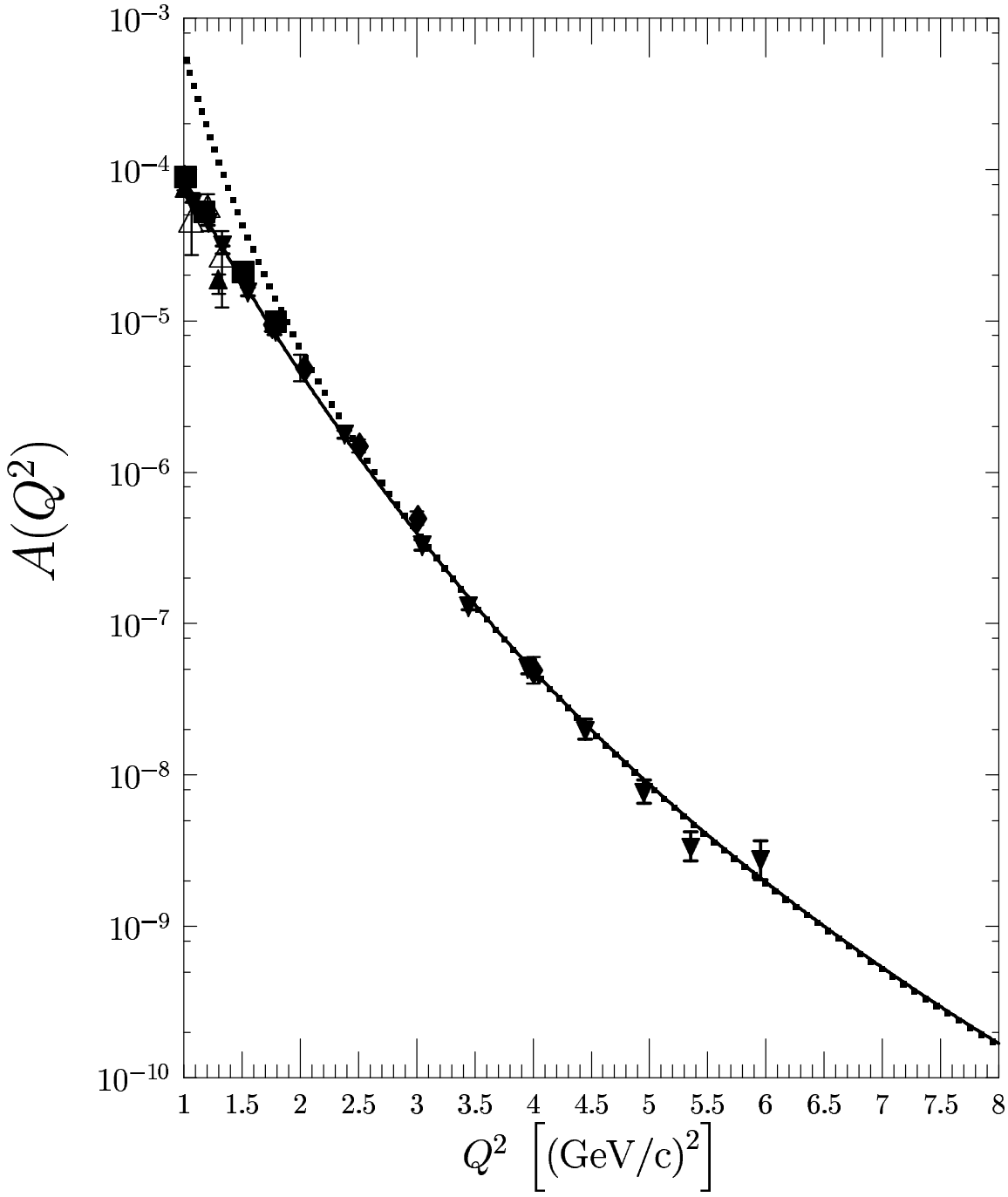

FIG. 23: The deuteron elastic structure function $A(Q^2)$ for $Q^2 > 1$ GeV/c^2. The data are from [35], [33], [36], [37], [38], [39], [40], [41], [42]. The solid line is the model fit from [46]; the dotted line is the pQCD asymptotic behavior extrapolated to lower momentum transfer.

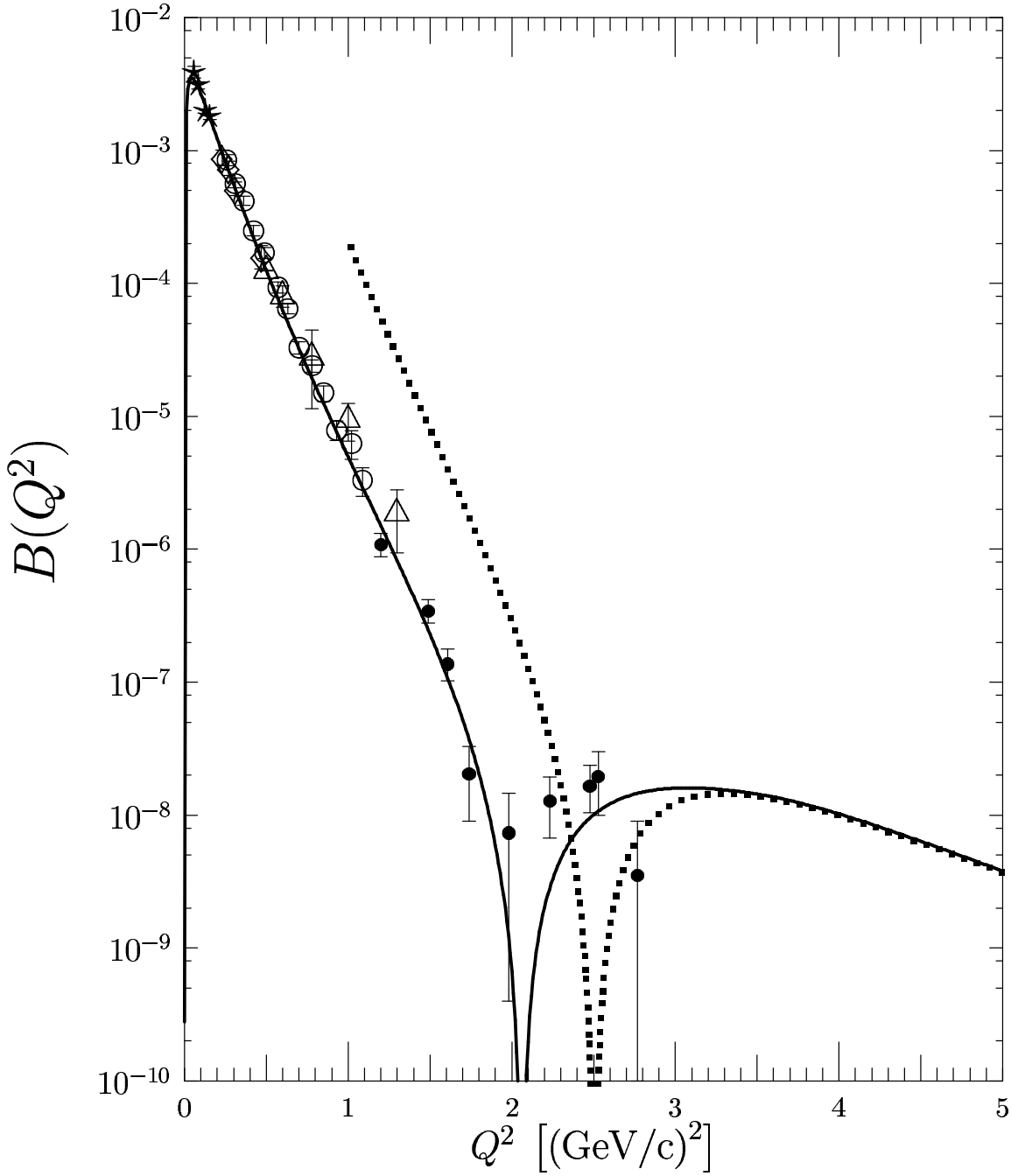

FIG. 24: The deuteron elastic structure function $B(Q^2)$. The data are from [43], [37], [38], [44], [45]. The solid line is the model fit from [46]; the dotted line is the pQCD asymptotic behavior extrapolated to lower momentum transfer.

define dimensionless structure functions [48] (see figure 25 for the graph of F_2^D):

$$F_{1D} = M_D W_{1D}(\nu, Q^2), \tag{58a}$$

$$F_{2D} = \frac{\nu W_{2D}(\nu, Q^2)}{M_D}. \tag{58b}$$

As the momentum transfer goes to infinity, we can use the form convenient for a comparison with the parton model and QCD predictions [48] (these, as well as all the formulas from this reference, are written in the light-cone approximation):

$$F_{1D} = \int \sum_{N=p,n} F_{1,N}(\frac{x}{\alpha}, Q^2)\rho_D^N(\alpha, k_\perp)\frac{2}{\alpha}\frac{d\alpha d^2k_\perp}{\alpha}, \tag{59a}$$

$$F_{2D} = \int \sum_{N=p,n} F_{2,N}(\frac{x}{\alpha}, Q^2)\rho_D^N(\alpha, k_\perp)\frac{d\alpha d^2k_\perp}{\alpha}, \tag{59b}$$

where the density matrix

$$\rho_D^N(\alpha, k_\perp) = \frac{\psi_D^2(\alpha, k_\perp)}{2-\alpha} = \frac{\sqrt{M_D^2 + k^2}}{2-\alpha}(U^2(k) + W^2(k)); \tag{60}$$

$$\alpha = 1 + \frac{k_3}{\sqrt{m^2 + k^2}} \tag{61}$$

is the light cone momentum fraction, and

$$k = \sqrt{\frac{m^2 - k_\perp^2}{\alpha(2-\alpha)} - m^2} \tag{62}$$

corresponds to the nucleon momentum in the center of mass system, $\psi_D(\alpha, p_\perp)$ is the deuteron wavefunction, U and W are S- and D-state deuteron wavefunctions in momentum representation, $x = Q^2/(qP_D)$ with q being the momentum transfer, P_D is the deuteron 4-momentum, and the factor $2-\alpha$ is due to the two-nucleon phase space. In the lab frame, $\alpha = \frac{E-p_z}{M_D/2}$ where z points along the direction of $\hat{q}$.

Equations (59) have a simple parton interpretation: the probability of finding a parton in the deuteron carrying a fraction of the deuteron momentum $x/2$ is equal to the product of the probability of finding a nucleon with a fraction of the deuteron momentum $\alpha/2$ and the probability of finding a parton in the nucleon with a fraction of nucleon momentum x/α.

II.8 TAGGED STRUCTURE FUNCTIONS

After decades of studies of the partonic structure of nucleons, our knowledge of the relative d and u quark densities in the large Bjorken x region is still unsatisfactory

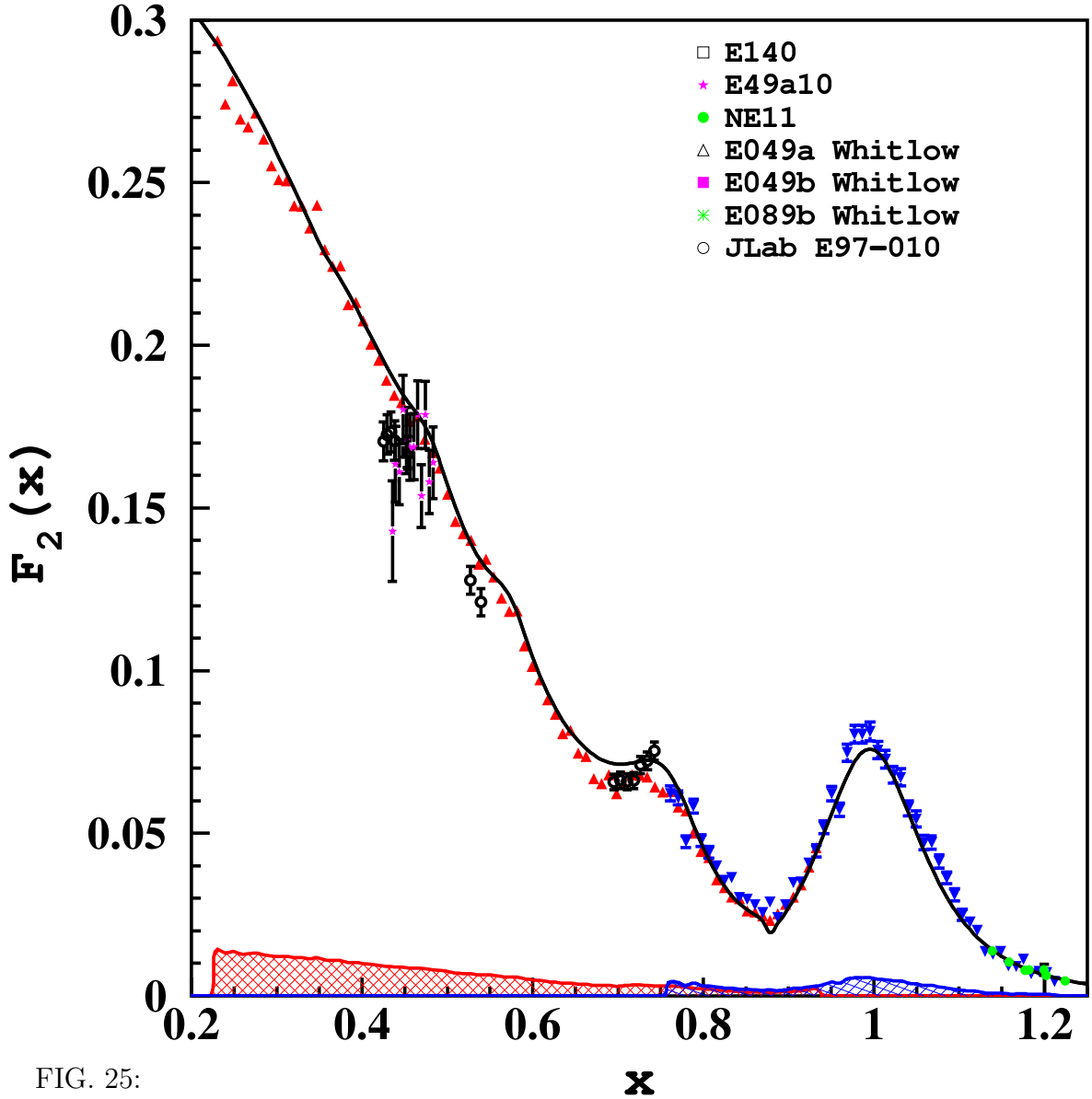

FIG. 25:
The deuteron structure function F_2^D per nucleon at $Q^2 = 1.925$ GeV/c^2. The red and blue points show the CLAS data from E6a and E1d run periods respectively; others are indicated on the graph. The curve is the phenomenological model from [47].

(see, for example, figure 17). Different methods have been proposed in order to obtain the large-x n/p (or equivalently d/u distribution) ratio, but all of them have been plagued with model uncertainties and too large nuclear corrections. None of them have been able to discriminate between different limits on the ratio F_{2n}/F_{2p} as $x \to 1$ (see figure 17). The promising experiments utilizing neutrino and anti-neutrino scattering off proton targets, that can measure u and d distributions separately, suffer from relatively low statistics [50].

The measurement of tagged structure functions in semi-inclusive deep inelastic scattering with slow recoil proton detected in the backward hemisphere

$$e + D \to e + p + X \tag{63}$$

can help us resolve the ambiguities introduced by nuclear model dependence and extract the ratio of neutron to proton structure functions at high-x region, hence accessing the long-sought d/u distribution ratio.

The measurements performed on bound nucleons yield "effective" structure functions that are not guaranteed to be very close to free nucleon structure functions. Nevertheless, by selecting only the slowest recoil protons and backward scattering angles we are able to measure them in the region where the target nucleon is almost on-shell, thus enabling ourselves to extract the F_{2n} structure function with minimal model uncertainties.

II.8.1 Spectator tagging

The general formula for the cross-section of process (63) is [50]

$$\frac{d\sigma}{dxdQ^2d^3p_s/E_s} = \frac{4\pi\alpha_{em}^2}{xQ^4}\left(1 - y - \frac{x^2y^2m_N^2}{Q^2}\right)$$
$$\times \left(F_L^D + \left(\frac{Q^2}{2q^2} + \tan^2\left(\frac{\theta_e}{2}\right)\right)\frac{\nu}{m_N}F_T^D + \left(\frac{Q^2}{2q^2} + \tan^2\left(\frac{\theta_e}{2}\right)\right)^{1/2}\cos\phi F_{TL}^D + \cos(2\phi)F_{TT}^D\right), \tag{64}$$

where the four-momentum of the virtual photon is $q \equiv (\nu, \vec{q})$, Q^2 is the usual $-q^2$, the recoil nucleon has four-momentum $p_s \equiv (E_s, \vec{p_s})$, $y = \nu/E_e$, where E_e is the initial electron energy, m_N is the nucleon mass, ν is the energy transfer, α_{em} is the electromagnetic coupling constant, and ϕ is the azimuthal angle of the recoil nucleon (the z axis is aligned with the direction of $\vec{q}$). The four nuclear structure functions

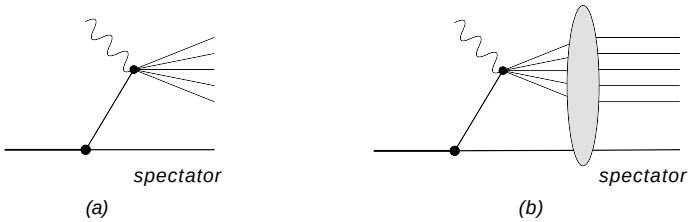

FIG. 26: Two main diagrams contributing to the reaction (63) in the region of $\alpha > 1$. The diagram (a) represents the usual impulse approximation describing the interaction of the virtual photon with only one nucleon with no further rescattering. The diagram (b) describes final state interactions: after the interaction of the virtual photon with a nucleon, products of the reaction interact between themselves.

$F^D_{L,T,TL,TT}$ depend on Q^2, x, α_s, $p_{s\perp}$, where α_s is the light-cone momentum fraction of the spectator. After azimuthal angle integration, (64) becomes

$$\frac{d\sigma}{dxdQ^2d^3p_s/E_s} = \frac{4\pi\alpha^2_{em}}{xQ^4}\left(1-y-\frac{x^2y^2m_N^2}{Q^2}\right)\left(F^{SI}_{2D}+2\tan^2\left(\frac{\theta_e}{2}\right)\frac{\nu}{m_N}F^{SI}_{1D}\right), \quad (65)$$

where

$$F^{SI}_{2D}(x,Q^2,\alpha_s,p_\perp) = F^D_L + \frac{Q^2}{2q^2}\frac{\nu}{m_N}F^D_T, \quad (66a)$$

$$F^{SI}_{1D}(x,Q^2,\alpha_s,p_\perp) = F^D_T/2. \quad (66b)$$

There are two possible reactions that can produce (63): the direct process in which the electron scatters off the nucleon going backwards in the deuteron rest frame (nucleon with $\alpha > 1$) and the spectator reaction itself in which scattering takes place on the unobserved nucleon, which gets knocked out and therefore releases its neighbor-spectator. It has been shown [48] that in the kinematic region where $\alpha > 1$ the contribution of the direct process is negligible, thus enabling us to utilize this region for the study of the spectator reaction.

In this kinematic region two main diagrams will contribute to (63) [50]: the impulse approximation diagram 26a, and the "final state interactions" diagram 26b which accounts for rescattering of the spectator nucleon off the debris of the DIS scattering.

I will return to final state interactions in section II.8.2. For now I will concentrate on the impulse approximation described by figure 26a.

In the nuclear impulse approximation, we can write down the scattering amplitude as [50]

$$A^{\mu}_{IA} = \langle X|J^{\mu}_{em}(Q^2,\nu,p_s)\frac{\not{p}_d - \not{p}_s + m}{m_N^2 - t}\bar{u}(p_s)\Gamma_d, \tag{67}$$

where $t = (p_d - p_s)^2$. Γ_d is the covariant $d \to pn$ transition vertex, and $J^{\mu}_{em}(Q^2,\nu,p_s)$ is the electromagnetic DIS operator of electron scattering of the bound nucleon. $\not{p} = \gamma^{\mu}p_{\mu}$, γ^{μ} being Dirac matrices.

Taking the recoil nucleon to be on-mass-shell and using

$$\not{p}_d - \not{p}_s + m \approx \sum_{spins} u(p_d - p_s)\bar{u}(p_d - p_s), \tag{68}$$

we can factorize the amplitude (67) into two parts: the DIS current of the bound nucleon, $J^{\mu}_{X,N} = \langle X|J^{\mu}_{em}(Q^2,\nu,p_s)u(p_d - p_s)$ and the wave function of the deuteron.

With this factorization the nuclear DIS structure functions can be expressed through the convolution of bound nucleon DIS structure functions and the nuclear spectral function, S [50]:

$$F^{SI}_{1D}(x,Q^2,\alpha_s,p_\perp) = \frac{S(\alpha_s,p_\perp)}{n}\left(F^{eff}_{1N}(\tilde{x},Q^2,\alpha,p_\perp) + \frac{p_\perp^2}{2pq}F^{eff}_{2N}(\tilde{x},Q^2,\alpha,p_\perp)\right) \tag{69a}$$

$$F^{SI}_{2D}(x,Q^2,\alpha_s,p_\perp) = \frac{S(\alpha_s,p_\perp)}{n}\frac{m_N\nu}{pq}\left((1+\cos\delta)^2\left(\alpha + \frac{pq}{Q^2}\alpha_q\right)^2 + \frac{1}{2}\sin^2\delta\frac{p_\perp^2}{m_N^2}\right) \times F^{eff}_{2N}(\tilde{x},Q^2,\alpha,p_\perp), \tag{69b}$$

where F^{eff}_{1N} and F^{eff}_{2N} are the structure functions of the bound nucleon, $\sin^2\delta = Q^2/q^2$; the modified Bjorken x, $\tilde{x}$, is described in appendix B; the nuclear spectral function S describes the probability of finding an interacting nucleon in the target with momentum $(\alpha, p_\perp)$ and a recoil nucleon in the final state of the reaction with momentum $(\alpha_s, p_{s\perp})$ (in impulse approximation, $\alpha_s + \alpha = 2$, $\mathbf{p}_\perp = -\mathbf{p}_{s\perp}$). n is also model dependent. In the light cone approximation

$$n = 2 - \alpha_s. \tag{70}$$

This gives us basically the same as the density matrix from the equation (60), with a different "normalization". Indeed, in the light-cone approximation

$$S^{IA}_{LC}(\alpha_s,p_{s\perp}) = \frac{E_k}{2-\alpha_s}\psi^2_D(\alpha_s,p_{s\perp}) = E_k\rho(\alpha_s,p_{s\perp}). \tag{71}$$

Using (69), (65) takes the following form:

$$\begin{aligned}\frac{d\sigma}{dxdQ^2d^3p_s/E_s} &= \frac{4\pi\alpha_{em}^2}{xQ^4}\left(1-y-\frac{x^2y^2m_N^2}{Q^2}\right)\\ &\times\frac{S(\alpha_s,p_\perp)}{n}\left(\frac{m_N\nu}{pq}\left((1+\cos\delta)^2\left(\alpha+\frac{pq}{Q^2}\alpha_q\right)^2+\frac{1}{2}\sin^2\delta\frac{p_\perp^2}{m_N^2}\right)\right.\\ &\times F_{2N}^{eff}(\tilde{x},Q^2,\alpha,p_\perp)+2\tan^2\left(\frac{\theta_e}{2}\right)\frac{\nu}{m_N}\\ &\times\left.\left(F_{1N}^{eff}(\tilde{x},Q^2,\alpha,p_\perp)+\frac{p_\perp^2}{2pq}\;F_{2N}^{eff}(\tilde{x},Q^2,\alpha,p_\perp)\right)\right),\end{aligned} \tag{72}$$

where $\alpha_q \equiv (\nu - |\mathbf{q}|)/m_N$.

II.8.2 Corrections to impulse approximation

Equations (69) present a nice way of accessing bound nucleon structure functions. Extrapolating them to the nucleon pole will allow us to find free nucleon structure functions. However, when final state interactions (FSI), off-shellness and model uncertainties are accounted for, things can get complicated. Nevertheless, the choice of backward kinematic combined with using slow momentum spectator protons minimize these effects, such as final state interactions, on-shell extrapolation, deuteron wavefunction ambiguity, and target fragmentation. Let us look more closely at these sources of uncertainty.

Spectral function ambiguity

The nuclear spectral function S is a model dependent quantity whose form depends on the formalism used to describe the interaction (*i.e.* instant form *vs* light cone formulation). However, it turns out that at spectator momenta $|\vec{p}_s| \lesssim 0.5$ GeV/c, the difference between these approaches is not very large [51]. Figure 27 (from [51]) illustrates the α_s and $p_\perp$ dependence of the ratio of spectral functions calculated in instant form and light cone approaches. For $p_\perp \leq 0.1$ GeV/c the light cone and instant form approaches differ up to 20% for $\alpha_s \leq 1.5$. The uncertainty in the spectral function can be further reduced by choosing the isolated values of $\alpha \leq 1.2$ or $\alpha \sim 1.4$. In these cases the difference does not exceed 10%.[u]

[u] In the BONuS experiment, we restricted the kinematic region of interest to $p_\perp \leq 0.1$, $1.0 < \alpha \leq 1.1$

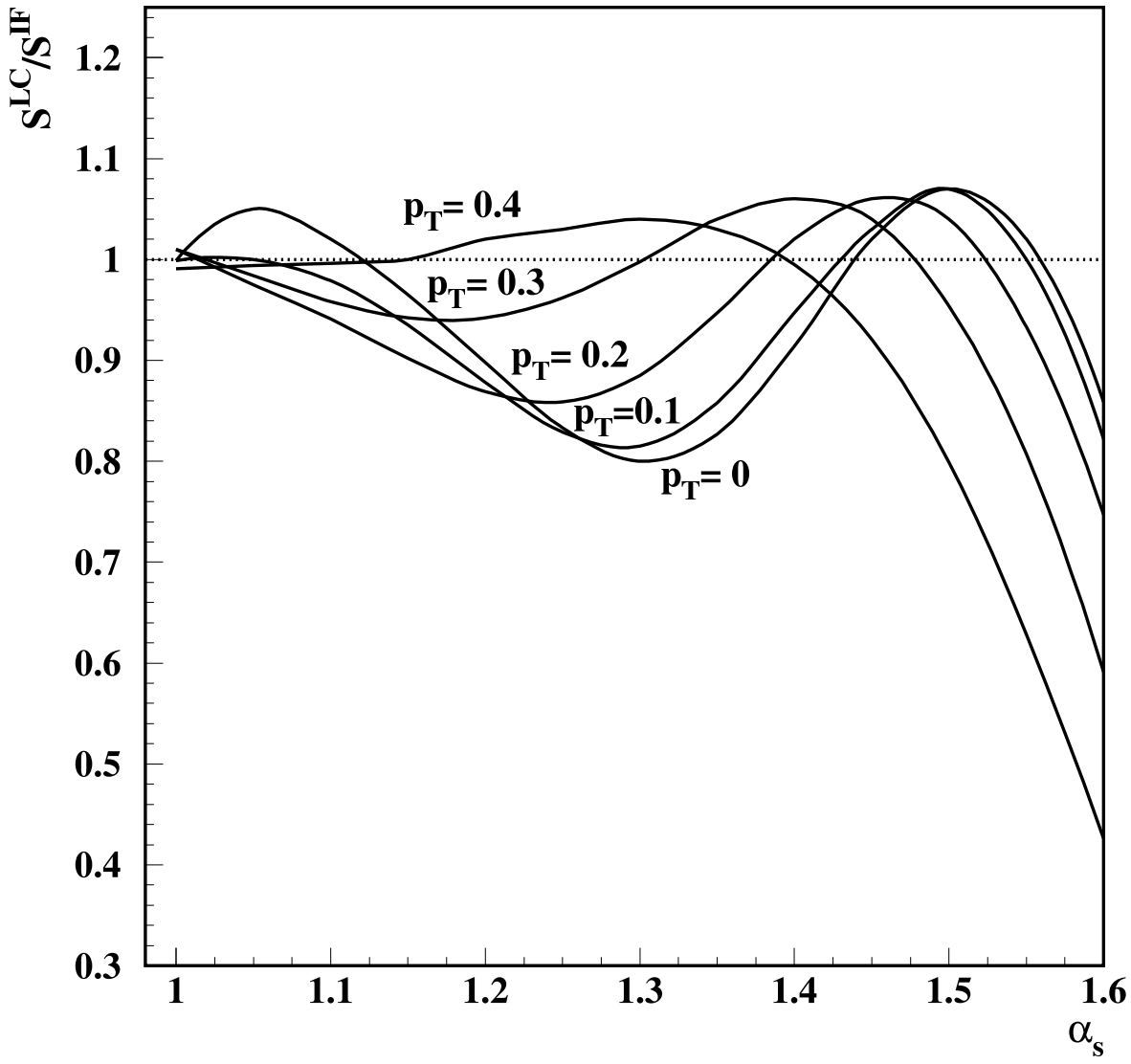

FIG. 27: The ratio of nuclear spectral functions calculated in the light cone and instant form formalisms as a function of light cone momentum fraction α_s. The dependence is shown for five values of the transverse momentum close to the kinematic region of interest. From [51].

Target fragmentation

A large rapidity gap between the spectator proton and the hadronic debris from the struck neutron ensures a very small production of low momentum protons originating from the latter. Contributions from the direct quark to proton fragmentation can be large in the current fragmentation region (forward hemisphere) whereas they are strongly suppressed in the target fragmentation region (backward hemisphere). The decrease in the spectator proton momentum should also decrease the direct fragmentation contribution. As it can be seen from figure 28, the effects of target fragmentation are noticeable in the forward hemisphere (current fragmentation region) only, and are totally negligible in the region of interest (target fragmentation region).

Off-shell effects

The degree to which the struck neutron is off-shell is

$$M^2 - p^2 \approx 2\vec{p}_s^{\,2} + 2M|\epsilon|, \tag{73}$$

where ϵ = -2.2 MeV is the deuteron binding energy. Thus, the lower spectator momentum we have, the closer to on-shell the neutron is and the simpler the extrapolation of the structure functions to their on-shell values will be. In convolution models, off-shell effects in the leading twist arise either kinematically or dynamically. Kinematic effects, coming from the transverse motion, can be calculated with very little model dependence [24]. Dynamic effects, emerging due to modifications of bound nucleon intrinsic structure, are unfortunately model-dependent and need some further discussion. Let us look at some models for the dynamic effects and estimate the plausibility of the on-shell extrapolation in each of them.

1. **Covariant spectator model.** In this model [56], nucleon-quark-diquark interactions in deep inelastic scattering are parameterized by *relativistic vertex functions*. The functions are constrained by fitting to the on-shell proton functions and comparing the calculated deuteron structure function with the inclusive F_2^d data. The ratio of the bound to free neutron structure functions calculated in this model (see figure 29) is rather close to unity at low (around 100 MeV/c) spectator momenta. For the highest shown Bjorken x (x=0.6) curve, it is within 1% of unity and even closer for lower x.

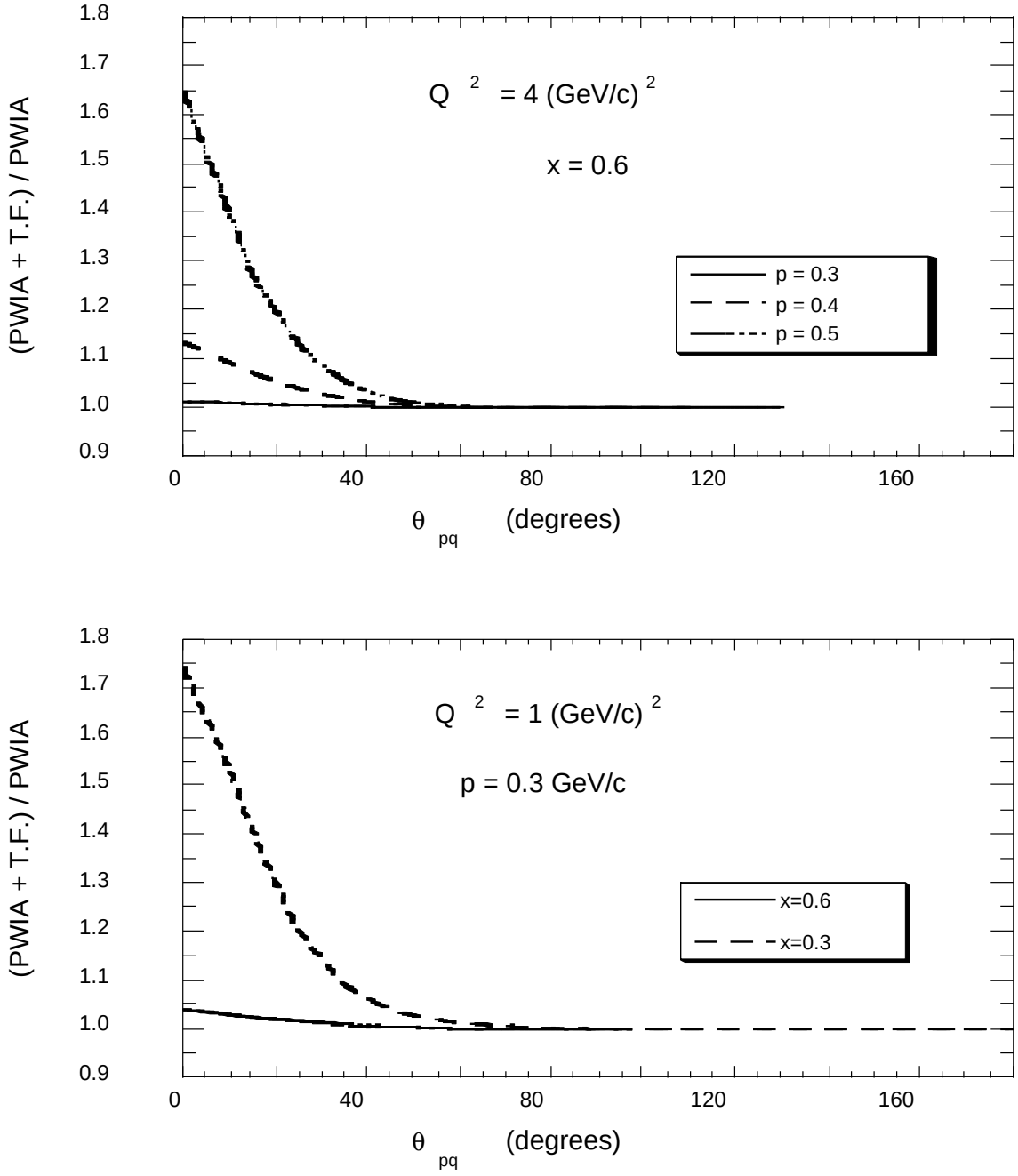

FIG. 28: Ratio of the plane wave impulse approximation (PWIA) corrected for the target fragmentation (TF) to the pure PWIA calculation as a function of the center of mass angle, θ_{pq}, between the spectator proton and the virtual photon shown for two values of the momentum exchange: Q^2=4 GeV/c^2 (upper panel) and Q^2=1 GeV/c^2 (lower panel) (from reference [53]).

2. **Relativistic quark spectral function.** Here the bound nuclear structure function is evaluated as the free nucleon structure function at a shifted value of the quark light-cone momentum fraction α [24]. The shift depends on the mass of the spectator diquark system, the bound nucleon momentum, and the binding energy. The ratio of the bound to free neutron structure functions calculated in this model (see figure 30) is within 2% of unity for small (around 100 MeV/c) spectator momenta values. The general behavior of the spectator momentum dependence is consistent with that of the covariant spectator model with the biggest difference being the less pronounced Bjorken x dependence of the result in this model.

3. **Instant form approach.** Here the bound nuclear structure function is evaluated as the free structure function at a shifted energy transfer value [25]. The shift depends on the binding energy. The ratio of the bound to free neutron structure functions calculated in this model (see figure 31) at $Q^2 = 1$ GeV/c is within 1% for all the angles for small momenta (around 100 MeV/c).

4. **Color screening model.** In this model [26], the bulk of the EMC effect is attributed to a medium modification of the bound nucleon, not to the nuclear binding. A larger deviation of the bound to free structure function ratio from unity is calculated by this model. Still, this deviation is proportional to $2\vec{p}_s^{\,2} + 2M|\epsilon|$, thus making the extrapolation to the free nucleon pole possible once the ratio is found for several values of p_s.

To summarize, in all the models from the representative sample discussed above the deviation of the bound structure function from the free structure function is either very small (within a couple of percent) or a relatively easy extrapolation to the free nucleon pole is deemed possible. At the lower edge of our momentum acceptance ($|\vec{p}_s| \approx 70$ MeV/c), the neutron is only 7 MeV/c off its mass shell thus making off-shell effects small and making on-shell extrapolation relatively painless.

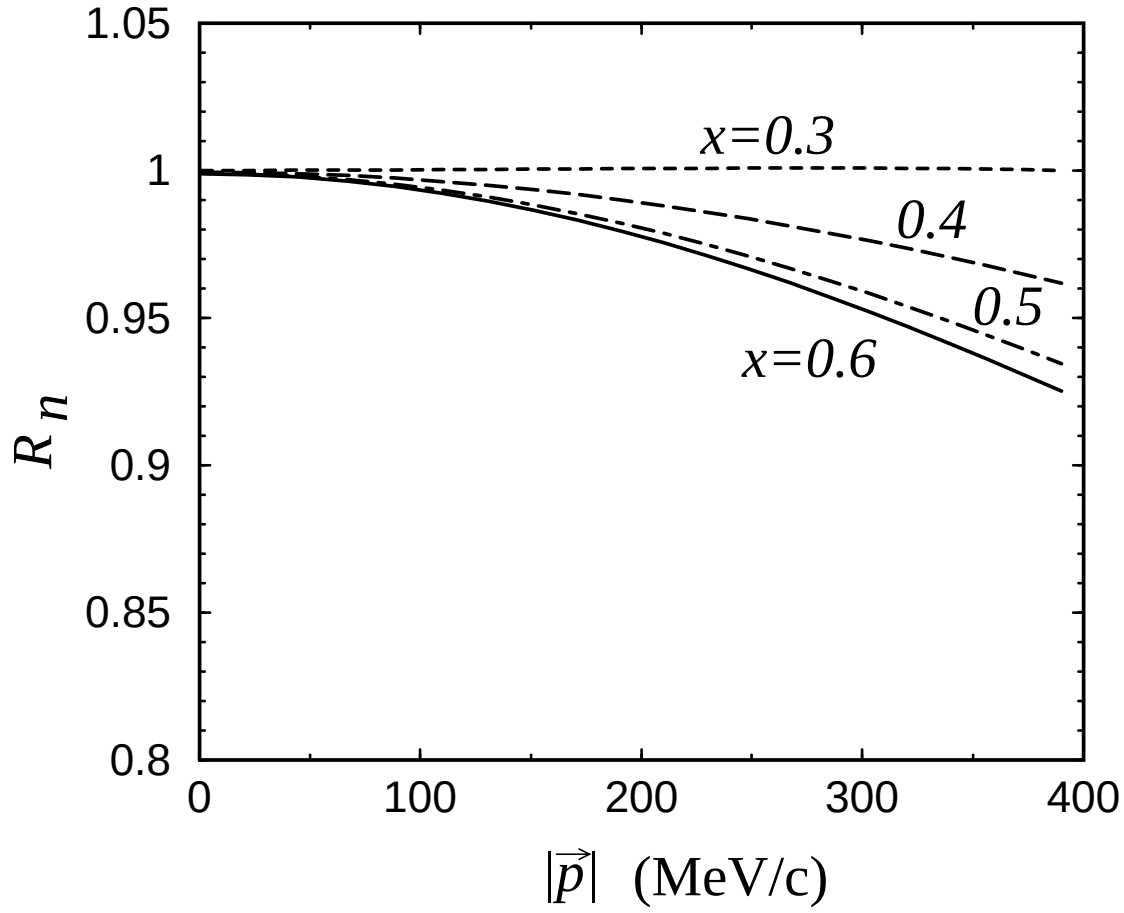

FIG. 29: Ratio $R_n \equiv F_2^{n(eff)}(W^2, Q^2, p^2)/F_2^n(W^2, Q^2)$ of the bound to free neutron structure functions as a function of the spectator proton momentum in the covariant spectator model for several values of x. For the calculations shown, $Q^2 \sim 4\text{GeV}/c^2$, although the Q^2 dependence is rather weak for $Q^2 > 1$ GeV/c^2. In the model of [56].

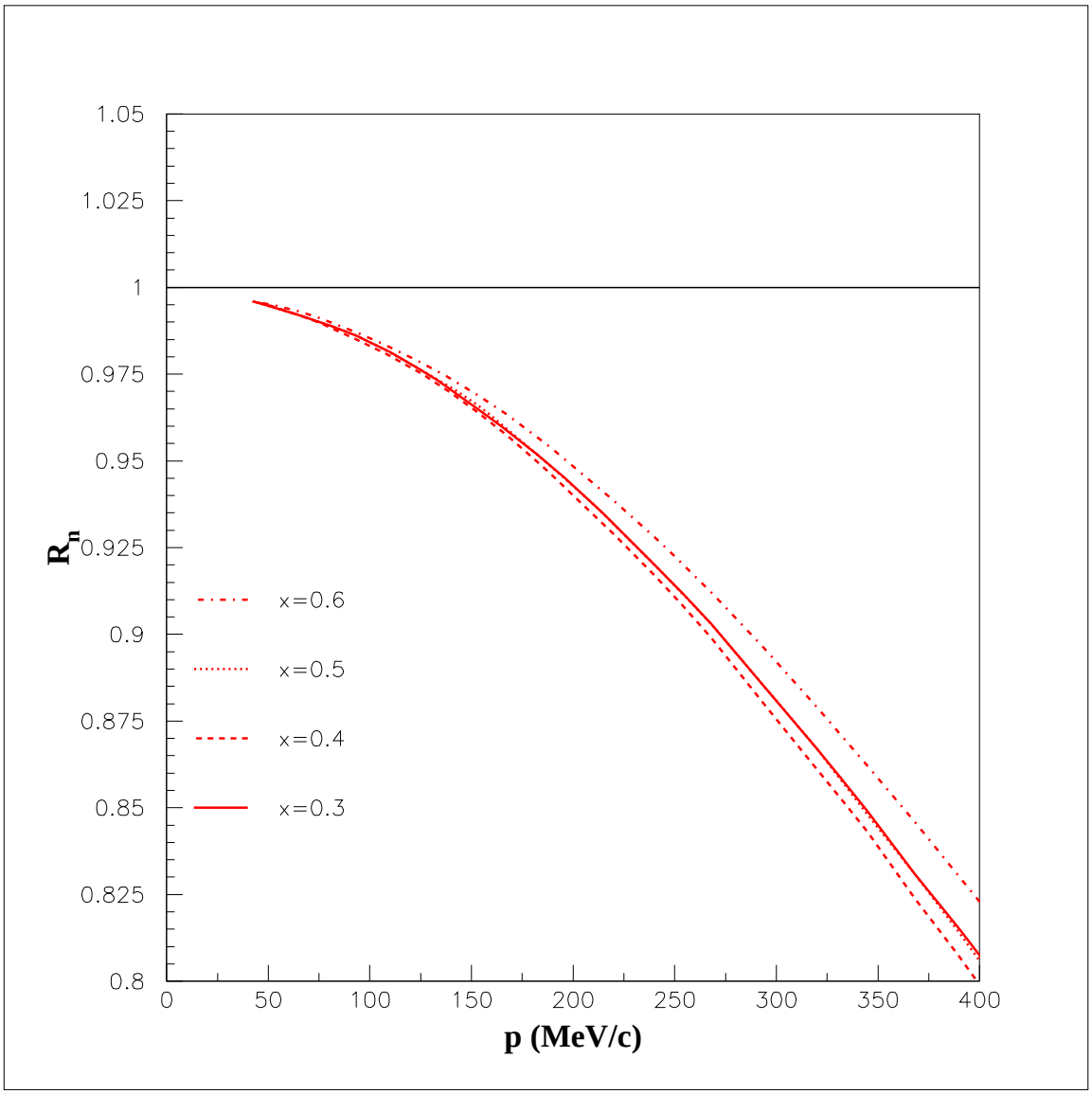

FIG. 30: Ratio $R_n \equiv F_2^{n(eff)}(W^2, Q^2, p^2)/F_2^n(W^2, Q^2)$ of the bound to free neutron structure functions as a function of the spectator proton momentum in the relativistic quark spectral function approach for several values of x. In the model of [24].

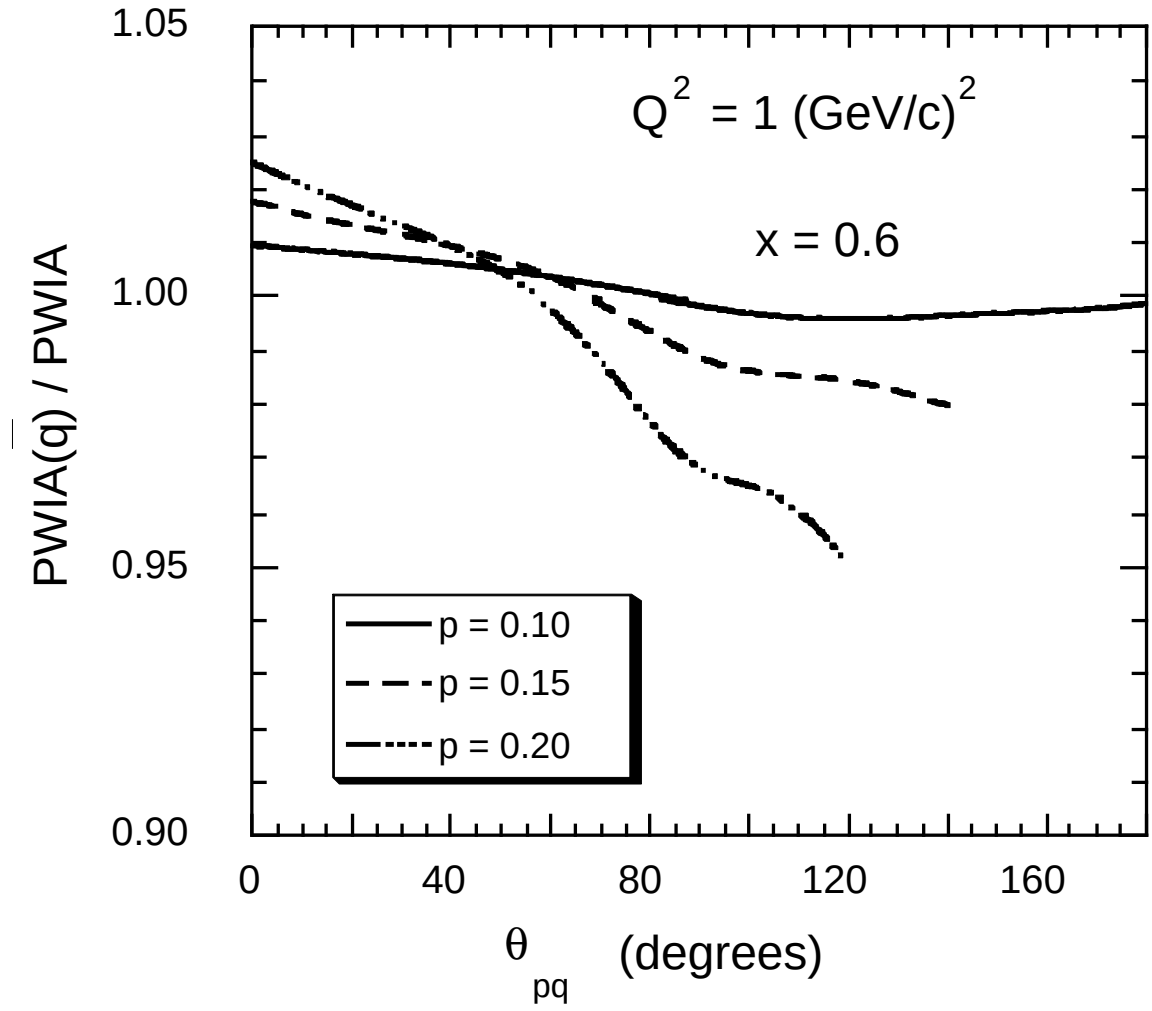

FIG. 31: Ratio of the bound to free neutron structure functions calculated in the instant form approach as a function of the angle θ_{pq}. The bound structure function in this model is calculated from the free structure function by shifting the energy exchange ν and thus shifting x and Q^2 at which the nucleon structure function is evaluated. Both are calculated in the plane wave impulse approximation. Graphs for 3 values of the spectator momentum are shown calculated in the model of [57].

Final state interactions

Let us return to the second diagram describing the spectator proton scattering, figure 26b. It can be represented [50] in the most general form as

$$A_{FSI} = \sum_{X'} \int \frac{d^4 p_{s'}}{(2\pi)^4} \langle X, s | \hat{A}_{FSI} \cdot G(X') \cdot \hat{J}^{em}(Q^2, x) \frac{\not{p}_d - \not{p}_{s'} + m_N}{(p_d - p_{s'})^2 - m_N^2 + i\epsilon} \frac{\not{p}_{s'} + m_{N_2}}{p_{s'}^2 - m_{N_1}^2 + i\epsilon} \Gamma_d, \tag{74}$$

where $\hat{J}^{em}(Q^2, x)$ and $\hat{A}_{FSI}$ represent operators of DIS and FSI scattering and $G(X')$ is a notation for the propagation of the intermediate state X'. The amplitude (74) is too general to perform any realistic calculations, but one important fact can be deduced from its form [50]: it is not singular at the nucleon pole, thus allowing the extraction of the free nucleon structure by extrapolating to the pole.

Having established the possibility of extrapolating to the pole in principle, let us turn to evaluating FSI in order to estimate the practical plausibility of the procedure. Backward angles chosen for the BoNuS experiment served the purpose of minimizing rescattering of the spectator proton by deep inelastic remnants of the scattered neutron (also known as FSI). Although the direct calculation of the FSI is not possible at the moment, we can look at what different theoretical models tell us about the FSI.

In the distorted wave approximation [51], the model due to W. Melnitchouk *et al*, the effect of FSI would be to modify the spectral function: $S \rightarrow S^{DWIA}$, where

$$S^{DWIA}(\alpha, p_\perp \approx 0) \sim S(\alpha, p_\perp \approx 0) \left(1 - \frac{\sigma_{eff}(Q^2, x)}{8\pi \langle r_{pn}^2 \rangle} \frac{|\psi_d(\alpha, \langle p_\perp \rangle) \psi_d(\alpha, 0)|}{S(\alpha, p_\perp \approx 0) / \sqrt{E_s E_s(\langle p_\perp^2 \rangle)}} \right), \tag{75}$$

where $\langle r_{pn}^2 \rangle$ is the average separation of the nucleons within the deuteron, E_s is the spectator energy, $E_s(\langle p_\perp^2 \rangle) = \sqrt{M^2 + p_{zs}^2 + \langle p_\perp^2 \rangle}$ is the energy evaluated at the average transverse momentum transferred for the hadronic soft core interactions with effective cross-section σ_{eff}.[v] Due to the steep momentum dependence of the deuteron wavefunction, FSI effects are suppressed in backward kinematics, $p_\perp \approx 0$, where FSI contribute less than 5% to the overall uncertainty of the cross-section for $\alpha < 1.5$ (see figure 32).

[v] The effective pX cross-section can be approximated [16] by that extracted from soft neutron production in the high energy DIS of muons from heavy nuclei, where $\sigma_{eff} \approx 20$ mb can be used as an upper limit of the cross-section. The average transverse momentum for this value of the cross-section can be taken to be 200-300 MeV/c.

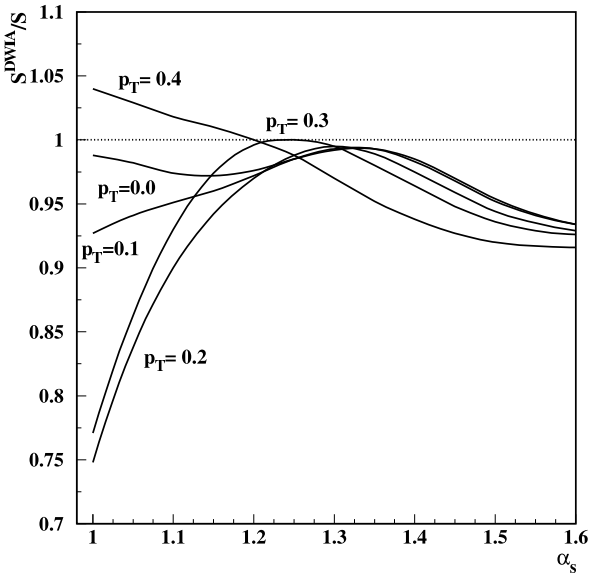

FIG. 32: The α_s dependence of the ratio of the light cone spectral function with FSI effects included calculated in DWIA framework, to that without FSI effects [51]. The dependence is shown for five values of transverse momentum p_T.

In a model due to Ciofi degli Atti *et al* in which FSI are due to the struck nucleon debris propagation and hadronization [52], the effective cross-section is not constant, but grows logarithmically as a function of time (or longitudinal distance z) as quarks get further away from each other, the color tube stretches and radiates gluons (see figure 33). Including effects of both color tube breaking and gluon bremsstrahlung, the effective cross-section can be written as

$$\sigma_{eff}(t) = \sigma_{tot}^{NN} + \sigma_{tot}^{\pi N}(n_M(t) + n_G(t)), \tag{76}$$

where σ_{tot}^{NN} and $\sigma_{tot}^{\pi N}$ are the total nucleon-nucleon and pion-nucleon cross-sections, $n_M(t)$ and $n_G(t)$ are the effective numbers of created mesons and radiated gluons correspondingly. Then the cross-section can be evaluated [52] by replacing the struck nucleon momentum distribution with the distorted momentum distribution

$$S^{PWIA}(\vec{p}_s) \to S^{FSI}(\vec{p}_s) = \frac{1}{3}\frac{1}{(2\pi)^3}\sum_{M_d} |\int d\vec{r}\Psi_{1,M_d}(\vec{r})S(\vec{r})\chi_f^{\dagger}e^{(-i\vec{p}_s\cdot\vec{r})}|^2, \tag{77}$$

where $\vec{r} = \vec{b} + z\vec{q}/|\vec{q}|$ is the relative coordinate, z is the longitudinal component, b is the transverse component, χ_f is the spin wavefunction of the final state, $S(\vec{r})$ is the

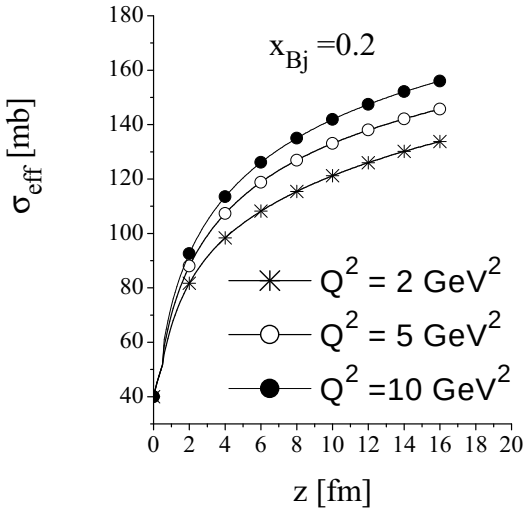

FIG. 33: The debris-nucleon effective cross-section, σ_{eff}, as a function of the longitudinal distance z [54].

S-matrix for the FSI interaction between the debris and spectator nucleon:

$$S(\vec{r}) = 1 - \Theta(z)\frac{\sigma_{eff}(z)(1-i\beta)}{4\pi b_0 2} e^{(-b^2/2b_0^2)}, \tag{78}$$

where $\Theta(z)$ is the step function, and β is the ratio of the real to imaginary parts of the scattering amplitude. The FSI in this model are not large at small spectator momenta, p_s, and large scattering angles, θ (see figure 34) continuing the familiar trend.

To summarize the discussion of the corrections to the impulse approximation for the spectator scattering, these corrections, including the off-shell corrections, target fragmentation, and final state interactions, are minimized at small spectator momenta, $p_s \lesssim 100$ MeV/c, and backward scattering angles, $\theta_{pq} > 120$ degrees, thus making the extraction of the free neutron structure information from the bound neutron data a doable task. And for the rare models that have those corrections non-negligible, getting a few data points in the small momentum-large angle region and extrapolating to the nucleon pole is still quite a plausible procedure (see the next section).

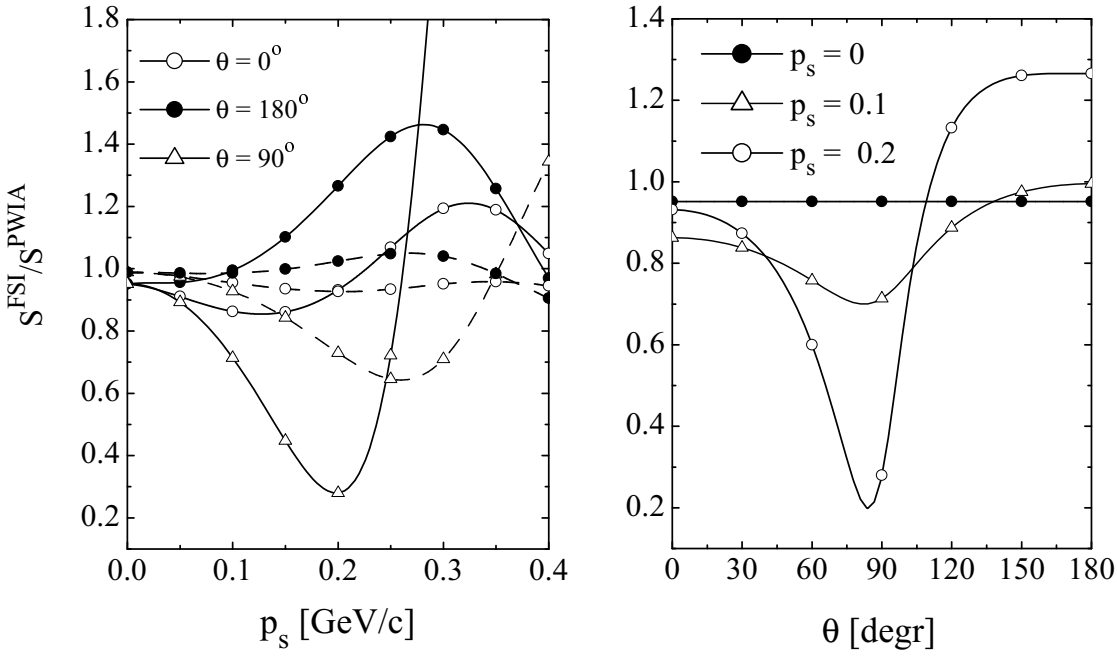

FIG. 34: The momentum and angular dependence of the ratio of the spectral function calculated accounting for FSI to the spectral function calculated in the impulse approximation, for $Q^2 = 5$ GeV/c^2, and x=0.2. On the left panel containing the momentum dependence, the dashed line illustrates the case of constant effective cross-section, σ_{eff}= 20 mb, the solid line illustrates the case of the effective cross-section changing with time and momentum exchange (*cf* figure 33) [55].

II.8.3 Alternative way of extracting F_2 structure function

To finish the discussion of the spectator tagging, let us consider a procedure of extracting the free F_2 structure function for the struck nucleon that does not demand backward scattering angles and negligible FSI [50].

The procedure is based on the pole extrapolation, the technique mentioned above for the model with relatively large FSI. Let us introduce an extraction factor:

$$I(p_s,t)=\frac{1}{E_s}\frac{(m_N^2-t)^2}{[Res(\Psi_d(T_{pole}))]^2}\frac{1}{\frac{m_N\nu}{pq}[(1+\cos\delta)^2(\alpha+\frac{pq}{Q^2}\alpha_q)^2+\frac{1}{2}\sin^2\delta\frac{p_\perp^2}{m_N^2}]}, \qquad (79)$$

where T_{pole} is the kinetic energy at the nucleon pole,

$$T_{pole}=-\frac{\epsilon_d}{2}\left(1+\frac{m_n 2m_p}{M_d}\right)\approx-\frac{\epsilon_d}{2}, \qquad (80)$$

ϵ_d being the deuteron binding energy; the residue (see appendix C for more on residues) of the deuteron wavefunction at the pole is

$$Res(\Psi_d(T_{pole}))=\frac{C}{\sqrt{2}\pi 2m_N}\,\mathrm{GeV}^{1/2}, \qquad (81)$$

where C is a number that slightly depends on the potential used to calculate deuteron wavefunction (for example, C=0.3939 for Paris potential, C=0.3930 for Bonn potential). Using $I(p_s,t)$ we can define the extracted structure function as

$$F_{2N}^{extr}(Q^2,x,t)=I(p_s,t)\cdot F_{2D}^{SI}(x,q^2,\alpha_s,p_\perp), \qquad (82)$$

where F_{2D}^{SI} is defined in (65). In PWIA we could use (69) with the regular spectral function to calculate F_{2D}^{SI}. In this case, the extrapolation of t to m_N would give $F_{2N}^{extr}\to F_{2N}^{eff}(x,Q^2,\alpha=1,p_\perp=0)=F_{2N}^{free}(x,Q^2)$.

When FSI effects are considered, we need to evaluate the extracted structure function within the DWIA framework, in which case we have to use the spectral function of equation (75). And again, we can extrapolate F_{2D}^{SI} to the values of $t\to m_N^2$.

It was noted [50] that if the spectator kinetic energy is much less than the energy scale corresponding to higher mass singularities in the deuteron wavefunction, equation (82) is a quadratic function of $t'\equiv t-m_N^2$. This means that we can successfully extrapolate to the nucleon pole by using a quadratic fit of the data constructed according to (82) for small and finite values of t'. There are additional problems

arising due to the deviation of (82) from the quadratic form because of the change of other kinematic variable involved in the reaction (α dependence of F_{2N}^{extr}, higher twist effects due to the sensitivity of the structure function to the final mass of the DIS scattering at intermediate Q^2). However, as it was demonstrated in reference [50], equation (82) has a nice quadratic form in the region of $\alpha \approx 1$. This means that the uncertainties due to the other kinematic variables will be minimized, and we can extract the structure function F_2 with minimum model dependence in this region.

In practice, this means that we should conduct our measurement at $\theta_{pq} \approx 90^\circ$ (where $\alpha \approx 1$). Ideally, we should probe as high Q^2 region as possible since higher twist effects are reduced when Q^2 gets large. Plotting the extracted structure function in this region as a function of $t - m_N^2$ with subsequent extrapolation to 0, using a quadratic functional form, should give us the structure function value at the free nucleon pole ($t = m_N^2$).

CHAPTER III

EXPERIMENTAL SETUP

The BONuS experiment was conducted in Hall B of the Thomas Jefferson National Accelerator Facility. A deuterium target, the Continuous Electron Beam Accelerator Facility (CEBAF) electron beam, the CEBAF Large Acceptance Spectrometer (CLAS) and a novel Radial Time Projection Chamber (RTPC), designed specially for this experiment, were used.

III.1 ACCELERATOR FACILITY

The CEBAF accelerator is a superconducting radio frequency (RF) electron accelerator facility (see figure 35). The accelerator uses a state-of-the-art photo-cathode gun system that is capable of delivering beams of high polarization and high current to Hall A and Hall C while maintaining high polarization, low current beam delivery to Hall B. An RF chopping system operating at 499 MHz is used to develop a 3-beam 1497 MHz bunch train at 100 keV. The beam is then longitudinally compressed in the bunching section to provide 2 picosecond bunches, which are then accelerated to just over 1% of the total machine energy in the remaining injector section. The beam polarization, optics and energy are verified in the injector matching region prior to injection into the main machine. The beam from the injector is accelerated through a recirculating beam line, with two linear accelerators (linacs) joined by two 180° arcs with a radius of 80 meters. Twenty cryomodules, each containing eight superconducting niobium cavities, line the two linear accelerators. Liquid helium, produced at the Lab Central Helium Liquefier (CHL), keeps the accelerating cavities superconducting at a temperature of 2 Kelvin. The linac energies are each set identically and the RF cavities are phased to provide maximum acceleration. Subsequent passes through the accelerator are phased to maximum energy gain by adjusting the length of travel in the dogleg section of the preceding arc. Quadrupole and dipole magnets in the tunnel steer and focus the beam as it passes through each arc. More than 2,200 magnets are necessary to keep the beam on a precise path and tightly focused. Beam is directed into a hall transport channel using magnetic or RF extraction. The RF scheme uses 499 MHz cavities, which kick every third bunch out of the machine. The accelerator can deliver any one of the first four passes to one hall only. The fifth

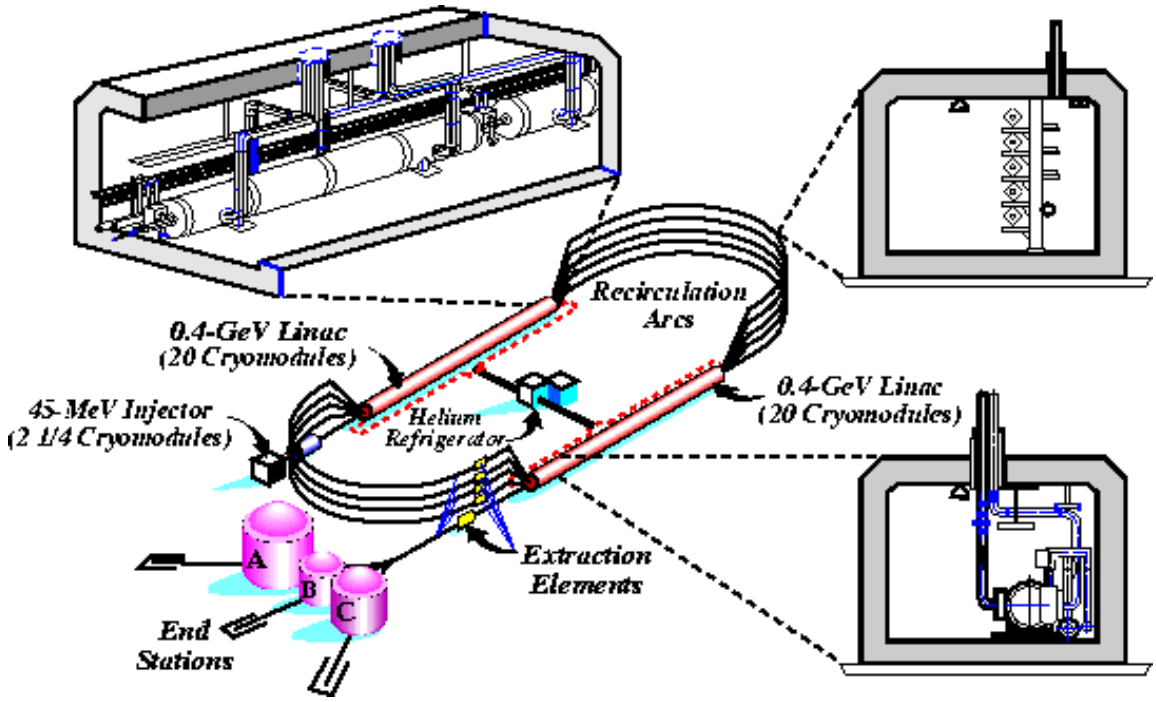

FIG. 35: The schematics of the accelerator.

pass can be sent to all three halls simultaneously.

At the time of the BONuS experiment, the accelerator could produce electron beams of up to 5.5 GeV of energy (down from 5.8 GeV achievable a few years ago), with polarization up to 86%. An upgrade that will increase the output energy to around 12 GeV has been approved and will soon be under construction.

During the BONuS experiment, beam energies of 1.100, 2.142, 4.226, and 5.268 GeV were used.[a] Beam currents of 2 - 55 nA were used. The polarization of the beam was 23%, 73.9%, 78.5%, 81%, and 85 - 87 %.

III.2 HALL B AND CLAS

The Hall B end station, the smallest of three, houses CLAS, the largest acceptance particle detector at Jeffeson Lab (see figure 36). CLAS provides an almost 4π angular coverage, covering a θ range of 8° - 142° and approximately 80% of 2π in ϕ. It is

[a]Nominal beam energies are quoted, the actual beam energies received can differ up to 10 MeV from the quoted values.

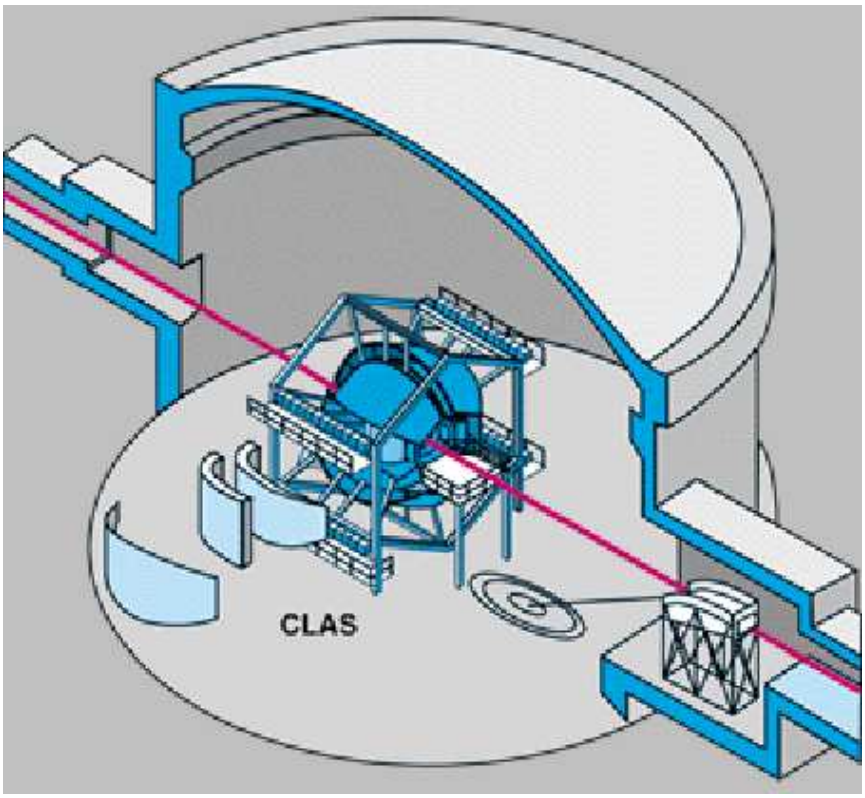

FIG. 36: CLAS in Hall B.

designed to track charged particles with initial momenta ≥ 200 MeV/c, with a track resolution for 1 GeV/c particles of $\delta p/p \leq 0.5\%$ for reconstructed momenta, and $\delta\theta$, $\delta\phi \leq 2$ mrad for reconstructed angles.

It is built around a magnet, which consists of six iron-free superconducting coils, providing a toroidal magnetic field bending charged particles in the θ direction. The coils separate CLAS into 6 independent tracking areas known as sectors, with particle detectors repeating in different sectors.

CLAS consists of several particle detectors (see figures 37, 38):

1. Drift chambers, which determine charged particle trajectories;
2. Cherenkov detectors for electron-pion separation;
3. Scintillation counters for time-of-flight measurements;
4. Calorimeters to identify electrons and neutral particles.

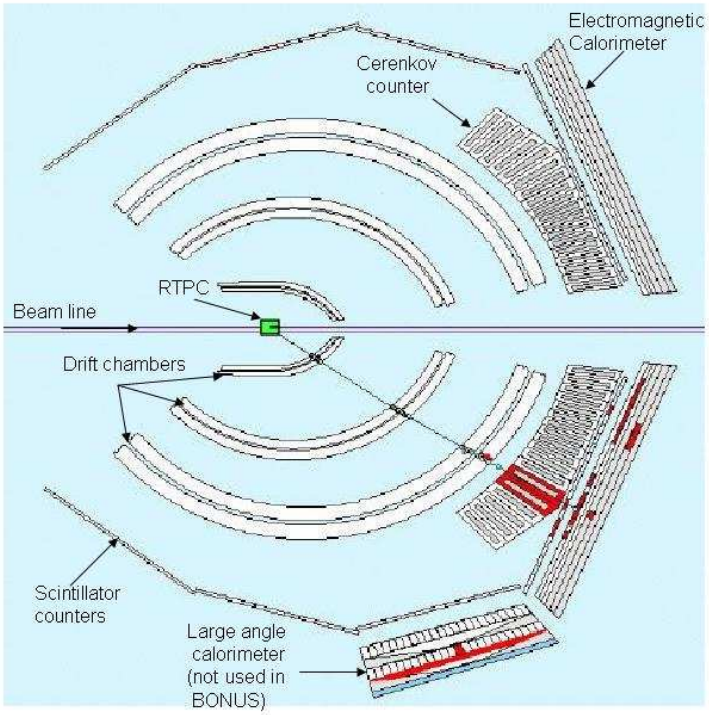

FIG. 37: CLAS, 2-dimensional view, showing the cross-section through 2 opposite sectors. The standard CLAS configuration with the added BONuS RTPC in the middle and one scattering event is shown. The standard CLAS detectors are described in the text.

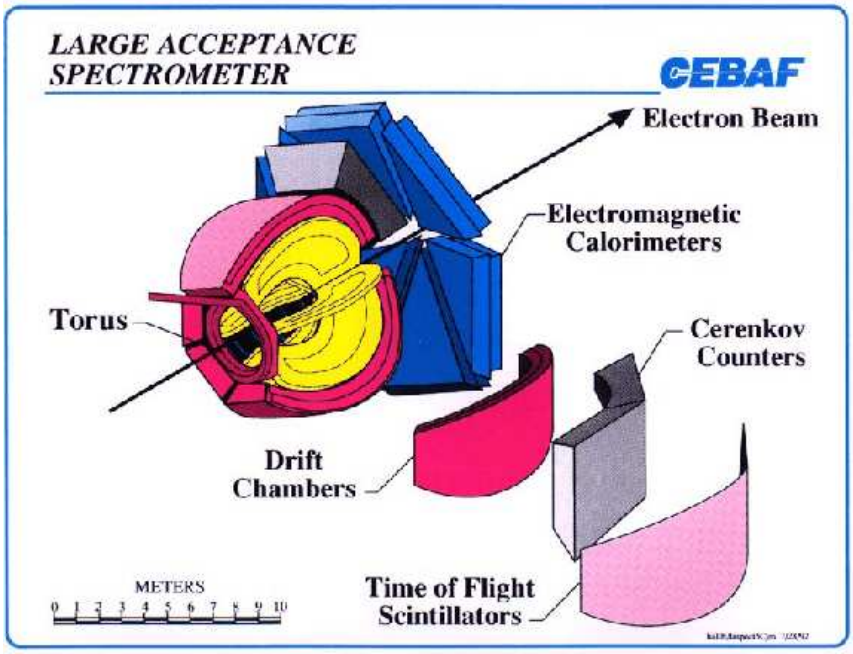

FIG. 38: CLAS, 3-dimensional view.

III.2.1 Drift chambers

Drift chambers (DC) are particle detectors capable of determining the trajectory of a charged particle. The DC is a cousin of the multi-wire (or simply wire) chamber, which, in turn, was an advancement of the Geiger counter and the proportional counter. In the Geiger counter, a wire at high voltage is enclosed in a tube filled with a gas, which is ionized by passing charged particles, and this ionization triggers the detector. In the proportional counter, the energy of the charged particle can be determined, since the ability of a particle to ionize gas changes with the particle kinetic energy and mass. Putting a lot of wires together in a box will produce a wire chamber. They will allow us to approximately find the particle trajectory by looking at which wires have been triggered by the passing particle.

If one knows the time it took the ions to "drift" from the ionization point to the wire, the accuracy of the knowledge of a particle trajectory will be greatly increased and we will have what is known as a **drift chamber**.

Drift chambers play an important role in the CLAS detector, allowing for the

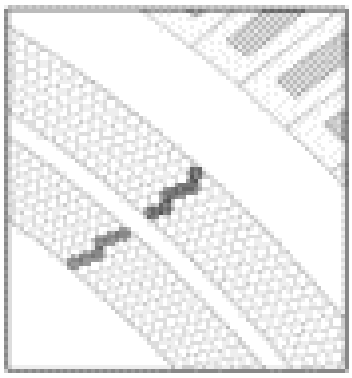

FIG. 39: Representation of a portion of the layout of a Region 3 chamber, showing the layout of its two superlayers. In the upper right corner, the edges of several Cherenkov modules are visible.

determination of particle momenta and trajectories. There are three multi-layer drift chambers at different radial locations, which are called DC "regions", in each of the six CLAS sectors, for tracking charged particles produced in a target situated on the axis of the toroidal magnet. The region 1 DC surrounds the target in the area of low magnetic field, the region 2 DC is located between the magnet coils in the area of high magnetic field, and the region 3 DC is located outside of the magnet coils. In each region, layers of wires are grouped into two "superlayers", one parallel to the magnetic field, and the other tilted at a 6° stereo angle to provide some azimuthal information (see figure 39). Overall, there are 18 drift chambers with a total of 35,148 individually instrumented hexagonal drift cells (see figure 41).

The structure of the DC facilitates achieving the aforementioned construction goals of momentum and angular track resolution ($\delta p/p \leq 0.5\%$, $\delta\theta, \delta\phi \leq 2$ mrad for 1 GeV/c particles). To achieve these goals, the tracks need to be measured at the three regions along their trajectories to an accuracy of 100 μm in the bend plane of the magnetic field and 1 mm in the direction perpendicular to the bend plane. Also, the total amount of material in the tracking region of the detector was required to be less than 1% of a radiation length. A high purity gas mixture of 90% argon - 10% CO_2 was used as a drift gas.

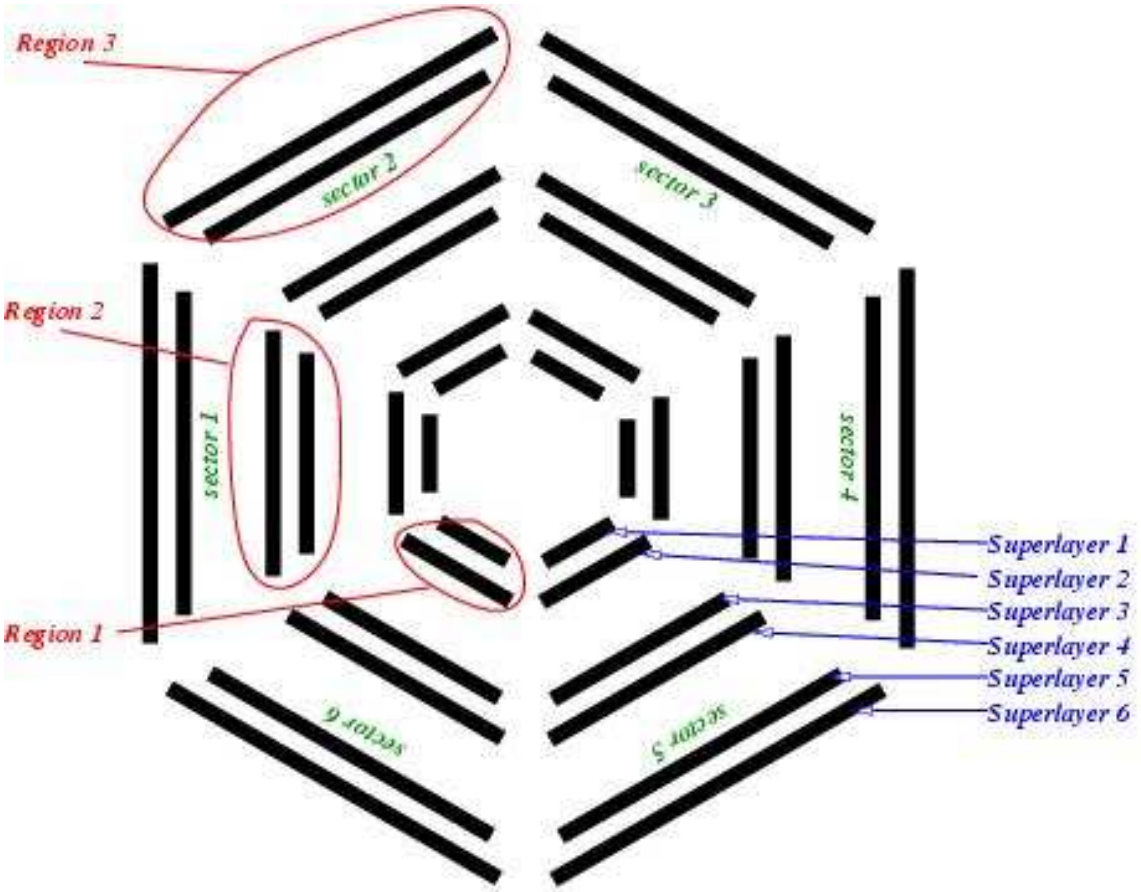

FIG. 40: Vertical cut of the drift chambers transverse to the beam line.

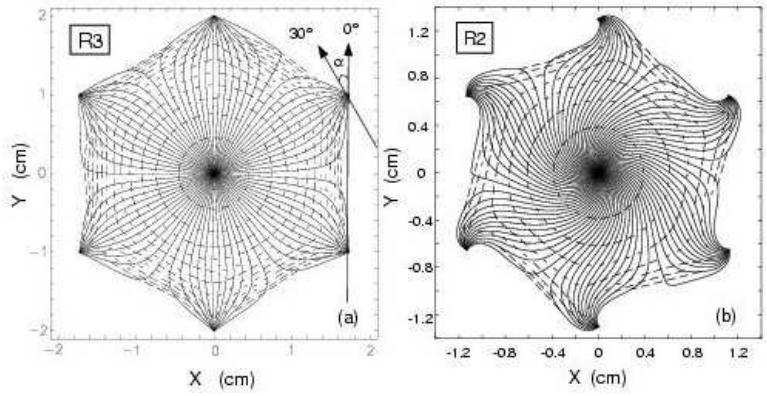

FIG. 41: Hexagonal cell drift lines without (left) and with (right) magnetic field.

III.2.2 Cherenkov counters

A Cherenkov counter (CC) is a particle detector that utilizes the velocity-dependent threshold of Cherenkov radiation, thus distinguishing between lighter and heavier particles. Cherenkov radiation is a type of radiation emitted by a charged particle passing through an insulator at speeds faster than the speed of light in that medium. As a charged particle travels, it disrupts the local electromagnetic field of the medium. Electrons in the atoms of the medium get displaced and polarized by the electromagnetic field of the particle. Photons are emitted after electrons restore themselves to equilibrium after the disruption has passed. Normally, these photons destructively interfere with each other and no radiation is registered. However, when the disruption travels faster than the photons themselves travel, the photons constructively interfere and intensify the observed radiation, analogously to the sonic boom caused by a supersonic aircraft.

The angle at which Cherenkov radiation is emitted is related to the velocity of the charged particle causing the radiation by:

$$\cos\theta = \frac{1}{n\beta}, \tag{83}$$

where θ is the angle at which the radiation is emitted, n is the index of refraction of the medium, and β is the speed of the particle in the units of the speed of light in vacuum. If there is a separate detector determining the momentum of the particle, one can use this information to extract the mass of the particle and thus identify the particle.

The Cherenkov counters are used in CLAS to identify electrons and separate them from other particles, mainly pions. The CC response is used in the level 1 trigger. The CC is positioned between the DC region 3 and the time of flight scintillator system (see figures 37, 38). They cover the region of polar angles $\theta = 7°$-$48°$ in forward direction. Each of the 6 sectors of CLAS consists of 18 segments. C_4F_{10} is used as the radiator gas. Its refraction index is 1.00153, which gives the threshold for particle energy of

$$E = \frac{m}{\sqrt{1-\beta^2}} = \sqrt{\frac{n^2}{n^2-1}}m = 18.09m, \tag{84}$$

where m is the mass of the particle, and β is its speed in units of the speed of light. This leads to a threshold for pion detection of $p_\pi \approx 2.5$ GeV/c. Thus, the CC can distinguish between pions and electrons up to momenta of approximately 2.5 GeV/c.

III.2.3 Time of flight detector

A time of flight (TOF) detector is a particle detector which can discriminate between lighter and heavier elementary particles of the same momentum using their time of flight. In its simplest form, it consists of two scintillators. The first of the scintillators activates a clock upon being hit while the other stops the clock when hit. The time of flight difference between two highly relativistic particles of masses m_1 and m_2 with velocities of v_1 and v_2 and momentum p is

$$\delta t = L(\frac{1}{v_1} - \frac{1}{v_2}) \approx \frac{Lc}{2p^2}(m_1^2 - m_2^2), \tag{85}$$

where L is the distance between scintillators and δt is the resolution of the time of flight system.

In CLAS, the TOF is a much bigger detector than the simplest form described in the previous paragraph. It consists of many scintillator counters (SC) that cover an area of 206 m^2 [59]. The system measures time of flight of the particles; it can also participate in the level 1 trigger.

The counters cover the θ range between 8° and 142° and the entire active range in ϕ. The scintillators are located radially outside the DC and CC, but in front of the calorimeters (see figures 37, 38). The scintillator thickness is 5.08 cm, chosen to give a large signal for traversing minimum ionizing particles. Each scintillator is positioned so that it is perpendicular to the average local particle trajectory. The forward counters (those positioned at $\theta < 45°$) are 15 cm wide, and the large angle counters are 22 cm wide. Each TOF counter is made of Bicron BC-408 with a photomultiplier tube (PMT) on each end.

In CLAS, the flight time can be calculated as the difference between the vertex time (found by using the electron beam bunch) and the time at the end of the particle trajectory reported by SC. For electron beam experiments, the beam bunch is determined by identifying the final state electron and tracing it back to the interaction point.[b] For tagged photon experiments, independent information about the beam bucket is obtained from the start counter[c].

The time resolution of the counters has been measured using cosmic rays and can

[b] At JLab energies, electrons are considered to be $\beta = 1$ particles.
[c] A system of thin counters surrounding the target.

be parameterized as [59]:

$$\sigma_{TOF}(ns) = \sqrt{\sigma_0^2 + \frac{\sigma_1^2 + (\sigma_P L/2)^2}{N_{pe}\exp(-L/2\lambda)}}, \quad (86)$$

where σ_0=0.062 ns is the intrinsic resolution of the electronic measuring systems and other processes that are independent of light level, σ_1=2.1 ns is the combined single photoelectron response of the scintillator and PMT, σ_P=0.0118 ns/cm accounts for path length variations in the light collection, L is the length of the counter, and λ is the attenuation length of the counter, which can be approximated by λ=134cm+0.36L for forward angle counters and by 430 cm for large angle counters. N_{pe} is the number of photoelectrons seen by a hypothetical counter without attenuation. The time resolution of the system was between 70 (for shortest counters) and 165 (for longest counters) ps, better than the design goal of 120 ps at the smallest angles (shortest counters) and 250 ps at angles above 90 degrees (longest counters) [59].

III.2.4 Electromagnetic calorimeter

A calorimeter is an experimental apparatus that measures the energy of particles traversing it. Some types of particles initiate a particle shower upon entering the calorimeter and the sum of all particle energies is collected and measured, in order to determine the energy of the original particle. The energy of a neutral particle can be measured this way by measuring the energy of the shower. The entire energy may be deposited and thus measured, or it may be sampled. Two types of calorimeters are generally used: an electromagnetic calorimeter, which is designed to measure the energy of particles that interact primarily via the electromagnetic interaction, and a hadronic calorimeter, the main focus of which is particles interacting via the strong nuclear force. Both calorimeters can be sampling calorimeters, in which the particle shower is created by one kind of material, but the detecting part is made of a different kind of material.

Two electromagnetic calorimeters are used in CLAS: the forward electromagnetic calorimeter (EC), which covers the θ range up to 45°, and the large angle electromagnetic calorimeter (LAC), which covers θ between 45° and 75° in sectors one and two, providing 120° coverage in ϕ.

The main functions of the EC are detection of and triggering on electrons at energies above 0.5 GeV, detection of photons at energies above 0.2 GeV, and detection

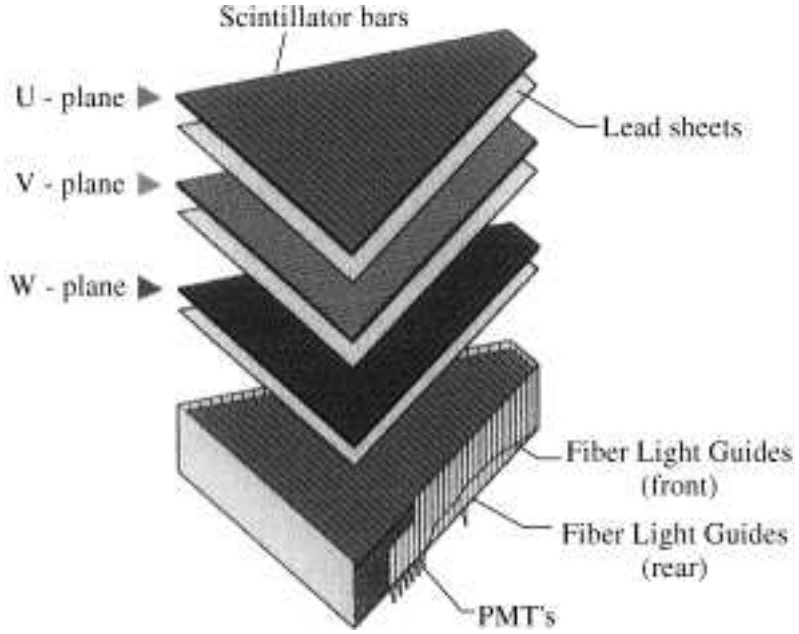

FIG. 42: Exploded view of one of the six CLAS EC modules [60].

of neutrons. It is made of alternating layers of scintillator strips and lead sheets with a total thickness of 16 radiation length, with total thicknesses of 39 cm of scintillator and 8.4 cm of lead per module.

A module consists of 39 layers with 10 mm of scintillator and 2.2 mm of lead in each layer. The area of each successive layer of scintillators increases linearly with increasing distance to the target. Each scintillator layer consists of 36 strips parallel to one side of the triangle, with the orientation of the strips rotated by 120° in successive layers (see figure 42). The three orientations (U, V, and W), with 13 layers in each direction, provide spatial information on the location of energy deposition. In each of the sectors, EC scintillators are divided into two groups: 15 layers closer to the target make up the inner calorimeter, 24 layers further from the target make up the outer calorimeter. This additional subdivision facilitates longitudinal separation of deposited energy.

The energy resolution of the EC for electrons can be parameterized as

$$\frac{\sigma}{E} = \frac{10.3\%}{\sqrt{E}} \tag{87}$$

with a negligible constant term [60]. The sampling fraction is approximately 0.3

for electrons of 3 GeV and greater, and for smaller energies, there is a monotonic decrease to about 0.25 for electrons of 0.5 GeV. The average rms resolution is 2.3 cm for electron showers with more than 0.5 GeV of energy deposited in the scintillator. The timing resolution of EC for electrons averages to 200 ps over the entire detector [61]. Although the EC is capable of detecting both electrons and hadrons, a larger fraction of the particle energy is deposited in the EC in the case of electrons via a bremsstrahlung-pair production "shower", than in case of hadrons.

The LAC provides detection of scattered electrons and neutral particles such as neutrons and photons coming from radiative processes or decays. It was not used in the BONuS experiment.

III.2.5 Target

A 7 atmosphere deuterium gas target 284.1 mm long (with an active length, within the BONuS detector, of 169.4 mm) and 6.1 mm in diameter was used in the BONuS experiment (see figure 43). It was constructed from a 50 micron kapton wall with aluminum endcaps. Four centimeters of the target adjacent to the upstream endcap were enclosed by an aluminum shroud, which prevented slow particles from the upstream window from entering the detector. The target cell was surrounded by helium gas at atmospheric pressure. This kept the material density low, thus keeping the material that spectator protons had to traverse on the way to the detector to a minimum, while still allowing a surrounding gas detector to have thin windows. Some helium target contamination originating from this setup was a necessary evil, addressed in the analysis. Hydrogen and helium targets were used for calibration purposes. The target gas system was static, *i.e.* the system was purged and charged with the appropriate gas, then valved off at the appropriate pressure. At each target gas exchange, the system was flushed a few times to minimize old gas presence in the new target gas, but it could not be done perfectly and so provided a possible source of errors, which are taken care of in the data analysis.

The target was located in the beam line at z = -58.0 cm in the CLAS coordinate system. The upstream end of the tube was fixed to an aluminum cylinder that provided gas plumbing. The target was surrounded by the BONuS RTPC (see section III.4) and the DVCS solenoid (see section III.2.6). The downstream end of the tube extended into a larger cylindrical volume filled with helium to minimize electron interactions downstream of the target.

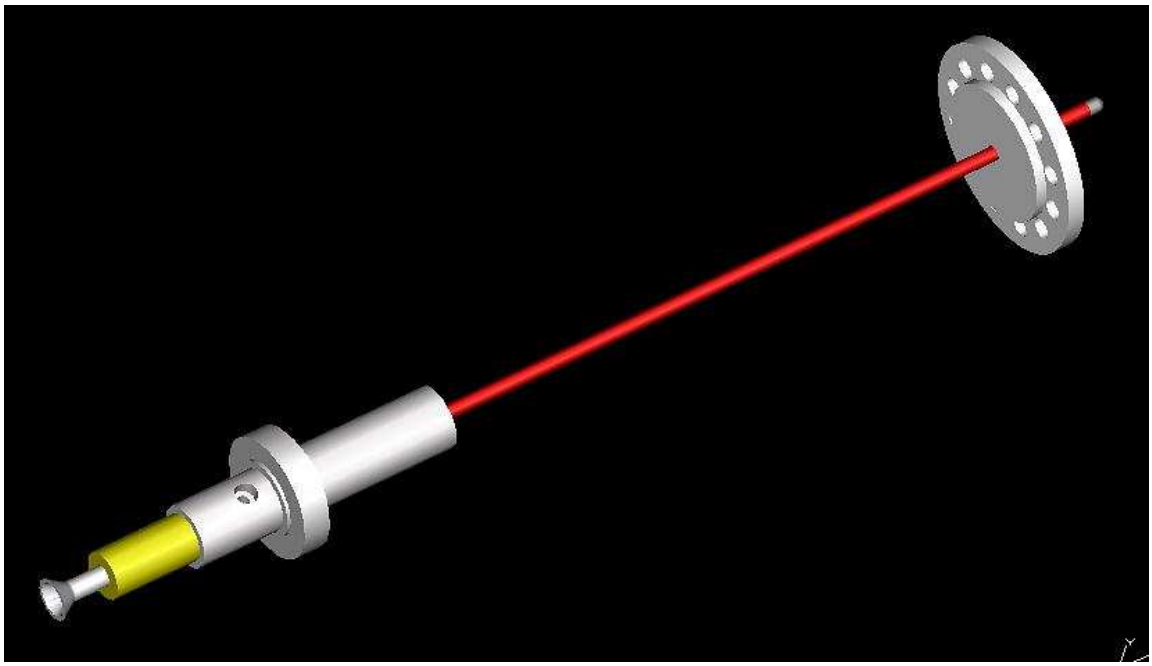

FIG. 43: Target tube with fixtures attached.

III.2.6 DVCS magnet

An existing solenoid magnet constructed for another experiment[d] was used to prevent Moeller electrons from getting into the RTPC sensitive volume (see figure 48) and to create trajectory curvature for spectator protons thus making momentum measurements possible.

The magnet is a superconducting magnet, designed and built in Saclay. It provides a 4.7 T nominal field at its center point. An additive superconducting compensation coil ensures external magnetic shielding. To reach the requested nominal field, the maximum usable current is 550 A. See table 4 for the compilation of magnet characteristics.

[d] An older experiment was dedicated to Deeply Virtual Compton Scattering (DVCS), hence the "DVCS magnet" name.

TABLE 4: DVCS magnet dimensions.

Aperture diameter	270 mm
External diameter	910 mm
Magnet length	910 mm
Total length	2776 mm
Total height	1661 mm
Total width	1143 mm
Cold mass at 4 K	700 kg
Cold mass at 50 K	200 kg
Total mass	1500 kg
Liquid helium capacity	65 liters

III.3 RADIAL TIME PROJECTION CHAMBER

As was mentioned earlier, to identify events in which a proton is a mere spectator to the electron-neutron collision, we need to select events in which a scattered proton is backwards moving and possesses a low (around or below 100 MeV/c) momentum. To register such protons, we need a detector that would provide good coverage in the backward (with respect to the direction of the electron beam) hemisphere, and be close enough to the target to be able to detect heavily ionizing low energy protons before they get stopped. A Radial Time Projection Chamber (RTPC) utilizing Gas Electron Multipliers (GEMs) was specially constructed for the experiment to fulfil these requirements.

III.3.1 Time projection chambers

The time projection chamber (TPC) is an ionization detector capable of providing a complete 3D picture of the particle trajectory in the detector volume as well as particle identification through its specific energy loss, dE/dx. Both gas and liquid sensitive volumes are used. The TPC combines concepts from both Multi-Wire Proportional Chamber (MWPC) and drift chamber.

Figure 44 depicts a scheme of a classical TPC, based on the one invented by Dave Nygren in the late 1970s [62]. The shown configuration represents a gas filled cylinder with a thin cathode plane at the center producing a strong electric field along the axis of the TPC. A magnetic field parallel to the electric field is applied by a solenoid (not shown).

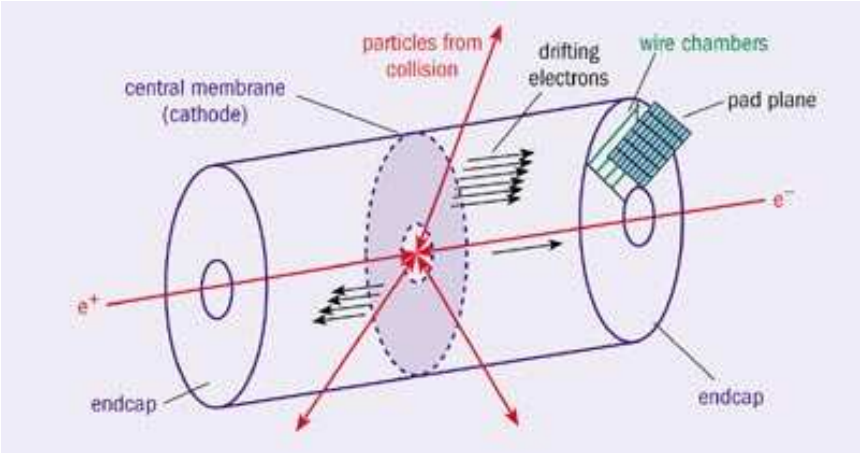

FIG. 44: The classical TPC with gaseous sensitive volume.

Charged particles produced in the center of the TPC move through the sensitive volume ionizing molecules. The produced ionization electrons drift to one of the two endcaps. The solenoidal magnetic field minimizes transverse diffusion of the electrons (which is necessary since the drift path can reach meters) and bends the charged particles allowing the momentum measurement.

The endcaps are divided into six sectors, each one containing a MWPC. Anode wires of the MWPCs detect drift electrons providing one of the three needed space coordinates of the charged particle trajectory. The second coordinate is determined by cathode pads located under the wires. Using the center-of-gravity method (basically looking at the way the charge from the signal was shared between pads), this coordinate can be determined with great accuracy. The third coordinate is given by the drift time of the drift electrons in the same fashion it is done in drift chambers. Thus, the full particle trajectory is reconstructed in three dimensions.

When an electron produces an avalanche on an anode wire, a cloud of positively charged ions stays behind, in the drift volume. To prevent the distortion of the detector electric field by these ions, a grid at ground potential is placed before the anode wires. It captures the positive ions that attempt to drift back towards the cathode.

Since the charge collected at the endcaps is proportional to the energy loss of the particle, the signal amplitude from the anode wires also provides the information

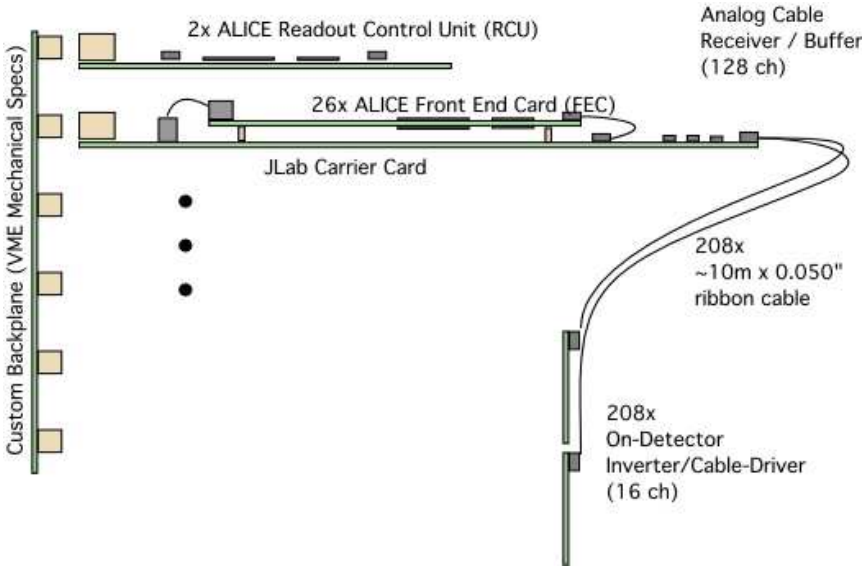

FIG. 45: BONuS data readout scheme.

on the specific energy loss of the particle. Since the momentum of the particle can be found from the curvature of its trajectory in the magnetic field, the particle can be identified. This requires sufficient resolution in dE/dx, necessitating collecting huge amounts of information and thus imposing a condition on how slow the readout can be. The readout equipment progressed from using charged coupled devices in earlier experiments to a switched capacitor array, and then to custom integrated circuits, which can read out data 1000 times per second, built for a huge TPC used in the ALICE heavy-ion experiment. The ALICE readout was used in the BONuS experiment (see figure 45).

Nowadays, two new technologies are replacing wire chambers in TPCs: the aforementioned GEMs and Micromesh gaseous structure chambers (Micromegas). GEMs represent thin plastic foils, metal coated on both sides, with holes punched through them and potential difference delivered to the two sides of the foil. Micromegas use a thin metal mesh instead of anode wires. Both GEMs and Micromegas are flexible, relatively low cost structures, which can be used in a variety of detectors and, as an additional benefit, can be placed very near readout pads decreasing charge diffusion. The BONuS experiment used the GEM technology.

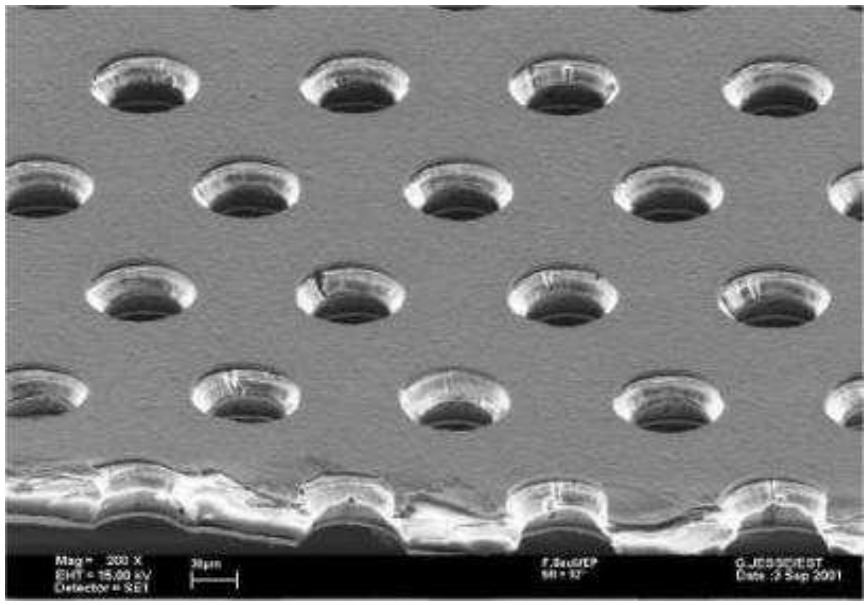

FIG. 46: An enlarged view of a GEM electrode. The diameter of the holes is 50μm.

Gas Electron Multipliers

GEMs are a new electron multiplication technique developed at CERN [65]. They combine robustness, low cost, high rate capabilities, can be used in detectors of varying shapes, and possess high energy resolution and space localization accuracy. Some advantages of using GEMs over the conventional wire chambers include the elimination of wire sag, and the possibility of placing them very closely to readout pads, thus reducing diffusion after amplification. Also, positive ions generated in the avalanche, naturally drift away from the amplification region, eliminating charge build-up.

A GEM consists of a thin, metal-clad chemically pierced polymer foil, with density of holes reaching over 50 per 100 mm^2 (see figure 46). After a potential difference is applied, electrons released by the gas on one side of the foil drift into the holes, multiply, and drift into the collection region. Thus, each hole acts as a proportional amplifier (see figure 47). The multiplier can be used as an individual detector or as a preamplifier in a many foil structure.

The main characteristics of GEM detectors [66], [67]:

- Operate with many gases, including noble;

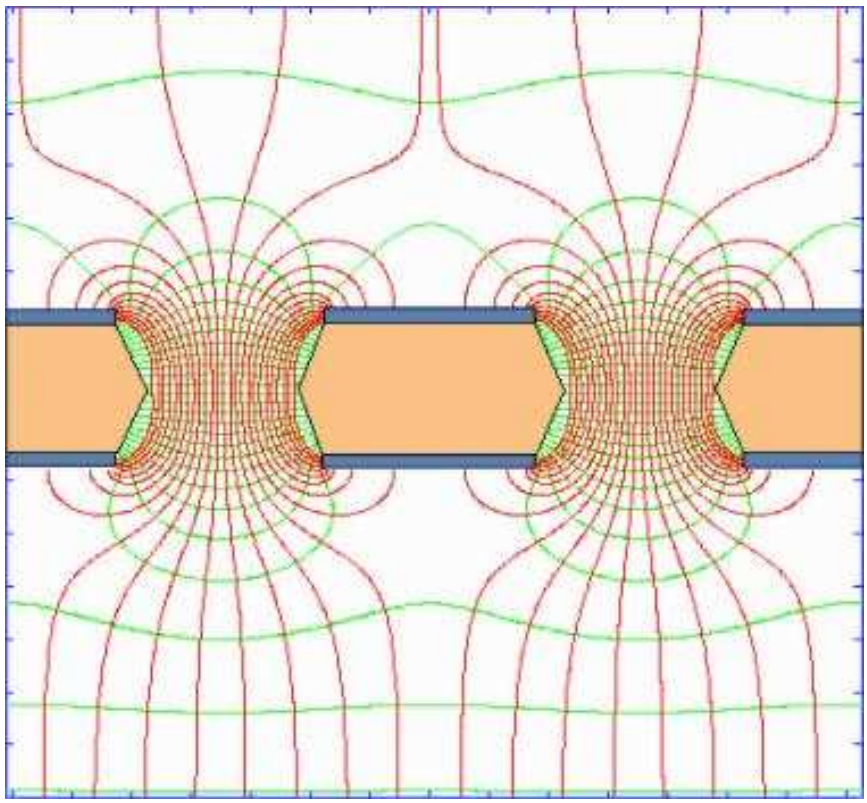

FIG. 47: Electric field lines and equipotential lines in GEM holes.

- Proportional gains higher than 10^5 are possible;
- Energy resolution 18% FWHM at 5.9 keV;
- Space localization accuracy better than 60μm RMS;
- Active areas up to 1000 cm^2;
- Rate capability higher than 10^5 counts/mm^2 sec.

Due to these characteristics and the aforementioned robustness, low cost and flexibility, GEMs have become a popular choice as amplifiers for modern detectors. The BONuS experiment became the first experiment to use curved GEMs. Multiple tests were performed to verify their satisfactory performance, and they were found adequate for the task.

III.4 BONUS RTPC

Sometimes longitudinally drifting electrons may not be optimal. Some collaborations like STAR [63] and CERES [64] have built and used TPCs in which electrons drift radially outwards from a cylindrical central cathode to the anode located on a concentric cylinder. Such TPCs are called Radial Time Projection Chambers (RTPCs). The electric and magnetic fields are no longer parallel, which leads to complex electron drift trajectories. Curved pad planes are then required. For these reasons RTPCs have a more complex structure and poorer resolution than their non-radial counterparts.

The spectator protons of interest for BONuS have momenta of 70 to 120 MeV/c. At these energies, protons are very heavily ionizing particles, which can be stopped by little material. This requires the use of as low density detectors as possible (the same considerations affect the target design, as was previously mentioned). This consideration suggests the use of TPCs, since they have inherently low mass density.

The detector had to surround the beamline and fit inside the available DVCS solenoidal magnet. The magnet length was less than its diameter, and so it did not have magnetic field lines parallel to each other over a reasonable range, complicating the use of an axial TPC. Furthermore, forward moving high-momentum particles, which were detected with CLAS, required minimizing the endcap density, the region where a lot of equipment is normally situated in axial TPCs. The natural solution to

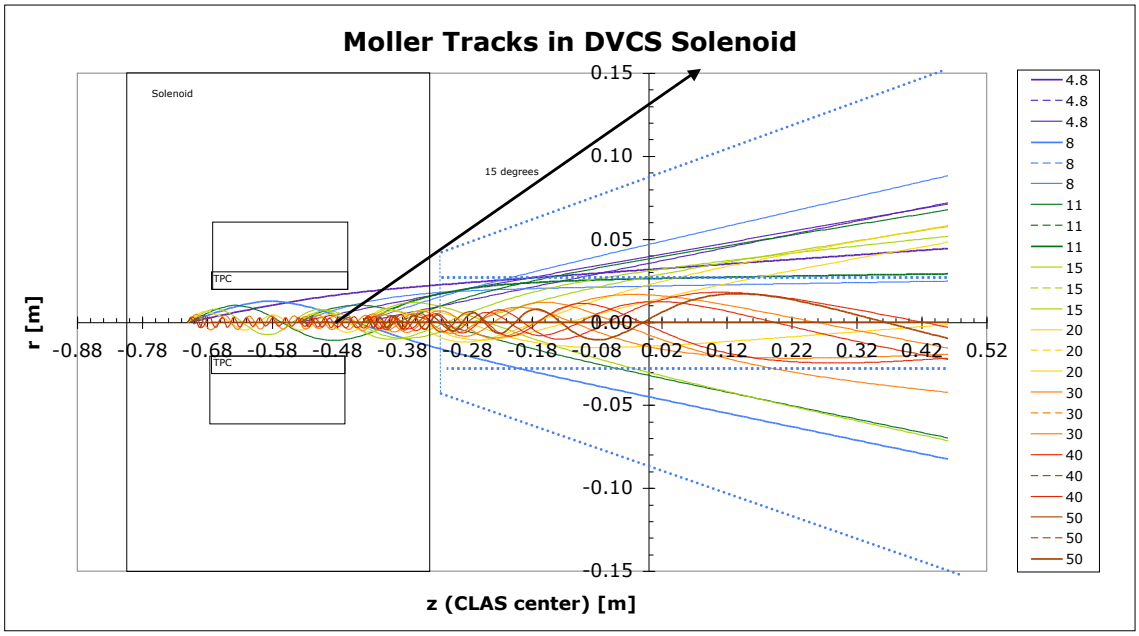

FIG. 48: Simulation of Moeller tracks in the DVCS solenoid (S. Kuhn). Moeller tracks at different angles to the axis (angle values in degrees are shown in the table to the right of the picture) are shown. The RTPC outline between z of -0.48 and -0.68, and between r of $\pm$0.03 and $\pm$ 0.06 is shown. A Moeller catcher that prevents the tracks from getting into the CLAS detector is shown with a dashed blue line.

these problems was to use an RTPC. The last constraint on the RTPC was the necessity to stay clear of the Moeller electrons (see figure 48), thus making it impossible to put it too close to the target.

Figure 49 shows the BONuS RTPC. The 7 atmosphere gas target is shown in the middle. The detector is situated close to the target, with its center moved backwards with respect to the center of the target for better coverage of the backwards hemisphere, where spectator protons are expected. Upon exiting the target and traversing the volume filled with 1 atmosphere helium gas (providing low mass density volume for spectator protons to pass and Moeller electrons to escape), the proton passes a ground plane that was located at the radius of two centimeters, and then the cathode surface located at the radius of three centimeters. Upon traversing the cathode, the proton enters the sensitive volume, filled with an approximately 80% He/20% dimethyl ether (DME) mixture, at the radius of 30 mm from the central

axis. This 30 mm distance allowed plenty of space for Moeller electrons to escape without entering the sensitive volume (see figure 48). Having helium as the main component of the mixture provided the necessary low density, which minimized the energy loss of the slow protons. When traversing the sensitive volume, the spectator ionizes the gas and the released electrons drift towards the GEMs, where they are multiplied and delivered to readout pads. The drift region of the RTPC was kept at 1500 V for all runs (see table 5 for voltages on different components). The resulting electric field produced a sufficiently short clearing time in the drift region without making the cathode voltage so high that a breakdown could occur. The GEM gain was set at a maximum voltage at which non-linearities (saturation) did not occur for slow spectator protons. This made the RTPC fairly insensitive to the lighter ionizing particles (i.e. electrons) [68].

The first GEM layer was at 60 mm radius, and the padboard was at 69 mm radius, after two more GEM layers, with the space between the padboard and the solenoidal magnet reserved for preamplifiers and cables. The interior walls of the drift region were made of printed-circuit boards patterned with metal traces forming the field cage necessary to make the drift field between the concentric cylinders as close to that between two infinite concentric cylinders as possible. A ground plane was located at the radius of two centimeters.

The RTPC was made of two half-cylinders, each of which represented a self-supporting structure. Figure 50 shows the exploded view of the detector, with each half having supports for the window, cathode, cascade of three GEMs, and padboard. The length of the detector was 20 cm. Phi (azimuthal angle) coverage was around 300°. Wedges on the top and bottom of the assembly serving for combining the halves covered the rest of the phi acceptance. The readout pads had dimensions of 5 mm in the phi direction, thus covering approximately 3.5°, and 4.45 mm in the z direction (along the axis of the cylinder). Pad rows along the axis of the RTPC were shifted with respect to each other to minimize the probability of a whole track being contained in the same row of pads, thus improving the track resolution. The RTPC was capable of detecting spectator protons with momenta from 70 to 150 MeV/c. Below this range, protons are stopped too soon to leave a substantial track in the RTPC, and above that range, protons are too fast and the curvature of their trajectories is not large enough to confidently reconstruct their momenta (often, they are seen as infinite momentum particles).

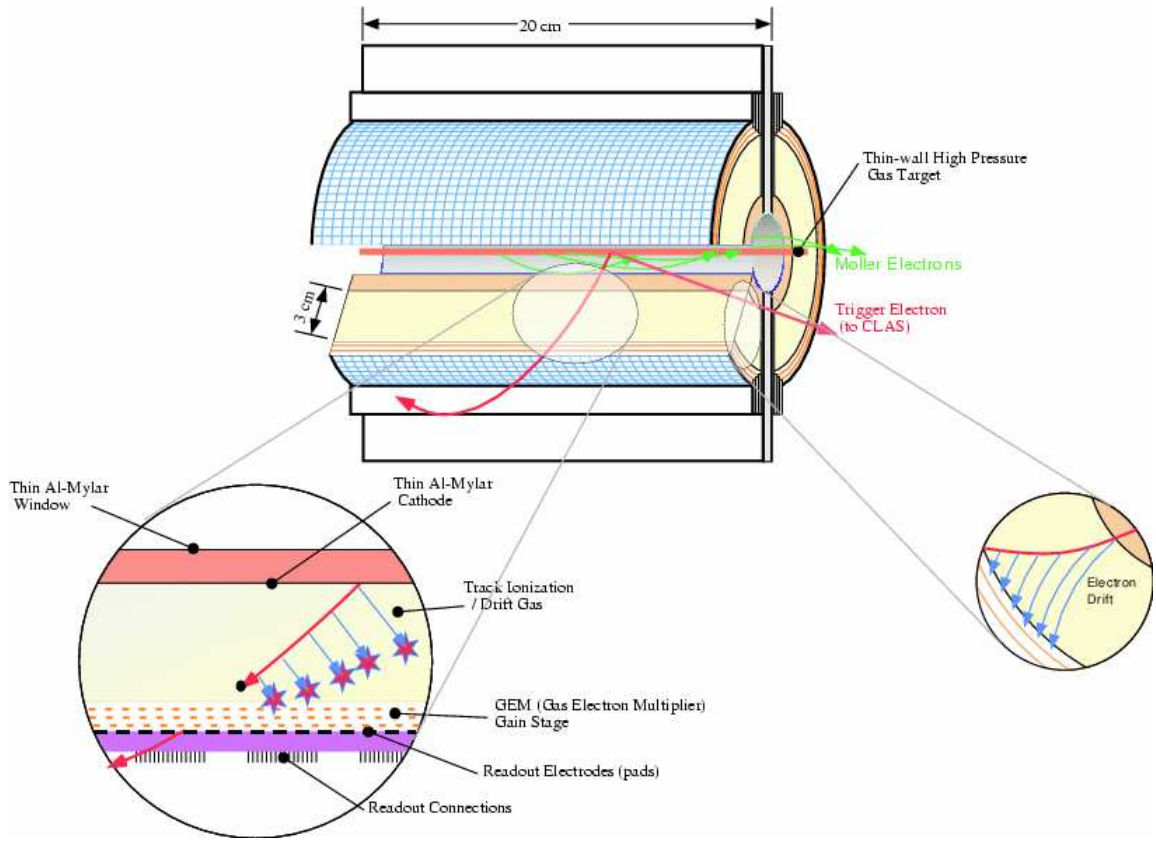

FIG. 49: Schematics of the BONuS RTPC. See text for details.

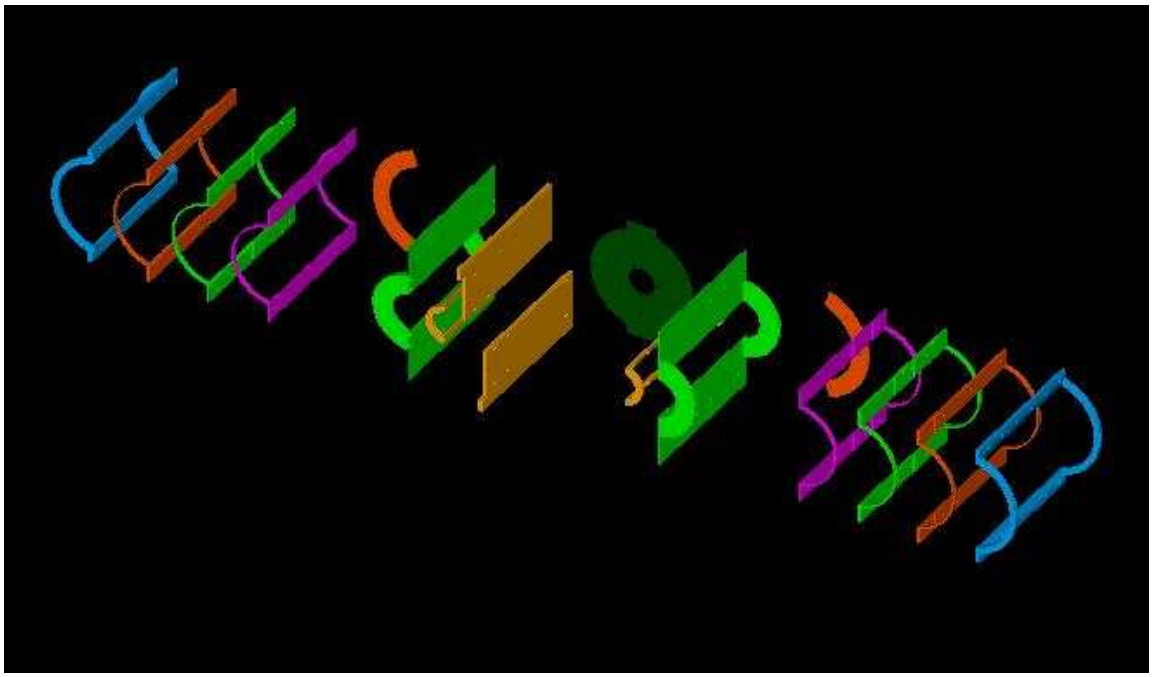

FIG. 50: Exploded view of the BONuS RTPC. Supporting structures for the window, cathode, three GEMs, and padboard in both half-cylinders, as well as the central support combining two halves, are shown.

Figure 51 shows an RTPC event as seen on the event display. Two candidate tracks curved by the solenoid field are shown. The charge collected on the readout pads was traced back to the time when it was released from the gas by ionizing it, and converted to the distance from the beam axis by the usual TPC methods (see section III.3.1 for those). The time to distance conversion will be discussed as part of the preliminary data analysis below. The other two coordinates were given by pad locations (after correcting for the electron drift in the combined $\vec{E}$ and $\vec{B}$ fields). The size of the rectangle indicates the amount of charge collected on a pad.

Each of the pads was connected to a connector, each of which carried sixteen pad signals and four ground connections and supported a preamplifier card. Two hundred cards were required to instrument the whole RTPC [68]. The preamplifier cards projected radially from the surface of the detector and connected to the ribbon cables in such a way that the cable length was parallel to the chamber axis thus increasing the electronics package density. The readout system was borrowed from the ALICE experiment (ALICE TPC readout - ALTRO, see figure 45), with some necessary modifications required due to the shortage of space in the BONuS experiment. ALTRO readout controllers (U2F) supervised the communications in the VME crates (which accepted RTPC signals) and transferred the compacted digital data to a pair of single-board (VME) computers via USB-2 interfaces. These processors served as Readout Controllers within the standard CLAS data acquisition system. This system provided readout of approximately 1kB events at a rate of about 500 Hz.

The BONuS event readout was initiated by the standard CLAS electron trigger system selecting interactions with a high probability of having an electron track in CLAS. The data recorded for each event is composed of the times (114 ns samples) and amplitudes (10 bits) of all TPC pad signals above threshold for a time period extending from 1.7 μs before to 9.7 μs after a trigger. This interval is about 1.5 times the maximum drift time in the RTPC.

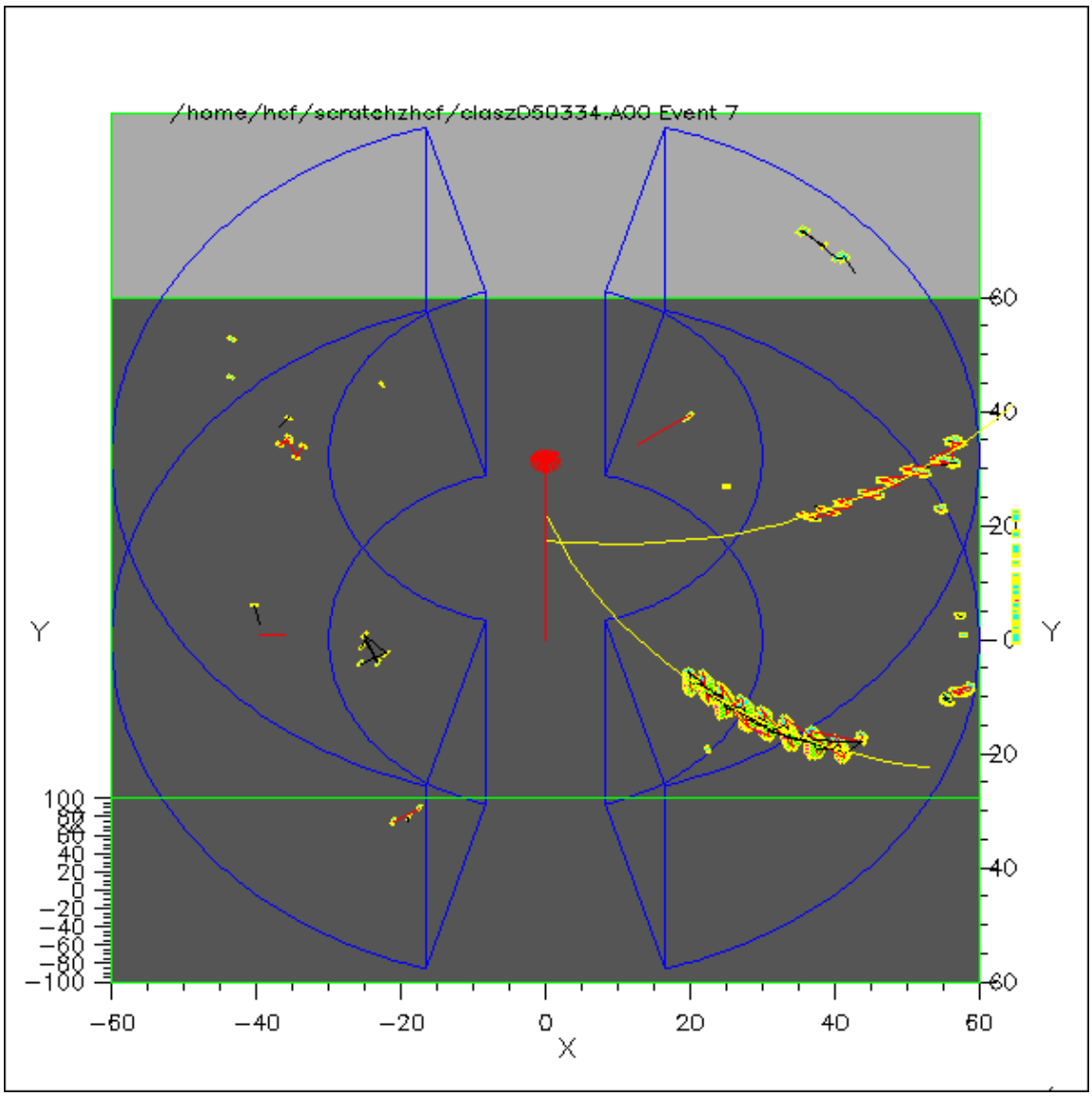

FIG. 51: An RTPC event.

TABLE 5: Supply settings and electrode voltages in the RTPC during operation of the experiment. The suffixes on the GEM label refer to the inner (i) and outer (o) surfaces of the GEMs. All voltages are of negative polarity and are referenced to ground. The table is taken from H. Fenker [68].

Detector element	Heavily ionizing tracks		Minimum ionizing tracks	
	Left Half	Right Half	Left Half	Right half
HVPC-C	4550	4350	4950	4750
HVPC-G	3050	2850	3450	3250
Window	0	0	0	0
Cathode	4532	4329	4931	4729
GEM-1i	2869	2656	3242	3026
GEM-1o	2579	2374	2915	2705
GEM-2i	2087	1918	2359	2185
GEM-2o	1798	1642	2031	1871
GEM-3i	1143	1040	1292	1185
GEM-3o	845	764	955	871
Padboard	0	0	0	0

CHAPTER IV

DATA ANALYSIS

IV.1 RUNNING CONDITIONS

Overall, the BONuS experiment had 1350 runs, from run 49000 to run 50349, each of which with one to ten separate data files. In the following discussion I will ignore the first 462 runs at the beginning of the running period that were recorded at the time of the experiment setting up and fine tuning. The real data were recorded in runs 49462 - 50349.

The BONuS experiment recorded data at four beam energies with nominal energy values (the ones written in the database, see section IV.2.5 for more on the actual values of the beam energy) of 5.268, 4.226, 2.142 and 1.100 GeV. Overall around 861 million triggers were collected on the deuterium target and around 95 million triggers were collected on the hydrogen target. Table 6 has a detailed list. Additionally, empty target runs for background estimation and ^{4}He runs for evaluation of ^{4}He contamination were conducted. Several dedicated runs for DC alignment and TOF calibrations were also conducted.

Each of the magnets had two settings during the experiment: the CLAS toroidal magnet was used at 1500 A and 2250 A, whereas the DVCS solenoid magnet was used at 400 A (corresponding to 3.5 Tesla field) and 534 A (corresponding to 4.7 Tesla field). The trigger for the BONuS experiment was provided by the electron in CLAS. A coincident signal from the CC and the EC formed the CLAS trigger with thresholds of 75 mV for CC, 72 mV for the inner calorimeter (inner EC) and for the outer calorimeter (outer EC) the threshold was set at 147, 200, and 260 mV at different times.

On the RTPC side, for all physics runs, the magnitude of the cathode power supply voltage was maintained 1500 V higher than the GEM supply voltage. See table 5 for working voltages on the RTPC. Additional calibration RTPC runs were conducted with raised voltages in order to provide sensitivity to minimum ionizing particles. The detector gas was a mixture of He and DME with approximately 80% He and 20% DME.

TABLE 6: Triggers collected in the BONuS experiment.

Beam energy, GeV	Triggers, millions	
	D_2 target	H_2 target
1.100	8	5
2.142	91	15
4.226	306	11
5.262	456	64

IV.2 PRELIMINARY ANALYSIS

Detectors in CLAS measure relevant quantities by producing electric impulses that have to be further interpreted as corresponding to particular energy, time, etc., measurements. The formidable task of converting voltages that are produced by the detectors to the physical quantities of interest with one to one correspondence is called calibration of the detectors. The complicated structure of CLAS, which has many detectors and large luminosity makes this procedure involved.

IV.2.1 Drift chambers

The drift chambers (see section III.2.1) are an important part of CLAS providing, in particular, momentum information for the particles passing through the detector. Due to stringent requirements on the knowledge of the momenta, drift chambers should be aligned and calibrated to a high degree of accuracy.

Drift chamber alignment

The relative wire to wire and chamber to chamber positions are needed to determine momenta of particles traversing the drift chambers (DC). The design momentum resolution of $\delta p/p \leq 0.5\%$ at a particle momentum of 1 GeV [69] requires knowledge of hit positions along a track to be better than 0.8 mm [70]. However, it was impossible to install the DC with an accuracy of a few hundred microns. Hence the necessity to verify the relative positions of the chambers after each removal and/or repair (see references [70], [71] for some of the noted cases of alignment procedures being performed). Both the first region of DC and one of the sectors of the third region had been moved before the Bonus experiment, thus necessitating DC alignment for accurate data analysis. The procedure finds offsets of the DC geometry from the

design geometry and writes those offsets to the database used in data processing. There are six offsets: shifts along each of the coordinate axis (dx, dy, dz) and rotations along each of the axes (θ_{x}, θ_{y}, θ_{z}).

The following was assumed:

1. Wire positions inside a single DC region and sector are fixed.
2. Intra-sector alignment only will be performed.
3. Region one DC will be used as a reference since they were constructed as a single unit with sector to sector accuracy of 0.2 mm [70].

The torus magnetic field was turned off for the alignment run. In its absense, particle trajectories should be straight lines. Thus, by minimizing the deviation of the trajectories from a straight line the best set of offset parameters was found. The minimized quantity was:

$$\chi^2 = \sum_{tracks} \sum_{hits} \frac{(|D_{track,hit}| - |D_{hit}|)^2}{\sigma^2_{track,hit} + \sigma^2_{hit}}, \tag{88}$$

where $D_{track,hit}$ is the calculated distance of closest approach of the track to the wire, D_{hit} is the drift distance as reported by the x_vs_t function for that wire (see section IV.2.1), $\sigma_{track,hit}$ is the uncertainty of the track position at that hit, and σ_{hit} is the time based resolution of the hit. The sum of spacial residuals of the hit

$$Res = \sum D_{track,hit} - D_{hit} \tag{89}$$

was used to represent the quality of the alignment parameters.

As mentioned above, region 1 was used as a reference. Then one of the other regions (2 or 3) was fitted, and both of them were used as the reference for fitting the remaining region. The sequence of region fitting was varied and results compared to achieve the best possible alignment. Data with and without having applied the DC distance versus time calibration (see section below for description) were compared in order to resolve differences between methods described in references [70] and [71] (R. Feuerbach [70] did not perform the DC calibration on the alignment run, noting that it could have led to wide residual distributions for region 2, whereas S. Morrow and M. Mestayer [71] claim that performing a calibration for the alignment run was an improvement over the previous technique).

After performing the above-mentioned procedure outlined in references [70] and [71], offsets in the database were altered by hand to improve the alignment. Figures 52 and 53 illustrate the residual distributions before and after the described procedure. The residuals are much closer to each other and to zero in the right panel, indicating that the alignment was successful.

Drift chamber calibration

The reconstruction of a track in the DC is performed in two stages: hit-based tracking and time-based tracking.

In hit-based tracking the wires that got signals from a passing particle are combined in segments by superlayers, which are subsequently linked with each other. The physical positions of wires are used as points along the trajectory. Since the drift cell size is small and the number of wire layers is big, the track momentum can be reconstructed with a resolution of 3-5% [72].

We need a better resolution than that. For this, we need to know a particle trajectory better, namely where exactly the particle traversed each of the drift cells. Using information from other detectors, it is possible to determine the drift time for ionization electrons from the particles passing to reach the sense wire with great accuracy. Then drift times can be converted to drift distances (see below). Finally, the parameters for the track are adjusted in the fit procedure that constitutes time-based tracking.

The drift time for a hit can be determined by

$$t_{drift} = t_0 - t_{start} - t_{TDC} - t_{prop} - t_{walk}, \tag{90}$$

where t_0 is a fixed delay for a given wire determined by hardware characteristics such as cable lengths, t_{start} is the event start time provided by the time-of-flight system and corrected for the calculated flight time of the electron using a momentum estimate and the distance from the target to SC, t_{TDC} is the raw time as measured by the TDC (time-digital converter), t_{flight} is the flight time from the reaction vertex to the wire, t_{prop} is the signal propagation time along the wire, and t_{walk} is a time-walk correction. From this, the initial estimate of the distance from the wire at which the particle passed can be made. The remaining ambiguity, namely on which side of the wire the particle passed, can be resolved within the superlayer by comparing χ^2 assuming it passing on one and the other side.

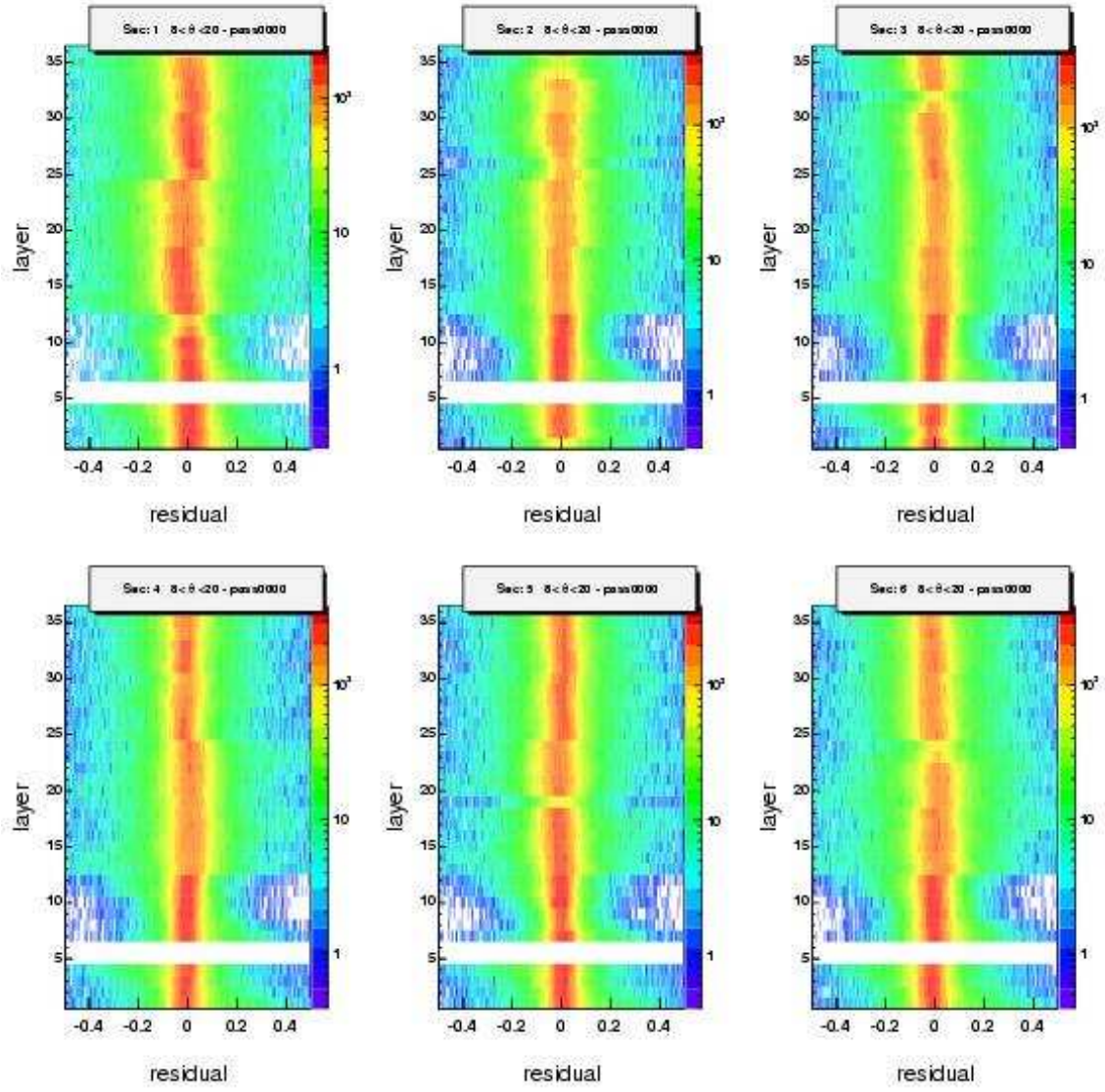

FIG. 52: Residuals for six sectors before the alignment.

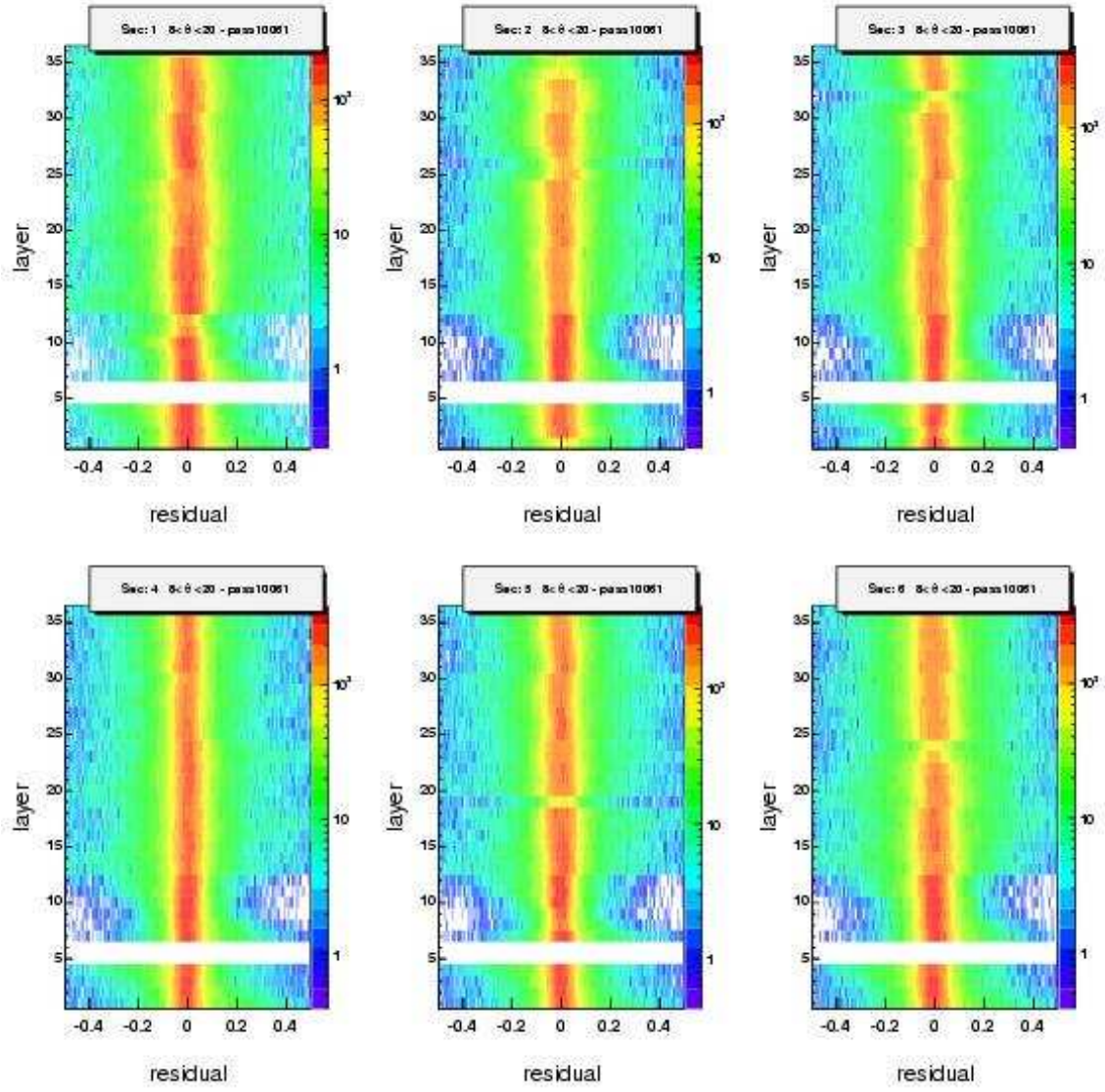

FIG. 53: Residuals for six sectors after the alignment.

Since the drift time-to-distance relationship is not constant, affected even by the weather outside, we need to review coefficients for the functions determining the time to distance relationship. These functions are:

$$x(\hat{t}) = v_0\hat{t} + \eta\hat{t}^p + \kappa\hat{t}^q, \tag{91a}$$

$$x(\hat{t}) = a\hat{t} + b\hat{t}^2 + c\hat{t}^3 + d\hat{t}^4 + (x_{max} - a - b - c - d)\hat{t}^5, \tag{91b}$$

where the power law form (91a) is used for region 3 and the polynomial form (91b) is used for regions 1 and 2. In equations (91a) and (91b) v_0 is the value of the saturated drift velocity near $t = 0$, $\hat{t} = t/t_{max}$ is the normalized time, where the normalization t_{max} is the drift time for tracks that pass near the outer edge of the drift cell, so that the ionization electrons drift for the longest time, and x_{max} is the cell linear size corrected for the local angle. Each of the equations has 4 parameters that are varied in the minimization procedure (η, p, κ, q, a, b, c, d).

The time-to-distance function has to satisfy the boundary constraint

$$x(\hat{t} = 1, \alpha) = C \cdot \cos(30^\circ - \alpha), \tag{92}$$

where the angle α is the track entrance angle and C is the cell size.

In the region 2 DC the inhomogeneous magnetic field rotates and shrinks the isochrones. To account for that, the effective entrance angle and maximum drift time have to be modified. The correction to the entrance angle is determined from a GARFIELD simulation:

$$\alpha_c = arccos(1 - aB), \tag{93}$$

where a is a constant and B is the magnetic field strength.

The maximum time is extracted directly from data and is parameterized as

$$t_{max}(B) = t_{max}(0) + bB^2, \tag{94}$$

where b is a constant and B is the magnetic field strength. At any given local magnetic field point, the time-to-distance function included an additional correction term $\beta(\hat{t})$ to describe the magnetic field dependence:

$$x(\hat{t}, \alpha, B) = x(\hat{t}, \alpha - \alpha_c, B_0) + (B - B_0)\beta(\hat{t}), \tag{95}$$

where B_0 is the average magnetic field value for the full fitted data sample. The magnetic field dependence is included only for region 2, since regions 1 and 3 are located outside the torus cryostats.

As a result of the minimization procedure, the values of the 4 parameters for each of the equations (91) and each superlayer are determined. In addition, the average local angle at which tracks enter the drift cells, the average magnetic field strength, t_0 and t_{max} are found.

The calibration was performed with the help of "dc3", the program developed by David Lawrence to automate and standardize the drift chamber calibration procedure. The up-to-date description of dc3 can be found at

`http://www-meg.phys.cmu.edu/\%7Ebellis/dc/dc3_manual.ps.`

The package itself was retrieved from CVS at /packages/reccal/dc3. The calibration procedure followed guidelines from the dc3 manual:

1. **Choosing runs for calibration.** As mentioned above, the drift time-distance correspondence can "drift" with time, thus necessitating the re-calibration of the parameters every once in a while. The DC calibration was performed for 7 runs more or less equally spaced over the BONuS run period with at least one calibration run corresponding to each beam energy and torus current combination. The chosen runs were: 49200, 49289, 49485, 49544, 49835, 50282, and 50333.

2. **Setting up the environment.** Necessary environmental variables were set up in the .cshrc file, the most important of which is the proper RunIndex, the SQL table, in which constants for the given run period are stored.

3. **"Cooking" chosen runs.** This jargon means subjecting the raw data, written to tape during the run period, to the reconstruction program that converted raw detector signals to physical quantities, reconstructed particle trajectories, identified particles, etc. This was performed by V. Tvaskis, our analysis coordinator at the time.

4. **Producing ntuple files using the trk_mon program.** This step consists of converting the "cooking" output into the particular form readable by the DC calibration program. This is done by running the *trk_mon* program. The program is run twice. When running the first time, only input and output files are given as parameters:

   ```
   trk_mon -ooutputfile.hbook inputfile.A00.00
   ```

By looking at histograms produced by this command, cuts on χ^2 and local angles are chosen. These cuts are then used in running the program for the second time. This second run produces cleaned ntuples (a particular form of storing data) ready to be used in the calibration.

5. **Fitting in DC3.** This is the heart of the calibration procedure; everything before this step was done to prepare files to use as an input to dc3.

   - *Finding T0.* $T0$ is the value of the time at which the calculated distance is equal to 0. It is primarily determined by passive cable delays and therefore needs to be determined only once per run period (barring some extraordinary changes in the CLAS setup). $T0$ was determined using *the leading edge distribution*, that is fitting to the leading edge of the time distribution.
   - *Finding Tmax.* Done by a simple click of a button, this means finding the time corresponding to 97% (default, can be changed) of the time integral for regions 2 and 3 , and corresponding to 99% (default, can be changed) of the time integral for region 1. Using this time as the limit of calibration as opposed to using time at 100% of the integral eliminates "edge effects" of the drift cells.
   - *Fitting.* After limits of the fits were determined in the previous steps, we can do the fitting itself. First, we choose the *xvst* fit to find the initial parameter set for equations (91a) and (91b) (later, we can use the *resid* fit to fine-tune the parameters). The fit is initially done for one sector of one superlayer, then the resulting parameters are copied for other sectors/superlayers to provide initial values for those, and the global fit is performed.
   - *Preliminary checking.* A table of χ^2 is generated to perform a preliminary check of the parameters.
   - *Write parameters to the database.*

6. **Checking calibration quality.** First we re-analyze raw data using the newly found parameters. Using the re-analyzed data, we then prepare files for *dc3*, and start the program. Using the *calibration quality* tab of the program interface, we can check the calibration quality. Average tracking χ^2 should be below 2.0,

the time based over hit based ratio should be around 0.7 or more, and the number of hits per time based track should be 30 or more.

See figure 54 for resulting DC resolutions for DC sectors in different superlayers. The resolutions are found as the RMS of the time residual distributions. The time residuals are found as follows

$$TRESI = abs(DOCA) - abs(DIST), \tag{96}$$

where $DOCA$ (Distance Of Closest Approach) is the distance from the fitted track to the sense wire; $DIST$ is the calculated (using drift time and other parameters) distance from the sense wire to the track. Both $DOCA$ and $DIST$ are signed quantities whose signs are determined by the side of the wire on which the track passed. The values shown are within the allowable limits of 500 microns when averaged over the sectors.

IV.2.2 Time of flight system

The time of flight (TOF) system in CLAS (see section III.2.3 for more) provides the timing information for charged particles in each event. Other detectors use this information, and thus the quality of data reconstruction heavily depends on how well the time of flight system is calibrated.

TOF calibration

The reconstructed time and energies in a scintillator of the TOF are given by (see reference [74])

$$t_L = c_{norm} \cdot (t_w - c_{LR}/2 + c_{c2c} + c_{p2p}) \tag{97}$$

$$t_R = c_{norm} \cdot (t_w + c_{LR}/2 + c_{c2c} + c_{p2p}) \tag{98}$$

$$\bar{t} = (t_L + t_R)/2 \tag{99}$$

$$E_L = \frac{k(A-P)}{M0_L} \tag{100}$$

$$E_R = \frac{k(A-P)}{M0_R} \tag{101}$$

$$E = \sqrt{E_L \cdot E_R} \tag{102}$$

$$y = \frac{v_{eff}}{2}(t_L - t_R - y_{offset}), \tag{103}$$

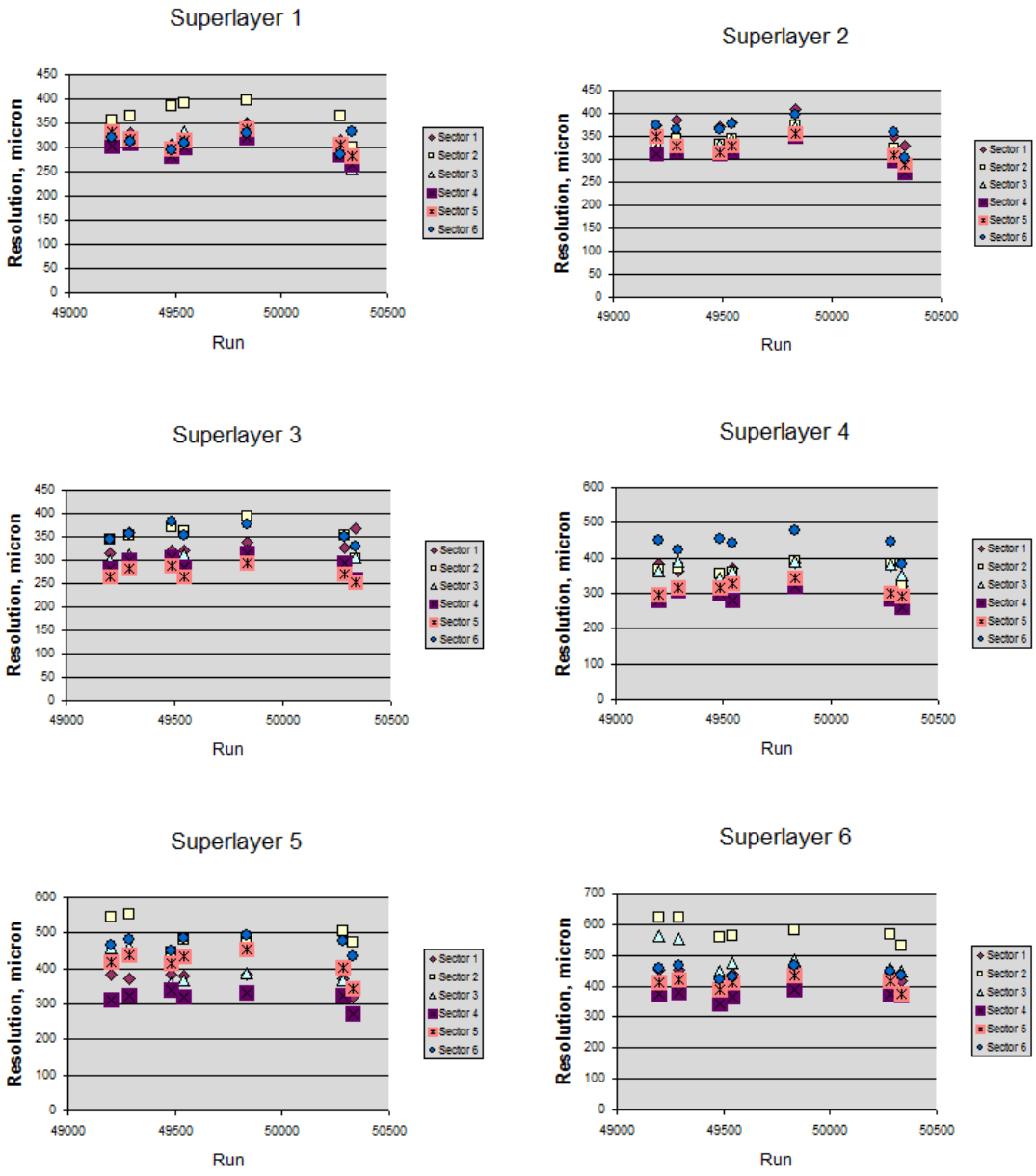

FIG. 54: DC resolutions after the DC calibration for six DC superlayers. The resolution for each of six sectors is shown for each of the superlayers. Points are shown for the runs used to do the calibration.

where t_L and t_R are adjusted times on the left and right PMTs, average time $\bar{t}$ is a position independent determination of time of particle impact, E_L and E_R are the normalized pulse heights on the left and right PMTs, E is a position independent measure of the energy deposited in the scintillator, and y is the position of the hit in the scintillator measured with respect to the center of the counter.

To compute these quantities the following quantities must be measured/calibrated

- Pedestals (P). The pedestal is the base voltage on an ADC channel when no data are present. It is measured by taking data with a pulse-trigger.

- TDC calibration constants c_0, c_1, c_2 are extracted from calibrating time:

$$t = c_o + c_1 T + c_2 T^2, \tag{104}$$

  where T is the raw time in units of TDC channels and t is the converted time in nanoseconds.

- Time-walk correction. Since the leading edge of the discriminator does not rise instantaneously, there is pulse-height dependent uncertainty due to the time the leading edge to rise. To account for this, the correction of the form

$$t_w = t - f_w\left(\frac{A-P}{Th}\right) + f_w\left(\frac{600}{Th}\right) \tag{105}$$

  is used, where Th is the channel corresponding to the leading-edge discriminator threshold of 20 mV ($\sim$ 35 channels), A is the raw value of the ADC, P is the pedestal, and $f_w(x)$ is the time walk correction function

$$f_w(x) = \frac{w_2}{x^{w_3}} \quad \text{if} \quad x < w_0 \tag{106a}$$

$$f_w(x) = \frac{w_2}{w_0^{w_3}}(1+w_3) - \frac{w_2 w_3}{w_0^{w_3+1}}x \quad \text{if} \quad x > w_0, \tag{106b}$$

  where w_0, w_2, and w_3 are fit parameters determined for each PMT using a laser calibration system.

- Left-right delay constants (c_{LR}) are the relative time reported by PMTs from the opposite ends of the same counter.

- Counter-to-counter offsets (c_{c2c}), also known as paddle-to-paddle constants, are relative time shifts of the measured times from counter to counter.

- Panel-to-panel offsets (c_{p2p}) are the offsets between scintillator panels (currently set to zero).

- Attenuation length (λ) is found separately for each counter. It is found from measuring pulse heights on the left and right PMTs

$$A_L - P = \frac{M0_L}{k} E_L e^{-y/\lambda}, \tag{107a}$$

$$A_R - P = \frac{M0_R}{k} E_R e^{y/\lambda}. \tag{107b}$$

- Effective velocity (v_{eff}) is the measured propagation time of light in each counter. It is defined relative to time t_0 at the center of the counter

$$t_L = t_o + y/v_{eff}, \tag{108a}$$

$$t_R = t_o - y/v_{eff}. \tag{108b}$$

- Pulse height normalizations on left and right PMTs ($M0_L$ and $M0_R$) are the peak height for minimum ionizing particles normally incident at the center of the counter.

- Pulser normalization (c_{norm}), the overall time scale for time measurements, measures the possible absolute scale offset of the pulser used in calibration runs with respect to the accelerator radio frequency (RF) time

The TOF system was successfully calibrated for BONuS by Narbe Kalantarians. Figure 55 shows the geometric mean (in ADC channels) of the minimum ionizing peak. The geometric mean is a position-independent handle on the energy deposition in the counter given as:

$$gmean = \sqrt{ADC_L \cdot ADC_R}, \tag{109}$$

where ADC_L and ADC_R are the left and right ADC values for a particular energy deposition. Figure 56 demonstrates how well the RF (radio frequency) offsets were calibrated.[a] This shows the overall timing resolution of the TOF, which is rather good according to figure 56. Figure 57 shows the ratio of logarithms of energy attenuation as reported by the right and left PMTs. The nice straight line indicates a satisfactory attenuation length calibration.

[a]RF offset is the difference between the predicted vertex time of electrons and the RF accelerator time.

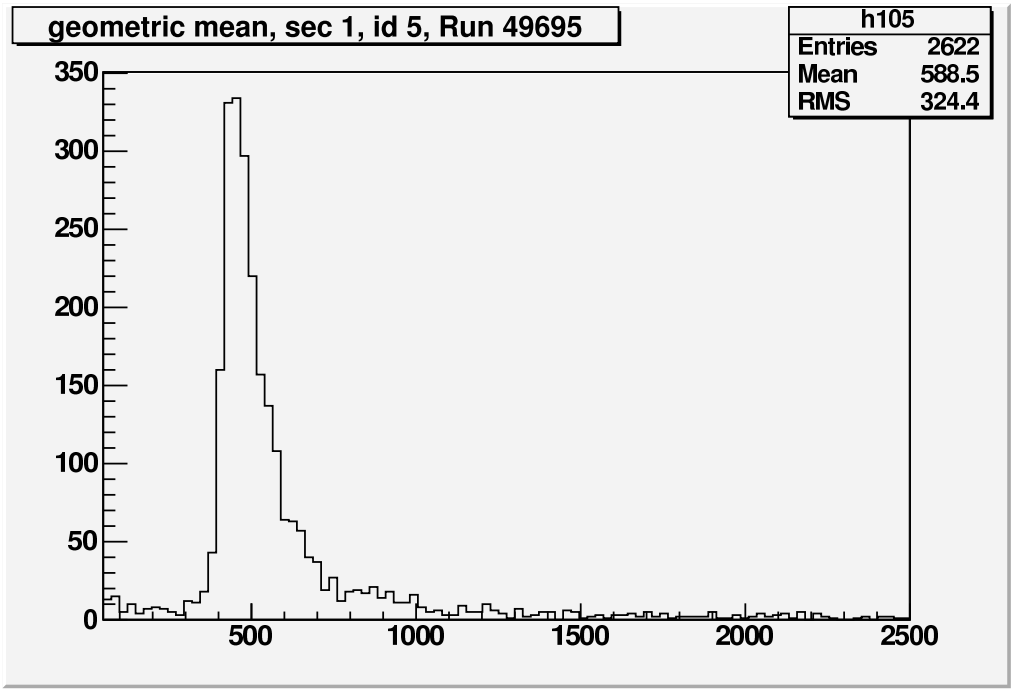

FIG. 55: The geometric mean in ADC counts for the fifth paddle of the first sector.

IV.2.3 Forward electromagnetic calorimeter

Distinguishing electrons from pions, which is one of the responsibilities of the electromagnetic calorimeter (EC) (see section III.2.4), necessitates a good energy resolution in the EC. The EC response to energy deposited should be independent of the place of the hit, which requires us to calibrate the EC before the actual data analysis.

EC energy calibration

In general, the energy of an electron passing through CLAS can be deduced using other detectors, thus making the EC calibration a seemingly trivial task, in which PMT (photomultiplier) gains need to simply be adjusted in such a way that the EC response matches the energy reported by the other detectors. Due to the complicated structure of the EC (see figure 42), each hit in the EC involves a minimum of 6 PMTs and the reconstructed energy can be represented as

$$E_{tot} = \sum_{s=1}^{2} \sum_{v=1}^{3} \sum_{n=1}^{N} E_n^{sv}/f_s, \tag{110}$$

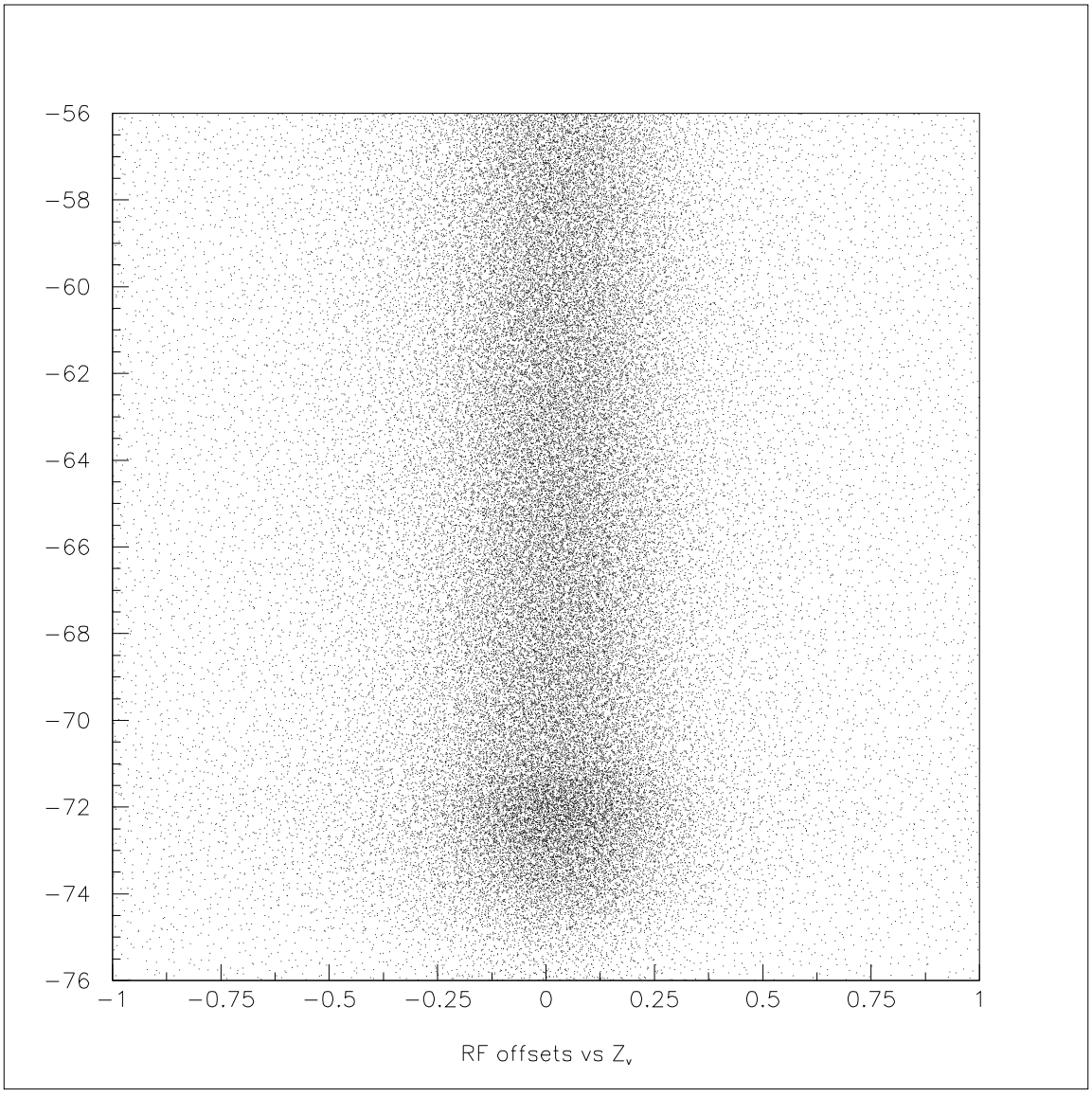

FIG. 56: The RF offset (horizontal axis) in ns *vs* the vertex z coordinate (vertical axis) in cm. Data are for run 49560.

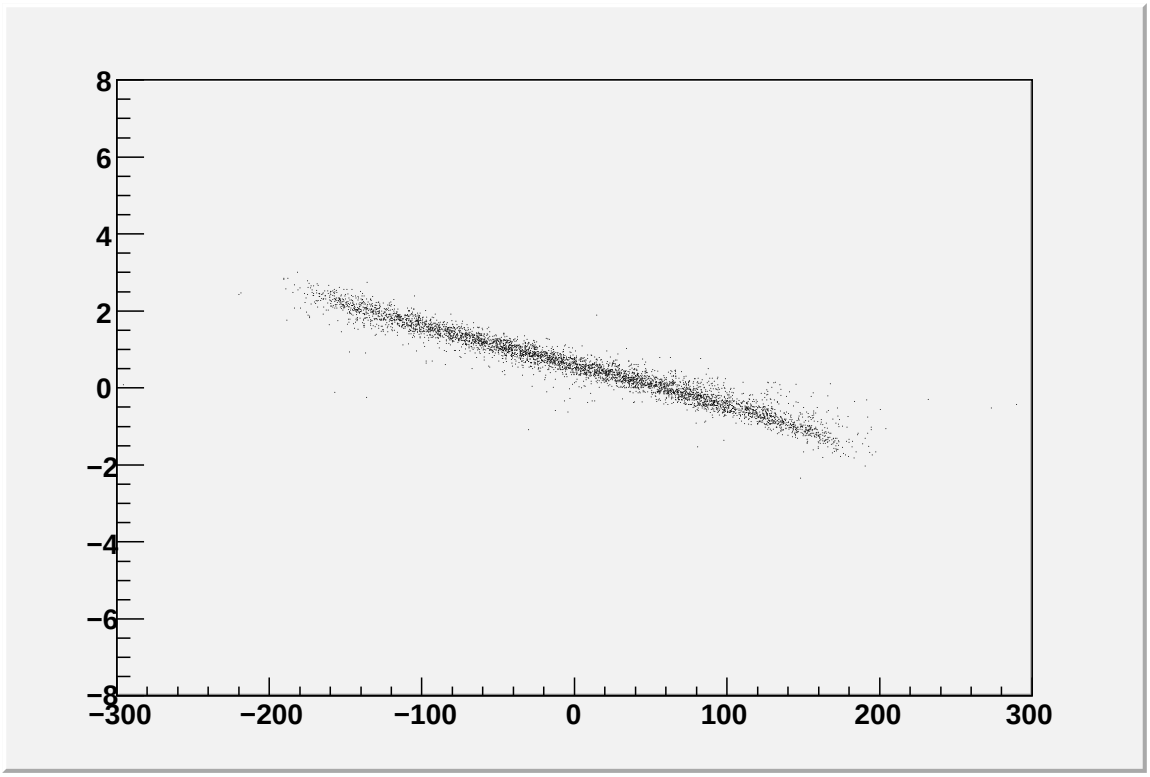

FIG. 57: The ratio of logarithms of energy attenuation as reported by the left and right PMTs ($\ln AL/\ln AR$ *vs* the hit position x (in cm) along the scintillator. These data are from paddle 22, sector 2). Data are for run 49560.

where E_n^{sv} is the energy seen by the nth PMT contributing to the peak in view v and stack s

$$E_n^{sv} = \frac{G(A_{sig} - A_{ped})}{\exp(-x/\lambda)}, \tag{111}$$

where G is the PMT gain, λ is the effective attenuation length, f_S is the overall sampling fraction, A_{sig} is the ADC channel corresponding to the digitized PMT signal, A_{ped} is the ADC pedestal and x is the PMT-reconstructed hit distance. G, λ, and f_s are the parameters to be determined in the calibration.

Since the EC is a complicated structure with a threefold stereo readout, a global optimization would require fitting 433 parameters ([73]) per sector. This fit might be very slow to converge and have problems reaching a stable solution. To avoid this complication, cosmic muons have been used to simplify the calibration. Cosmic runs have been performed and only events activating a single pixel in the EC were accepted thus minimizing the spread in energy deposition. Plotting the mean of the energy deposition vs the distance to the PMT, one can extract the gain G and the effective attenuation length λ for each PMT. Then a uniform overall response can be achieved by adjusting the PMT high voltage. Afterwards, beam data taken with electrons are used to estimate the sampling fraction f_s and to cross-check the calibration.

IV.2.4 RTPC calibration

There are two kinds of calibrations needed in the RTPC:

- We need to know the drift velocity and trajectories of released electrons so that the spatial point at which they were released from the gas by an ionizing particle can be reconstructed (thus allowing trajectory reconstruction). This is called drift velocity calibration.

- The RTPC pads register the charge of the ions that drifted to them. We need to know to what ionization energy this charge corresponds in order to find dE/dx for the passing particle (which will allow identification of the particle). This is called gain calibration.

Drift velocity calibration

Since both the magnetic and electric fields in the RTPC were not constant, thus complicating the analytic calculations of the drift velocity and trajectory, the program

MAGBOLTZ [75] was used to generate initial electron paths. Parameterizations of the electric and magnetic fields and an approximate composition of the drift gas were used as inputs to the program. As a result we determined a function converting a pad signal to a spatial point [68]:

$$P_{xyz} = P_{xyz}(I, T_{sig}; V_{cathode}, V_{GEM}, R_{gas}), \tag{112}$$

where I is the pad number, T_{sig} is the time at which a signal was recorded, $V_{cathode}$ is the cathode voltage, V_{GEM} is the voltage on the GEMs, and R_{gas} is the fraction of helium in the drift gas, which was a He/DME mixture.

Due to the imperfect knowledge of the magnetic field and gas mixture, this function had to be further calibrated using information from the CLAS detector. A special run with an increased RTPC voltage was conducted so that electrons registered in CLAS were also visible in the RTPC. Cross-checking information from the two detectors allowed us to further improve the RTPC calibration. Figure 58 demonstrates RTPC - CLAS cross-checks for three coordinates of the track, illustrating the satisfactory quality of the calibration. Nathan Baillie did this very involved work to perform the calibration (see [91]).

Gain calibration

No RTPC channels were found whose response to a test pulse during bench tests prior to installation was more than a few percent away from the mean response [68]. Nevertheless, later it was found that the effective detector gain varied considerably across the surface of the RTPC [68]. Therefore, we had to accurately determine the relative responses of all 3200 pads before useful dE/dx information could be extracted from the data.

Using the drift velocity/trajectory calibration described above, each track's momentum was determined. Using the momentum, the average dE/dx expected for a proton was determined for the track using the Bethe-Bloch formula (see, for example, [76]). Using the drift paths obtained in the drift velocity/trajectory calibration, the amount of ionized electrons drifting to each pad was determined. Since the charge obtained by the pad is known, the energy-charge calibration is possible. For each track (i) and pad (j) the following mean response ratio was computed [68]

$$G1_j = \sum_{i=1}^{N} (Q_{i.j}/E_{i,j})/N, \tag{113}$$

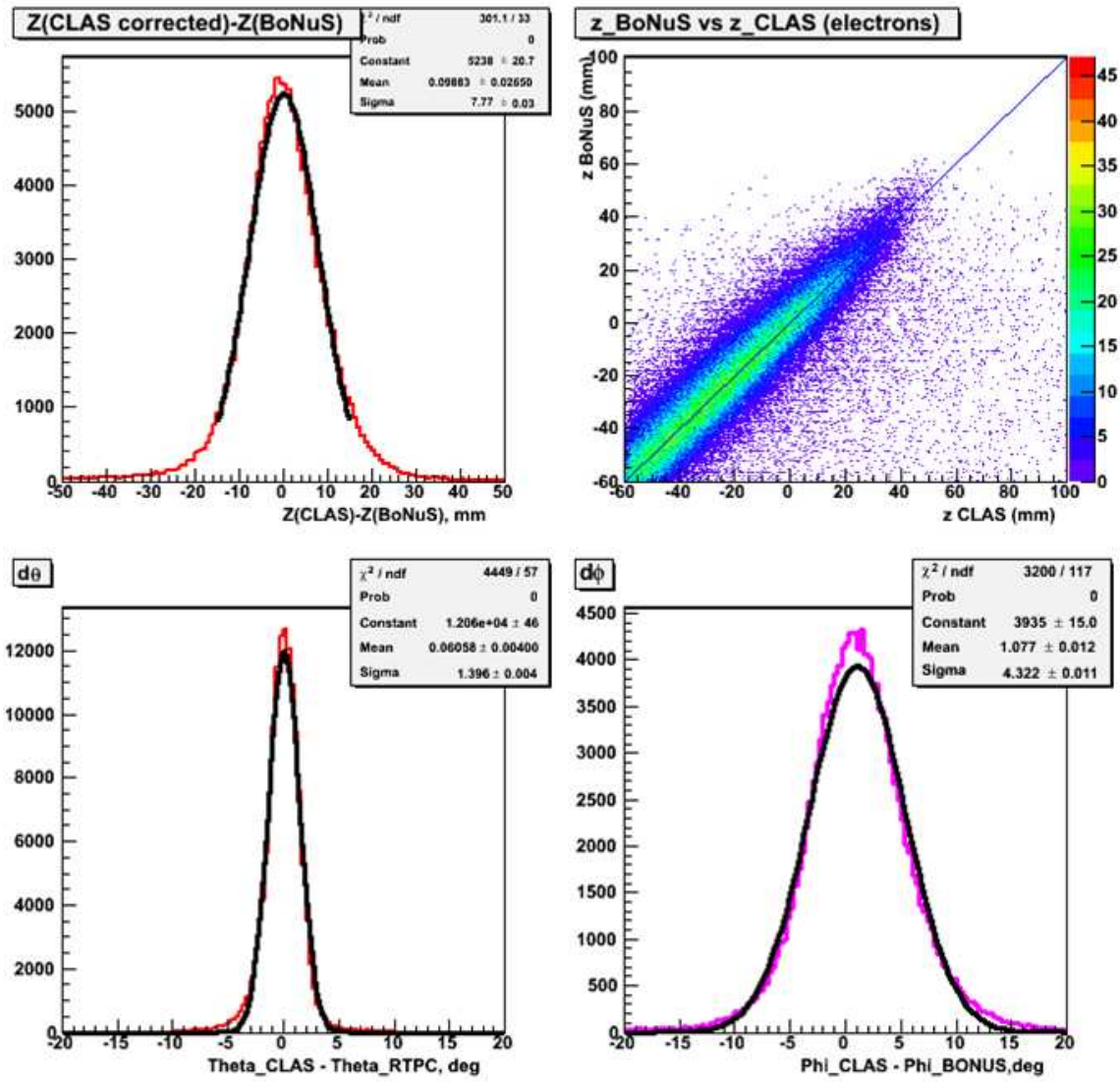

FIG. 58: Comparison of coordinates as reported by the CLAS and RTPC. The upper panels show the comparison of the z vertex of the reaction. The difference of the z coordinate as reported by the CLAS and by the RTPC is shown on the left, and the two coordinates plotted versus each other are shown on the right. The lower panel shows the comparison of the track initial angles by showing differences in the values as reported by the CLAS and by the RTPC. The polar angle θ difference is shown on the right, and the azimuthal angle ϕ difference is shown on the left.

where the sums over i for each pad run over those track segments that were predicted to produce a signal in pad j, $Q_{i,j}$ is the time integrated pulse height measured on the pad for the given track, and $E_{i,j}$ is the predicted energy loss of the track i whose ionization electron should have drifted to the pad j.

The obtained gain-normalization factors, $G1_j$, were used to scale the raw pulse heights and the same calculation was performed again excluding tracks whose measured dE/dx was inconsistent with that of protons. The second pass gain-normalization factors were retained and used for the final analysis. See figures 59 and 60 for dE/dx distributions before and after the gain calibration with Bethe-Bloch curves overlayed. The data point bands around the curves in the "after" picture (60) clearly indicate that the calibration was successful.

IV.2.5 Momentum corrections

Even after all the alignment and calibration procedures the particle momenta reconstructed by CLAS are not accurate which is illustrated in particular by the elastic peak being shifted from its nominal value (proton mass) and broader than the CLAS resolution would indicate (see figure 61), as well as in a polar and azimuthal angle dependence of the momentum (see figure 66) [77]. These deviations have several possible sources of origin:

- Inaccurate knowledge of wire positions because of the drift chamber residual misalignment, wire sag, thermal and stress distortion of the drift chambers, etc.
- Imperfect knowledge of the torus magnetic field.
- An axis offset of the solenoid magnet with respect to the torus axis.
- A beam position offset from the nominal position.
- Multiple scattering of particles.
- Energy loss of particles between the target and the detectors.
- Inaccurate knowledge of the beam energy (which does not affect the determination of the particle momentum directly, but needs to be taken care of since the whole procedure was based on momentum-energy conservation).

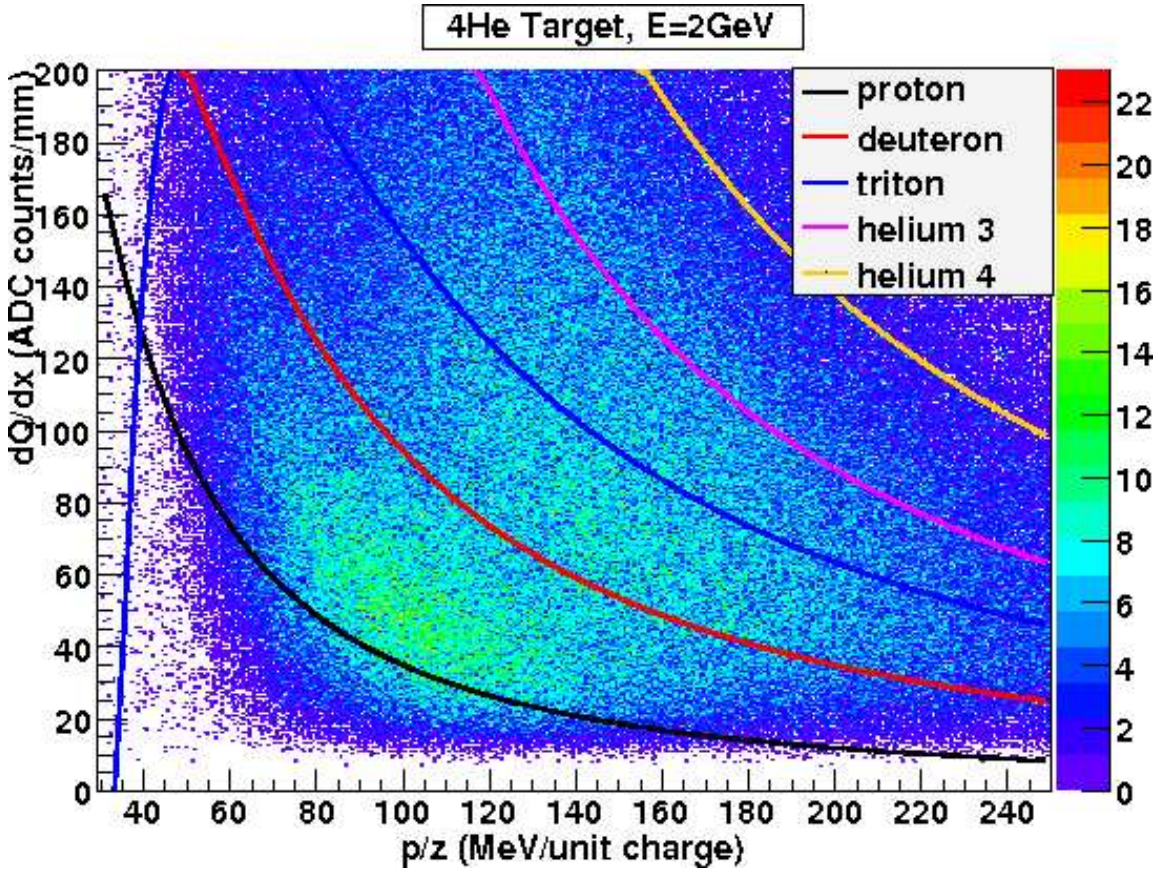

FIG. 59: The dE/dx distribution of particles registered by the RTPC before the RTPC gain calibration. The solid curves are calculated dE/dx curves for various particles.

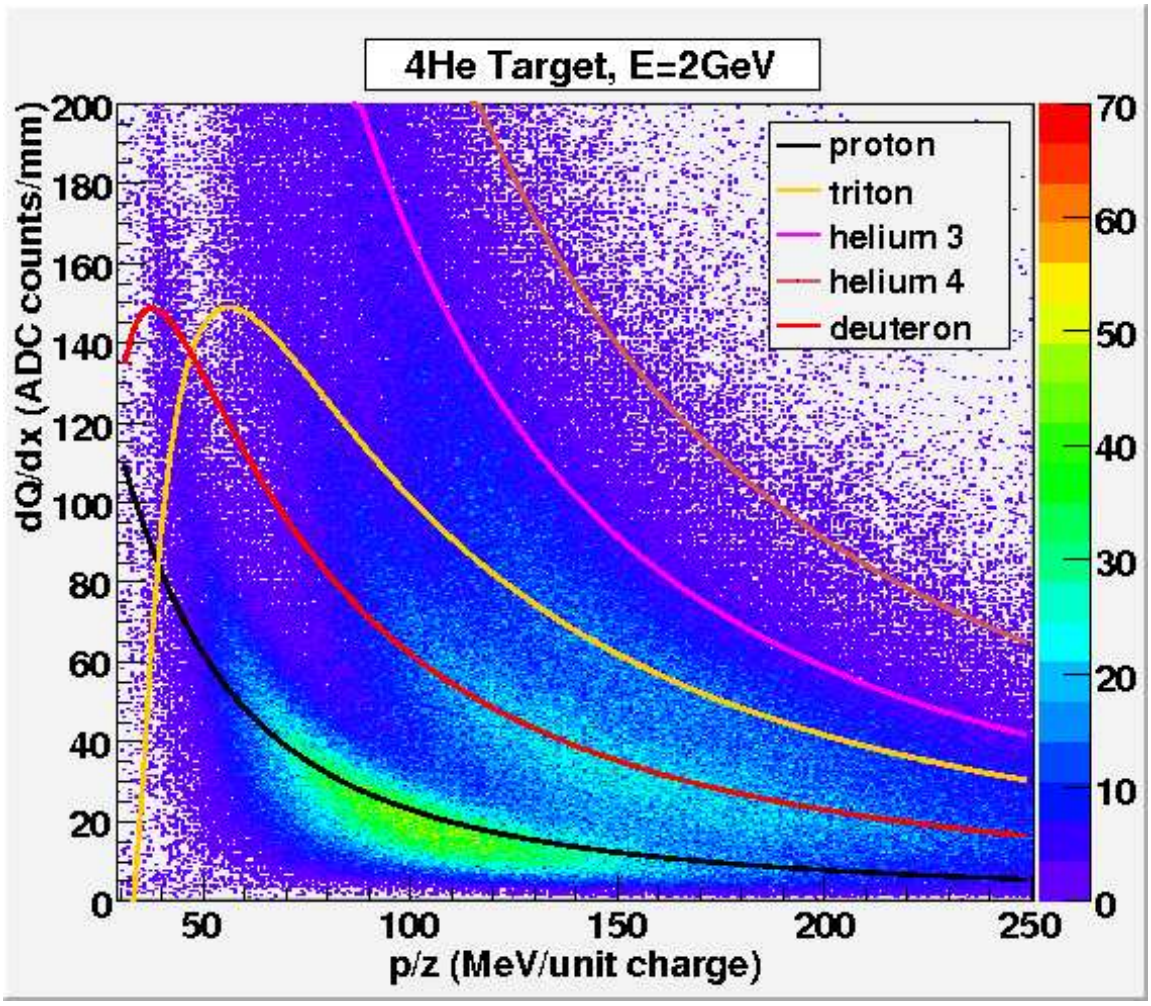

FIG. 60: The dE/dx distribution of particles registered by the RTPC after the RTPC gain calibration. The solid curves are calculated dE/dx curves for various particles.

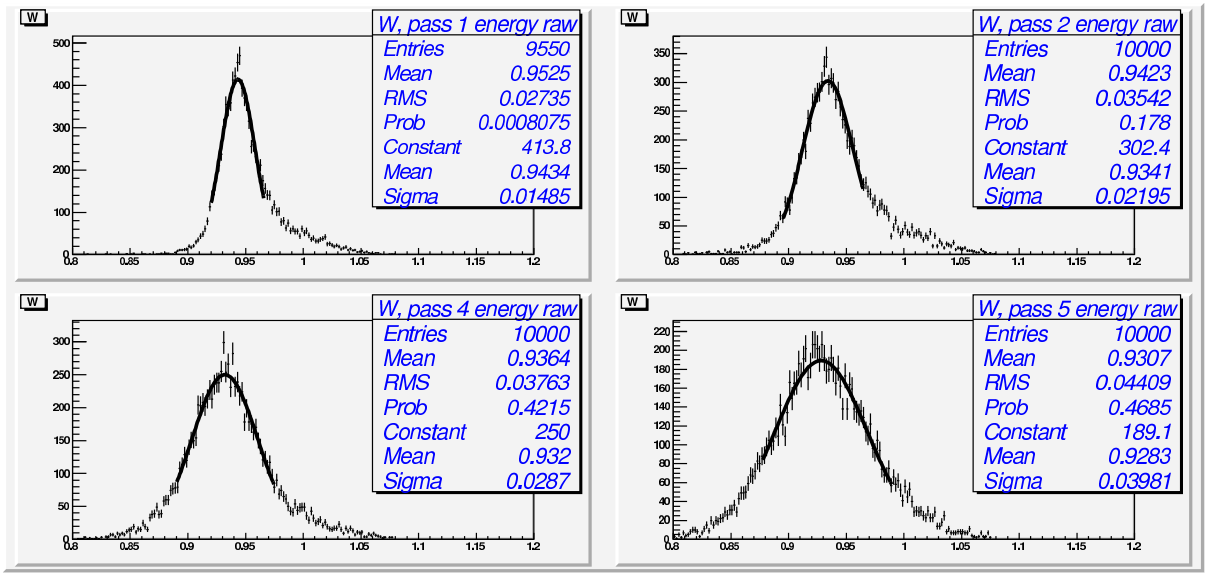

FIG. 61: Invariant mass, W, distribution for the p(e,e′)p reaction before momentum corrections. Beam energies are 1.099 GeV (top left), 2.140 GeV (top right), 4.223 GeV (bottom left), and 5.262 GeV (bottom right)
.

To solve these problems, a procedure of bringing particle momenta to their optimized values, known as momentum correction, was performed.

Procedure background

The iterative procedure for momentum corrections took care of the aforementioned problems one by one, followed by a return to the beginning, re-evaluation of the results of each step, and possible re-iteration. Each of the steps was assessed and the best recipe for each as well as the best sequence of corrections were determined.

Our method is an extension of the one described in [77] and as such has the same approach to the procedure, namely imposing conservation of momentum and energy by minimizing the missing momentum and energy of a reaction. Basic assumptions about the form of the necessary corrections were made. The number of parameters we used is slightly larger than the one in [77], with 12 parameters common for all the sectors being added to the original 14 per sector. Then a fitting procedure using a large data sample including elastic as well as inelastic events at different

beam energies was applied to fix the parameters. As a result, a set of "universal" parameters for correcting particle momenta in different reactions at different energy settings was developed.

Drift chamber displacement

To correct this problem a set of 8 parameters per sector was used. These parameters would try to correct displacements along the z- and x-axes as well as ϕ-dependent x and z displacements for each region 2 and region 3 drift chambers. The effect of these can be written as a change in the polar angle and momentum:

$$\Delta\theta = (par_1 + par_2\phi)\frac{\cos\theta}{\cos\phi} + (par_3 + par_4\phi)\sin\theta \tag{114a}$$

$$\frac{\Delta p}{p} = \left((par_5 + par_6\phi)\frac{\cos\theta}{\cos\phi} + (par_7 + par_8\phi)\sin\theta\right)\frac{p}{qB_{tor}}, \tag{114b}$$

where $par_1 \ldots par_8$ are the parameters to be determined, q is the particle charge in units of the electron charge, ϕ is the local sector azimuthal angle, θ is the polar angle, and p is the particle momentum value. B_{tor} stands for $\int B_{trans} d\ell$ along the path of the track multiplied with the speed of light in the units of m/ns ($c = 0.29979$ m/ns). The ratio $\frac{qB_{tor}}{p}$ is proportional to the amount of curvature of the track, which determines the effect of the drift chamber misalignment. A simple parameterization of this integral in terms of the polar angle was found [77]

$$B_{tor} = 0.76\frac{I_{tor}\sin^2(4\theta)}{3375\,\theta/\mathrm{rad}} \quad \text{for} \quad \theta < \frac{\pi}{8} \tag{115a}$$

$$B_{tor} = 0.76\frac{I_{tor}}{3375\,\theta/\mathrm{rad}} \quad \text{for} \quad \theta \geq \frac{\pi}{8} \tag{115b}$$

where I_{tor} is torus current.

Parameters par_1 and par_5 describe radial outward displacements, parameters par_2 and par_6 describe ϕ-dependent radial displacements, par_3 and par_7 describe displacements along the beam axis, and par_4 and par_8 account for a rotation along the radial direction.

Torus field map imperfections

Differences between the actual spatial magnetic field distribution and whatever is encoded in reconstruction programs is an origin of possible deviations of reconstructed

momenta from real ones. The parameterization

$$\frac{\Delta p}{p} = (par_9 \cos\theta + par_{10} \sin\theta + par_{11} \sin 2\theta) + (par_{12} \cos\theta + par_{13} \sin\theta + par_{14} \sin 2\theta)\phi, \tag{116}$$

where $par_9 \ldots par_{14}$ are 6 more fitting parameters, seems to do a decent job in fixing this problem.

Once a new polar angle $\theta_{new} = \theta_{old} + \Delta\theta$ and $\Delta p/p$ are found, the new momentum absolute value can be found as

$$p_{new} = p_{old} \cdot (1 + \frac{\Delta p}{p}), \tag{117}$$

and new momentum components are

$$\begin{aligned} p_{x,new} &= p_{new} \cos\phi \sin\theta_{new} \\ p_{y,new} &= p_{new} \sin\phi \sin\theta_{new} \\ p_{z,new} &= p_{new} \cos\theta_{new}. \end{aligned} \tag{118}$$

Solenoid axis offset

If the axis of the solenoid does not coincide with the beam line, then the solenoid magnetic field through which the reconstruction program calculates the particle trajectory is wrong, the particle trajectory is bent by the wrong amount, and angles (polar and azimuthal) calculated by the reconstruction are wrong. To correct for that, angle corrections of the following form are introduced:

$$d\phi = \frac{qB(par_{15} \cos\phi - par_{16} \sin\phi)}{p \sin\theta} \tag{119a}$$

$$d\theta = \frac{qB(par_{17} \sin\phi - par_{18} \cos\phi)}{p}, \tag{119b}$$

where ϕ and θ are azimuthal and polar angles correspondingly. In (119) q is the particle charge, B is the solenoid magnetic field, p is the particle momentum, $par_{15} \ldots par_{18}$ are parameters determined by fitting. Then the corrected angles are determined

$$\phi_{new} = \phi_{old} + d\phi \tag{120a}$$

$$\theta_{new} = \theta_{old} + d\theta, \tag{120b}$$

and the corrected momentum components are found

$$p_x = p\cos\phi_{new}\sin\theta_{new} \tag{121a}$$

$$p_y = p\sin\phi_{new}\sin\theta_{new} \tag{121b}$$

$$p_z = p\cos\theta_{new}. \tag{121c}$$

Beam position offset

In the standard reconstruction routine it is assumed that the electron beam goes strictly along the axis of the CLAS coordinate system and thus all reactions take place at $(x, y) = (0, 0)$ in this coordinate system. As usual, real life introduces deviations from this simple picture. The beam, as good as it is, comes into the hall at a tiny angle, which is large enough, though, to produce a noticeable difference between the reaction vertex x and y coordinates and the assumed pair of zeroes. This causes the ϕ angle of the particle track to be reported wrong and its x- and y-momentum components to have the wrong values.

To correct for this, a two-step procedure was used. First, by using multiple track CLAS events, the (x, y) vertex coordinate for each event was found as the coordinate of the point where these tracks intersect. Vertex x and y positions were assumed to be a linear function of the z coordinate and fit accordingly. This work was performed by Jixie Zhang [92]. This information, in turn, was used to correct the ϕ angles:

$$\phi_{corr} = \phi_{raw} + \frac{qBx'/100}{33.356\ p\sin\theta}, \tag{122}$$

where ϕ_{corr} and ϕ_{raw} are the corrected and raw angles, q is the particle charge in units of the electron charge, B is the solenoid field expressed in kGauss, p is the momentum of the particle, and θ is its polar angle. The factor of 100 converts centimeters to meters and 33.356 is the inverted speed of light in the proper units. x' is found as

$$x' = \frac{x\cos\phi_s + y\sin\phi_s}{\cos(\phi - \phi_s)}, \tag{123}$$

where x and y are coordinates of the vertex in cm, and ϕ_s is the azimuthal angle of the center of the sector in which the particle was detected. Then the z-position of the vertex is corrected as

$$z_{corr} = z_{raw} + \frac{x'}{\tan\theta} + par_{19}\frac{\theta - \theta_{ini}}{\sin^2\theta}, \tag{124}$$

where θ_{ini} is the polar angle at the beginning of the fitting iteration, θ is the polar angle after all the previous corrections, and par_{19} is a fitting parameter whose physical meaning is the distance from the vertex to the first region of DC ($\sim$ 60 cm).

Knowing the ϕ angle and considering the transverse momentum $p_\perp = \sqrt{p_x^2 + p_y^2}$ to be unaltered by the beam position change, we can calculate the proper x and y momentum components as

$$p_x = p_\perp \cos\phi_{corr} \tag{125a}$$

$$p_y = p_\perp \sin\phi_{corr} \tag{125b}$$

Multiple scattering

A particle encounters a lot of scattering centers while traversing the CLAS volume. As a result of the interaction with some of them, its polar and azimuthal angles registered by the detectors are not the same as the angles at the reaction vertex. This introduces an additional ambiguity into how the particle momentum is distributed among the components. In addition, its vertex position can be shifted, and as a result, the reconstruction program will try to bend the particle track by the wrong amount, trying to get it to the wrong vertex. This introduces an error into the momentum value. Luckily, we have events with more than one particle, and it is possible to use information from multiple tracks to improve our knowledge of the actual vertex position, and subsequently correct track angles and momentum.

The average z of the vertex was found by taking the weighted average of the z positions of all the charged particles in the event:

$$\langle z \rangle = \frac{\sum z_{part}/z_{res}^2}{\sum 1/z_{res}^2}, \tag{126}$$

where the sums are over all the well-identified charged particles in the event, z_{part} is the z position for each of the particles, and "resolution" in z is

$$z_{res} = \frac{0.4}{\beta p_\perp}, \tag{127}$$

where β is the particle speed in units of the speed of light, and $p_\perp$ is the component of the particle momentum perpendicular to the z-axis.

Having found the weighted average, we "force" all the particles to originate from

that vertex and correct the angles by the amounts

$$d\theta = \Delta z \frac{par_{20} \sin^2 \theta + par_{21}}{p} \tag{128a}$$

$$d\phi = \frac{par_{22} q B \Delta z}{p_z} \tag{128b}$$

for the polar and azimuthal angles, respectively. In equations (128) Δz is the distance from the reconstructed vertex z for the particle to the weighted average defined by (126), p is the reconstructed momentum of the particle, p_z is the z component, q is the charge of the particle, B is the solenoid magnetic field, and $par_{20} \ldots par_{22}$ are parameters found by fitting.

Then the new angles $\theta_{new} = \theta_{old} + d\theta$ and $\phi_{new} = \phi_{old} + d\phi$ are found, and the new components of the momentum are

$$p_x = p \cos \phi_{new} \sin \theta_{new} \tag{129a}$$

$$p_y = p \sin \phi_{new} \sin \theta_{new} \tag{129b}$$

$$p_z = p \cos \theta_{new}. \tag{129c}$$

Energy loss

Energy loss of particles was accounted for using a simulation package combining a GEANT4 based simulation of the target and RTPC developed for our experiment and the GEANT3 based package GSIM describing the standard CLAS configuration. A number of particles were generated with random momenta, vertex z and vertex angles ϕ and θ. Then they were led through the simulated detectors using the aforementioned simulation package, with subsequent reconstruction of the tracks back to vertices using the standard CLAS reconstruction software. The difference between the "true" momenta with which the particles were generated and the momenta as reported by the reconstruction software was minimized using a function based on the Bethe-Bloch formula [76] with four fitting parameters. These parameters were tabulated for a range of polar angle, vertex z and momentum bins for different particles.

The parameters were used to find the energy loss for individual particles in real data in the following way. The measured kinetic energy of a particle is

$$T_f = \sqrt{m^2 + p^2} - m, \tag{130}$$

where m is the mass of the particle, and p is its momentum as reported by the CLAS

reconstruction. From this, its "true" (initial) kinetic energy was reconstructed:

$$T_i = (T_f^b + am^{b-1.0})^{1/b} + c + d * \log(p/m), \tag{131}$$

where a, b, c, and d are parameters found in the fitting procedure. Then the "true" initial energy was found as

$$E_i = T_i + m. \tag{132}$$

Beam energy

Since we are trying to reconstruct the proper momentum values by minimizing the missing energy, we need to know the initial energy of the reaction, and hence the beam electron energy. Unfortunately, this energy is not measured in Hall B, and what is written in the database is the set accelerator energy which can be off by 10-20 MeV [81]. The actual energy can be deduced from the measured momenta in elastic reactions $ep \to ep$ as

$$E_{beam} = \frac{m_N}{1 - \cos\theta_e} \left(\cos\theta_e + \cos\theta_p \frac{\sin\theta_e}{\sin\theta_p} - 1 \right), \tag{133}$$

where m_N is the nucleon mass, θ_e and θ_p are polar angles of the electron and proton, respectively. The problem is that we need the beam energy to determine the new components of the momenta and hence the angles.

Alternatively, we can use a beam energy measurement from other halls and convert it to the Hall B beam energy by

$$E_{Hall\,B} = E_{another\,Hall} \frac{n_B + 0.056}{n_o + 0.056}, \tag{134}$$

where n_B and n_o are the number of beam passes on the way to Hall B and the other Hall, respectively. This method gives an energy value much closer to the "true" energy, and values determined in this way (see table 7) were used as initial values for the energies in the fitting procedure. These energies were later used as fitting parameters.

Event selection

The correction method at hand uses momentum-energy conservation. Thus, it is very important to use exclusive events, otherwise the whole procedure does not make sense . The simplest reaction accessible would be exclusive $ep \to ep$. To cover lower particle

TABLE 7: Beam energy values deduced from Hall A measurements, GeV

Beam pass	1	2	4	5
Beam energy	1.099	2.140	4.223	5.262

momenta and decouple momenta and scattering angles, we need to also use exclusive reactions with more than two particles in the final state, for which $ep \rightarrow ep\pi^-\pi^+$ was chosen. Although reactions with different torus polarities would be desirable to decouple parameters in equations (114) that depend on the torus sign from those of equations (115) that do not, we did not have such a luxury; all the BONuS data were taken at one torus polarity.

To ensure exclusivity, only events with missing energy less than 0.1 GeV, and all missing momentum components below 0.1 GeV/c were selected. Fiducial, electron ID, geometric solenoid and trigger efficiency cuts (see below) were applied to all the events. Particle IDs were identified comparing time of flight as reported by CLAS with the time of flight that a physical particle of the given mass and momentum would have. A timing cut of 2 ns was applied to the difference between them. Then for the events that had the necessary numbers of particles, cuts of 0.1 GeV on the absolute values of the missing momentum/energy were applied to ensure the reaction was exclusive. Additionally, to ensure that identified elastic event candidates were indeed elastic, the difference between electron and proton azimuthal angles was required to be within 2 degrees of 180 degrees and the invariant mass of the reaction was required to be between 0.8 and 1.1 GeV.

Fitting procedure and results

The MINUIT minimization package was used for optimizing the momentum correction parameters [78]. The fitting was done in two steps. In the first step events with missing energy and momentum $|E_{miss}| \leq 0.1$ GeV, $|p_{z,miss}| \leq 0.1$ GeV/c, $|p_{x,miss}| \leq 0.07$ GeV/c, and $|p_{y,miss}| \leq 0.07$ GeV/c were chosen. The elastic candidates were subjected to additional $\Delta\phi = 180 \pm 1.5^\circ$ ($\Delta\phi$ being the difference between

TABLE 8: Uncertainties for missing energy and momentum spreads for 4 beam energies, GeV.

Beam pass	1	2	4	5
Uncertainty for E_{miss}	0.015	0.030	0.036	0.038
Uncertainty for $p_{x,miss}$	0.013	0.017	0.019	0.021
Uncertainty for $p_{y,miss}$	0.013	0.017	0.019	0.021
Uncertainty for $p_{z,miss}$	0.017	0.028	0.035	0.039

electron and proton azimuthal angles) and W cuts:

$$0.91 \leq W \leq 0.96 \quad \text{for 1 pass events} \tag{135a}$$

$$0.90 \leq W \leq 0.97 \quad \text{for 2 pass events} \tag{135b}$$

$$0.89 \leq W \leq 0.98 \quad \text{for 4 pass events} \tag{135c}$$

$$0.88 \leq W \leq 0.99 \quad \text{for 5 pass events.} \tag{135d}$$

The selected events were fit using the procedure described below, after which another step, with events selected by stricter cuts (with cut values already corrected using parameters from the first step) was taken. Cuts for the second step were: $|E_{miss}| \leq 0.06$ GeV, $|p_{z,miss}| \leq 0.06$ GeV/c, $|p_{x,miss}| \leq 0.05$ GeV/c, $|p_{y,miss}| \leq 0.05$ GeV/c, $\Delta\phi = 180 \pm 1.0°$. The W cuts were the same as for the first step.

In each of the steps, the procedure was the same. For each selected event, the corrections outlined in section IV.2.5 were applied one by one. After all the corrections and energy loss were applied, the minimization χ^2 was calculated. Its main contributions came from the missing energy and momentum to which each event added

$$\Delta\chi^2 = \frac{E_{miss}^2}{\sigma_{E_{miss}}^2} + \frac{p_{x,miss}^2}{\sigma_{p_{x,miss}}^2} + \frac{p_{y,miss}^2}{\sigma_{p_{y,miss}}^2} + \frac{p_{z,miss}^2}{\sigma_{p_{z,miss}}^2}, \tag{136}$$

where the σ's are reasonable uncertainties for the corresponding variables, listed in table 8 for 4 possible beam energies. They were found by plotting missing energy and momentum distributions for raw data.

Also, for each event a sum of squared differences between the weighted average z-position of the particles and the z-position of each particle was added to "force" the particles to the same vertex. One more per-event contribution for p(e,e′p) events came from forcing the invariant mass of the reaction, W, to be the same as the mass

of the target (proton), which added

$$\Delta\chi^2 = \frac{(W - M_p)^2}{\sigma^2_{E_{miss}}}, \tag{137}$$

where M_p is the proton mass.

After going over all the events and adding the χ^2 contributions pertaining to each of them, contributions from each of the parameters were added to avoid parameter "run-away" to some corners of parameter space. For the majority of the parameters, we added

$$\Delta\chi^2 = \frac{param^2}{\sigma^2_{param}}, \tag{138}$$

where *param* stands for a parameter value at the end of the iteration, σ_{param} is the "reasonable uncertainty" for the parameter (σ_{param} for the 14 "per sector" parameters were 0.005, 0.01, 0.005, 0.01, 0.002, 0.005, 0.002, 0.005, 0.002, 0.002, 0.002, 0.005, 0.005, 0.005; σ_{param} for the beam energy parameters were 5 MeV; σ_{param} for the solenoid correction parameters were 0.0003; σ_{param} for the beam correction parameter was 1cm; σ_{param}'s for multiple scattering parameters were 0.01). For a few parameters that had physically motivated starting values (beam energy parameters, beam offset parameter), the contribution was

$$\Delta\chi^2 = \frac{(param - start\ value)^2}{\sigma^2_{param}} \tag{139}$$

to avoid parameters departing too far away from where they should be.[b] Representative figures 62 and 63 show invariant mass distributions for events in which fitting was performed (figure 62) and for random inclusive events (figure 63) for 5 pass data before and after the momentum correction was applied. In both cases, the corrected distribution has a smaller sigma and the mean is much closer to the expected value (proton mass, 0.938 GeV). The remaining 2-3 MeV of difference between the means and the expected value can be attributed to radiative effects not accounted for by the procedure. The data for other beam energies also showed a reasonable improvement, thus indicating that the procedure was successful.

Figure 64 shows missing energy distributions before and after the corrections for

[b]All starting values were zeroes except for five parameters: the initial values of beam energies were 1.099, 2.140, 4.223, and 5.262 GeV (parameters 85-88), and the distance to the first region of drift chambers was given an initial value of 60 cm (parameter 93).

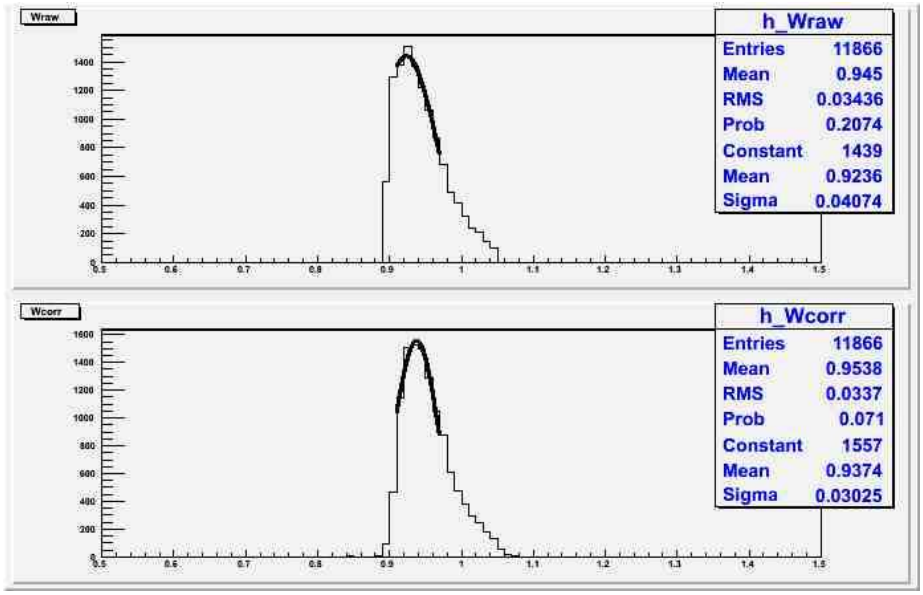

FIG. 62: Raw (upper panel) and corrected (lower panel) invariant mass distributions for pre-selected 5 pass events that were used in the fit.

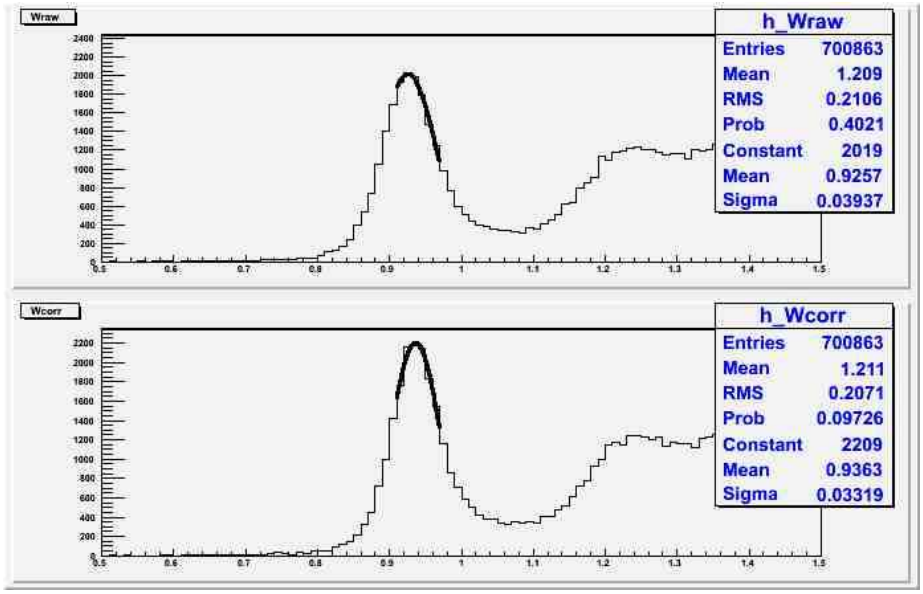

FIG. 63: Raw (upper panel) and corrected (lower panel) invariant mass distributions for inclusive 5 pass events from runs 49929-49935. These events are not necessarily those fit for the momentum corrections.

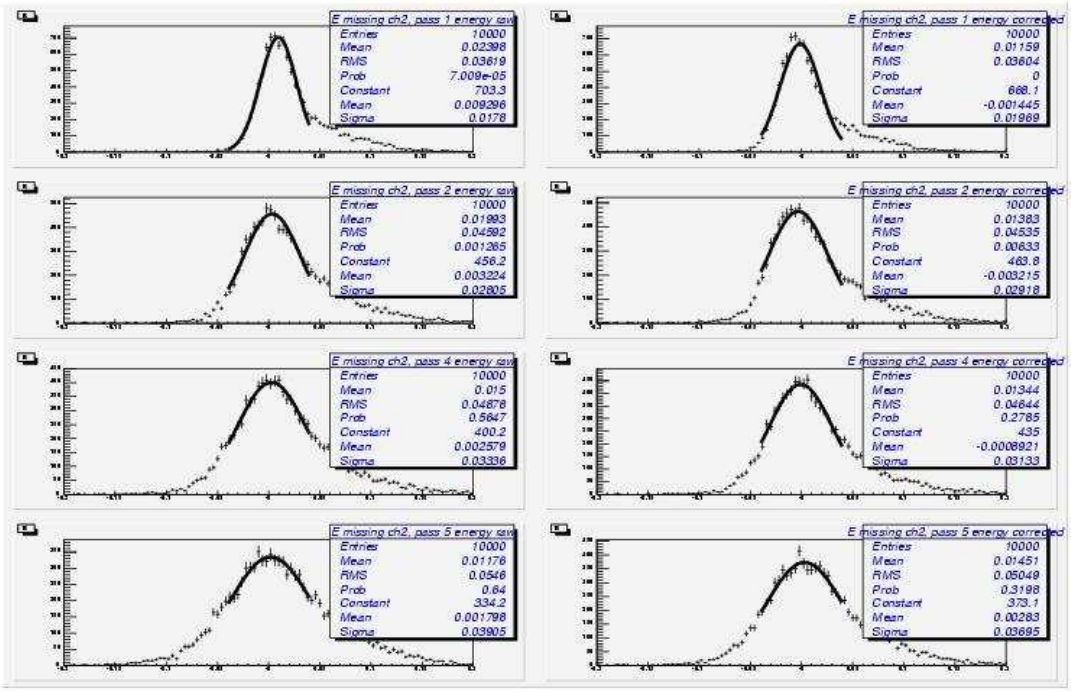

FIG. 64: Missing energy distributions before (left side) and after (right side) the momentum corrections. Results are shown for elastic ep → ep events events for four beam energies.

all four energies. On average[c], the mean and sigma are better for the corrected distributions. Figure 65 shows distributions of the z component of the missing momentum. Once again, on average, the corrected distributions are better.

Figures 66 and 67 show the percentage differences of expected electron momenta from elastic scattering (as before, calculated using the beam energy and scattering angles) from the measured momenta. The corrected momentum distributions (figure 67) are more flat and closer to zero thus indicating that the momenta were brought closer to expected values by the correction procedure.

[c]The performed procedure of correcting momenta found a set of "universal" parameters that would work for all the energies. While it was possible to find better solutions for each of the energies separately, we preferred to choose a set of common parameters to improve the distributions on average.

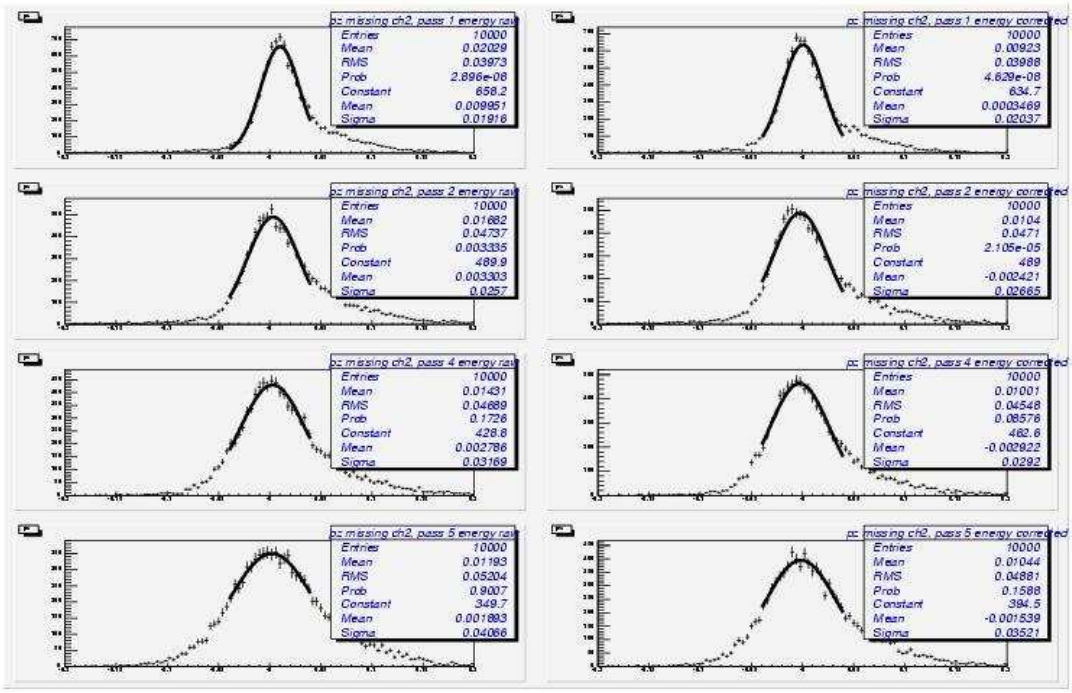

FIG. 65: z component of missing momentum distributions before (left side) and after (right side) the momentum corrections. Results are shown for elastic ep $\rightarrow$ ep events for four beam energies.

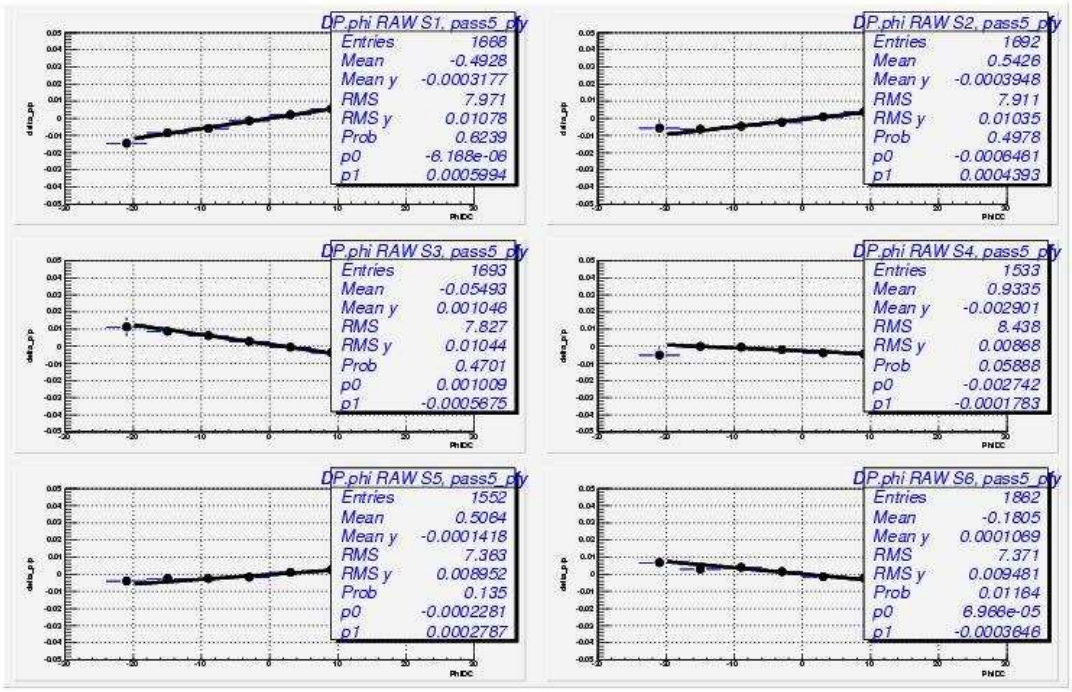

FIG. 66: The difference between expected (calculated from beam energy and scattering angle, $p_{expected} = E_{beam}/(1+(E_{beam}/M_p)*(1-\cos\theta))$ and measured momenta, divided by the expected momentum value, before the momentum corrections *vs* ϕ, the azimuthal angle relative to the sector mid-plane, for each sector. ep $\rightarrow$ ep data for the 5 GeV beam energy are shown.

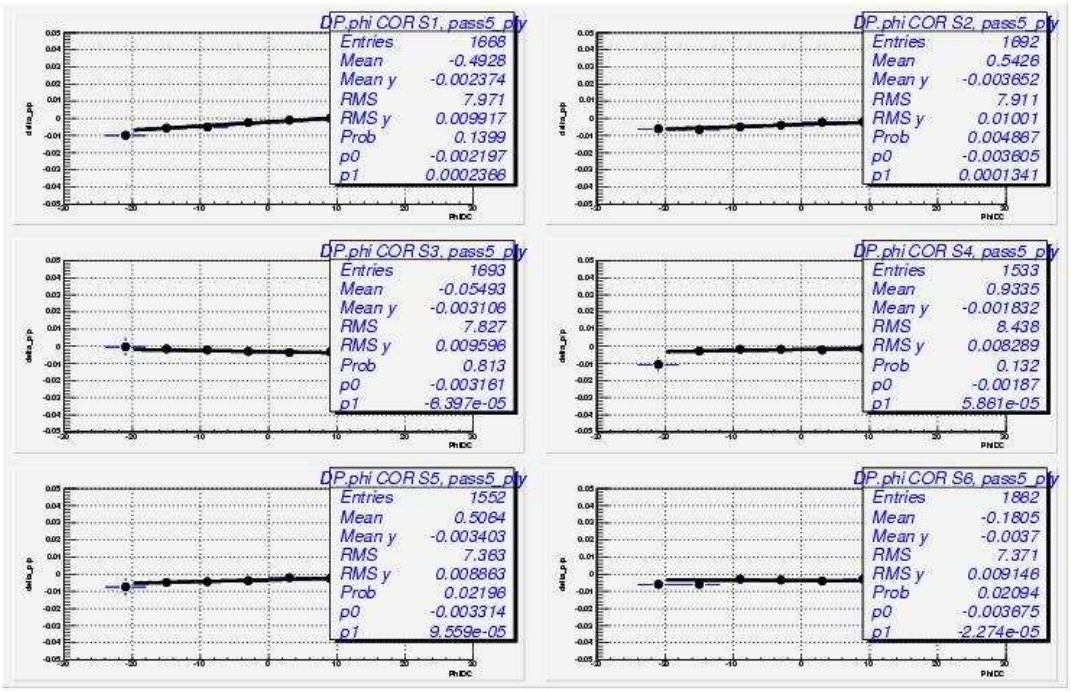

FIG. 67: The difference between expected (calculated from beam energy and scattering angle, $p_{expected} = E_{beam}/(1+(E_{beam}/M_p)*(1-\cos\theta))$ and measured momenta, divided by the expected momentum value, after momentum corrections *vs* ϕ, the azimuthal angle relative to the sector mid-plane, for each sector. ep $\rightarrow$ ep data for the 5 GeV beam energy are shown.

IV.2.6 RTPC momentum corrections

Although the RTPC is a simpler detector than CLAS, momentum corrections had to be applied to the RTPC data as well. Two RTPC momentum corrections were applied:

1. Correcting momenta themselves to extract the proper initial momentum value given the radius of curvature of the track. An extension of this correction also provides a corrected value of the polar angle θ of the spectator proton. This correction was needed to account for the energy loss of spectator protons.

2. The first correction took the energy loss into account, but some other limitations of the momentum reconstruction were not accounted for. These include imperfect description of electron paths in the drift region, limited statistics and clustering of ionization points. To correct for these, we corrected radii of curvature of trajectories in the RTPC for systematic shifts by using CLAS data to predict the proper radius of curvature.

The first correction was based on a GEANT4 simulation by J. Zhang. A number of events in a range of z (coordinate along the beam axis), θ (spectator proton polar angle), and p_s (spectator proton momentum) were generated. They were subsequently run through the RTPC simulation and the radius of curvature and angle θ of the tracks recorded by the simulated RTPC were compared with the thrown momenta and θ. Utilizing this comparison, J. Zhang was able to provide a one-to-one correspondence between the detected radius of curvature and the true spectator momentum, which corrects for effects like energy loss (see figure 68 for results of two iterations of this correction). See [92] for more details.

The momentum distribution provided by this correction was not perfect. Its deviation from the distribution expected from the deuteron wavefunction was noticeable, whereas the distribution of spectator proton momenta extracted from the CLAS data (utilizing events with a missing mass equal to that of the proton, and assuming that the missing momentum is that of the spectator proton) agreed rather well with the aforementioned theoretical distribution.

For this we used fully exclusive $\mathrm{d(e,e'p}_{CLAS}\pi^-\mathrm{p}_{RTPC})$ events to compare predicted (based on the CLAS data) and measured (by the RTPC) spectator momentum distributions to find a systematic shift in the measured momenta due to incorrect momentum reconstruction in the RTPC due to aforementioned problems.

The discrepancy in the momentum measurements was taken care of by minimizing the difference between momenta reported by the RTPC and expected from the CLAS information, modifying the raw radius of curvature and angles of the spectator as follows:

$$R_{new} = R_{old}/(p_1 \cdot R_{old} + p_2) \tag{140a}$$

$$\theta_{new} = p_3 \cdot \theta_{old} + p_4 \tag{140b}$$

$$\phi_{new} = p_5 \cdot \phi_{old} + p_6, \tag{140c}$$

with subsequent fitting of parameters $p_1 \ldots p_6$ to minimize the RTPC - CLAS momentum difference.

The RTPC momentum distribution after these two corrections was closer to the expected one. The p_s spectrum still falls off faster than predicted. This can be attributed to the not completely understood RTPC reconstruction efficiency at low charge per unit length of a track registered by the RTPC for higher spectator momenta.

IV.3 CUTS AND CORRECTIONS TO THE DATA

IV.3.1 Experimental data

We applied the following cuts:

- Counters (ec, cc, dc, sc) for any particle are not larger than 200 and the stat variable for the trigger particle is positive.
- Target is deuterium.
- Trigger particle is a good electron:
  - Negative charge.
  - For electron momenta less than or equal to 3.0 GeV/c, the number of photoelectrons in the Cherenkov counter must be at least 1.5, and at least 1.0 for other momentum values.
  - The energy registered by the inner calorimeter is larger than 0.06 GeV, and the total energy in the calorimeter divided by the particle momentum is smaller than 0.34 and larger than $0.016p + 0.15$, where p is the particle momentum.

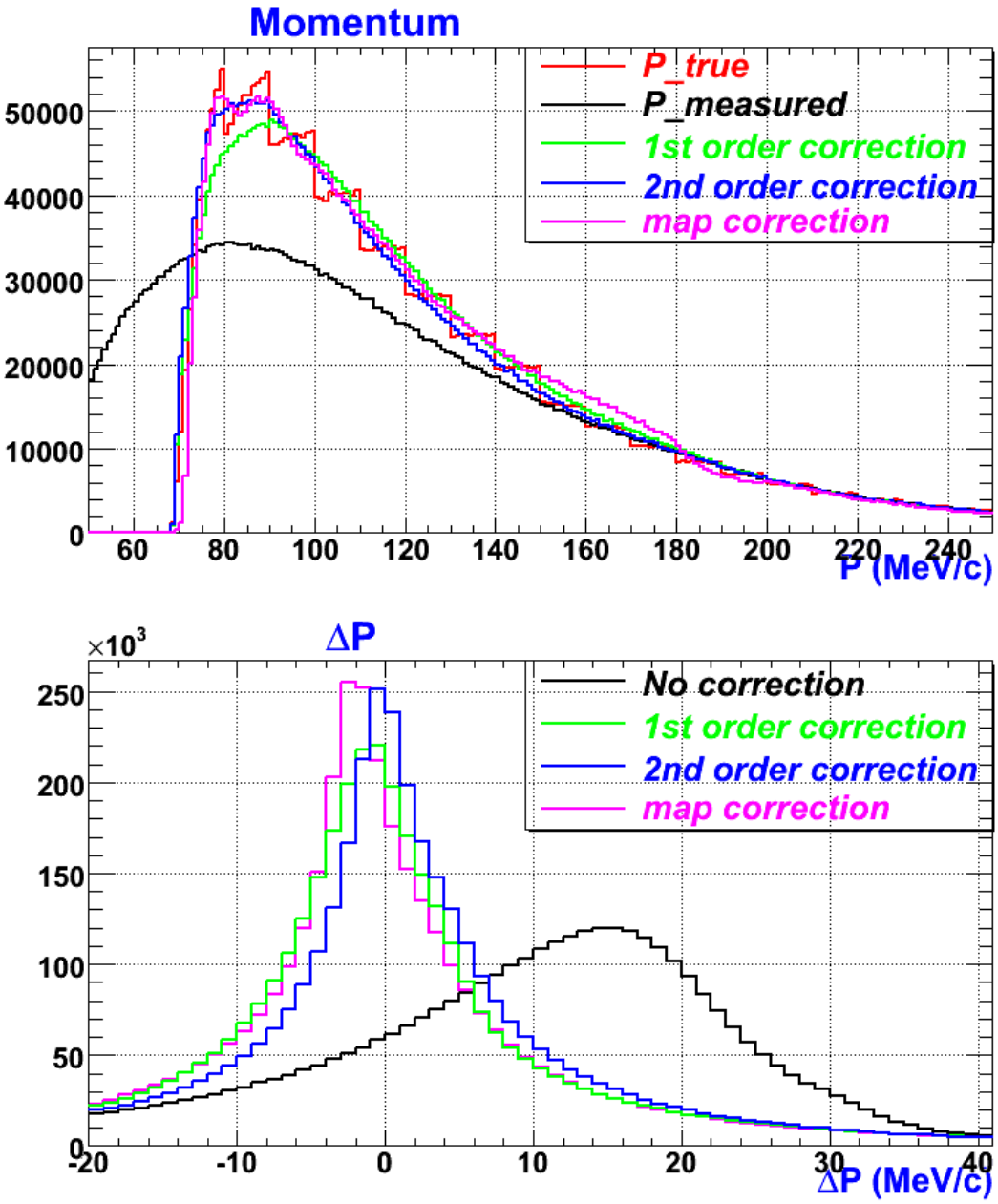

FIG. 68: Proton momentum distribution in the RTPC (top panel) and the difference between the measured and true spectator momentum (bottom panel) are shown. Raw measured distributions are shown in black, the results after the first order energy loss RTPC correction are shown in green, and results after the second order energy loss RTPC correction are shown in blue. An attempt to correct the RTPC momentum not discussed in the text is shown in pink.

  - The Osipenko cut [95] (geometrical and temporal matching between the CC signal and the measured track is required to eliminate coincidences between CC noise and pion tracks, which can result in pions masquerading as electrons. These coincidences used to be the largest source of pion contamination in CLAS.) is passed.
  - The fiducial cut (a geometrical cut serving to eliminate events in which electrons went through regions of the CC known to be inefficient) is passed. See figure 69 for an example of a fiducial cut.
  - "θ-z" cut is passed. This is a simple cut making sure that a particle did not hit the DVCS solenoid. For each z coordinate, only particles going through a particular range of the polar angle θ should be able to clear the solenoid. If the reported particle polar angle and z coordinate pairing was not possible geometry-wise, the particle was thrown out.
  - Trigger is in the same sector as the 1st electron in the event.

- The trigger electron momentum is larger than 20% of the beam energy.
- Spectator cuts:
  - dq/dx[d] of the candidate is not more than two sigmas larger and not less than three sigmas smaller than the dq/dx expected for a proton (see figure 60 for an example).
  - The distance between either end of the ionization trail and the closest chamber boundary is less than 5 mm.
  - Vertex z is inside the fiducial target region (between -60 and 100 mm in the RTPC coordinate system[e]).
  - The difference between the vertex z as reported by CLAS and as reported by the RTPC is no more than 15 mm.
  - χ^2 of the fitted track in the RTPC is less than 4.
  - Radius of curvature of the track is positive (positively charged particle).
  - More than 5 pads register above-threshold charge in the event.

[d]Denotes charge per unit length of a track registered by the readout pads.

[e]With respect to the center of the RTPC. It can be converted to the CLAS coordinate system by subtracting 58 cm, since the RTPC was at -58.0 cm in the CLAS coordinate system.

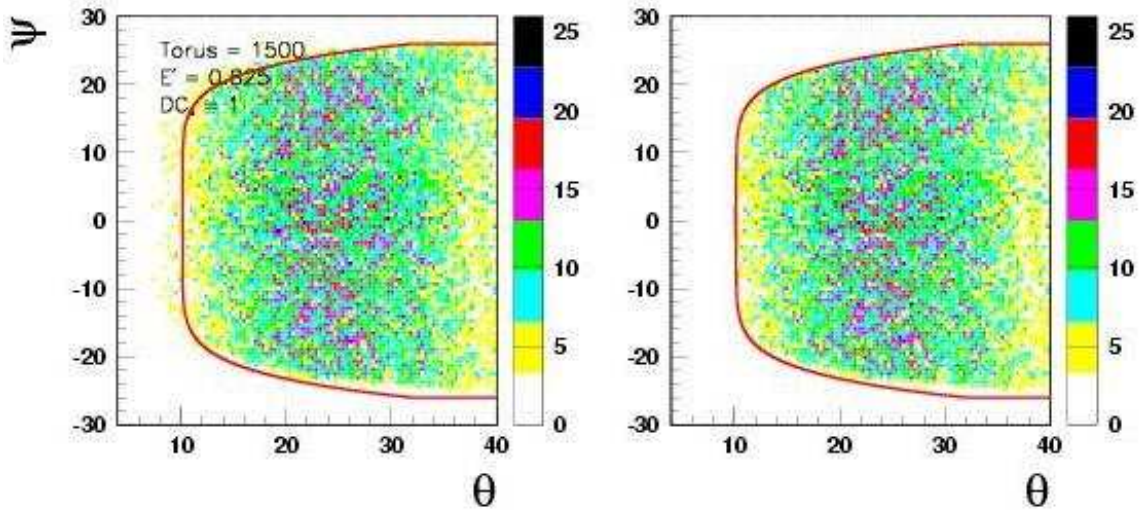

FIG. 69: The electron distribution shown as a function of the azimuthal angle relative to the sector mid-plane (vertical axis) and the polar angle (horizontal axis). Such distribution plots were used to find angular regions, in which the electron detection is less efficient (shown as less densely populated on the plot). Events with electrons going to these regions (outside of the red line on the plot) were not used in the analysis. The red line represents the fiducial cut. The 2 GeV beam energy data are shown.

– Total charge collected by the RTPC is larger than 0.

Corrections:

- RTPC proton momentum correction (see section IV.2.6).
- CLAS particle momentum corrections (see section IV.2.5).

IV.3.2 Accidental background subtraction

The aforementioned cut on the difference between the trigger electron vertex z and the spectator proton candidate vertex z (in conjunction with other cuts) left us with a rather clean sample of tagged events. Unfortunately, there still were accidental coincidences in a fraction of these events.

To eliminate such events, we assumed that the accidental background had a triangular shape and fit Δz ($\Delta z = z_{electron} - z_{spectator}$) with the sum of the Gaussian

representing the signal and the triangular background. This was done before the 15 mm cut was applied so that the "wings" of the distribution, which are pure background, would be used to estimate the background (see figure 70 for the fits). The vertical lines in figure 70 show the 15 mm Δz "signal" cut, events inside of which were considered to come mainly from the signal. Events with $|\Delta z|$ larger than 20 mm and smaller than 160 mm were considered to come from accidental coincidences ("wing" cut). We found the number of background events to the right of the "wing" cut ($\Delta z > 20$ mm), N_{right}, to the left of the "wing" cut ($\Delta z < -20$ mm), N_{left}, and inside the "signal" cut (-15 mm $< \Delta z <$ 15 mm), $N_{central}$, based on the triangular fit. We also assumed that in all of our kinematic bins accidental coincidences sneaking inside the cut represent the same fraction of overall events. Then, we counted the number of events falling outside the Δz cut for each bin $N_{bg,bin}$, and scaled it with the ratio $R_{bg} = N_{central}/(N_{right} + N_{left})$ of events inside and outside the cut that we got from the overall distribution. Thus, the sample of events free of accidental coincidences for a given bin was

$$N_{clean,bin} = N_{raw,bin} - R_{bg}N_{bg,bin}, \tag{141}$$

where $N_{raw,bin}$ is the number of raw events in a bin.

IV.3.3 Simulated data

For the simulated data, the same cuts are applied as for the real data, except for the CC and EC cuts. The CC and EC cuts were not used since the acceptance/calibration of these detectors was not fully understood. In particular, the hardware threshold for the EC trigger input was set rather high and varied throughout the experiment. This was remedied by additionally running the full inclusive simulation (ignoring spectator protons) and comparing it with the data (see figure 71). There were no CC and EC cuts in the inclusive simulation either. Comparison of the distribution of scattering angles and energies of the simulated electrons with inclusive experimental data allowed us to extract the trigger electron detection efficiency as a function of scattering angle and energy. The efficiency was used in the main analysis by weighing simulated counts and thus compensating our lack of understanding of the detector efficiency (see chapter V and figure 71 for more on this efficiency).

For the simulated data, only the first of the RTPC momentum corrections was used (see IV.2.6). No radius of curvature rescaling was applied. Similarly, the full

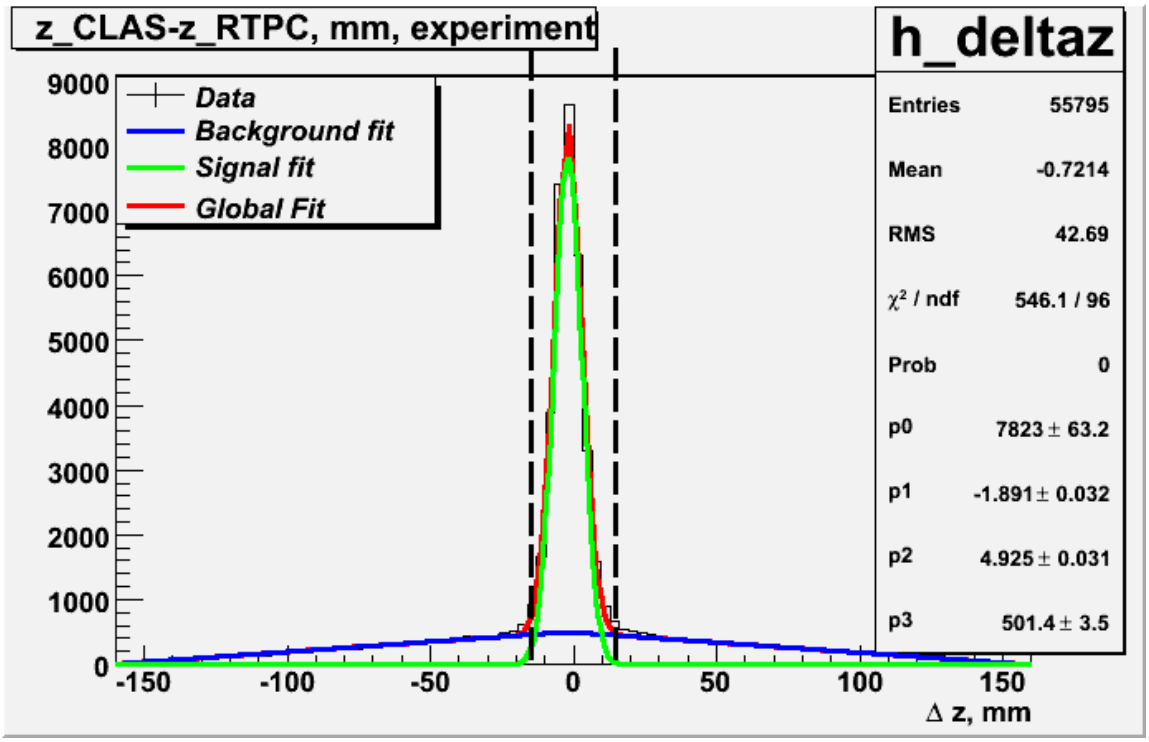

FIG. 70: The distribution of $\Delta z = z_{electron} - z_{spectator}$ for 2 GeV events before the Δz cut was applied. The experimental distribution (black line) was fit with a sum of the Gaussian representing the signal (green line) and the triangular background (blue line). The dashed vertical lines represent the ± 15 mm cut applied to the events in the analysis.

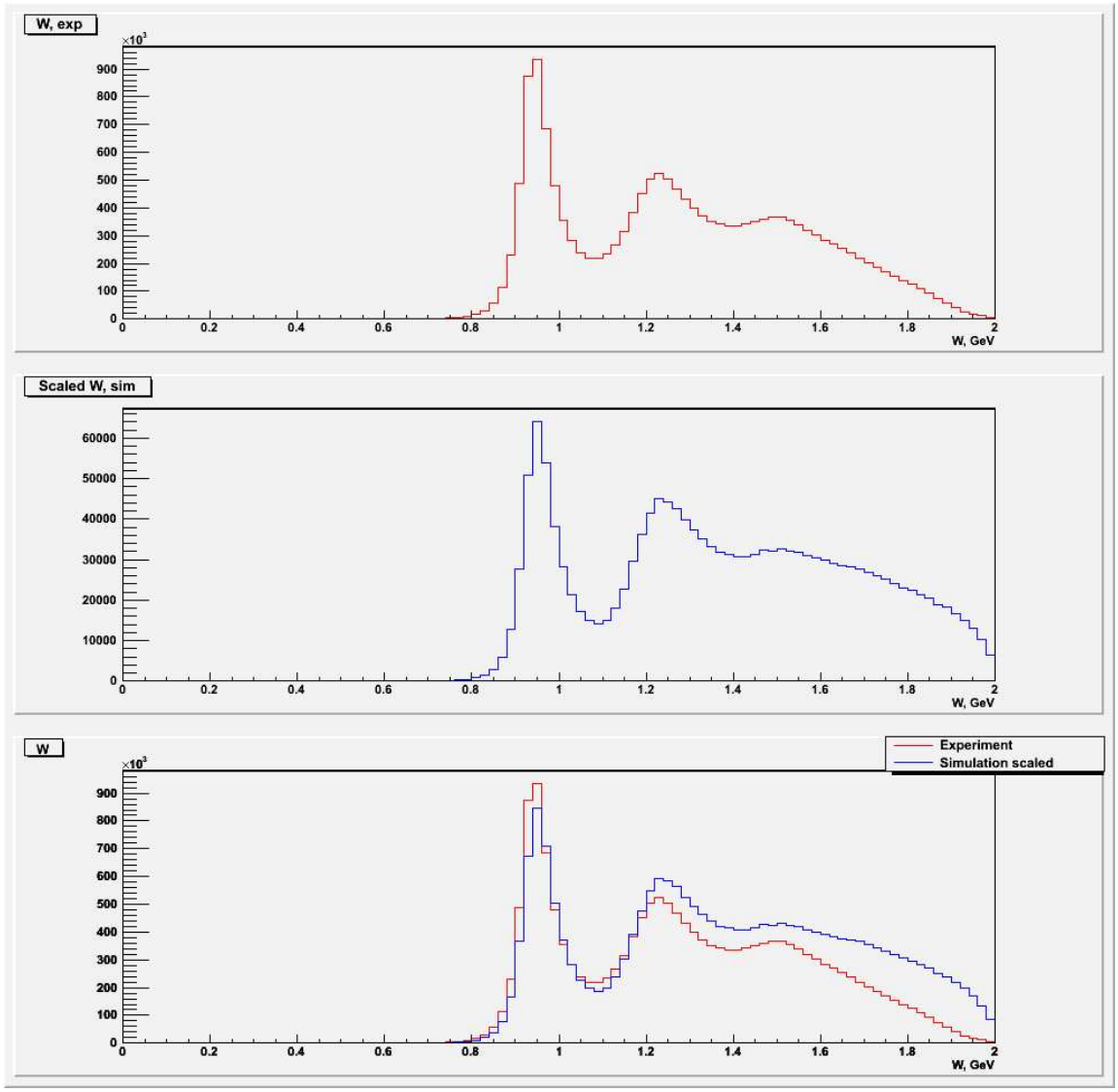

FIG. 71: Inclusive W distributions for experimental (red) and simulated (blue) data. Simulated data was scaled by a factor of 13.2 to account for the difference between experimental and simulated luminosity. The beam energy is 2.140 GeV.

CLAS momentum correction was not used; only the energy loss correction was applied. No accidental background subtraction was applied to the simulated data.

IV.4 HIGH LEVEL PHYSICS ANALYSIS

The physics analysis had the following goals:

- Check the spectator approximation (see section II.8.1).
- Study the off-shell F_{2n} structure function dependence on the spectator momentum p_s. We were not completely successful in this due to the p_s distribution being distorted because of unknown RTPC inefficiency at high p_s.
- Study the tagged[f] cross-section dependence on the angle between the spectator proton and the virtual photon θ_{pq}.

To achieve these goals the following steps were taken.

IV.4.1 Experimental data

First, events that pass certain cuts (details below) are filled into an array of structures containing:

- "Index" of the event - the number of the event as it was read in.
- Trigger electron momentum, GeV.
- Square of the momentum transfer (Q^2, GeV/c^2)
- Event invariant mass (W, GeV)
- Flag whether event was tagged (flag is true) or not (false).
- Spectator momentum, GeV (set to -10.0 if not tagged).
- Cosine of the angle between the direction of the spectator and the direction of the momentum transfer (set to -10.0 if not tagged).
- Invariant mass accounting for the neutron motion (W^*, GeV) (set to -10.0 if not tagged).

[f]Tagged events are events with a spectator proton registered in the RTPC.

- Polar scattering angle of the spectator, radians.
- z coordinate of the reaction vertex as reported by the RTPC, cm.
- Difference in the z coordinate of the vertex as reported by the RTPC for the spectator and registered by CLAS for the trigger electron.

IV.4.2 Simulated data

To estimate detector acceptance and inefficiencies, we need to utilize a simulation with subsequent comparison to real data. Additionally, if we want to compare the data with a certain model, we need to simulate events generated according to that model and compare them with the data.

Generating events

Events used in this analysis were generated using a generator written by Sebastian Kuhn. The generator is based on the RCSLACPOL code developed at SLAC [82]. The three purposes for which we need simulated events in this analysis are: subtracting the elastic tail from the inelastic event distribution, accounting for detector acceptance and inefficiencies, and comparing the experimental data with the spectator model. To satisfy these needs, three kinds of events were generated: 1) simulation of quasi-elastic scattering of electrons off the neutron inside deuterium in the plane wave spectator approximation including electromagnetic radiative effects, 2) simulation of inelastic scattering off the neutron in the same framework (with radiative effects), 3) Fully inclusive scattering $d(e,e')X$ off the deuteron (with radiative effects).

Events with quasi-elastic scattering of the electron off a moving neutron in the spectator picture are produced as follows. Initially, the electron is assigned random kinematics within the boundaries (Q^2 and ν) defined in the configuration file. In the spectator picture, the energy and momentum of the off-shell bound nucleon (E_N and $\vec{p}_N$) are related to the spectator nucleon momentum $\vec{p}_s$ as

$$E_N = M_D - \sqrt{M_p^2 + p_s^2} \tag{142a}$$

$$\vec{p}_N = -\vec{p}_s. \tag{142b}$$

And the target nucleon mass is

$$M^* = \sqrt{(M_D - \sqrt{M_p^2 + p_s^2})^2 - p_s^2}. \tag{143}$$

The initial momentum of the struck nucleon is distributed according to

$$P(\vec{p}_N) = |\psi(\vec{p}_N)|^2, \tag{144}$$

where $\psi(\vec{p}_N)$ is the Paris deuteron wavefunction [83] rescaled using light-cone formalism [86] (see equations (60) - (62)). The events were then generated according to the cross-section given by equation (16) (the equation is given for the proton, but it has the same form for the neutron with the proton form factors substituted by the corresponding neutron form factors) in the rest reference frame of the target nucleon. The elastic radiative tail is calculated using the full prescription of Mo and Tsai [87]. The reduction of the quasi-elastic peak itself due to the internal radiation is given by

$$\left(\frac{d\sigma}{d\Omega}\right)_{rad} = e^{\delta} \left(\frac{d\sigma}{d\Omega}\right)_{Born}, \tag{145}$$

where the expression for the parameter δ is given in [87]. The event generator also simulated external radiative energy loss *before* scattering due to material in the beam.

The inelastic data were generated similarly to the quasi-elastic data. The cross-section was evaluated using

$$\frac{d\sigma}{dE'\,d\Omega} = \left(\frac{d\sigma}{d\Omega}\right)_{Mott} \frac{2MxF_2(x,Q^2)}{\epsilon Q^2} \frac{1 + \epsilon R(x,Q^2)}{1 + R(x,Q^2)}, \tag{146}$$

where $R = \sigma_L/\sigma_T$, σ_L and σ_T being the longitudinal and transverse cross-sections. The polarization of the virtual photon, ϵ, is given by

$$\frac{1}{\epsilon} = 1 + 2\left(1 + \frac{Q^2}{4M^2x^2}\right)\tan^2\frac{\theta}{2}. \tag{147}$$

Equation (146) is just another form of equation (34) written this way for convenience. The New Muon Collaboration (NMC) fit to SLAC, BSDMS and NMC data on the proton and deuteron structure functions was used [88]. The neutron structure function was obtained by Bosted *et al.* [93] by a fit to proton and deuteron data including Fermi smearing. The parameterization of the R ratio from [89] was used. Radiative effects were simulated using the output of the SLACPOLRAD program [82]. SLACPOLRAD calculates the ratio of radiated to Born (unradiated) cross-section

for DIS without the elastic tail. These ratios were applied to scale the generated unradiated cross-section.

The fully inclusive events were generated by adding quasi-elastic and inelastic events from both the neutron and the proton (integrated over all spectator momenta), plus the radiative elastic tail from $D(e,e')D$.

Detector simulation

The generated events were then run through the full experimental setup simulation including external radiation losses. The target and RTPC part of the setup were simulated in all the details using a GEANT4-based [90] simulation package written for our experiment (the same setup that was used for the RTPC momentum corrections, see section IV.2.6). The standard CLAS part of the setup was simulated using an existing GEANT3-based package, called GSIM, a standard CLAS software package describing all the other detectors besides the RTPC. Particle paths through the RTPC were simulated. The output information was written to files which served as input for the GSIM package. To simulate inefficiencies of the CLAS detector, the output of the GSIM served as an input to the GSIM Post Processing package (GPP), which accounted for such things as finite resolution of DC and SC, broken DC wires, etc.

After the generated events went through the simulated detectors, we obtained files with simulated detector responses for the generated events. Finally, these files were processed by the usual data processing program (RECSIS), the same one that was used for processing experimental events. The outputs of RECSIS for experimental and simulated events were directly compared and used in the analysis. Figures 72 and 73 show plots of the W and W^* distributions for quasi-elastic 4 and 5 GeV beam energy simulations, respectively, as examples of simulation results. Then quasi-elastic simulated events that pass certain cuts were filled into the array of structures identical to those for the experimental data. The same was followed with inelastic simulated events. Figures 74 and 75 show plots of the W and W^* distributions for inelastic 4 and 5 GeV beam energy simulations, respectively, as examples of simulation results.

The fully inclusive events (both data and simulation) were binned in E' and θ (ignoring any spectator tracks in the RTPC). The three arrays are passed to the plotting routine that performs necessary binning of the data with subsequent filling

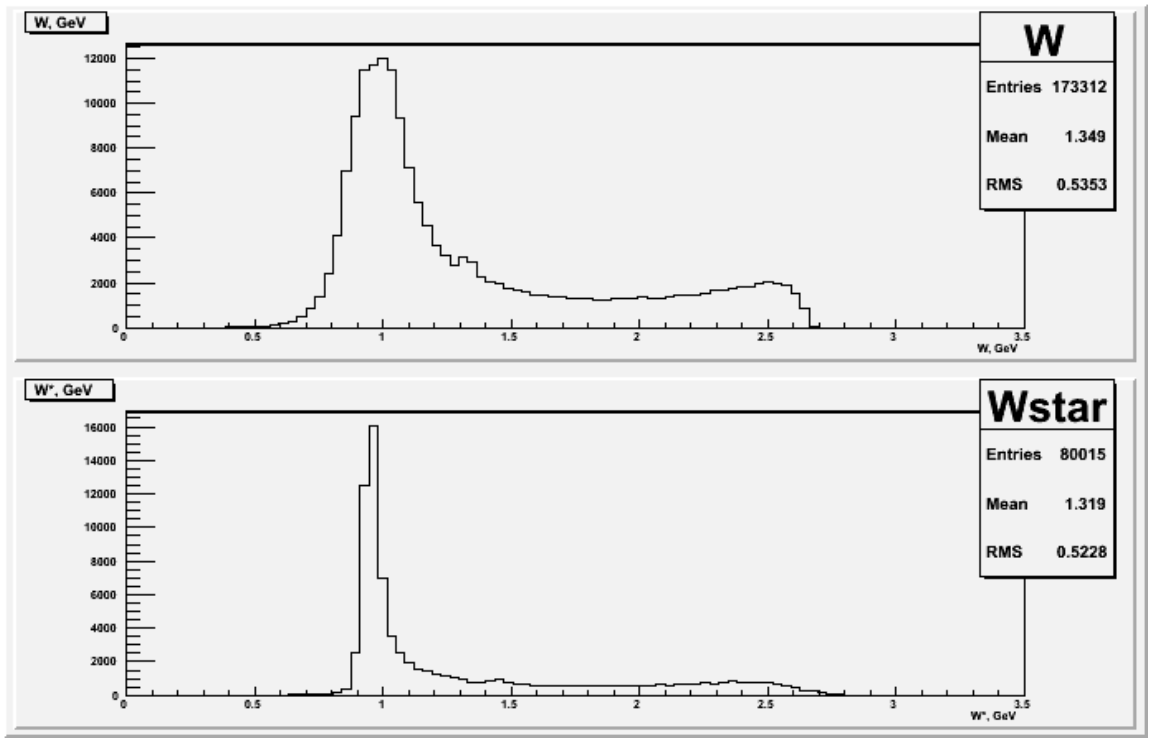

FIG. 72: The W and W^* distributions of the quasi-elastic simulation for the 4 GeV data.

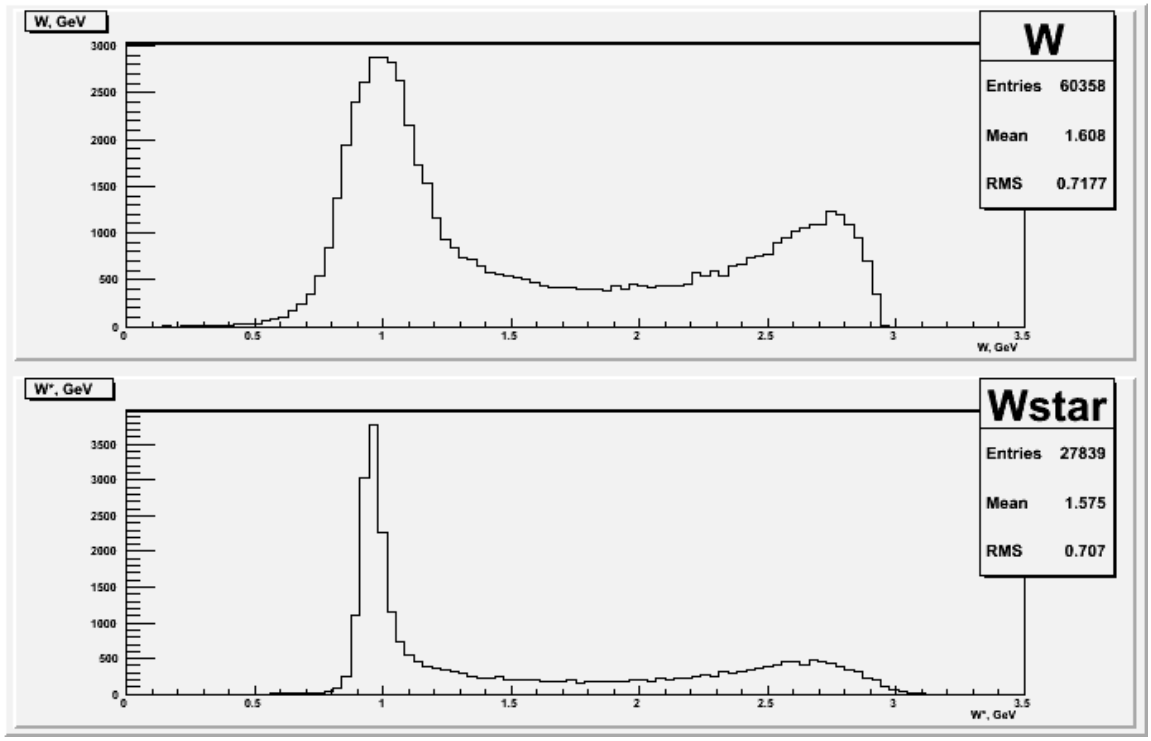

FIG. 73: The W and W^*distributions of the quasi-elastic simulation for 5 GeV beam energy.

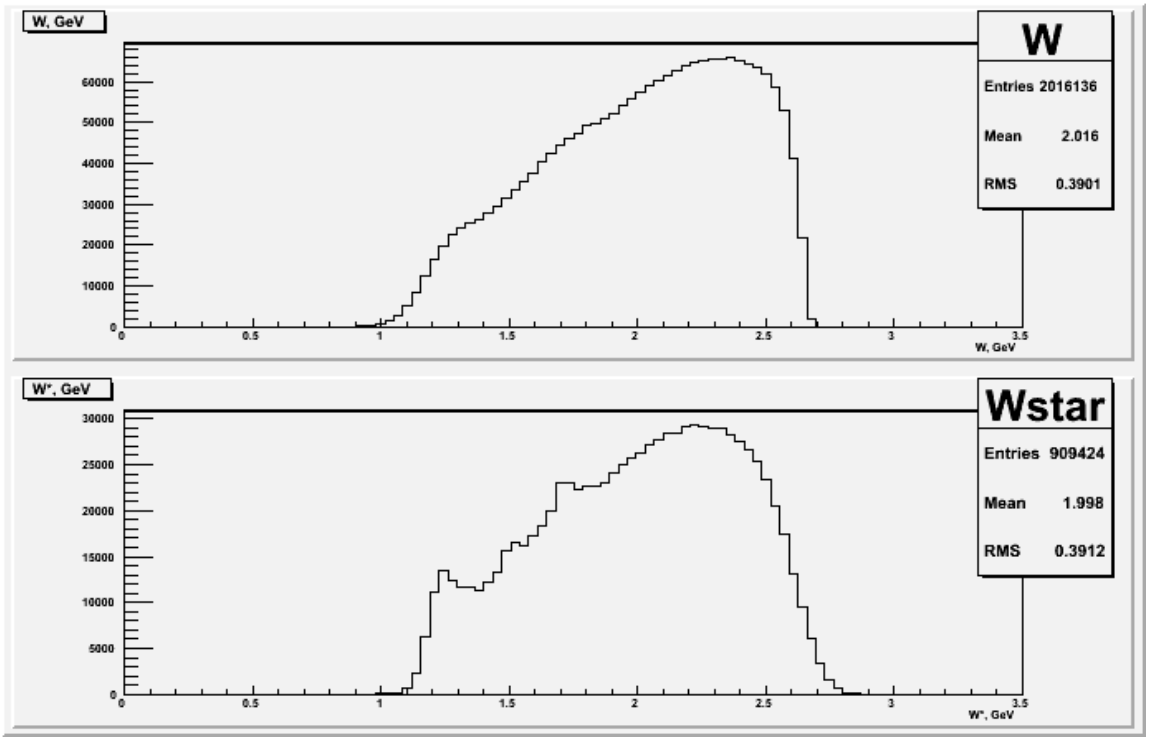

FIG. 74: The W and W^* distributions of the inelastic simulation for the 4 GeV data.

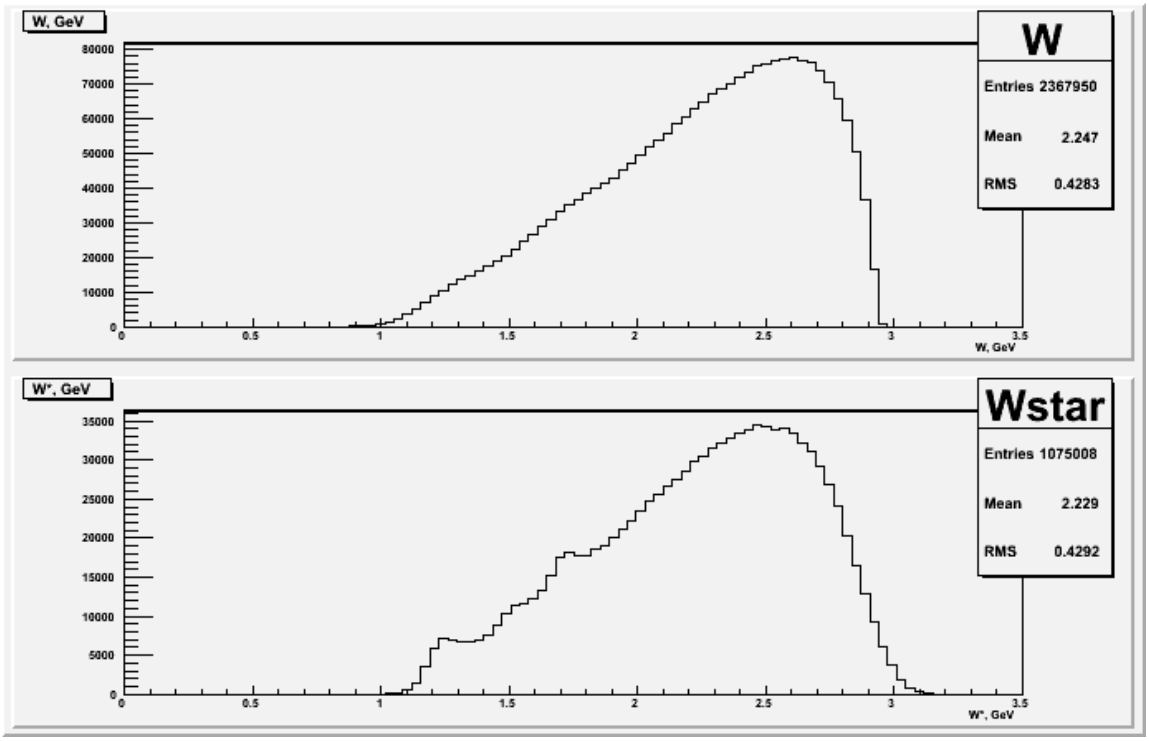

FIG. 75: The W and W^*distributions of the inelastic simulation for 5 GeV beam energy.

and plotting of needed histograms and graphs (see below).

IV.5 PRESENTATION OF DATA

A loop over all experimental events that passed the cuts (see section IV.3) was performed. If an event was tagged, the W^*, Q^2, $\cos(\theta_{pq})$, and spectator momentum bins corresponding to the values recorded in the structure were found. Binning in W^* is performed twice: once with 6 bins for making plots in other variables for events belonging to the given bin, and the other with 90 bins, for plotting other variables *vs* these bins. In the same fashion 2 possible sets of $\cos(\theta_{pq})$ bins were made: 3 bins for making plots in other variables, 10 bins for making plots with $\cos\theta_{pq}$ plotted on the horizontal axis. In detail, we use the following bins:

- $\cos(\theta_{pq})$ bins:
  - "Small" bins: 10 equal bins between -1 and 1.
  - "Big" bins: 3 bins, lower bounds being: -0.75, -0.25, 0.25, upper bounds being -0.25, 0.25, 0.75.
- Spectator momentum bins - 4 bins, lower bounds: 0.07, 0.09, 0.11, 0.13 GeV; upper bounds: 0.09, 0.11, 0.13, 0.15 GeV.
- Q^2 bins:
  - For 2 GeV beam energy: 3 bins, lower bounds: 0.2227, 0.4524, 0.7697 GeV/c; upper bounds: 0.4524, 0.7697, 1.0969 GeV/c.
  - For 4 GeV beam energy: 3 bins, lower bounds: 0.7697, 1.0969, 2.2277 GeV/c; upper bounds: 1.0969, 2.2277, 4.5243 GeV/c.
  - For 5 GeV beam energy: 2 bins, lower bounds: 1.0969, 2.2277 GeV/c; upper bounds: 2.2277, 4.5243 GeV/c.
- W^* bins:
  - "Big" bins, for plotting other variables - 6 bins, lower bounds: 0.88, 1.00, 1.35, 1.60, 1.85, 2.20 GeV; upper bounds: 1.00, 1.35, 1.60, 1.85, 2.20, 2.68 GeV.
  - "Small" bins, for horizontal axis - 90 bins equally spaced between 0.88 and 2.68 GeV.

As a result of the binning procedure three arrays are filled: tag_counts_exp - "small" bins in $\cos(\theta_{pq})$, "big" bins in W^*; tag_byreg_exp - "big" W^* bin, "big" $\cos(\theta_{pq})$ bin, tag_wplots_exp - "small" W^* bins, "big" $\cos(\theta_{pq})$ bins.

IV.6 EXTRACTION OF F_{2N}

After the experimental data were binned, almost identical loops were performed over the simulated events, first from the elastic simulation, then from the inelastic simulation. Simulated counts were then multiplied by the trigger electron detection efficiency (see section IV.3.3).

The quasi-elastic radiative tail was subtracted from the data distribution using the quasi-elastic simulation. For this purpose, quasi-elastic simulation and data were cross-normalized in the vicinity of the quasi-elastic peak, and the cross-normalized quasi-elastic simulation was subtracted from the experimental data. For this, cross-normalization factors (denoted as *ratio*'s below) between the quasi-elastic simulation and the elastic region of the experimental distribution were calculated using numbers of events in the corresponding elastic bin, the bin with W^* being between 0.88 and 1.00 GeV and with bins in the other variables being the same as for the bin for which the cross-normalization is being performed. The data from the simulation of inelastic tagged scattering (see section IV.4.2) was then cross-normalized with the experimental data. The cross-normalization factors were found by summing experimental and simulated counts over a specific region in W^*, Q^2 and $\cos\theta_{pq}$, where (according to the theoretical expectations) the spectator picture should be most appropriate. The region in each of the variables was: for 2 GeV data, W^* between 1.7 and 1.8 GeV, Q^2 between 0.4524 and 0.7697 $(\mathrm{GeV}/c)^2$, and $\cos(\theta_{pq})$ between -0.75 and -0.25; for 4 GeV data, W^* between 2.0 and 2.2 GeV, Q^2 between 1.0969 and 2.2277 $(\mathrm{GeV}/c)^2$, and cosine of θ_{pq} between -0.75 and -0.25; for 5 GeV data, W^* between 1.9 and 2.1 GeV, Q^2 between 1.0969 and 2.2277 $(\mathrm{GeV}/c)^2$, and $\cos(\theta_{pq})$ between -0.75 and -0.25. This region was chosen so that the spectator picture works well in it and we are beyond the resonant region. Because of our lack of understanding of the momentum dependence efficiency spectator proton detection in the RTPC, these factors were found and applied separately in each spectator momentum bin.

After this, several kinds of histograms are filled, most notable being: histograms for Q^2, W^* ("big" bins), p_s (spectator momentum) bins with $\cos\theta_{pq}$ ("small" bins)

being the horizontal axis and histograms for Q^2, $\cos\theta_{pq}$ ("big" bins), p_s bins with W^* ("small" bins) being the horizontal axis.

In the first case, when plots are *vs* $\cos\theta_{pq}$, "small" bins in cosine, "big" bins in W^* are used (tag_counts... arrays). Different plots for the following quantities are generated:

1. The simplest one, the number of experimental counts (black squares in figure 76).

2. The number of experimental counts with accidental background subtracted (blue crosses in figure 76).

3. The number of experimental counts with accidental background and elastic radiative background from the elastic simulation, which is shown in red in figure 76, subtracted.

4. The number from the previous item divided by the number of inelastic simulated counts:

$$ratio = cleaned_prelim/inelsimcount, \tag{148}$$

where *inelsimcount* is the normalized number of inelastic simulated counts in the bin. This *ratio* plot lets us eliminate detector effects (acceptance, inefficiency), thus directly providing access to the physics of the problem; the most obvious use of them would be comparing them with flat lines to check the validity of the spectator picture. See chapter V for a more detailed description.

In the second case, when plots are *vs* W^*, tag_Wplots... arrays are used for the number of counts ("small" W, "big" cosine bins), whereas *ratio* is calculated using tag_byreg... arrays ("big" W bins, "big" cosine bins, since in this binning bin 0 in W corresponds to the elastic peak, and the number of cosine bins is identical to the one used in calculating counts). But now W^* is plotted on the horizontal axis, and "big" cosine bins are used instead of "big" W^* bins.

As mentioned in section IV.4.2, the differential cross-section can be written as

$$\frac{d\sigma}{dE'\,d\Omega} = \left(\frac{d\sigma}{d\Omega}\right)_{Mott} \frac{2MxF_2(x,Q^2)}{\epsilon Q^2} \frac{1+\epsilon R(x,Q^2)}{1+R(x,Q^2)}, \tag{149}$$

where $R = \sigma_L/\sigma_T$, σ_L and σ_T being the longitudinal and transverse cross-sections. As also shown in section IV.4.2, all factors in equation (149) (and all additional

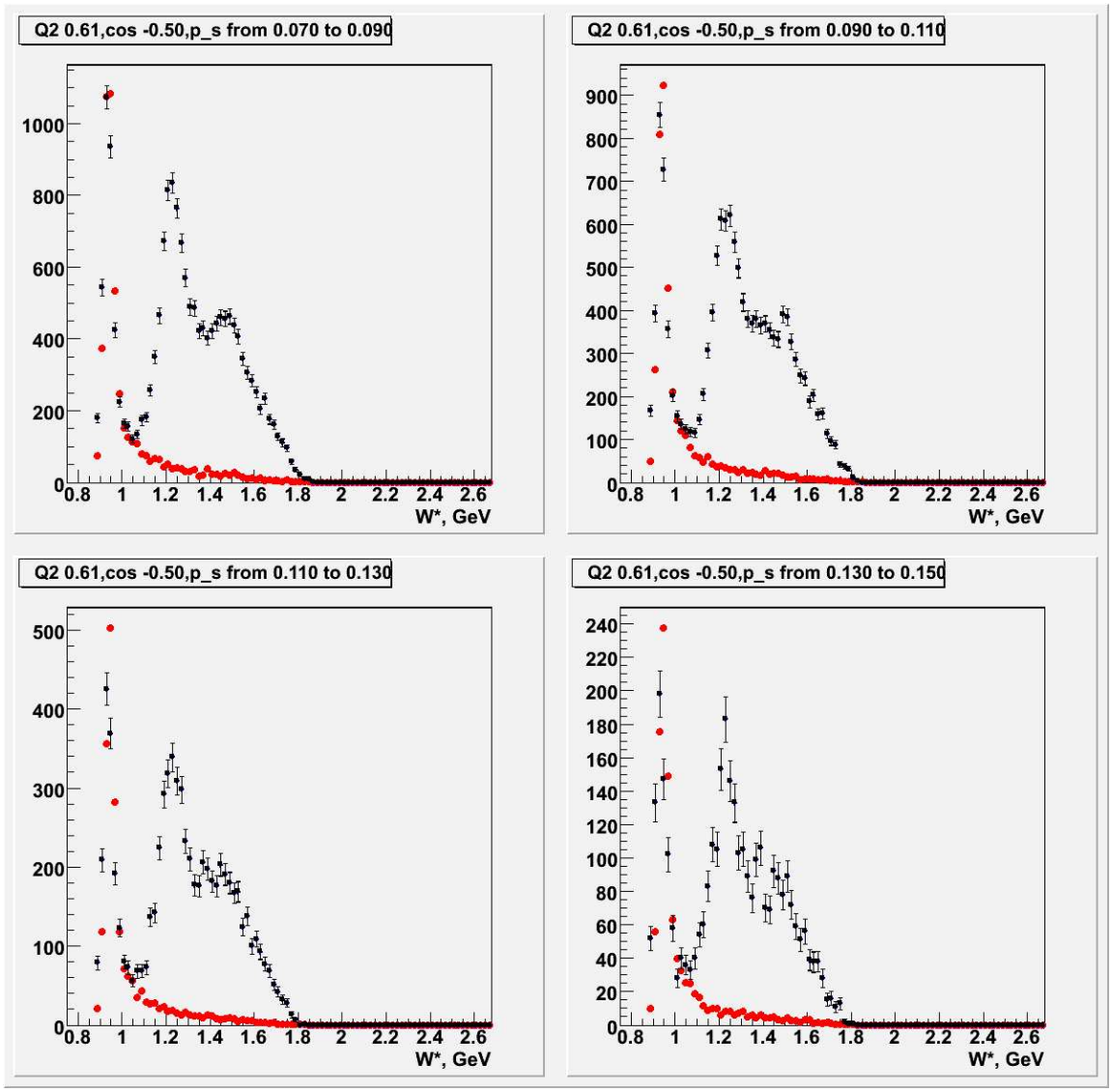

FIG. 76: Raw data (black squares), raw data with subtracted accidental background (blue crosses, barely visible behind the black squares), and elastic simulation cross-normalized with experimental data (red circles) are shown for four typical p_s bins, Q^2 between 0.45 to 0.77 $(\mathrm{GeV}/c)^2$, and $\cos(\theta_{pq})$ between -0.75 and -0.25. The beam energy is 2.140 GeV.

factors due to radiation, smearing, acceptance, and efficiency) are modeled by our simulation. Thus, if the simulation is done properly, the aforementioned scheme leaves you with the ratio of experimental (effective) and simulated (model) structure functions $F_{2n}^{eff}/F_{2n}^{model}$. In this case, structure function F_{2n}^{eff} plots are obtained from the *ratio* plots by multiplying them by the value of F_{2n}^{model} (used in producing the simulated data) for a given (Q^2, W^*) value. F_{2n} is then plotted as a function of W^*. Consequently, these plots are converted into F_{2n} *vs* x^* plot by relating W^* to x^* as

$$x^* = \frac{Q^2}{(W^*)^2 - M_N^2 + Q^2}, \tag{150}$$

where M_N is the nucleon mass.

CHAPTER V

RESULTS

The goal of this work is to analyze the dependence of the extracted effective neutron structure function F_{2n}^{eff} on the kinematic conditions, namely the spectator proton momentum p_s and spectator proton scattering angle θ_{pq}. As mentioned in the analysis chapter, to achieve that, we took the ratio of the experimental d(e,e$'p_s$) data (where the experimental F_{2n}^{eff} was convoluted with acceptance, efficiency, binning and other effects) to the simulated data (where the model F_{2n}^{model} used in the simulation was convoluted with the same acceptance, efficiency, binning and other effects), subtracted the accidental background and elastic tail. Multiplying the ratio with the model structure function leaves you with the experimental structure function, that is, we arrive at the final goal of this research. The experimental F_{2n}^{eff} could be distorted (and acquire a $\cos\theta_{pq}$ dependence) through FSI, or if the used spectator model does not have the correct spectator momentum distribution. Thus, studying the dependence mentioned earlier will allow us to check the FSI role as well as the spectator model.

V.1 SYSTEMATIC ERRORS

The systematic error can be defined as a bias in measurement which leads to the situation where the mean of many separate measurements differs significantly from the actual value of the measured attribute. CLAS detectors, as well as the RTPC, have such biases. Since we are analyzing a ratio of the experimental data to the simulated data, we look here for systematic errors that are not overall scaling factors.

- **Accidental background subtraction.** The background subtraction is performed by first plotting the distribution of all events for the given energy as a function of Δz, the distance along the beamline between the reaction vertex as reported by CLAS for the trigger electron and as reported by the RTPC for the spectator proton, with the idea being that particles that are too far away from each other in space are accidental coincidences in time. Then the fraction of the accidental background is estimated as the ratio of the events in the "wings" of the Δz distribution and events under the signal peak. For

this purpose, "wings" are taken to be between 20 and 160 cm for $|\Delta z|$, and the signal is between -15 and 15 cm (see section IV.3.2).

The "wings" could be chosen between different limits, and the effect of the choice of these limits is estimated in this systematic error. For this purpose, the number of events between 20 and 90 cm for $|\Delta z|$ was counted. The background was then found using these new limits as well as with the original (20 - 160 cm) limits. The background is found by multiplying the number of counts in the "wings" in each of the chosen bins by the ratio found by taking the ratio of "signal" to "wings" (see the previous paragraph). Due to 2 different choices of the "wings", there are also 2 ratios that were found using 2 sets of "wing" Δz limits. They multiply the counts in corresponding "wings" to find the number of background counts in each of the limit sets. The systematic error due to the choice of the limits was found as

$$error^2 = (count_{old\ limits} - count_{new\ limits})^2, \tag{151}$$

where $count_{old\ limits}$ denotes the number of background-subtracted events found with limits of (20 - 160 cm), and $count_{new\ limits}$ is the number of events found with limits of (20 - 90 cm). The *error* shown here applies directly to the background subtracted data.

- ***E′−θ* dependent acceptance and efficiency error.** This is the uncertainty on the estimate of the detection efficiency of the CLAS trigger electrons. Since the CLAS electron detection efficiency was not 100%, we needed to account for this. This was done by performing an inclusive event simulation and comparing the simulated distribution to the experimental one (see figure 71 for plots of the inclusive experimental and scaled - to account for difference in luminosity - simulated W distributions). The efficiency of the detection was found as a function of E', the energy of the scattered electron, and θ, the electron scattering angle. By performing a two-dimensional multi-linear fit of the efficiency as a function of these two variables, and estimating point-to-point fluctuations in the efficiency, the $E' - \theta$ error was found to be 8.5%. This means that the value of the experimental to simulated data ratio for a given bin is assigned an additional error equal to the value of the ratio multiplied by 0.085 due to the uncertainty in the trigger electron detection efficiency.

- F_{2n} **model dependence.** The simulations used in this research utilized an input model F_{2n}. The systematic error due to this model dependence was estimated to be 5%. It is not shown on plots 78 - 184 since it affects all $\cos\theta$, p_s bins equally and since we cross-normalize.

- **Experiment - simulation cross-normalization.** Experimental and simulated data were cross-normalized by taking the ratio in a chosen Q^2 - $\cos(\theta_{pq})$- W^* bin for each energy (see analysis description for more). The cross-normalization dependence on the choice of this bin in each of these variables was estimated to be 30% for 2 GeV data, 15% for 4 GeV data, and 10% for 5 GeV data. This error was estimated by checking the spread of the values for the bins other than the one for which the cross-normalization was performed. This uncertainty is not shown on plots 78 - 184, since it affects all the bins in a given distribution uniformly.

- **Monte-Carlo simulations.** The ratio of the experimental to the simulated data was found for each bin as

$$ratio = \frac{exp - bg - elas_tail}{inelsimcount}, \tag{152}$$

where *exp* is the experimental data count for the bin, *bg* is the accidental background, *elas_tail* is the normalized elastic tail found using simulated data, *inelsimcount* is the number of counts in this bin from the simulated data multiplied by the trigger electron detection efficiency and cross-normalized with the experimental data count. The error on this quantity due to the uncertainty in Monte-Carlo (MC) counts can be found by chain differentiation as

$$\Delta ratio_{MCcount} = \frac{\partial(ratio)}{\partial(MCcount)} \Delta ratio_{MCcount}, \tag{153}$$

where $\Delta ratio_{MCcount}$ is the uncertainty on the ratio due to the MC count uncertainty and $MCcount$ is the number of MC counts in the bin. The uncertainty found consisted of two parts:

1. **Monte-Carlo statistics.** The error due to the simulation statistics was found for each bin for the experiment to simulation ratio according to

$$error^2 = \left(\frac{elsimcount}{inelsimcount}\right)^2 / pure_elas_count + \frac{ratio^2}{pure_inelas_count}, \tag{154}$$

where *elsimcount* is the cross-normalized with experiment number of events in this bin from the elastic simulation, *inelsimcount* is the cross-normalized with experiment number of events in this bin from the inelastic simulation, *ratio* is the aforementioned experiment to simulation ratio for the bin, *pure_elas_count* is the number of events from the elastic simulation for this bin, and *pure_inelas_count* is the number of events from the inelastic simulation for this bin.

2. **Monte-Carlo systematics.** A systematic error due to the simulation was found as

$$error^2 = \left(\frac{0.1\ elsimcount}{inelsimcount} \right)^2, \tag{155}$$

where *elsimcount* is the cross-normalized with experiment number of events in this bin from the elastic simulation, *inelsimcount* is the cross-normalized with experiment number of events in this bin from the inelastic simulation. The factor of 0.1 is the potential cross-normalization error between quasi-elastic simulation and experimental data, due to a somewhat different shape in W^* of the corresponding quasi-elastic peaks (see figure 76).

The systematic errors due to $E' - \theta$ efficiency, background subtraction, and Monte - Carlo simulation (both parts) were added in quadratures, and the square root of this sum is shown on the plots as a point to point systematic error for the ratios of the experimental to simulated data. To convert these values to systematic errors of the F_{2n} structure function, they are multiplied by the value of model F_{2n} in the bin for which the error is calculated.

V.2 RESULTS AND DISCUSSION

As mentioned before, the goal is to find the effective neutron structure function F_{2n}^{eff} as a function of W^* and θ_{pq}.[a] This will allow us to:

1. Check the validity of different FSI theories and/or their range of applicability since different theories predict different dependence of FSI on the outgoing proton angle (see section II.8.2 for details).

[a]Only the ratio of experimental to simulated data was obtained for the plots *vs* $\cos(\theta_{pq})$. This ratio (its deviation from 1) describes the deviation of the experimental data from the simulation, and thus (since the simulation is based on the spectator model) from the spectator model. This lets us perform analysis mentioned in the first two items.

2. Check the general validity and/or range of validity of the PWIA spectator picture in both spectator angle and momentum since dependence of the effective structure function F_{2n}^{eff} on these quantities is different in different models (see section II.8.2 for details).

3. Eventually extrapolate the effective structure function values to the on-shell nucleon pole, thus finding the free neutron structure function F_{2n} (not covered in this work).

The full data set in all of our bins is shown, for each beam energy in sequence, in figures 78 - 184. In the following, we discuss the dependence of ratios and extracted effective structure functions on W^* and $\cos\theta_{pq}$.

V.2.1 W^* dependence

The aforementioned ratio dependence on W^* for different Q^2 regions and four spectator momentum regions split into backward, forward and intermediate regions[b] of the spectator proton scattering lets us analyze:

1. How well the PWIA spectator model and the used model for the free F_{2n} describe the scattering process for all final state invariant masses and all spectator momenta.

2. Whether at different values of the proton recoil momentum and angle this agreement is better or worse.

3. Dependence of these results on Q^2. There are structure function Q^2-dependent effects (F_{2n} is different at different Q^2), but there are also reaction mechanism Q^2-dependent effects, such as resolving different distance scales at different Q^2. We must investigate the possibility of decoupling these two competing sources of variation in results in the used model.

2 GeV energy

For the lowest Q^2 bin, Q^2 between 0.22 and 0.45 $(\mathrm{GeV}/c)^2$, (figures 78 - 80) all the ratio plots exhibit a resonance-like "bump" in the vicinity of $W^* = 1.5$ GeV.

[b]The "nomenclature" I use here for the bins introduced in IV.5 is: $\cos\theta_{pq} = -0.75 \ldots -0.25$ - backward region; $\cos\theta_{pq} = -0.25 \ldots 0.25$ - intermediate region; $\cos\theta_{pq} = 0.25 \ldots 0.75$ - forward region.

This bump is an indication that resonance contribution may be underestimated in our model for F_{2n}. Other than that, the ratios are consistent with 1, except for the forward region, especially as the spectator momentum gets high. This trend is consistent with the spectator model, which should work worse (if at all) for higher momenta and more forward angles. There is a rise at low W^*, which is a remnant of the elastic tail, which may not be completely subtracted (this could also be due to an incompletely simulated resolution effect, where the simulated data fall off more sharply as $W^* \rightarrow 1.08$, than the real ones). The structure function plots (figures 87 - 89 and 96 - 98), which are direct descendants of the ratio plots, consequently exhibit reasonable agreement between the model and data points (with a slight disagreement at $W^* \sim 1.5$), except for the forward region where the disagreement gets worse with increasing p_s (this is expected since the spectator model should work better at lower p_s [51]) and W^* (this is expected from the target fragmentation and FSI models of [53] and [55]).

Plots for the next Q^2 bin, Q^2 between 0.45 and 0.77 $(\mathrm{GeV}/c)^2$ (see figures 81 - 83 for ratios, 90 - 92 for plots of F_{2n} *vs* W^*, and 99 - 101 for plots of F_{2n} *vs* x^*), demonstrate all the attributes described for the lower bin plots. Namely, there is a resonance-like structure between W^* of 1.4 and 1.6 GeV; the agreement with the spectator model gets worse as we go to the forward region, especially for higher p_s bins. There is a rise at low W^*, which is a remnant of elastic tail subtraction.

In plots for the highest Q^2 bin at this energy, Q^2 between 0.77 and 1.10 $(GeV/c)^2$ (see figures 84 - 86 for ratios, 93 - 95 for plots of F_{2n} *vs* W^*, and 102 - 104 for plots of F_{2n} *vs* x^*), the statistics are much worse and it is difficult to draw conclusions, except to note that reasonable agreement of the distributions with 1 and the deviation from one in the forward region, especially in higher p_s bins. Overall, there seems to be little dependence of the ratio $F_{2n}^{eff}/F_{2n}^{model}$ on Q^2.

4 GeV energy

For the lowest Q^2 bin, Q^2 between 0.77 and 1.10 $(\mathrm{GeV}/c)^2$, (see figures 115 - 117 for ratios, 124 - 126 for plots of F_{2n} *vs* W^*, and 133 - 135 for plots of F_{2n} *vs* x^*) all the ratio plots are consistent with one (except for some structure between W^* of 1.2 and 1.4 GeV that can be again attributed for resonance effects not accounted for in model F_{2n}), and, as a consequence, the effective structure function points lie on top of the model structure function.

This also holds for the next Q^2 bin, Q^2 between 1.10 and 2.23 $(\mathrm{GeV}/c)^2$ (see figures 118 - 120 for ratios, 127 - 129 for plots of F_{2n} *vs* W^*, and 136 - 138 for plots of F_{2n} *vs* x^*).

For the highest Q^2 bin, Q^2 between 2.23 and 4.52 $(\mathrm{GeV}/c)^2$ (see figures 121 - 123 for ratios, 130 - 132 for plots of F_{2n} *vs* W^*, and 139 - 141 for plots of F_{2n} *vs* x^*), the statistics is worse than in lower Q^2 bins making it harder to draw accurate conclusions, but, within errors, the distributions are not inconsistent with the descriptions given for the lower Q^2 bins.

The lowest Q^2 bin agrees reasonably well with the same Q^2 bin in 2 GeV, but is much smoother due to better statistics. It shows a much lesser increase at forward θ_{pq} and higher p_s.

5 GeV energy

For the lowest Q^2 bin, Q^2 between 1.10 and 2.23 $(\mathrm{GeV}/c)^2$ (see figures 157 - 159 for ratios, 163 - 165 for plots of F_{2n} *vs* W^*, and 169 - 171 for plots of F_{2n} *vs* x^*), the ratios are consistent with 1 for the backwards and forward regions, but they are slightly below 1 for two higher p_s bins in the intermediate region, which could be attributed to FSI that are supposed to be large in the intermediate region (see section II.8.2). Resonance-like bumps can be seen for both W^* between 1.2 and 1.4 GeV and W^* between 1.4 and 1.6 GeV (*cf* lower beam energies).

For the next Q^2 bin, Q^2 between 2.23 and 4.52 $(\mathrm{GeV}/c)^2$ (see figures 160 - 162 for ratios, 166 - 168 for plots of F_{2n} *vs* W^*, and 172 - 174 for plots of F_{2n} *vs* x^*), the statistics get worse, but the distributions for the ratio plots are still consistent with 1, and F_{2n}^{eff} distributions are consistent with model F_{2n}.

Some factors that added uncertainty to the analysis of the described results are:

- Since p_s resolution is not very good, there might be an overlap of different p_s bins.

- Insufficiently understood momentum dependent efficiency of the RTPC made it necessary to cross-normalize experiment and simulation separately for each p_s bin. This could hide systematic offsets of ratios from 1, and, consequently, F_{2n}^{eff} from model F_{2n}.

The results exhibit a nearly perfect agreement of $F_{2n}^{eff}(W^*)$ with the model for all but the lowest Q^2 and all W^* for the lowest p_s bin and backward θ_{pq}.

V.2.2 θ_{pq} dependence

The dependence of the data-to-simulation ratio on the cosine of the angle θ_{pq} for different Q^2 regions and four spectator momentum regions, split into six W^* bins (see section IV.5) roughly following resonance regions lets us analyze:

1. The applicability of the PWIA description as a function of $\cos(\theta_{pq})$
2. How the agreement with PWIA expectations (flat angular dependence) depends on final state W^*, Q^2 and spectator momentum.
3. Dependence of the results on the Q^2 value, showing the presence or absence of such dependence.

2 GeV energy

For the lowest Q^2 bin, Q^2 between 0.22 and 0.45 $(\mathrm{GeV}/c)^2$ (figures 105 - 108), the curve is close to a flat line for the 2 lower p_s bins and the lowest W^* bin. With the increase of W^* and p_s, the distribution starts deviating from the flat line, exhibiting two competing effects: a dip at around 90° and a rise towards the forward direction where one expects a contribution from the current fragmentation region.

For the next Q^2 bin, Q^2 between 0.45 and 0.77 $(\mathrm{GeV}/c)^2$ (figures 109 - 111), the data start developing the aforementioned structure even in the lowest p_s bins and the lowest W^* bin, with deviations from 1 being much more pronounced with the increase of p_s in each W^* bin.

For the next Q^2 bin, Q^2 between 0.77 and 1.10 $(\mathrm{GeV}/c)^2$ (figures 112 - 114), the rise towards forward scattering angles dominates over the dip at the perpendicular kinematics, which is barely noticeable on a minority of the plots.

The described results are in agreement with the target fragmentation and FSI models described in chapter II. The increase of the distribution in the forward direction is described well by the target fragmentation model of [53] (*cf* figure 28), and the dip at the intermediate angles is described well by the FSI model of [55] (*cf* figure 34). Additionally, it is worth noting that the dip in the experimental ratio increases with the increase of the spectator momentum in accordance with the FSI model (*cf* figure 34).

4 GeV energy

For the lowest Q^2 bin, Q^2 between 0.77 and 1.10 $(\mathrm{GeV}/c)^2$ (figures 142 - 146), each W^* bin exhibits the presence of both the dip at intermediate angles and the forward rise. The features are more pronounced in the two higher p_s bins than in the two lower ones in each W^* bin, except in the lowest W^* bin.

For the next Q^2 bin, Q^2 between 1.10 and 2.23 $(\mathrm{GeV}/c)^2$ (figures 147 - 151), all the remarks for the previous Q^2 bin hold, including the last one, about the features being more pronounced in the lower p_s bins of the lowest W^* bin than those of the other W^* bins.

For the next Q^2 bin, Q^2 between 2.23 and 4.52 $(\mathrm{GeV}/c)^2$ (figures 152 - 156), statistical fluctuations are too large to draw any precise conclusions, but the general trend is consistent with that of the lower Q^2 bins at this energy.

5 GeV energy

For the lowest Q^2 bin, Q^2 between 1.10 and 2.23 $(\mathrm{GeV}/c)^2$ (figures 175 - 179), and the two lower p_s bins, the ratio dependence on $\cos(\theta_{pq})$ are close to a flat line at 1 for each W^* bin, except for the lowest one, whereas higher p_s bins exhibit the aforementioned effects of the dip at the perpendicular kinematics and the rise at forward angles. The two lower p_s bins of the lowest W^* bin have these two features as well.

For the next Q^2 bin, Q^2 between 2.23 and 4.52 $(\mathrm{GeV}/c)^2$ (figures 180 - 184), we have the same features. They are somewhat less pronounced than for the lower Q^2 bin, presumably due to statistical fluctuations.

Overall, with the possible exception of the lowest W^* bin, the $\cos(\theta_{pq})$ is very close to flat in the backward angular region for low p_s (the region in which the spectator model should work well), for most $Q^2 - W^*$ bins. This confirms that this kinematics is described well by the spectator picture and therefore well-suited to extract (nearly) free neutron structure functions.

V.3 SUMMARY

The results shown tend to agree with the target fragmentation model of [53] (see figure 28), and the final state interaction model of [55] (*cf* figure 34): our data show an enhancement over PWIA in the target fragmentation region (in accordance with

[53]), especially for 2 GeV, and dip in the vicinity of $\theta_{pq} = 90°$ (in accordance with [55]).

The PWIA spectator model works well for the lowest spectator momentum bin (p_s=70...90 MeV/c), as expected from the models of [56] (see figure 29) and [24] (see figure 30), especially in the backward θ_{pq} region.

The resonance-like structure present in the ratio of the experimental data to the simulated data shows that our model for F_{2n} may underestimate the resonant contribution at some values of W^* and Q^2. On the other hand, the agreement between data and model for the 2 highest Q^2 bins and 5 GeV beam energy, over the whole range in W^*/x^*, is quite good in the region where the spectator picture should work (p_s between 0.07 and 0.09 GeV and $\cos(\theta_{pq})$ between -0.75 and -0.25) (see figure 77). This confirms that in the DIS region, the F_{2n} model provides a good description of a (nearly) free neutron up to $x^* \approx 0.6$, within our systematic errors of 10 - 15%.

Superimposing structure functions for different Q^2 for 5.254 GeV beam energy data (see figure 77) indicates, that while the data agree with the spectator picture, they might not scale with Q^2 as nicely as one might expect.

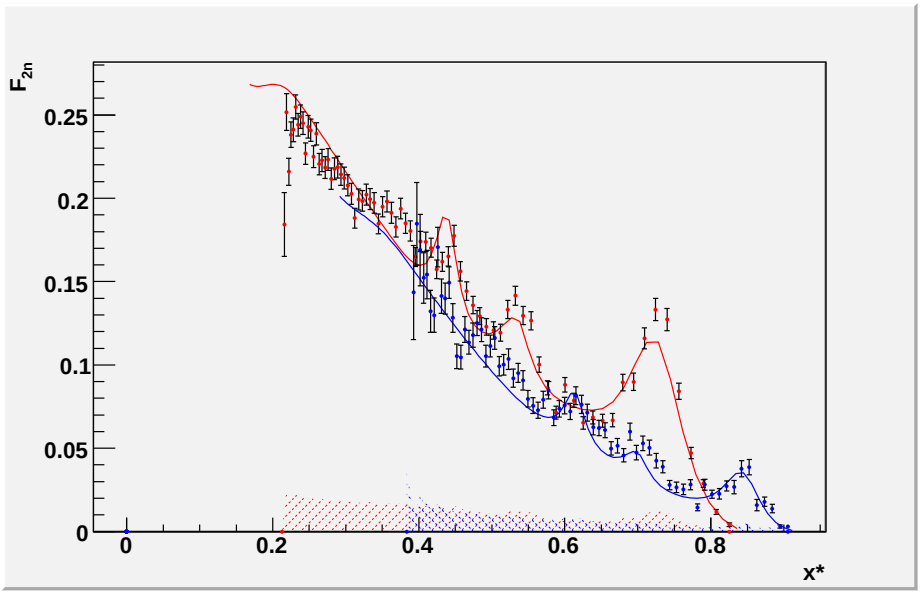

FIG. 77: Model (lines) and effective (markers) F_{2n} are shown as functions of x^* for two Q^2 bins: from 1.10 to 2.23 (GeV/c)^2 (red) and from 2.23 to 4.52 (GeV/c)^2 (blue). Results are shown for backward angles ($\cos(\theta_{pq})$ between -0.75 and -0.25) and low spectator momenta (p_s between 70 and 90 MeV/c), for which the spectator model should be a good description. The beam energy is 5.254 GeV.

Some uncorrected reconstruction and efficiency effects for CLAS and the RTPC limited our resolution in W^*/x^* and they have washed out some of the details. A larger statistics runs at higher beam energies, with a better understanding of the detectors, should improve the data and extend them to higher Bjorken x [96]. A follow-up experiment after the energy upgrade of CEBAF to 12 GeV has been approved for this purpose.

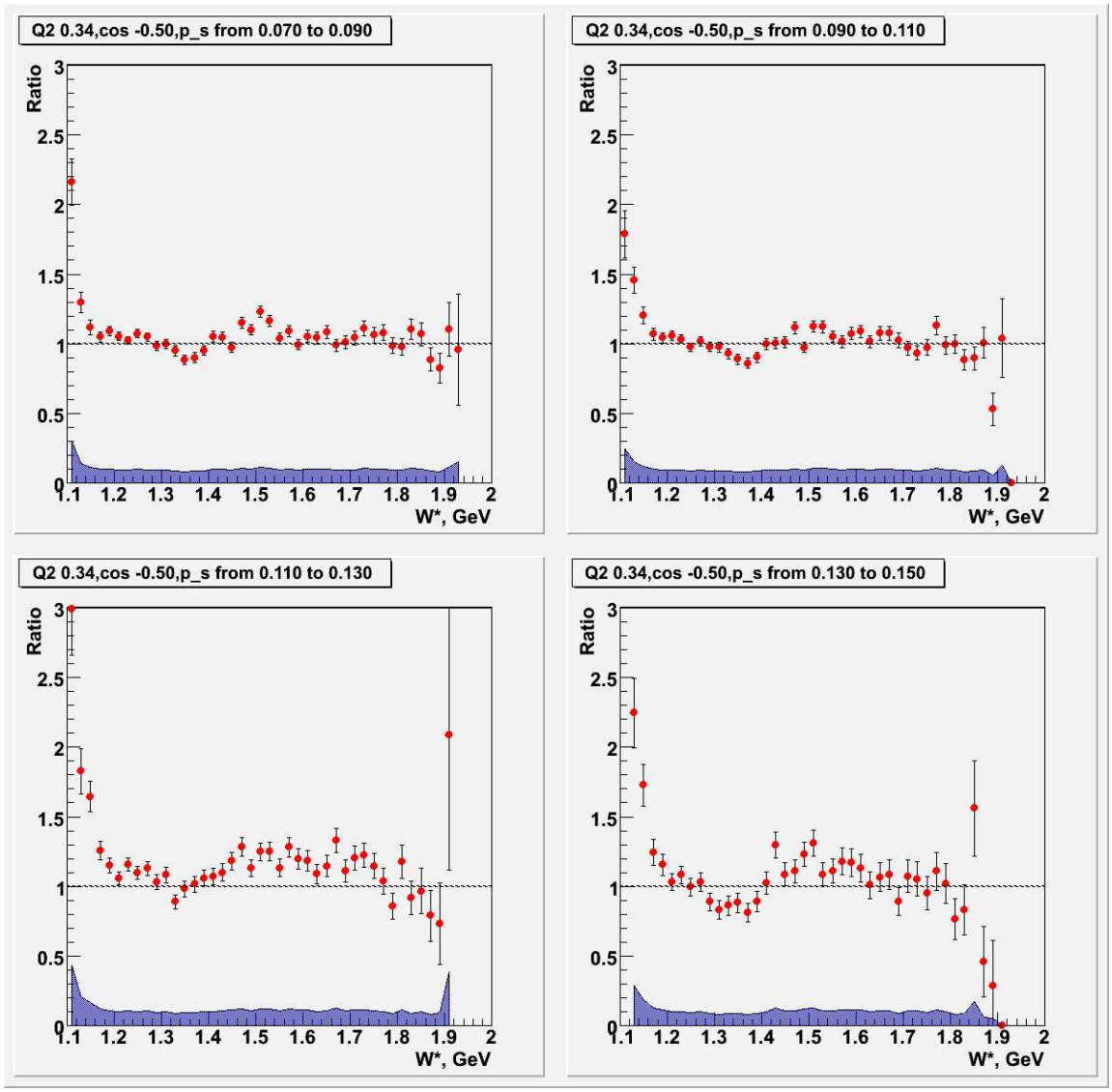

FIG. 78: Ratio of experimental data with subtracted accidental background and elastic tail to the full simulation in the PWIA spectator picture is shown as a function of W^*. Data are for Q^2 from 0.22 to 0.45 $(\mathrm{GeV}/c)^2$, $\cos\theta_{pq}$ from -0.75 to -0.25. The beam energy is 2.140 GeV. Error bars are statistical only. Systematic errors are shown as a blue band.

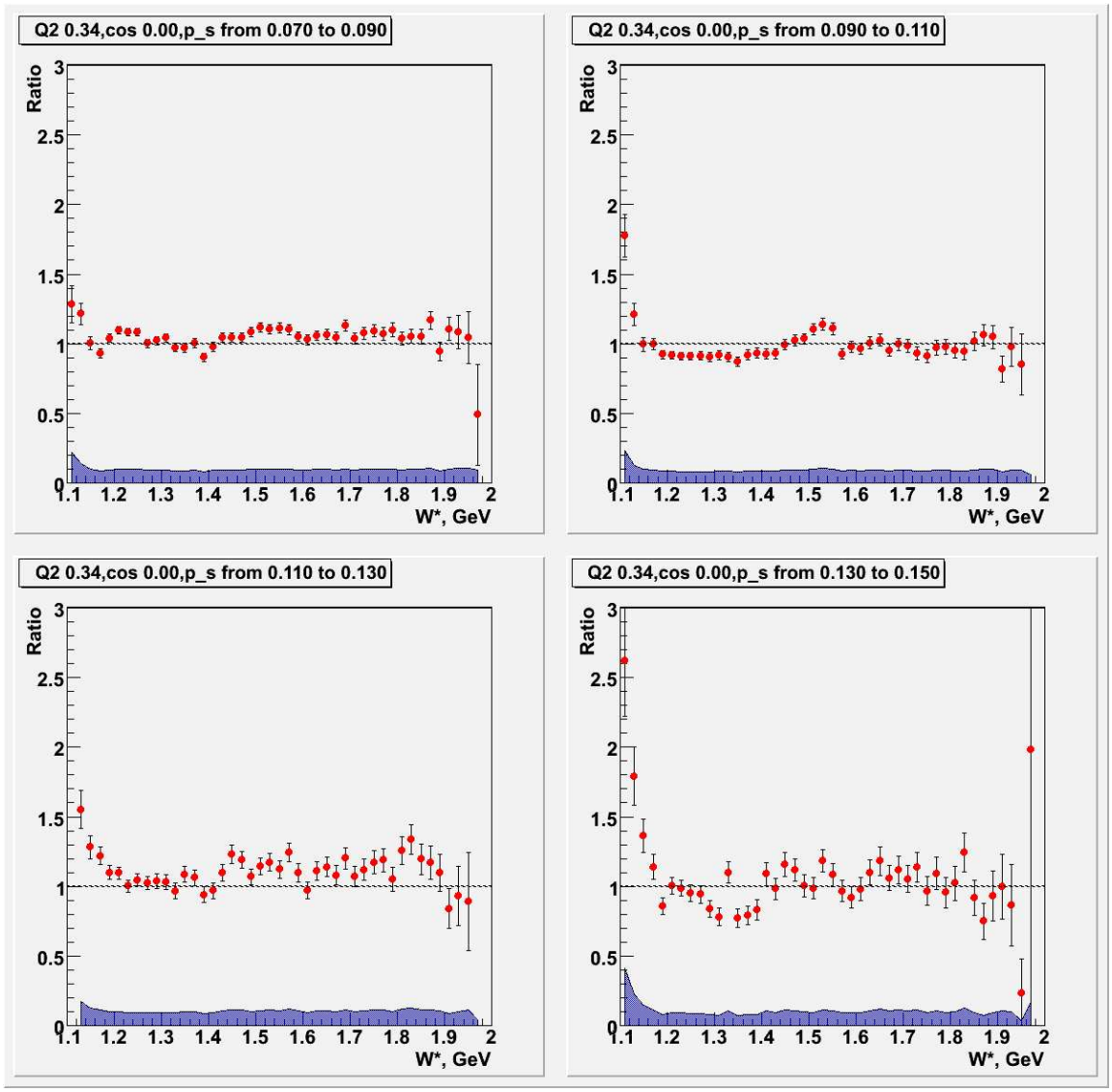

FIG. 79: Ratio of experimental data with subtracted accidental background and elastic tail to the full simulation in the PWIA spectator picture is shown as a function of W^*. Data are for Q^2 from 0.22 to 0.45 $(\mathrm{GeV}/c)^2$, $\cos\theta_{pq}$ from -0.25 to 0.25. The beam energy is 2.140 GeV. Error bars are statistical only. Systematic errors are shown as a blue band.

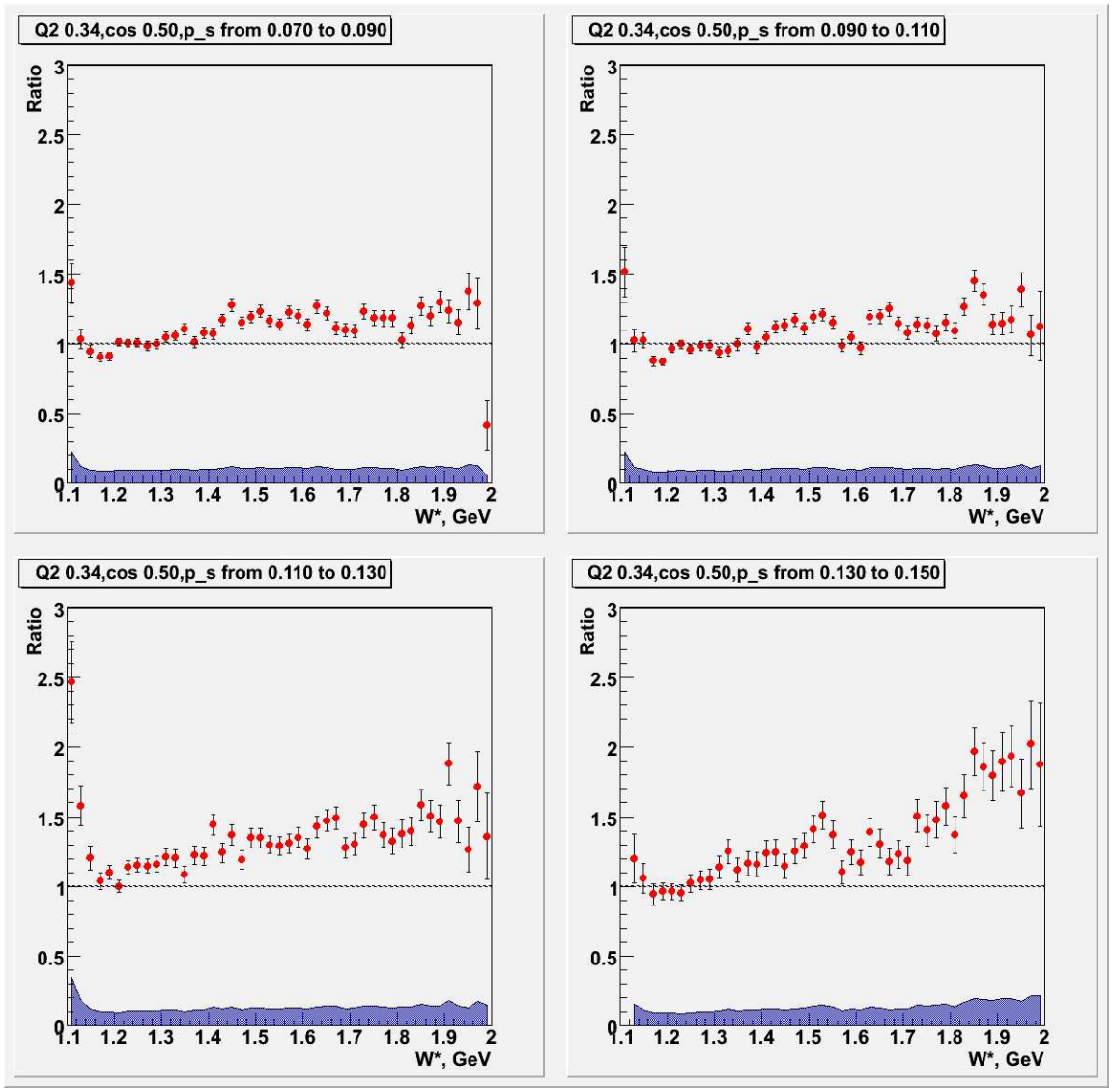

FIG. 80: Ratio of experimental data with subtracted accidental background and elastic tail to the full simulation in the PWIA spectator picture is shown as a function of W^*. Data are for Q^2 from 0.22 to 0.45 $(\mathrm{GeV}/c)^2$, $\cos\theta_{pq}$ from 0.25 to 0.75. The beam energy is 2.140 GeV. Error bars are statistical only. Systematic errors are shown as a blue band.

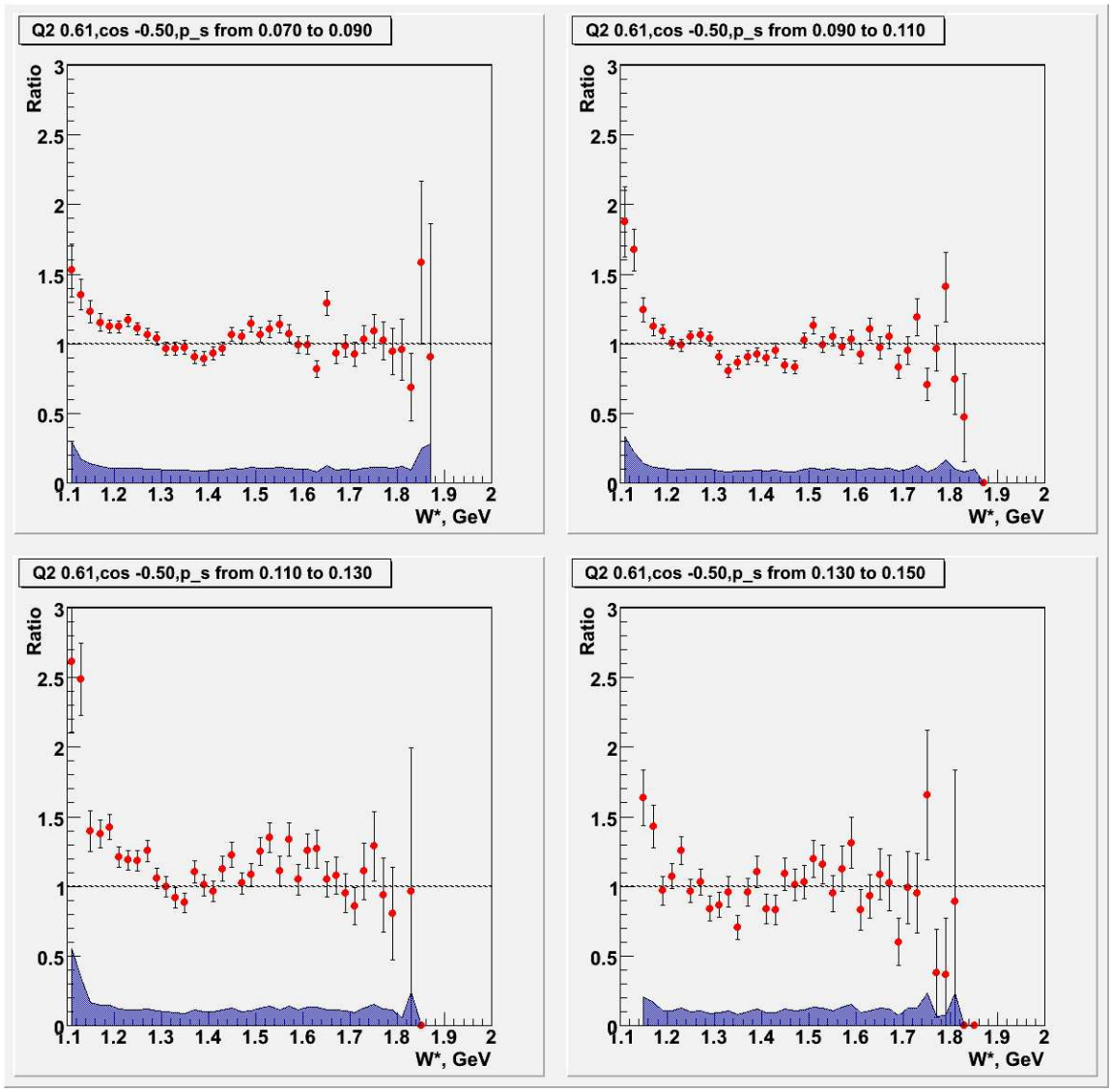

FIG. 81: Ratio of experimental data with subtracted accidental background and elastic tail to the full simulation in the PWIA spectator picture is shown as a function of W^*. Data are for Q^2 from 0.45 to 0.77 $(\mathrm{GeV}/c)^2$, $\cos\theta_{pq}$ from -0.75 to -0.25. The beam energy is 2.140 GeV. Error bars are statistical only. Systematic errors are shown as a blue band.

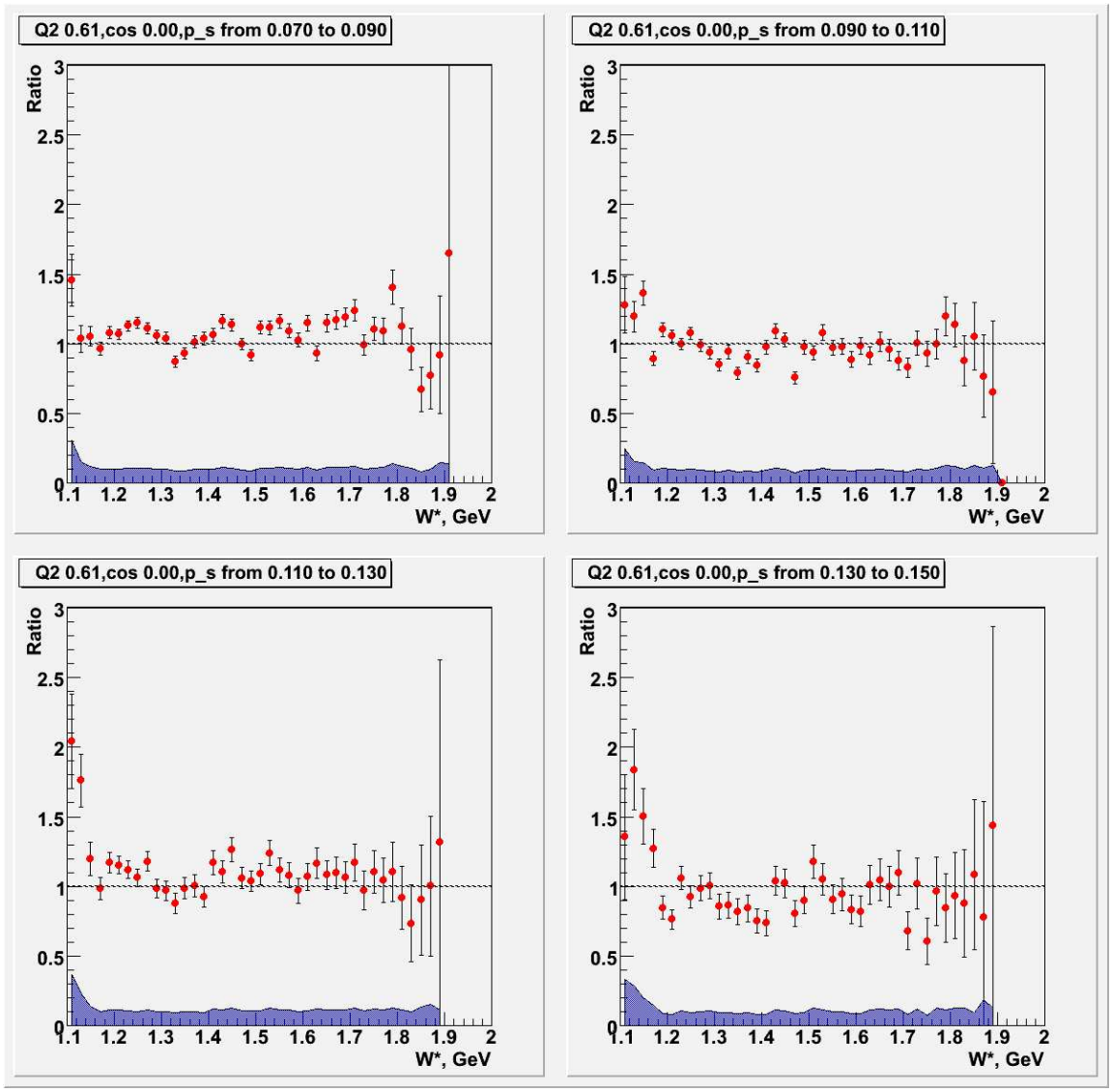

FIG. 82: Ratio of experimental data with subtracted accidental background and elastic tail to the full simulation in the PWIA spectator picture is shown as a function of W^*. Data are for Q^2 from 0.45 to 0.77 $(\mathrm{GeV}/c)^2$, $\cos\theta_{pq}$ from -0.25 to 0.25. The beam energy is 2.140 GeV. Error bars are statistical only. Systematic errors are shown as a blue band.

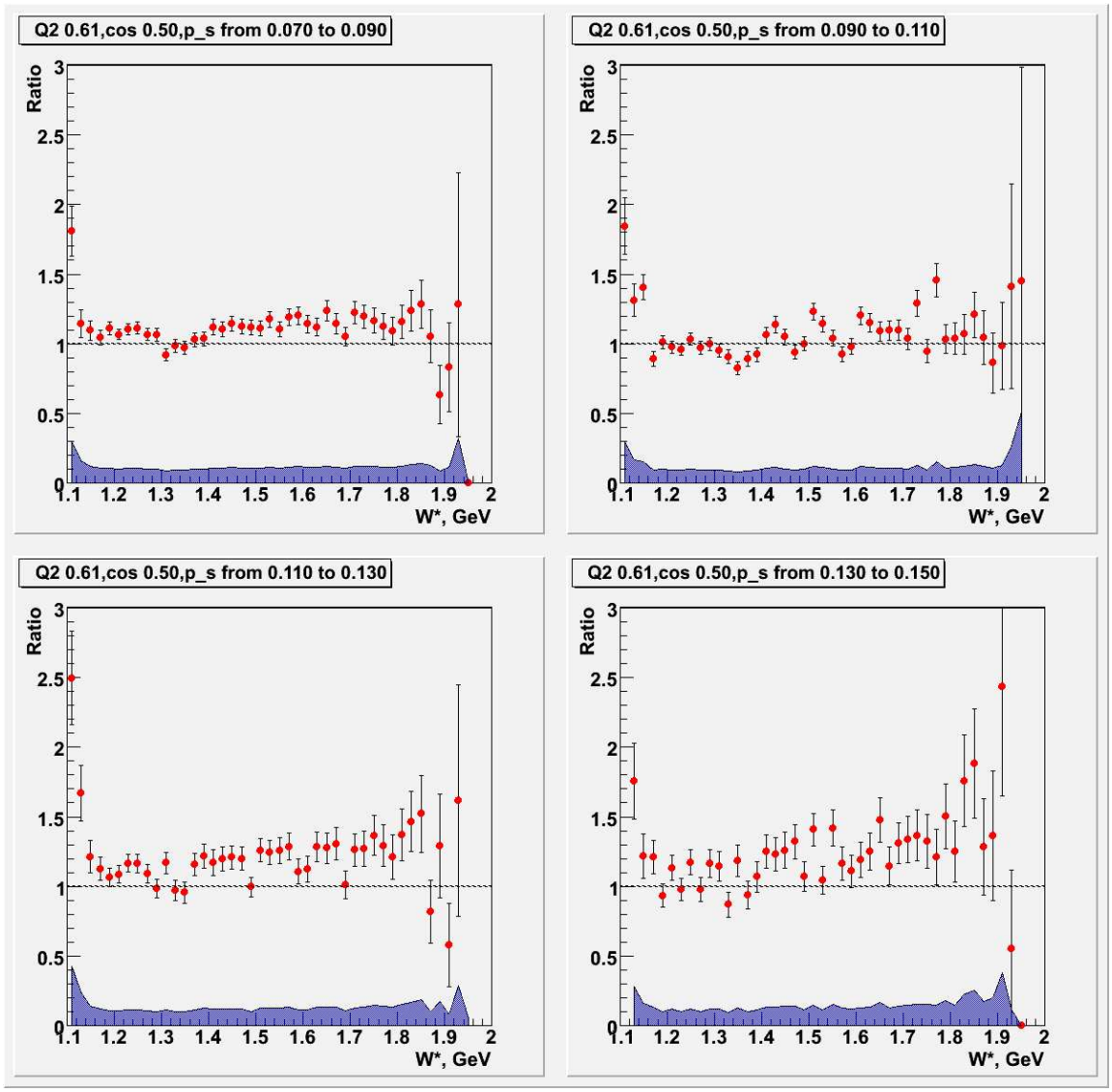

FIG. 83: Ratio of experimental data with subtracted accidental background and elastic tail to the full simulation in the PWIA spectator picture is shown as a function of W^*. Data are for Q^2 from 0.45 to 0.77 $(\mathrm{GeV}/c)^2$, $\cos\theta_{pq}$ from 0.25 to 0.75. The beam energy is 2.140 GeV. Error bars are statistical only. Systematic errors are shown as a blue band.

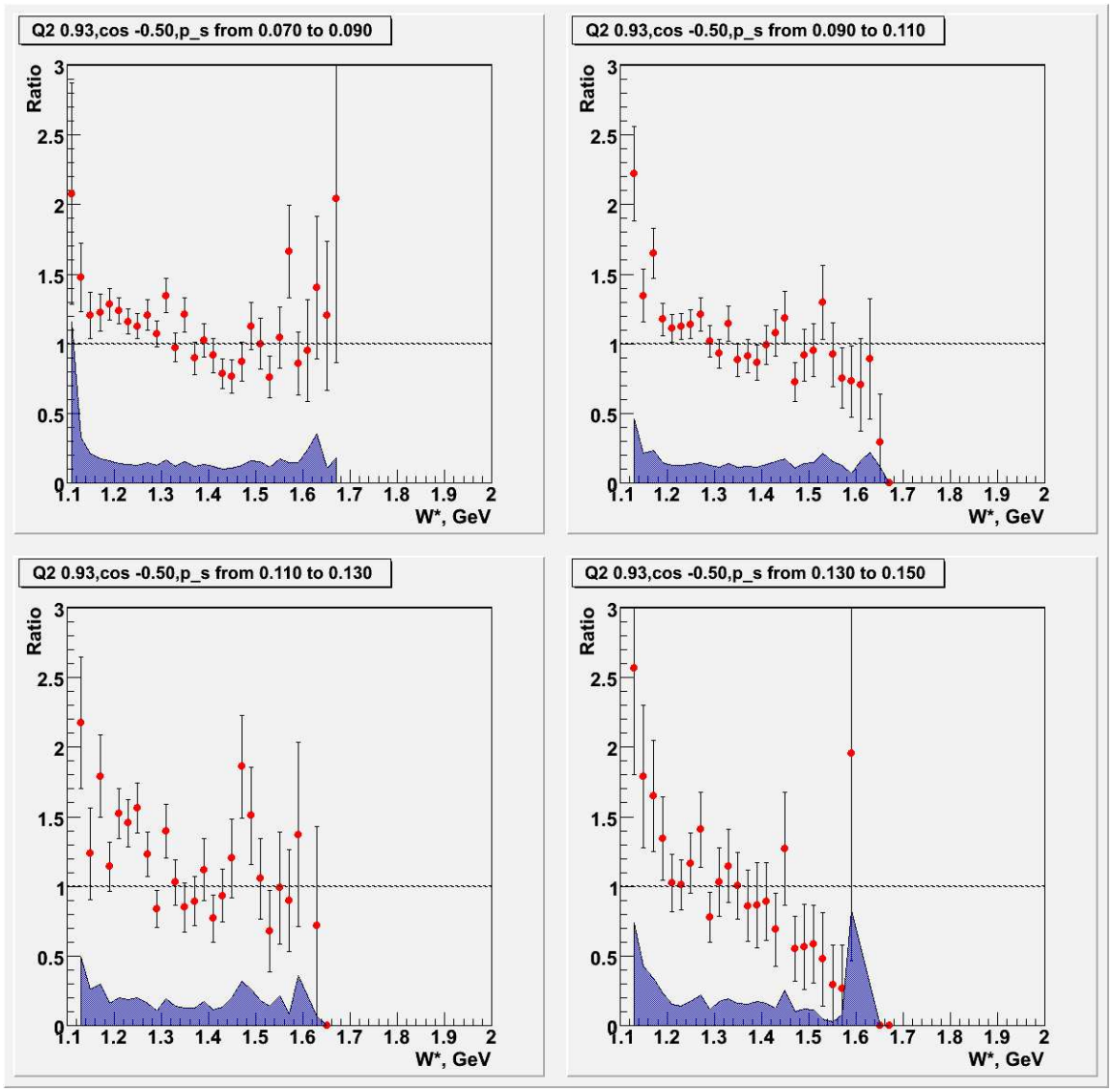

FIG. 84: Ratio of experimental data with subtracted accidental background and elastic tail to the full simulation in the PWIA spectator picture is shown as a function of W^*. Data are for Q^2 from 0.77 to 1.10 $(\mathrm{GeV}/c)^2$, $\cos\theta_{pq}$ from -0.75 to -0.25. The beam energy is 2.140 GeV. Error bars are statistical only. Systematic errors are shown as a blue band.

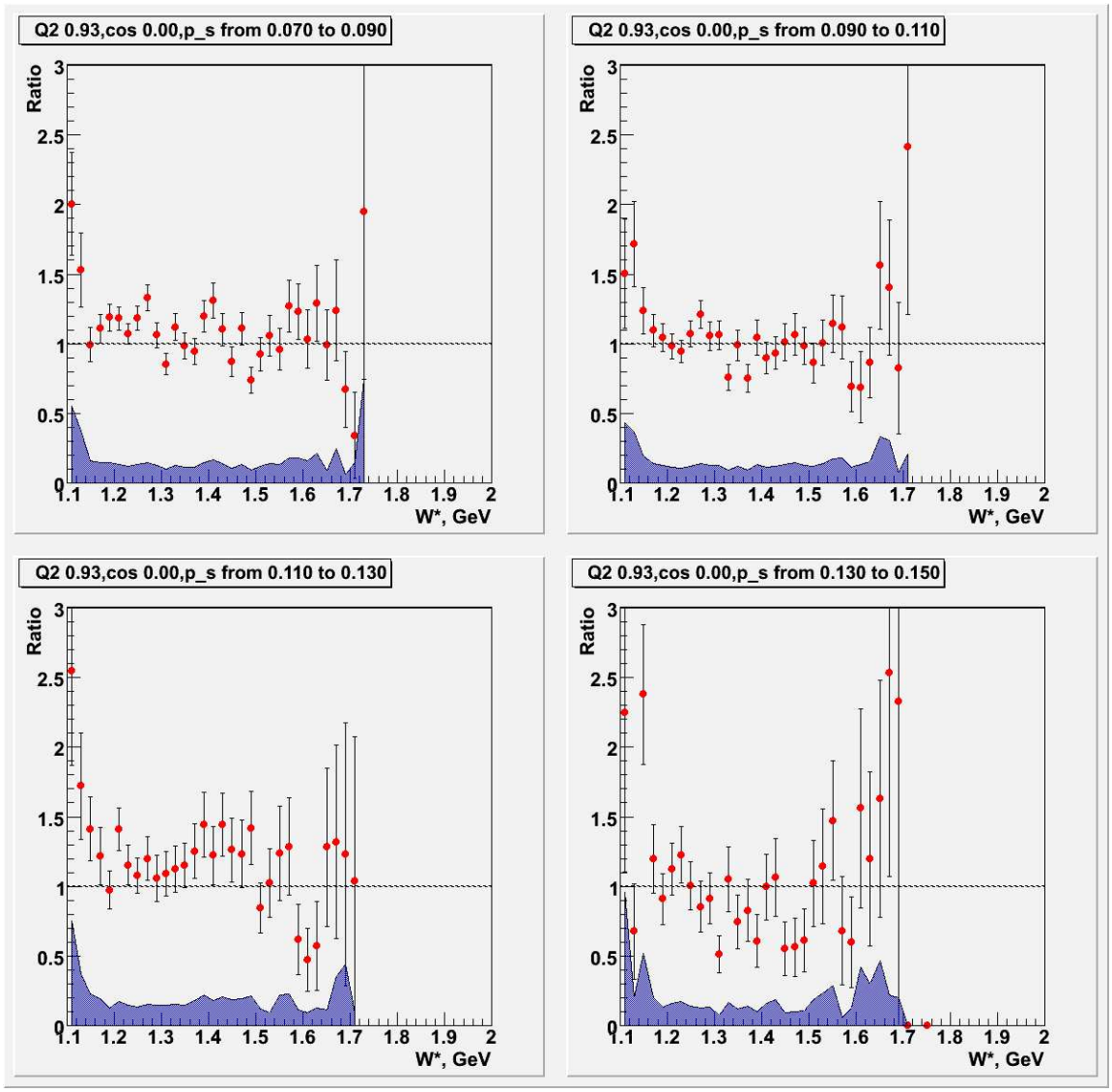

FIG. 85: Ratio of experimental data with subtracted accidental background and elastic tail to the full simulation in the PWIA spectator picture is shown as a function of W^*. Data are for Q^2 from 0.77 to 1.10 $(\mathrm{GeV}/c)^2$, $\cos\theta_{pq}$ from -0.25 to 0.25. The beam energy is 2.140 GeV. Error bars are statistical only. Systematic errors are shown as a blue band.

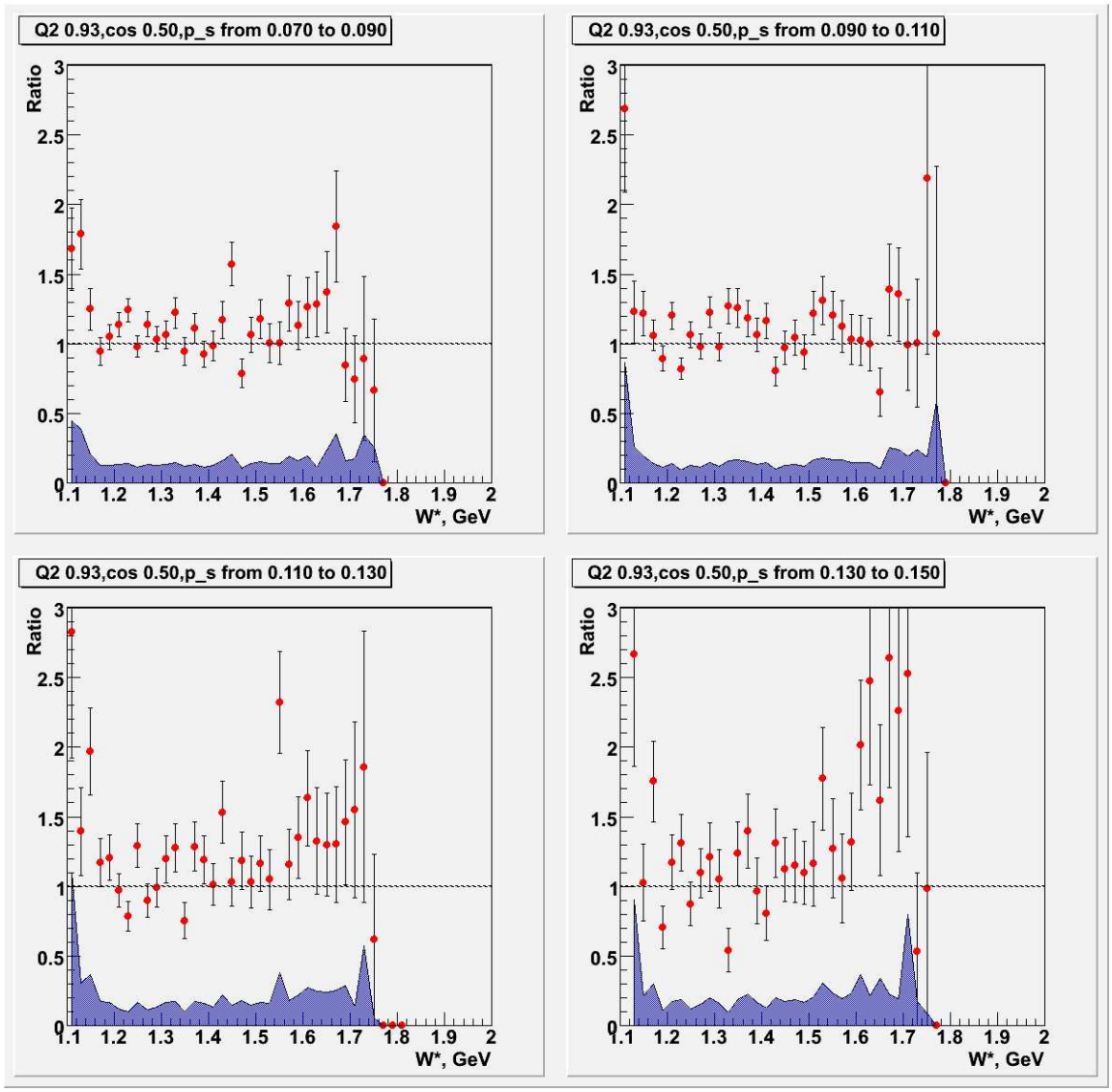

FIG. 86: Ratio of experimental data with subtracted accidental background and elastic tail to the full simulation in the PWIA spectator picture is shown as a function of W^*. Data are for Q^2 from 0.77 to 1.10 $(\mathrm{GeV}/c)^2$, $\cos\theta_{pq}$ from 0.25 to 0.75. The beam energy is 2.140 GeV. Error bars are statistical only. Systematic errors are shown as a blue band.

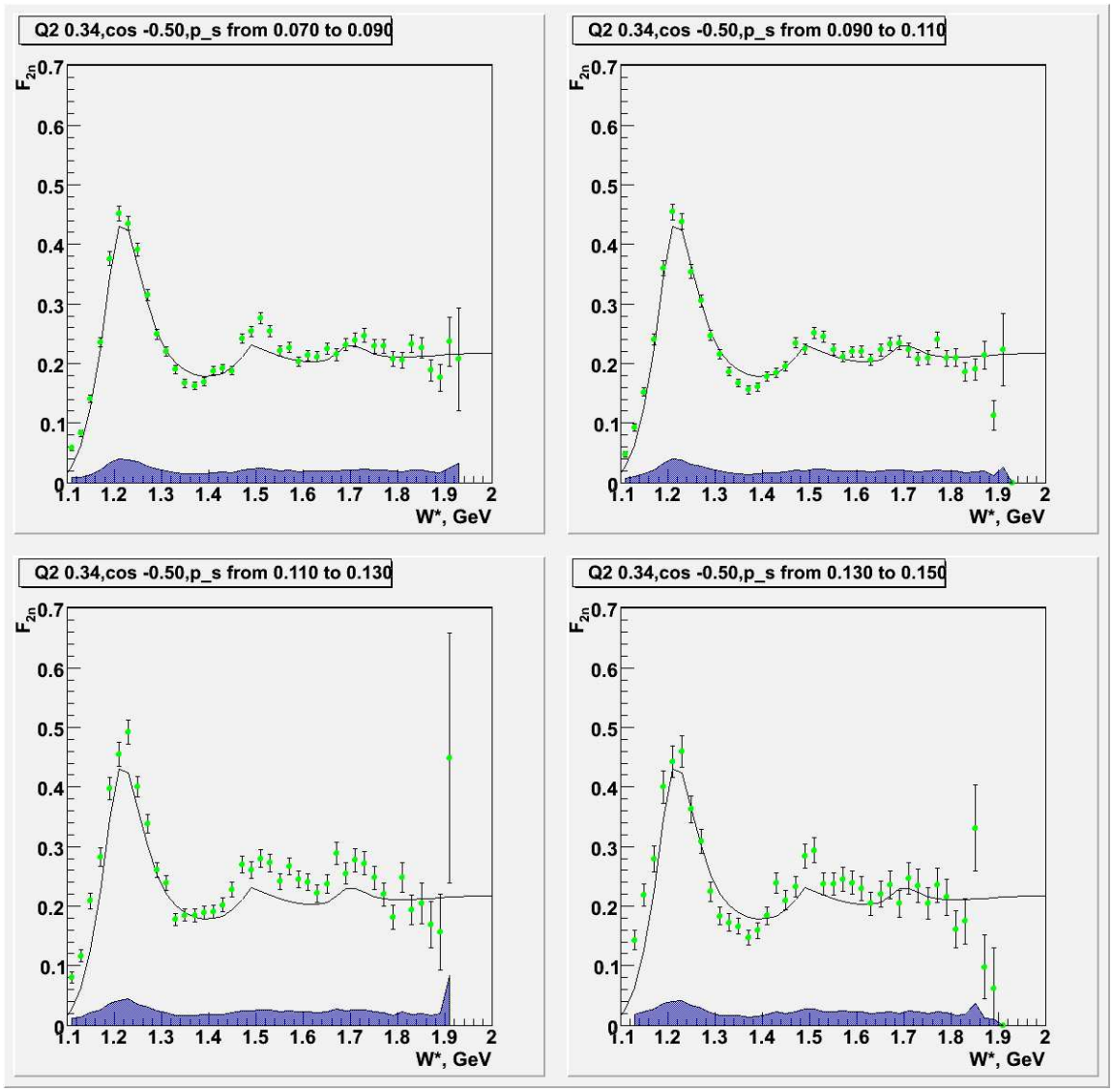

FIG. 87: Effective F_{2n} (green markers) structure function is shown as a function of W^*. Black line is the model F_{2n}. Data are for Q^2 from 0.22 to 0.45 $(\mathrm{GeV}/c)^2$, $\cos\theta_{pq}$ from -0.75 to -0.25. The beam energy is 2.140 GeV. Error bars are statistical only. Systematic errors are shown as a blue band.

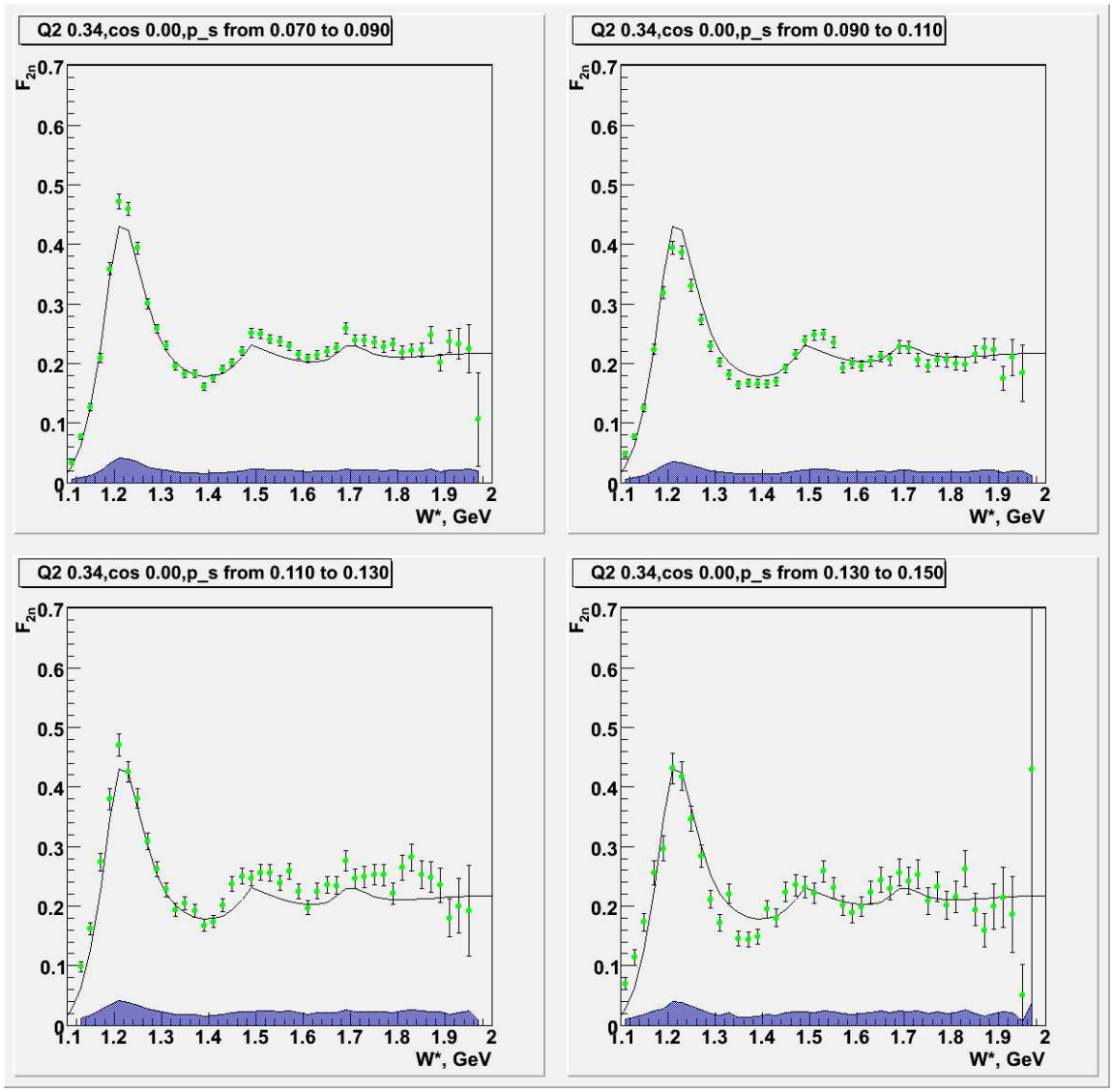

FIG. 88: Effective F_{2n} (green markers) structure function is shown as a function of W^*. Black line is the model F_{2n}. Data are for Q^2 from 0.22 to 0.45 $(\mathrm{GeV}/c)^2$, $\cos\theta_{pq}$ from -0.25 to 0.25. The beam energy is 2.140 GeV. Error bars are statistical only. Systematic errors are shown as a blue band.

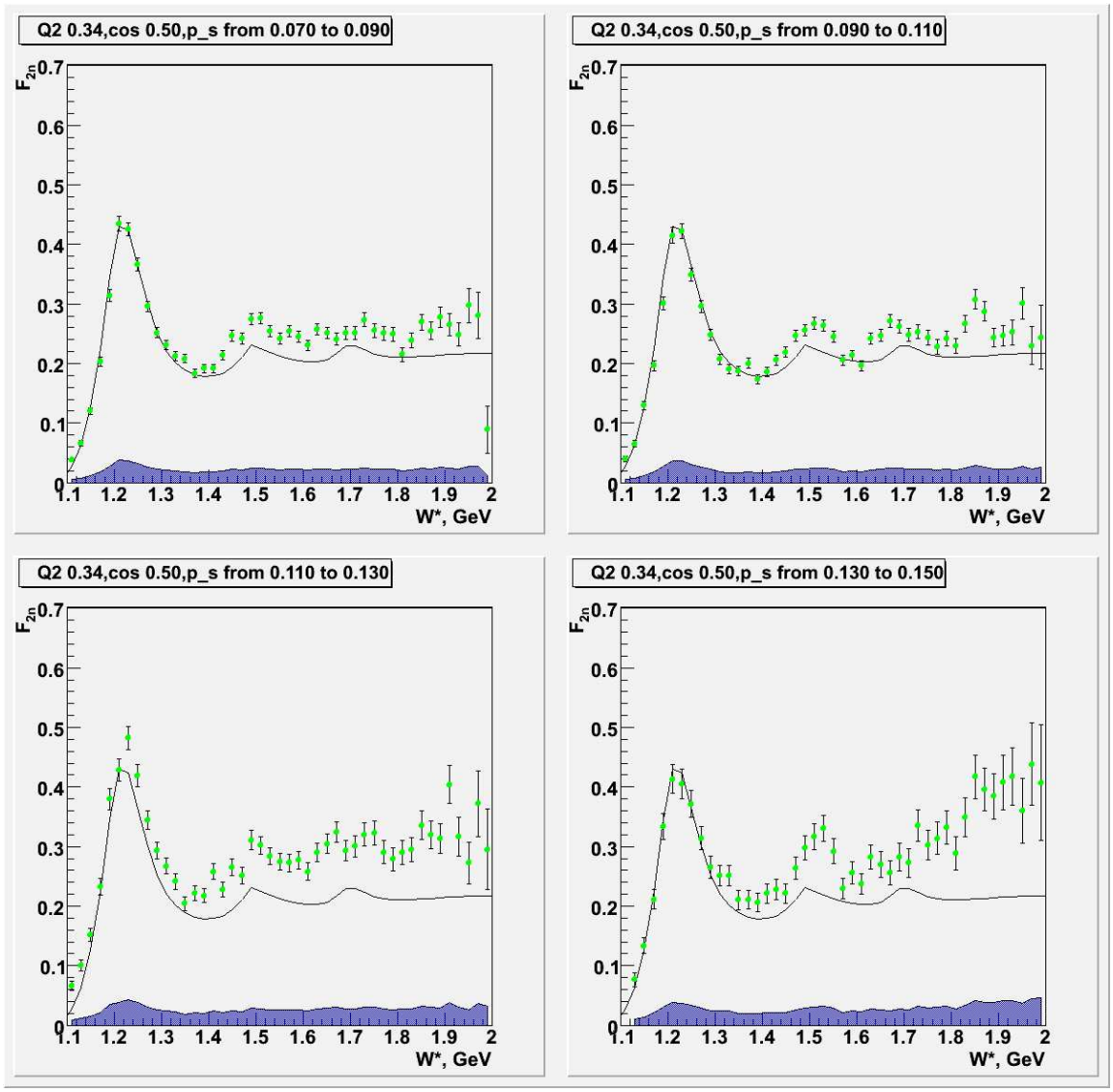

FIG. 89: Effective F_{2n} (green markers) structure function is shown as a function of W^*. Black line is the model F_{2n}. Data are for Q^2 from 0.22 to 0.45 $(\mathrm{GeV}/c)^2$, $\cos\theta_{pq}$ from 0.25 to 0.75. The beam energy is 2.140 GeV. Error bars are statistical only. Systematic errors are shown as a blue band.

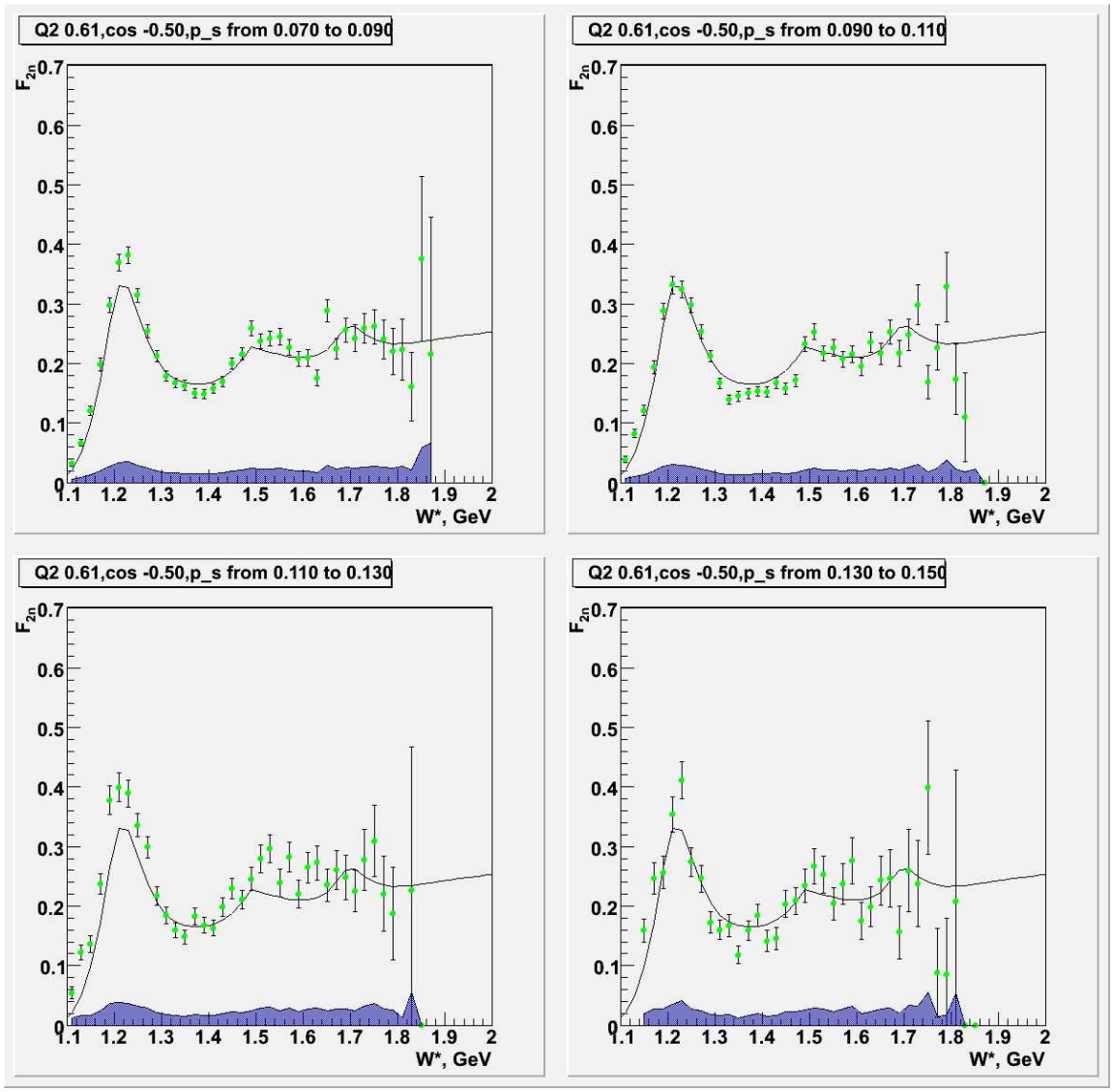

FIG. 90: Effective F_{2n} (green markers) structure function is shown as a function of W^*. Black line is the model F_{2n}. Data are for Q^2 from 0.45 to 0.77 $(\mathrm{GeV}/c)^2$, $\cos\theta_{pq}$ from -0.75 to -0.25. The beam energy is 2.140 GeV. Error bars are statistical only. Systematic errors are shown as a blue band.

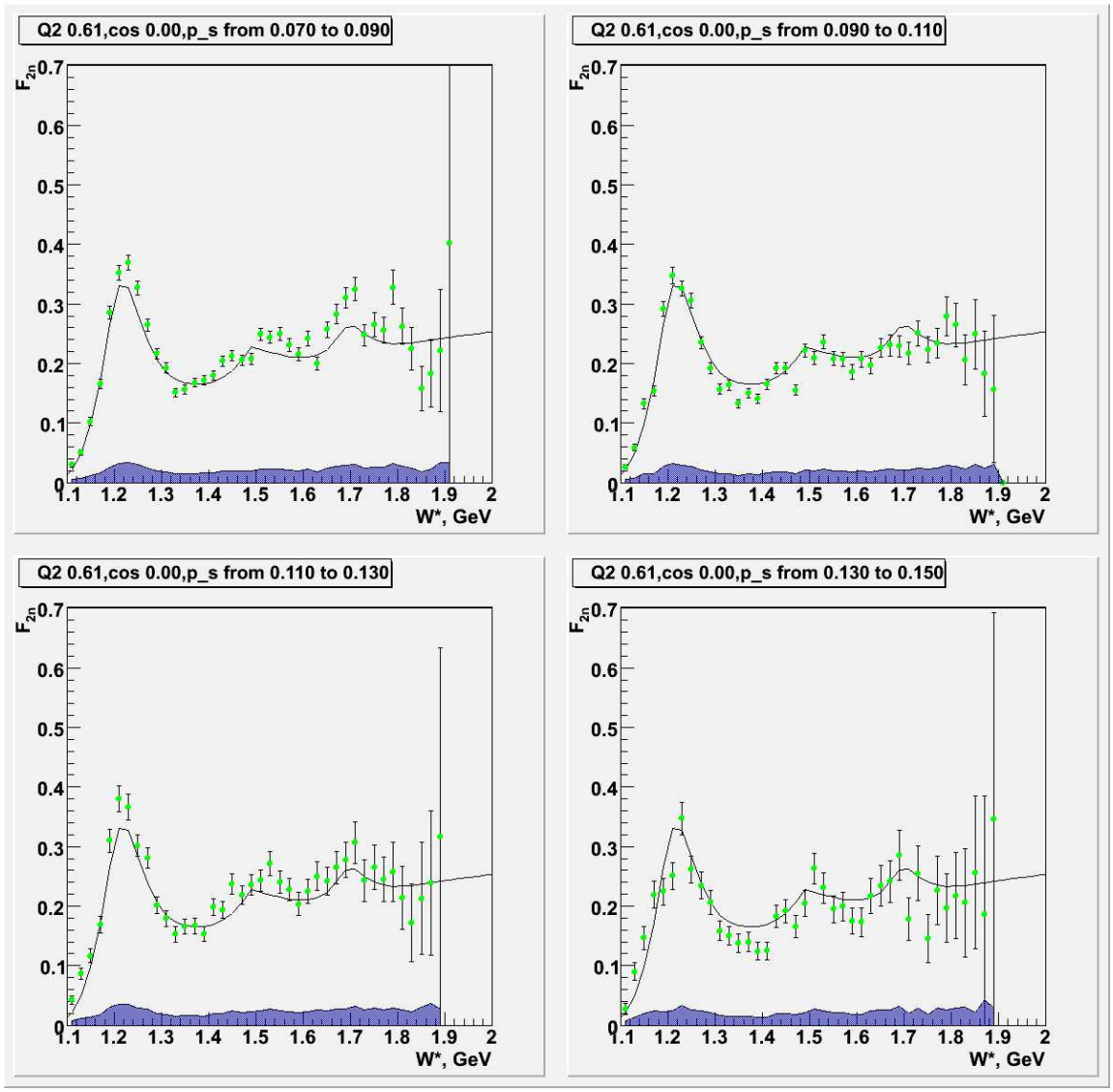

FIG. 91: Effective F_{2n} (green markers) structure function is shown as a function of W^*. Black line is the model F_{2n}. Data are for Q^2 from 0.45 to 0.77 $(\mathrm{GeV}/c)^2$, $\cos\theta_{pq}$ from -0.25 to 0.25. The beam energy is 2.140 GeV. Error bars are statistical only. Systematic errors are shown as a blue band.

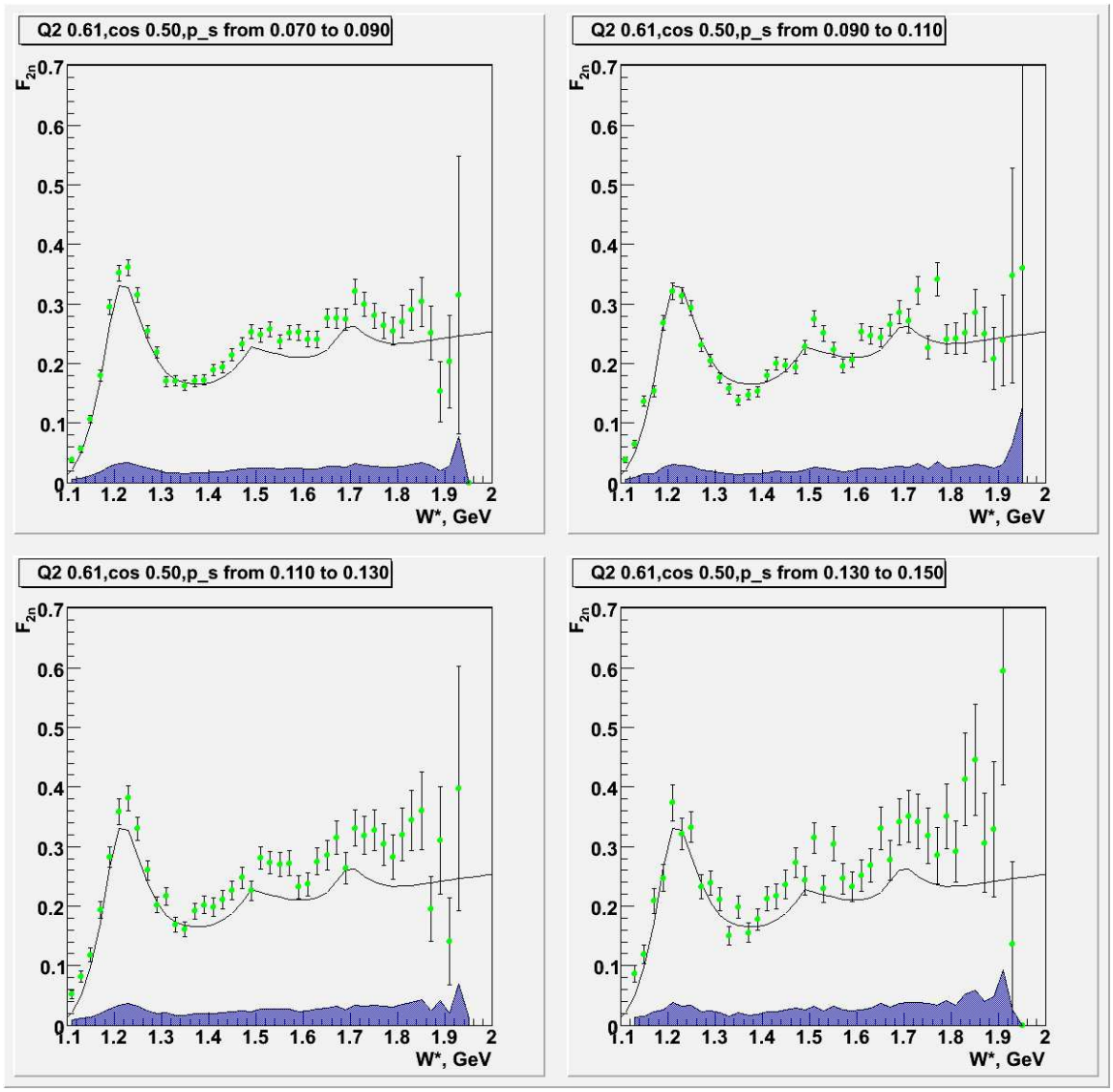

FIG. 92: Effective F_{2n} (green markers) structure function is shown as a function of W^*. Black line is the model F_{2n}. Data are for Q^2 from 0.45 to 0.77 $(\mathrm{GeV}/c)^2$, $\cos\theta_{pq}$ from 0.25 to 0.75. The beam energy is 2.140 GeV. Error bars are statistical only. Systematic errors are shown as a blue band.

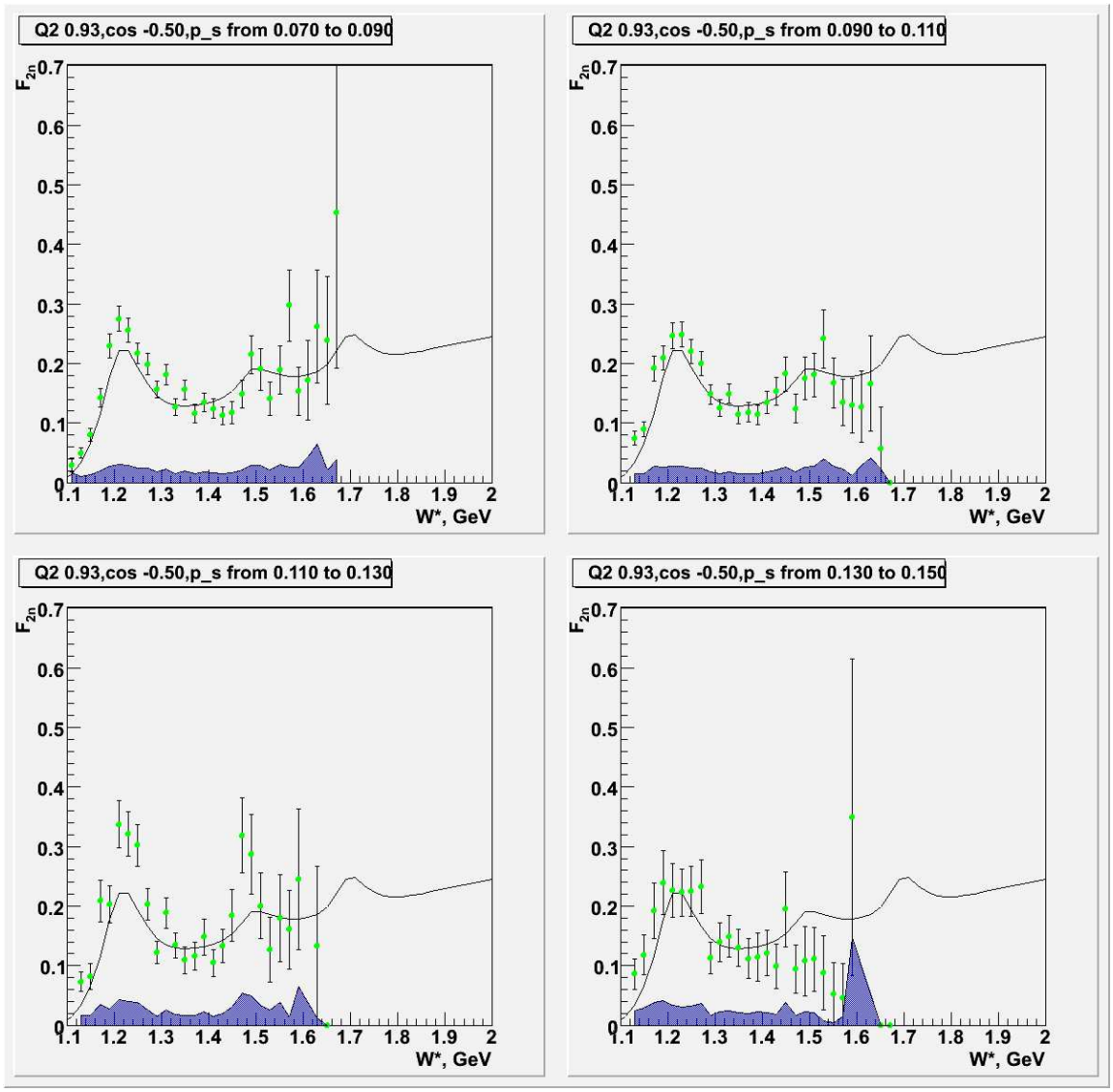

FIG. 93: Effective F_{2n} (green markers) structure function is shown as a function of W^*. Black line is the model F_{2n}. Data are for Q^2 from 0.77 to 1.10 $(\mathrm{GeV}/c)^2$, $\cos\theta_{pq}$ from -0.75 to -0.25. The beam energy is 2.140 GeV. Error bars are statistical only. Systematic errors are shown as a blue band.

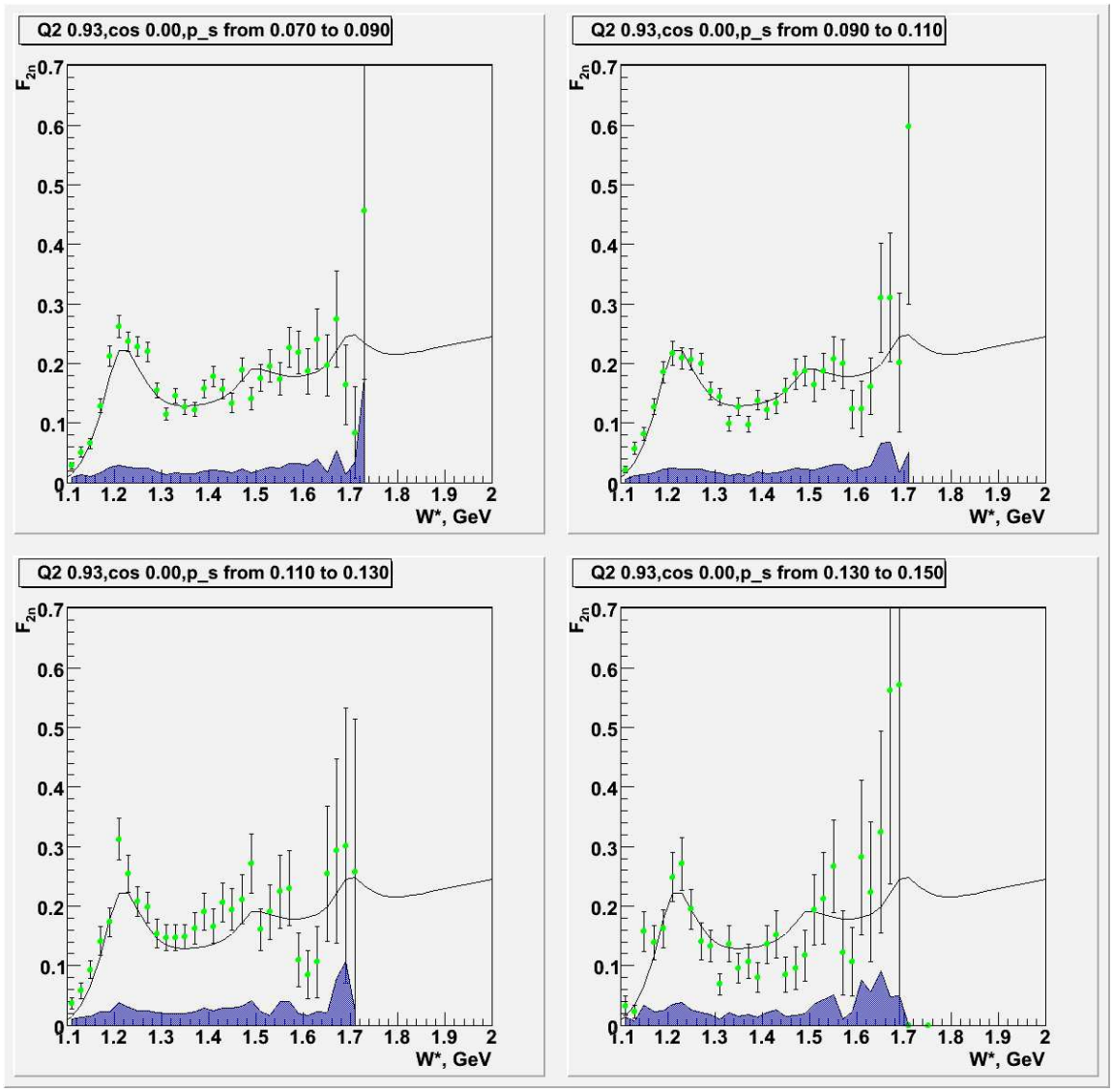

FIG. 94: Effective F_{2n} (green markers) structure function is shown as a function of W^*. Black line is the model F_{2n}. Data are for Q^2 from 0.77 to 1.10 $(\mathrm{GeV}/c)^2$, $\cos\theta_{pq}$ from -0.25 to 0.25. The beam energy is 2.140 GeV. Error bars are statistical only. Systematic errors are shown as a blue band.

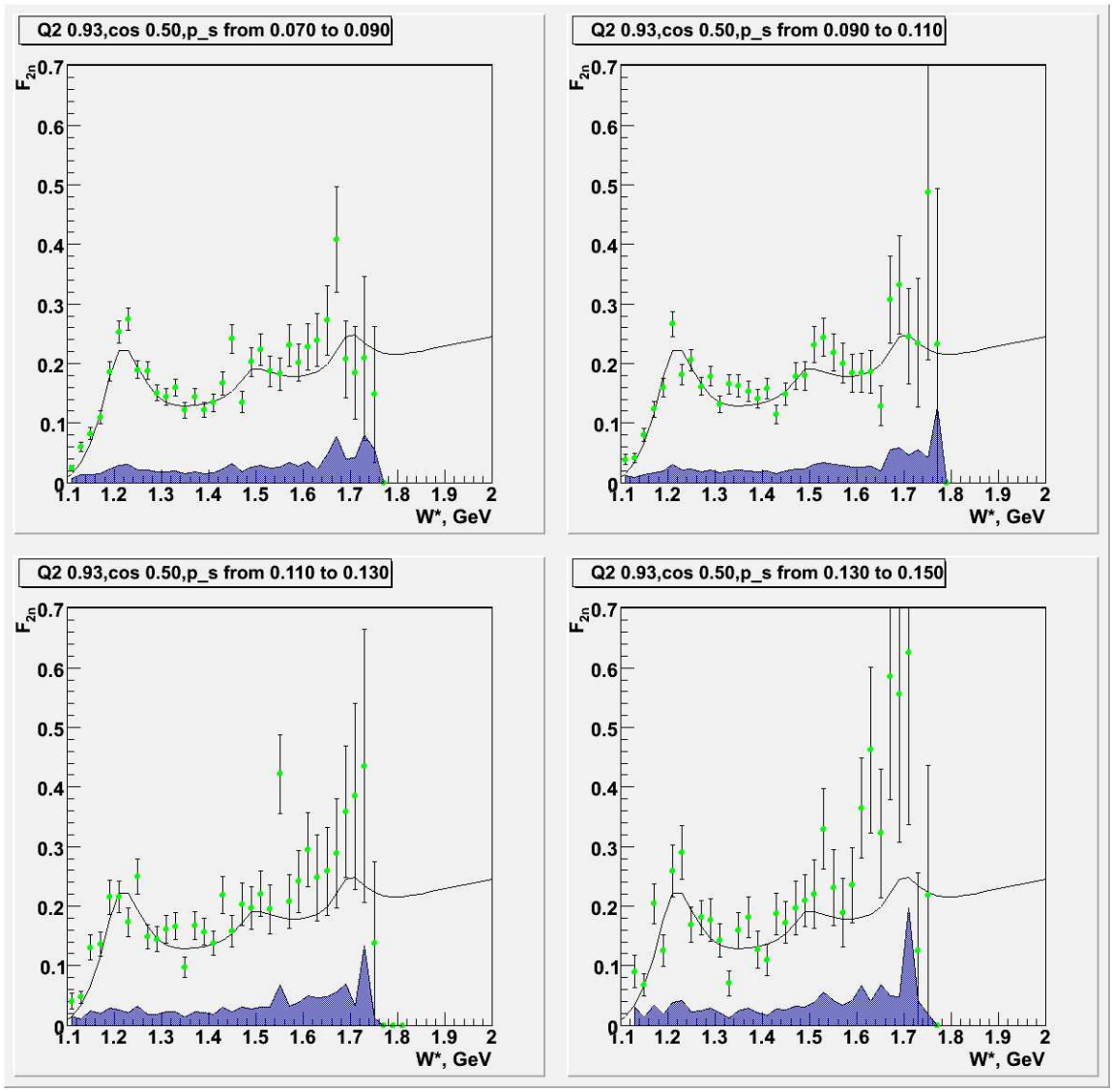

FIG. 95: Effective F_{2n} (green markers) structure function is shown as a function of W^*. Black line is the model F_{2n}. Data are for Q^2 from 0.77 to 1.10 $(\mathrm{GeV}/c)^2$, $\cos\theta_{pq}$ from 0.25 to 0.75. The beam energy is 2.140 GeV. Error bars are statistical only. Systematic errors are shown as a blue band.

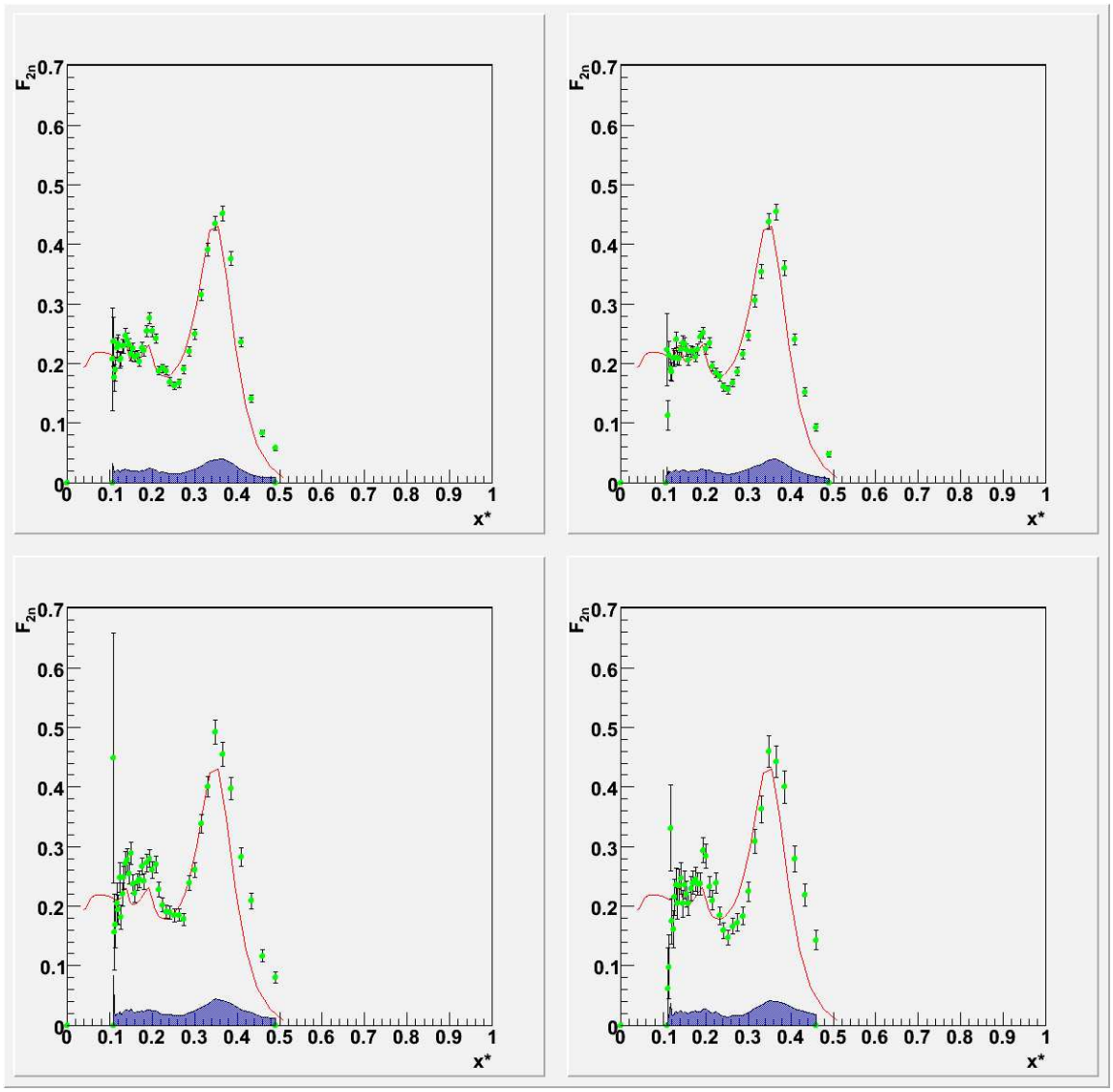

FIG. 96: Effective F_{2n} (green markers) structure function is shown as a function of x^*. Red line is the model F_{2n}. Data are for Q^2 from 0.22 to 0.45 $(\mathrm{GeV}/c)^2$, $\cos\theta_{pq}$ from -0.75 to -0.25. The beam energy is 2.140 GeV. Error bars are statistical only. Systematic errors are shown as a blue band.

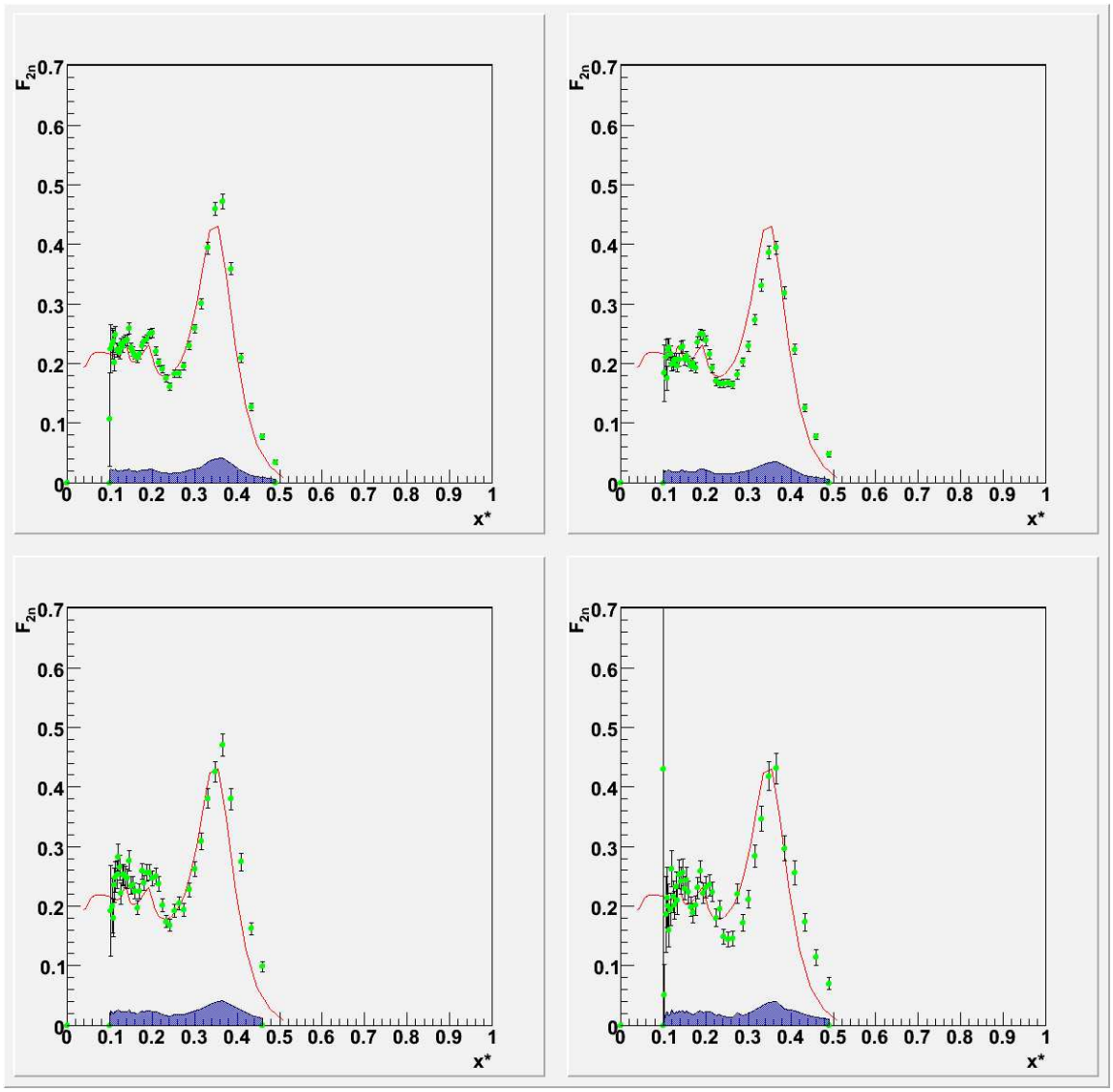

FIG. 97: Effective F_{2n} (green markers) structure function is shown as a function of x^*. Red line is the model F_{2n}. Data are for Q^2 from 0.22 to 0.45 $(\mathrm{GeV}/c)^2$, $\cos\theta_{pq}$ from -0.25 to 0.25. The beam energy is 2.140 GeV. Error bars are statistical only. Systematic errors are shown as a blue band.

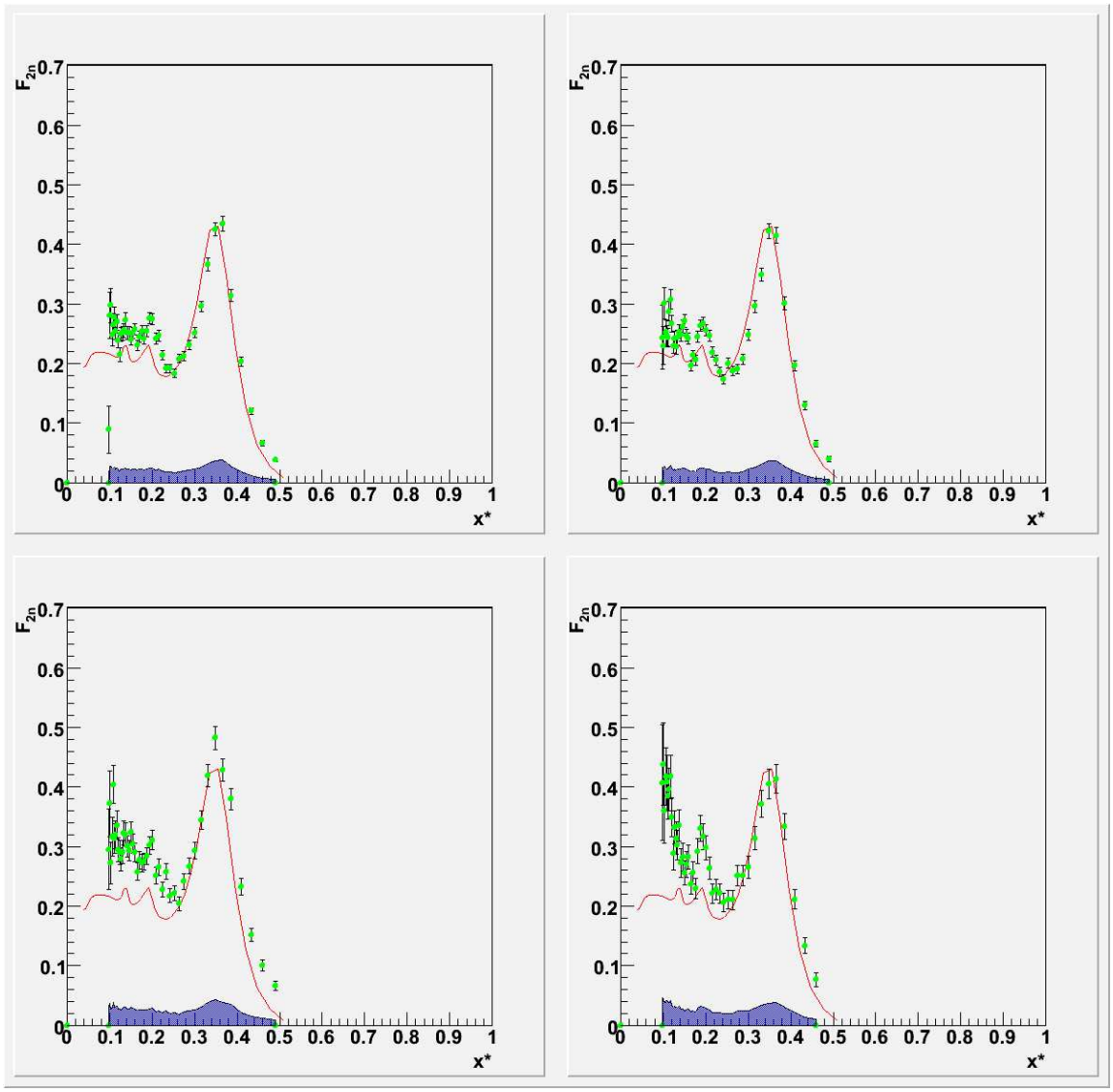

FIG. 98: Effective F_{2n} (green markers) structure function is shown as a function of x^*. Red line is the model F_{2n}. Data are for Q^2 from 0.22 to 0.45 $(\mathrm{GeV}/c)^2$, $\cos\theta_{pq}$ from 0.25 to 0.75. The beam energy is 2.140 GeV. Error bars are statistical only. Systematic errors are shown as a blue band.

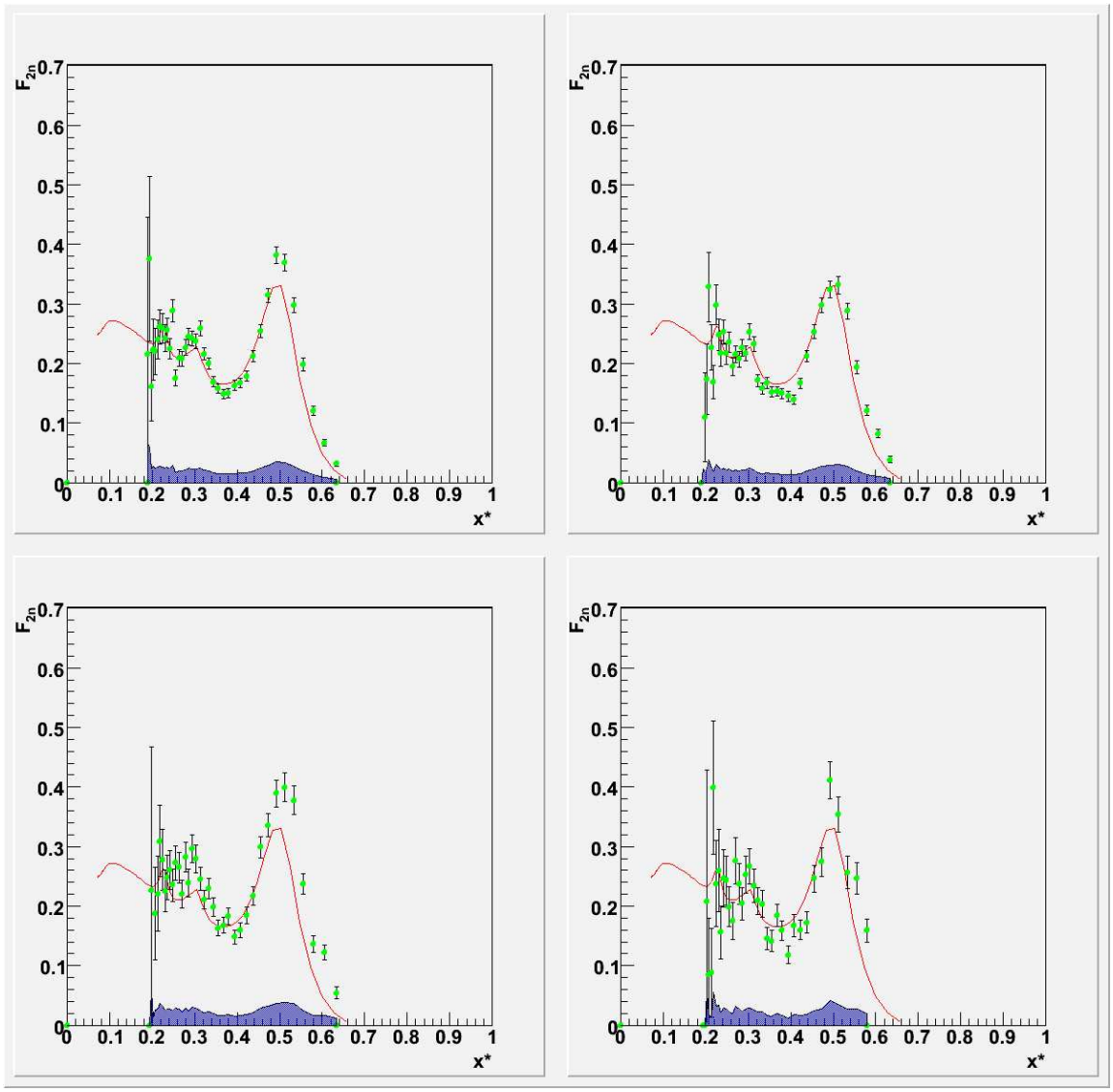

FIG. 99: Effective F_{2n} (green markers) structure function is shown as a function of x^*. Red line is the model F_{2n}. Data are for Q^2 from 0.45 to 0.77 $(\mathrm{GeV}/c)^2$, $\cos\theta_{pq}$ from -0.75 to -0.25. The beam energy is 2.140 GeV. Error bars are statistical only. Systematic errors are shown as a blue band.

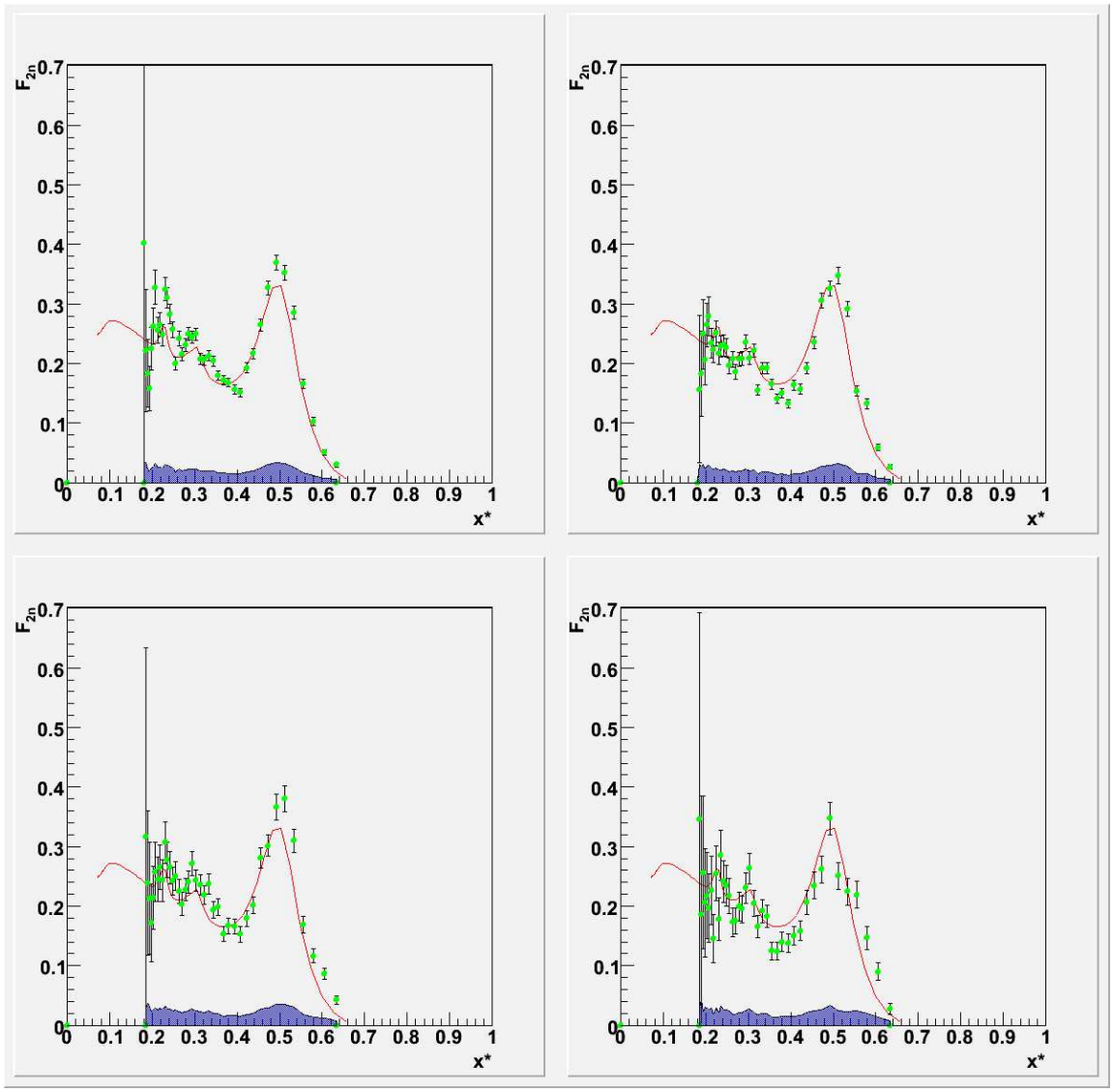

FIG. 100: Effective F_{2n} (green markers) structure function is shown as a function of x^*. Red line is the model F_{2n}. Data are for Q^2 from 0.45 to 0.77 $(\mathrm{GeV}/c)^2$, $\cos\theta_{pq}$ from -0.25 to 0.25. The beam energy is 2.140 GeV. Error bars are statistical only. Systematic errors are shown as a blue band.

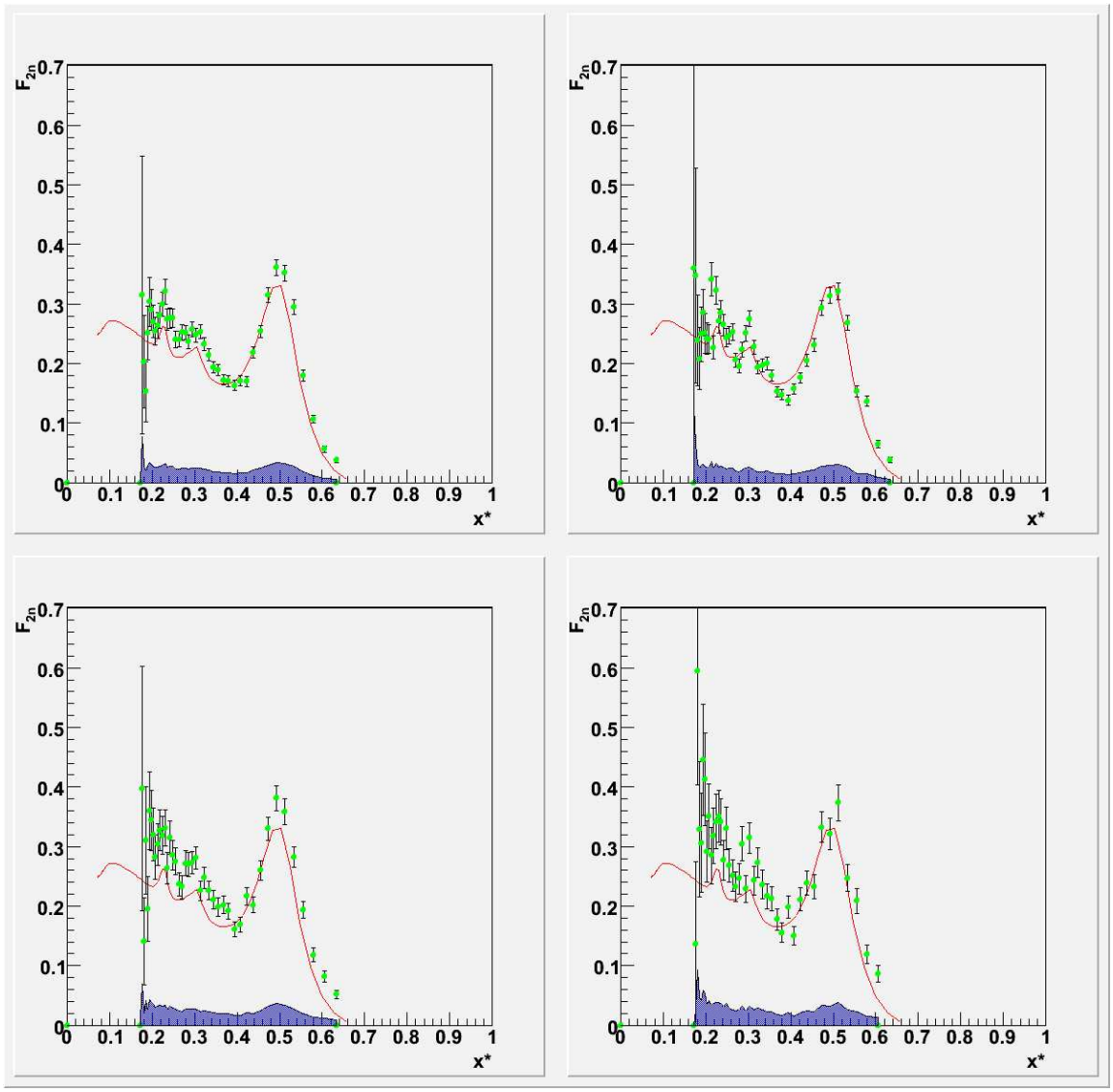

FIG. 101: Effective F_{2n} (green markers) structure function is shown as a function of x^*. Red line is the model F_{2n}. Data are for Q^2 from 0.45 to 0.77 $(\mathrm{GeV}/c)^2$, $\cos\theta_{pq}$ from 0.25 to 0.75. The beam energy is 2.140 GeV. Error bars are statistical only. Systematic errors are shown as a blue band.

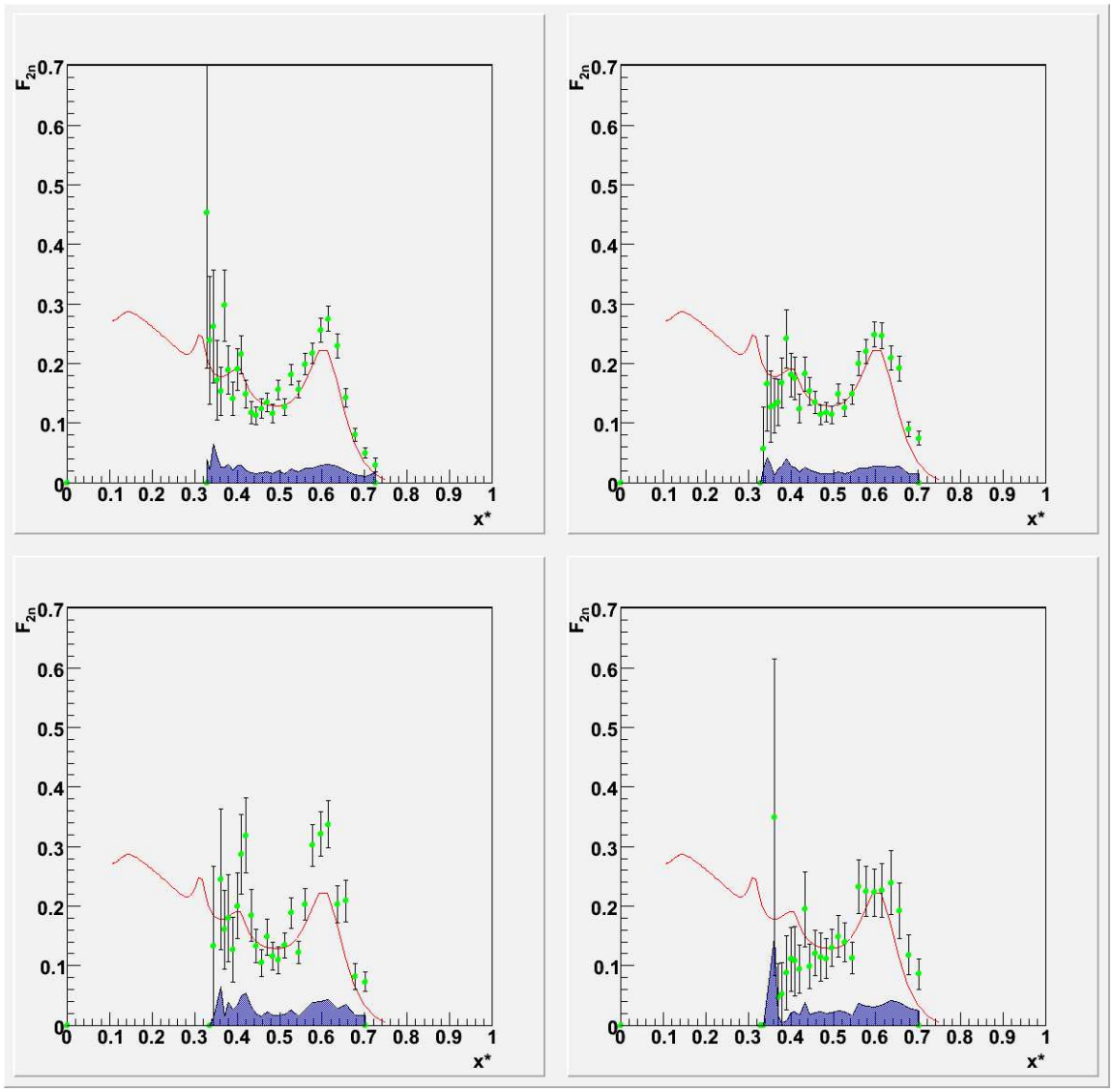

FIG. 102: Effective F_{2n} (green markers) structure function is shown as a function of x^*. Red line is the model F_{2n}. Data are for Q^2 from 0.77 to 1.10 $(\mathrm{GeV}/c)^2$, $\cos\theta_{pq}$ from -0.75 to -0.25. The beam energy is 2.140 GeV. Error bars are statistical only. Systematic errors are shown as a blue band.

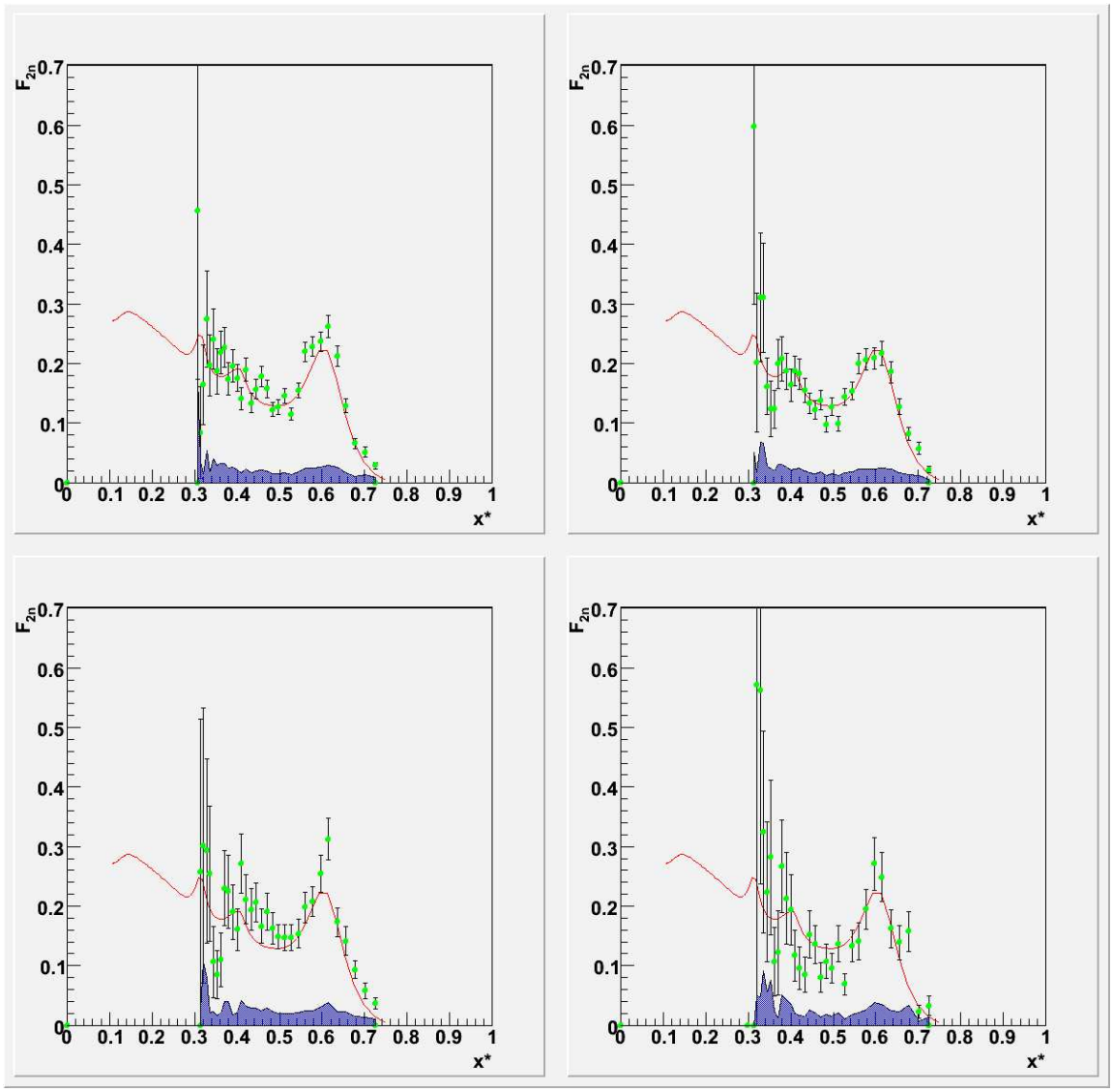

FIG. 103: Effective F_{2n} (green markers) structure function is shown as a function of x^*. Red line is the model F_{2n}. Data are for Q^2 from 0.77 to 1.10 $(\mathrm{GeV}/c)^2$, $\cos\theta_{pq}$ from -0.25 to 0.25. The beam energy is 2.140 GeV. Error bars are statistical only. Systematic errors are shown as a blue band.

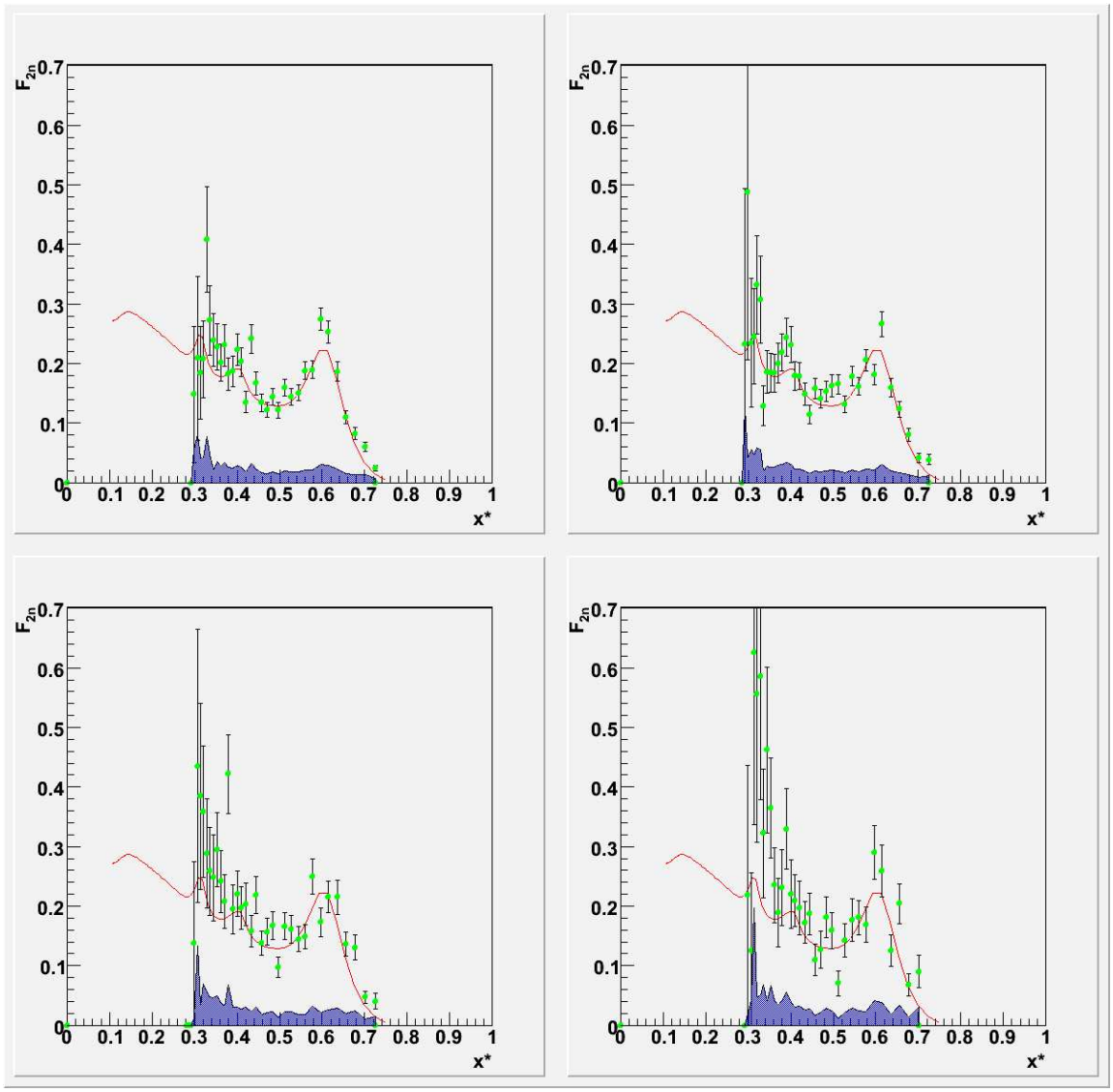

FIG. 104: Effective F_{2n} (green markers) structure function is shown as a function of x^*. Red line is the model F_{2n}. Data are for Q^2 from 0.77 to 1.10 $(\mathrm{GeV}/c)^2$, $\cos\theta_{pq}$ from 0.25 to 0.75. The beam energy is 2.140 GeV. Error bars are statistical only. Systematic errors are shown as a blue band.

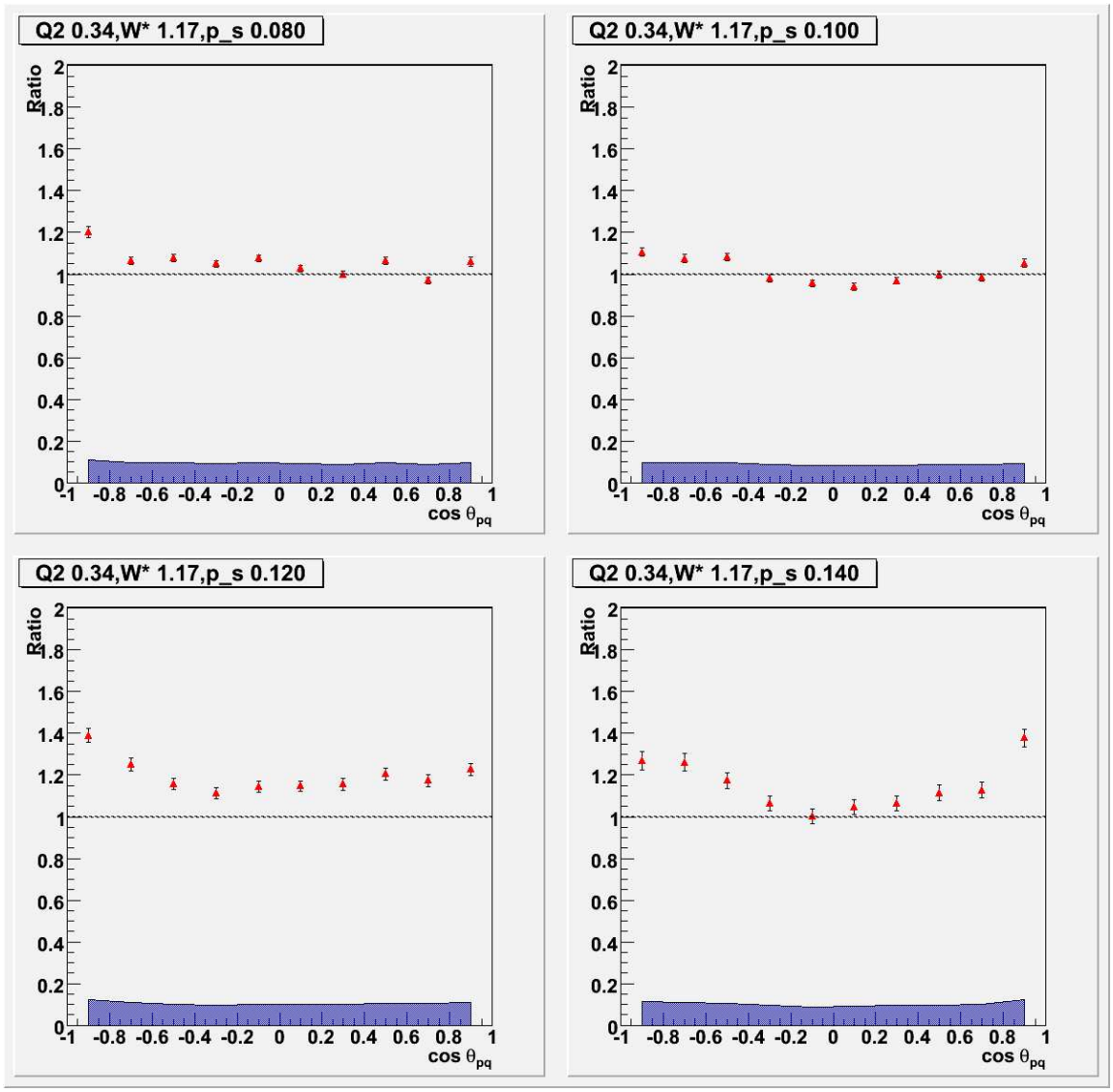

FIG. 105: Ratio of experimental data with subtracted accidental background and elastic tail to the full simulation in the PWIA spectator picture is shown as a function of $\cos\theta_{pq}$. Data are for Q^2 from 0.22 to 0.45 $(\mathrm{GeV}/c)^2$, W^* from 1.00 to 1.35 GeV. The beam energy is 2.140 GeV. Systematic errors are shown as a blue band.

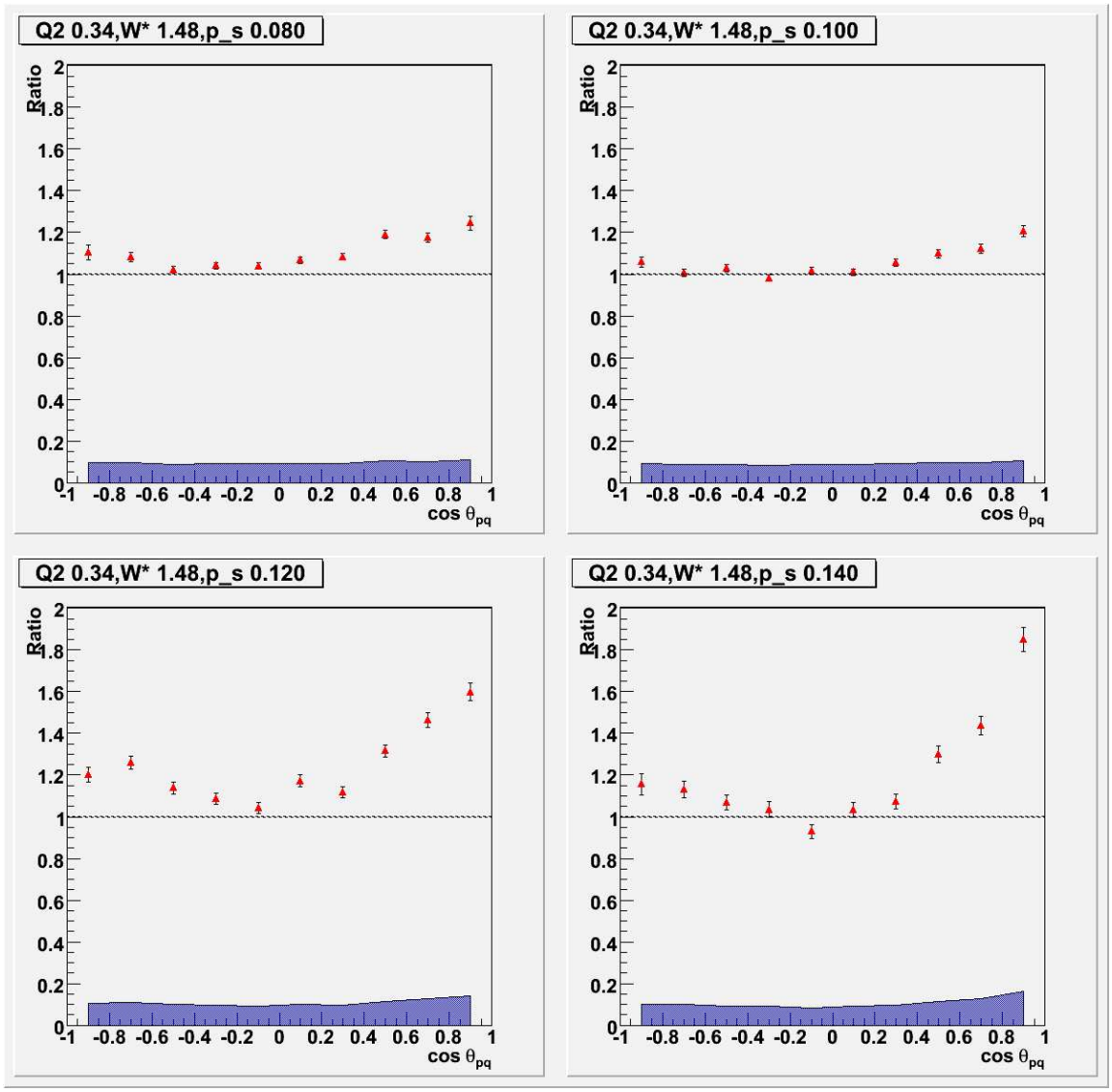

FIG. 106: Ratio of experimental data with subtracted accidental background and elastic tail to the full simulation in the PWIA spectator picture is shown as a function of $\cos\theta_{pq}$. Data are for Q^2 from 0.22 to 0.45 $(\mathrm{GeV}/c)^2$, W^* from 1.35 to 1.60 GeV. The beam energy is 2.140 GeV. Error bars are statistical only. Systematic errors are shown as a blue band.

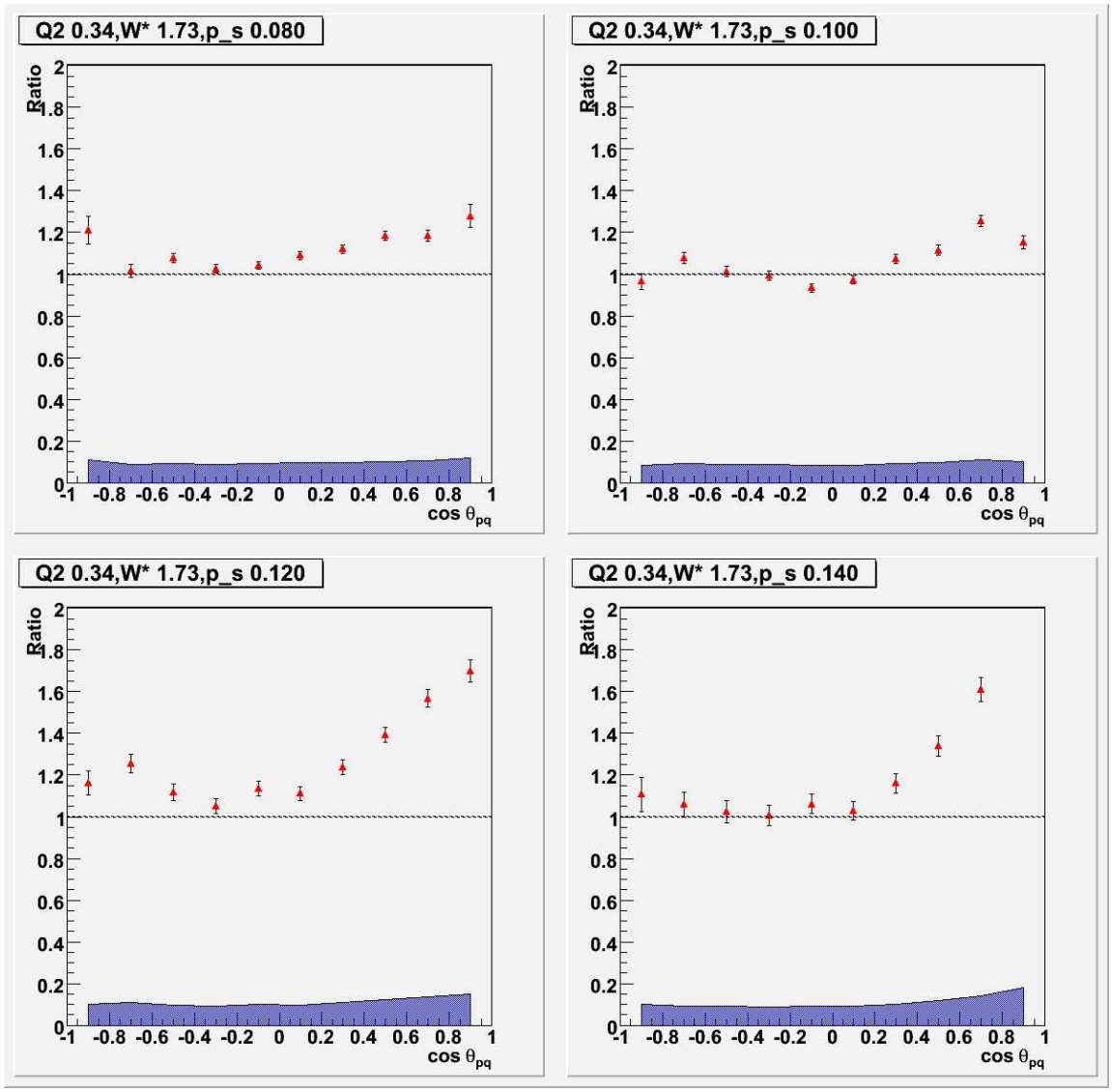

FIG. 107: Ratio of experimental data with subtracted accidental background and elastic tail to the full simulation in the PWIA spectator picture is shown as a function of $\cos\theta_{pq}$. Data are for Q^2 from 0.22 to 0.45 $(\mathrm{GeV}/c)^2$, W^* from 1.60 to 1.85 GeV. The beam energy is 2.140 GeV. Error bars are statistical only. Systematic errors are shown as a blue band.

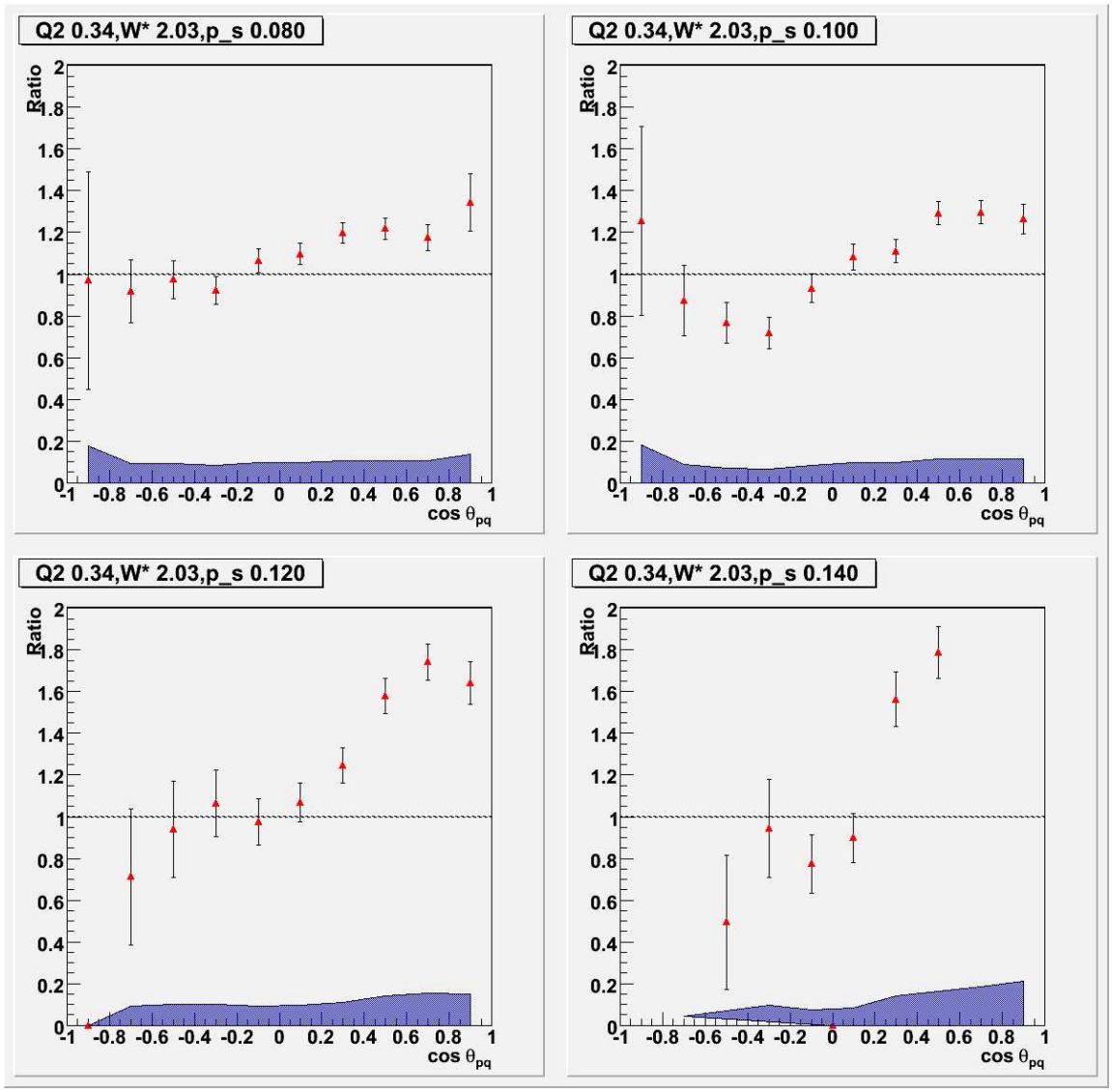

FIG. 108: Ratio of experimental data with subtracted accidental background and elastic tail to the full simulation in the PWIA spectator picture is shown as a function of $\cos\theta_{pq}$. Data are for Q^2 from 0.22 to 0.45 $(\mathrm{GeV}/c)^2$, W^* from 1.85 to 2.20 GeV. The beam energy is 2.140 GeV. Error bars are statistical only. Systematic errors are shown as a blue band.

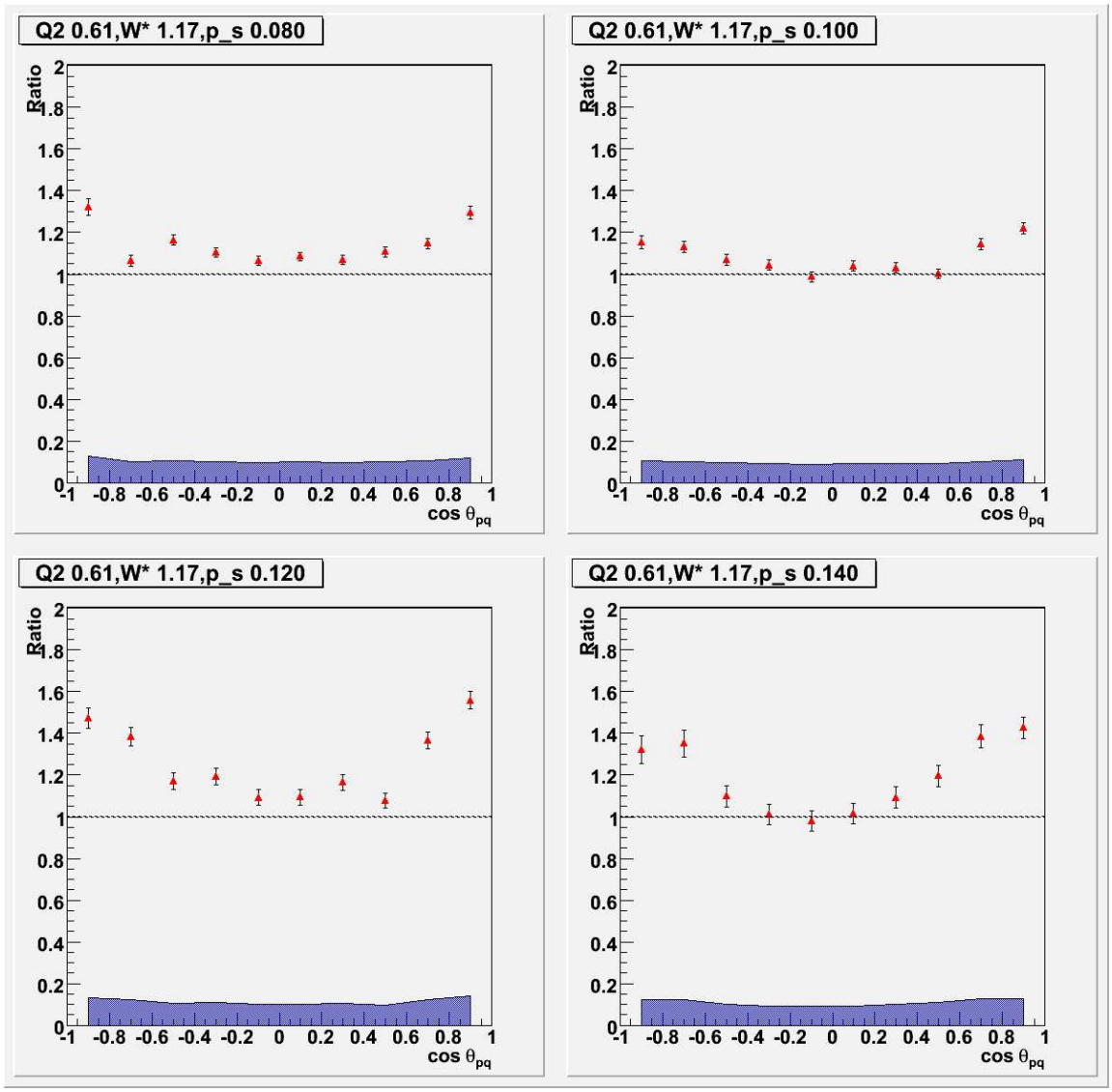

FIG. 109: Ratio of experimental data with subtracted accidental background and elastic tail to the full simulation in the PWIA spectator picture is shown as a function of $\cos\theta_{pq}$. Data are for Q^2 from 0.45 to 0.77 $(\mathrm{GeV}/c)^2$, W^* from 1.00 to 1.35 GeV. The beam energy is 2.140 GeV. Error bars are statistical only. Systematic errors are shown as a blue band.

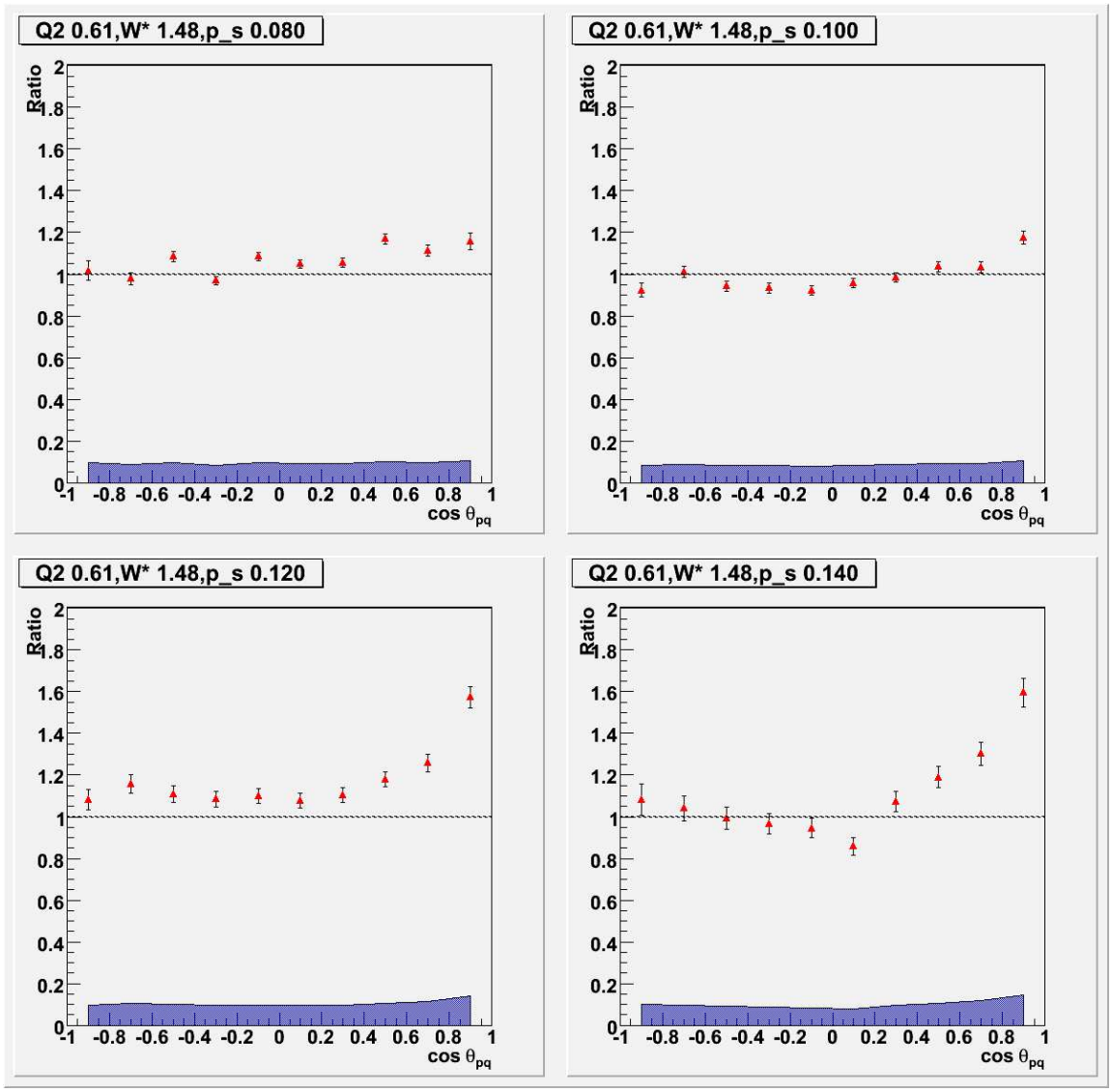

FIG. 110: Ratio of experimental data with subtracted accidental background and elastic tail to the full simulation in the PWIA spectator picture is shown as a function of $\cos\theta_{pq}$. Data are for Q^2 from 0.45 to 0.77 $(\mathrm{GeV}/c)^2$, W^* from 1.35 to 1.60 GeV. The beam energy is 2.140 GeV. Error bars are statistical only. Systematic errors are shown as a blue band.

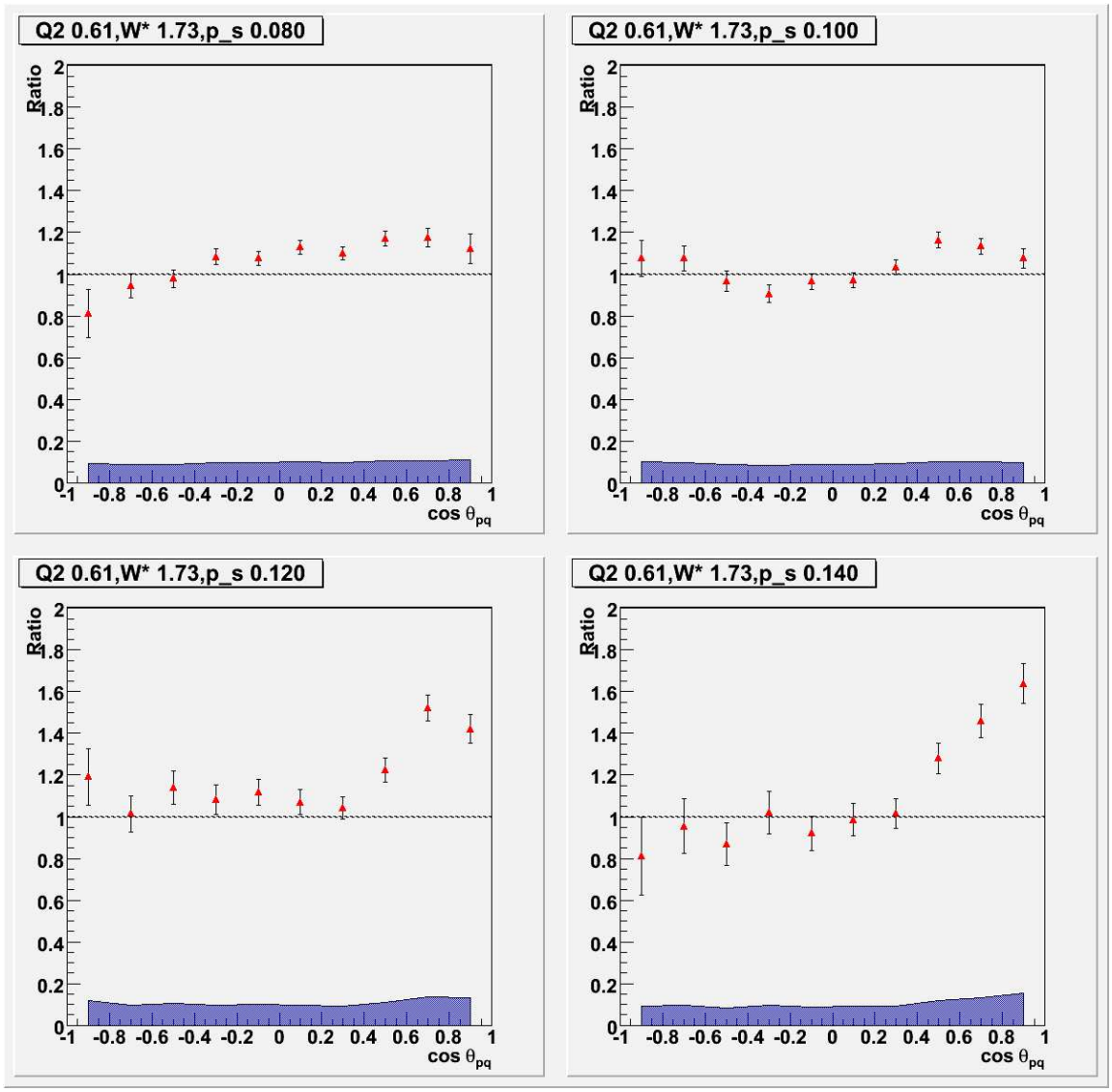

FIG. 111: Ratio of experimental data with subtracted accidental background and elastic tail to the full simulation in the PWIA spectator picture is shown as a function of $\cos\theta_{pq}$. Data are for Q^2 from 0.45 to 0.77 $(\mathrm{GeV}/c)^2$, W^* from 1.60 to 1.85 GeV. The beam energy is 2.140 GeV. Error bars are statistical only. Systematic errors are shown as a blue band.

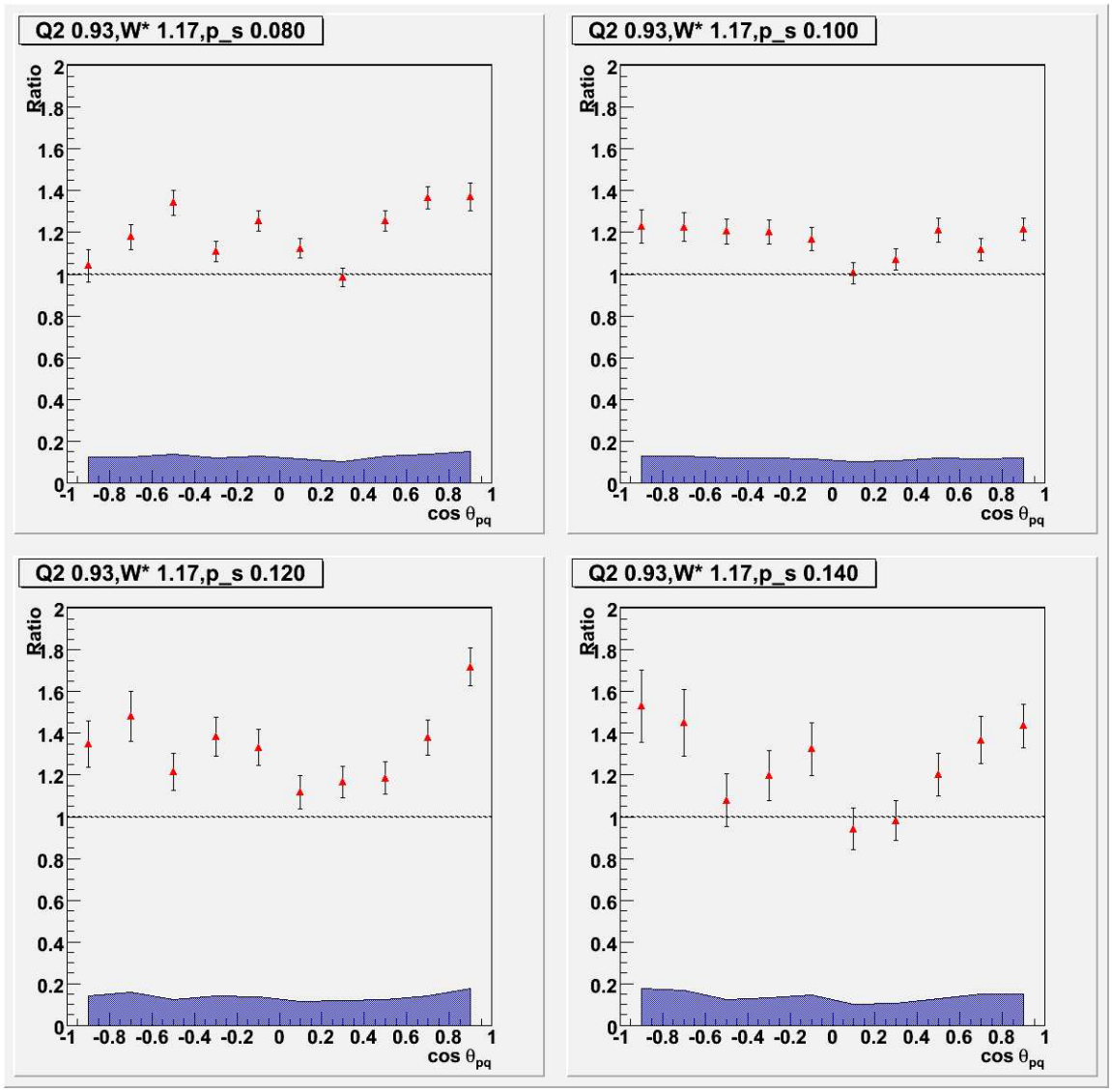

FIG. 112: Ratio of experimental data with subtracted accidental background and elastic tail to the full simulation in the PWIA spectator picture is shown as a function of $\cos\theta_{pq}$. Data are for Q^2 from 0.77 to 1.10 $(\mathrm{GeV}/c)^2$, W^* from 1.00 to 1.35 GeV. The beam energy is 2.140 GeV. Error bars are statistical only. Systematic errors are shown as a blue band.

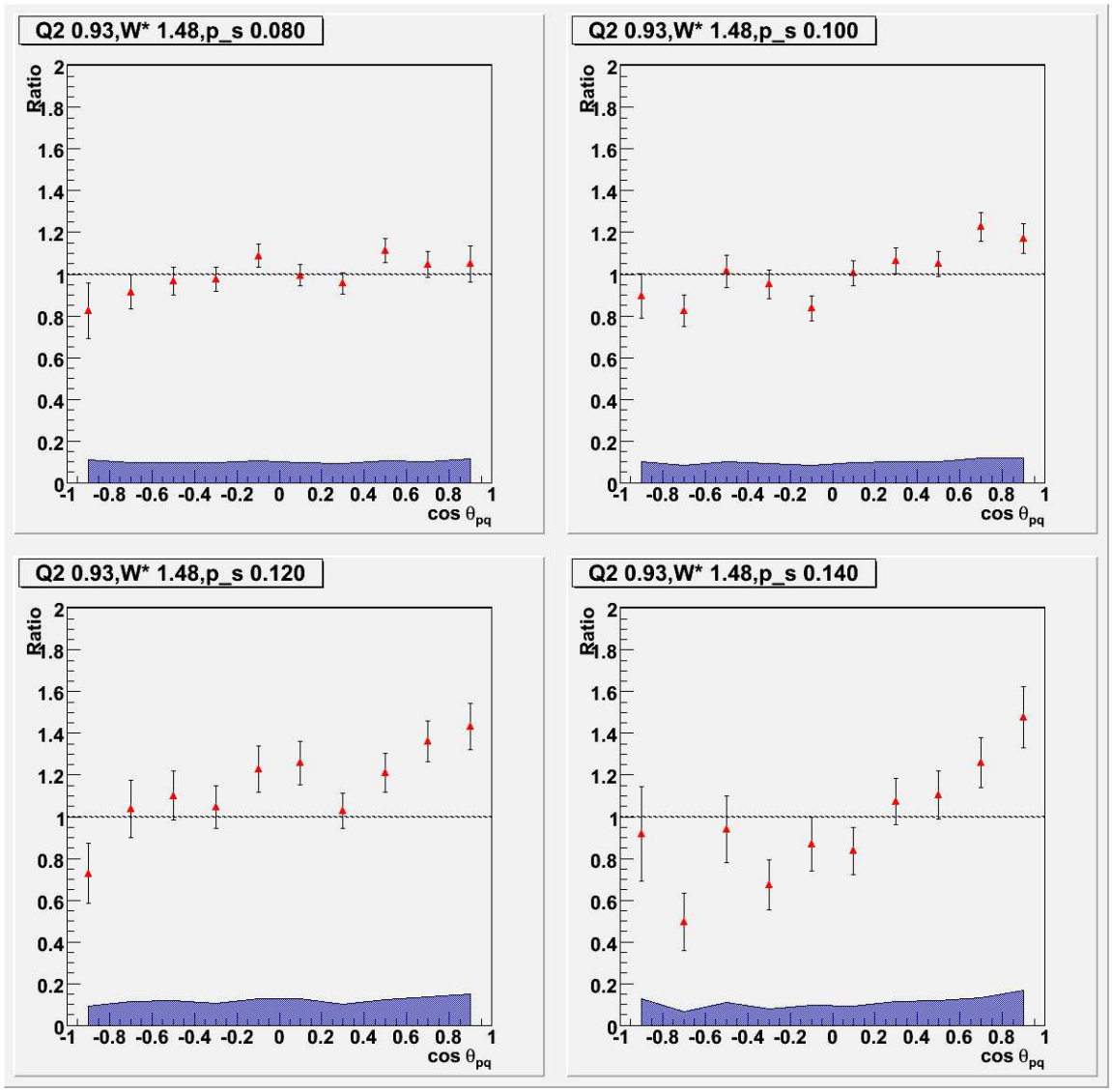

FIG. 113: Ratio of experimental data with subtracted accidental background and elastic tail to the full simulation in the PWIA spectator picture is shown as a function of $\cos\theta_{pq}$. Data are for Q^2 from 0.77 to 1.10 $(\mathrm{GeV}/c)^2$, W^* from 1.35 to 1.60 GeV. The beam energy is 2.140 GeV. Error bars are statistical only. Systematic errors are shown as a blue band.

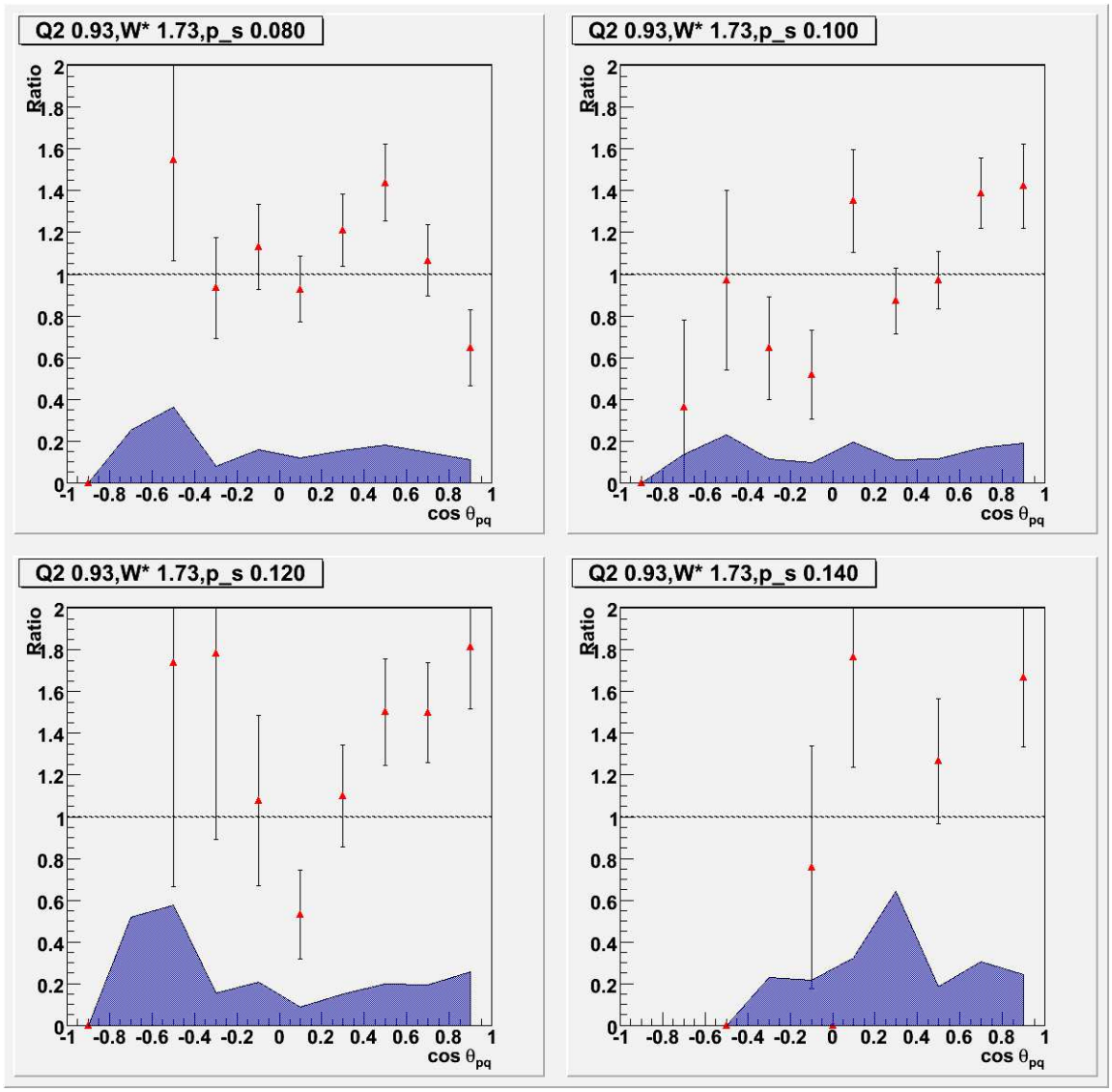

FIG. 114: Ratio of experimental data with subtracted accidental background and elastic tail to the full simulation in the PWIA spectator picture is shown as a function of $\cos\theta_{pq}$. Data are for Q^2 from 0.77 to 1.10 $(\mathrm{GeV}/c)^2$, W^* from 1.60 to 1.85 GeV. The beam energy is 2.140 GeV. Error bars are statistical only. Systematic errors are shown as a blue band.

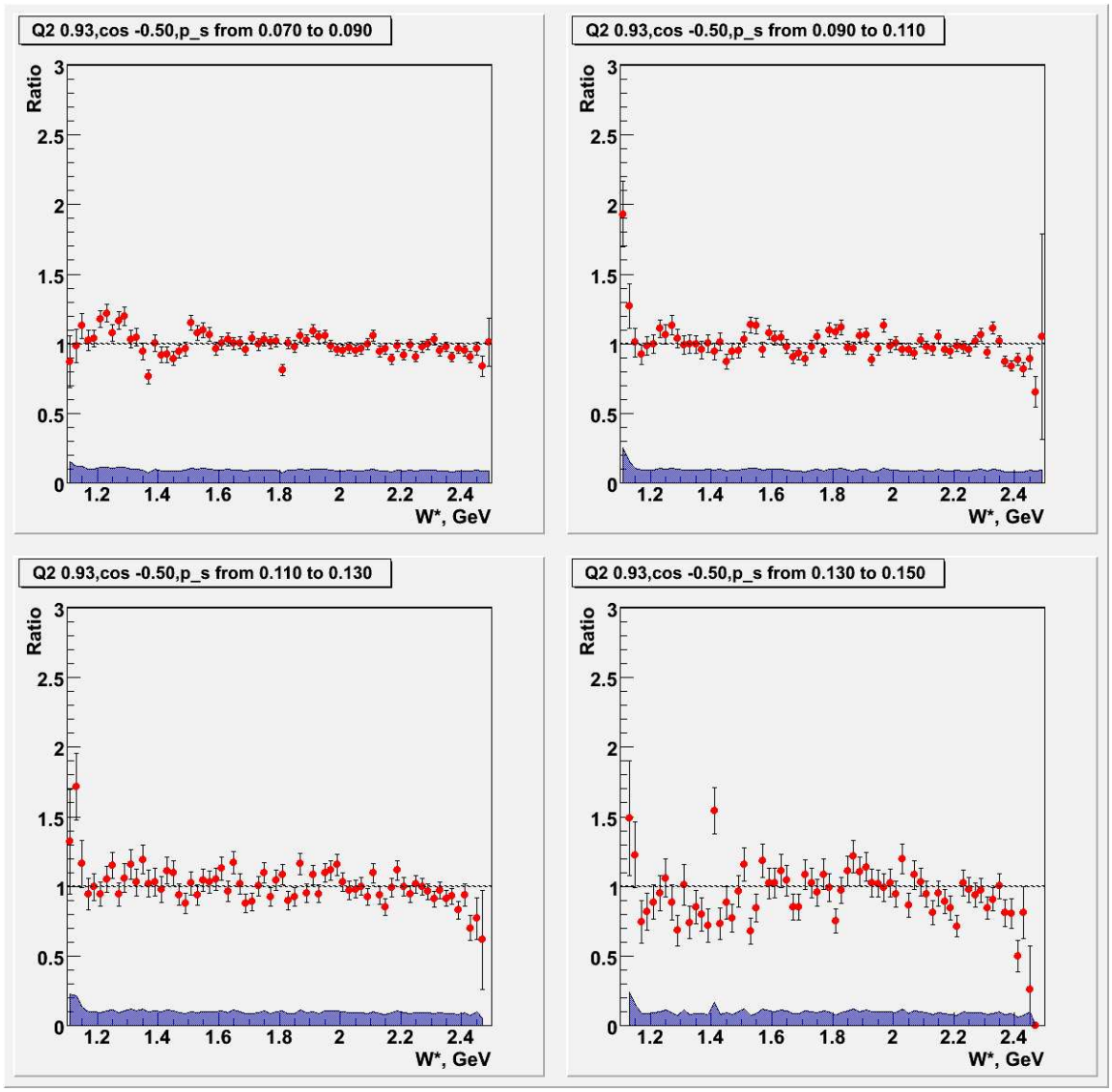

FIG. 115: Ratio of experimental data with subtracted accidental background and elastic tail to the full simulation in the PWIA spectator picture is shown as a function of W^*. Data are for Q^2 from 0.77 to 1.10 $(\mathrm{GeV}/c)^2$, $\cos\theta_{pq}$ from -0.75 to -0.25. The beam energy is 4.217 GeV. Error bars are statistical only. Systematic errors are shown as a blue band.

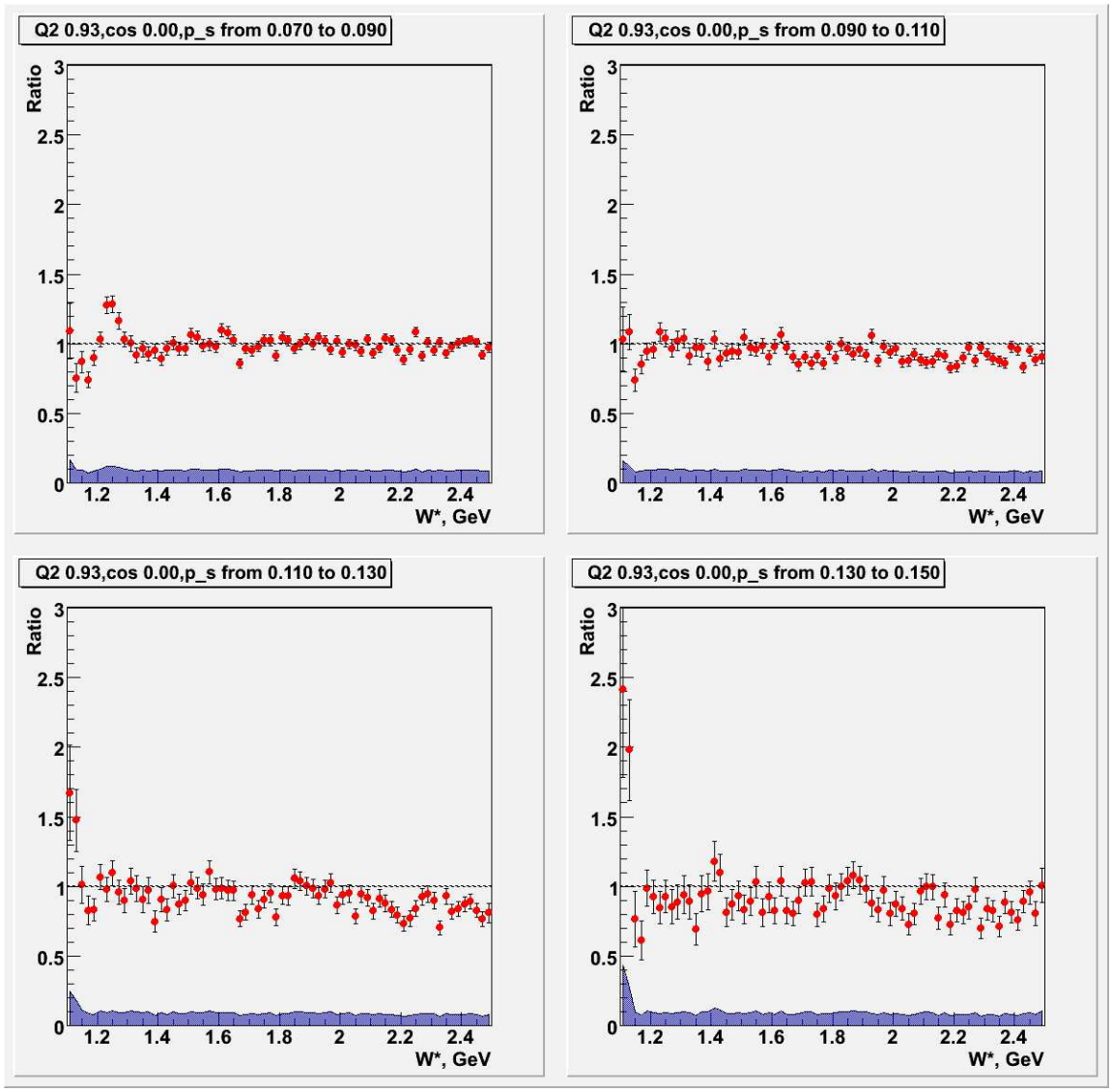

FIG. 116: Ratio of experimental data with subtracted accidental background and elastic tail to the full simulation in the PWIA spectator picture is shown as a function of W^*. Data are for Q^2 from 0.77 to 1.10 $(\mathrm{GeV}/c)^2$, $\cos\theta_{pq}$ from -0.25 to 0.25. The beam energy is 4.217 GeV. Error bars are statistical only. Systematic errors are shown as a blue band.

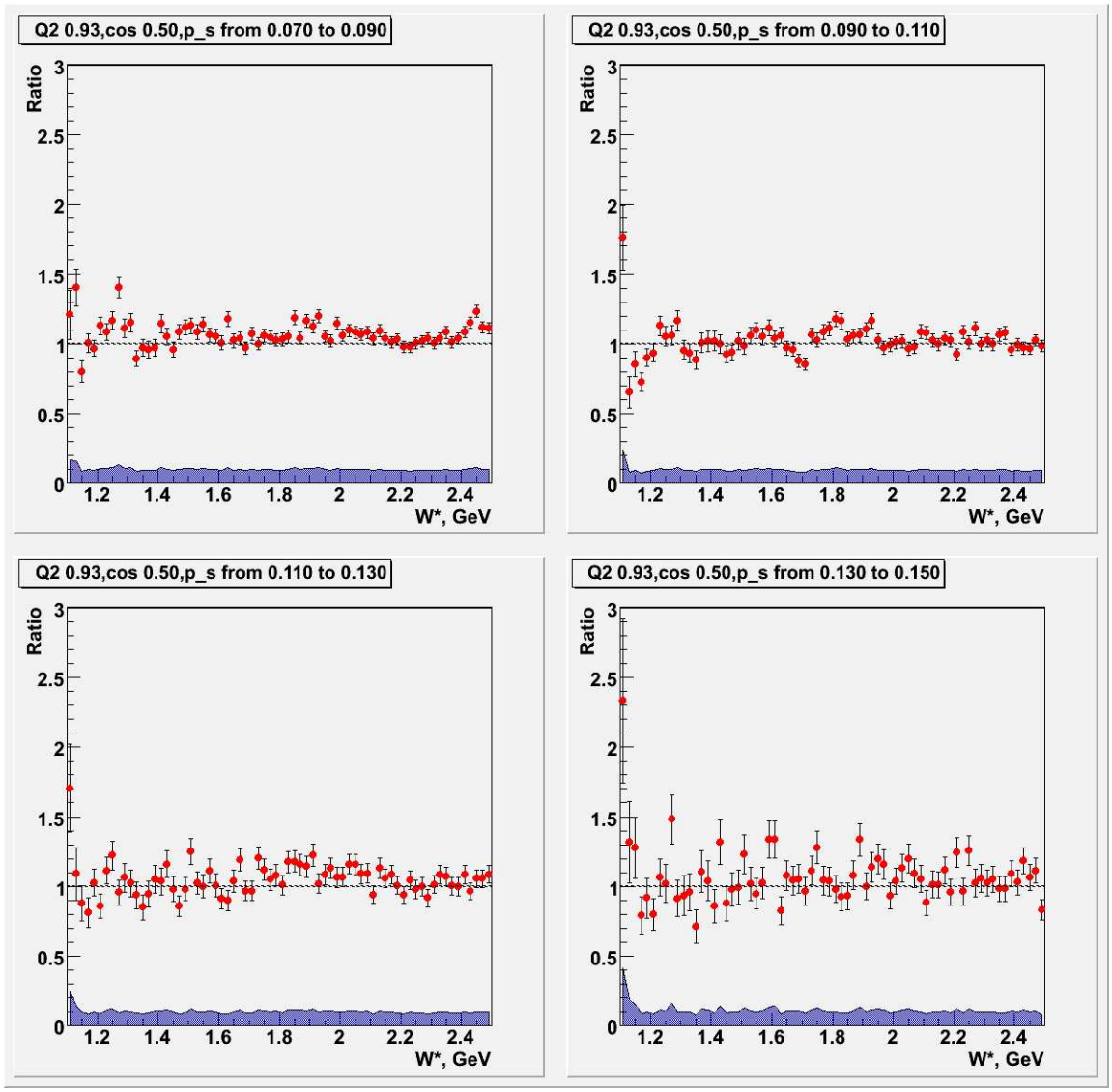

FIG. 117: Ratio of experimental data with subtracted accidental background and elastic tail to the full simulation in the PWIA spectator picture is shown as a function of W^*. Data are for Q^2 from 0.77 to 1.10 $(\mathrm{GeV}/c)^2$, $\cos\theta_{pq}$ from 0.25 to 0.75. The beam energy is 4.217 GeV. Error bars are statistical only. Systematic errors are shown as a blue band.

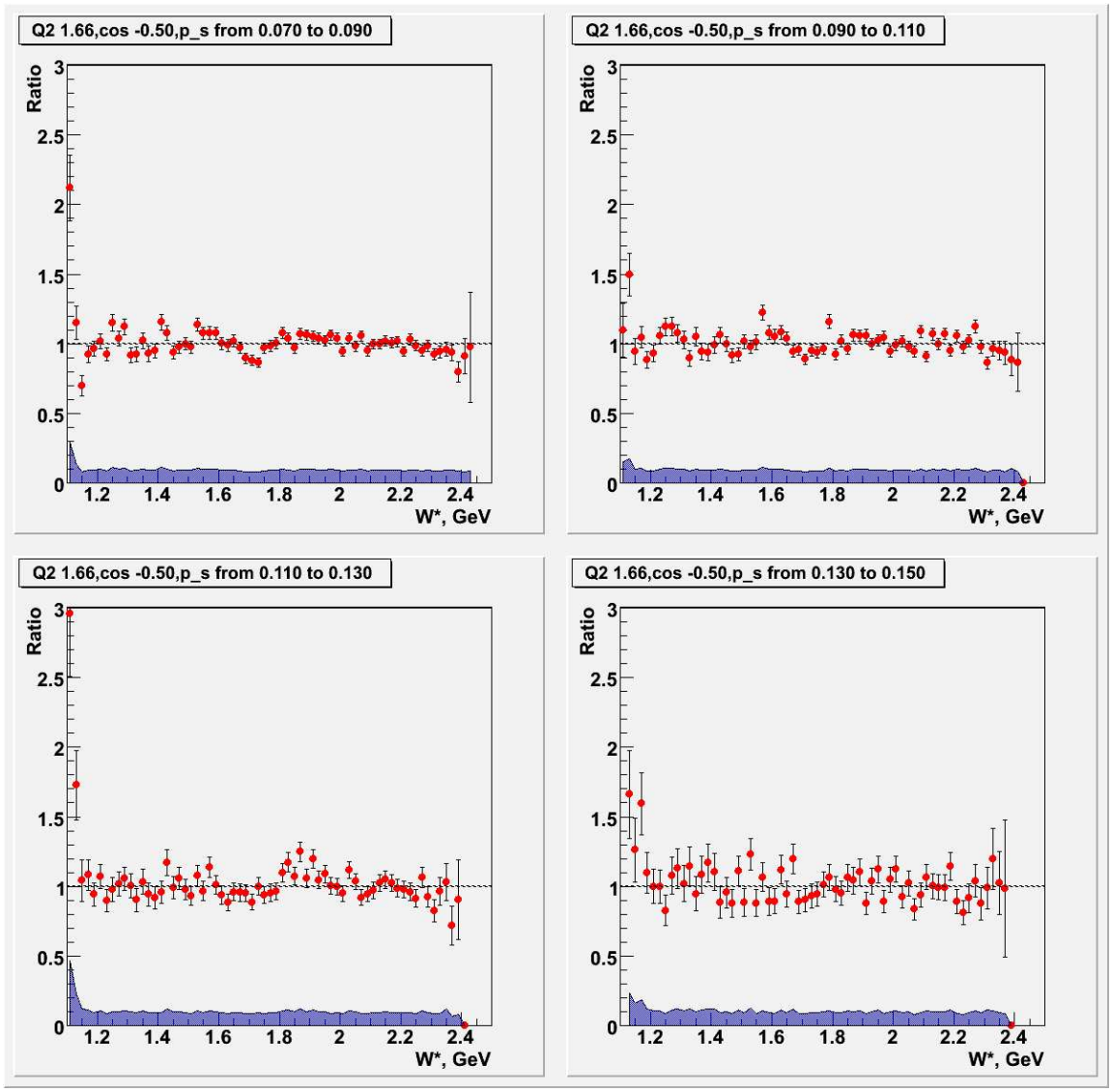

FIG. 118: Ratio of experimental data with subtracted accidental background and elastic tail to the full simulation in the PWIA spectator picture is shown as a function of W^*. Data are for Q^2 from 1.10 to 2.23 $(\mathrm{GeV}/c)^2$, $\cos\theta_{pq}$ from -0.75 to -0.25. The beam energy is 4.217 GeV. Error bars are statistical only. Systematic errors are shown as a blue band.

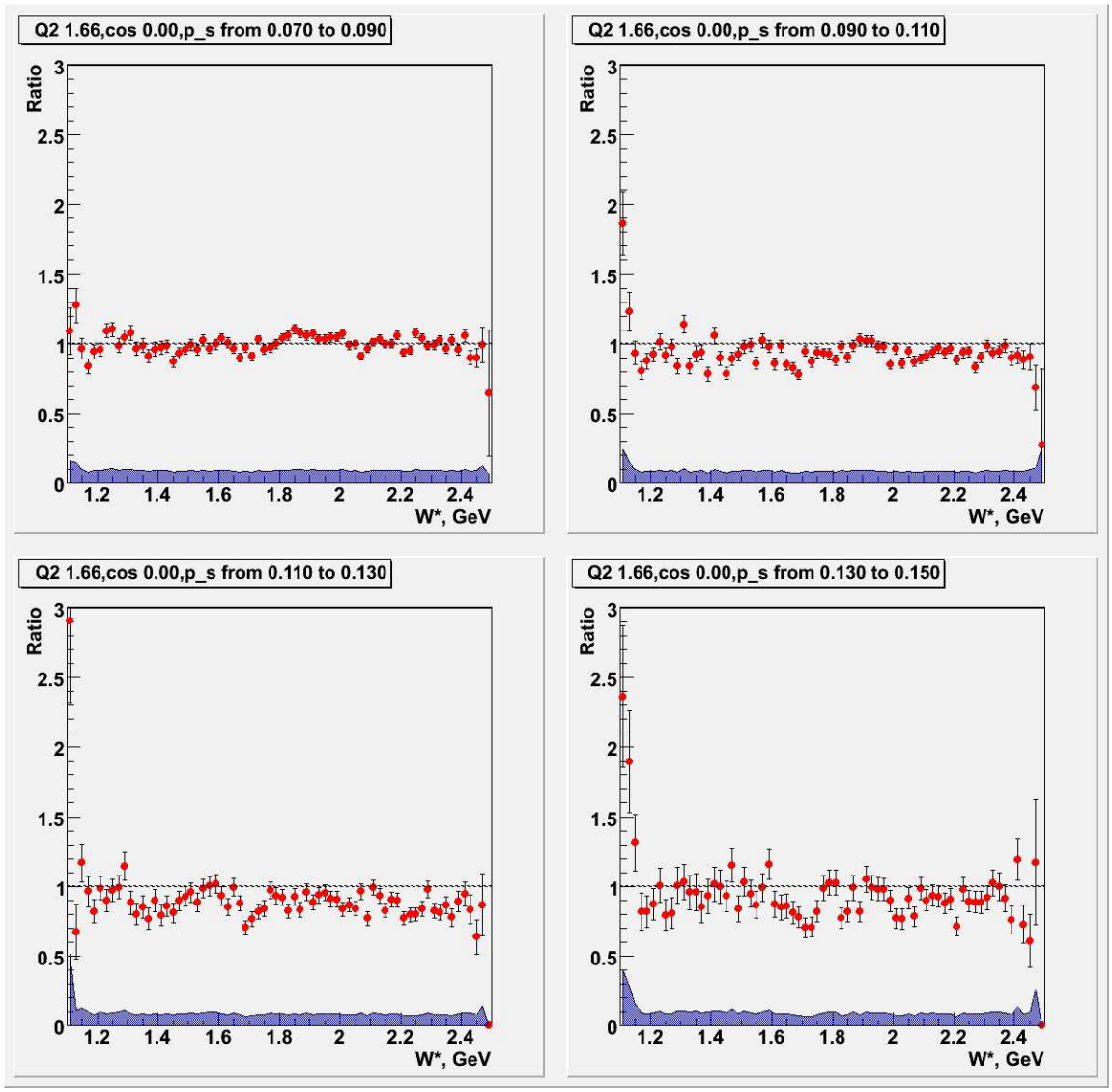

FIG. 119: Ratio of experimental data with subtracted accidental background and elastic tail to the full simulation in the PWIA spectator picture is shown as a function of W^*. Data are for Q^2 from 1.10 to 2.23 $(\mathrm{GeV}/c)^2$, $\cos\theta_{pq}$ from -0.25 to 0.25. The beam energy is 4.217 GeV. Error bars are statistical only. Systematic errors are shown as a blue band.

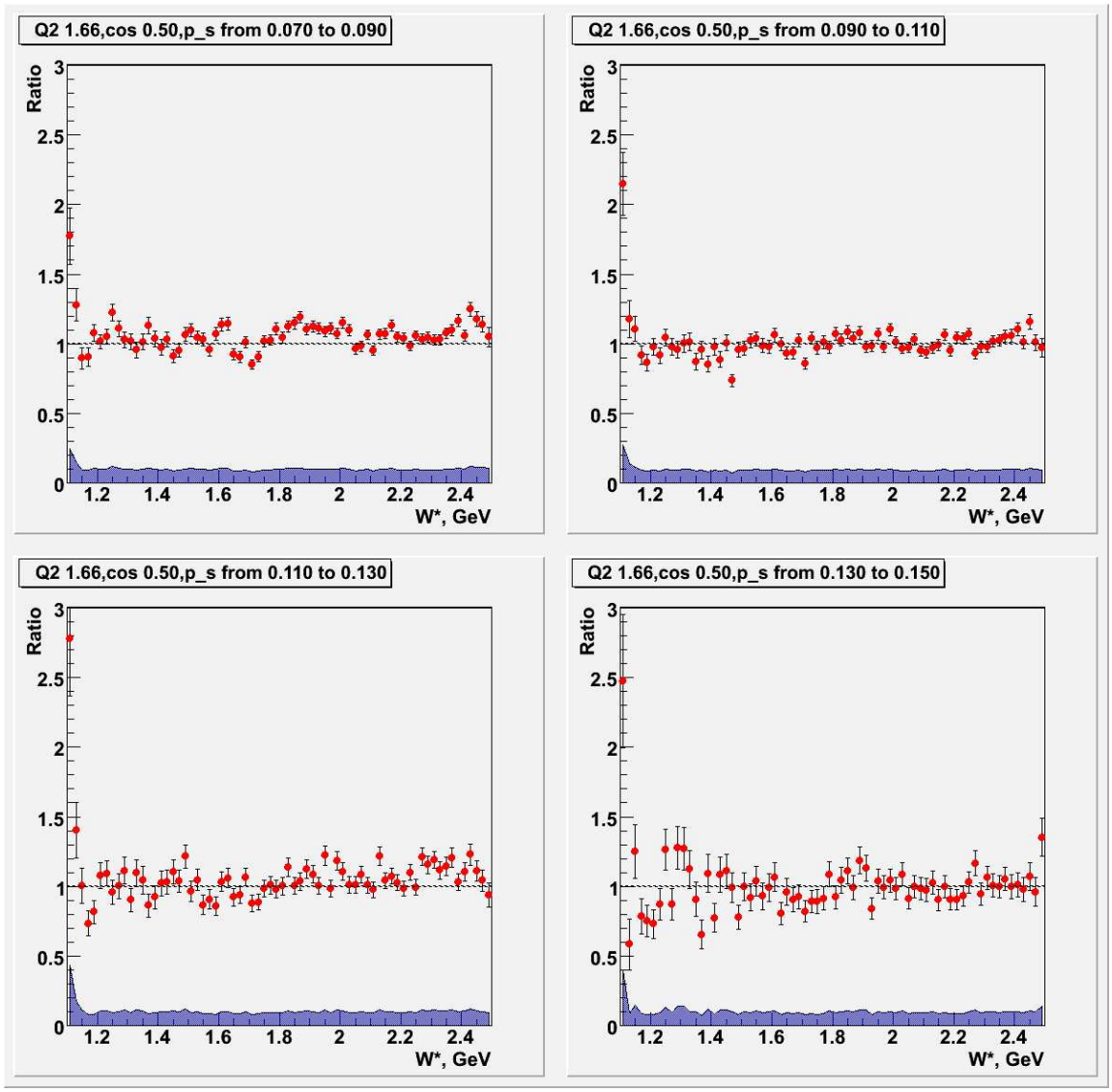

FIG. 120: Ratio of experimental data with subtracted accidental background and elastic tail to the full simulation in the PWIA spectator picture is shown as a function of W^*. Data are for Q^2 from 1.10 to 2.23 $(\mathrm{GeV}/c)^2$, $\cos\theta_{pq}$ from 0.25 to 0.75. The beam energy is 4.217 GeV. Error bars are statistical only. Systematic errors are shown as a blue band.

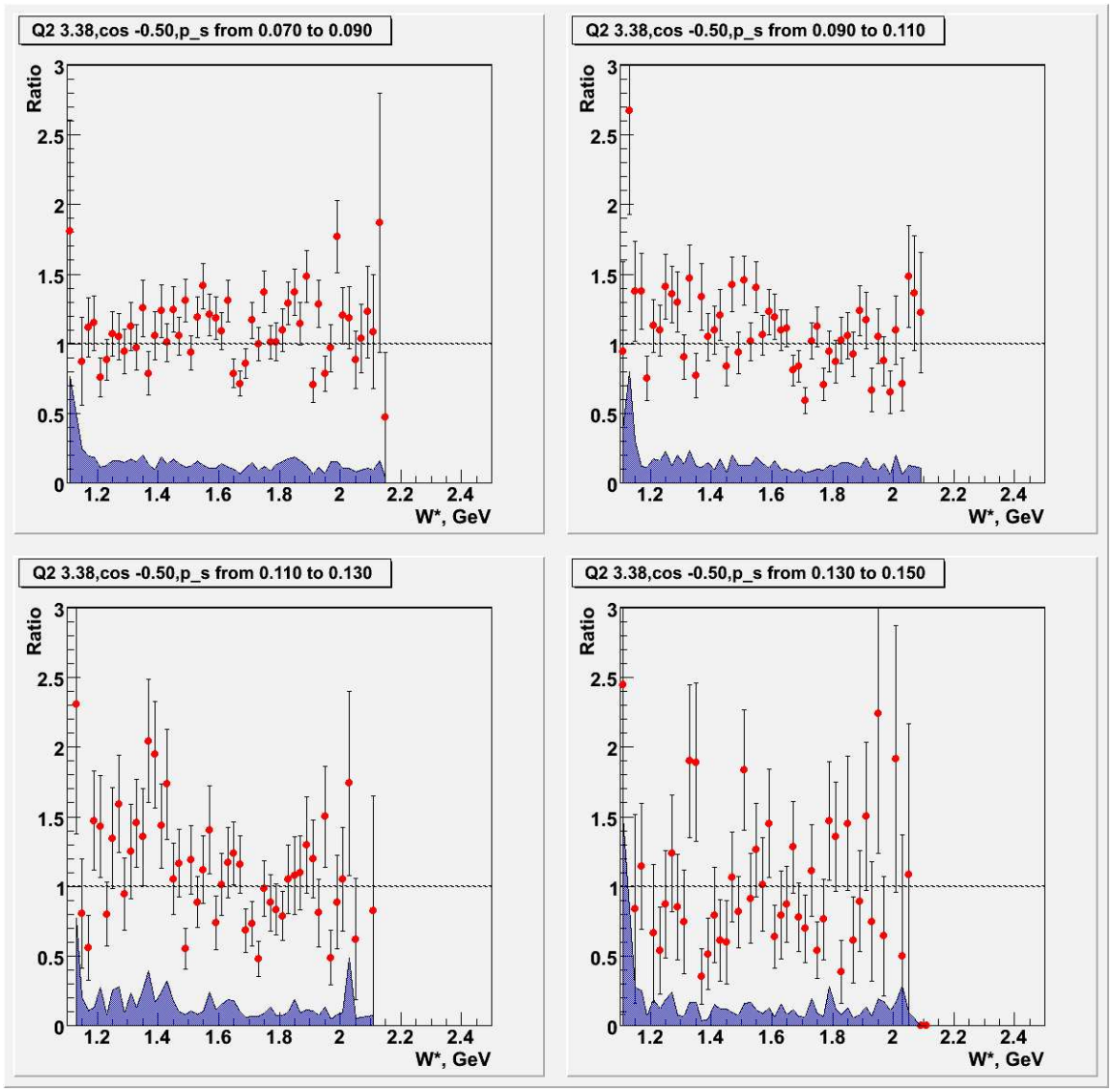

FIG. 121: Ratio of experimental data with subtracted accidental background and elastic tail to the full simulation in the PWIA spectator picture is shown as a function of W^*. Data are for Q^2 from 2.23 to 4.52 $(\mathrm{GeV}/c)^2$, $\cos\theta_{pq}$ from -0.75 to -0.25. The beam energy is 4.217 GeV. Error bars are statistical only. Systematic errors are shown as a blue band.

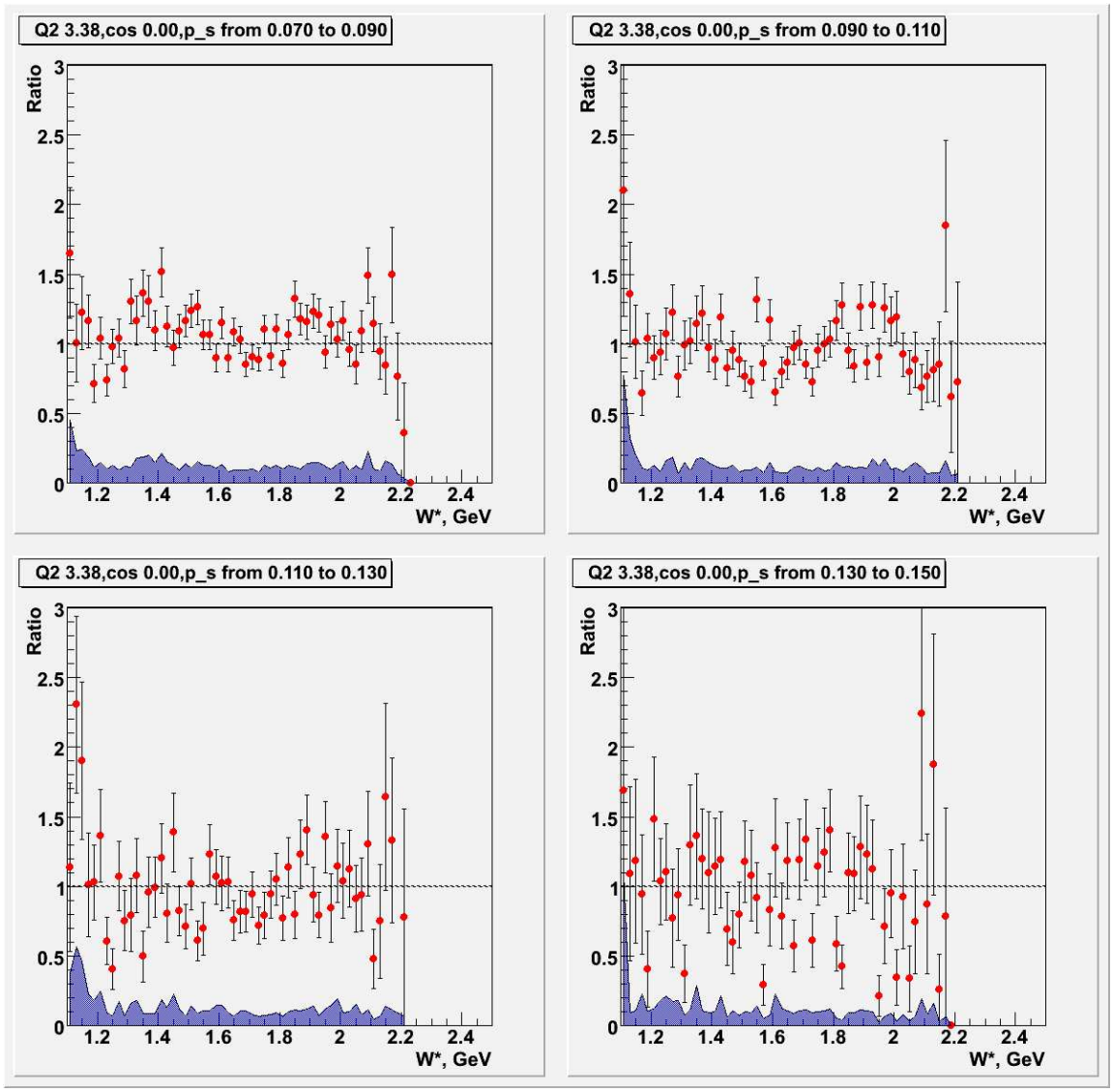

FIG. 122: Ratio of experimental data with subtracted accidental background and elastic tail to the full simulation in the PWIA spectator picture is shown as a function of W^*. Data are for Q^2 from 2.23 to 4.52 $(\mathrm{GeV}/c)^2$, $\cos\theta_{pq}$ from -0.25 to 0.25. The beam energy is 4.217 GeV. Systematic errors are shown as a blue band.

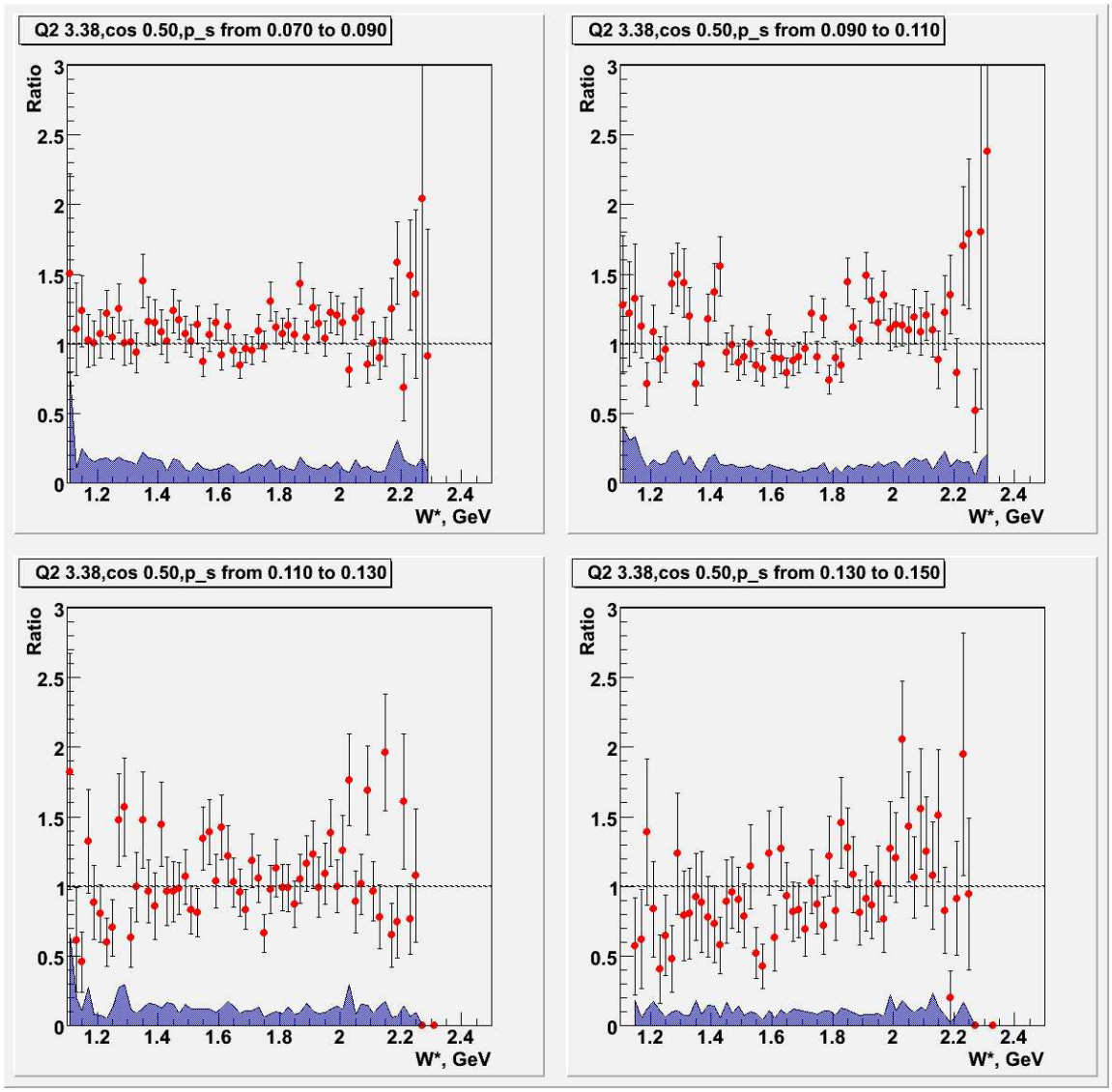

FIG. 123: Ratio of experimental data with subtracted accidental background and elastic tail to the full simulation in the PWIA spectator picture is shown as a function of W^*. Data are for Q^2 from 2.23 to 4.52 $(\mathrm{GeV}/c)^2$, $\cos\theta_{pq}$ from 0.25 to 0.75. The beam energy is 4.217 GeV. Error bars are statistical only. Systematic errors are shown as a blue band.

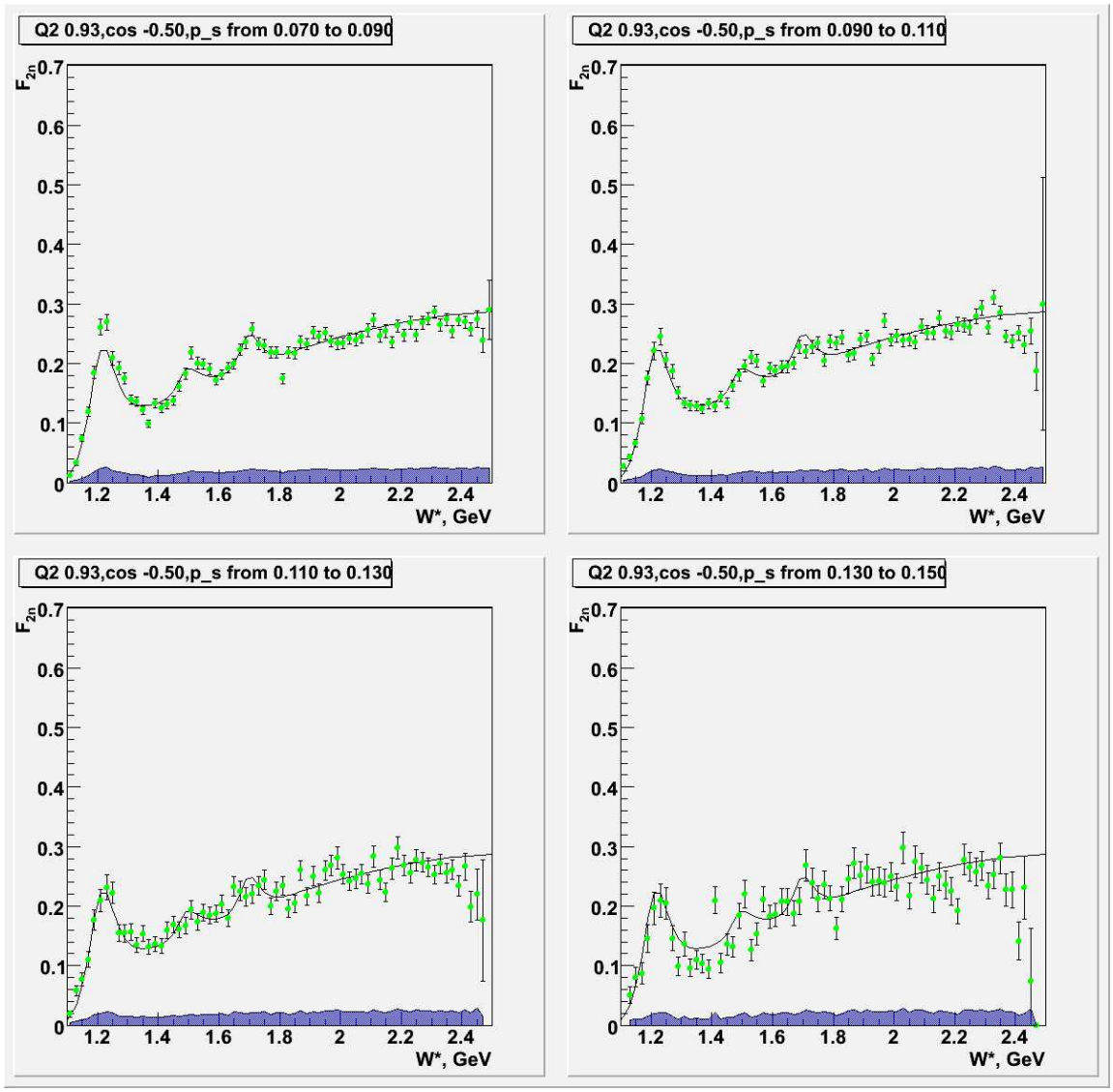

FIG. 124: Effective F_{2n} (green markers) structure function is shown as a function of W^*. Black line is the model F_{2n}. Data are for Q^2 from 0.77 to 1.10 $(\mathrm{GeV}/c)^2$, $\cos\theta_{pq}$ from -0.75 to -0.25. The beam energy is 4.217 GeV. Error bars are statistical only. Systematic errors are shown as a blue band.

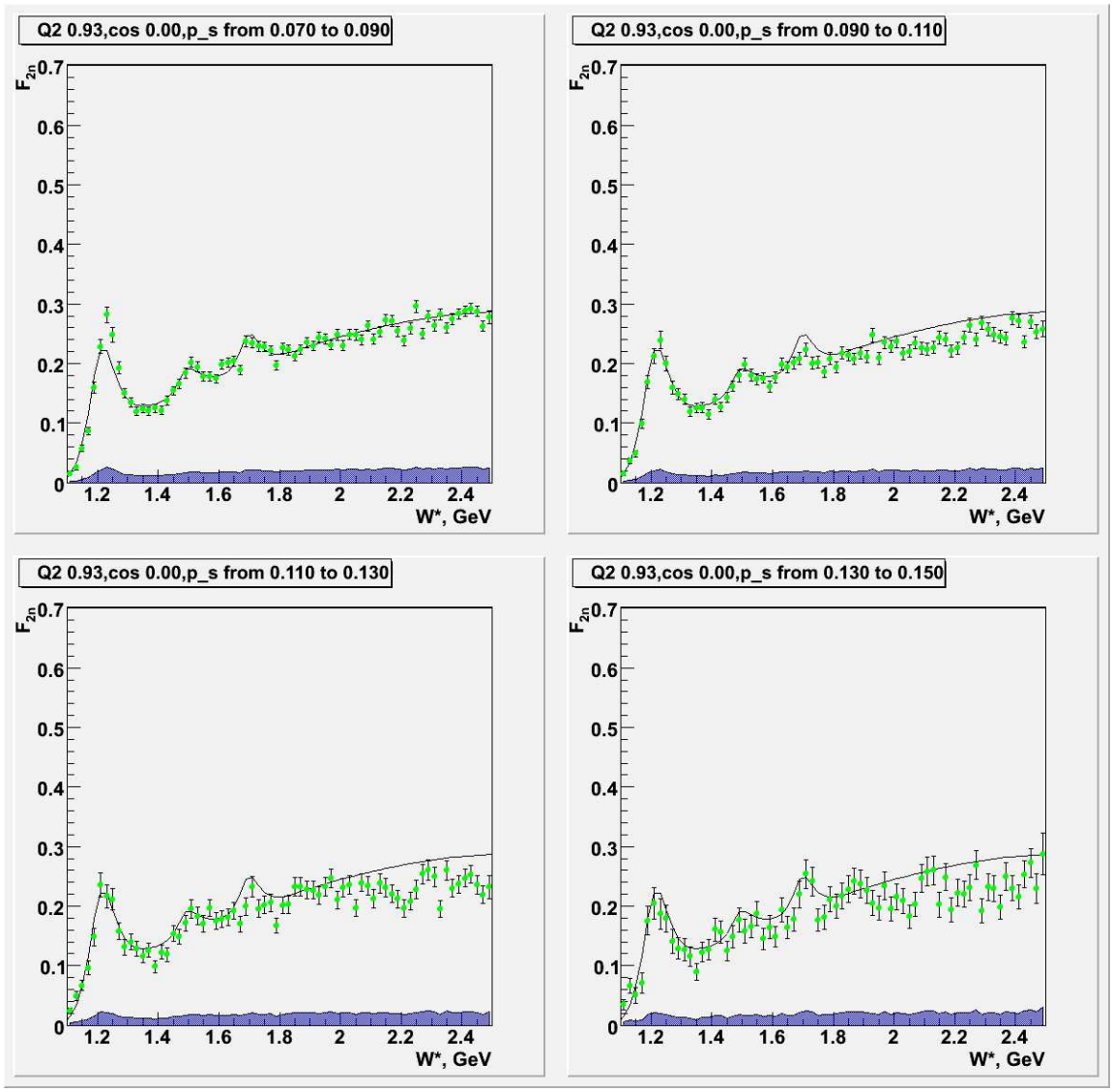

FIG. 125: Effective F_{2n} (green markers) structure function is shown as a function of W^*. Black line is the model F_{2n}. Data are for Q^2 from 0.77 to 1.10 $(\mathrm{GeV}/c)^2$, $\cos\theta_{pq}$ from -0.25 to 0.25. The beam energy is 4.217 GeV. Error bars are statistical only. Systematic errors are shown as a blue band.

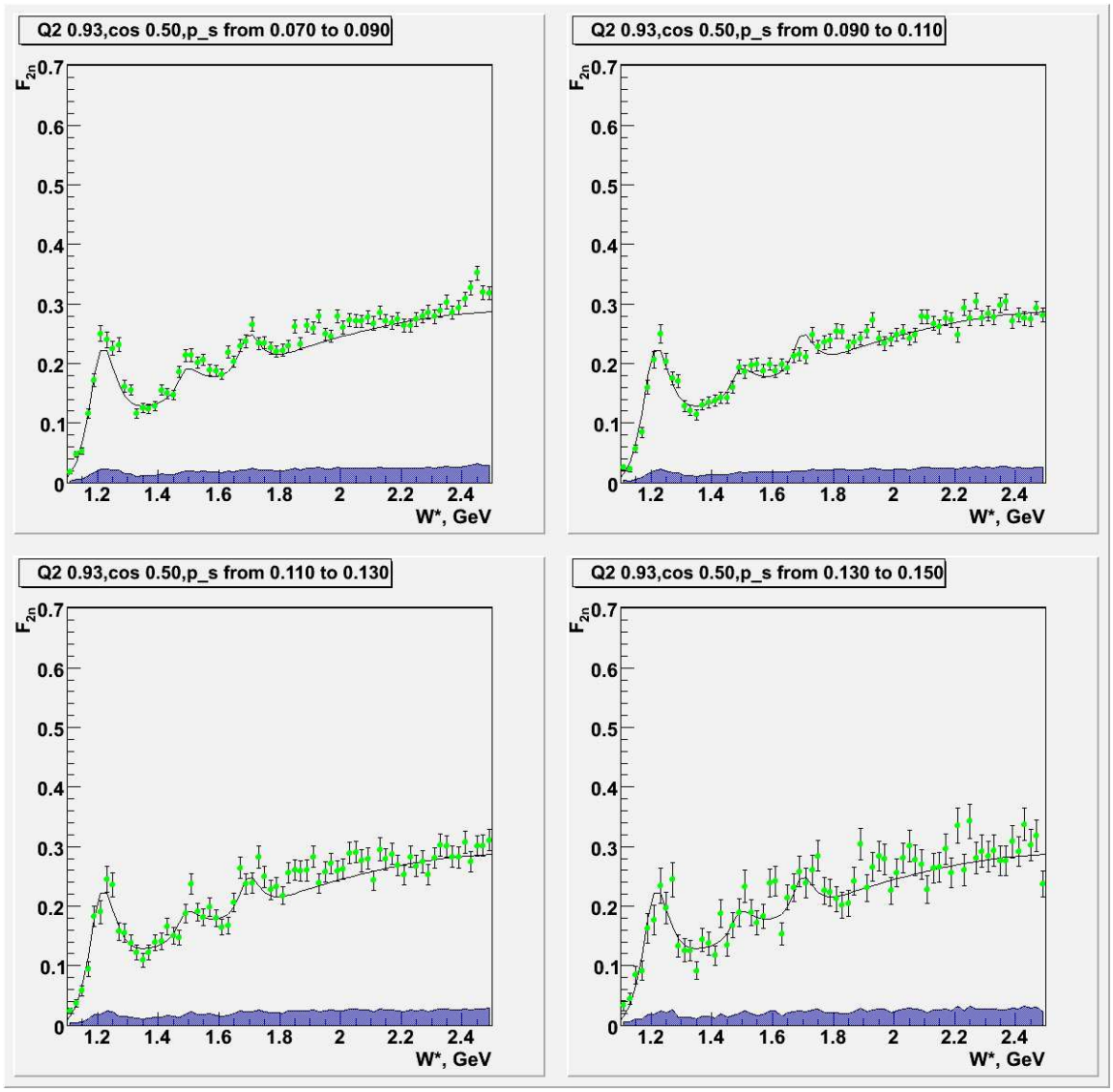

FIG. 126: Effective F_{2n} (green markers) structure function is shown as a function of W^*. Black line is the model F_{2n}. Data are for Q^2 from 0.77 to 1.10 $(\mathrm{GeV}/c)^2$, $\cos\theta_{pq}$ from 0.25 to 0.75. The beam energy is 4.217 GeV. Error bars are statistical only. Systematic errors are shown as a blue band.

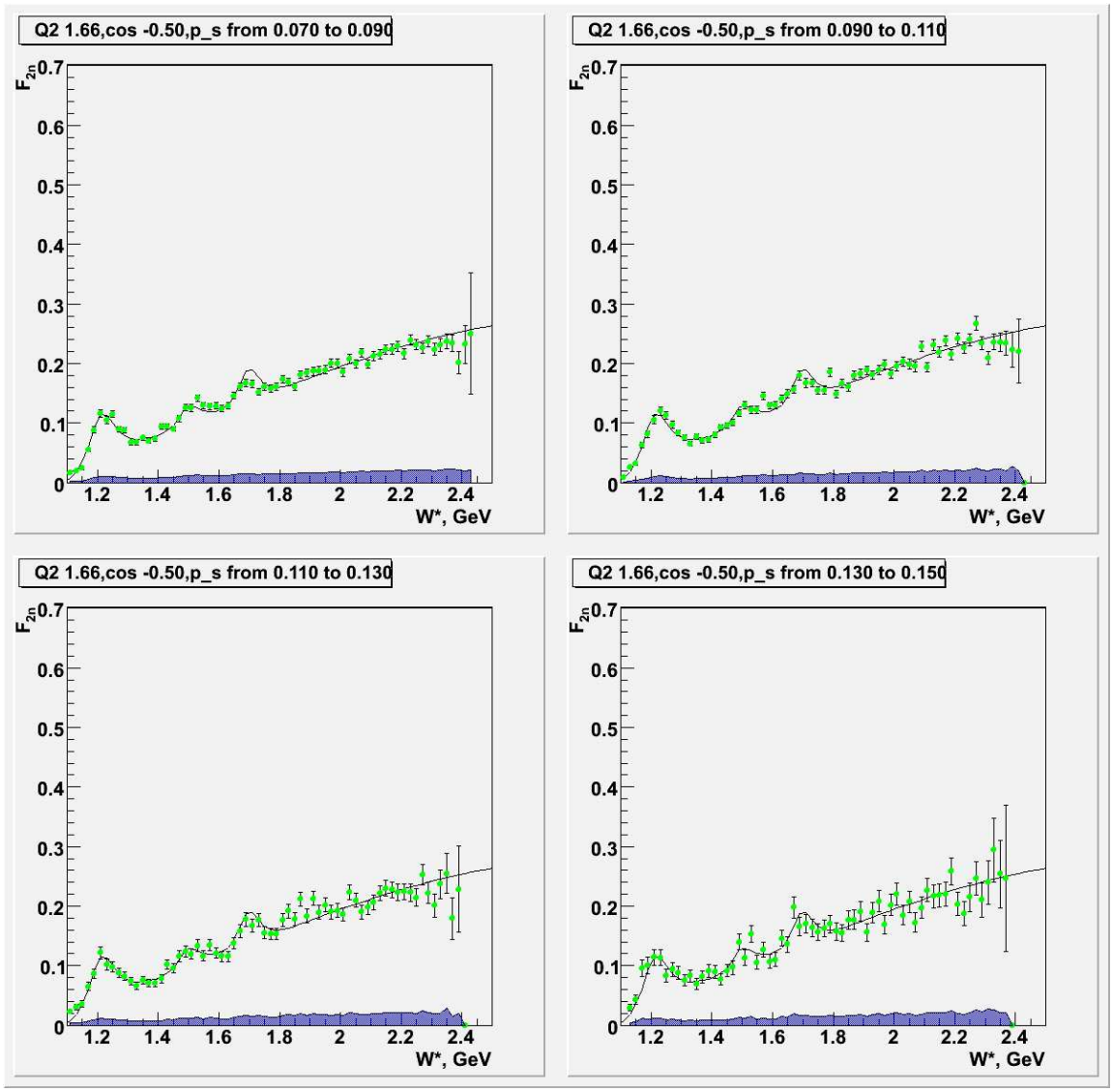

FIG. 127: Effective F_{2n} (green markers) structure function is shown as a function of W^*. Black line is the model F_{2n}. Data are for Q^2 from 1.10 to 2.23 $(\mathrm{GeV}/c)^2$, $\cos\theta_{pq}$ from -0.75 to -0.25. The beam energy is 4.217 GeV. Error bars are statistical only. Systematic errors are shown as a blue band.

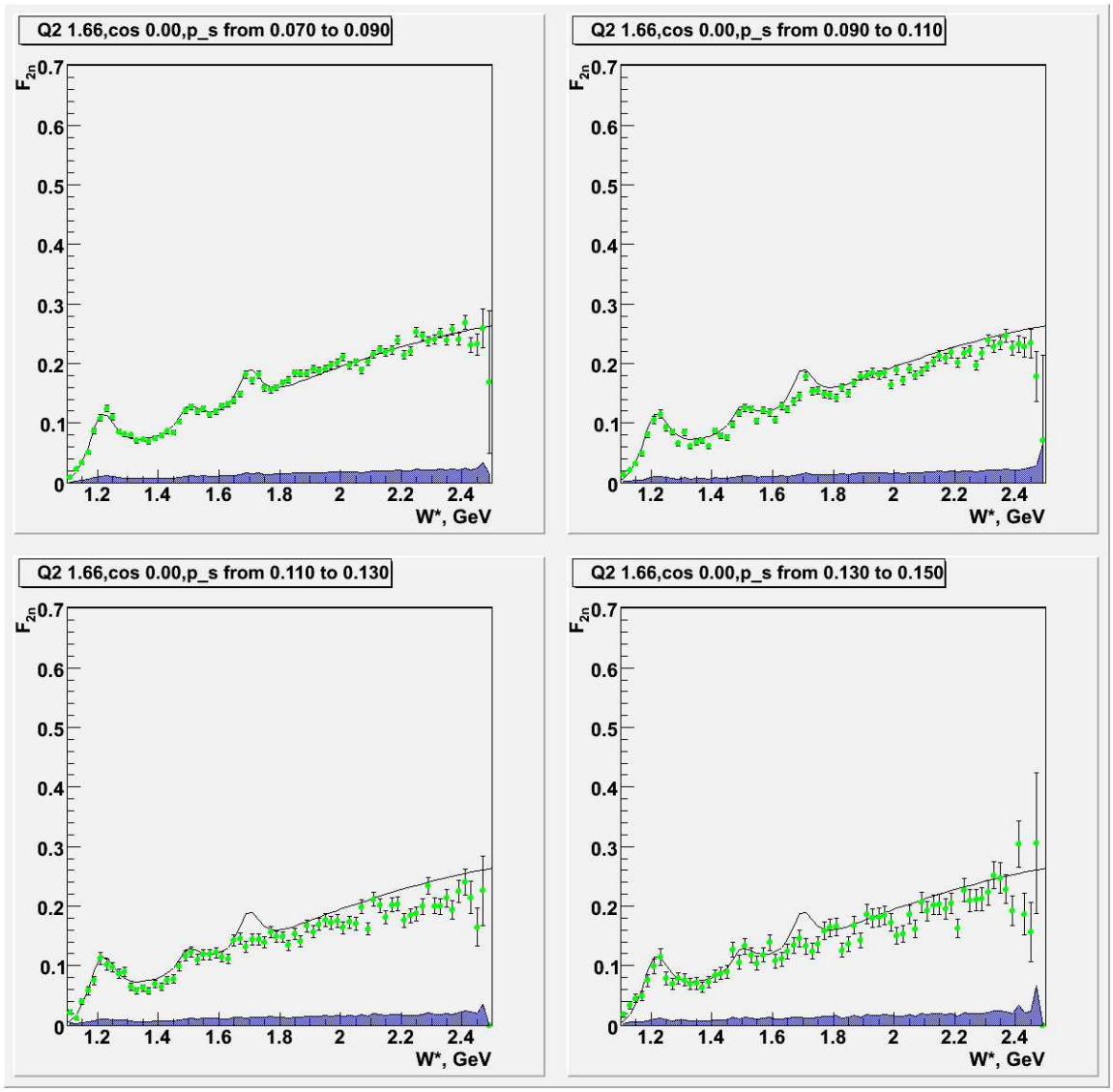

FIG. 128: Effective F_{2n} (green markers) structure function is shown as a function of W^*. Black line is the model F_{2n}. Data are for Q^2 from 1.10 to 2.23 $(\mathrm{GeV}/c)^2$, $\cos\theta_{pq}$ from -0.25 to 0.25. The beam energy is 4.217 GeV. Error bars are statistical only. Systematic errors are shown as a blue band.

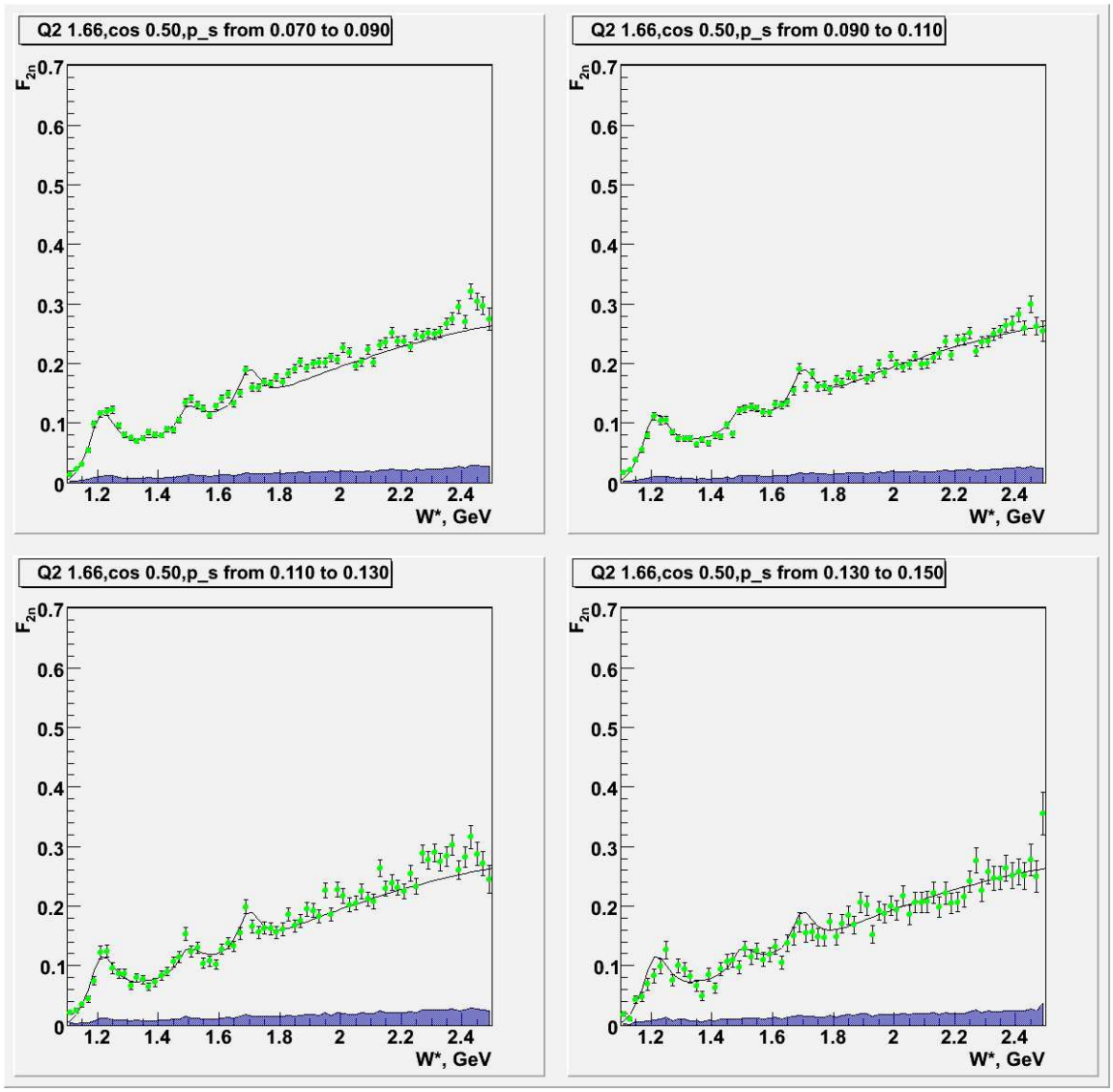

FIG. 129: Effective F_{2n} (green markers) structure function is shown as a function of W^*. Black line is the model F_{2n}. Data are for Q^2 from 1.10 to 2.23 $(\mathrm{GeV}/c)^2$, $\cos\theta_{pq}$ from 0.25 to 0.75. The beam energy is 4.217 GeV. Error bars are statistical only. Systematic errors are shown as a blue band.

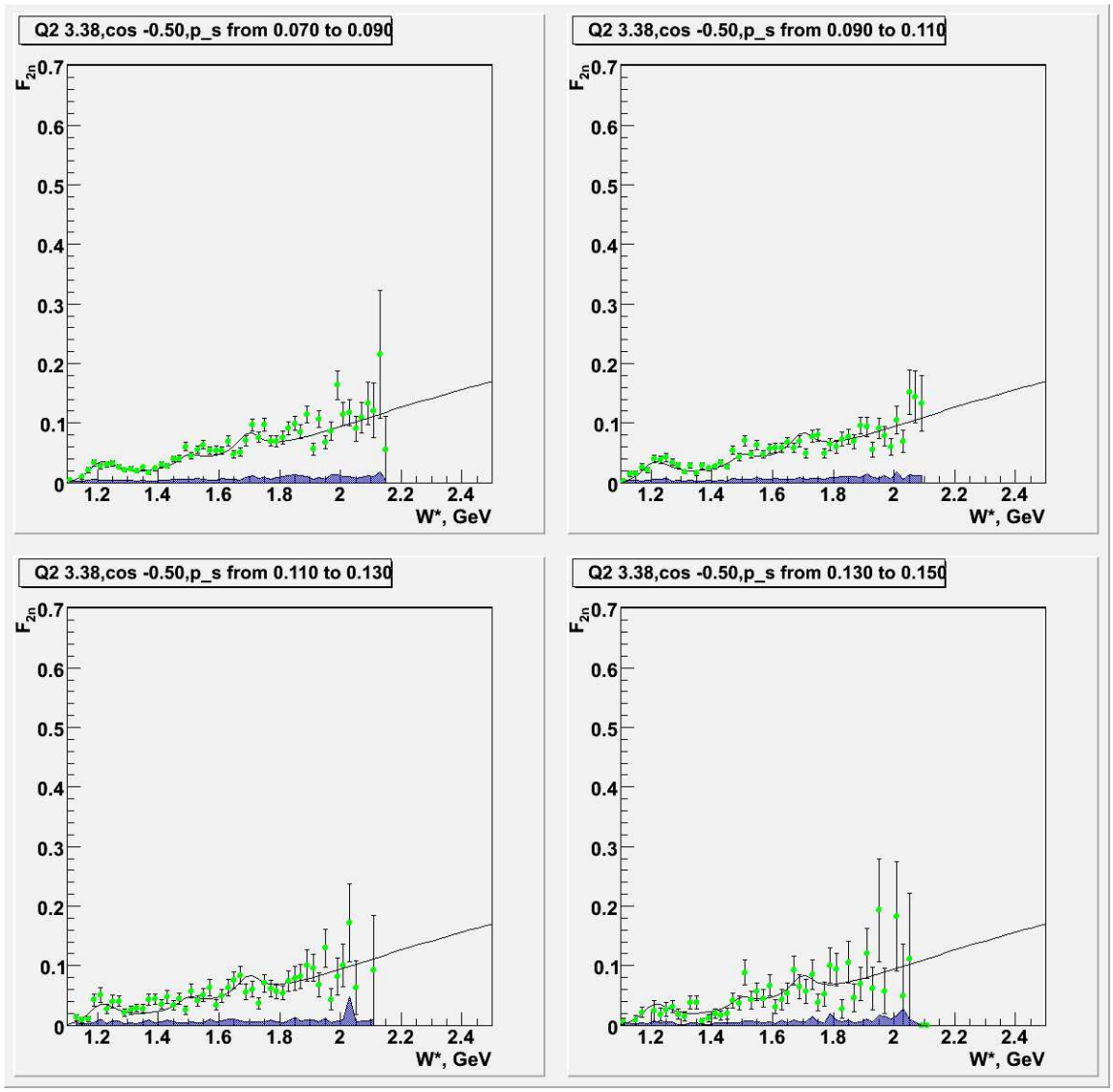

FIG. 130: Effective F_{2n} (green markers) structure function is shown as a function of W^*. Black line is the model F_{2n}. Data are for Q^2 from 2.23 to 4.52 $(\mathrm{GeV}/c)^2$, $\cos\theta_{pq}$ from -0.75 to -0.25. The beam energy is 4.217 GeV. Error bars are statistical only. Systematic errors are shown as a blue band.

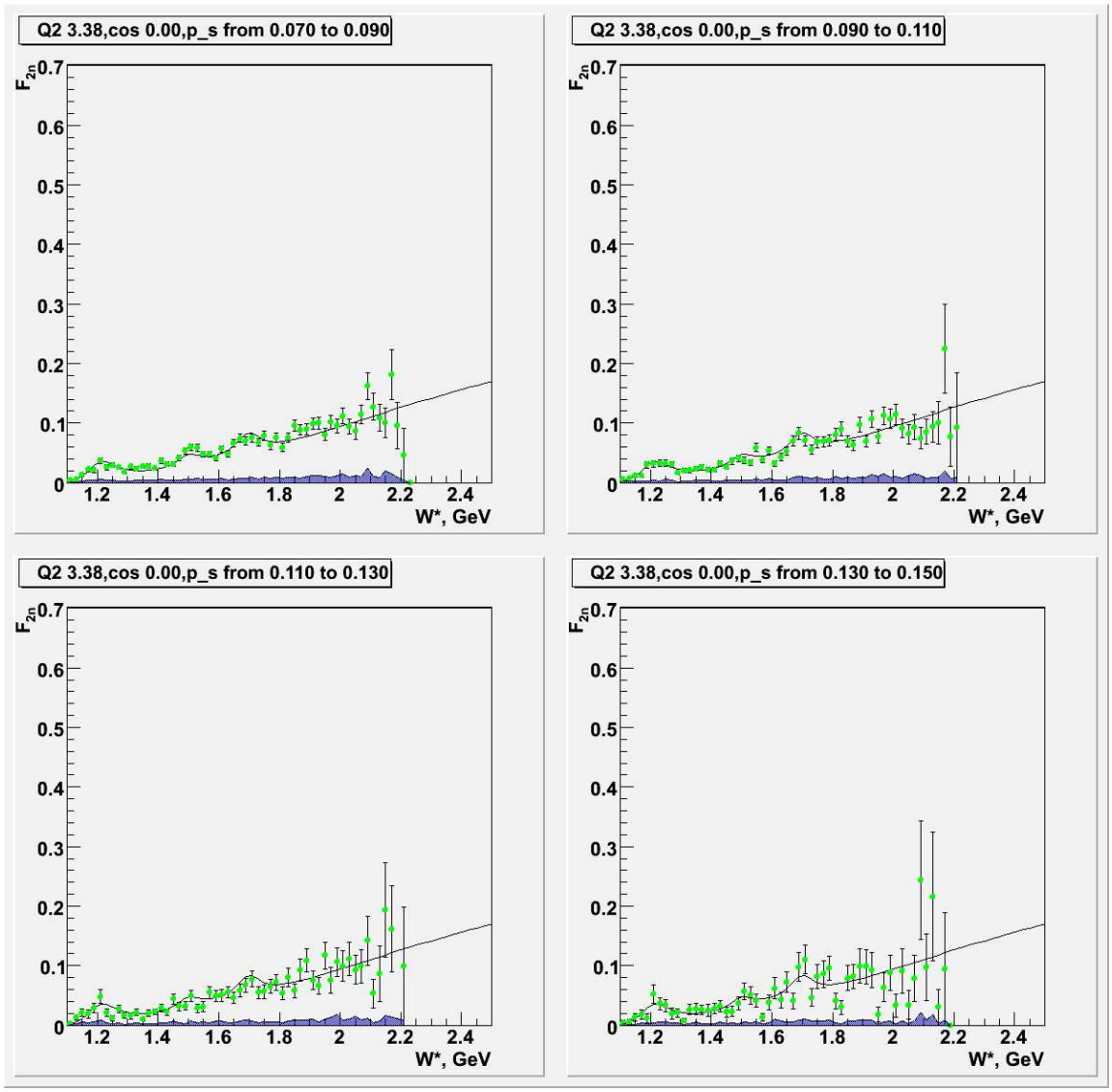

FIG. 131: Effective F_{2n} (green markers) structure function is shown as a function of W^*. Black line is the model F_{2n}. Data are for Q^2 from 2.23 to 4.52 $(\mathrm{GeV}/c)^2$, $\cos\theta_{pq}$ from -0.25 to 0.25. The beam energy is 4.217 GeV. Systematic errors are shown as a blue band.

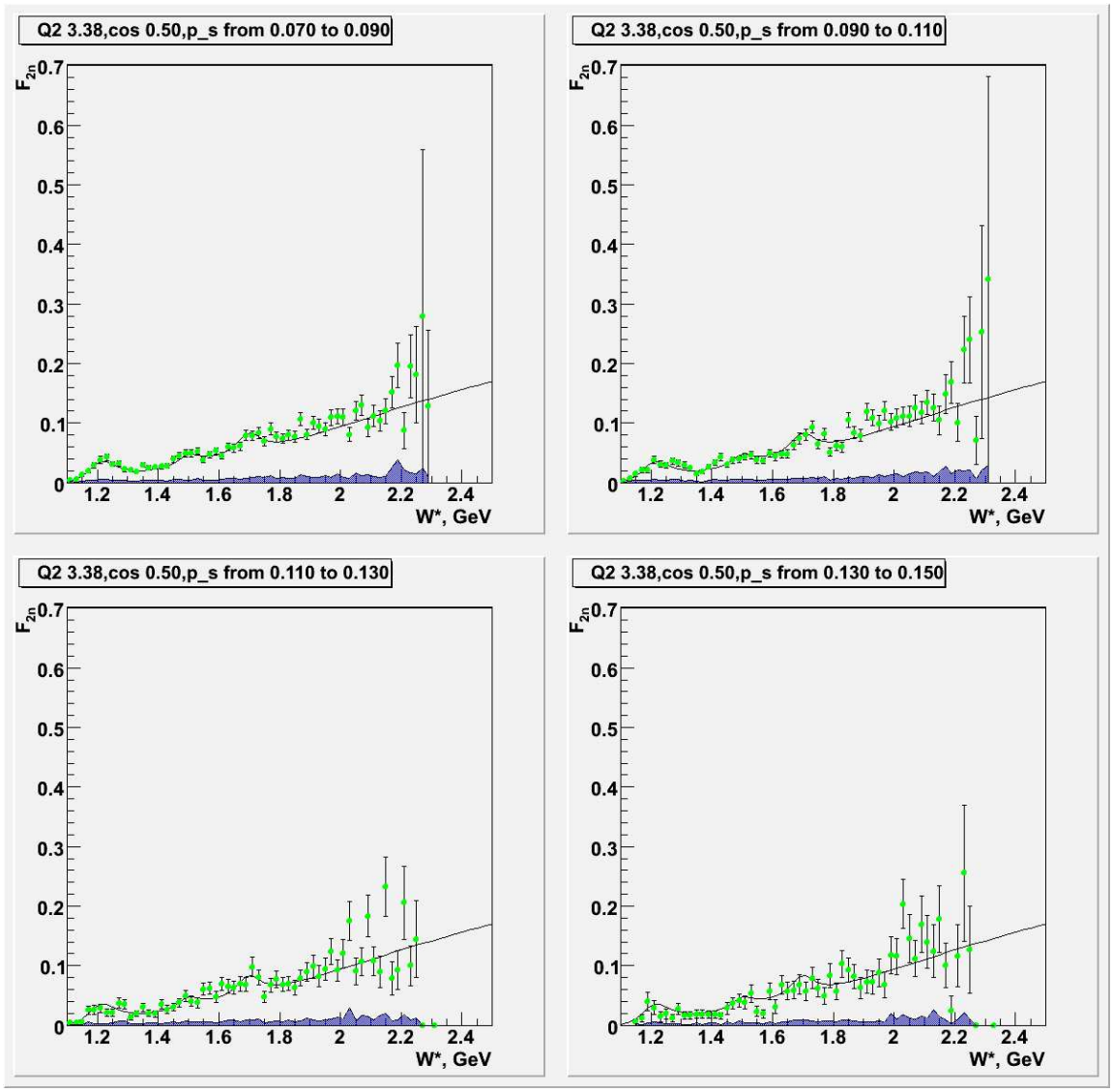

FIG. 132: Effective F_{2n} (green markers) structure function is shown as a function of W^*. Black line is the model F_{2n}. Data are for Q^2 from 2.23 to 4.52 $(\mathrm{GeV}/c)^2$, $\cos\theta_{pq}$ from 0.25 to 0.75. The beam energy is 4.217 GeV. Error bars are statistical only. Systematic errors are shown as a blue band.

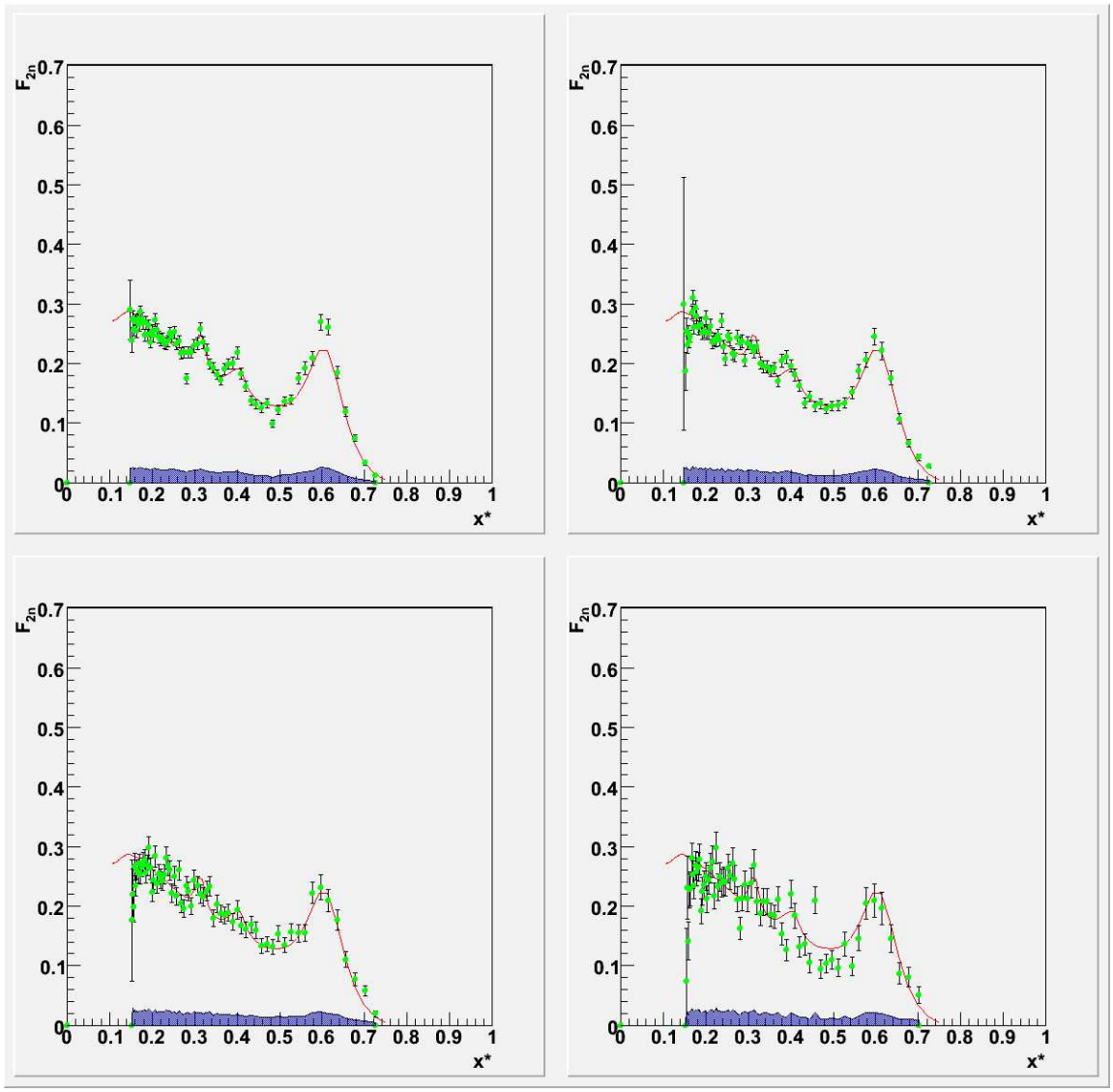

FIG. 133: Effective F_{2n} (green markers) structure function is shown as a function of x^*. Red line is the model F_{2n}. Data are for Q^2 from 0.77 to 1.10 $(\mathrm{GeV}/c)^2$, $\cos\theta_{pq}$ from -0.75 to -0.25. The beam energy is 4.217 GeV. Error bars are statistical only. Systematic errors are shown as a blue band.

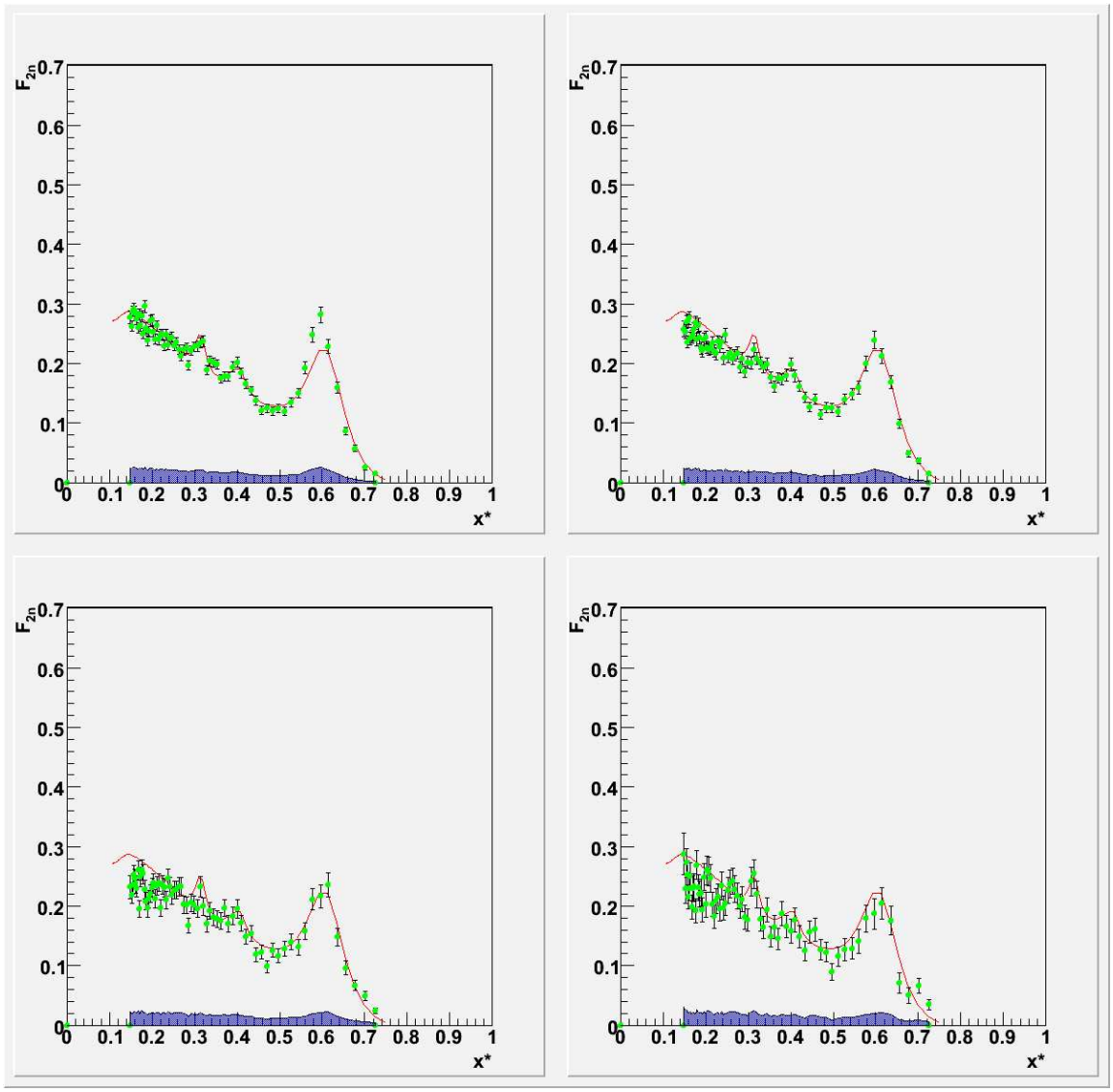

FIG. 134: Effective F_{2n} (green markers) structure function is shown as a function of x^*. Red line is the model F_{2n}. Data are for Q^2 from 0.77 to 1.10 $(\mathrm{GeV}/c)^2$, $\cos\theta_{pq}$ from -0.25 to 0.25. The beam energy is 4.217 GeV. Error bars are statistical only. Systematic errors are shown as a blue band.

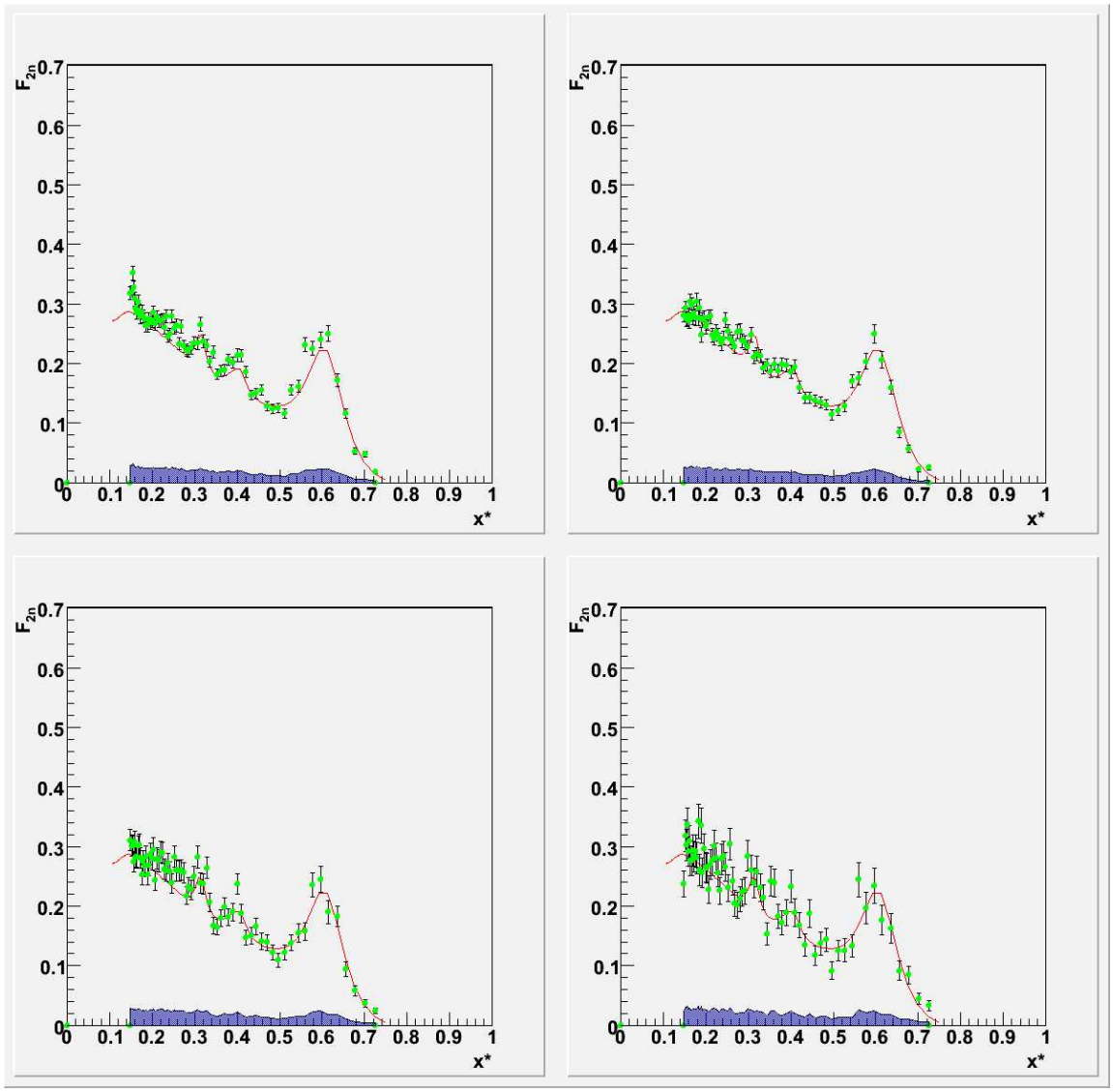

FIG. 135: Effective F_{2n} (green markers) structure function is shown as a function of x^*. Red line is the model F_{2n}. Data are for Q^2 from 0.77 to 1.10 $(\mathrm{GeV}/c)^2$, $\cos\theta_{pq}$ from 0.25 to 0.75. The beam energy is 4.217 GeV. Error bars are statistical only. Systematic errors are shown as a blue band.

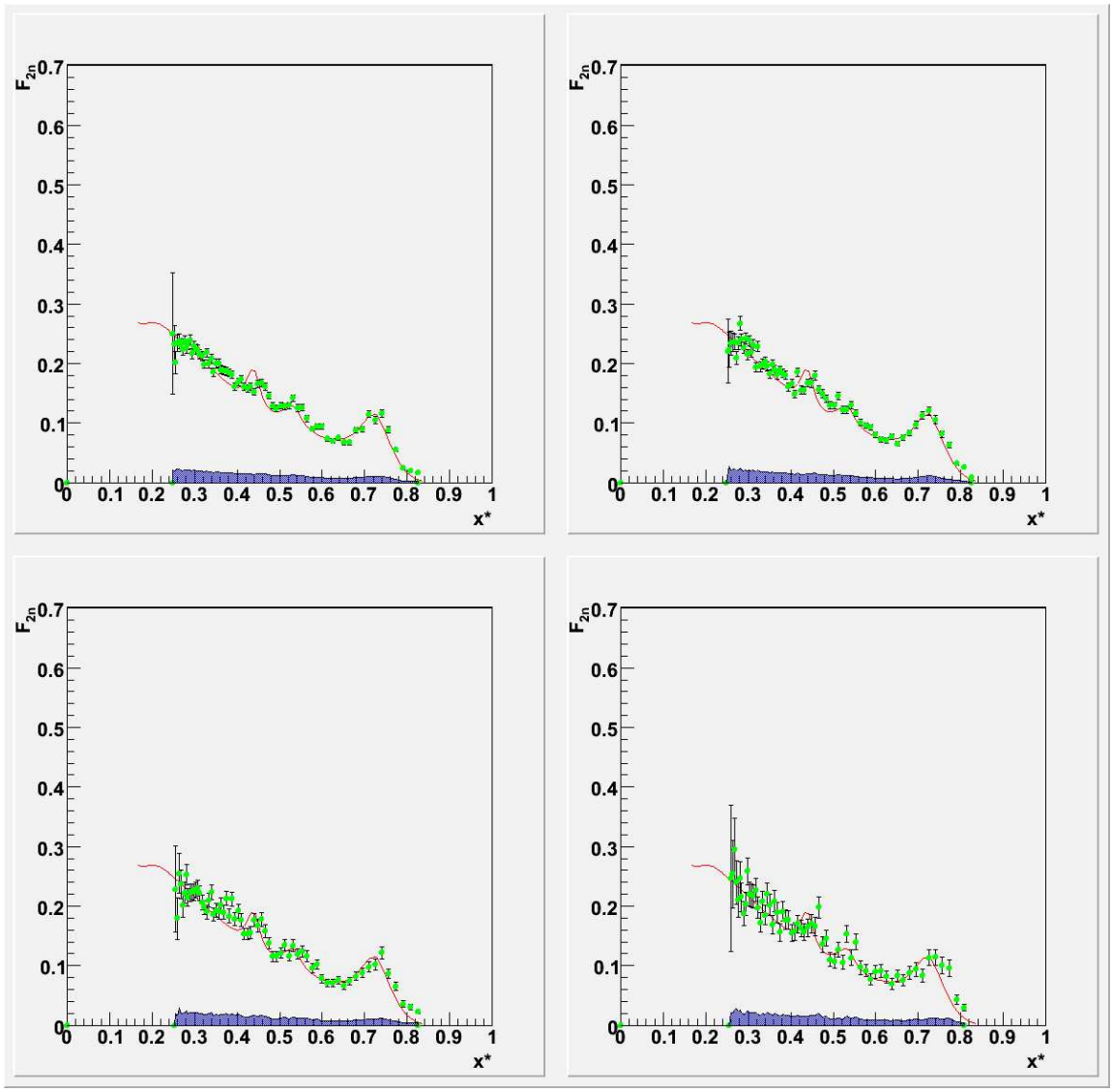

FIG. 136: Effective F_{2n} (green markers) structure function is shown as a function of x^*. Red line is the model F_{2n}. Data are for Q^2 from 1.10 to 2.23 $(\mathrm{GeV}/c)^2$, $\cos\theta_{pq}$ from -0.75 to -0.25. The beam energy is 4.217 GeV. Error bars are statistical only. Systematic errors are shown as a blue band.

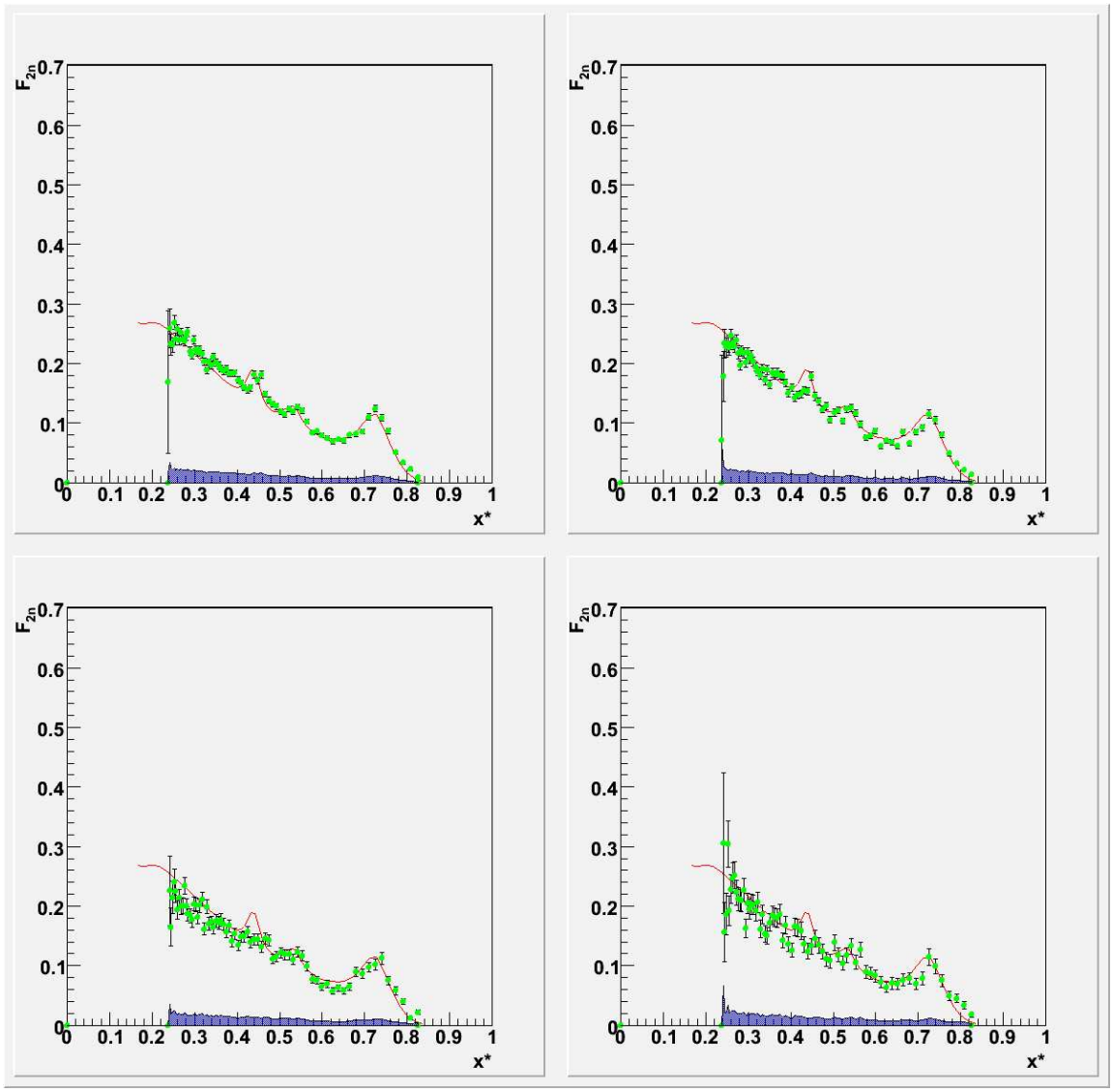

FIG. 137: Effective F_{2n} (green markers) structure function is shown as a function of x^*. Red line is the model F_{2n}. Data are for Q^2 from 1.10 to 2.23 $(\mathrm{GeV}/c)^2$, $\cos\theta_{pq}$ from -0.25 to 0.25. The beam energy is 4.217 GeV. Error bars are statistical only. Systematic errors are shown as a blue band.

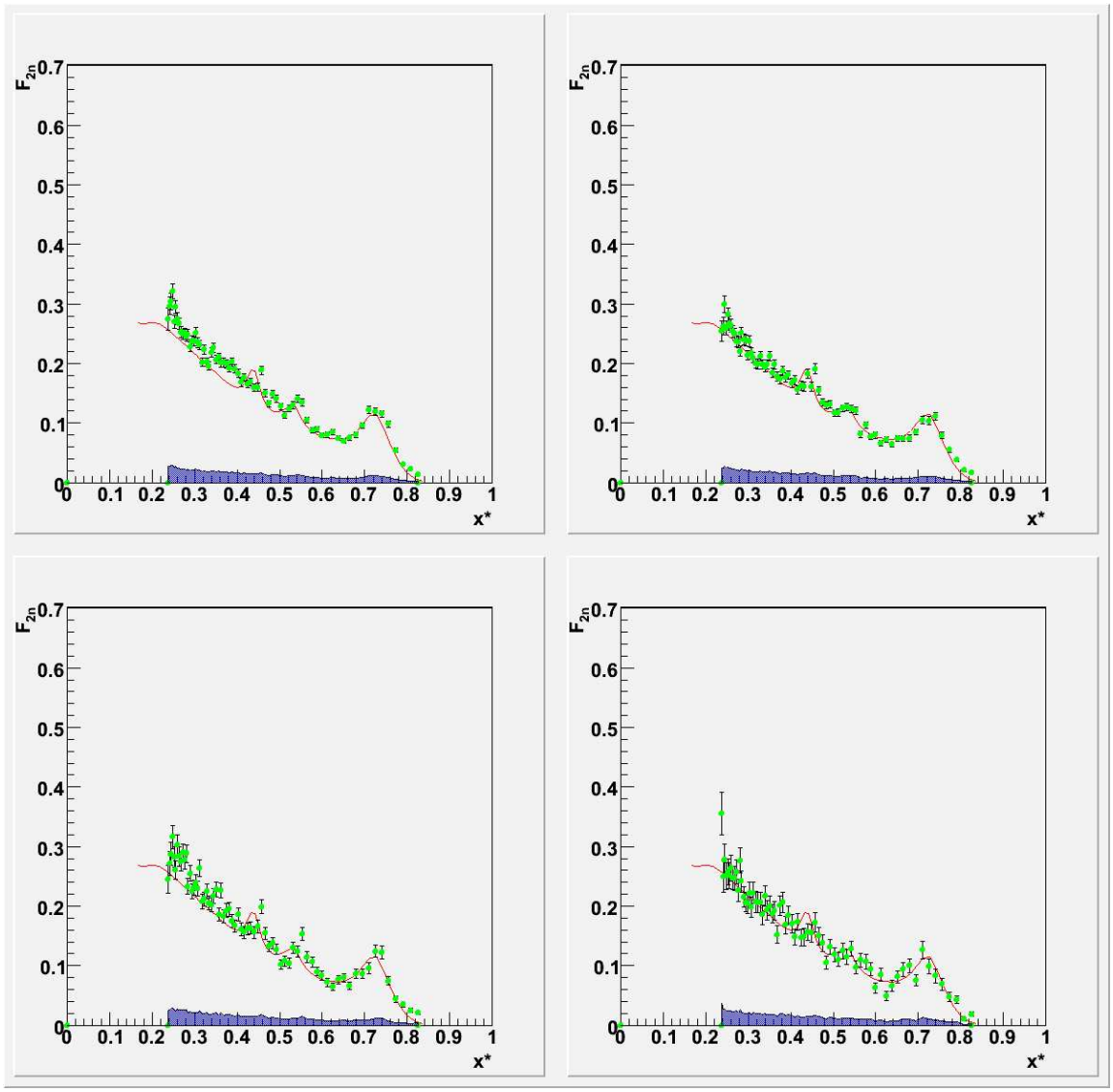

FIG. 138: Effective F_{2n} (green markers) structure function is shown as a function of x^*. Red line is the model F_{2n}. Data are for Q^2 from 1.10 to 2.23 $(\mathrm{GeV}/c)^2$, $\cos\theta_{pq}$ from 0.25 to 0.75. The beam energy is 4.217 GeV. Error bars are statistical only. Systematic errors are shown as a blue band.

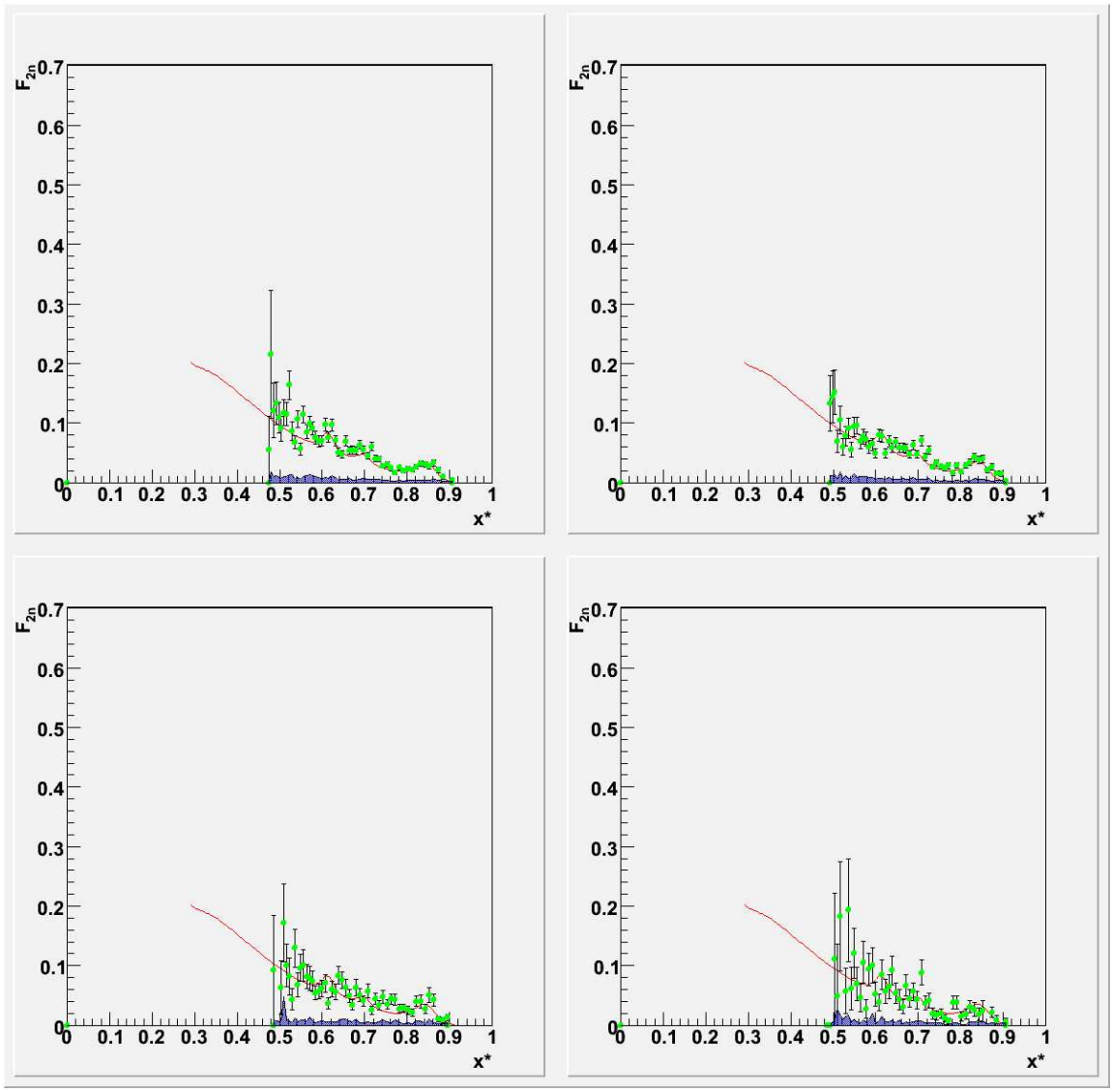

FIG. 139: Effective F_{2n} (green markers) structure function is shown as a function of x^*. Red line is the model F_{2n}. Data are for Q^2 from 2.23 to 4.52 $(\mathrm{GeV}/c)^2$, $\cos\theta_{pq}$ from -0.75 to -0.25. The beam energy is 4.217 GeV. Error bars are statistical only. Systematic errors are shown as a blue band.

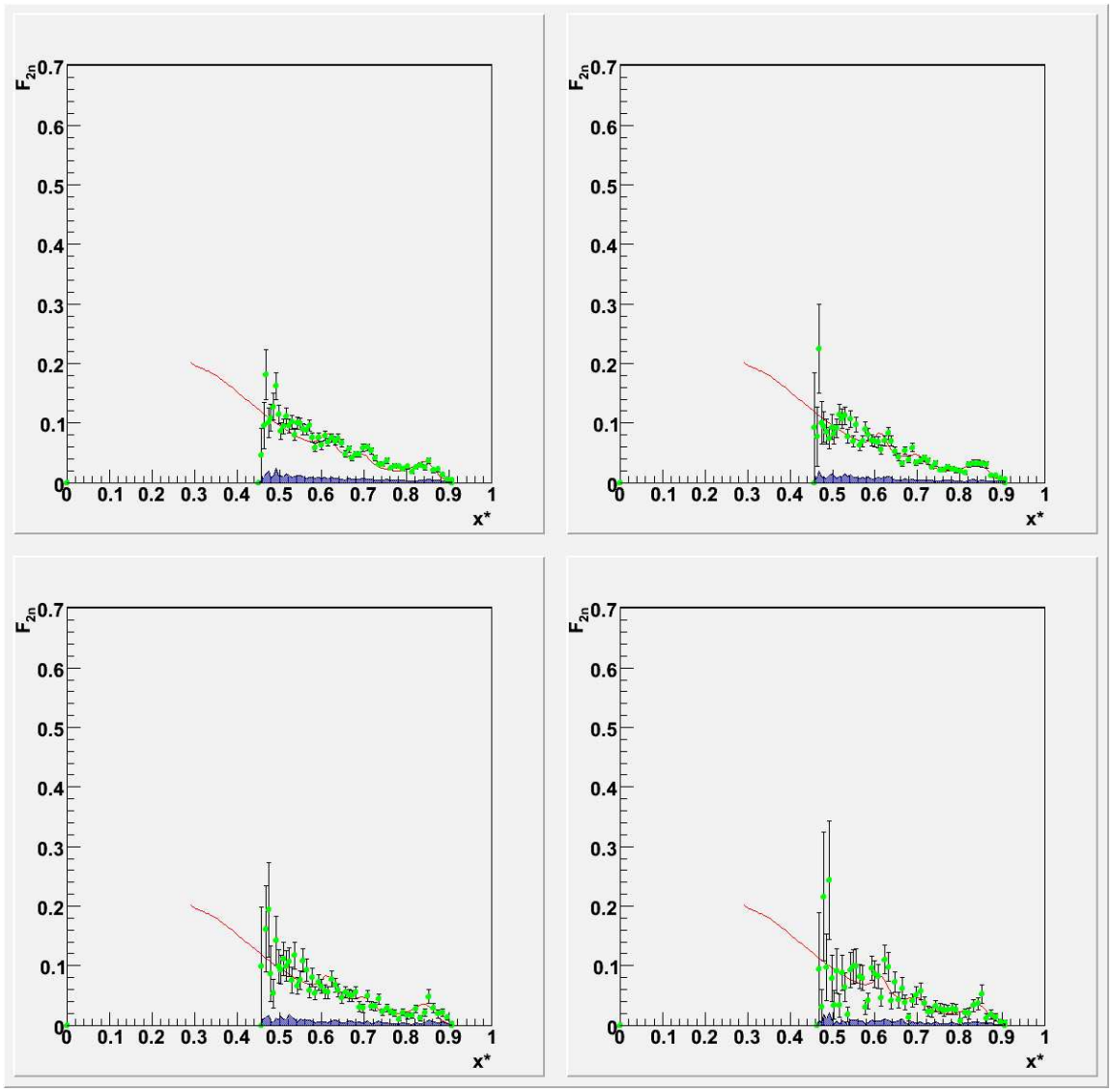

FIG. 140: Effective F_{2n} (green markers) structure function is shown as a function of x^*. Red line is the model F_{2n}. Data are for Q^2 from 2.23 to 4.52 $(\mathrm{GeV}/c)^2$, $\cos\theta_{pq}$ from -0.25 to 0.25. The beam energy is 4.217 GeV. Systematic errors are shown as a blue band.

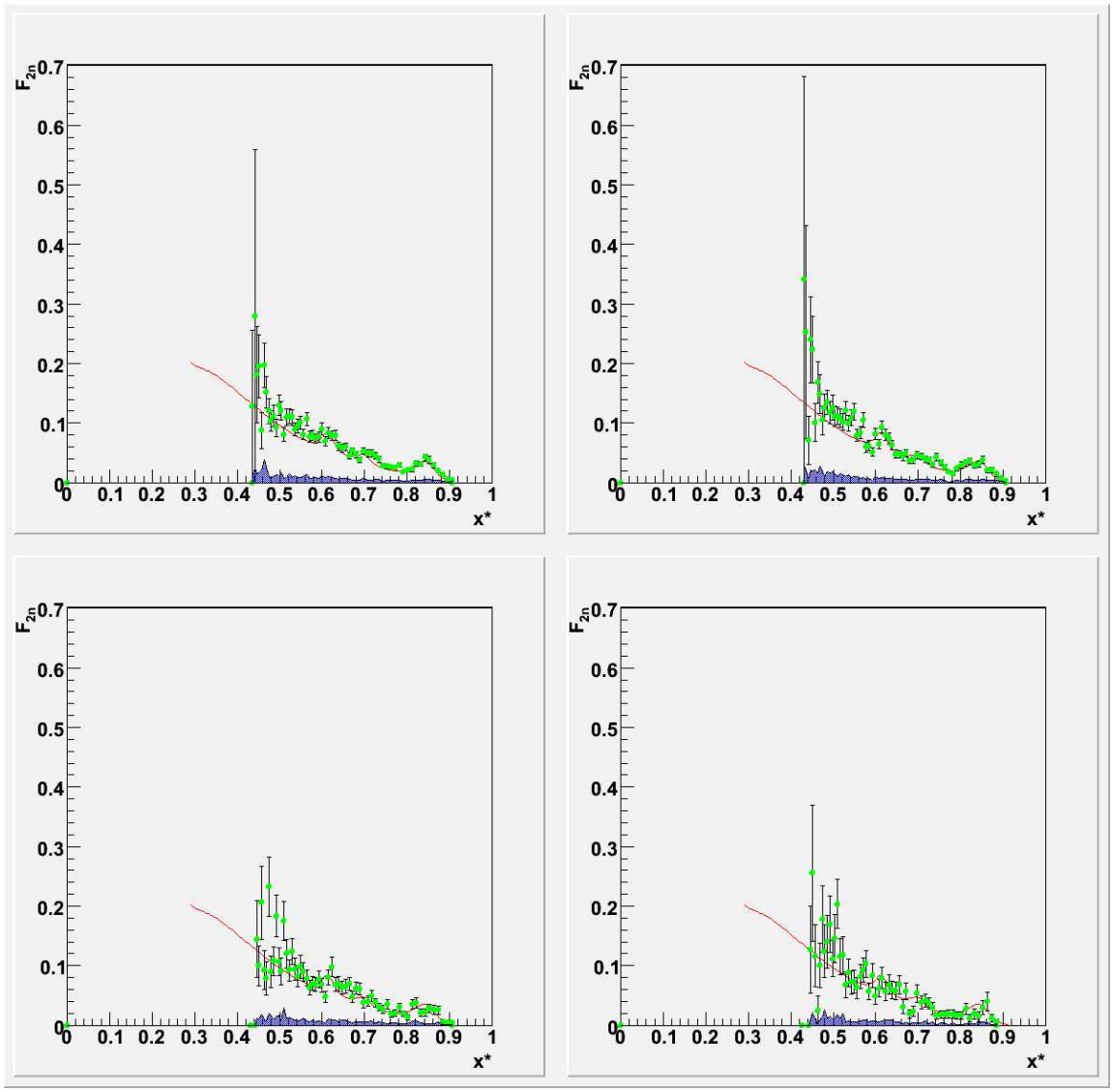

FIG. 141: Effective F_{2n} (green markers) structure function is shown as a function of x^*. Red line is the model F_{2n}. Data are for Q^2 from 2.23 to 4.52 $(\mathrm{GeV}/c)^2$, $\cos\theta_{pq}$ from 0.25 to 0.75. The beam energy is 4.217 GeV. Error bars are statistical only. Systematic errors are shown as a blue band.

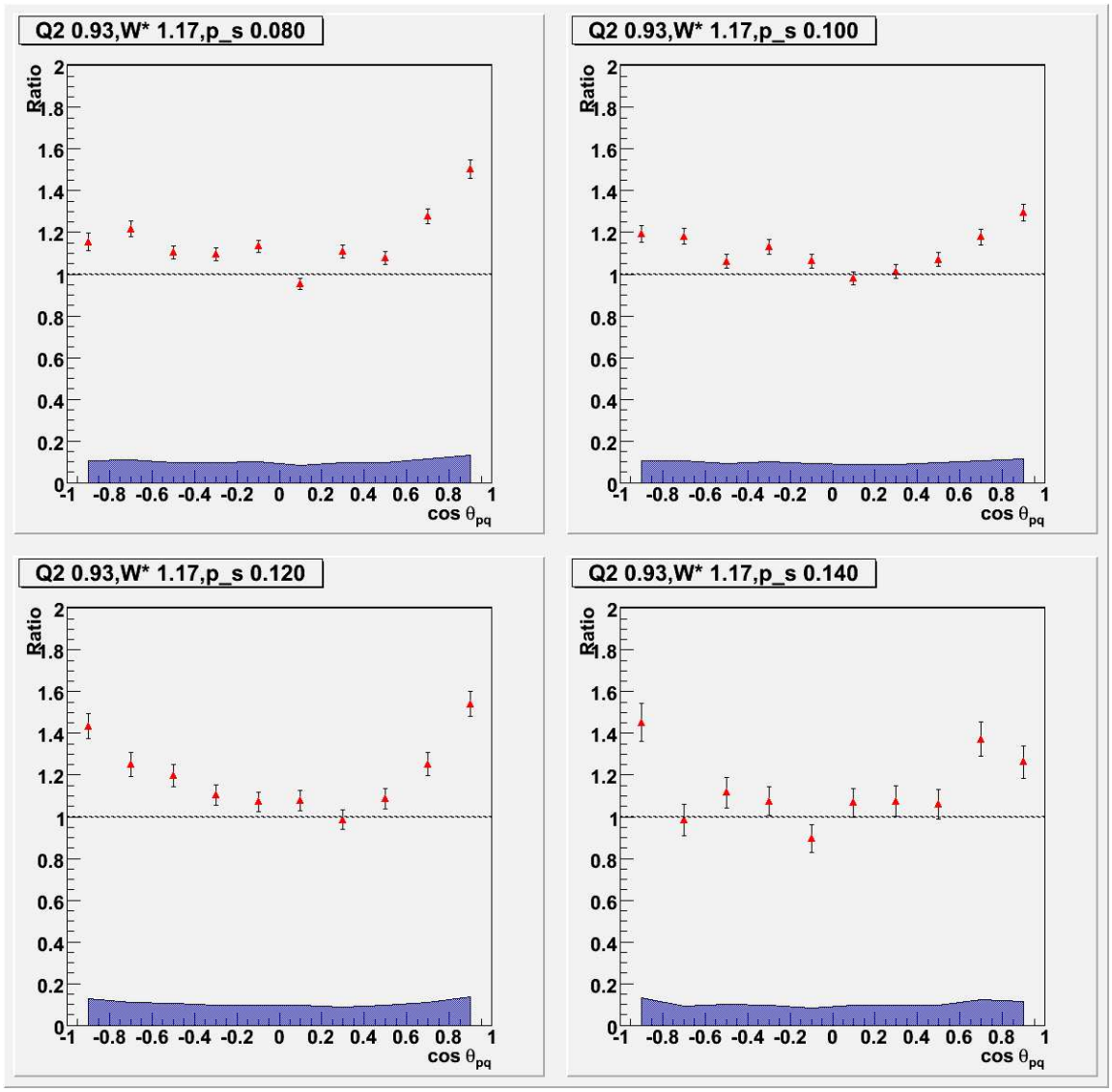

FIG. 142: Ratio of experimental data with subtracted accidental background and elastic tail to the full simulation in the PWIA spectator picture is shown as a function of $\cos\theta_{pq}$. Data are for Q^2 from 0.77 to 1.10 $(\mathrm{GeV}/c)^2$, W^* from 1.00 to 1.35 GeV. The beam energy is 4.217 GeV. Error bars are statistical only. Systematic errors are shown as a blue band.

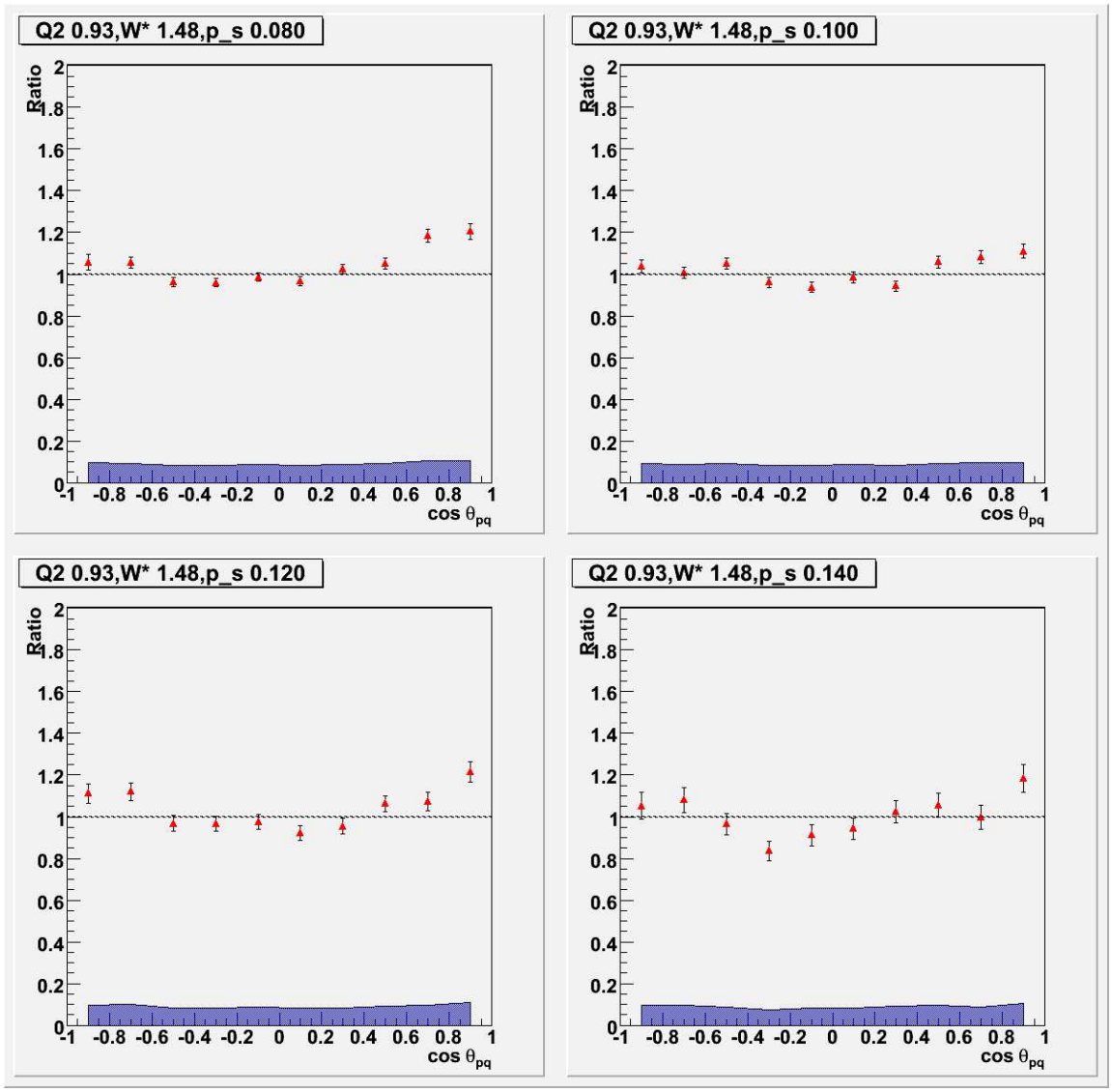

FIG. 143: Ratio of experimental data with subtracted accidental background and elastic tail to the full simulation in the PWIA spectator picture is shown as a function of $\cos\theta_{pq}$. Data are for Q^2 from 0.77 to 1.10 $(\mathrm{GeV}/c)^2$, W^* from 1.35 to 1.60 GeV. The beam energy is 4.217 GeV. Error bars are statistical only. Systematic errors are shown as a blue band.

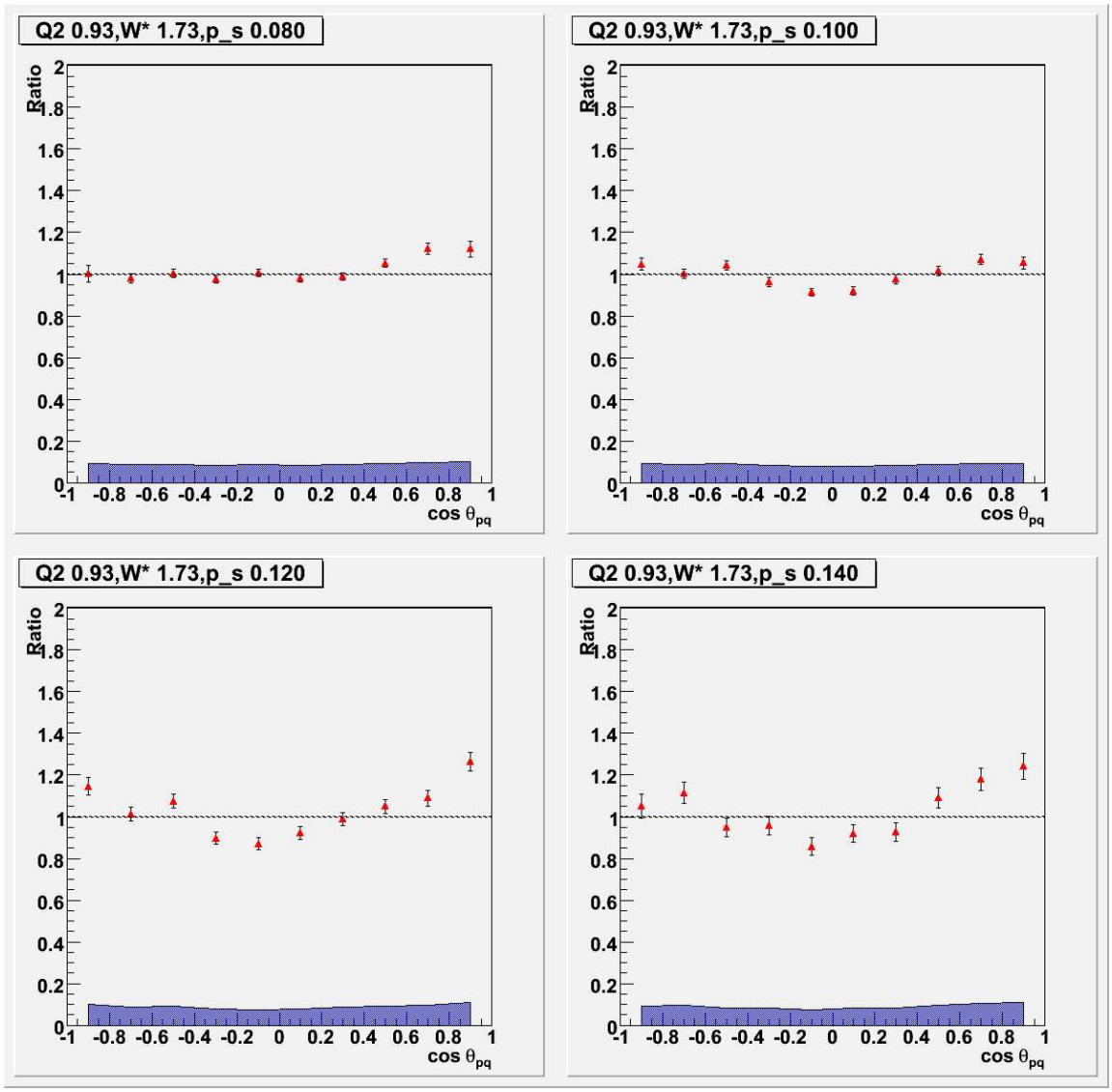

FIG. 144: Ratio of experimental data with subtracted accidental background and elastic tail to the full simulation in the PWIA spectator picture is shown as a function of $\cos\theta_{pq}$. Data are for Q^2 from 0.77 to 1.10 $(\mathrm{GeV}/c)^2$, W^* from 1.60 to 1.85 GeV. The beam energy is 4.217 GeV. Error bars are statistical only. Systematic errors are shown as a blue band.

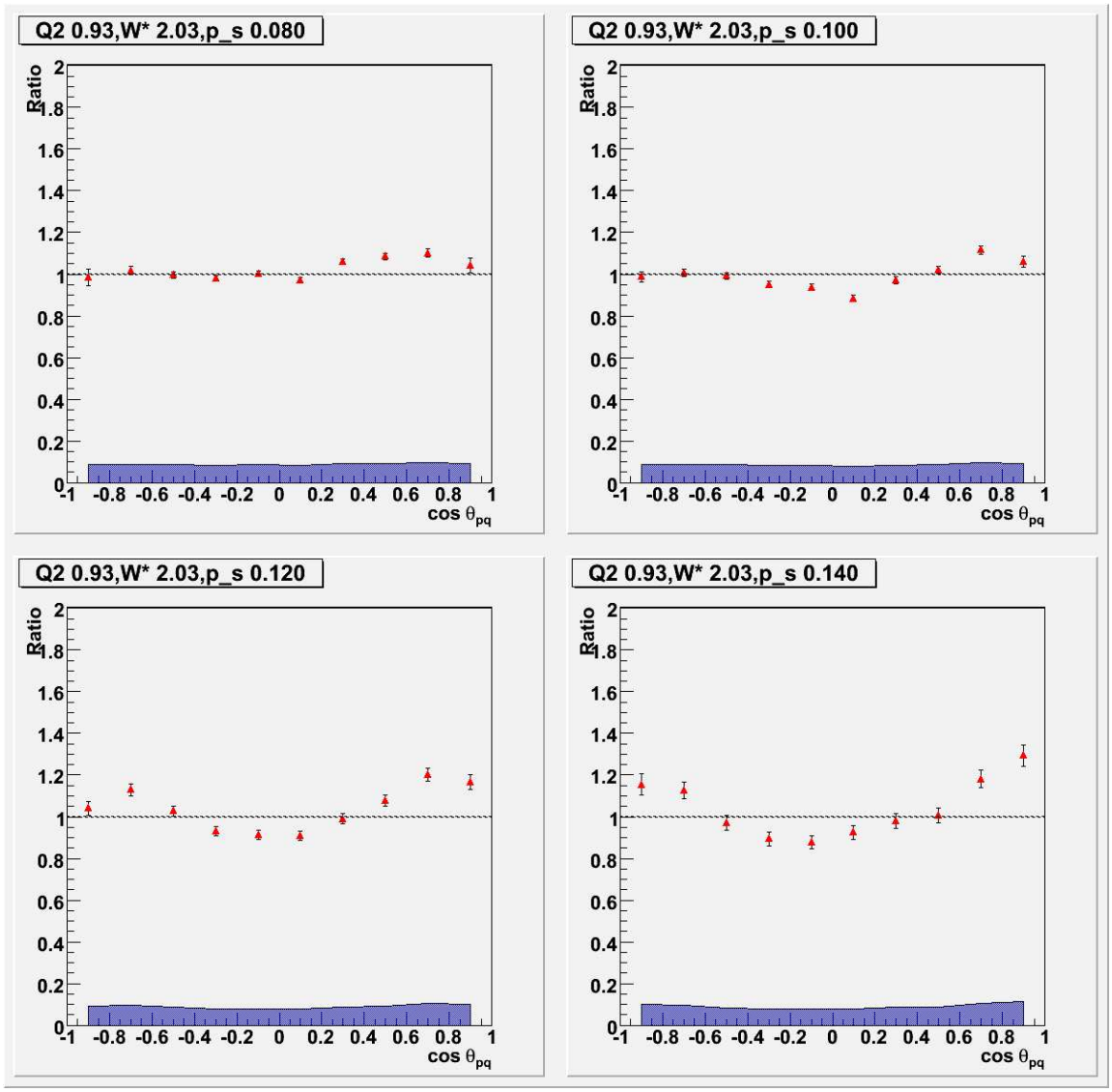

FIG. 145: Ratio of experimental data with subtracted accidental background and elastic tail to the full simulation in the PWIA spectator picture is shown as a function of $\cos\theta_{pq}$. Data are for Q^2 from 0.77 to 1.10 $(\mathrm{GeV}/c)^2$, W^* from 1.85 to 2.20 GeV. The beam energy is 4.217 GeV. Error bars are statistical only. Systematic errors are shown as a blue band.

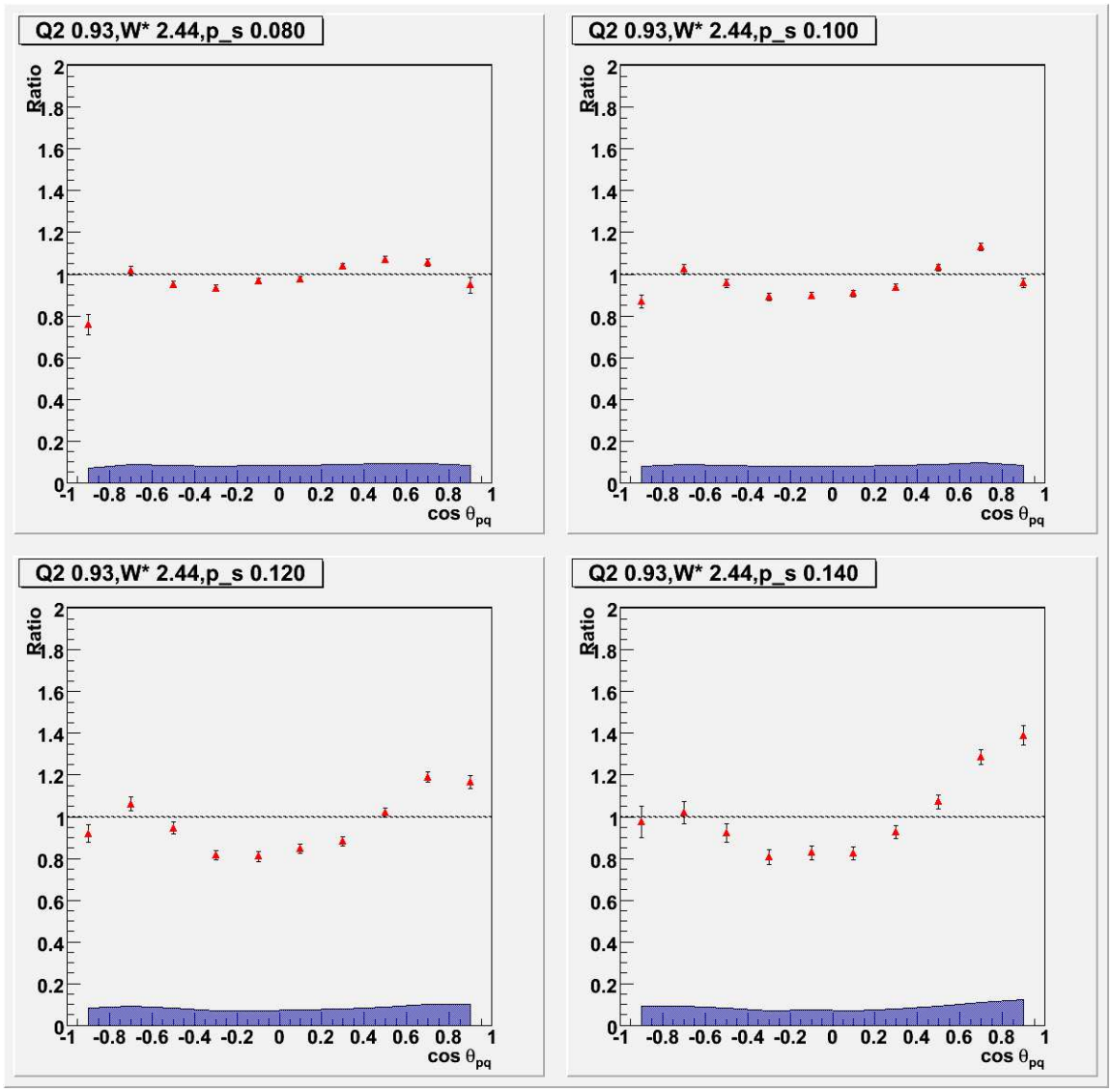

FIG. 146: Ratio of experimental data with subtracted accidental background and elastic tail to the full simulation in the PWIA spectator picture is shown as a function of $\cos\theta_{pq}$. Data are for Q^2 from 0.77 to 1.10 $(\mathrm{GeV}/c)^2$, W^* from 2.20 to 2.68 GeV. The beam energy is 4.217 GeV. Error bars are statistical only. Systematic errors are shown as a blue band.

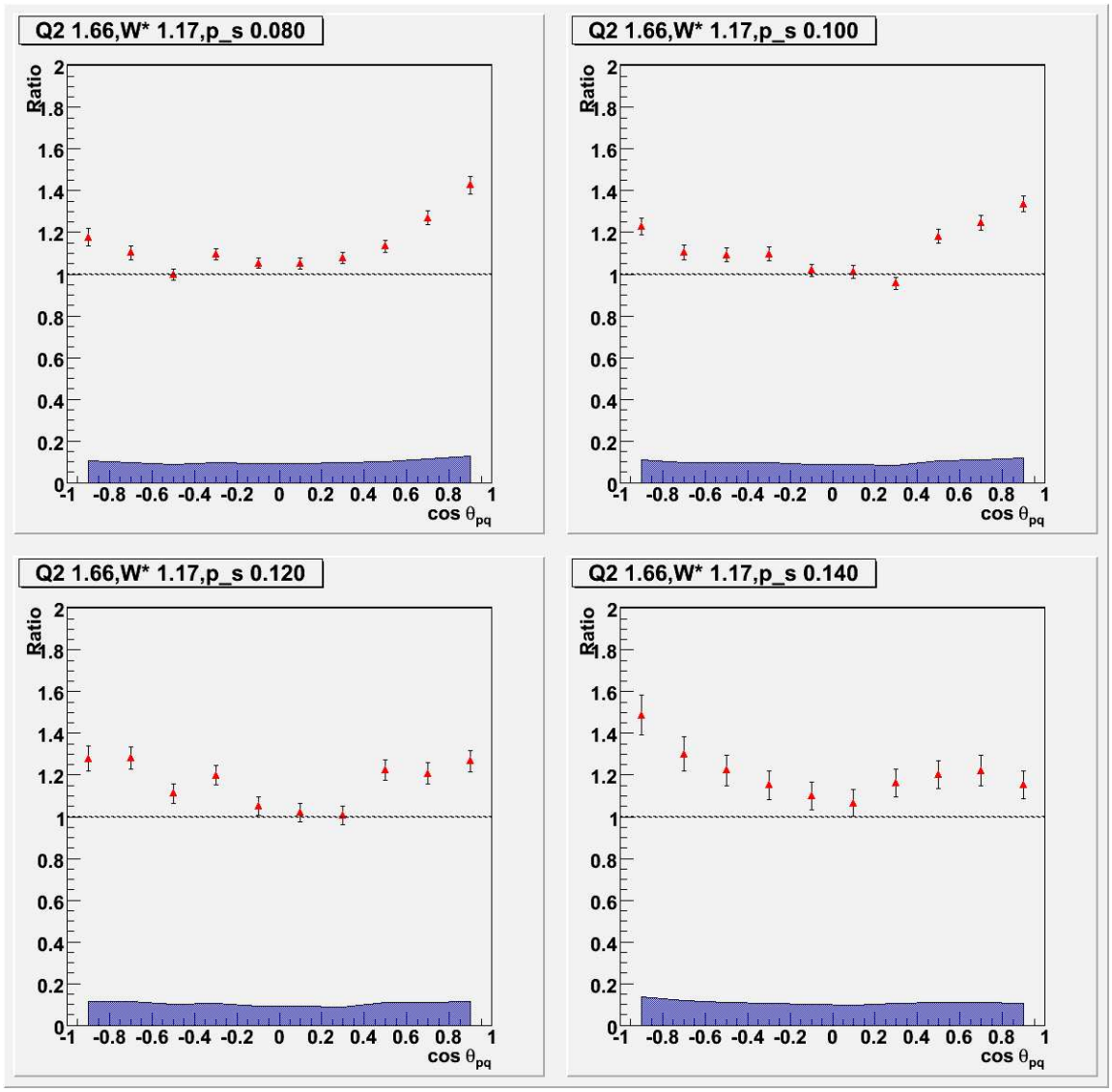

FIG. 147: Ratio of experimental data with subtracted accidental background and elastic tail to the full simulation in the PWIA spectator picture is shown as a function of $\cos\theta_{pq}$. Data are for Q^2 from 1.10 to 2.23 $(\mathrm{GeV}/c)^2$, W^* from 1.00 to 1.35 GeV. The beam energy is 4.217 GeV. Error bars are statistical only. Systematic errors are shown as a blue band.

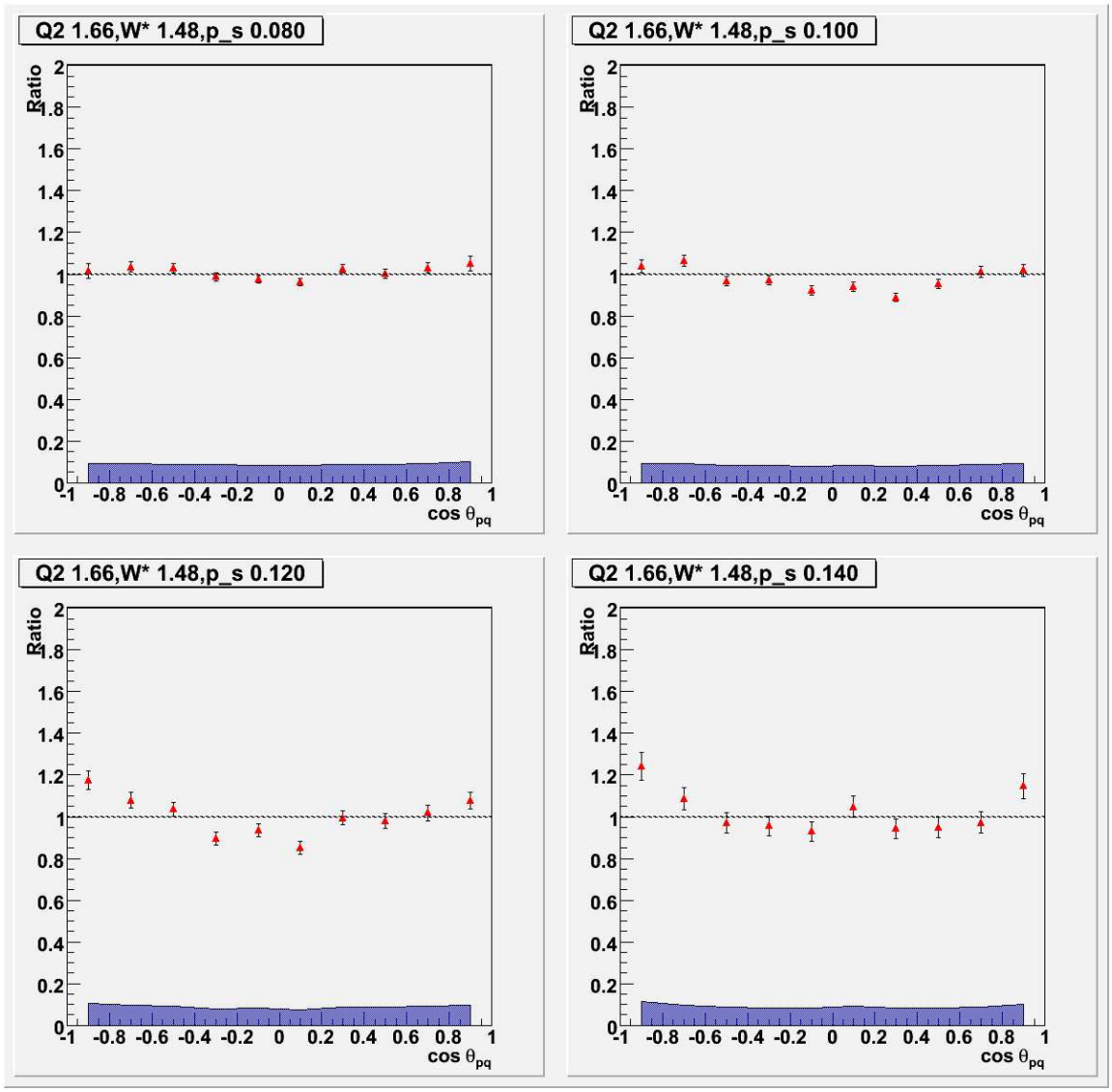

FIG. 148: Ratio of experimental data with subtracted accidental background and elastic tail to the full simulation in the PWIA spectator picture is shown as a function of $\cos\theta_{pq}$. Data are for Q^2 from 1.10 to 2.23 $(\mathrm{GeV}/c)^2$, W^* from 1.35 to 1.60 GeV. The beam energy is 4.217 GeV. Error bars are statistical only. Systematic errors are shown as a blue band.

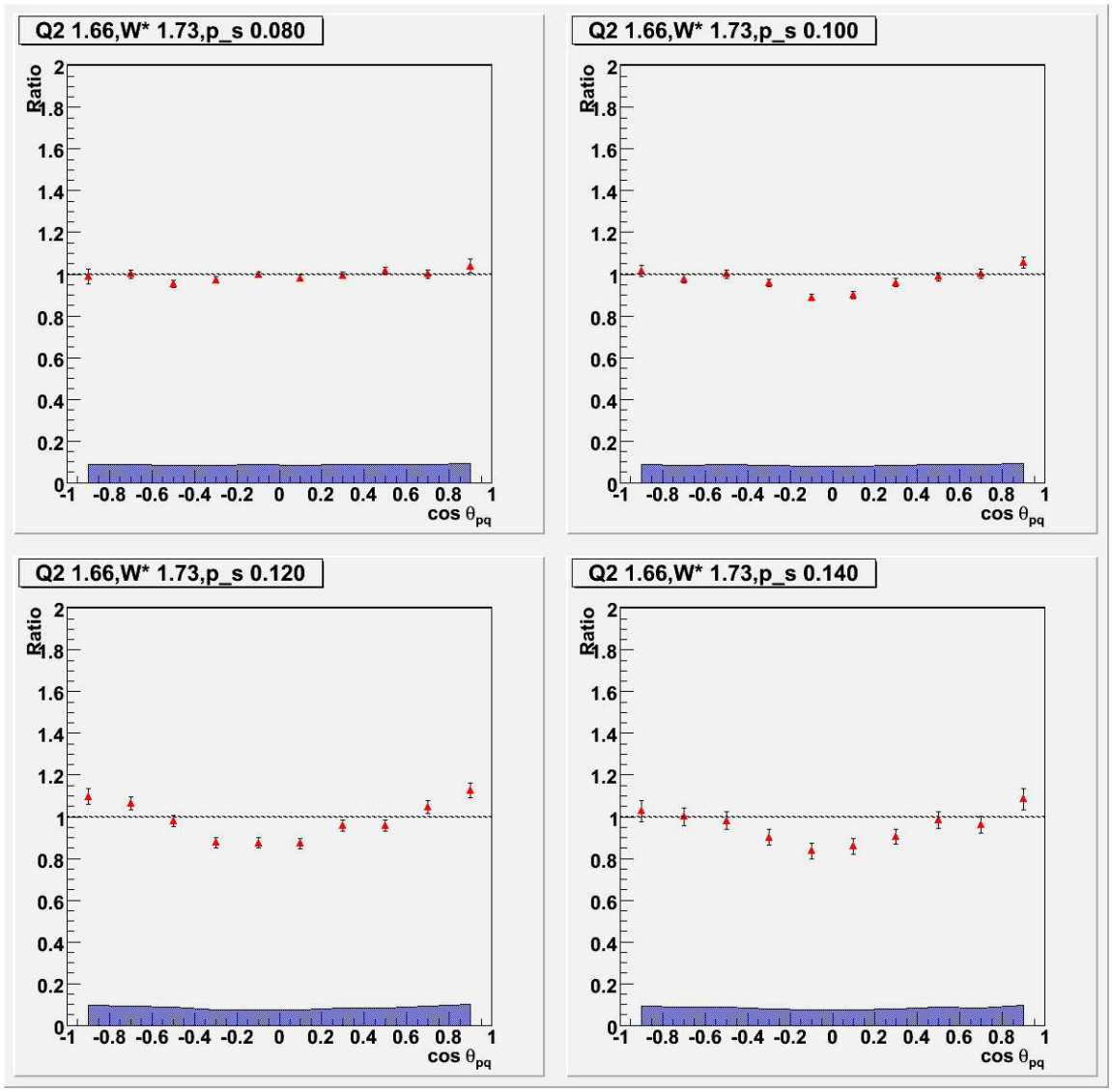

FIG. 149: Ratio of experimental data with subtracted accidental background and elastic tail to the full simulation in the PWIA spectator picture is shown as a function of $\cos\theta_{pq}$. Data are for Q^2 from 1.10 to 2.23 $(\mathrm{GeV}/c)^2$, W^* from 1.60 to 1.85 GeV. The beam energy is 4.217 GeV. Error bars are statistical only. Error bars are statistical only. Systematic errors are shown as a blue band.

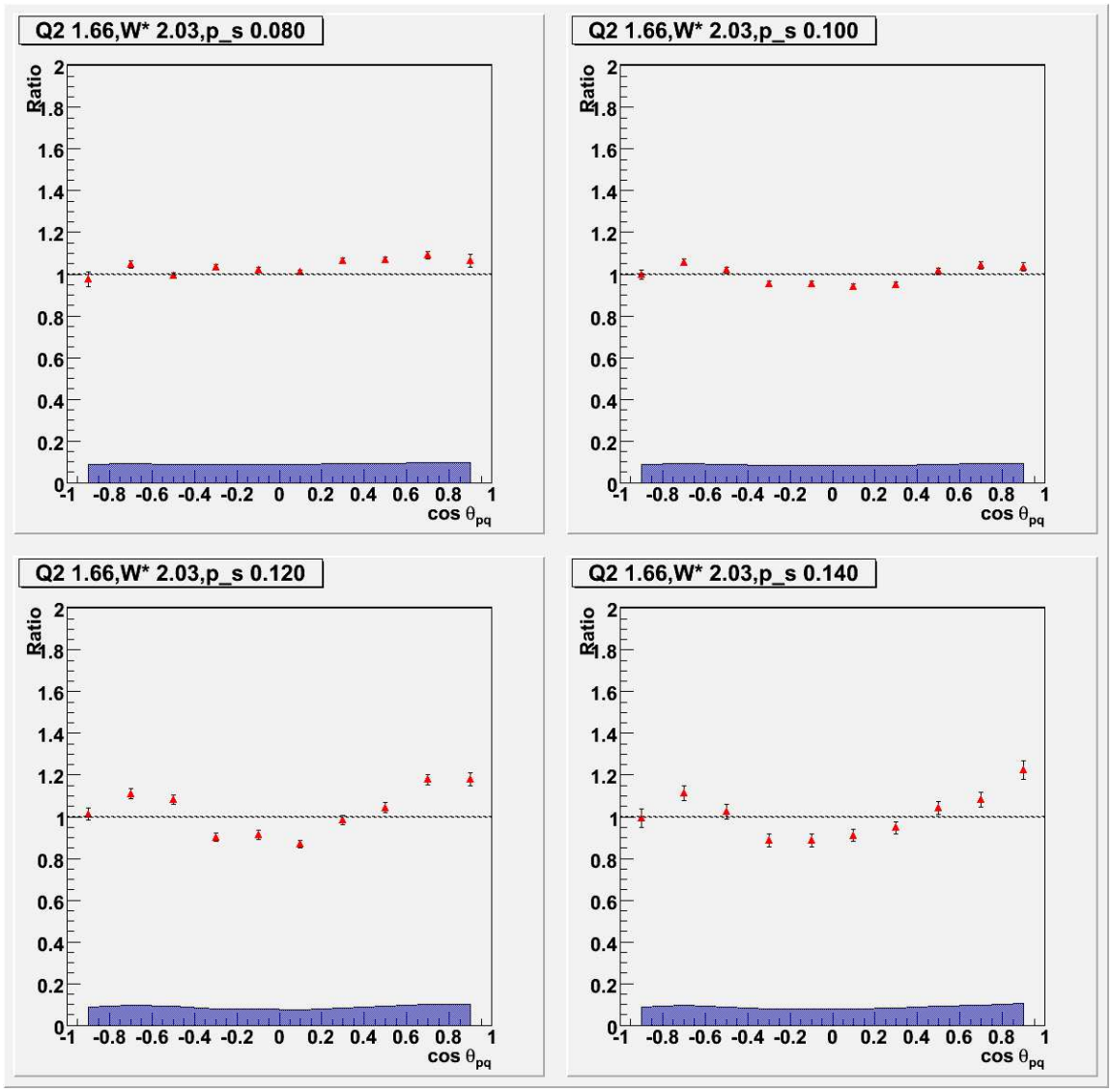

FIG. 150: Ratio of experimental data with subtracted accidental background and elastic tail to the full simulation in the PWIA spectator picture is shown as a function of $\cos\theta_{pq}$. Data are for Q^2 from 1.10 to 2.23 $(\mathrm{GeV}/c)^2$, W^* from 1.85 to 2.20 GeV. The beam energy is 4.217 GeV. Error bars are statistical only. Systematic errors are shown as a blue band.

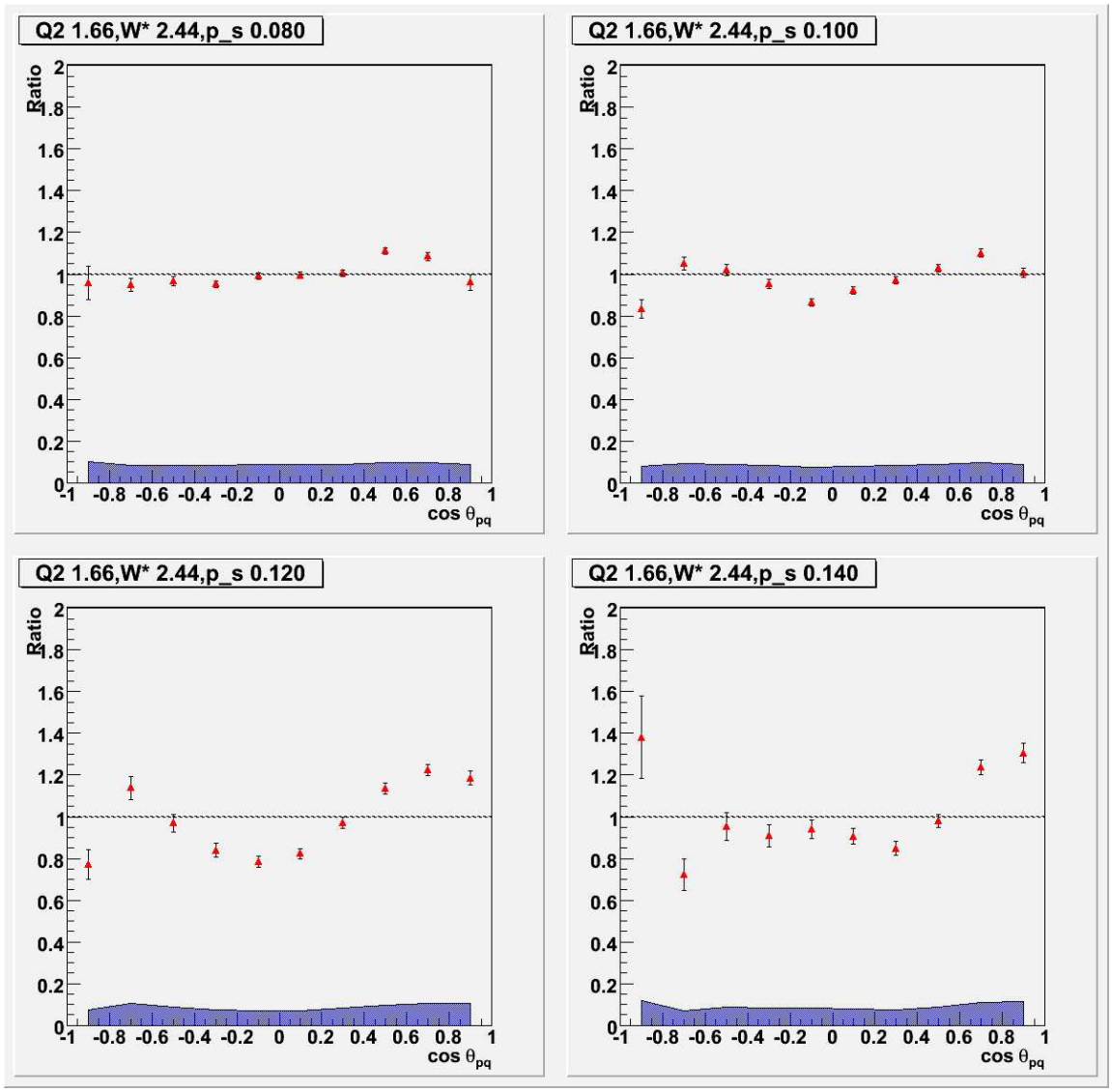

FIG. 151: Ratio of experimental data with subtracted accidental background and elastic tail to the full simulation in the PWIA spectator picture is shown as a function of $\cos\theta_{pq}$. Data are for Q^2 from 1.10 to 2.23 $(\mathrm{GeV}/c)^2$, W^* from 2.20 to 2.68 GeV. The beam energy is 4.217 GeV. Error bars are statistical only. Systematic errors are shown as a blue band.

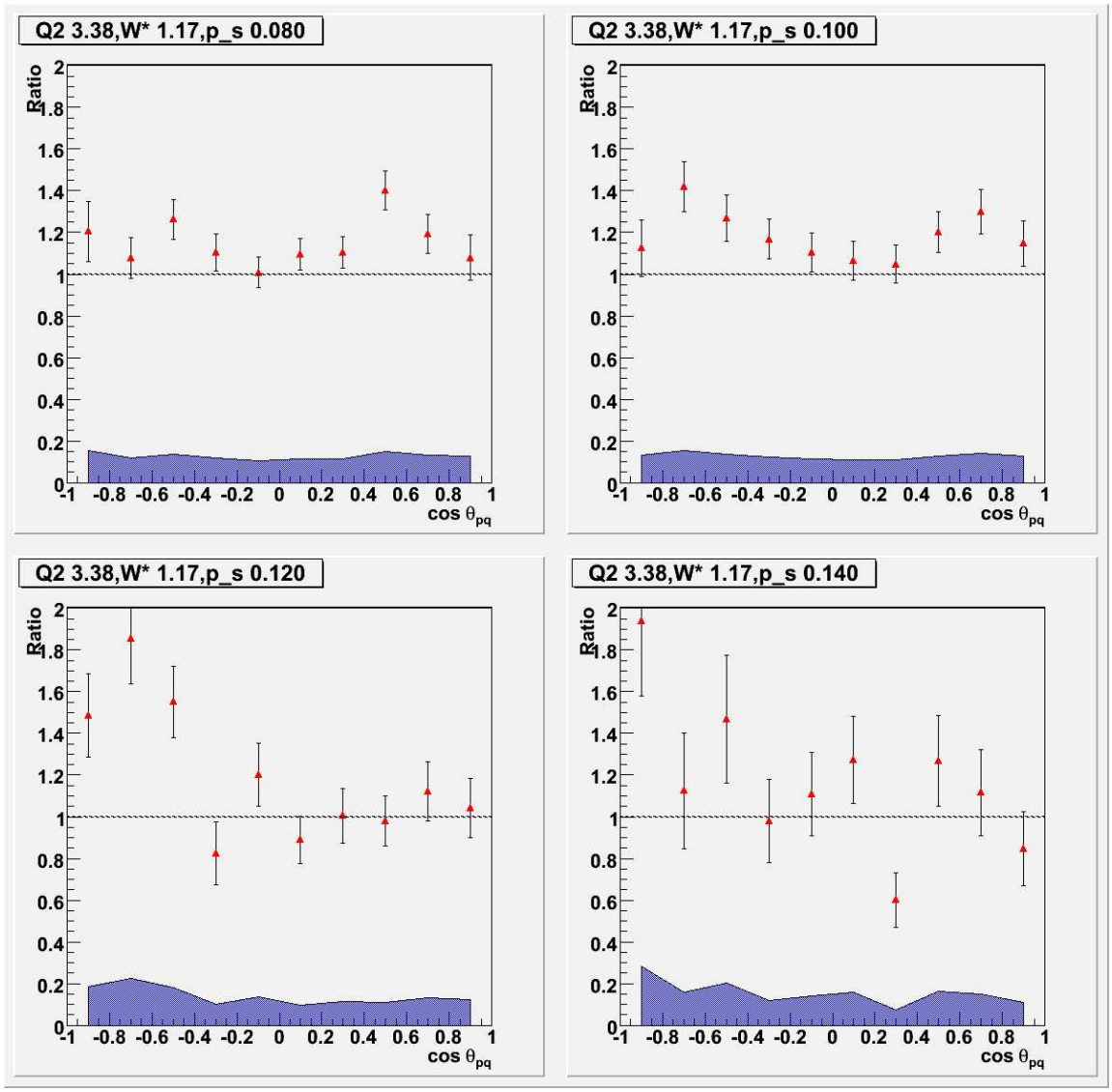

FIG. 152: Ratio of experimental data with subtracted accidental background and elastic tail to the full simulation in the PWIA spectator picture is shown as a function of $\cos\theta_{pq}$. Data are for Q^2 from 2.23 to 4.52 $(\mathrm{GeV}/c)^2$, W^* from 1.00 to 1.35 GeV. The beam energy is 4.217 GeV. Error bars are statistical only. Systematic errors are shown as a blue band.

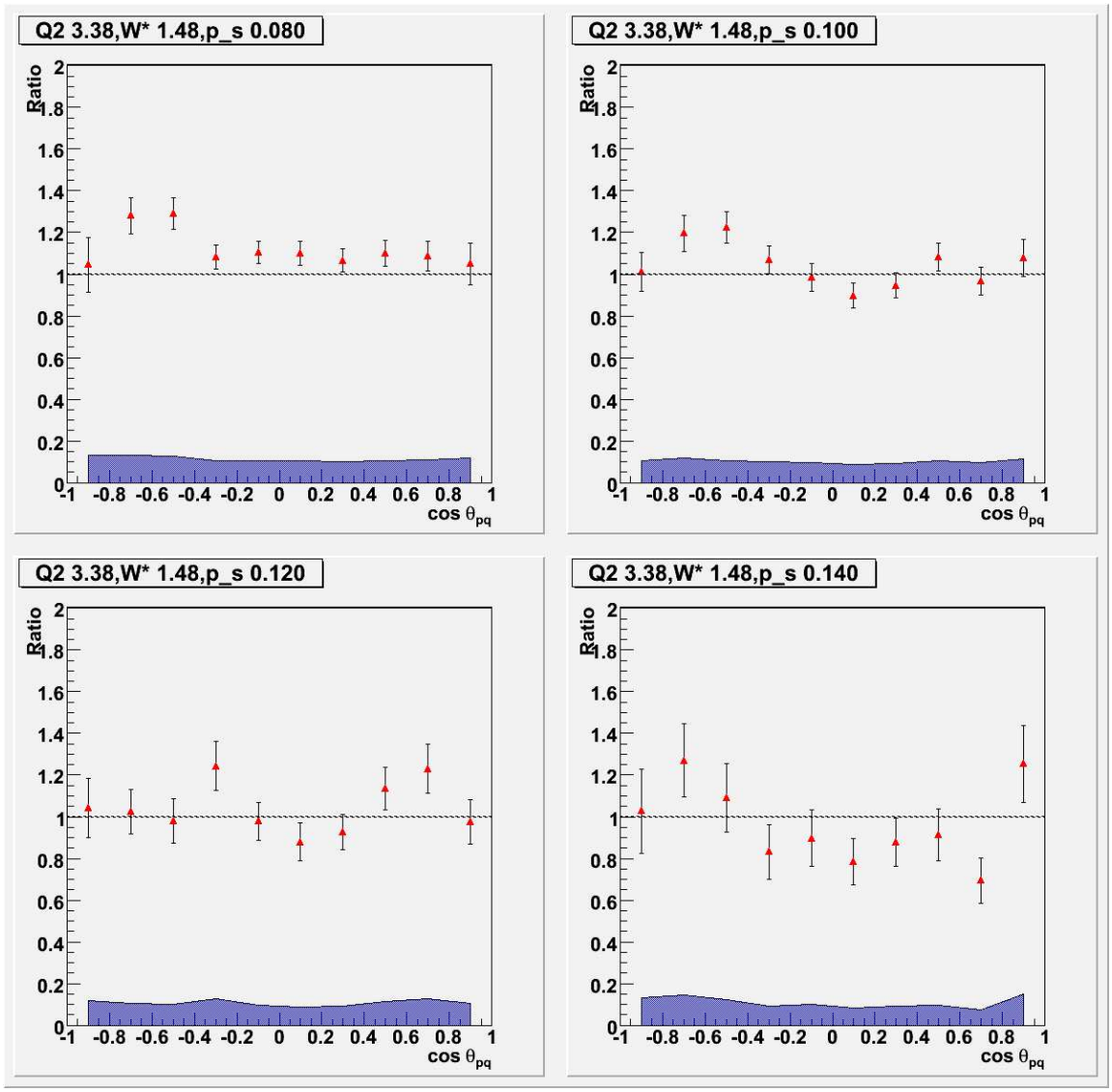

FIG. 153: Ratio of experimental data with subtracted accidental background and elastic tail to the full simulation in the PWIA spectator picture is shown as a function of $\cos\theta_{pq}$. Data are for Q^2 from 2.23 to 4.52 $(\mathrm{GeV}/c)^2$, W^* from 1.35 to 1.60 GeV. The beam energy is 4.217 GeV. Error bars are statistical only. Systematic errors are shown as a blue band.

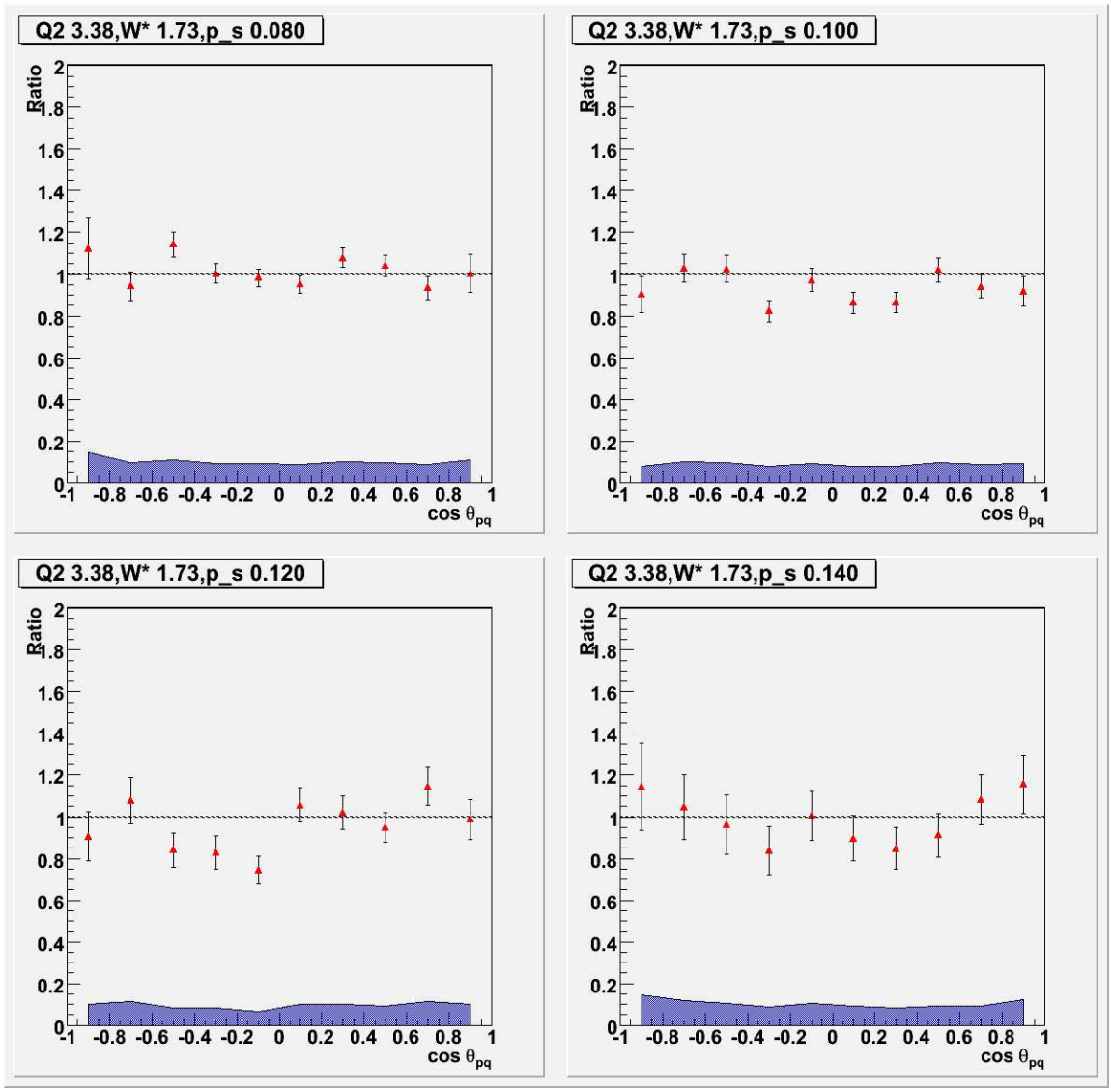

FIG. 154: Ratio of experimental data with subtracted accidental background and elastic tail to the full simulation in the PWIA spectator picture is shown as a function of $\cos\theta_{pq}$. Data are for Q^2 from 2.23 to 4.52 $(\mathrm{GeV}/c)^2$, W^* from 1.60 to 1.85 GeV. The beam energy is 4.217 GeV. Error bars are statistical only. Systematic errors are shown as a blue band.

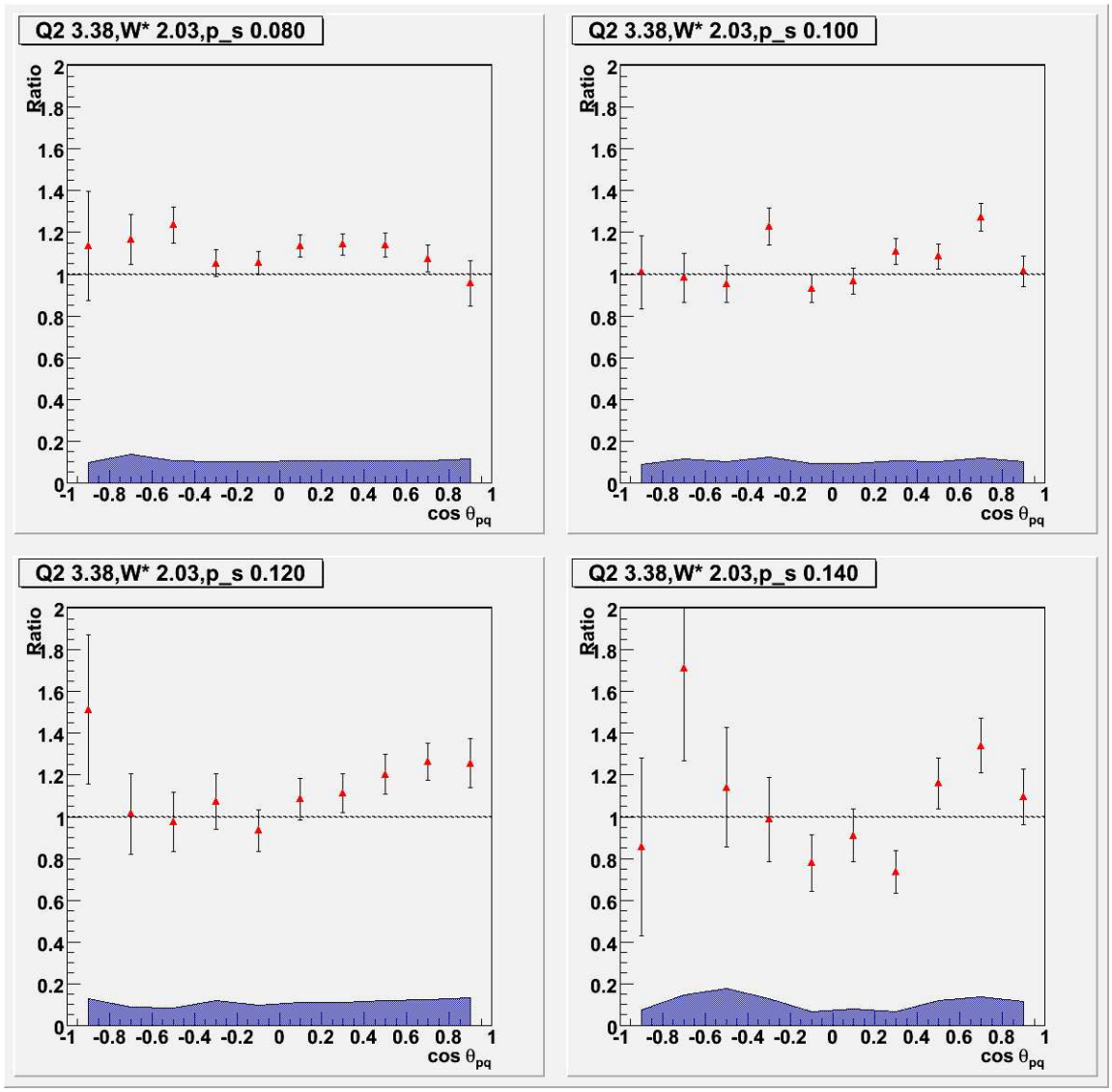

FIG. 155: Ratio of experimental data with subtracted accidental background and elastic tail to the full simulation in the PWIA spectator picture is shown as a function of $\cos\theta_{pq}$. Data are for Q^2 from 2.23 to 4.52 $(\mathrm{GeV}/c)^2$, W^* from 1.85 to 2.20 GeV. The beam energy is 4.217 GeV. Error bars are statistical only. Systematic errors are shown as a blue band.

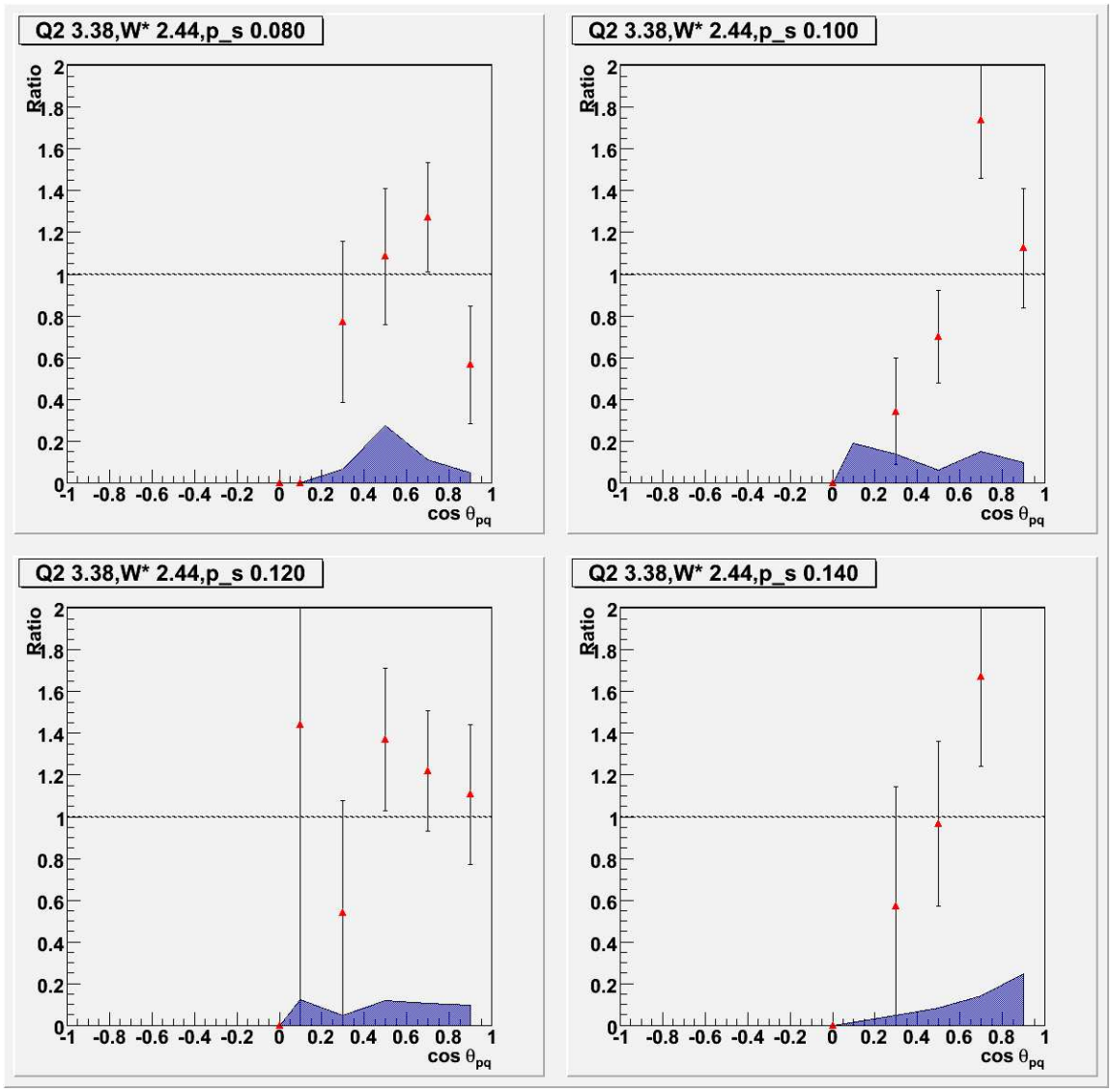

FIG. 156: Ratio of experimental data with subtracted accidental background and elastic tail to the full simulation in the PWIA spectator picture is shown as a function of $\cos\theta_{pq}$. Data are for Q^2 from 2.23 to 4.52 $(\mathrm{GeV}/c)^2$, W^* from 2.20 to 2.68 GeV. The beam energy is 4.217 GeV. Error bars are statistical only. Systematic errors are shown as a blue band.

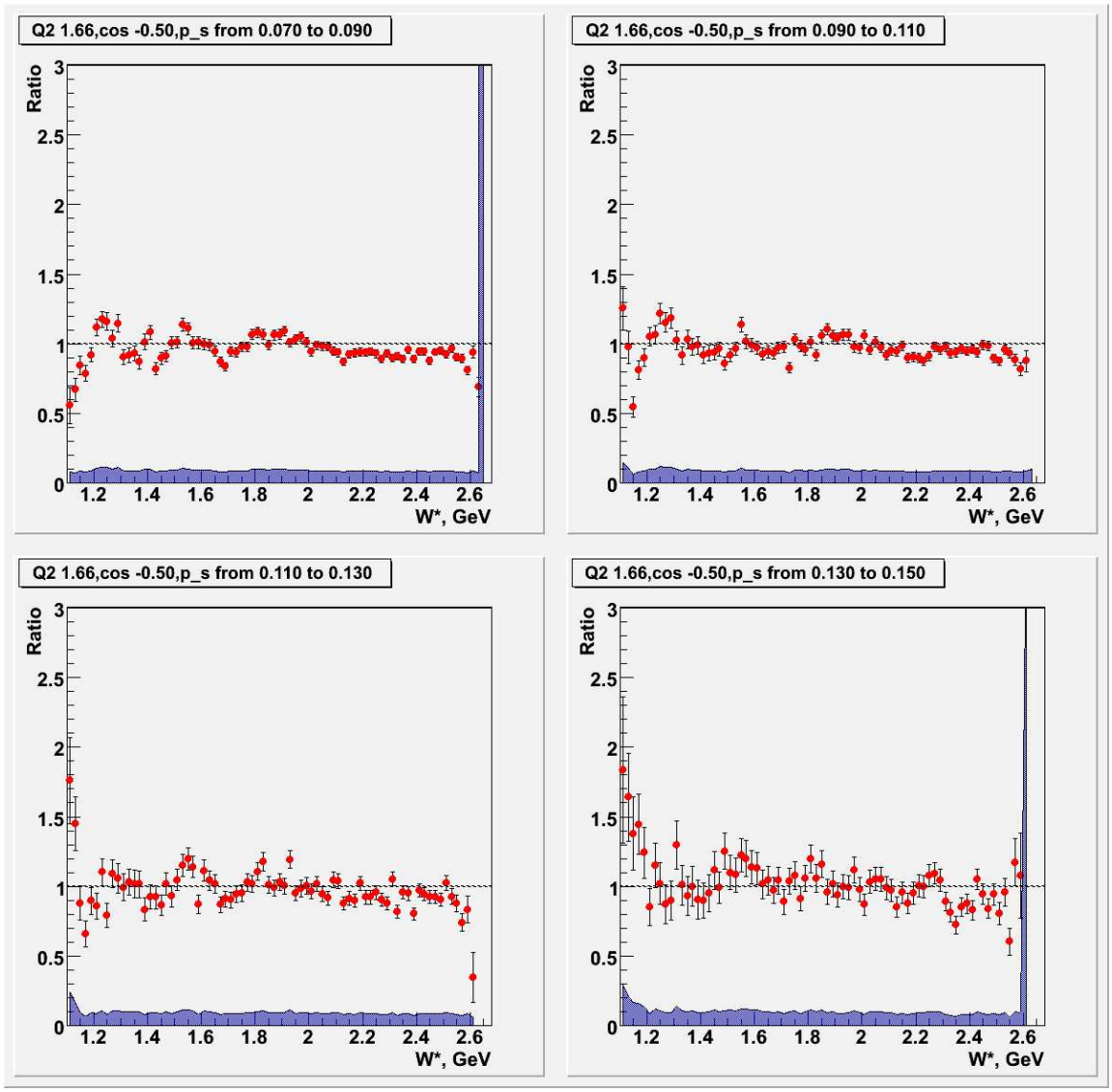

FIG. 157: Ratio of experimental data with subtracted accidental background and elastic tail to the full simulation in the PWIA spectator picture is shown as a function of W^*. Data are for Q^2 from 1.10 to 2.23 $(\mathrm{GeV}/c)^2$, $\cos\theta_{pq}$ from -0.75 to -0.25. The beam energy is 5.254 GeV. Error bars are statistical only. Systematic errors are shown as a blue band.

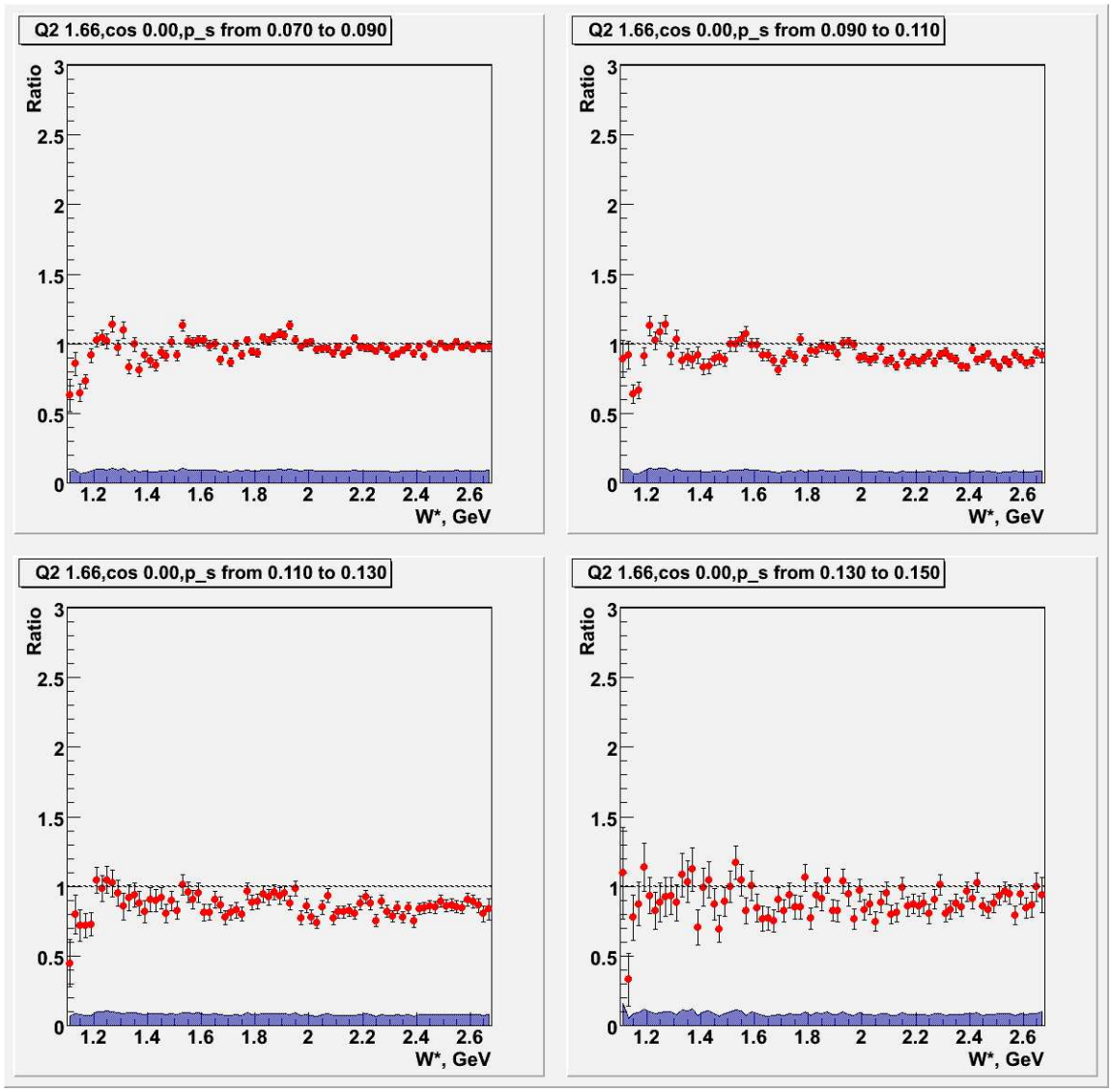

FIG. 158: Ratio of experimental data with subtracted accidental background and elastic tail to the full simulation in the PWIA spectator picture is shown as a function of W^*. Data are for Q^2 from 1.10 to 2.23 $(\mathrm{GeV}/c)^2$, $\cos\theta_{pq}$ from -0.25 to 0.25. The beam energy is 5.254 GeV. Error bars are statistical only. Systematic errors are shown as a blue band.

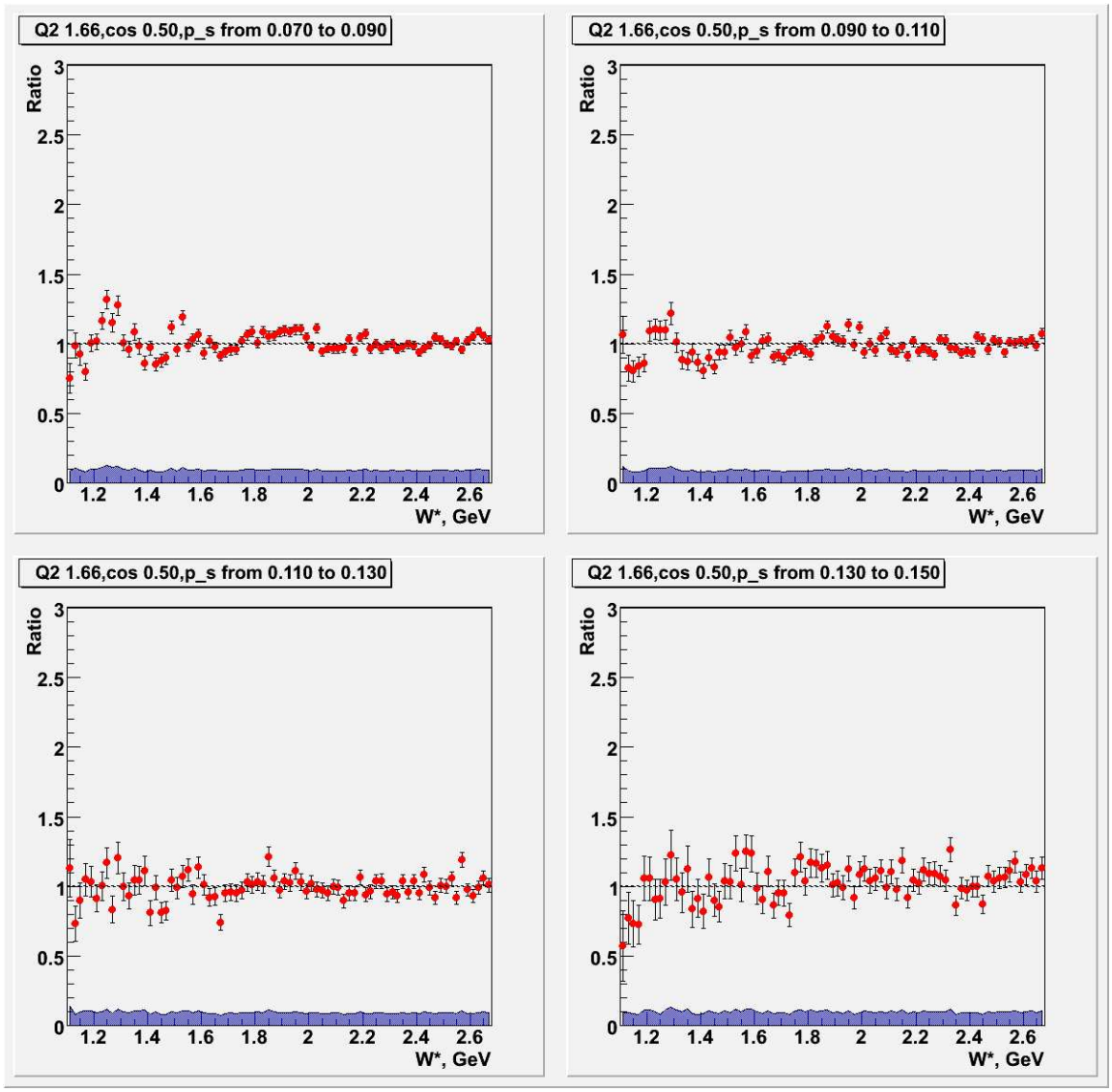

FIG. 159: Ratio of experimental data with subtracted accidental background and elastic tail to the full simulation in the PWIA spectator picture is shown as a function of W^*. Data are for Q^2 from 1.10 to 2.23 $(\mathrm{GeV}/c)^2$, $\cos\theta_{pq}$ from 0.25 to 0.75. The beam energy is 5.254 GeV. Error bars are statistical only. Systematic errors are shown as a blue band.

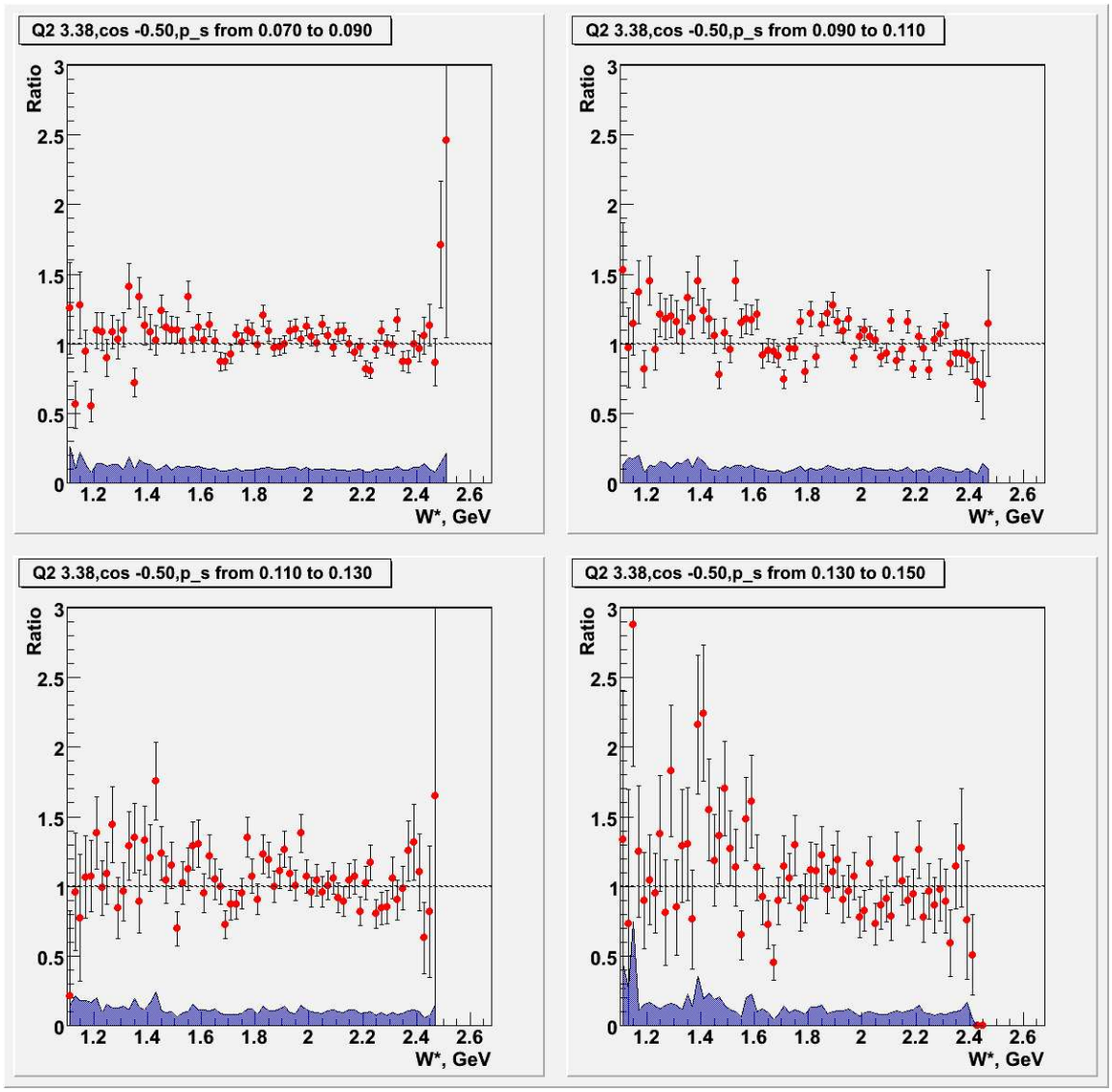

FIG. 160: Ratio of experimental data with subtracted accidental background and elastic tail to the full simulation in the PWIA spectator picture is shown as a function of W^*. Data are for Q^2 from 2.23 to 4.52 $(\mathrm{GeV}/c)^2$, $\cos\theta_{pq}$ from -0.75 to -0.25. The beam energy is 5.254 GeV. Error bars are statistical only. Systematic errors are shown as a blue band.

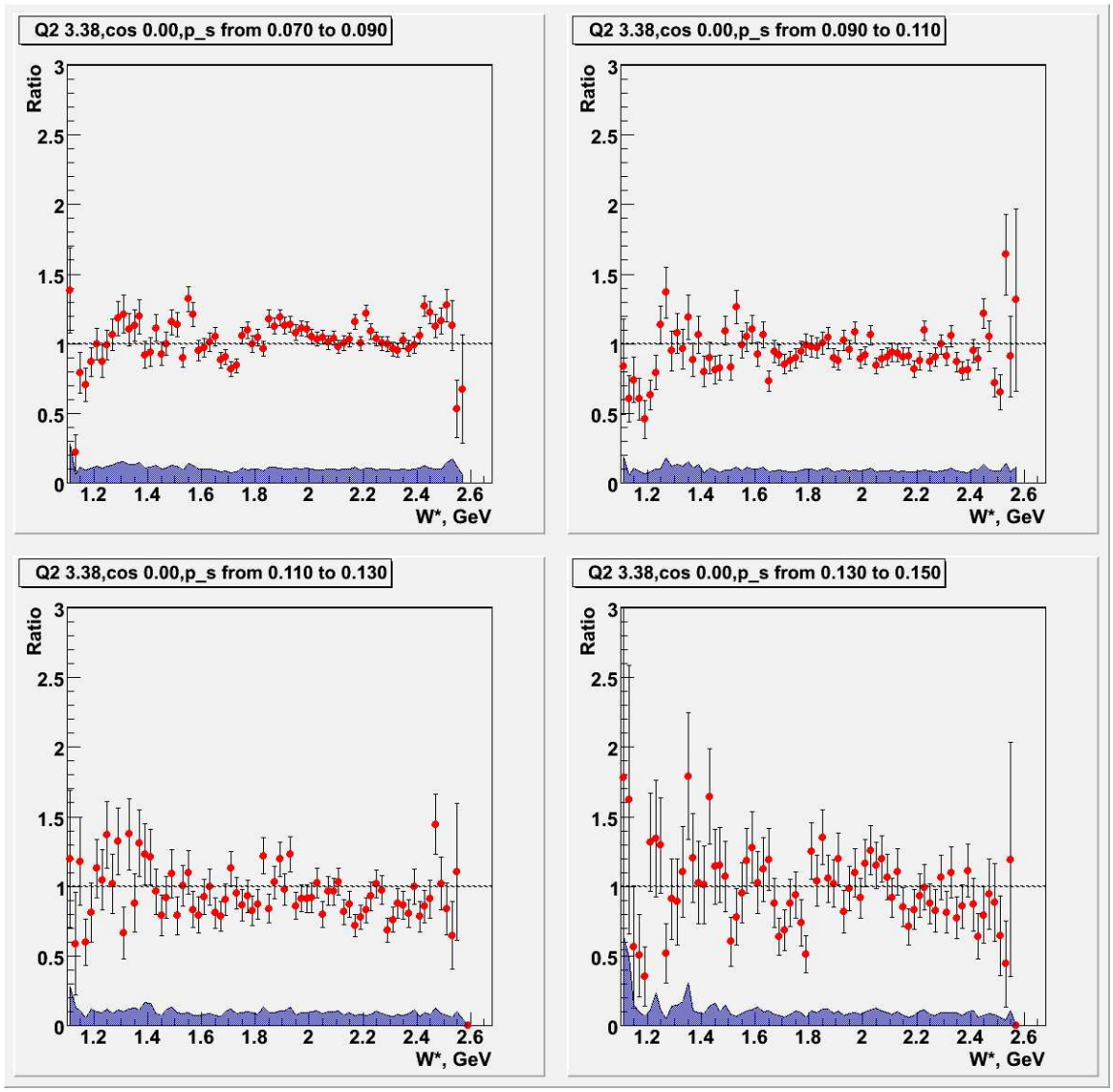

FIG. 161: Ratio of experimental data with subtracted accidental background and elastic tail to the full simulation in the PWIA spectator picture is shown as a function of W^*. Data are for Q^2 from 2.23 to 4.52 $(\mathrm{GeV}/c)^2$, $\cos\theta_{pq}$ from -0.25 to 0.25. The beam energy is 5.254 GeV. Systematic errors are shown as a blue band.

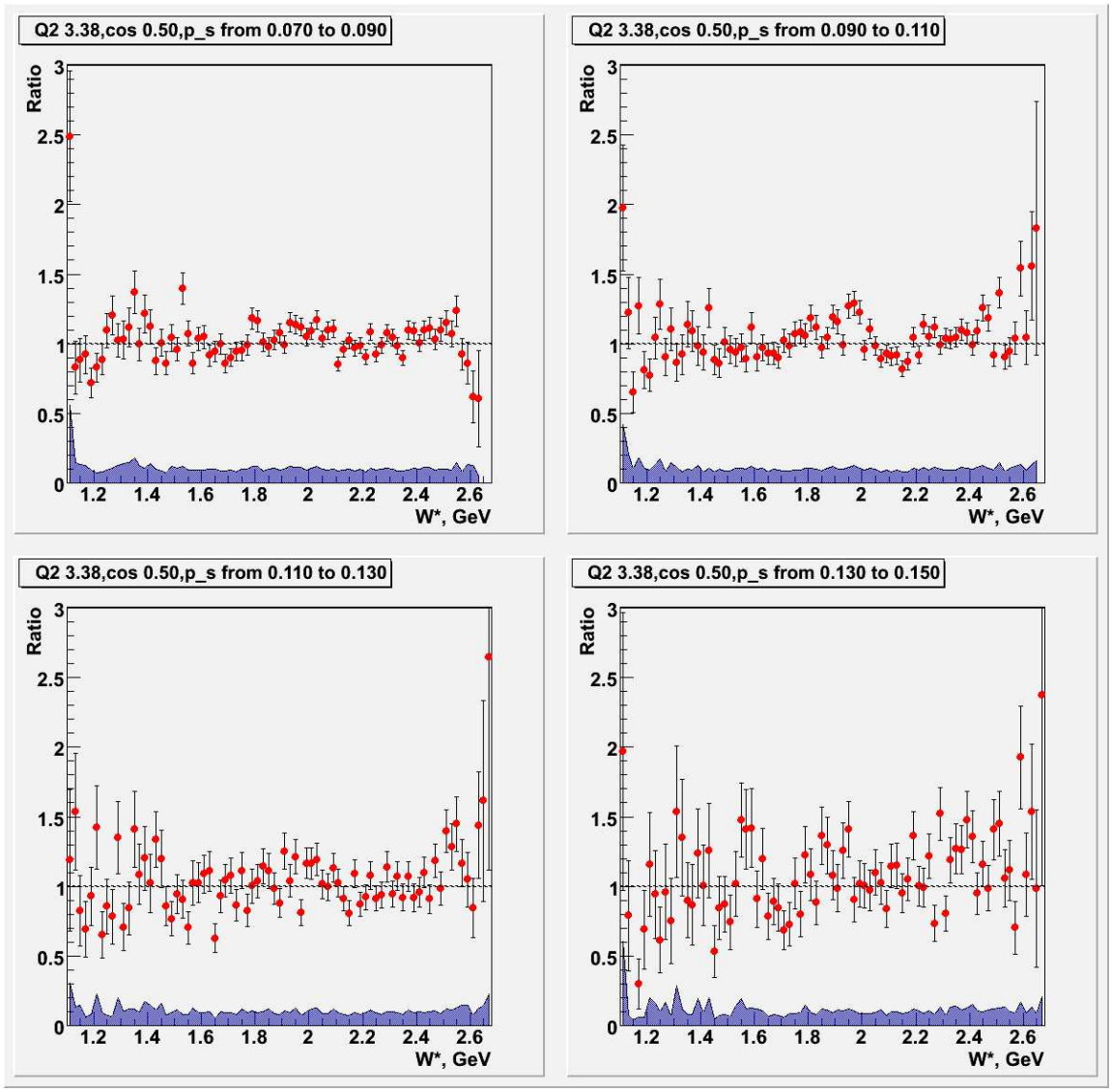

FIG. 162: Ratio of experimental data with subtracted accidental background and elastic tail to the full simulation in the PWIA spectator picture is shown as a function of W^*. Data are for Q^2 from 2.23 to 4.52 $(\mathrm{GeV}/c)^2$, $\cos\theta_{pq}$ from 0.25 to 0.75. The beam energy is 5.254 GeV. Error bars are statistical only. Systematic errors are shown as a blue band.

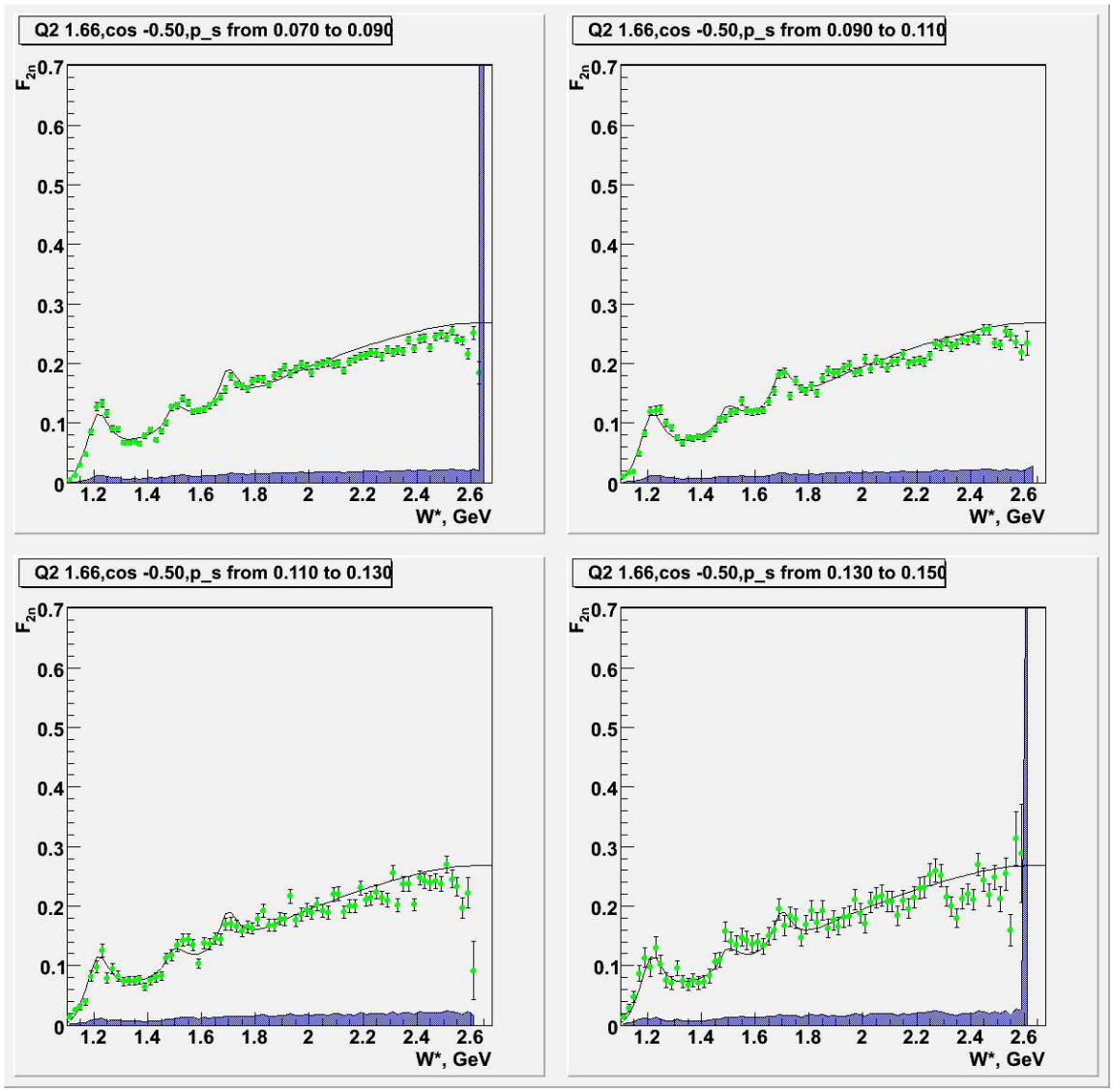

FIG. 163: Effective F_{2n} (green markers) structure function is shown as a function of W^*. Black line is the model F_{2n}. Data are for Q^2 from 1.10 to 2.23 $(\mathrm{GeV}/c)^2$, $\cos\theta_{pq}$ from -0.75 to -0.25. The beam energy is 5.254 GeV. Error bars are statistical only. Systematic errors are shown as a blue band.

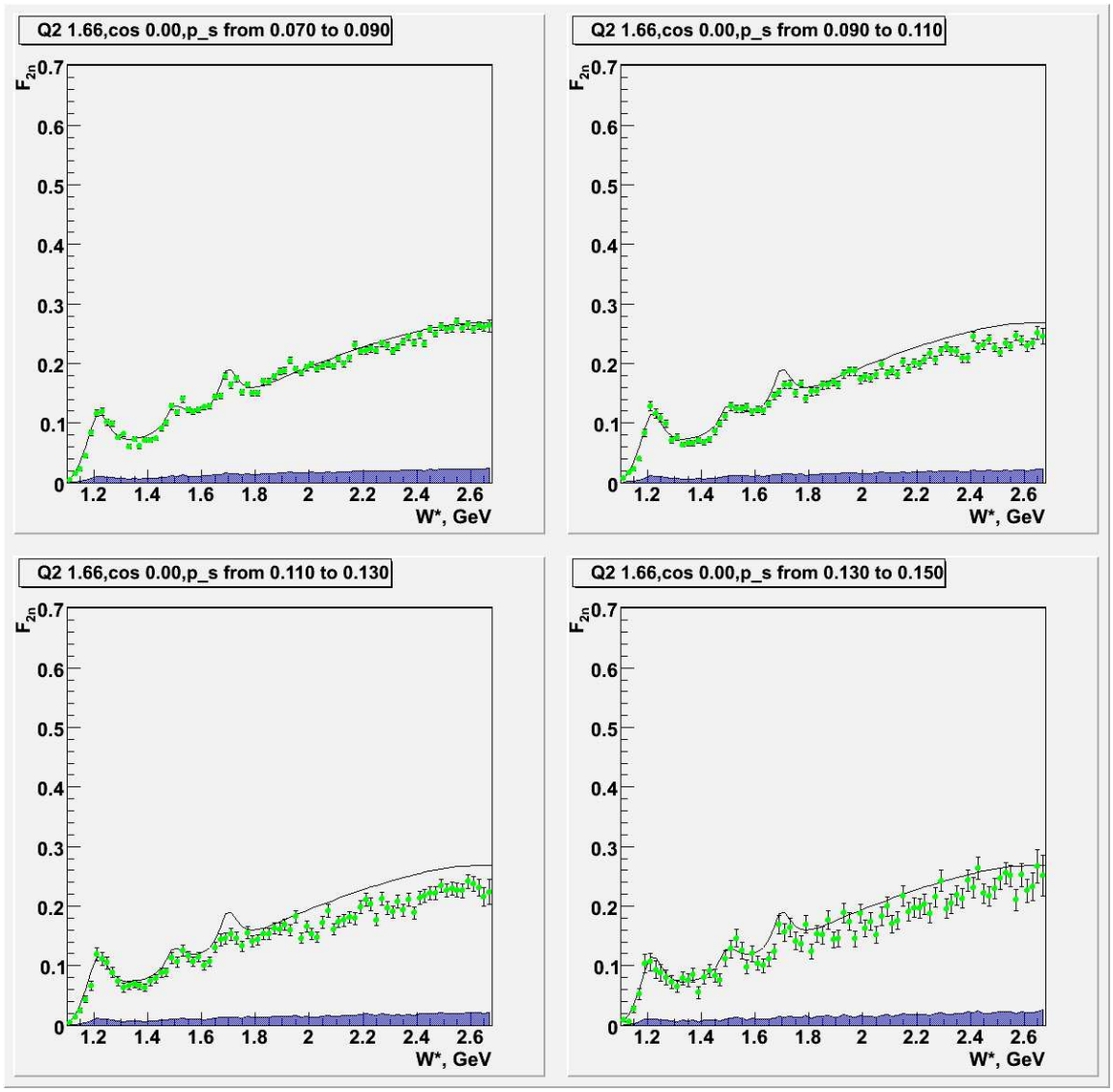

FIG. 164: Effective F_{2n} (green markers) structure function is shown as a function of W^*. Black line is the model F_{2n}. Data are for Q^2 from 1.10 to 2.23 $(\mathrm{GeV}/c)^2$, $\cos\theta_{pq}$ from -0.25 to 0.25. The beam energy is 5.254 GeV. Error bars are statistical only. Systematic errors are shown as a blue band.

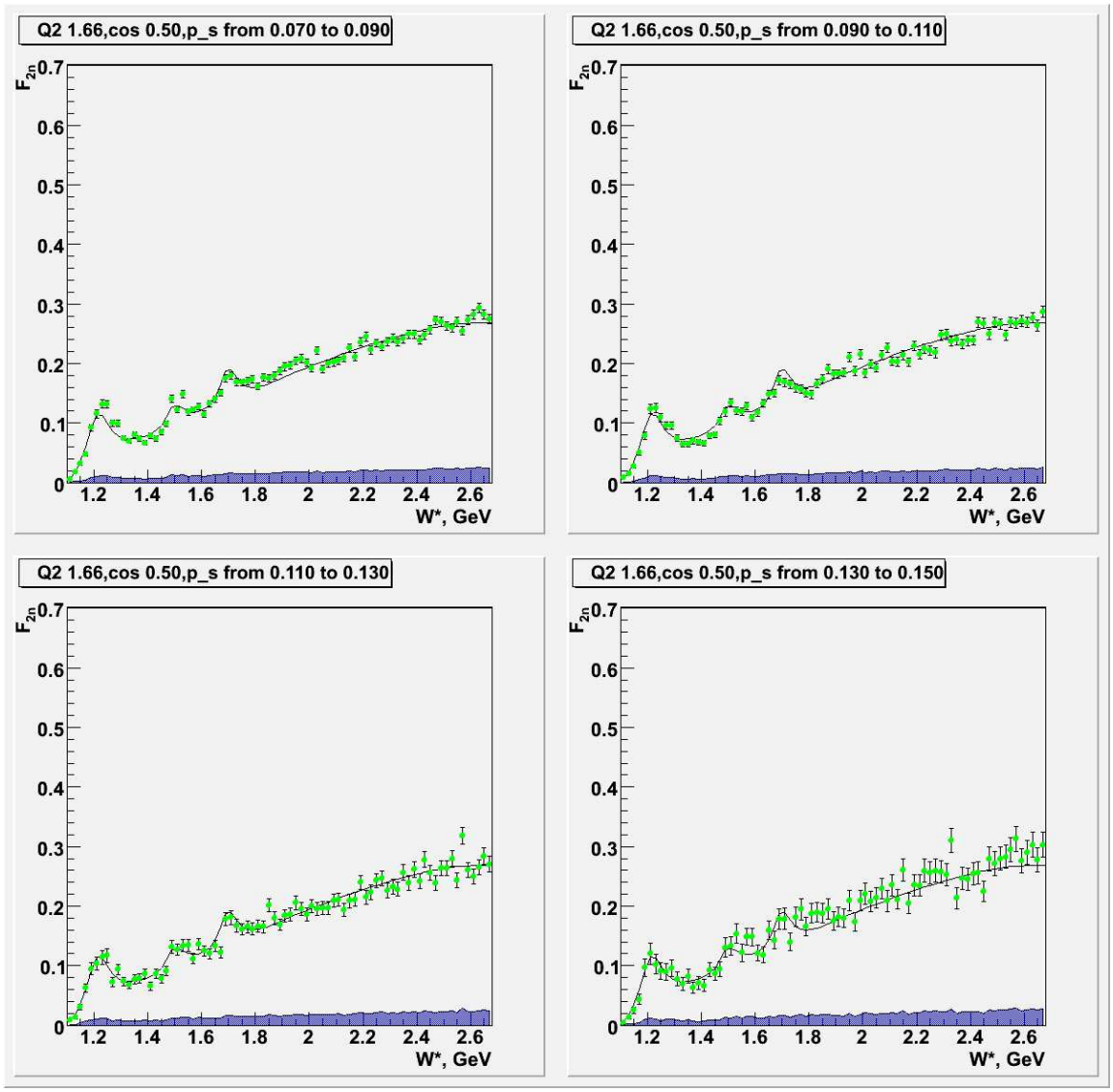

FIG. 165: Effective F_{2n} (green markers) structure function is shown as a function of W^*. Black line is the model F_{2n}. Data are for Q^2 from 1.10 to 2.23 $(\mathrm{GeV}/c)^2$, $\cos\theta_{pq}$ from 0.25 to 0.75. The beam energy is 5.254 GeV. Error bars are statistical only. Systematic errors are shown as a blue band.

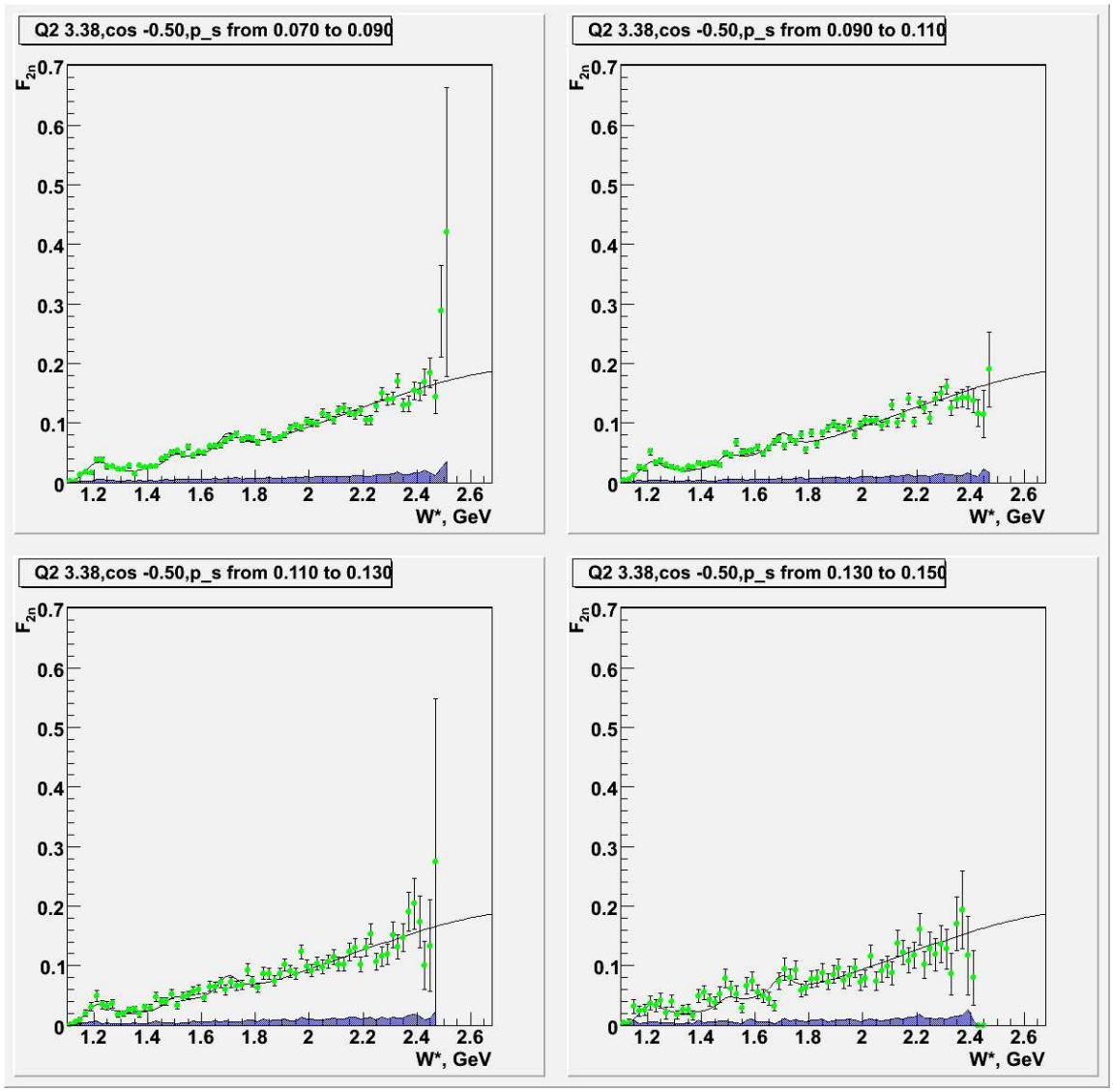

FIG. 166: Effective F_{2n} (green markers) structure function is shown as a function of W^*. Black line is the model F_{2n}. Data are for Q^2 from 2.23 to 4.52 $(\mathrm{GeV}/c)^2$, $\cos\theta_{pq}$ from -0.75 to -0.25. The beam energy is 5.254 GeV. Error bars are statistical only. Systematic errors are shown as a blue band.

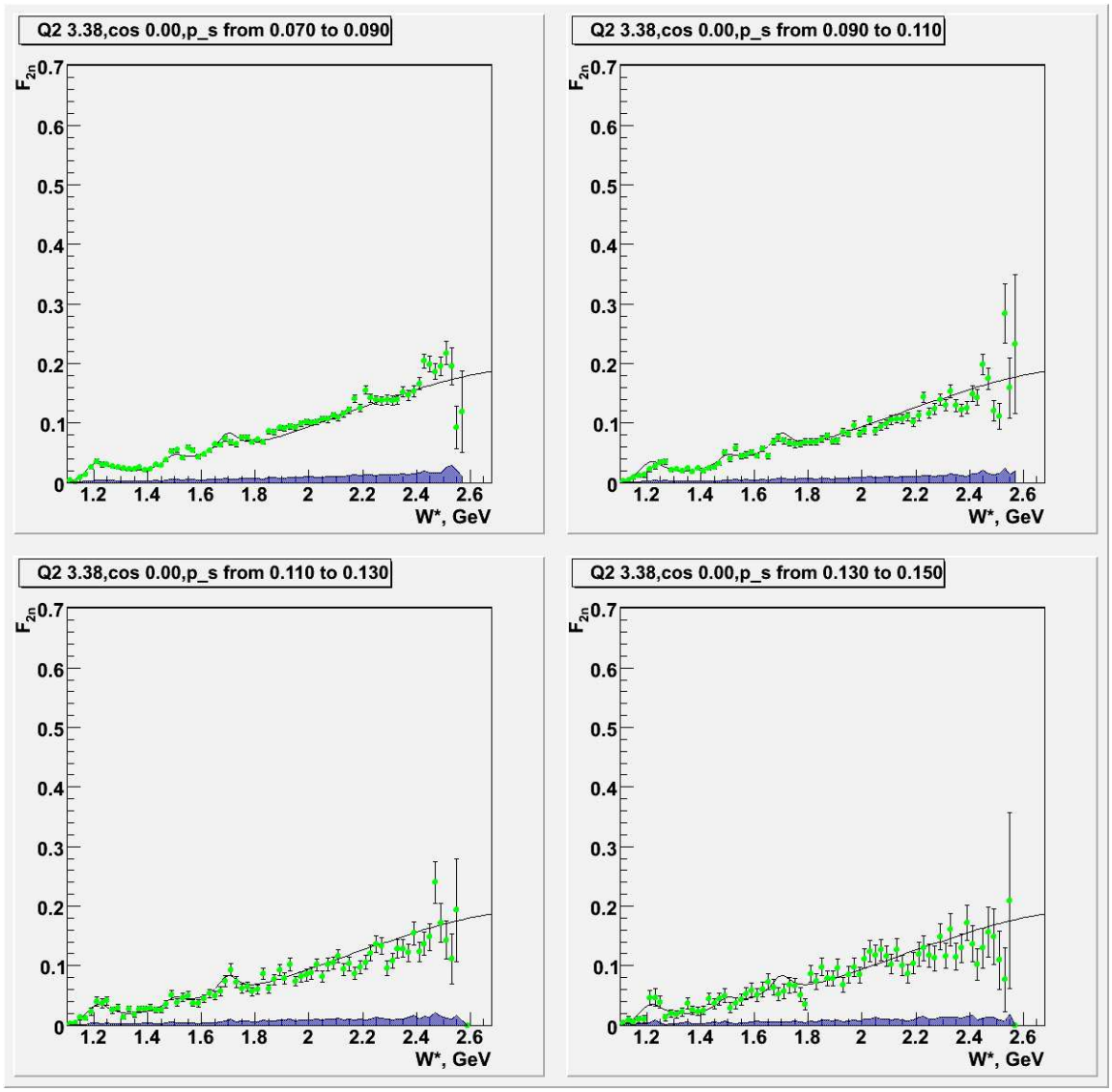

FIG. 167: Effective F_{2n} (green markers) structure function is shown as a function of W^*. Black line is the model F_{2n}. Data are for Q^2 from 2.23 to 4.52 $(\mathrm{GeV}/c)^2$, $\cos\theta_{pq}$ from -0.25 to 0.25. The beam energy is 5.254 GeV. Systematic errors are shown as a blue band.

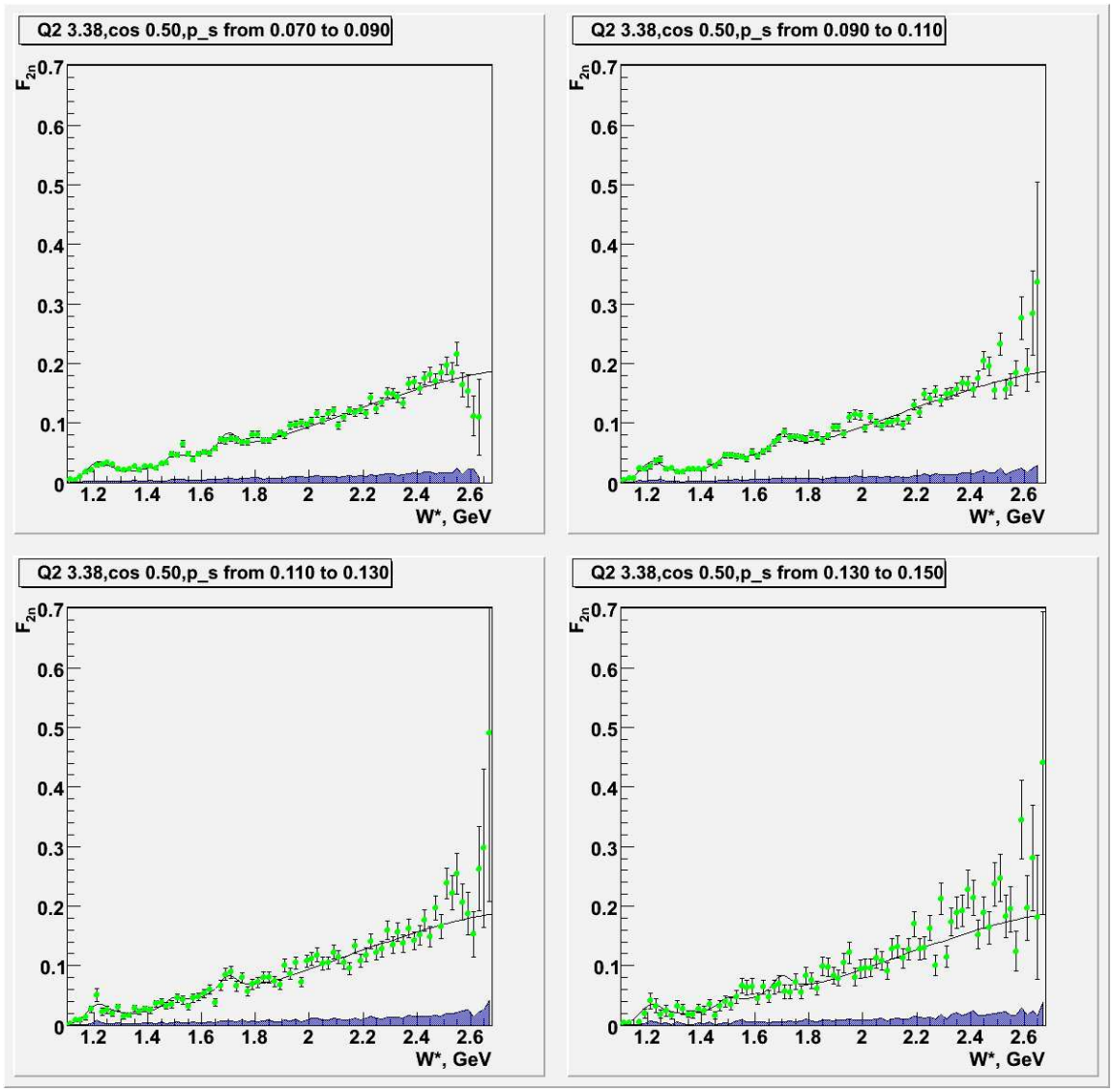

FIG. 168: Effective F_{2n} (green markers) structure function is shown as a function of W^*. Black line is the model F_{2n}. Data are for Q^2 from 2.23 to 4.52 $(\mathrm{GeV}/c)^2$, $\cos\theta_{pq}$ from 0.25 to 0.75. The beam energy is 5.254 GeV. Error bars are statistical only. Systematic errors are shown as a blue band.

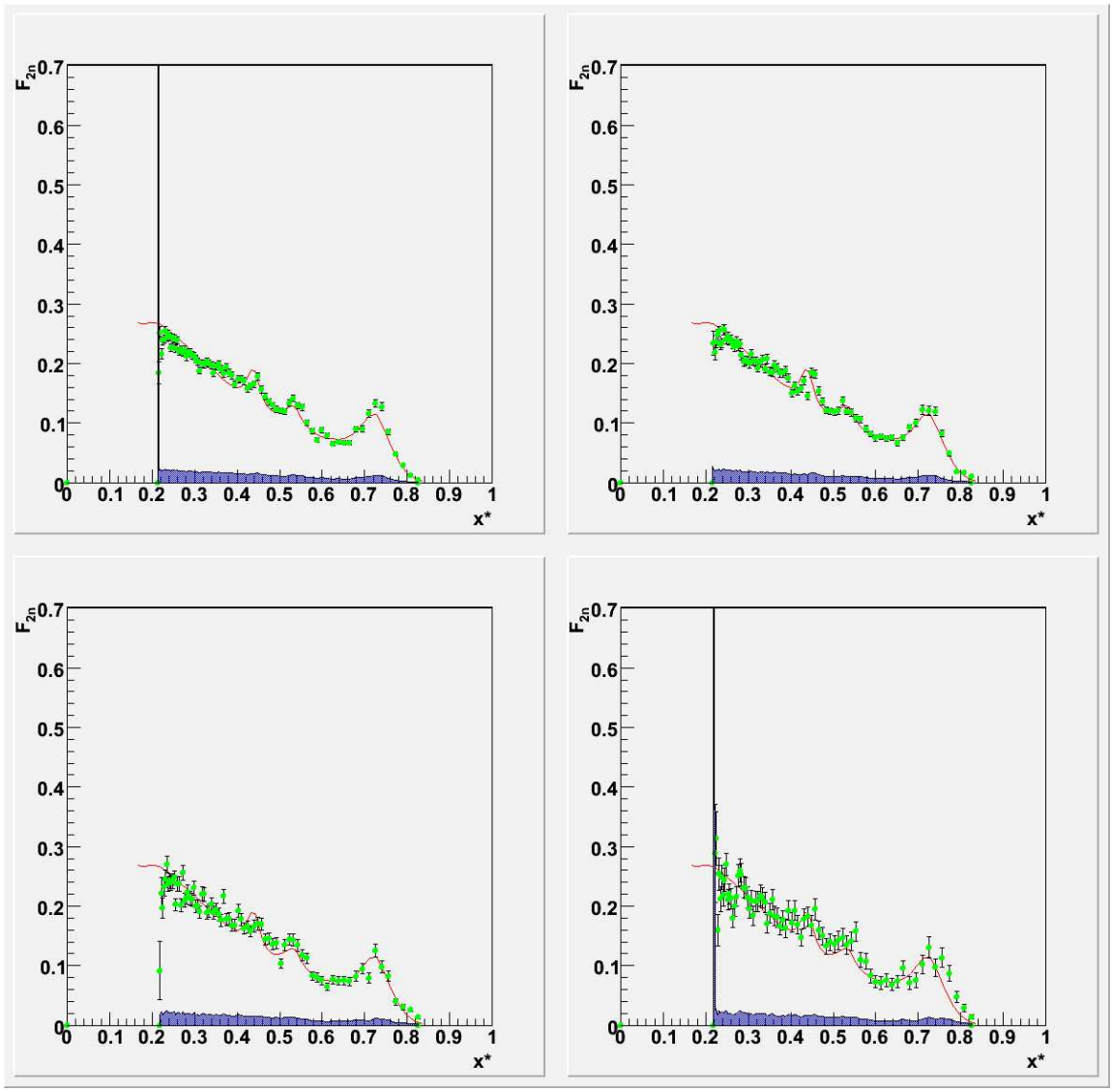

FIG. 169: Effective F_{2n} (green markers) structure function is shown as a function of x^*. Red line is the model F_{2n}. Data are for Q^2 from 1.10 to 2.23 $(\mathrm{GeV}/c)^2$, $\cos\theta_{pq}$ from -0.75 to -0.25. The beam energy is 5.254 GeV. Error bars are statistical only. Systematic errors are shown as a blue band.

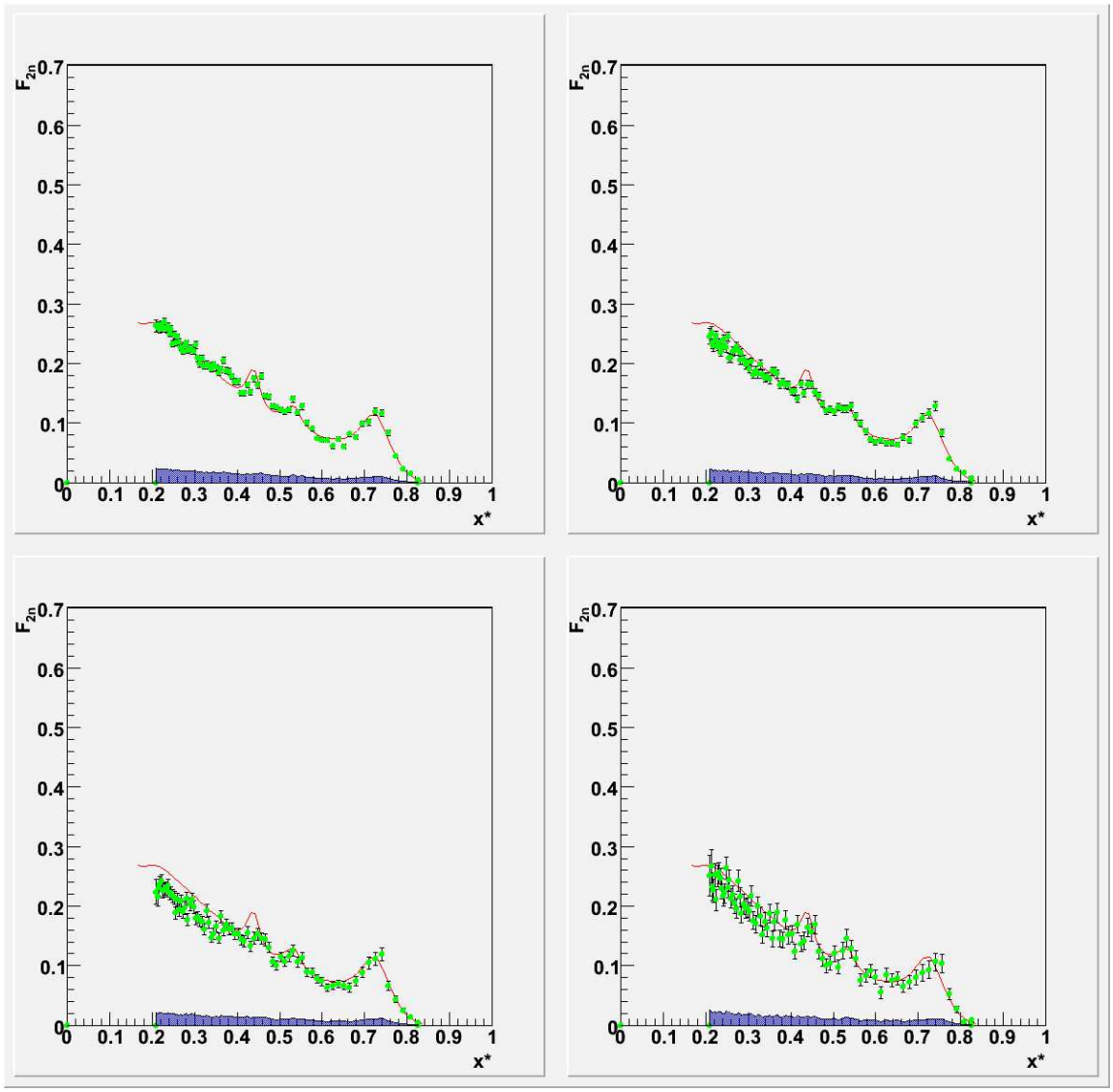

FIG. 170: Effective F_{2n} (green markers) structure function is shown as a function of x^*. Red line is the model F_{2n}. Data are for Q^2 from 1.10 to 2.23 $(\mathrm{GeV}/c)^2$, $\cos\theta_{pq}$ from -0.25 to 0.25. The beam energy is 5.254 GeV. Error bars are statistical only. Systematic errors are shown as a blue band.

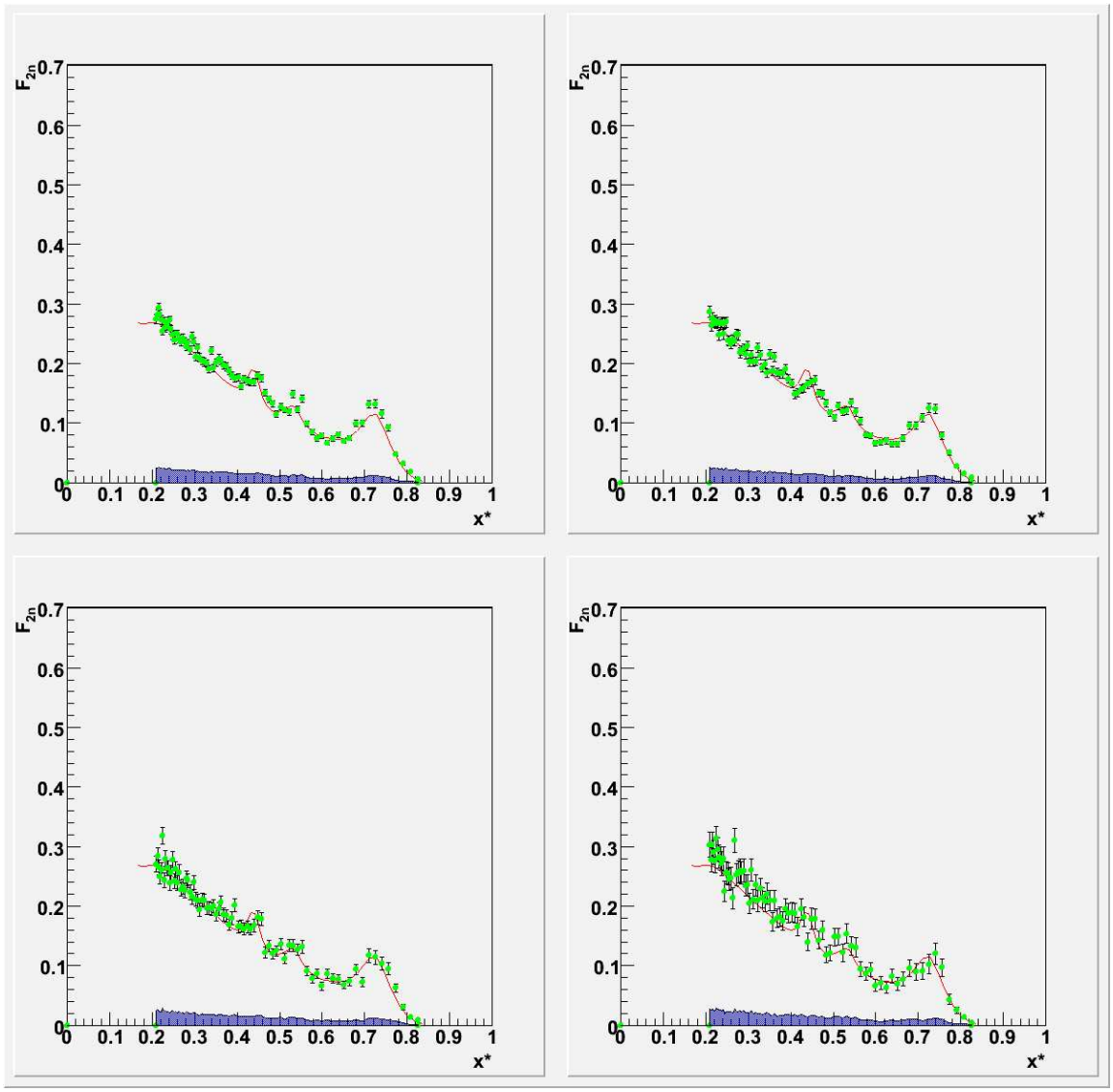

FIG. 171: Effective F_{2n} (green markers) structure function is shown as a function of x^*. Red line is the model F_{2n}. Data are for Q^2 from 1.10 to 2.23 $(\mathrm{GeV}/c)^2$, $\cos\theta_{pq}$ from 0.25 to 0.75. The beam energy is 5.254 GeV. Error bars are statistical only. Systematic errors are shown as a blue band.

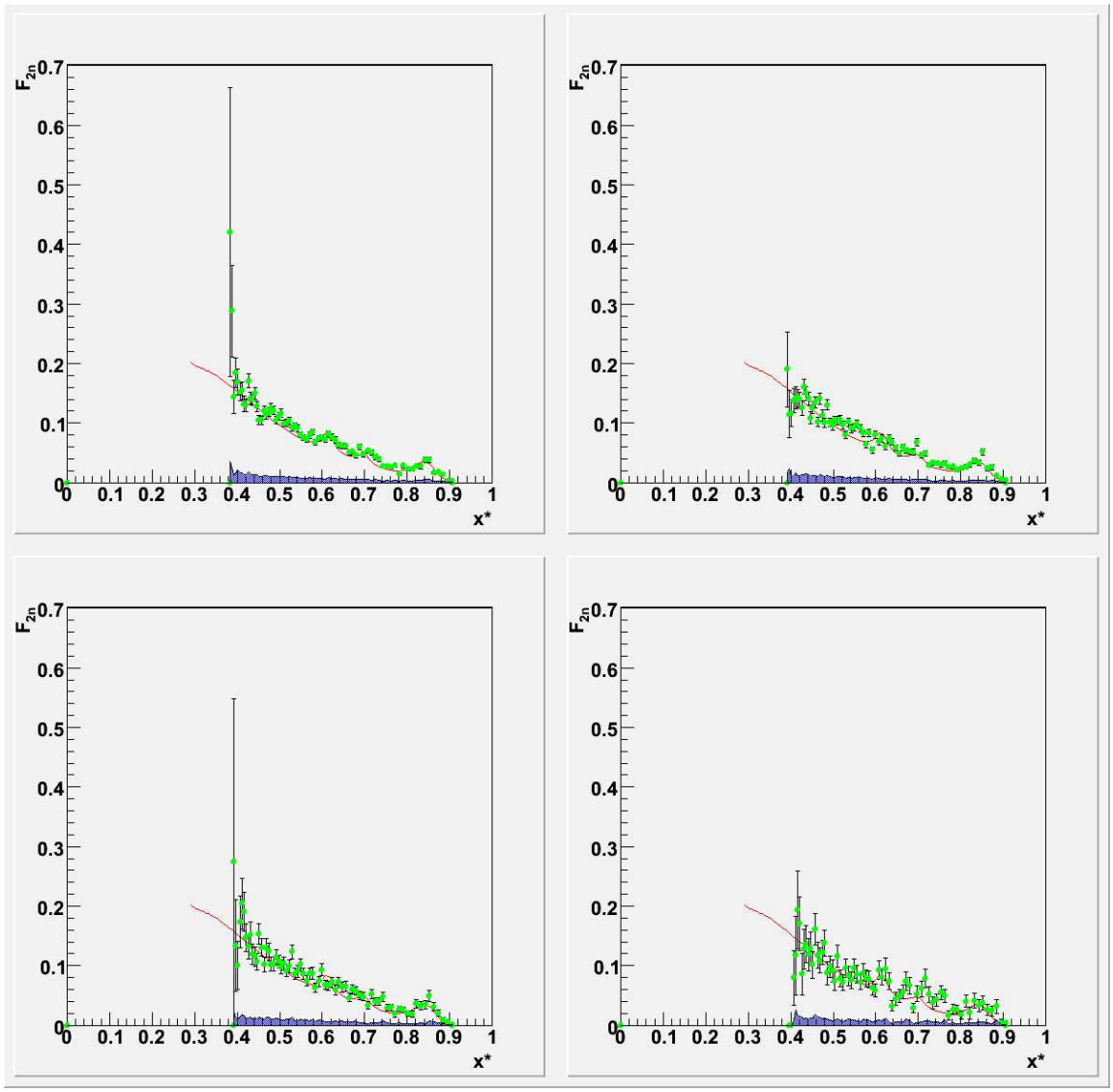

FIG. 172: Effective F_{2n} (green markers) structure function is shown as a function of x^*. Black line is the model F_{2n}. Data are for Q^2 from 2.23 to 4.52 $(\mathrm{GeV}/c)^2$, $\cos\theta_{pq}$ from -0.75 to -0.25. The beam energy is 5.254 GeV. Error bars are statistical only. Systematic errors are shown as a blue band.

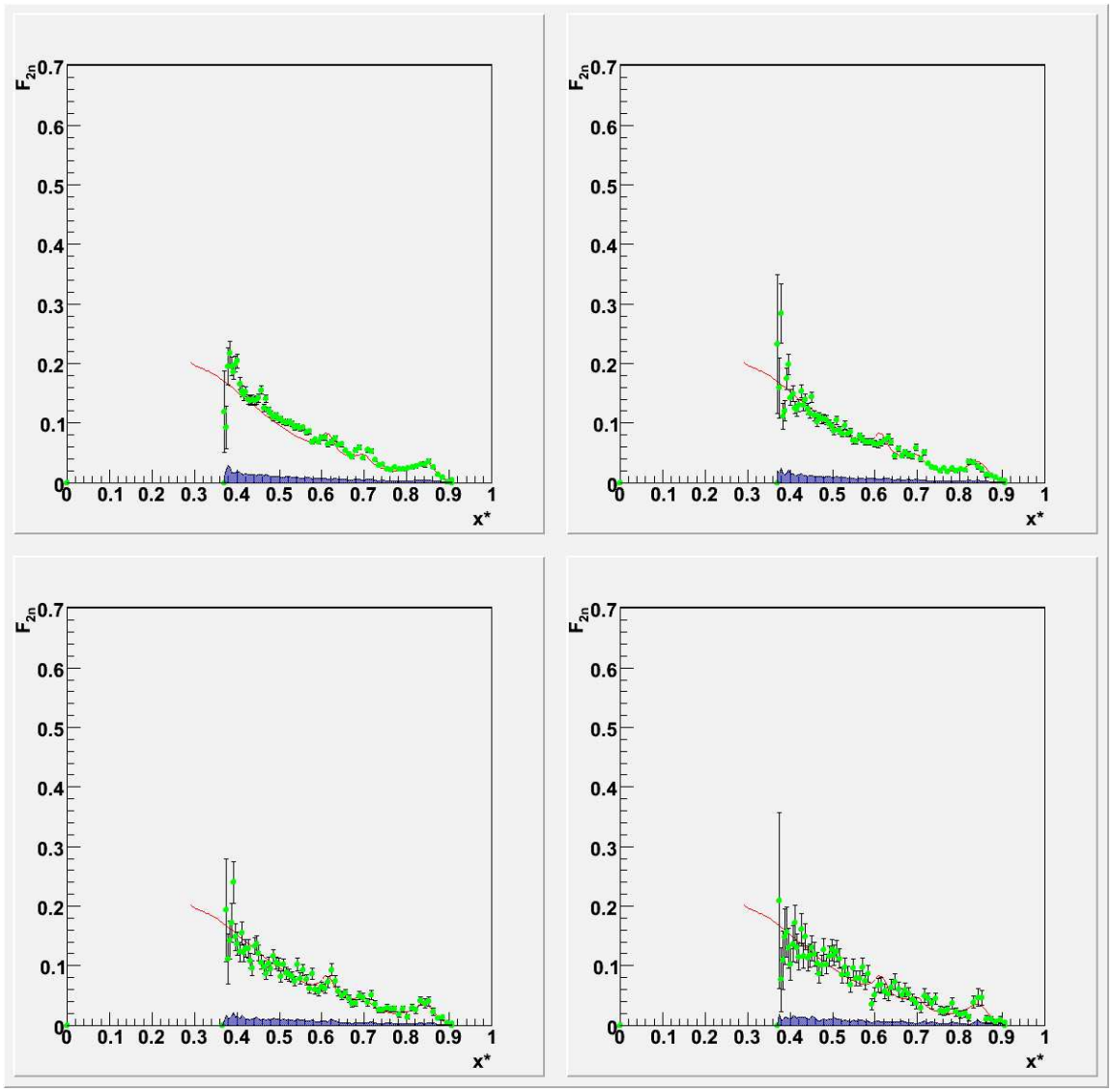

FIG. 173: Effective F_{2n} (green markers) structure function is shown as a function of x^*. Black line is the model F_{2n}. Data are for Q^2 from 2.23 to 4.52 $(\mathrm{GeV}/c)^2$, $\cos\theta_{pq}$ from -0.25 to 0.25. The beam energy is 5.254 GeV. Systematic errors are shown as a blue band.

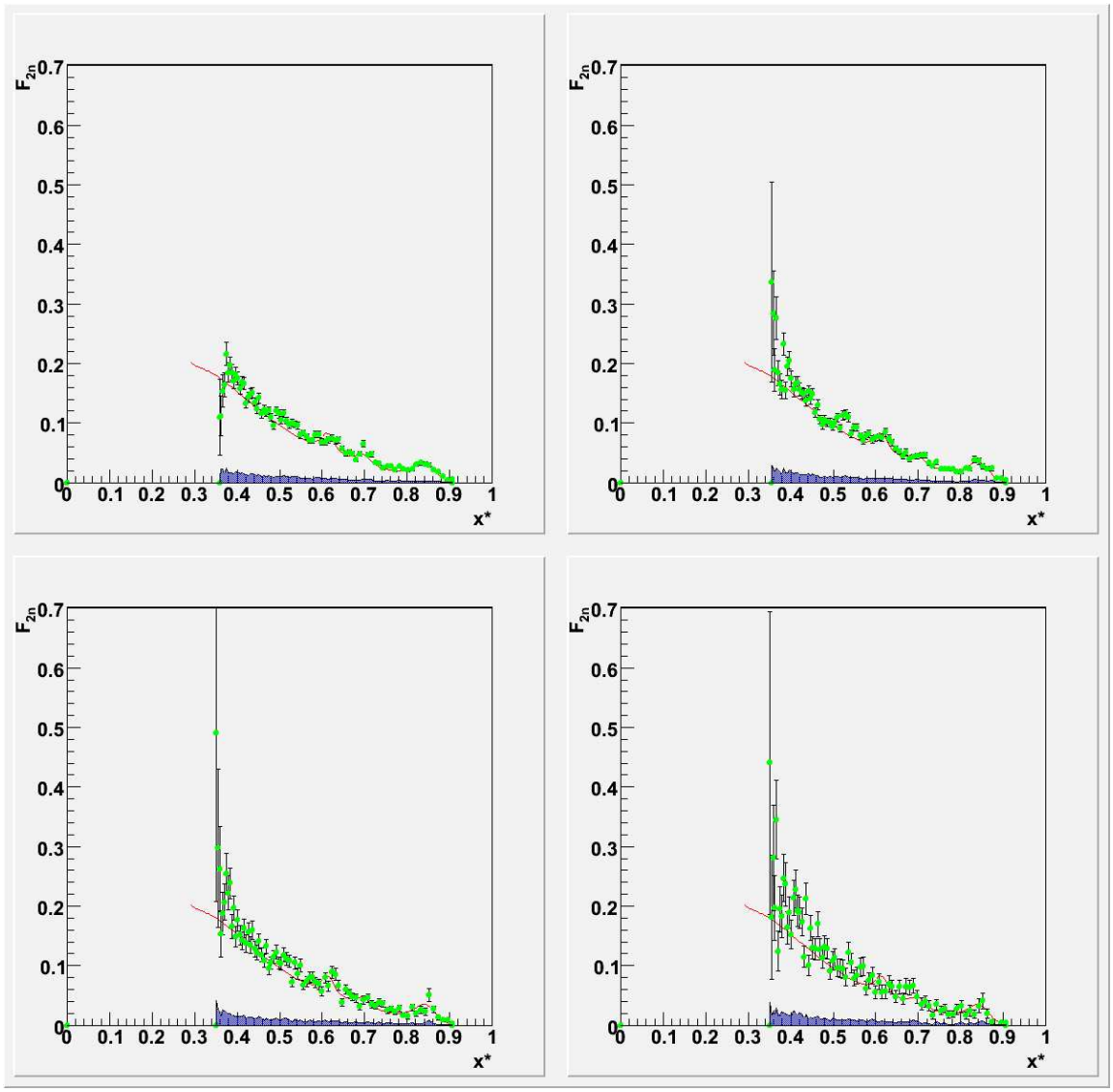

FIG. 174: Effective F_{2n} (green markers) structure function is shown as a function of x^*. Black line is the model F_{2n}. Data are for Q^2 from 2.23 to 4.52 $(\mathrm{GeV}/c)^2$, $\cos\theta_{pq}$ from 0.25 to 0.75. The beam energy is 5.254 GeV. Error bars are statistical only. Systematic errors are shown as a blue band.

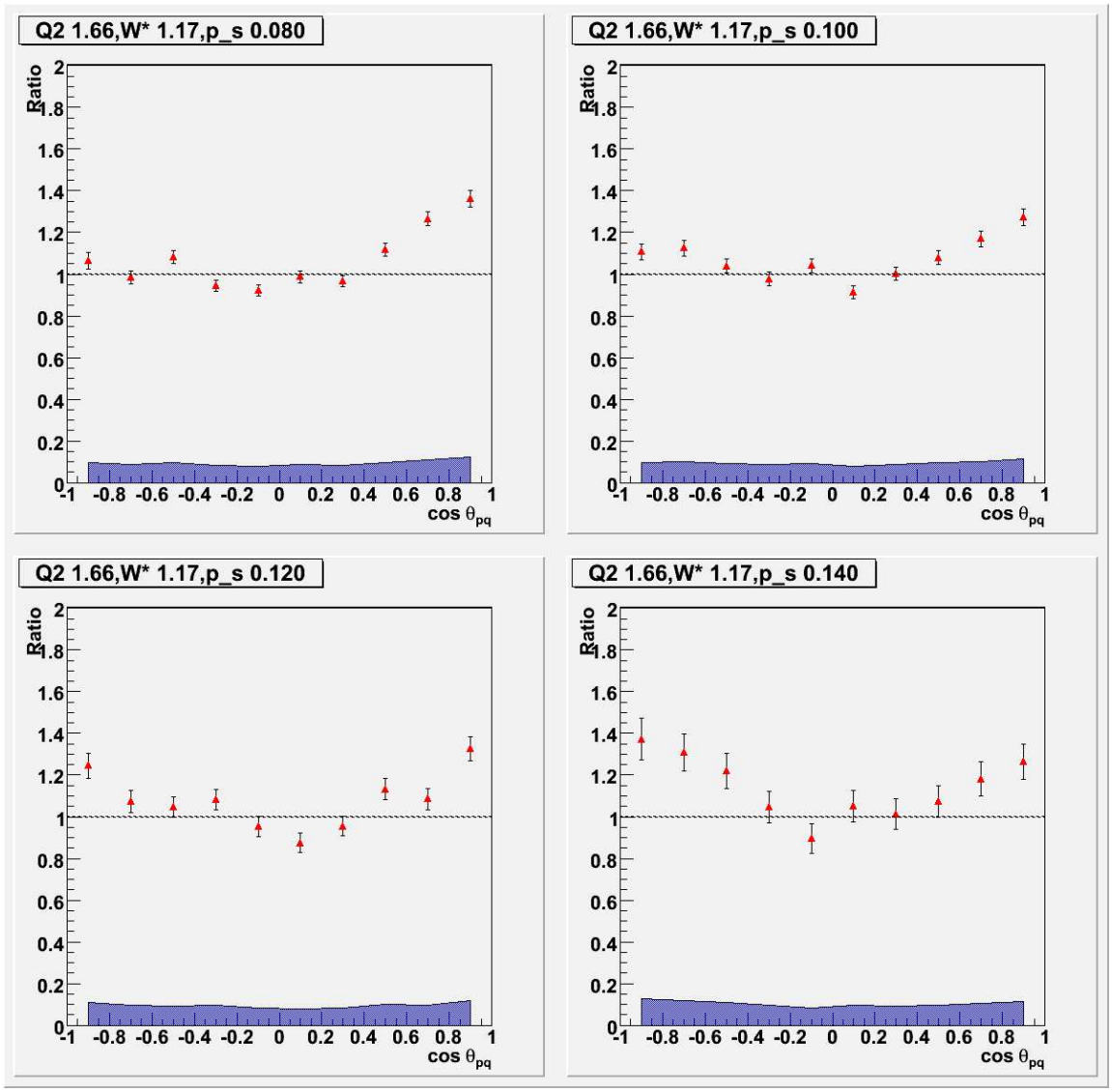

FIG. 175: Ratio of experimental data with subtracted accidental background and elastic tail to the full simulation in the PWIA spectator picture is shown as a function of $\cos\theta_{pq}$. Data are for Q^2 from 1.10 to 2.23 $(\mathrm{GeV}/c)^2$, W^* from 1.00 to 1.35 GeV. The beam energy is 5.254 GeV. Error bars are statistical only. Systematic errors are shown as a blue band.

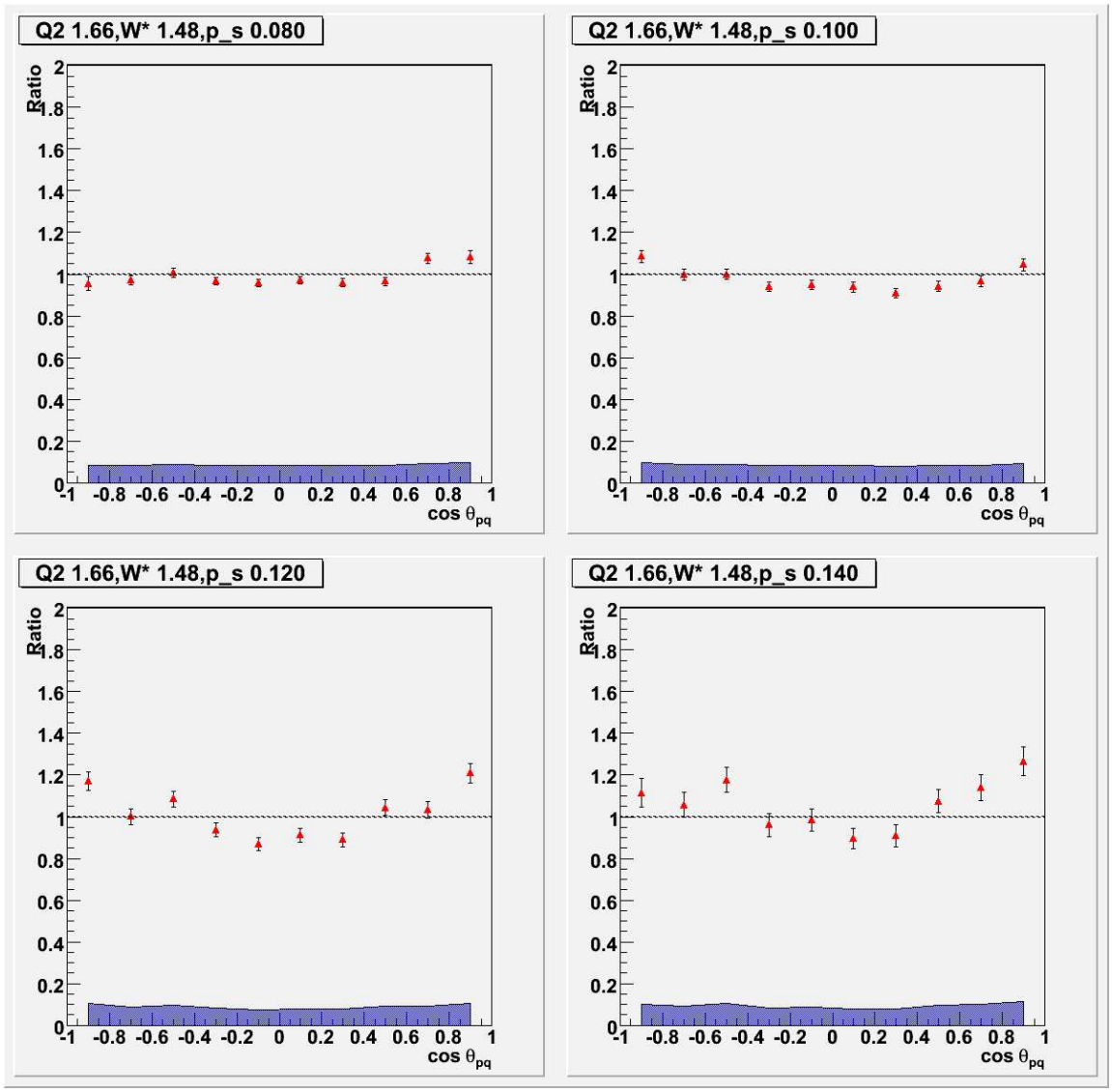

FIG. 176: Ratio of experimental data with subtracted accidental background and elastic tail to the full simulation in the PWIA spectator picture is shown as a function of $\cos\theta_{pq}$. Data are for Q^2 from 1.10 to 2.23 $(\mathrm{GeV}/c)^2$, W^* from 1.35 to 1.60 GeV. The beam energy is 5.254 GeV. Error bars are statistical only. Systematic errors are shown as a blue band.

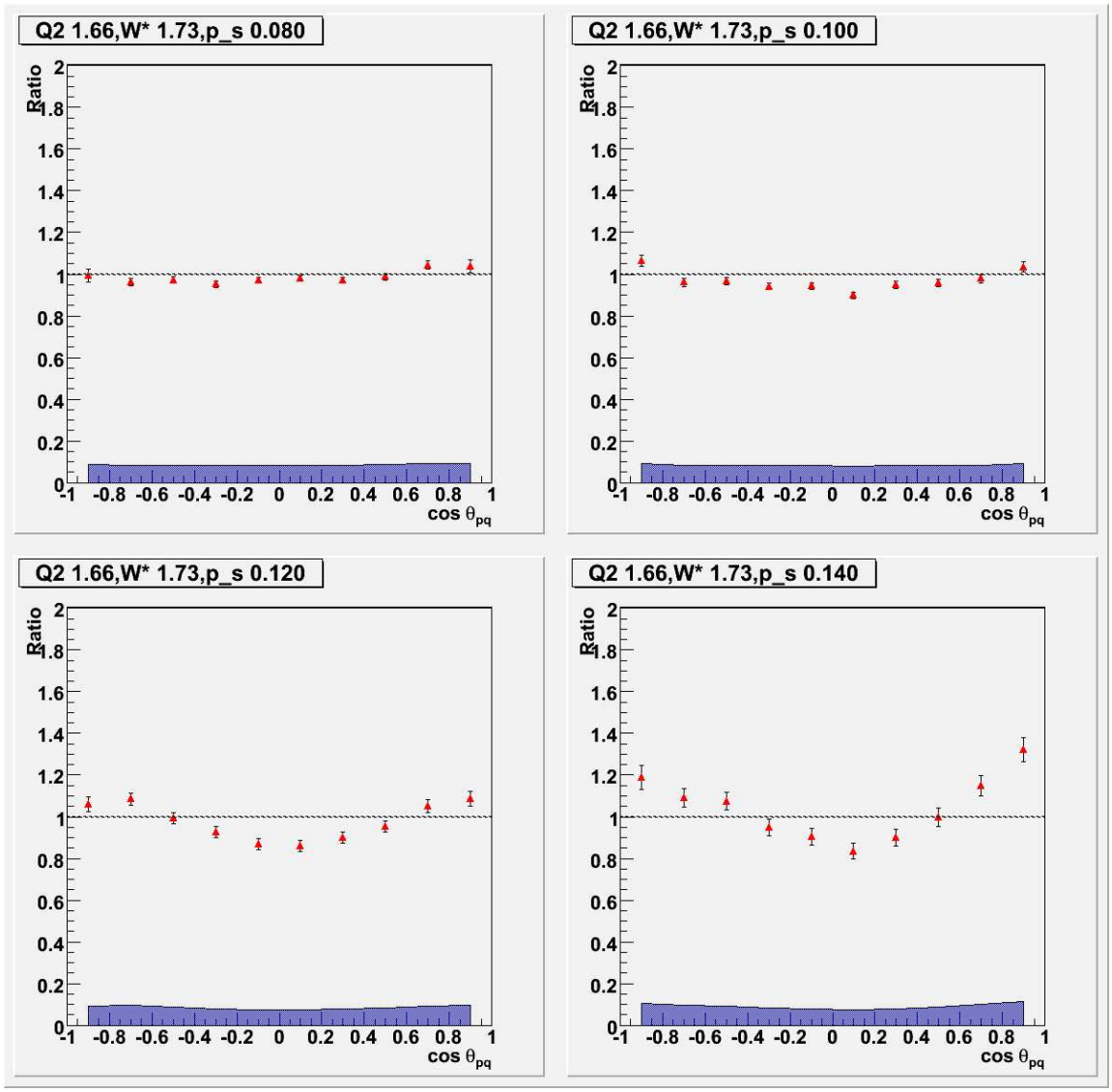

FIG. 177: Ratio of experimental data with subtracted accidental background and elastic tail to the full simulation in the PWIA spectator picture is shown as a function of $\cos\theta_{pq}$. Data are for Q^2 from 1.10 to 2.23 $(\mathrm{GeV}/c)^2$, W^* from 1.60 to 1.85 GeV. The beam energy is 5.254 GeV. Error bars are statistical only. Systematic errors are shown as a blue band.

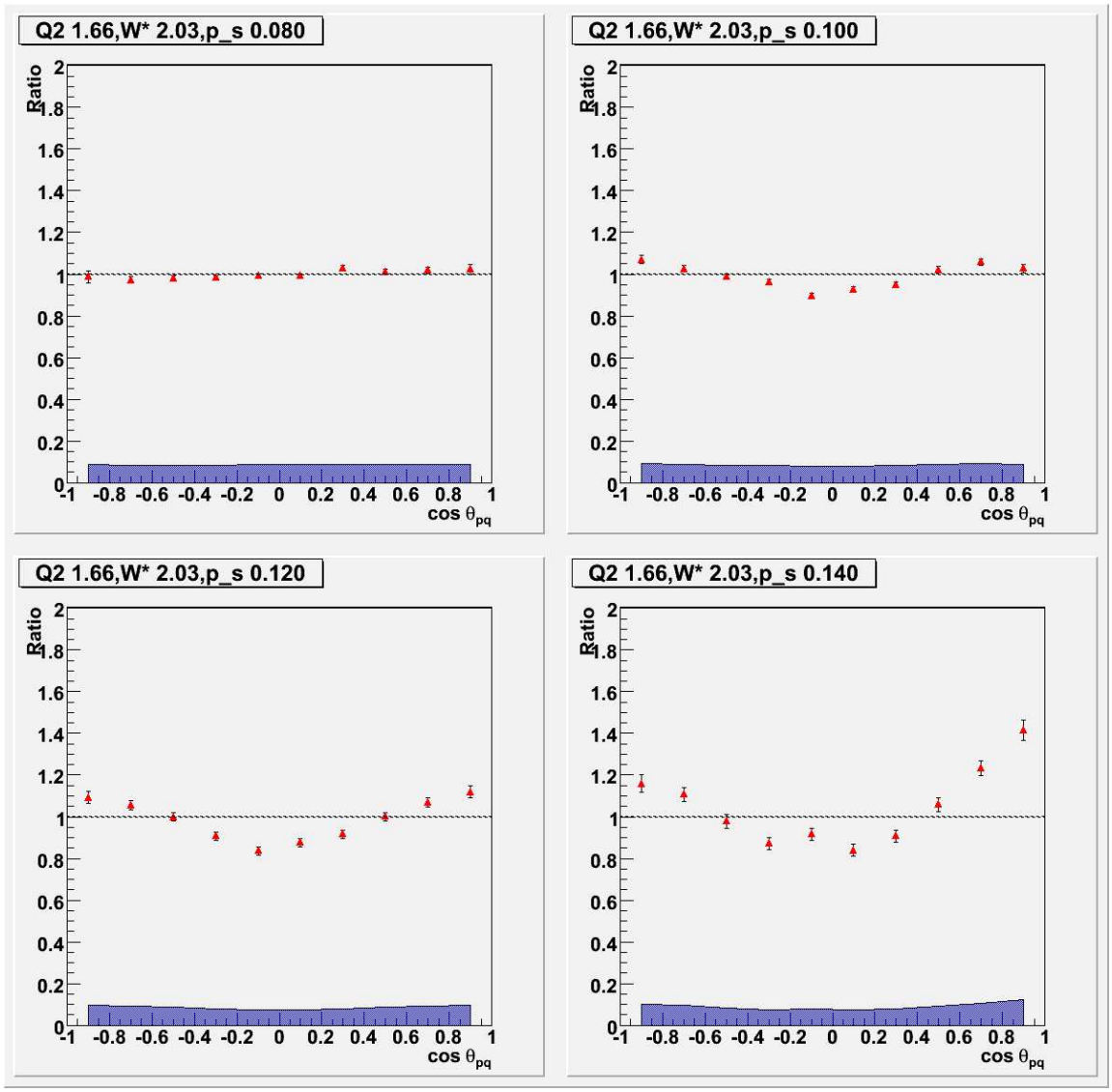

FIG. 178: Ratio of experimental data with subtracted accidental background and elastic tail to the full simulation in the PWIA spectator picture is shown as a function of $\cos\theta_{pq}$. Data are for Q^2 from 1.10 to 2.23 $(\mathrm{GeV}/c)^2$, W^* from 1.85 to 2.20 GeV. The beam energy is 5.254 GeV. Error bars are statistical only. Systematic errors are shown as a blue band.

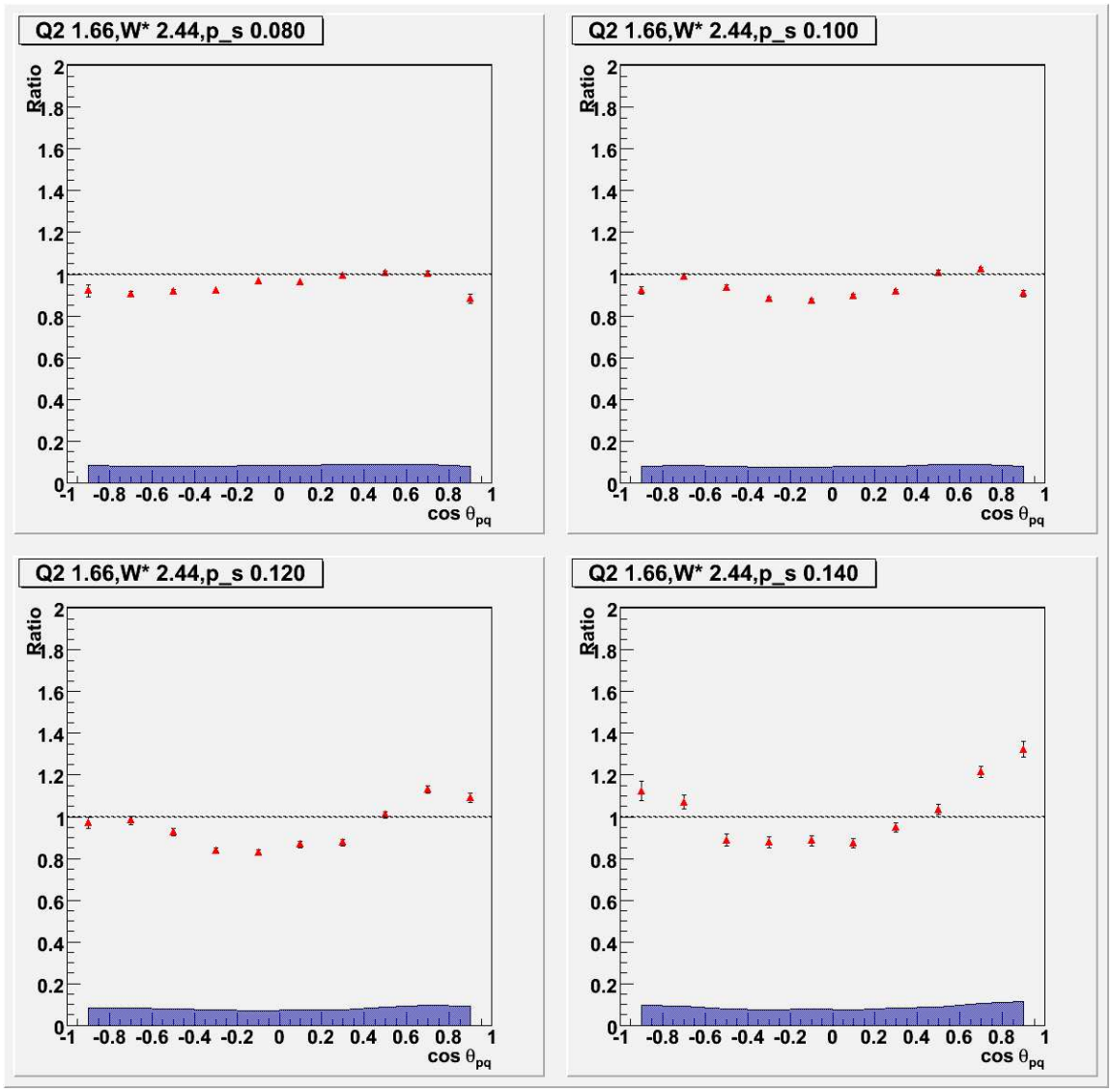

FIG. 179: Ratio of experimental data with subtracted accidental background and elastic tail to the full simulation in the PWIA spectator picture is shown as a function of $\cos\theta_{pq}$. Data are for Q^2 from 1.10 to 2.23 $(\mathrm{GeV}/c)^2$, W^* from 2.20 to 2.68 GeV. The beam energy is 5.254 GeV. Error bars are statistical only. Systematic errors are shown as a blue band.

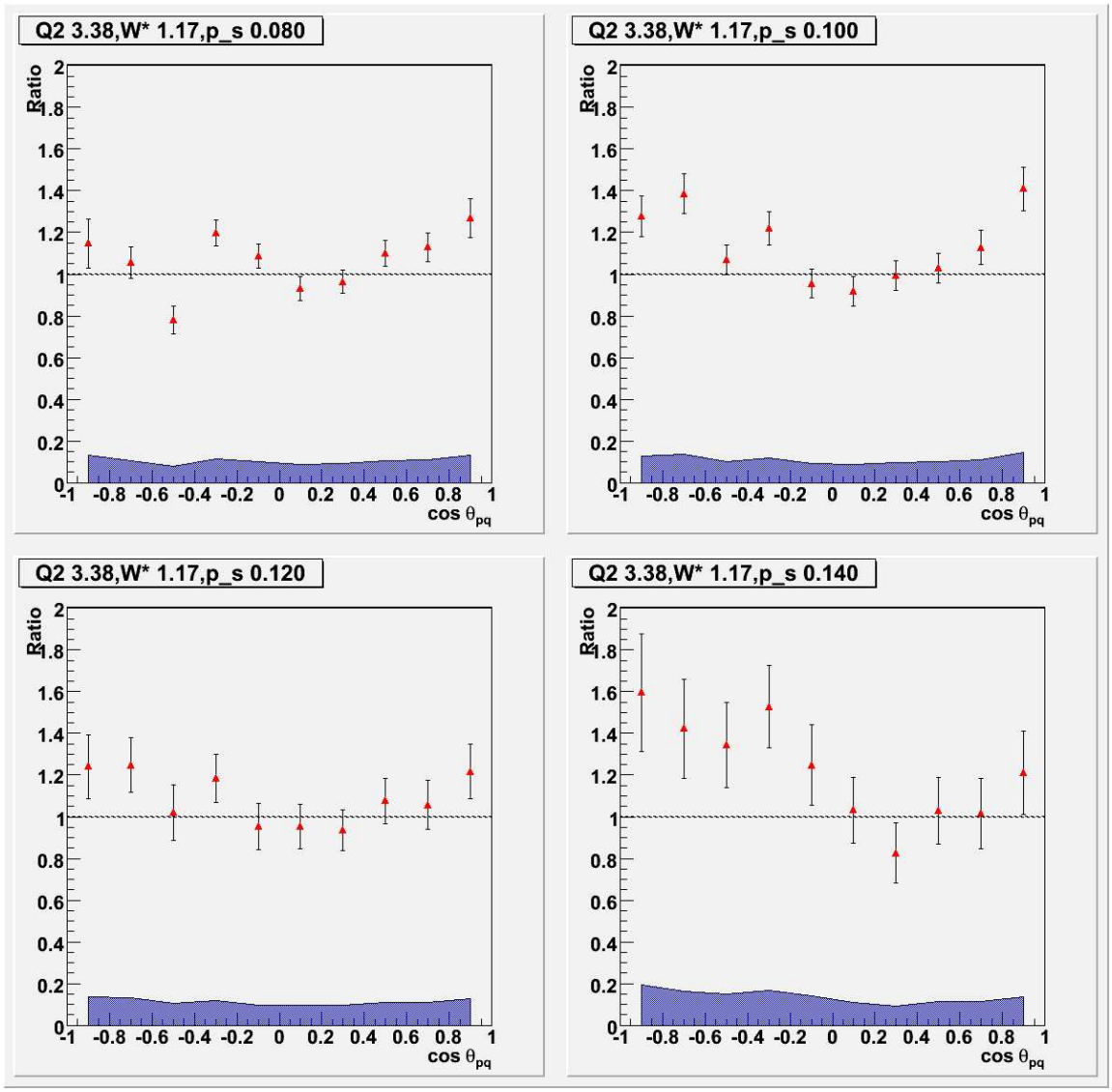

FIG. 180: Ratio of experimental data with subtracted accidental background and elastic tail to the full simulation in the PWIA spectator picture is shown as a function of $\cos\theta_{pq}$. Data are for Q^2 from 2.23 to 4.52 $(\mathrm{GeV}/c)^2$, W^* from 1.00 to 1.35 GeV. The beam energy is 5.254 GeV. Error bars are statistical only. Systematic errors are shown as a blue band.

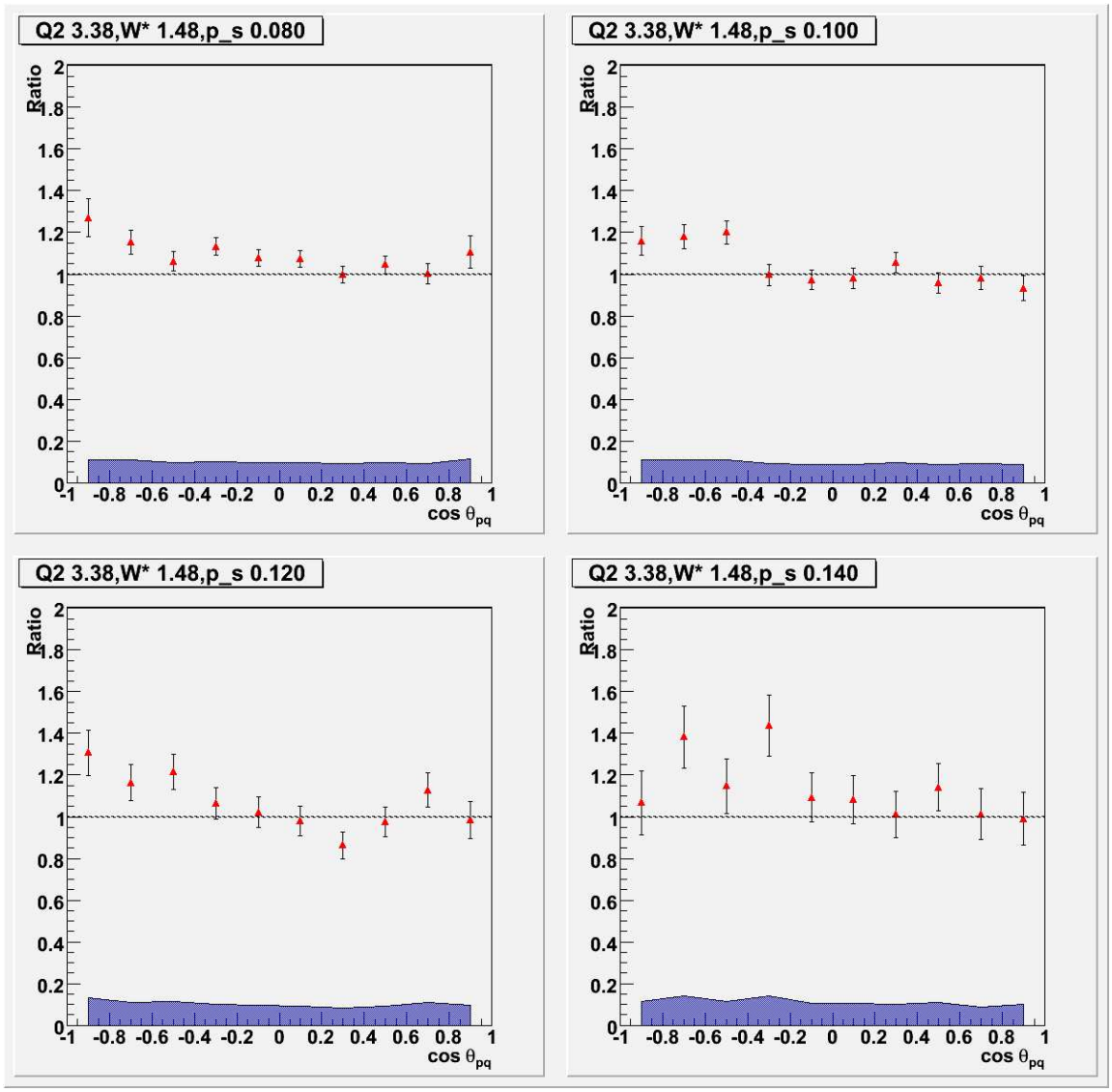

FIG. 181: Ratio of experimental data with subtracted accidental background and elastic tail to the full simulation in the PWIA spectator picture is shown as a function of $\cos\theta_{pq}$. Data are for Q^2 from 2.23 to 4.52 $(\mathrm{GeV}/c)^2$, W^* from 1.35 to 1.60 GeV. The beam energy is 5.254 GeV. Error bars are statistical only. Systematic errors are shown as a blue band.

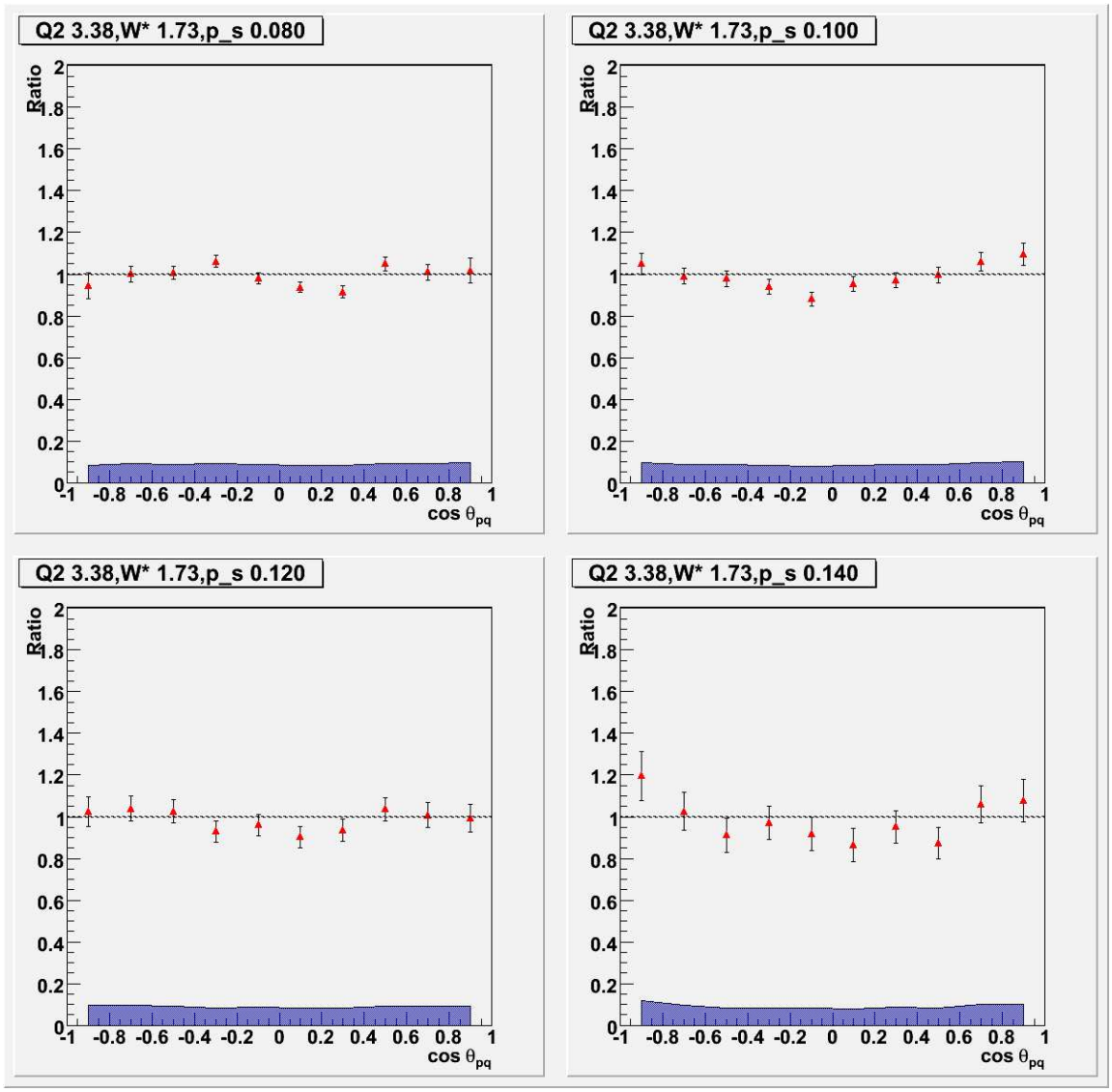

FIG. 182: Ratio of experimental data with subtracted accidental background and elastic tail to the full simulation in the PWIA spectator picture is shown as a function of $\cos\theta_{pq}$. Data are for Q^2 from 2.23 to 4.52 $(\mathrm{GeV}/c)^2$, W^* from 1.60 to 1.85 GeV. The beam energy is 5.254 GeV. Error bars are statistical only. Systematic errors are shown as a blue band.

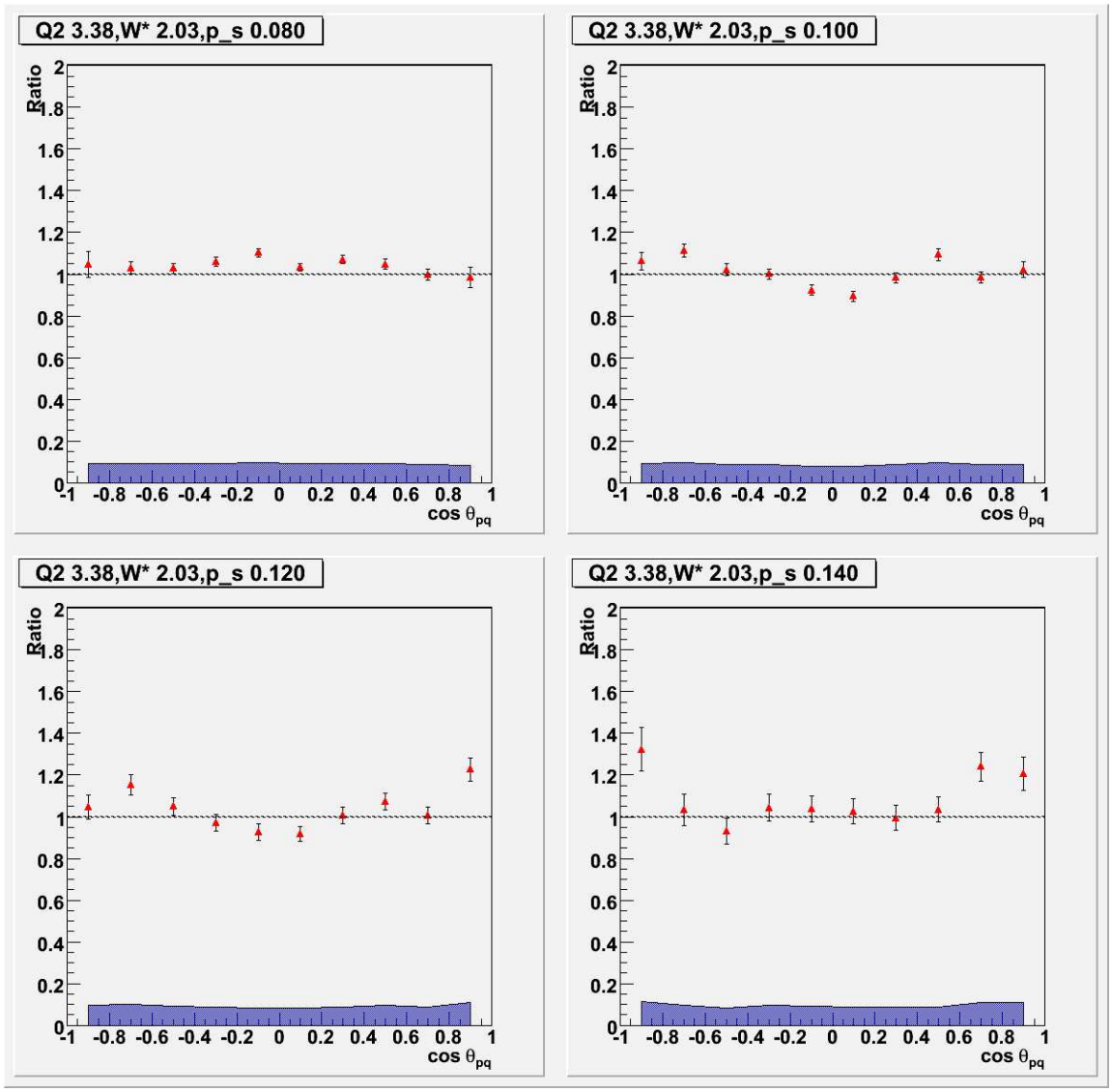

FIG. 183: Ratio of experimental data with subtracted accidental background and elastic tail to the full simulation in the PWIA spectator picture is shown as a function of $\cos\theta_{pq}$. Data are for Q^2 from 2.23 to 4.52 $(\mathrm{GeV}/c)^2$, W^* from 1.85 to 2.20 GeV. The beam energy is 5.254 GeV. Error bars are statistical only. Systematic errors are shown as a blue band.

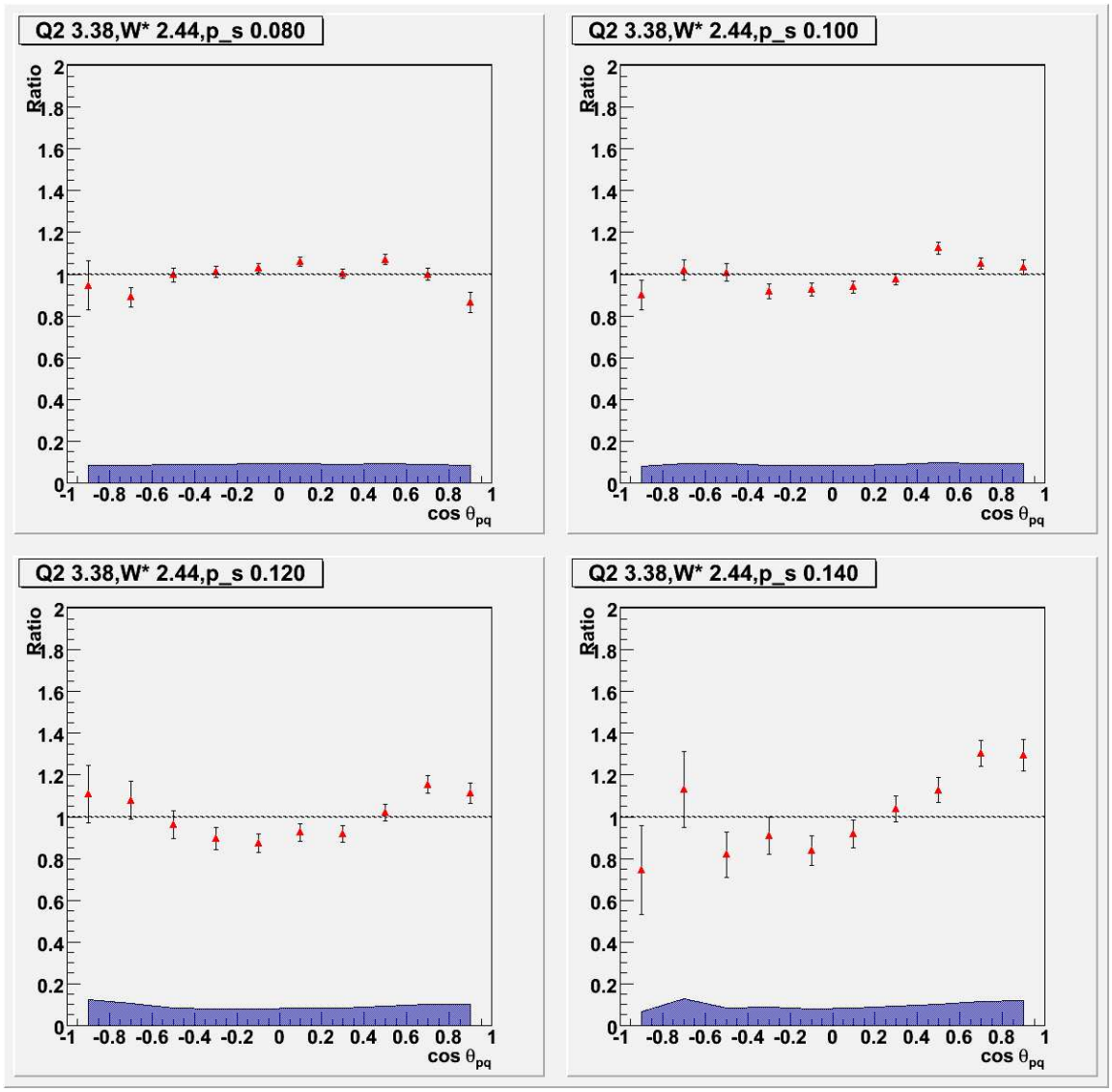

FIG. 184: Ratio of experimental data with subtracted accidental background and elastic tail to the full simulation in the PWIA spectator picture is shown as a function of $\cos\theta_{pq}$. Data are for Q^2 from 2.23 to 4.52 $(\mathrm{GeV}/c)^2$, W^* from 2.20 to 2.68 GeV. The beam energy is 5.254 GeV. Error bars are statistical only. Systematic errors are shown as a blue band.

APPENDIX A

PARTONS: QUARKS AND GLUONS

As was mentioned in the main text, nucleons consist of so called partons, which are of two kinds: quarks and gluons. In this appendix, I am going to give a brief description of partons, as well as elaborate on their connection with DIS structure functions (section II.5).

Quarks are elementary structureless (at least considered such now) fermions, which are, along with leptons, the basic constituents of matter. Six kinds of quarks are known; the summary of their properties is given in tables 9 and 10.

TABLE 9: Summary of quark properties (light quarks), from reference [6]

Quark	Down (d)	Up (u)	Strange (s)
Q, e- units	$-\frac{1}{3}$	$\frac{2}{3}$	$-\frac{1}{3}$
I	$\frac{1}{2}$	$\frac{1}{2}$	0
I_z	$-\frac{1}{2}$	$\frac{1}{2}$	0
m	1.5-4.0 MeV	4.0-8.0 MeV	80-130 MeV

TABLE 10: Summary of quark properties (heavy quarks), from reference [6]

Quark	Charm (c)	Bottom (b)	Top (t)
Q, e- units	$\frac{2}{3}$	$-\frac{1}{3}$	$\frac{2}{3}$
I	0	0	0
I_z	0	0	0
m	1.15-1.35 GeV	4.1-4.4 GeV	$\approx$178 GeV

The six quarks are arranged in three doublets (called families or generations):

$$\begin{pmatrix} u \\ d \end{pmatrix} \quad \begin{pmatrix} s \\ c \end{pmatrix} \quad \begin{pmatrix} b \\ t \end{pmatrix}.$$

The c, b, t quarks are so heavy that they do not play a big role in the nucleon. Neither is it easy to obtain a quark-antiquark pair by means of vacuum fluctuation for these quarks. Thus, when discussing ordinary hadrons, I will limit myself to u, d, s quarks.

Quarks determining quantum numbers of baryons are called valence quarks. Besides these three quarks, there is a practically infinite number of quark-antiquark

pairs created and annihilated every second: those are so called sea quarks. The sea quarks play an important role in the region $x \leq 0.4$, but their contribution becomes negligible at high x. Sometimes, an effective degree of freedom called constituent quark is defined, where a valence quark "dressed" in a number of quark antiquark pairs and gluons, is the carrier of hadron quantum numbers.

Let us look at the DIS structure functions. I will concentrate on F_2, since we can easily get F_1 from it (see (35)). Expanding the second of equations (35), and considering only three light quarks (u, s, d), we can write for proton and neutron correspondingly:

$$F_2^p(x) = x \cdot [\frac{1}{9}(d_{\mathrm{v}}^p + d_s + \bar{d}_s) + \frac{4}{9}(u_{\mathrm{v}}^p + u_s + \bar{u}_s) + \frac{1}{9}(s_s + \bar{s}_s)], \tag{156a}$$

$$F_2^n(x) = x \cdot [\frac{1}{9}(d_{\mathrm{v}}^n + d_s + \bar{d}_s) + \frac{4}{9}(u_{\mathrm{v}}^n + u_s + \bar{u}_s) + \frac{1}{9}(s_s + \bar{s}_s)]. \tag{156b}$$

Where $d_{\mathrm{v}}^{p,n}$, $u_{\mathrm{v}}^{p,n}$ are distributions of down and up valence quarks in protons and neutrons; d_s, u_s are distributions of sea quarks (proton/neutron subscripts were dropped under the assumption that sea quarks distributions are identical in protons and neutrons); s_s are distributions of strange quarks (only sea strange quarks are present). "Barred" quantities denote distributions of corresponding antiquarks. Since the proton and neutron can be transformed into each other using isospin symmetry, this symmetry also relates their quark distributions:

$$u_{\mathrm{v}}^p(x) = d_{\mathrm{v}}^n(x) \equiv u_{\mathrm{v}}, \tag{157a}$$

$$d_{\mathrm{v}}^p(x) = u_{\mathrm{v}}^n(x) \equiv d_{\mathrm{v}}, \tag{157b}$$

$$u_s^p(x) \approx d_s^p(x) = d_s^n(x) \approx u_s^n(x). \tag{157c}$$

Thus, if we operate in the region where sea quarks can be neglected,

$$\frac{F_2^n}{F_2^p} \approx \frac{1 + 4d_{\mathrm{v}}/u_{\mathrm{v}}}{4 + d_{\mathrm{v}}/u_{\mathrm{v}}}, \tag{158}$$

and measuring DIS structure functions gives us direct access to quark momentum distributions.

Careful experiments measuring quark momentum distributions found that only half of baryon momentum can be assigned to quarks. This is how the idea of *gluons* emerged. Gluons are carriers of strong interactions. They do not interact either weakly or electromagnetically, being quanta of the strong field. Quarks and gluons share a unique quantum number called *color*. Gluons couple to color charge, thus

propagating strong interactions. Every quark and gluon has color charge. Particles can only exist in color neutral combinations. That is why quarks (or gluons for that matter) have never been seen in a free state, necessitating the introduction of *color confinement*, the theoretical basis of which is still being investigated.

APPENDIX B

SOME KINEMATIC VARIABLES

Figure 185 shows an electron scattering off a proton. Initial momenta of the electron and proton are k and p, final momenta are k' and p' correspondingly. The 4-momentum transfered from the electron to the proton is shown as q:

$$q = k - k'. \tag{159}$$

Some common kinematic variables associated with this reaction would be:

- The exchange energy of the reaction:

$$\nu = E - E', \tag{160}$$

  where E is the energy of the incident electron, E' is the energy of the scattered electron.

- The momentum transfer squared:

$$Q^2 = -q^2 \underset{lab}{=} 4EE' \sin^2 \frac{\theta}{2}, \tag{161}$$

  where θ is the scattering angle of the electron, q is the transfered momentum (see equation (159)).

- Missing mass of the inclusive reaction (sometimes called total mass or final mass):

$$W^2 = (p+q)^2 = p^2 + 2p \cdot q + q^2 \underset{lab}{=} M^2 + 2M\nu - Q^2, \tag{162}$$

  where M is the target (proton) mass, and other variables are discussed above.

- Bjorken x:

$$x = \frac{Q^2}{2p \cdot q} \underset{lab}{=} \frac{Q^2}{2M\nu}, \tag{163}$$

  where all the variables have been defined in the earlier equations. The common interpretation of this variable is the fraction of the nucleon momentum carried by the struck quark. While this is an accurate interpretation only in the Bjorken limit where $Q^2, \nu \to \infty$, we usually consider scattering at high enough momenta that we can work in an infinite momentum frame, where it is a good enough aproximation.

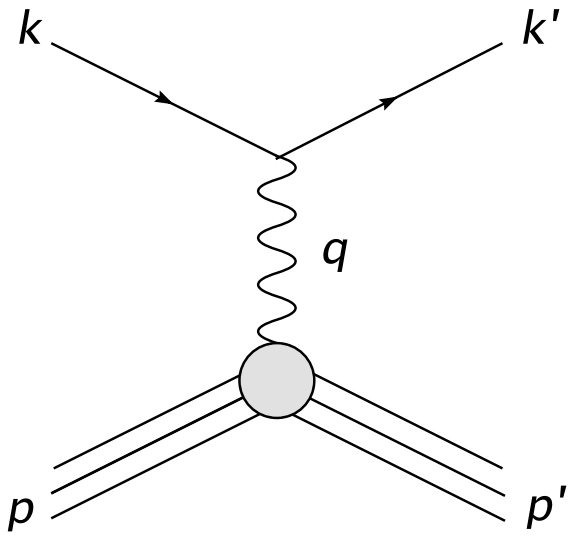

FIG. 185: Scattering of an electron with initial 4-momentum k off a proton with initial momentum p. Final momenta of the electron and proton are k' and p' correspondingly. The 4-momentum transfered from the electron to proton is q (see text for more).

- Nachtman scaling variable:

$$\xi = \frac{2x}{1 + \sqrt{1 + 4m^2x^2/Q^2}}, \tag{164}$$

  where x is Bjorken x (see equation (163)), m is the target mass. This variable is often used to study the Bloom-Gilman duality.

Equation (162) assumes the target to be stationary (in this case 4-momentum $p = M, 0, 0, 0$), which is not exactly true in real life. Nevertheless, this formula is usually used since its inaccuracy is not too large, and figuring out the motion of the target is a very complicated task. If we do know how the target is moving (BONuS experiment *forte*), we can calculate the missing mass of the inclusive reaction more precisely. Let us denote it with a '*' to distinguish from the W from equation (162) and calculate in case of the BONuS scattering on the neutron in deuterium with proton being a spectator:

$$(W^*)^2 = (p_n + q)^2 = p_n^\mu p_{n\mu} + 2((M_D - E_S)\nu + \vec{p_s} \cdot \vec{q}) - Q^2. \tag{165}$$

Here p_n denotes the neutron 4-momentum, M_D is the deuteron mass, and E_S and $\vec{p_s}$ are the spectator proton energy and momentum (in case of spectator scattering $p_n = (M_D - E_S, -\vec{p}_S)$). The other variables are discussed above.

The same inaccuracy (the assumption of the target being stationary) we find in the second half of the equation (163). To account for the target motion, we need to rewrite it as

$$\tilde{x} \underset{lab}{\approx} \frac{Q^2}{2M\nu(2-\alpha)}, \tag{166}$$

where α is the spectator light-cone momentum fraction.

APPENDIX C

RESIDUES

Given a point z_0 where $f(z)$ is either analytic or has an isolated singularity, the residue of $f(z)$ is the coefficient of $(z - z_0)^{-1}$ in the Laurent series expansion of $f(z)$ about z_0, or

$$Res(z_0) = b_1 = \frac{1}{2\pi i} \int_C f(z)dz. \tag{167}$$

If $f(z)$ is either analytic or has a removable singularity at z_0, then $b_1 = 0$ there. If z_0 is a pole of order m, then

$$b_1 = \frac{1}{(m-1)!} \frac{d^{m-1}}{dz^{m-1}} [(z - z_0)^m f(z)]|_{z=z_0}. \tag{168}$$

For every simple closed contour C enclosing at most a finite number of singularities $z_1, z_2, \ldots, z_n$ of an analytic function continuous on C,

$$\int_C f(z)dz = 2\pi i \sum_{k=1}^{n} Res(z_k), \tag{169}$$

where $Res(z_k)$ is the residue of $f(z)$ at z_k.

BIBLIOGRAPHY

[1] J. J. Aubert *et al.*, Phys. Lett. B **123**, 275 (1983).

[2] A. Benvenuti *et al.*, Phys. Lett. B **189**, 483 (1987).

[3] J. Gomez *et al.*, Phys. Rev. D **49**, 4348 (1994).

[4] J. Chadwick, Proc. Roy. Soc. **A136**, 692 (1932).

[5] N. Isgur, Phys. Rev. Let. **83**, 2 (1999).

[6] W.-M. Yao *et al.* (Particle Data Group), J. Phys. G **33**, 1 (2006).

[7] C. F. Perdrisat, V. Punjabi, and M. Vanderhaegen, Prog. Part. Nucl. Phys. **59**, 694 (2007).

[8] J. Arringron, C. D. Roberts, and J. M. Zanotti, J. Phys. G **34**, S23 (2007).

[9] I. A. Qattan, *Precision Rosenbluth Measurement of the Proton Elastic Electromagnetic Form Factors and Their Ratio at Q^2 = 2.64, 3.20, and 4.10 GeV^2*, PhD Thesis, NWU (2005).

[10] M. Peskin and D. Schroeder *An Introduction to Quantum Field Theory*, Addison-Wesley Publishing Company (1997).

[11] C. E. Hyde-Wright and K. de Jager, Ann. Rev. Nucl. Part. Sci. **54**, 217 (2004).

[12] E. Klempt, J.-M. Richard, *Baryon spectroscopy*, arXiv:0901.2055v1 (2009).

[13] P. Stoler, Phys. Rev. Let. **66**, 8 (1991).

[14] V. D. Burkert *et al.*, Phys. Rev. C **67**, 035204 (2003).

[15] P. Stoler, Phys. Rep. **226**, 3 (1993).

[16] S. E. Kuhn *et al*, The structure of the free neutron via spectator tagging, PR03-012 proposal.

[17] L. W. Whitlow *et al.*, Phys. Lett. B **282**, 475 (1992); A. Bodek, S. Dasu and S.E. Rock, in Tucson Part. Nucl. Phys., **768** (1991), SLAC-PUB-5598.

[18] N. Isgur, Phys. Rev. D **4**, 034013 (1999).

[19] A. D. Martin, R. G. Roberts, W. J. Stirling, and R. S. Thorne, Eur. Phys. J. C **14**, 133 (2000).

[20] G. R. Farrar and D. R. Jackson, Phys. Rev. Lett. **35**, 1416 (1975).

[21] E. Bloom and F. Gilman, Phys. Rev. Let. **25**, 1140 (1970).

[22] W. Melnitchouk, R. Ent, and C. E. Keppel, Phys.Rep. **406**, 3-4 (2005).

[23] I. Niculescu *et al*, Phys. Rev. Lett. **85**, 1182 (2000).

[24] F. Gross and S. Liuti, Phys. Rev. C **45**, 1374 (1992); S. Liuti and F. Gross, Phys. Lett. B **356**, 157 (1995).

[25] L. Heller and A. W. Thomas, Phys. ReV. C **41**, 2756 (1990).

[26] L. L. Frankfurt and M. I.Strikman, Nucl. Phys. B**250**, 1585 (1985); Phys. Rep **160**, 135 (1988).

[27] J. D. Bjorken and E. A. Paschos, Phys. Rev. **185**, 5 (1969).

[28] S. S. M. Wong *Introductory Nuclear Physics*, John Wiley and Sons, INC. (1998).

[29] I. I. Rabi, J. M. B. Kellogg, and J. R. Zacharias, Phys. Rev. **46**, 163 (1934).

[30] J. M. B. Kellogg *et al.*, Phys. Rev. **55**, 318 (1939).

[31] M. Garson and J. W. Van Orden, Adv. Nucl. Phys., **26**, 293 (2001).

[32] F. Halzen and A. D. Martin, *Quarks and Leptons: An Introductory Course in Modern Particle Physics*, John Wiley and Sons (1984).

[33] D. Abbott *et al.*, Phys. Rev. Lett. **82**, 1379 (1999).

[34] G. D. Yen and J. P. Vary, Phys. Rev. C **40**, 1 (1989).

[35] L. C. Alexa *et al.*, Phys. Rev. Lett. **82**, 1374 (1999).

[36] R. G. Arnold *et al.*, Phys. Rev. Lett. **35**, 776 (1975).

[37] C. D. Buchanan and R. Yearian, Phys. Rev. Lett. **15**, 303 (1965).

[38] R. Cramer *et al.*, Z. Phys. C **29**, 513 (1985).

[39] D. J. Drikley and L. N. Hand, Phys. Rev. Lett. **9**, 521 (1962).

[40] J. E. Elias *et al.*, Phys. Rev. **177**, 2075 (1969).

[41] S. Galster *et al.*, Nucl. Phys. B **32**, 221 (1971).

[42] S. Platchkov *et al.*, Nucl. Phys. A **510**, 740 (1990).

[43] P. E. Bosted *et al.*, Phys. Rev. C **42**, 38 (1990).

[44] S. Auffret *et al.*, Phys. Rev. Lett. **54**, 649 (1985).

[45] G. G. Simon *et al.*, Nucl. Phys. A **364**, 285 (1981).

[46] A. P. Kobushkin and Y. D. Krivenko, arXiv:nucl-th/0112009.

[47] M. Osipenko *et al.* [CLAS Collaboration], arXiv:hep-ex/0507098.

[48] L. L. Frankfurt and M. I. Strikman, Phys. Rep. **76**, 4 (1981).

[49] S. Okubo and R. E. Marshak, Ann. Rev. **4**, 166 (1958).

[50] M. Sargsian and M. Strickman Phys. Lett. B **639**, 223 (2006).

[51] W. Melnitchouk, M. Sargsian, and M. I. Strikman Z. Phys. A **359**, 99 (1997).

[52] C. Ciofi degli Atti, L. P. Kaptari, and D. Treleani, Phys. Rev. C **63**, 044601 (2001).

[53] C. Ciofi degli Atti and S. Simula, Phys. Lett. B **319**, 23 (1993); S. Simula, Phys. Lett. B **387**, 245 (1996).

[54] C. Ciofi degli Atti and B. Z. Kopeliovich, Eur. Phys. J. A **17**, 133 (2003); arXiv:nucl-th/0207001.

[55] C. Ciofi degli Atti, L. P. Kaptari, and B. Z. Kopeliovich, Eur. Phys. J. A **19**, 145 (2004).

[56] W. Melnitchouk, A. W. Schreiber, and A. W. Thomas, Phys. Lett. B **335**, 11 (1994); Phys. Rev. D **49**, 1183 (1994).

[57] S. I. Alekhin and S. A. Kulagin, S. Liuti, Phys. Rev. D **69**, 114009 (2004).

[58] D. Zwillinger, *Standard Mathematical Tables and Formulae*, CRC Press (1996).

[59] E.S. Smith *et al*, NIM A **432**, 265 (1999).

[60] M. Amaryan *et al*, NIM A **460**, 239 (2001).

[61] B.A. Mecking *et al*, NIM A **503**, 513 (2003).

[62] S. Klein, CERN Courier 44, issue 1 (2004).

[63] V. Eckardt *et al* arXiv:nucl-ex0101013v2.

[64] CERES collaboration, Nuclear Physics A **661**, 673 (1999).

[65] F. Sauli NIM A **386**, 531 (1997).

[66] F. Sauli NIM A **553**, 18 (2005).

[67] F. Sauli NIM A **580**, 971 (2007).

[68] H. Fenker *et al*, NIM A**592**, 273 (2008).

[69] M. Mestayer *et al.*, NIM A**449** (2000).

[70] R. Feuerbach, CLAS-NOTE **2001-22** (2001).

[71] S. A. Morrow and M. D. Mestayer, CLAS-NOTE **2002-010** (2002).

[72] D. Lawrence and M. Mestayer, Drift Chamber Calibration: Software and Procedures, CLAS-NOTE **1999-018** (1999).

[73] M. Amaryan *et al.*, NIM A**460**, 239 (2001).

[74] E. S. Smith *et al.*, CLAS-NOTE **1999-011** (1999).

[75] S. Biagi, MAGBOLTZ programme, version 2, CERNLIB, CERN, Geneva (2005).

[76] W. Leo, *Techniques For Nuclear And Particle Physics Experiments*, Springer-Verlag New York, LLC (1994).

[77] A. Klimenko and S. Kuhn, CLAS-NOTE **2003-005** (2003).

[78] F. James, CERN Program Library Long Writeup **D506** CERN, Geneva (1998).

[79] P. Bosted, S. Kuhn, and Y. Prok, CLAS-NOTE **2003-008** (2008).

[80] P. Bosted and H. Avakyan, CLAS-NOTE **2006-006** (2006).

[81] S. Stepanyan, CLAS-NOTE **2002-008** (2002).

[82] K. Abe *et al.*, Phys. Rev. D **58**, 112003 (1998).

[83] M. Lacombe, B. Loiseau, R. Vinh Mau, J. Cote, P. Pires, and R. de Tourreil, Phys. Lett. B **101**, 139 (1981).

[84] R. Machleidt, K. Holinde and Ch. Elster, Phys. Rep. **149** (1987) 1.

[85] R. B. Wiringa, V. G. J. Stoks and R. Schiavilla, Phys. Rev. C **51** (1995) 38.

[86] S. J. Brodsky, *Light-Cone Quantized QCD and Novel Hadron Phenomenology*, arXiv:hep-ph/9710288v2 (1997).

[87] L. W. Mo and Y. S. Tsai, Rev. Mod. Phys. **41**, 205 (1969).

[88] M. Arneodo *et al.*, Phys. Rev. Lett. B **364**, 107 (1995).

[89] K. Abe *et al.*, Phys. Lett. B **452**, 194 (1999).

[90] S. Agostinelli *et al.*, NIM A **506**,**3**, 250 (2003).

[91] N. Baillie, Ph.D. thesis, W&M (2009).

[92] J. Zhang, Ph.D. thesis, ODU, in preparation.

[93] P. E. Bosted and M. E. Christy, Phys. Rev. C **77**, 065206 (2008).

[94] A. Klimenko, *Electron Scattering From a High-Momentum Neutron in Deuterium*, PhD thesis, ODU (2004).

[95] M. Osipenko, A. Vlassov and M. Taiuti, CLAS-NOTE **2004-020** (2004).

[96] M. Amarian *et al.*, The structure of the free neutron at large x-Bjorken, PR12-06-113 proposal.

VITA

Svyatoslav Tkachenko
Department of Physics
Old Dominion University
Norfolk, VA 23529

Svyatoslav Tkachenko received the Degree of Specialist (equivalent of the Bachelor of Science degree) in robototechnics from Odessa State Polytechnic Institute (Odessa, Ukraine) in 1997. The same year he started graduate school in the University of Virginia, where he received a Master of Science degree in physics (Nuclear Physics) in 2004. The same year, 2004, he entered a Ph.D. program in physics in Old Dominion University (the specialty of Nuclear Physics). The projected date of graduation is December 2009. Svyatoslav Tkachenko is a member of the following professional organizations: American Physical Society, CEBAF (Continuous Electron Beam Accelerator Facility) Users group, CLAS (CEBAF Large Acceptance Spectrometer) collaboration, Deep Processes Physics Working Group.

Typeset using LaTeX.